BULGARIAN CHEMICAL COMMUNICATIONS

Crystal structure of a DNA sequence d(CGTGAATTCACG) at 130K

H. I. Sbirkova, B.L. Shivachev

Institute of Mineralogy and Crystallography "Acad. Ivan Kostov", Bulgarian Academy of Sciences, Acad. G. Bonchev str., bl. 107, 1113 Sofia, Bulgaria

The crystal structure of the oligonucleotide d(CGTGAATTCACG)has previously been reported as a B-type double helix at a resolution of 2.5 Å. Here, the structure of this sequence was determined at a higher resolution of 2.00Å in space group $P2_12_12_1$. The adjustmentsin crystal packing between the former and latter are described. The present structure allowed more in depth description of the interactions between the oligonucleotides and with the surrounding solvent: the presence of Mg and Cl ions, a greater number of water moleculesand non-classicalG⋯G hydrogen bonding interactions between adjacent DNA duplexes.

INTRODUCTION

The d(CGTGAATTCACG) DNAduplex is interesting because it features a *Eco*RI restriction site[1]. The crystal structure of the sequence has been previouslyreported at 2.7and2.5 Å resolution[2, 3].Interestingly,data collection has been carried out at 0ºC because the authors state that the useof lowertemperatures resulted in the absence of diffraction, associated with damage of the crystals[2]. In the present manuscript we report the structure of d(CGTGAATTCACG)$_2$ collected at 130 K and at a higher resolution of 2.0Å. This is the highest resolution reported for this structure. Thus, we are able to discern a number of detailsthat were not spotted in the previous reports: the presence of Mg and Cl ions, a greater number of water molecules) and non-classicalG⋯G hydrogen bonding interactions. One shouldnote that our aim was to co-crystalize the DNAwithDAPI and thus thecrystallization condition includedDAPI. It is unclear whether the presence of an intercalating agent is responsible for the stabilization of the crystal though we observed visually the degradation/destruction of the crystalsinthe drops afew dayslater.

EXPERIMENTAL

Sample crystallization

The dry oligonucleotide sequence CGTGAATTCACG was purchased from "EurofinMWG Genomics",dissolved in a buffer up to 1 mM and annealed at 75°Cbefore usein order to obtain dsDNA. The buffer solution consists of 60mM sodium cacodylate (pH 7.0), 17 mM MgCl$_2$, 2mMSpermine and 1.5 mM DAPI. Crystals were grown from hanging drops (3 µl) at room temperature, equilibratedagainst 50%*v/v*2-methyl-2,4-pentanediol (MPD).Large crystals (0.4 x 0.3 x 0.25 mm^3) suitable for single crystal X-ray studies formed within a month(Fig. 1).
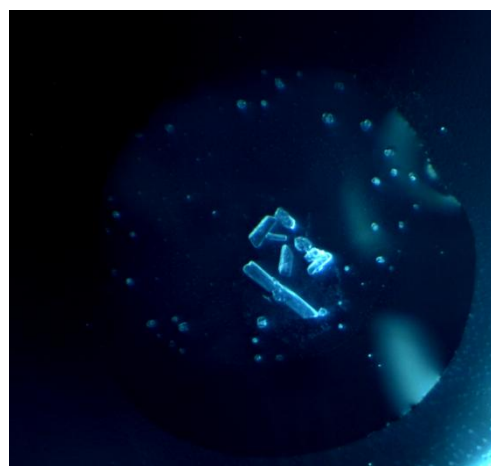

Fig. 1. Observed crystals of d(CGTGAATTCACG)

Data collection and crystal structure refinement

Crystals were mounted on loops and were flash frozen at 130 K directly under the nitrogen cryo stream (Cobra, Oxfordcryosystems). All data were collected at low temperature(130K) on an Oxford diffraction Supernova diffractometer using Cu-Kα radiation (λ = 1.54056 Å) from a micro-focus source. The determination of unit cell parameters, data integration, scaling and absorption correction were carried out using the CrysalisPro[4]. The phases were obtained by molecular replacement with a Phaser[5]using 1D29 [2] as the starting model.The refinement of the structure involved several cycles of refinementusing Refmac 5 [6] and Coot[7]programs.The water and heavier atoms (Mg and Cl) were positioned on the *Fo-Fc*difference

map using the interface of a Coot program.A summary of the fundamental crystal data and refinement indicators is provided in Table 1.Graphical analyses of the model and the electron-density maps were carried out using Coot[7].X3DNA [8] was used to carry out structural analysis and geometrical calculations of the DNA parameters. PyMOL[9] was used to prepare the figures. The coordinates and structure factors have been deposited in the PDB as entry 5JU4.

Table 1. Selected crystallographic data-collection statisticsand refinement indicators for 5JU4

Crystal system	Orthorhombic
Space group	$P2_12_12_1$
cell dimensions	
a, b, c, Å	24.503, 41.09, 65.184
α, β, γ, °	90, 90, 90
independent molecules	2
diffraction data	
wavelength, Å	1.54056
resolution, Å	2.0
reflections	4796
completeness, *%*	99.5
I/σ(I) at 2 Å	2.77
redundancy	8.2
R*merge* %	7.5(36.8)
Refinement	
reflections used	4524
resolution, Å	2.0
R (R*free*)%	21.8 (29.0)
no. of atoms	544
DNA	488
Mg, Cl/ion	2
Waters	74
average B fatcor, Å ^{2}	31.01
R.m.s.d.	
bond lengths, Å	0.009
bond angles,˚	1.776
PDB code	5JU4

RESULTS AND DISCUSSION

Single crystal data collection has been attempted for several different crystals. One should note that the dataset collected up to a resolution of2.00 Å was from a crystalthat was harvestedfromthedrop five(5) daysafter it was spotted. Crystals withsimilar or even bigger dimensions (size)that

were allowed to "stabilize" for more than a week in the crystallization drop diffracted usually at a resolution up to 2.5 Å.Attempts for datacollection at roomtemperature (19ºC) were performed on afew crystals, however the observedquality of the diffraction was not comparable with that for experiments conducted at130K.The presence of DAPI in the crystallization conditions may have played a role for crystal structure stabilization.

The asymmetric unit of 5JU4 consists of two chemically equivalent self-complementary strands (each strand is twelve base pairs in length)forming an anti-parallel right-handed DNA(Fig. 2).The B-type DNA duplex is formed by classical Watson-Crick (W-C) hydrogen bonding base-pairing interactions between the two strands: basesC1 to G12 from the first strand interact with basesG13 to C24from the opposite (second) strand (thenumbering corresponds to a sequence of thecrystal structure).Theminor grooveof the present double stranded oligonucleotide features a central TpAstep (AATT) surrounded by C or G rich regions. Its overall secondary structure is comparable to the previously reported structureswith the same sequence, PDB entry 1D29[2], with an *rmsd* of 1.61Å when the two structures are superposed (Fig. 2b).
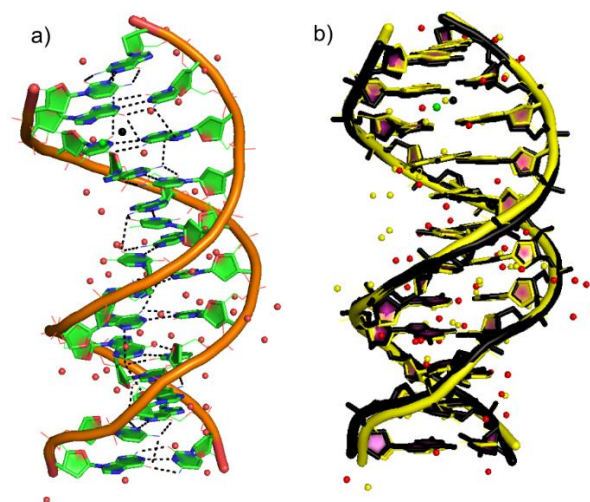

Fig. 2. View of the asymmetric unit of **a)**5JU4 including hydrogen bounds (dottedlines) and water moleculesand**b)** structural alignment of 1D29[2] (shown in yellow) and 5JU4 (the backbone is shown in black color, Mg in green, Cl in black and the water molecules in red).

The base-pair morphology values for theshear, stretch, stagger, buckle, open and propeller twist obtained using X3DNA[8] for 5JU4 and 1D29are shown in Table 2.While for the shear, stretch and staggerthe variationsbetween the two structures areminimal (average differences are 0.15, 0.23 and 0.12 respectively)the averaged differences for the

buckle, open and propeller twist values in the structures are moreevident(2.61, 5.07 and3.46 respectively). The mostpronounced differences are not in the core TpAregion butare seen mostlyat thetwoC-G ends, e.g."propeller" differences of 11.97 and 10.45 in C-G pairs 12-13 and2-23 and differences for "opening" of 8.01 and6.24 forC-G pairs 1-24 and 11-14.Consequently, althoughthe DNA sequence is slightlyalteredthe intrastrand interactions of 5JU4 produces a motifthatis in agreement withthe Dickerson-Drew dodecamerandclassical right-handed B-DNA duplex structuralfeatures[10, 11].

The asymmetric unit of 5JU4 contains 74 water molecules (whileonly 36 are located in 1D29). Many of these waters are first hydration-shell, ordered and welldefinedand may be responsible for providing additionalstabilization to the DNA duplex. In addition the *Fo-Fc*difference map, suggests thepresence ofheavier atoms (than water)e.g.Mg^{2+} and Cl^- ions. No such ions, compensating the DNA negative charge are present in the 1D29 structure.The 5JU4 model shows thatMg^{2+}interactsattwo levels – firstly withthe DNA moleculepresent in the ASU, near the ends of the strands and secondly with a neighboring DNA molecule (via symmetry operation), near the minor groove (Fig. 3).One should note that the position of this particular Mg^{2+} is evident in earlier studies of d(CGCGAATTCGCG)$_2$and it has been concluded that the binding to the minor groove does not drastically affectthe DNA helical parameters [12]. The above mentioned interaction led us to the conclusion that this Mg^{2+}may have implicationsforthe DNAstabilization and the three-dimensionalarrangement of the DNA molecules.
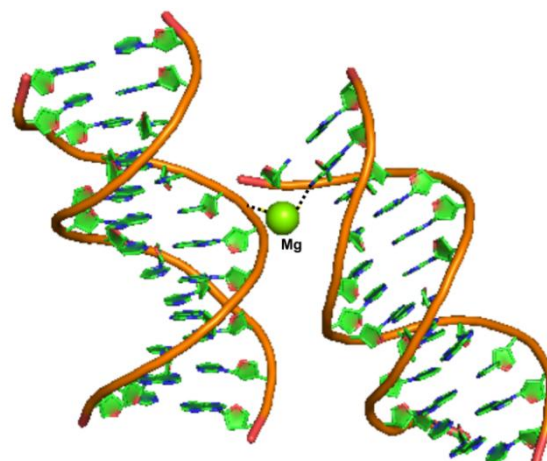

Fig. 3. Positioning of Mg^{2+} compensating the negative charge of the DNA phosphate backbone and acting as a bridge between the DNA molecules.

The 5JU4 crystal structure reveals a nonclassicalinterstrand hydrogen bonding interactionsinvolving G bases. The base pairs C1-G24, G2-C23and G12-C13, C11-G14,located at the ends of the duplexes form G...G bonds with the adjacent DNA duplexes. The discerned G…G hydrogen bonding does not correspond to Hoogsten[13]. Representative electron densities and hydrogen-bonding interactions are shown in (Fig. 4).

Based on the donor acceptordistances(*D…A*) the observed G…G hydrogen bonds are probably slightly weaker[14] thanclassical W-Cones(the *D…A*distance forG…G is around 3.0Å while in C…Git is around 2.85 Å). The G…Ginteractions are located at theends of the DNA strands whilethepreviously mentionedDNA … Mg^{2+} …DNAbridge (Figure 3) involves the AATT domain.

Table 2. X3DNA [8]results for Base-Pair morphology:shear, stretch, stagger, buckle, opening and propeller twist values in5JU4 and 1D29DNA crystal structures.

|	Pair	Shear		Stretch		Stagger		Buckle		Propeller		Opening	
		1D29	5JU4	1D29	5JU4	1D29	5JU4	1D29	5JU4	1D29	5JU4	1D29	5JU4
1-24	C-G	-0.4	0.39	-0.15	-0.22	-0.1	-0.13	3.49	4.99	-11.84	-10.24	-6.69	0.45
2-23	G-C	-0.25	-0.32	-0.33	-0.31	0.04	-0.04	-7.03	-4.24	-13.6	-3.12	-11.8	-6.15
3-22	T-A	-0.17	-0.3	-0.56	-0.07	0.19	-0.27	-5.65	4.58	-10.97	-6.3	-7.79	-2.78
4-21	G-C	-0.53	-0.48	-0.56	-0.18	-0.12	-0.07	7.21	10.06	-11.47	-5.61	-0.33	0.62
5-20	A-T	0.68	0.13	-0.38	-0.05	-0.26	-0.12	4.26	8.06	-12.17	-11.91	6.81	2.01
6-19	A-T	0.08	-0.08	0.06	-0.12	-0.01	0.09	2.83	3	-18.58	-17.08	-3	3.61
7-18	T-A	0.41	-0.02	-0.01	-0.03	-0.23	0.08	0.95	-0.63	-21.35	-15.28	2.34	1.8
8-17	T-A	0.32	0.02	-0.47	-0.11	-0.13	0.09	0.66	-3.97	-18.33	-15.32	5.65	3.81
9-16	C-G	0.39	0.26	-0.41	-0.06	-0.35	0.09	-8.39	-15.17	-18.68	-12.21	-3.77	-0.49
10-15	A-T	0.09	-0.08	-0.28	-0.22	0.33	0.16	-0.23	-0.06	-15.29	-6.92	5.49	3.8
11-14	C-G	-0.17	0.04	-0.44	-0.08	0.51	0.15	3.35	1.79	-16.27	-16.8	-8.1	0.09
12-13	G-C	-0.12	-0.19	-0.47	-0.16	0.12	-0.06	3.31	10.34	-4.5	16.47	-7.9	-4.39
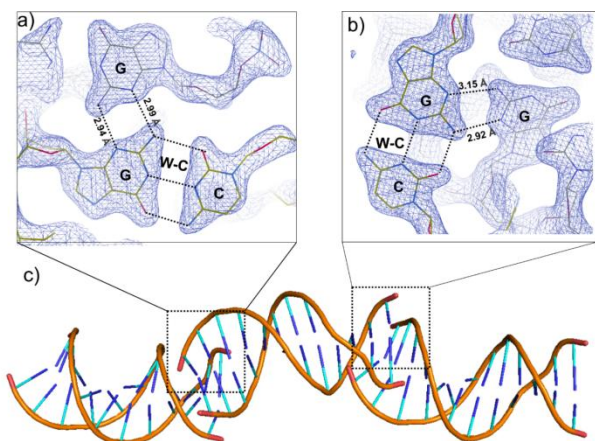
Fig.4. Representation of non-canonical base pairings within the adjacent DNA duplexes; (*a*) G…G Interaction I (*b*) G…G Interaction II and (*c*) Head-to-endarrangement of DNA duplexes generating interactions a) and b).

One can assumethat the "bulky" Mg^{2+}requiresmore space and thusoccupies the outside of theminor groove.On the other hand, the upper and lower surfaces of thepurine and pyrimidine rings are hydrophobic and the G…G interactions exploit the interaction of the edges of the bases (which are hydrophilic) thus eliminating the need of water molecules. Of course, whenno suitableinteraction is achievable thewater molecules interact with the available donors andacceptors. Thus theinterstrand interaction and stabilization of the three-dimensional crystal structure isachievedby evenly distributedweak interaction involvingDNA, ionsand waters molecules.

CONCLUSIONS

The crystal structure of the oligonucleotide d(CGTGAATTCACG)at 2.0 Åresolution is described.In addition to the classical intrastrandWatson-Crickhydrogen bonding interactions the present structure disclosed some noncanonicalG…Ginterstrandinteractions, which had not been previously reported. The presence of a

Mg^{2+} ion acting as a charge compensating ion has alsobeen discovered.The positioning of the Mg^{2+} is comparable to similar higher resolution structures of the Dickerson-DrewDNA dodecamer.Data collection showed that the time of crystal growth is crucial for the crystal quality.

REFERENCES

1. Y. Kim, J. Grable, R. Love, P. Greene, J. Rosenberg, *Science*, **249**, 1307(1990).
2. T.A. Larsen, M.L. Kopka, R.E. Dickerson, *Biochemistry*, **30**, (1991) 4443(1991).
3. N. Narayana, S.L. Ginell, I.M. Russu, H.M. Berman, *Biochemistry*, **30,** 4449 (1991).
4. Agilent Technologies, UK Ltd, Yarnton, England, 2011.
5. A.J. McCoy, R.W. Grosse-Kunstleve, P.D. Adams, M.D. Winn, L.C. Storonip R.J. Read, *J. Appl. Cryst.*, **40**, 658(2007).
6. G.N. Murshudov, P. Skubák, A.A. Lebedev, N.S. Pannu, R.A. Steiner, R.A. Nicholls, M.D. Winn, F. Long, A.A. Vagin, *Acta Cryst. D*, **67**, 355(2011).
7. P. Emsley, B. Lohkamp, W.G. Scott, K. Cowtan, *Acta Cryst. D*, **66**, 486(2010).
8. [8] G. Zheng, X.-J. Lu, W.K. Olson, *Nucleic Acids Res.*, **37**, W240(2009).
9. The PyMOL Molecular Graphics System, Version 1.6, Schrödinger, LLC, 2015.
10. D. Wei, W.D. Wilson, S. Neidle, *J. Am. Chem. Soc.*, **135**, 1369(2013).
11. R.M. Wing, P. Pjura, H.R. Drew, R.E. Dickerson, *EMBO J.*, **3**, 1201(1984).
12. T.K. Chiu, R.E. Dickerson, *J. Mol. Bio.*, **301**, 915(2000).
13. K. Hoogsteen, *Acta Cryst.*, **12**, 822(1959).
14. G.R. Desiraju, T. Steiner, The weak hydrogen bond in structural chemistry and biology, Oxford University Press, Oxford , New York, 1999.

Кристалнаструктурана ДНК последователностd(CGTGAATTCACG) при 130K

Х. И. Сбиркова, Б. Л. Шивачев

Институт по минералогия и кристалография "Акад. Иван Костов", Българска академия на науките ул. „Акад. Г. Бончев, бл. 107, 1113 София, България

Кристалната структура на двойно верижната ДНК секвенцияd(CGTGAATTCACG) е отснета и разшифрована с резолюция of 2.00Å в орторомбичната кристална система и пространствена група *P*2₁2₁2₁. Описани са различията между настоящата структура и отснетите преди това с резолюция 2.5 и 2.7 Å на стайна температура. Забелязва се наличие на Mg и Cl йони както наличие на нетипични G…Gвзаимодействия между съседни ДНК дуплекси.

Synthesis and characterization of polymer-anchored transition metal complexes

D. Kumar[1], A. Kumar[2*]

Received October 12, 2014; Revised September 4, 2015

[1]*Department of Chemistry, National Institute of Technology, Kurukshetra, 136119, Haryana*
[2]*Department of Chemistry, Haryana College of Technology & Management, Kaithal, 136027, Haryana, India*

The reaction between polystyrene 3-formylsalicylate and 2-aminophenol in DMF in the presence of ethyl acetate results in the formation of polystyrene N-(2-hydroxyphenyl)-2'-hydroxybenzylideneimine-3'-carboxylate (**I**). Reacting with mercaptoacetic acid, a benzene suspension of **I** undergoes cyclization and forms polystyrene N-(2-hydroxyphenyl)-C-(3'-carboxy-2'-hydroxyphenyl) thiazolidin-4-one, $PSCH_2$–LH_2 (**II**). A DMF suspension of **II** reacts with Zn(II), Co(II), Cu(II), Zr(OH)$_2$(IV) and MoO$_2$(VI) ions and forms the corresponding polystyrene-anchored coordination compounds, [$PSCH_2$–LHZn(OAc)(DMF)] (**III**), [$PSCH_2$–LHCo(OAc)(DMF)] (**IV**), [$PSCH_2$–LHCu(OAc)(DMF)] (**V**), [$PSCH_2$–LHZr(OH)$_3$(DMF)$_2$] (**VI**) and [$PSCH_2$–LHMoO$_2$(acac)] (**VII**), respectively. The polystyrene-anchored coordination compounds were characterized on the basis of elemental analyses, spectral (IR, reflectance, ESR) studies and magnetic susceptibility measurements. **II** acts as a monobasic bidentate OS donor ligand in all coordination compounds. The acetato groups behave as monodentate ligands in all compounds. A tetrahedral structure for **III**, a square-planar structure for **IV** and **V**, a pentagonal-bipyramidal structure for **VI** and an octahedral structure for **VII** are suggested.

Keywords: Thiazolidin-4-one, Polystyrene-anchored coordination compounds, Magnetic dilution, Strong field, Covalent character.

INTRODUCTION

Interest in the preparation of polymers incorporating metallic subunits is continuously growing in light of their chemical and physical properties, as well as their potential applications [1-2]. This mainly arises from the wide range of coordination numbers, oxidation states and geometries of transition elements that offer the possibility of accessing a large diversity of metal-containing polymeric materials with unusual conformational, mechanical and morphological characteristics [3-4].

Among transition metal based polymers, the complexes of polymeric Schiff bases and their derivatives are considered as a very important class of coordination compounds which have been extensively studied [5] owing to their wide applications in many biological, clinical, analytical and industrial activities, in addition to their important roles in catalysis and organic synthesis, as well as in various industrial applications [6].

Thiazolidin-4-ones show a broad spectrum of biological activities due to their ready accessibility and diverse chemical reactivity [7-8]. They show antimicrobial, antibacterial, anticonvulsant, antifungal, anti-inflammatory, antithyroid and antitubercular [9-11] activities and possess better pharmacological properties in the form of metal complexes [12].

These facts prompted us to explore the coordination behavior of polystyrene-anchored thiazolidin-4-one (**II**) derived from the Schiff base (**I**) (obtained from the condensation of polystyrene 3-formylsalicylate and 2-aminophenol) towards Zn(II), Co(II), Cu(II), Zr(OH)$_2$(IV) and MoO$_2$(VI) ions.

A perusal of the literature indicates that several polymer-anchored ligands containing oxygen atom(s) like crown ethers [13], acetylacetone [14], etc. have been reported. However, fewer reports are available on the coordination compounds of polymer-anchored ligands containing thiazolidin-4-one moiety [15].

In this manuscript, we describe the synthesis and characterization of polystyrene-anchored thiazolidin-4-one, $PSCH_2$–LH_2 (**II**) and its coordination compounds with the above mentioned ions.

I

II

.
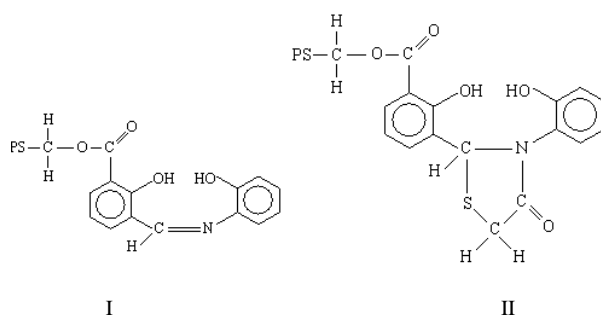
* To whom all correspondence should be sent:
E-mail: amit_vashistha2004@yahoo.co.in

EXPERIMENTAL

Materials

Chloromethylated polystyrene, $PSCH_2$–Cl (containing 1.17 mmol of Cl per g of resin and 1% crosslinked with divinylbenzene) was purchased from Sigma Chemical Co (USA). Copper(II) acetate monohydrate, zinc(II) acetate dihydrate [SD's Fine]; cobalt(II) acetate tetrahydrate, hexadecaaquaoctahydroxotetrazirconium(IV) chloride [BDH]; ammonium molybdate(VI) tetrahydrate, acetylacetone [Ranbaxy]; 2-aminophenol [Loba-Chemie (Mumbai)] were used for the synthesis as supplied. Polystyrene 3-formylsalicylate, bis(acetylacetonato)dioxo molybdenum(VI), hexadecaaquaoctahydroxotetra zirconium(IV) acetate and 3-formylsalicylic acid were synthesized according to reported procedures [15].

The elemental analyses, IR, reflectance, ESR spectral studies and magnetic susceptibility measurements were carried out as described in our previous report [15].

Synthesis of polystyrene N-(2-hydroxyphenyl)-2'-hydroxybenzylideneimine-3'-carboxylate (I)

Polystyrene 3-formylsalicylate (1.0 g) was allowed to suspend and swell in DMF (100 mL) for 45 min. To this suspension, a DMF solution (60 mL) of aminophenol (0.510 g, 4.68 mmol) and ethyl acetate (100 mL) were added, while stirring magnetically. The mixture was refluxed for 8 h and then cooled to room temperature. The obtained polystyrene-anchored Schiff base I was filtered, washed with DMF and ethyl acetate. It was dried *in vacuo* at room temperature.

Synthesis of polystyrene N-(2-hydroxyphenyl)-C-(3'-carboxy-2'-hydroxyphenyl) thiazolidin-4-one, $PSCH_2$–LH_2 (II)

Mercaptoacetic acid (0.32 g, 3.51 mmol) was added to the swollen suspension of I (1.0 g) in benzene (100 mL). The mixture was refluxed for 12 h on a water bath and then cooled to room temperature. The solid product was filtered and washed with 10% sodium bicarbonate solution followed by chilled distilled water. The product was dried as mentioned above. IR bands (KBr): 1690 cm^{-1} [v(C=O)(thiazolidinone ring)], 1575 cm^{-1} [v(C–N)(thiazolidinone ring)], 1530 cm^{-1} [v(C–O)(phenolic)] and 830 cm^{-1} [v(C–S)(thiazolidinone ring)].

Synthesis of coordination compounds of II

1.0 g of **II** was allowed to suspend and swell in DMF (100 mL) for 1 h. A DMF solution of the appropriate metal salt (2.34 mmol) was added to the above suspension. The mixture was refluxed on a water bath for 8-10 h and the products obtained were filtered, washed several times with ethyl acetate and DMF. The products were then dried as mentioned above.

RESULTS AND DISCUSSION

The reaction between polystyrene 3-formylsalicylate and 2-aminophenol in DMF in the presence of ethyl acetate results in the formation of polystyrene N-(2-hydroxyphenyl)- 2'-hydroxybenzylideneimine-3'-carboxylate (**I**). The cyclization of **I** with mercaptoacetic acid in benzene yields polystyrene N-(2-hydroxyphenyl)-C-(3'-carboxy-2'-hydroxyphenyl) thiazolidin-4-one, $PSCH_2$–LH_2 (**II**). A DMF suspension of **II** reacts with Zn(II), Co(II), Cu(II), Zr(OH)$_2$(IV) and MoO$_2$(VI) ions in a 1:2 molar ratio and forms the corresponding polystyrene-anchored coordination compounds of the types:

[$PSCH_2$–LHZn(OAc)(DMF)] (**III**),
[$PSCH_2$–LHCo(OAc)(DMF)] (**IV**),
[$PSCH_2$–LHCu(OAc)(DMF)] (**V**),
[$PSCH_2$–LHZr(OH)$_3$(DMF)$_2$] (**VI**) and
[$PSCH_2$–LHMoO$_2$(acac)] (**VII**), respectively.

The formation of **I** (by the reaction of polystyrene 3-formylsalicylate with 2-aminophenol, **II** (by cyclization of **I** with mercaptoacetic acid) and the coordination compounds of **II** with Co(II), Cu(II), Zn(II), Zr(OH)$_2$(IV) and MoO$_2$(VI) ions are depicted in Schemes **I**, **II** and **III**, respectively.

The percent reaction conversion of **III-VII** lies between 48.8-74.0 and the metal binding capacity of **II** lies between 0.34-0.55 mmol of corresponding metal per g of the resin (Table 1).

Infrared spectral studies

The infrared spectra of **I**-**VII** were recorded in KBr and the prominent peaks are shown in Table 2. The v(C=N)(azomethine) stretch of **I** occurs at 1625 cm^{-1}. This band disappears and a new band appears in **II** at 1575 cm^{-1} due to the v(C–N)(thiazolidinone ring) stretch [16], indicating the formation of the corresponding thiazolidin-4-one. The formation of **II** is further supported by the appearance of a new band at 830 cm^{-1} due to the v(C–S) (thiazolidinone ring) stretch [17]. The v(C–O) stretch [18] of **II** occurs at 1530 cm^{-1}. This band shifts to higher energy by 5-10 cm^{-1} in the coordination

compounds, indicating the involvement of a phenolic O atom of either 3-aldehydo-2-hydroxybenzoic acid or 2-aminopohenol moieties in the coordination. On the basis of steric grounds, we suggest the non-involvement of phenolic (2-aminophenol moiety) O atom in the coordination.

The ν(C=O)(thiazolidinone) stretch [19] of **II** occurs at 1690 cm^{-1}. This band remains unchanged in the coordination compounds showing its non-involvement in coordination. The [ν(C–N)(thiazolidinone ring)] stretch [16] of **II** occurs at 1575 cm^{-1} and also remains unchanged in the coordination compounds.

The [ν(C–S)(thiazolidinone ring)] stretch [17] of **II** occurring at 830 cm^{-1} shifts to lower energy by 20-35 cm^{-1} in all coordination compounds. The ν_{as}(COO) and ν_s(COO) stretches of free acetate ions occur at 1560 and 1416 cm^{-1}, respectively [20]. The ν_{as}(COO) and the ν_s(COO) stretches occur at 1575, 1350; and 1595, 1360 cm^{-1} in all coordination compounds. The magnitude of energy separation ($\Delta\nu$=225-240 cm^{-1}) between ν_{as}(COO) and ν_s(COO) is > 144 cm^{-1} and indicates the monodentate nature of acetato groups [20], since in the event of bidentate coordination, the energy separation between ν_{as}(COO) and ν_s(COO) is < 144 cm^{-1}. DMF shows a band at 1680 cm^{-1} due to the ν(C=O) stretch [21]. This band shifts to lower energy by 20-35 cm^{-1} in **III** to **VI** indicating the involvement of O

atom in the coordination [21]. The absence of a band between 835-955 cm^{-1}, characteristic of ν(Zr=O) stretch [22] in **VI** suggests that its structure is [PSCH$_2$–LHZr(OH)$_3$(DMF)$_2$] and not [PSCH$_2$–LHZrO(OH)(H$_2$O)(DMF)$_2$]. The appearance of a band at 1126 cm^{-1} due to the δ(Zr–OH) bending mode also supports the suggested structure of the compound [20]. **VII** exhibits the ν_s(O=Mo=O) and ν_{as}(O=Mo=O) stretch at 942 and 920 cm^{-1}, respectively and these bands occur in the usual range (892-964 cm^{-1}; 842-928 cm^{-1}) reported for the majority of MoO$_2$(VI) compounds [20]. The presence of ν_s(O=Mo=O) and ν_{as}(O=Mo=O) bands indicates a *cis*-MoO$_2$ structure, as the compounds with *trans*-MoO$_2$ structure exhibit only the ν_{as}(O=Mo=O) since the ν_s(O=Mo=O) is IR inactive [23].
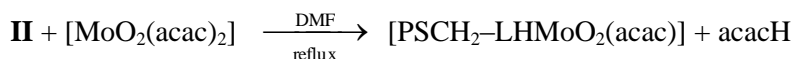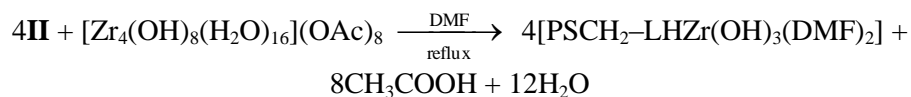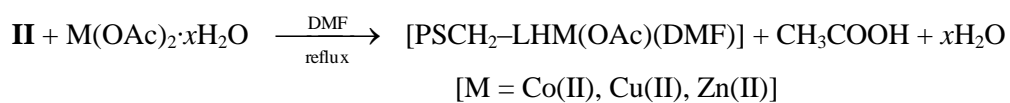
Magnetic measurements

The room temperature magnetic moments of the polystyrene-anchored coordination compounds of **II** are presented in Table 2. The magnetic moment of **V** is 1.90 B.M. This value lies within the range (1.70-2.20 B.M.) reported for the magnetically diluted Cu(II) compounds [24]. The magnetic moment of **IV** is 2.38 B.M. and the value lies in the range: 2.10–2.90 B.M., reported for low-spin square-planar Co(II) compounds. **III**, **VI** and **VII** are diamagnetic.
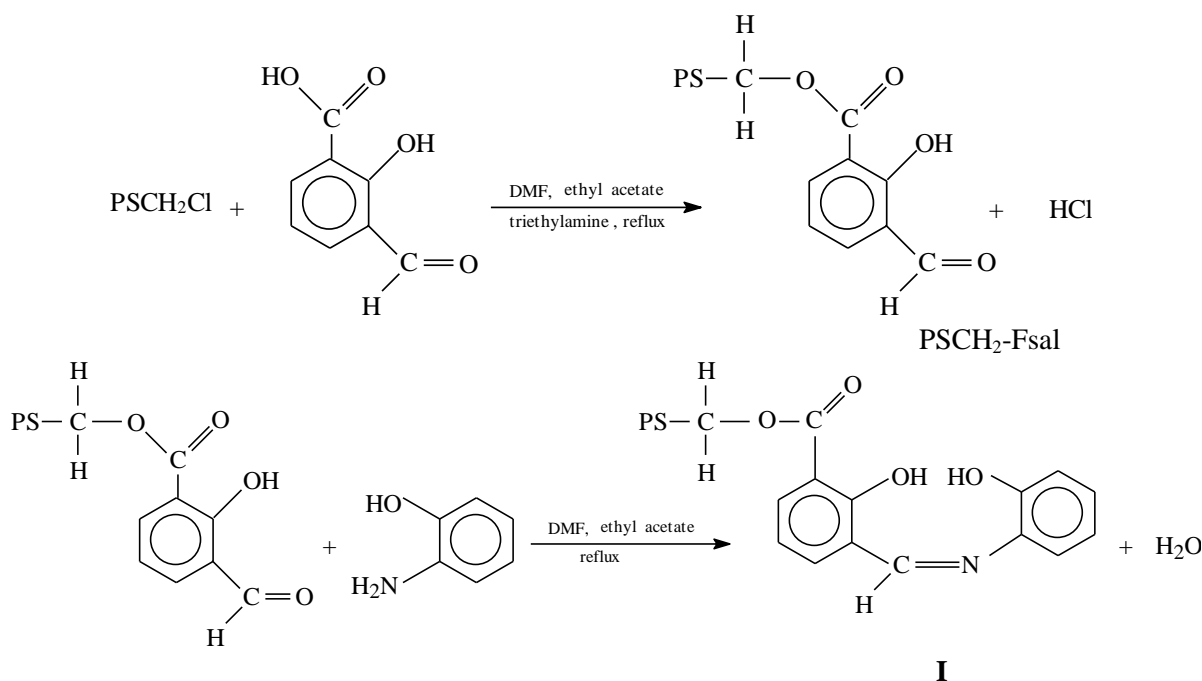
Scheme-I: Synthesis of Polystyrene-anchored Schiff Base

PSCH$_2$–LH$_2$ (**II**)
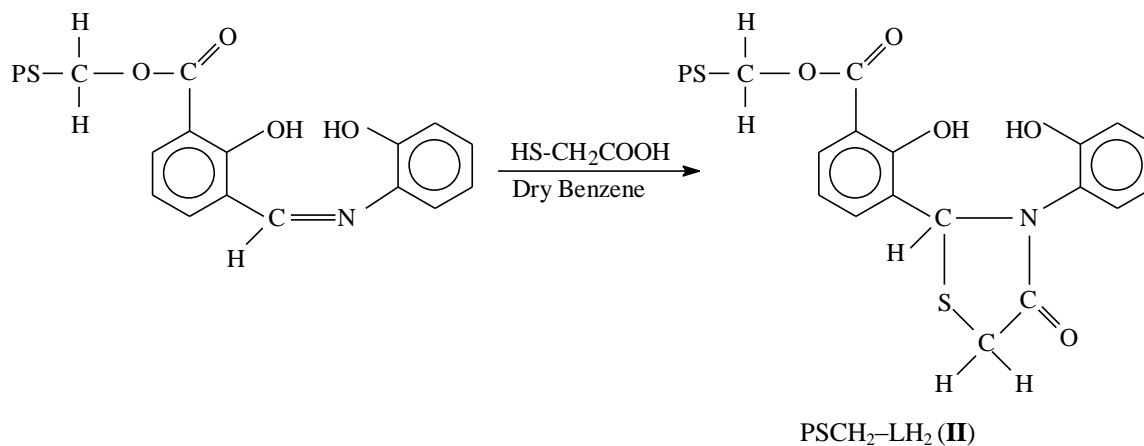
Scheme-II: Synthesis of Polystyrene-anchored Thiazolidin-4-one

II + M(OAc)$_2$·xH$_2$O $\xrightarrow[\text{reflux}]{\text{DMF}}$ [PSCH$_2$–LHM(OAc)(DMF)] + CH$_3$COOH + xH$_2$O

[M = Co(II), Cu(II), Zn(II)]

4**II** + [Zr$_4$(OH)$_8$(H$_2$O)$_{16}$](OAc)$_8$ $\xrightarrow[\text{reflux}]{\text{DMF}}$ 4[PSCH$_2$–LHZr(OH)$_3$(DMF)$_2$] + 8CH$_3$COOH + 12H$_2$O

II + [MoO$_2$(acac)$_2$] $\xrightarrow[\text{reflux}]{\text{DMF}}$ [PSCH$_2$–LHMoO$_2$(acac)] + acacH

Scheme-III: Syntheses of Polystyrene-anchored Coordination Compounds

III

IV

V

VI

VII

596
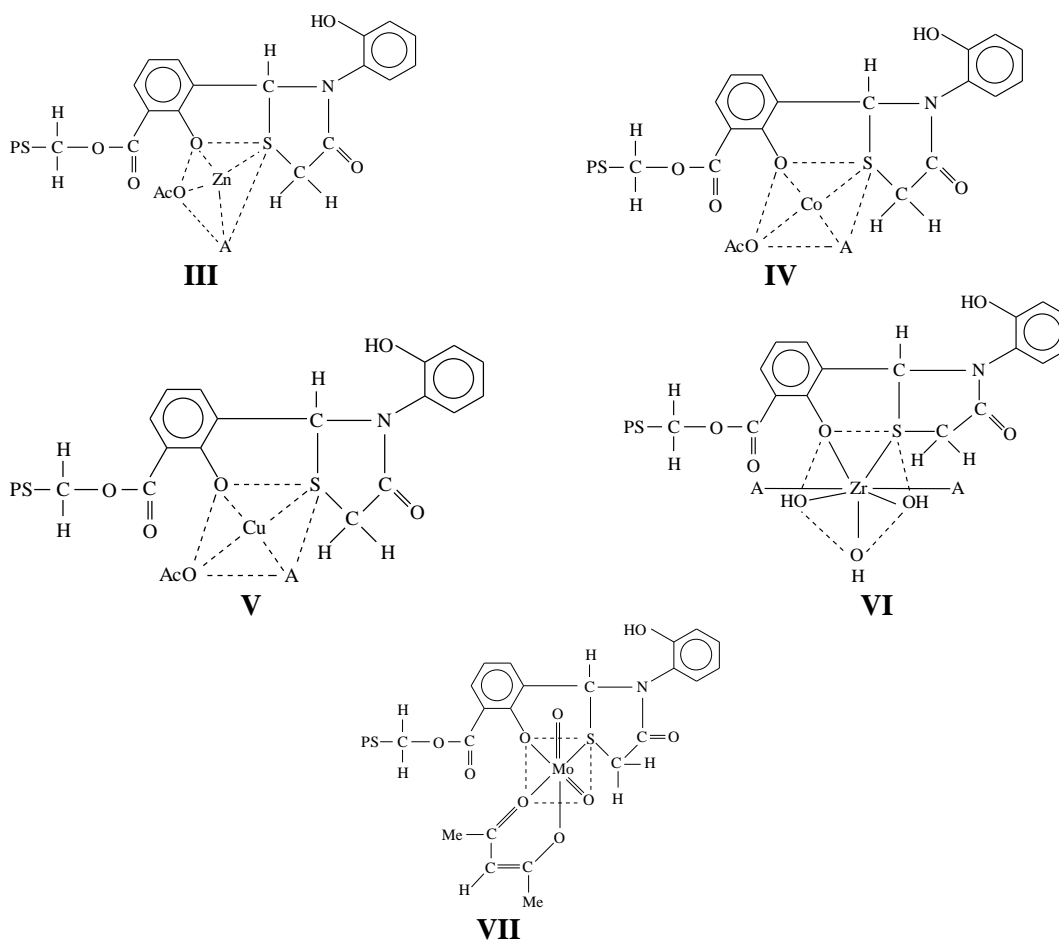
Table 1. Analytical, MBC and PRC values of polystyrene-anchored coordination compounds of II[a]

Compound	Observed(Calculated)%		MBC[b] (mmol/g of resin)	PRC[c]
	M	DMF		
[PSCH$_2$–LHCo(OAc)(DMF)]	2.6 (4.40)	3.2 (5.45)	0.44	59.1
[PSCH$_2$–LHCu(OAc)(DMF)]	3.5 (4.73)	4.1 (5.43)	0.55	74.0
[PSCH$_2$–LHZn(OAc)(DMF)]	3.2 (4.86)	3.5 (5.42)	0.49	65.8
[PSCH$_2$–LHZr(OH)$_3$(DMF)$_2$]	3.1 (6.35)	4.9 (10.16)	0.34	48.8
[PSCH$_2$–LHMoO$_2$(acac)]	3.7 (6.97)	–	0.39	53.08

[a]Abbreviations: PSCH$_2$–LH$_2$ = **II**

[b]MBC = [M% (observed) × 10] /(atomic weight of metal)

[c]PRC = [M% (observed) × 100] / M% (calculated) on the basis of 100% reaction conversion of polystyrene-anchored ligand to polystyrene-anchored coordination compounds.

Table 2. IR, reflectance spectral data (cm^{-1}) and magnetic moments of polystyrene-anchored coordination compounds

Compound	ν(C–S)	ν(C=O) (DMF)	ν$_{as}$ (COO) (acetate)	ν$_s$ (COO) (acetate)	N (C–O) (phenolic)	ν$_{max}$	Magnetic moment[a] (B.M.)
PSCH$_2$–LH$_2$ (II)	830	–	–	–	1530	–	Diamagnetic
[PSCH$_2$–LHCo(OAc)(DMF)]	810	1645	1575	1350	1535	8450, 22800	2.38
[PSCH$_2$–LHCu(OAc)(DMF)]	805	1660	1585	1355	1540	17250	1.90
[PSCH$_2$–LHZn(OAc)(DMF)]	800	1650	1590	1350	1538	–	Diamagnetic
[PSCH$_2$–LHZr(OH)$_3$(DMF)$_2$]	795	1645	1595	1360	1535	–	Diamagnetic
[PSCH$_2$–LHMoO$_2$(acac)]	805	–	–	–	1540	–	Diamagnetic

[a]$\mu_{eff.}$ = 2.83 ($\chi_M^{corr} \times T$)$^{1/2}$ B. M.

Reflectance spectral studies

[PSCH$_2$–LHCo(OAc)(DMF)] exhibits two bands, one at 8450 and another at 22800 cm^{-1} due to $^1A_{1g} \rightarrow {}^1B_{2g}$ and $^1A_{1g} \rightarrow {}^1B_{1g}$ transitions (Table 2).. These bands occur in the usual ranges (8400–8550 and 21000–24500 cm^{-1}) reported for the majority of square-planar compounds [25]. [PSCH$_2$–LHCu(OAc)(DMF)] exhibits a band at 17250 cm^{-1} due to $^2B_{1g} \rightarrow {}^2A_{1g}$, $^2B_{2g}$ and ^2E_g transitions for square-planar arrangement of ligands around Cu(II) ions [25]. The absence of a band in the range: 8000–10000 cm^{-1} precludes the presence of a tetrahedral structure.

ESR studies

The ESR spectrum of **V** exhibits $g_\parallel$ = 2.25 and $g_\perp$ = 2.10 indicating the presence of a tetragonal type symmetry about the Cu(II) ion [26]. The spectral parameters are: $A_\parallel$ = 1.683 × 10^{-2} cm^{-1}, $A_\perp$ = 3.74 × 10^{-3} cm^{-1}, G = 2.53, g_{av} = 2.15, α_{Cu}^2 = 0.80, $(\alpha')^2$ = 0.26, κ = 0.52 and P_d = 1.68 × 10^{-2} cm^{-1}. The trend that $g_\parallel > g_\perp$ and $A_\parallel > A_\perp$ is indicative of the presence of an unpaired electron in the d$_{x^2-y^2}$ orbital [27].

The $g_\parallel$ value (2.26) indicates that the metal-ligand bond in the compound is covalent. The G value

597

(2.53) indicates the strong field nature of the polystyrene-anchored ligand [28]. The values of α_{Cu}^2 (0.80) and $(\alpha')^2$ (0.26) indicate the covalent nature of the compound. The positive value of κ (0.52) suggests that $A_\parallel$ should be greater than $A_\perp$ [26] and this trend in $A_\parallel$ and $A_\perp$ values was also observed by us. The lower value (1.68 × 10^{-2} cm^{-1}) of P_d in comparison to that of the free ion value (3.5 × 10^{-2} cm^{-1}) indicates the covalent character of the metal-ligand bonding. The spectrum shows no band ~1500 G due to the $\Delta Ms = 2$ transition and this precludes the presence of M–M interaction.

CONCLUSIONS

The elemental analyses, IR, reflectance, ESR spectral and magnetic susceptibility measurements suggest a tetrahedral structure (**III**) for [PSCH$_2$–LHZn(OAc)(DMF)], a square-planar structure for [PSCH$_2$–LHCo(OAc)(DMF)] (**IV**), [PSCH$_2$–LHCu(OAc)(DMF)] (**V**), a pentagonal-bipyramidal structure (**VI**) for [PSCH$_2$–LHZr(OH)$_3$(DMF)$_2$] and an octahedral structure for [PSCH$_2$–LHMoO$_2$(acac)] (**VII**).

REFERENCES

1. T. Ravi P. Sankar, V. Ramana, *Journal of Applicable Chemistry*, **2**, 1459 (2013).
2. M.S. Mrudula, M.R. Gopinathan Nair, *Research J. Recent Sciences*, **3**, 319 (2014).
3. A.H. Ahmed, *International J. Chem. Tech. Research*, **6**, 36 (2014).
4. N. Novoa, J.P. Soto, R. Henríquez, C. Manzur, D. Carrillo, J.R. Hamon, *J. Inorganic and Organometallic Polymers and Materials*, **23**, 1247 (2013).
5. I.R. Parrey, S. Anayutullah, A.A. Hashmi, *Modern Research in Catalysis*, **3**, 107 (2014).
6. Sweta, S.Chand, S. Sinha, *J. Applied Polymer Science*, 130, 2127 (2013).
7. H. Behbehani, H.M. Ibrahim, *Molecules*, **17**, 6362 (2012).
8. S. Gaikwad, V. Suryawanshi, Y. Vijapure, V. Shinde, *J. Chemical and Pharma. Research*, **4**, 1851 (2012).
9. T.M. Bhagat, D.K. Swamy, S.G. Badne, S.V. Kuberkar, *Rasayan J. Chem*, **4**, 24 (2011).
10. M. Abhinit, M. Ghodke, N.A. Pratima, *International J. Pharmacy and Pharmaceutical Sci.*, **1**, 7 (2009).
11. H.H. Parekh, K.A. Parikh, A.R. Parikh, *Journal of Sciences, Islamic Republic of Iran*, **15**, 143 (2004).
12. H. Panwar, R.S. Verma, V. Srivastava, A. Kumar, *Indian J. Chem.*, **45B**, 2088 (2006).
13. V. Gududuru, *Bioorg. Med. Chem. Lett.*, **14**, 5289 (2004).
14. N.D. Sonawane, A.S. Verkman, *Bioorg. Med. Chem.*, **16**, 8187 (2008).
15. D. Kumar, A. Kumar, *E-J. Chem.*, **9**, 2532 (2012).
16. S.P Shrivastava, N. Seelam, R. Rai, *E-J. Chem.*, **9**, 825 (2012).
17. A. Solankee, S. Solankee, G. Patel, *Oriental J. Chem.*, **24**, 299 (2008).
18. D. Kumar, A. Kumar, *J. Chem.*, 1 (2014). Article ID 124790.
19. D. Kumar, A.Kumar, D.Dass, *Bull. Chem. Soc. Ethiop.*, **28**, 29 (2014).
20. B.N. Figgis, R.S. Nyholm, *J. Chem. Soc.*, 338 (1959).
21. A.B.P. Lever, Inorganic Electronic Spectroscopy, 2nd ed., and references therein, Elsevier, Amsterdam, 1984.
22. D.Kumar, A. Kumar, D. Dass, *International J. Inorganic Chemistry*, 1 (2013), Article ID 524179.
23. D.W. Warad, C.D. Satish, V.H. Kulkarni, C.S. Bajgur, *Indian J. Chem.*, **39A**, 415 (2000).
24. R.S. Drago, Physical Methods in Chemistry, 2nd edn., W.B. Saunders Co., Philadelphia, 1976.
25. B.B. Mahapatra, P. Ray, *J. Indian Chem. Soc.*, **79**, 609 (2002).
26. D. Kumar, A. Kumar, D. Dass, *Bulgarian Chemical Communications*, **46**, 238 (2014).
27. D. Kumar, P.K. Gupta, A.Syamal, *J. Chil. Chem. Soc.*, **59**, 2260 (2014).
28. D. Kumar, P.K.Gupta, A. Kumar, D. Dass, A. Syamal, *J. Coord. Chem.*, **64**, 590 (2011).

СИНТЕЗА И ХАРАКТЕРИЗИРАНЕ НА КОМПЛЕКСИ НА ПРЕХОДНИ МЕТАЛИ, ФИКСИРАНИ ВЪРХУ ПОЛИМЕРИ

Д. Кумар[1], А. Кумар[2*]

[1]*Департамент по химия, Национален технологичен институт, Курукшетра, 13611,Харияна, Индия*
[2]*Департамент по химия, Колеж по технология и управление, Кайтал, 136027 Харияна, Индия*

(Резюме)

В резултат на реакцията между полистирен-3-формамилсалицилат и 2-аминофенол в диметил-формамид вприсъствие на етилацетат се получава полистирен N-(2-хидроксифенил)-2'-хидроксибензилиденимин-3'-карбоксилат (**I**). При реакцията с меркапто-оцетна киселина суспензията на **I** в бензен протича циклизация и се образува полистирен N-(2-хидроксифенил)-C-(3'-карбокси-2'-хидроксифенил) тиазолидин-4-он, PSCH$_2$–LH$_2$ (**II**). Суспензията на **II** в диметил-формамид реагира с йоните Zn(II), Co(II), Cu(II), Zr(OH)$_2$(IV) и MoO$_2$(VI) и образува съоъветните координационни съединения, фиксирани върху полистирен, съответно [PSCH$_2$–LHZn(OAc)(DMF)] (**III**), [PSCH$_2$–LHCo(OAc)(DMF)] (**IV**), [PSCH$_2$–LHCu(OAc)(DMF)] (**V**), [PSCH$_2$–LHZr(OH)$_3$(DMF)$_2$] (**VI**) и [PSCH$_2$–LHMoO$_2$(acac)] (**VII**). Тези координационни съединения са охарактеризирани на базата на елементен анализ, спектрални методи (IR, отражателна, ESR) и измерване на магнития сусцептибилитет. Ацетатните групи се отнасят като монодентатни лиганди във всички съединения. Предлагат се тетраедрична структура за **III**, квадратно-планарна структура за **IV и V**, пентагонално бипирамидална структура за **VI** и октаедрична структура за **VII.**

Theoretical study on the cycloaddition reaction mechanism between azacyclopropenylidene and ethylene

X. J. Tan[1]*, W. H. Wang[2], P. Li[2]*

[1]*College of Biological Science and Technology, University of Jinan, Jinan, Shandong, 250022, People's Republic of China*

[2]*School of Chemistry and Chemical Engineering, Qufu Normal University, Qufu, Shandong, 273165, People's Republic of China*

The mechanism of the cycloaddition reaction between azacyclopropenylidene and ethylene was systematically investigated employing the second-order Møller-Plesset perturbation theory (MP2) method in order to better understand the reactivity of azacyclopropenylidene with the unsaturated compound ethylene. Geometry optimizations and vibrational analyses were performed for the stationary points on the potential energy surfaces of the system. From the potential energy profile, it is predicted that the cycloaddition reaction has three competitive pathways: (I) reaction of azacyclopropenylidene with ethylene to form a carbene compound P1 in two steps; (II) formation of an allene compound P2 from the two reactants in three steps; (III) after the formation of P1 by the reaction of azacyclopropenylidene with ethylene, further reaction of P1 with ethylene to form a stable bicyclic compound P3.

Keyword: Azacyclopropenylidene, Reaction mechanisms, MP2 method.

INTRODUCTION

Cyanopolyene molecules HC_nN have been detected in the interstellar space by radio telescopes for a long time [1-9]. This class of molecules plays an important role in astronomy and interstellar chemistry due to their astrophysical abundance and rather large dipole moments. One of the interesting cyanopolyenes, the molecule HCCN, was studied by electron spin resonance and UV/IR spectroscopy since the 1960s [10,11]. For the first time, Guélin *et al*. detected HCCN in the carbon star envelope IRC+10216, and discussed its formation mechanism [12]. Later, in 1996, HCCN was observed in the interstellar space [13]. A lot of experimental and computational methods were applied for finding out the structures and the relative energies of some isomers of the HCCN system. Many studies have revealed that there exist many isomers with different kinds of geometries (linear, bent or cyclic) or different multiplicity (singlet or triplet) having similar energies of the HCCN molecules [14-23]. Lee *et al*. have characterized the quasilinear triplet, bent singlet, and cyclic singlet HCCN isomers and determined their molecular properties with a series of highly accurate *ab initio* levels of theory [24]. The cyclic HCCN isomer, generally named as azacyclopropenylidene, is the most stable isomer of all singlet molecules. In addition, the cyclic HCCN isomer has been found to be an intermediate between the interconversion of other isomers on the hypersurface of neutral, anionic, and cationic species where the barriers are feasible [25,26]. Recently, vibrational spectroscopic constants and fundamental vibrational frequencies for isotopologues of the azacyclopropenylidene isomer have been investigated [27].

In 1998, matrix generations of singlet azacyclopropenylidene and singlet bromocyanocarbene (BrCCN) were reported by Maier and co-workers [28]. Casavecchia *et al*. reported the dynamics of a reaction of the nitrogen atom with an unsaturated hydrocarbon by combining crossed molecular beam experiments and *ab initio* molecular orbital calculations. They found that azacyclopropenylidene is one of the products of the reaction of the nitrogen atom with C_2H_2 in the upper atmosphere of Titan [29]. Thus, azacyclopropenylidene seems to be a good candidate for astrophysical detection, considering the various possible formation pathways and its large dipole moment [30]. Computational investigation of HCCN molecules will be very helpful to elucidate the reactivity and kinetic stability of these molecules. We have studied the reactions between azacyclopropenylidene and small ring compounds [31,32]. The calculational results demonstrated that azacyclopropenylidene can insert into small ring compounds to form ring-expanded products. However, no attention has been paid to the reactivity of azacyclopropenylidene with active species containing double bond compounds

---

* To whom all correspondence should be sent:
E-mail: chem.2001@163.com; lpsdu@sdu.edu.cn

until now. In the present study, we have performed a comprehensive theoretical investigation of the reaction mechanism between azacyclo-propenylidene and ethylene by employing the second-order Møller-Plesset perturbation theory (MP2) method in order to better understand the azacyclopropenylidene reactivity. The present results will enrich the available data for the relevant azacyclopropenylidene chemistry and discuss the possibility of formation of larger molecules by means of azacyclopropenylidene in the interstellar space.

CALCULATION METHOD

The second-order Møller-Plesset perturbation theory (MP2) method [33] in combination with the 6-311+G* basis set was employed to locate all stationary points along the reaction pathways without imposing any symmetry constraints. Frequency analyses were carried out to confirm the nature of minima and transition states. For example, the intermediates (IM) in the reactions are local minima with no imaginary frequencies. The transition states (TS) have only one imaginary frequency. The spin multiplicities of all transition states are singlet. Moreover, intrinsic reaction coordinate (IRC) calculations were also performed to further validate the calculated transition states connecting reactants and products. Additionally, the relevant energy quantities, such as the reaction energies and barrier heights, were corrected with the zero-point vibrational energy (ZPVE) corrections.

All calculations were performed using Gaussian 98 program [34].

RESULTS AND DISCUSSION

As displayed in Scheme 1, three possible pathways for the title reaction were proposed. The geometric parameters for the reactants (azacyclopropenylidene (R1) and ethylene (R2)), transition states (TS), intermediates (IM), and products (P) involved in the pathways (I), (II), and (III) are displayed in Fig. 1. The calculated relative energies for the available stationary points are summarized in Table 1. The corresponding reaction profile is illustrated in Fig. 2.

Pathway (I): formation of a carbene compound P1

There are step (a) and step (1) along the reaction pathway (I), where step (a) is a common step for the pathways (I) and (II).

The first intermediate IMa was formed along the reaction pathways (I) and (II) *via* a barrier of 51.7 kJ/mol. The calculated unique imaginary frequency

of the transition state TSa in the cycloaddition process of step (a) is 491i cm^{-1} at the MP2/6-311+G* level of theory.

As shown in Fig. 1, in TSa, the distance of C^1-C^3 and C^1-C^4 is 0.1930 and 0.2514 nm, respectively. The distance of C^3-C^4 in the R2 fragment is 0.1378 nm, which is elongated by 0.0039 nm in comparison with the isolated R2 molecule. Thus, in TSa, two new bonds of C^1-C^3 and C^1-C^4 are to be formed and the C^3-C^4 bond is to be simultaneously transformed from double bond to single bond. As shown in Fig. 3, these changes can be further validated by IRC calculations on the basis of TSa.
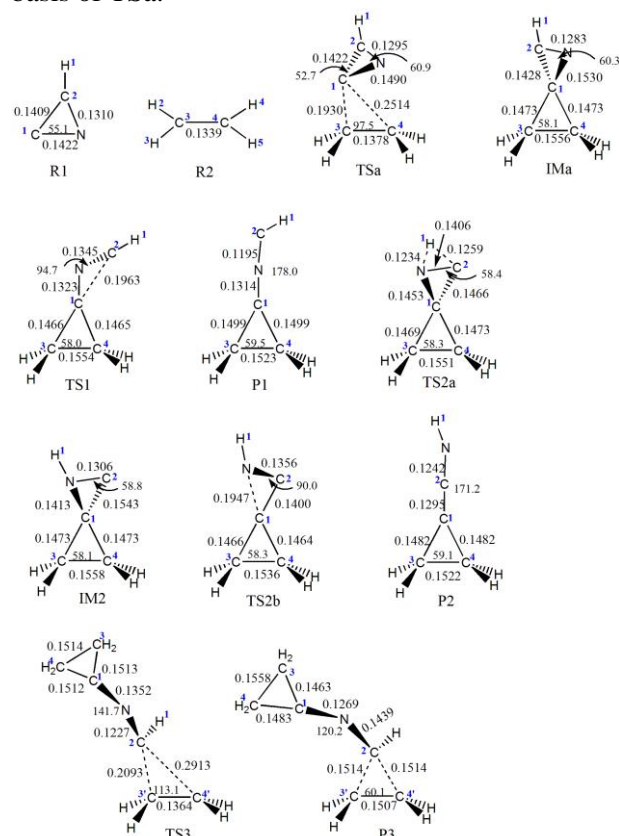
Fig. 1. Optimized structures of the reactants (azacyclopropenylidene and ethylene), transition states (TS), intermediates (INT), and products (P) in the reaction pathways (I), (II), and (III) at the MP2/6-311+G* level of theory, where bond length and bond angle are in angstrom and degree, respectively.

Qualitatively, the cycloaddition process can be understood ensuing from the frontier molecular orbital theory since the frontier orbitals (e.g., HOMO) of a chemical species are very important to define their reactivity and to determine the way in which the molecule interacts with other species [35]. As displayed in Fig. 4, the weak strength of the C^3-C^4 bond can be reflected from the HOMO of ethylene. Obviously, it is characterized by the π antibonding orbital. As for azacyclopropenylidene,

the activity of the C^1 site can be reflected from the largest contributions of the C^1 atom to the components of the whole HOMO. Therefore, the C^1 atom of azacyclopropenylidene can react with the C^3-C^4 bond of ethylene to form the spiro intermediate IMa.

As displayed in Fig. 1, compared with the isolated azacyclopropenylidene, the bond length of C^1-C^2 in IMa is extended by 0.0019 nm. The angle of C^1NC^2 in IMa is 60.3º, which is lower by 1.6º relative to that of the isolated azacyclopropenylidene. Therefore, the ring-tension of the R1 fragment in IMa is larger than that of the isolated R1. Because of the existing large tension in the three-membered ring, the C^1-C^2 bond in IMa will be broken. Therefore, the second step of the pathway (I) is the C^1-C^2 bond cleavage, followed by the formation of P1.
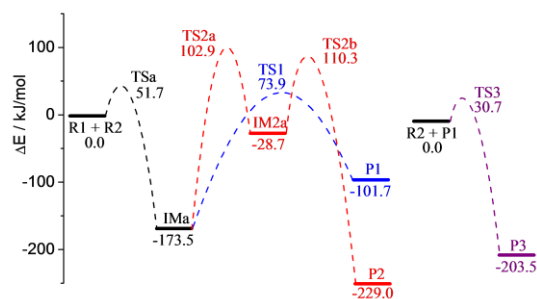
Fig. 2. Reaction profiles for the cycloaddition reaction pathways (I), (II), and (III) between azacyclopropenylidene and ethylene at the MP2/6-311+G* level of theory
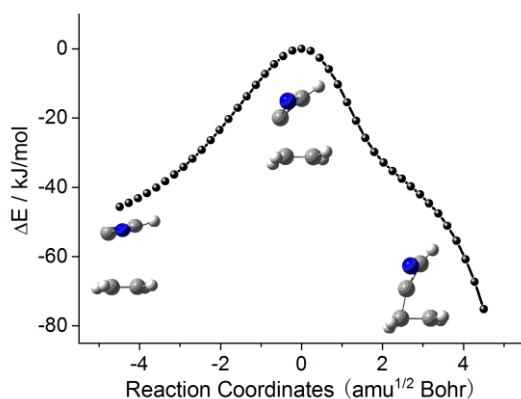
Fig. 3. IRC of TSa and geometry evolution.

Through the cleavage of the C^1-C^2 bond, IMa can be converted to P1 *via* TS1, where the barrier is 247.4 kJ/mol. The calculated unique imaginary frequency of TS1 is 435i cm^{-1}. IRC calculations were performed on the basis of the calculated TS1

to investigate the interactions between IMa and P1 in step (1) of the process (see Fig. 5).

As shown in Figs. 1 and 5 for the angle of C^1NC^2 in IMa, it increases along with the reaction. At the same time, the bond distance of C^1-C^2 increases along with the reaction process, implying the breakage of the three-membered ring involving C^1C^2N.
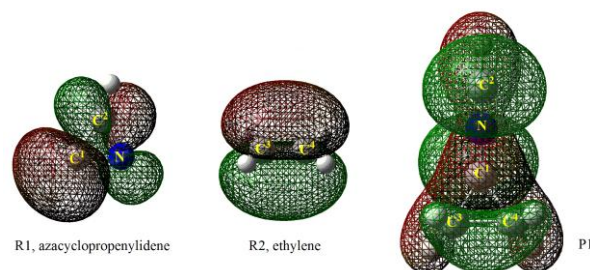
Fig. 4. Calculated HOMO orbitals for azacyclopropenylidene, ethylene, and P1.

In P1, the C^2 adopts sp^2 hybridization, it has a pair of lone electrons, making the P1 exhibit a carbene character. Therefore, P1 is very active, it is not only the product of pathway (I), but also the reactant of pathway (III). In the following reaction process, P1 can further react with ethylene to form the product P3.
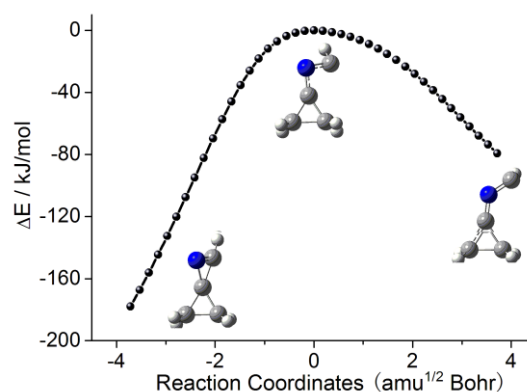
Fig. 5. IRC of TS1 and geometry evolution.
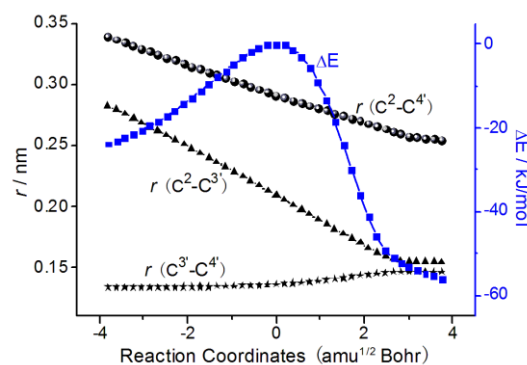
Fig. 6. Selected bond lengths change along the reaction coordinates on the basis of the IRC of TS3.

Pathway (II): formation of an allene compound P2

As the common intermediate of pathway (I) and (II), IMa can transform to P2 *via* steps (2a) and (2b).

The reaction step (2a) is a hydrogen transfer process from C^2 to the adjacent N, resulting in the conversion of IMa into IM2a *via* TS2a. Here, the calculated barrier is 276.4 kJ/mol and the unique imaginary frequency of TS2a is 1464i cm^{-1}. In detail, as shown in Fig. 1, the distance of C^2-H^1 in TS2a is elongated to 0.1259 nm, and the distance of N-H^1 reaches 0.1234 nm, which indicates that the H^1 atom can be transferred from C^2 to N.

Similar to the C^1C^2N ring in IMa, the C^1C^2N ring in IM2a can be opened at its weaker bond. Through the break of the C^1-N bond, IM2a can be converted to P2 *via* TS2b, where the barrier is 139.0 kJ/mol. The calculated imaginary frequency of transition state TS2b is 921i cm^{-1}.

In P2, the bond length of C^1-C^2 is 0.1295 nm, which falls in the range of the intermediate between C=C and C≡C bond length. Analogously, the bond length of C^2-N (0.1242 nm) lies between those of the C=N and C≡N bonds. The three atoms C^1, C^2, and N are approaching the same line ($\angle C^1C^2N$ is 171.2°). Therefore, P2 is an allene structure. Along the reaction profile, P2 is exothermic with a value of 229.0 kJ/mol compared with that of the reactants.

Pathway (III): formation of a bicyclic compound P3

As mentioned earlier, P1 exhibits a carbene character; it can further react with ethylene to form the product P3, which is named as the pathway (III). The geometric parameters for the species involved in the pathway (III) are displayed in Fig. 1. The calculated relative energies for the available stationary points are summarized in Table 1.

As shown in Fig. 1, in TS3, the distance of C^2-$C^{3'}$ and C^2-$C^{4'}$ is 0.2093 and 0.2913 nm, respectively. The distance of $C^{3'}$-$C^{4'}$ in the R2' fragment (0.1364 nm) is by 0.0025 nm longer than that in the isolated R2' molecule. Thus, in the transition state TS3, two new bonds of C^2-$C^{3'}$ and C^2-$C^{4'}$ are formed and the $C^{3'}$-$C^{4'}$ bond is simultaneously transformed from double bond to single bond. As shown in Fig. 6, those changes can be further validated by IRC calculations on the basis of TS3. Furthermore, similar with the explanation of the R1 reaction with ethylene, the HOMOs of P1 and ethylene are displayed in Fig. 4. Along the reaction profile, P3 is the important stable species, which is exothermic with a value of 203.5 kJ/mol compared with that of the reactants.
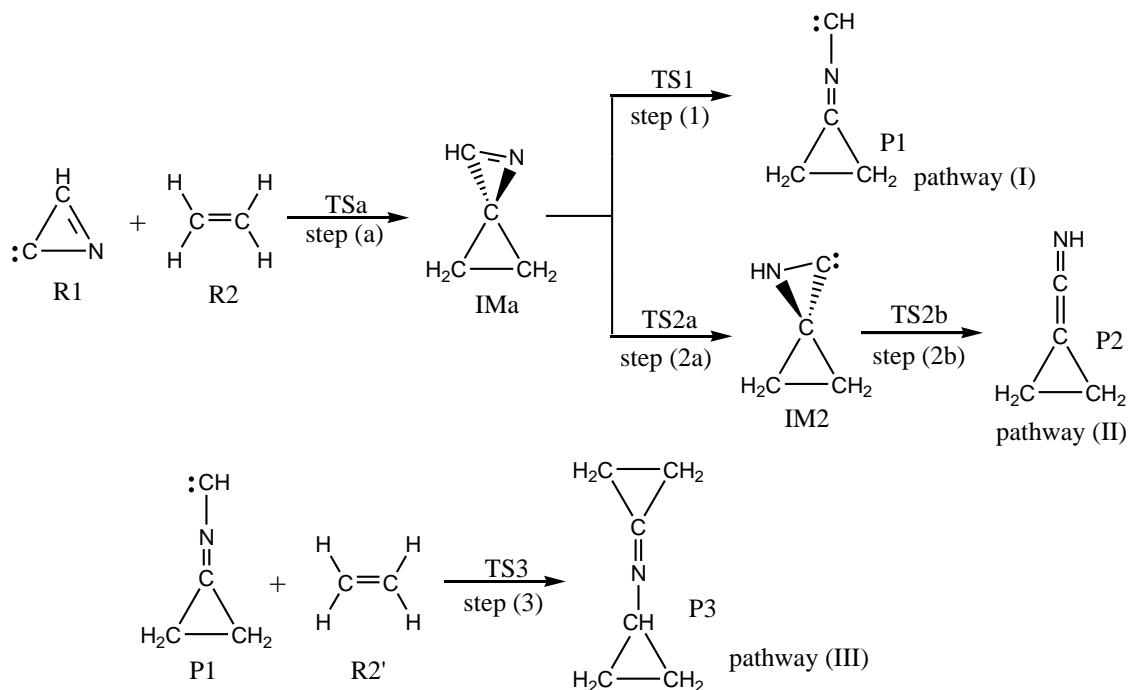
Scheme 1. The proposed three pathways for the reaction between azacyclopropenylidene and ethylene

Table 1. The calculated relative energy (in kJ/mol) with respect to the isolated reactants

Pathways	Relative Energies			
Pathway (I)	TSa	IMa	TS1	P1
	51.7	-173.5	73.9	-101.7
Pathway (II)	TS2a	IM2a	TS2b	P2
	102.9	-28.7	110.3	-229.0
Pathway (III)	TS3	P3		
	30.7	-203.5		

CONCLUSIONS

The cycloaddition reaction between azacyclopropenylidene and ethylene has three competitive pathways (I), (II), and (III); the corresponding products are: carbene compound P1, allene compound P2, and bicyclic compound P3, respectively. On the basis of the potential energy surface obtained with the MP2/6-311+G* method, it can be predicted that pathway (III) is the competitive dominant channel. The pathway (III) consists of three steps: (1) the two reactants (azacyclopropenylidene and ethylene) first form a spiro intermediate IMa *via* transition state TSa with energy barrier of 51.7 kJ/mol; (2) IMa isomerizes to a carbene compound P1 *via* transition state TS1a with an energy barrier of 247.4 kJ/mol; (3) P1 further reacts with ethylene (R2') to form a bicyclic compound P3 *via* transition state TS3 with an energy barrier of 30.7 kJ/mol. From the thermodynamic viewpoint, P3 is the important product, with energy lower by 203.5 kJ/mol than that of the reactants.

REFERENCES

1. R. A. Bernheim, R. J. Kempf, P. W. Humer, P. S. Skell, *J. Chem. Phys.,* **41**, 1156 (1964).
2. R. A. Bernheim, R. J. Kempf, J. V. Gramas, P. S. Skell, *J. Chem. Phys.*, **43**, 196 (1965).
3. M. J. Travers, M. C. McCarthy, P. Kalmus, C. A. Gottlieb, P. Thaddeus, *Astrophys. J. Lett.*, **469**, L65 (1996).
4. M. B. Bell, L. W. Avery, J. M. MacLeod, H. E. Matthews, *Astrophys. J.*, **400**, 551 (1992).
5. M. B. Bell, P. A. Feldman, L. W. Avery, *Astrophys. J.*, **396**, 643 (1992).
6. M. B. Bell, H. E. Matthews, *Astrophys. J.*, **291**, L63 (1985).
7. N. W. Broten, T. Oka, L. W. Avery, J. M. MacLeod, H. W. Kroto, *Astrophys. J.*, **223**, L105 (1978)..
8. C. A. Olano, C. M. Walmsley, T. L. Wilson, *Astron. Astrophys.*, **196**, 194 (1988).
9. I. Couturier-Tamburelli, N. Piétri, C. Crépin, M. Turowski, J.-C. Guillemin, R. Kołos, *J. Chem. Phys.*, **140**, 044329 (2014).
10. R. A. Bernheim, R. J. Kempf, J. V. Gramas, P. S. Skell, *J. Chem. Phys.*, **43**, 196 (1965).
11. A. Dendramis, G. E. Leroi, *J. Chem. Phys.,* **66**, 4334 (1977).
12. M. Guélin, J. Cernicharo, *Astron. Astrophys.*, **244**, L21 (1991).
13. D. McGonagle, W. M. Irvine, *Astron. Astrophys.*, **310**, 970 (1996).
14. M. C. McCarthy, C. A. Gottlieb, A. L. Cooksy, P. Thaddeus, *J. Chem. Phys.*, **103**, 7779 (1995).
15. N. Goldberg, A. Fiedler, H. Schwarz, *J. Phys. Chem.,* **99**, 15327 (1995).
16. K. Aoki, S. Ikuta, O. Nomura, *J. Chem. Phys.*, **99**, 3809 (1993).
17. F. Sun, A. Kosterev, G. Scott, V. Litosh, R. F. Curl, *J. Chem. Phys.*, **109**, 8851 (1998).
18. P. Y. Hung, F. Sun, N. T. Hunt, L. A. Burns, R. F. Curl, *J. Chem. Phys.*, **115**, 9331 (2001).
19. J. E. Rice, H. F. Schaefer, *J. Chem. Phys.*, **86**, 7051 (1987).
20. E. T. Seidl, H. F. Schaefer, *J. Chem. Phys.*, **96**, 4449 (1992).
21. P. Sung-Woo, L. Sungyul, *Bull. Korean Chem. Soc.*, **23**, 1553 (2002).
22. M. Z. Kassaee, S. M. Musavi, N. Jalalimaesh, *J. Theor. Comput. Chem.*, **7**, 367 (2008).
23. M. Z. Kassaee, M. Ghambarian, S. M. Musavi, *Heteroatom Chem.*, **19**, 377 (2008).
24. K. Jacek, *J. Phys. Chem. A,* **107**, 4717 (2003).
25. N. Inostroza, X. C. Huang, J. L. Timothy, J. Chem. Phys., **135**, 244310 (2011).
26. G. Maier, H. P. Reisenauer, K. Rademacher, *Chem. Eur. J.*, **4**, 1957 (1998).
27. N. Inostroza, R. C. Fortenberry, X. C. Huang, J. L. Timothy, *Astrophys. J.*, **778**, 1 (2013).
28. G. Maier, A. Bothur, J. Eckwert, H. P. Reisenauer, *Chem. Eur. J.*, **4**, 1964 (1998).

29. N. Balucani, M. Alagia, L. Cartechini, P. Casavecchia, G. G. Volpi, K. Sato, T. Takayanagi, Y. Kurosaki, *J. Am. Chem. Soc.*, **122**, 4443 (2000).
30. M. R. Nimlos, G. Davico, C. M. Geise, P. G. Wenthold, W. C. Lineberger, S. J. Blanksby, C. M. Hadad, G. A. Petersson, G. B. Ellison, *J. Chem. Phys.*, **117**, 4323 (2002).
31. X. J. Tan, W. H. Wang, Y. Jing, F. Wang, P. Li, *Monatsh. Chem.*, **145**, 1 (2014).
32. X. J. Tan, W. H. Wang, Q. Sun, Y. Jing, P. Li, *J. Mol. Model.*, **20**, 2088 (2014).
33. M. Head-Gordon, J. A. Pople, M. J. Frisch, *Chem. Phys. Lett.*, **153**, 503 (1988).
34. M. J. Frisch, G. W. Trucks, H. B. Schlegel, G. E. Scu_ seria, M. A. Robb, J. R. Cheeseman, V. G. Zakrzewski, J. A. Montgomery, R. E. Stratmann, Jr., J. C. Burant, S. Dapprich, J. M. Millam, A. D. Daniels, K. N. Kudin, M. C. Strain, O. Farkas, J. Tomasi, V. Barone, M. Cossi, R. Cammi, B. Mennucci, C. Pomelli, C. Adamo, S. Clifford, J. Ochterski, G. A. Petersson, P. Y. Ayala, Q. Cui, K. Morokuma, D. K. Malick, A. D. Rabuck, K. Raghavachari, J. B. Foresman, J. Cioslowski, J. V. Ortiz, A. G. Baboul, B. B. Stefanov, G. Liu, A. Liashenko, P. Piskorz, I. Komaromi, R.Gomperts, R. L. Martin, D. J. Fox, T. Keith, M. A. Al_Laham, M. A. Peng, A. Nanayakkara, C. Gonzalez, C. Challacombe, P. M. W. Gill, B. Johnson, W. Chen, M. W. Wong, J. L. Andres, C. Gonzalez, M. Head_Gordon, E. S. Replogle, J. A. Pople, Gaussian 98, Revision A.9, Gaussian Inc., Pittsburgh, PA, 1998.
35. I. Fleming, Frontier orbitals and organic chemical reactions. Wiley: London, 1976.

ТЕОРЕТИЧНО ИЗСЛЕДВАНЕ НА МЕХАНИЗМА НА ЦИКЛИЧНО ПРИСЪЕДИНЯВАНЕ МЕЖДУ АЗА-ЦИКЛОПРОПЕНИЛИДЕН И ЕТИЛЕН

С. Тан[1], У. Уанг[2], П. Ли[2]*

[1]*Колеж по биологически науки и технологии, Университет в Джинан, Шандонг. Китайска НР*
[2]*Училище по химия и химично инженерство, Университет в Куфу, Шандонг, Китайска НР*

(Резюме)

Системно е изследван механизма на циклично присъединяване между аза-циклопропенилиден и етилен с помощта на пертурбационната теория на Møller-Plesset от втори порядък(MP2). Така се постига по-добро разбиране на реактивоспособността на аза-циклопропенилидена с ненаситени съединения (етилен). Направени са геометрична оптимизация и вибрационен анализ за определянето на стационарните точки на повърхността на потенциалната енергия на системата. От профилите на потенциалната енергия се предсказва, че за реакцията на циклично присъединяване има три конкурентни маршрута: (I) дву-етапна реакция с образуване на карбеново съединение P1; (II) образуване на аленово съединение P2 в два етапа от двата реагента; (III) реакция с образуване на стабилно би-циклично съединение P3 след образуване на съединението P1.

Nano-BBr₃.SiO₂: a novel highly efficient heterogeneous catalyst for the one-pot synthesis of 3,4-dihydropyrimidin-2-(1H)-one derivatives

F. Hatamjafari*

Department of Chemistry, Faculty of Science, Islamic Azad University-Tonekabon Branch, P.O.Box 46841-61167, Tonekabon, I. R. of Iran.

This article describes a simple protocol for the efficient synthesis of 3,4-dihydropyrimidin-2(1H)-one derivatives using aromatic aldehydes, ethyl acetoacetate and urea in the presence of nano-BBr₃.SiO₂ as a catalyst. The structural features of the synthesized compounds were characterized by m.p., IR, MS, ^{1}H NMR, ^{13}C NMR, and CHN elemental analysis. We synthesized nano-BBr₃.SiO₂ for the first time as a nanocatalyst and characterized it by XRD, SEM and TEM techniques. High yields, mild conditions, easy availability, reusability, and green chemistry were some advantages of using this catalyst.

INTRODUCTION

It has been reported that 3,4-dihydropyrimidin-2(1H)-ones (DHPMs) possess many pharmacological qualities, such as antiviral, antibacterial, and antihypertensive activity, and are efficacious as calcium channel modulators and for multi drug resistance reversal [1-2]. The biological activity of some recently isolated alkaloids has also been attributed to the 3,4-dihydropyrimidin-2(1H)-ones moiety [3].

Biginelli (1893) reported that the first stage in the synthesis of DHPMs was the one-pot condensation of aldehyde, diketone and urea under acidic conditions. This method produces low yields, particularly in the case of some substituted aldehydes [4]. Various catalysts have been used to increase the efficiency of the Biginelli reaction. As is known, the Biginelli reaction has low product yields.

Recently, several improved methodologies have been developed such as microwave irradiation [5], ultrasound irradiation [6,7], use of ionic liquids [8], lanthanide triflate [9], silicasulfuric acid [10], HCOOH [11], copper (II) sulfamate [12], potassium tert-butoxide (t-BuOK) [13], ammonium dihydrogen phosphate [14], silica-gel [15], cyanuric chloride [16], TiO₂ [17], KHSO₄ [18,19], silica triflate [20], Li(glycine)(CF₃SO₃) [21], Brønsted acidic ionic liquid [Btto][*p*-TSA] [22], glutamic acid [23], use of solvent-free conditions [24], bismuth(III) sulfate trihydrate [25] and others. Some of these methods are expensive, environmentally unfriendly, produce low yields, and are incompatible with other functional groups, involving labor-intensive product isolation procedures. Therefore, a simple, efficient, and reusable procedure for one-pot dihydropyrimidinone synthesis under mild conditions is required.

In recent years, the use of eco-friendly, industrially applicable, and reusable green catalysts has been a matter of concern and interest. We define green chemistry as a set of principles that reduce or eliminate the use or generation of dangerous chemicals. This is part of our recent set of studies relating to the development of new methods in the synthesis of heterocyclic compounds [23-25].

Recently, nanoparticles have emerged as nanocatalysts alternative to conventional materials in various fields of chemistry. Nanoparticles are known to be promising heterogeneous catalysts in various organic reactions. Nanoparticles have a larger volume ratio for improved productivity, selectivity and performance of catalytic processes. The suitable choice of nanoparticles to the reaction produces less waste and less impurities, which leads to a more secure way and reduces environmental effect.

As an example, PbO nanoparticles have been studied as catalysts in organic reactions, including reactions such as paal-knorr [26], oxidative coupling of methane [27], synthesis of tetrahydrobenzopyrans and benzylidene malononitriles [28]. The catalyst's properties include: high yields, short reaction time, one-pot procedure, experimental simplicity. This prompted us to use nano-BBr₃.SiO₂ nanoparticles as a catalyst.

* To whom all correspondence should be sent:
E-mail: f_hatamjafari@tonekaboniau.ac.ir,
hatamjafari@yahoo.com

Here, Biginelli's reaction between benzaldehyde, ethylacetoacetate and urea to produce 3,4-dihydropyrimidin-2-(1H)-one derivatives using nano-BBr₃.SiO₂ as a nanocatalyst, is reported. The solid catalyst was synthesized by the reaction of nano-SiO₂ with BBr₃ by a hydrothermal method and was characterized by XRD, SEM and TEM techniques (Scheme 1).

EXPERIMENTAL

General Remarks

All chemicals were obtained from Merck or Fluka. Melting points were measured on an Electrothermal 9100 apparatus. Silica gel SILG/UV 254 plates were used for TLC. IR spectra were measured using a Shimadzu IR-470 spectrophotometer. ^{1}H NMR and ^{13}C NMR spectra were determined on a Bruker 300 DRX AVANCE instrument at 300 and 75 MHz, respectively. The elemental analyses (C, H, and N) were performed on a Carlo ERBA Model EA 1108 analyzer. Mass spectra were recorded on a Varian-Saturn 2000 gas chromatograph–mass spectrometer (MS). Scanning electron microscopy (SEM) of the nano-particles was performed on a VEGA/TESCAN scanning electron microscope. Transmission electron microscopy (TEM) was performed by Philips CM10-HT100KV. The X-ray diffraction (XRD) patterns of the materials were recorded by employing a Philips Xpert MPD diffractometer equipped with a Cu Kα anode (λ = 1.54 Å) in the 2θ range from 5 to 80°.

Preparation of nano-BBr₃.SiO₂

The catalyst was prepared by stirring a mixture of BBr₃ (1 ml) and nano silica gel (20 nm, 1 g) in 5 ml of chloroform for 1 h at room temperature. The slurry was filtered and washed with chloroform. The obtained solid (nano-BBr₃.SiO₂) was dried at ambient temperature for 2 h and then stored in a dry container.

Typical procedure for the synthesis of 3,4-dihydropyrimidinones(5a-j)

A mixture of aromaticaldehyde (1 mmol), ethyl acetoacetate (1 mmol), urea (1.2 mmol), nano-BBr₃.SiO₂ (0.05 g) and 10 ml of ethanol was refluxed for 1 h. The progress of reaction was monitored by TLC. After finishing, the reaction mixture was poured into crushed ice while stirring. The crude product was filtered, washed with cold water, dried, and recrystallized from ethanol 95% to give the pure products (5a-j) (91%–97%). All compounds were characterized by m.p., IR, CHN, MS, ^{1}H NMR, and ^{13}C NMR spectroscopy. The structures of all synthesized compounds (5a-j) are depicted in Table 2.

5–(Ethoxycarbonyl)–6–methyl–4–phenyl–3,4–dihydropyrimidin–2(1H)–one **(5a).** White solid; yield 95%; mp 203–205 °C; IR (KBr, $v$max, cm⁻¹): 3255, 3110, 3005, 1720, 1688, 1636; ^{1}H NMR (300.13 MHz, DMSO-d₆, δ/ppm): 1.10(t, *J*=7.10 Hz, 3H, CH₃); 2.26(s, 3H, CH₃); 3.88(q, *J*= 7.10 Hz, 2H, CH₂); 5.42(s, H, CH); 7.32-7.54(m, 5H, Ar-H); 7.72(s, H, NH); 9.24(s, H, NH); ^{13}C NMR (75 MHz, DMSO-d₆, δ/ppm): 18.30, 19.00, 53.42, 58.63, 103.32, 111.27, 115.15, 124.54, 130.41, 148.24, 158.34, 166.71; MS(ESI): *m/z* 261 (M+H)⁺; Anal. Calc. for C₁₄H₁₆N₂O₃: C, 64.62; H, 6.15; N, 10.72; found: C, 64.50; H, 6.14; N, 10.68.

5–(Ethoxycarbonyl)–4–(4-chlorophenyl)–6–methyl–3,4–dihydropyrimidin–2(1H)–one **(5b).** White solid; yield 95%; mp 213–215°C; IR (KBr, $v$max, cm⁻¹): 3253, 3125, 3000, 1708, 1648, 1611; ^{1}H NMR (300.13 MHz, DMSO- d₆, δ/ppm): 1.18(t, *J*=7.20 Hz, 3H, CH₃); 2.21(s, 3H, CH₃); 3.63(q, *J*=7.20 Hz, 2H, CH₂); 5.27(s, H, CH); 7.14-7.28(m, 4H, Ar–H); 7.77(S, H, NH); 9.23(s, H, NH); ^{13}C NMR (75 MHz, DMSO-d₆, δ/ppm): 16.47, 19.34, 57.06, 60.77, 101.02, 120.12, 133.42, 144.23, 153.64, 156.80, 158.66, 165.48; MS(ESI): *m/z* 295 (M+H)⁺; Anal. Calc. for C₁₄H₁₅ClN₂O₃: C, 57.12; H, 5.08; N, 9.55; found: C, 57.02; H, 5.03; N, 9.56.
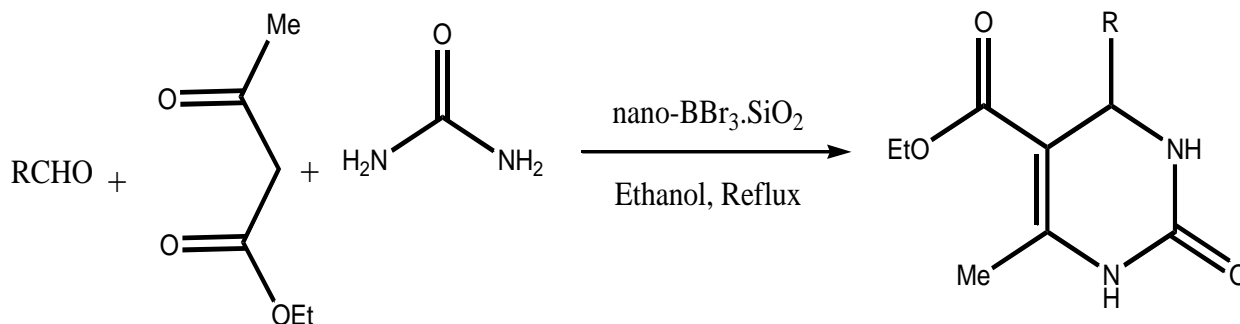
Scheme 1. Nano-BBr₃.SiO₂-catalyzed Biginelli reaction.

5–(Ethoxycarbonyl)–4–(4-hydroxyphenyl)–6–methyl–3,4–dihydropyrimidin–2(1H)–one **(5c).** White solid; yield 91%; mp 231-233°C; IR (KBr, v_{max}, cm^{-1}): 3442, 3345, 3107, 1710, 1680, 1629; ^{1}H NMR (300.13 MHz, DMSO-d₆, δ/ppm): 1.22 (t, 3H, *J*=7.50 Hz, CH₃), 2.45 (s, 3H, CH₃), 4.23 (q, 2H, *J*=7.50 Hz, CH₂), 6.10 (s, H, CH), 6.77 (s, 1H, OH), 7.15-7.80 (m, 4H, Ar–H), 7.89 (s, 1H, NH), 8.26 (d, 2H, *J*=8.2, Ar-H), 9.14 (s, 1H, NH); ^{13}C NMR (75 MHz, DMSO-d₆, δ/ppm): 15.2, 19.15, 54.31, 59.75, 101.90, 122.5, 132.23, 140.5, 155.66, 155.88, 158.5, 167.75; MS(ESI): *m/z* 277 (M+H)$^+$; Anal. Calc. for C₁₄H₁₅N₃O₅: C, 55.06; H, 4.92; N, 13.74; found: C, 55.15; H, 4.90; N, 13.70.

5–(Ethoxycarbonyl)–4–(4–methoxyphenyl)–6–methyl–3,4–dihydropyrimidin–2(1H)–one **(5d).** White solid; yield 94%; mp 202–203°C; IR (KBr, v_{max}, cm^{-1}): 3241, 3122, 3010, 1703, 1647, 1517; ^{1}H NMR (300.13 MHz, DMSO-d₆, δ/ppm): 1.07(t, *J*=7.08 Hz, 3H, CH₃); 2.23(s, 3H, CH₃); 3.89(s, 3H, CH₃); 3.97(q, *J*=7.08 Hz, 2H, CH₂); 5.09(s, H, CH); 7.14-7.64(m, 4H, Ar–H); 7.66(s, H, NH); 9.15(s, H, NH); ^{13}C NMR (75 MHz, DMSO-d₆, δ/ppm): 14.11, 20.45, 57.73, 58.40, 60.90, 101.37, 114.03, 125.38, 136.76, 148.22, 158.25, 159.75, 164.27; MS(ESI): *m/z* 291 (M+H)$^+$; Anal. Calc. for C₁₅H₁₈N₂O₄: C, 62.06; H, 6.25; N, 9.65; found: C, 61.98; H, 6.20; N, 9.59.

5–(Ethoxycarbonyl)–4–(3-bromophenyl)–6–methyl–3,4–dihydropyrimidin–2(1H)–one **(5e).** White solid; yield 95%; mp 183–185°C; IR (KBr, v_{max}, cm^{-1}): 3319, 3211, 3015, 1695, 1634, 1544; ^{1}H NMR (300.13 MHz, DMSO- d₆, δ/ppm): 1.08 (t, *J*=7.11 Hz, 3H, CH₃), 2.18 (s, 3H, CH₃), 3.77 (q, *J*=7.11 Hz, 2H, CH₂), 5.67 (s, H, CH), 7.14-7.25 (m, 4H, Ar-H), 7.66 (s, 1H, NH), 9.31 (s, 1H, NH); ^{13}C NMR (75 MHz, DMSO-d₆, δ/ppm): 15.11, 18.94, 56.56, 61.35, 100.68, 122.44, 127.56, 128.50, 129.07, 135.22, 142.55, 154.34, 160.77, 165.55; MS(ESI): *m/z* 340 (M+H)$^+$; Anal. Calc. for C₁₄H₁₅ClN₂O₃: C, 57.14; H, 5.10; N, 9.50; found: C, 57.09; H, 5.05; N, 9.45.

5-Ethoxycarbonyl-4-(2-hydroxyphenyl)-6-methyl-3,4-dihydropyrimidin-2(1H)-one **(5f).** White solid; yield 91%; mp 209–211 °C; IR (KBr, v_{max}, cm^{-1}): 3456, 3232, 2883, 1712, 1641, 1594 cm^{-1}: ^{1}H NMR (300.13 MHz, DMSO- d₆, δ/ppm): 1.15 (t, *J*=7.5 Hz , 3H, CH₃), 2.21 (s, 3H, CH₃), 3.82 (q, *J*=7.5, Hz, 2H, CH₂), 5.21 (s, H, CH), 6.10 (S, 1H, Ar-OH), 6.8-7.40 (m, 4H, Ar-H), 8.33 (s,1H, NH), 9.25 (s, 1H, NH); ^{13}C NMR (75 MHz, DMSO-d₆, δ/ppm): 17.22, 19.38, 55.46, 62.42, 102.33, 121.32, 125.23, 126.92, 127.28, 130.63, 139.71, 148.55, 161.85, 163.36; MS(ESI): *m/z* 277 (M+H)$^+$; Anal.

Calcd for C₁₄H₁₆N₂O₄: C, 60.86; H, 5.80; N, 10.14; Found: C, 60.80; H, 5.72; N, 10.12.

5-Ethoxycarbonyl-4-(2-chlorophenyl)-6-methyl-3,4-dihydropyrimidin-2(1H)-one **(5g).** White solid; yield 93%; mp 204–206 °C; IR (KBr, v_{max}, cm^{-1}): 3433, 3211, 2890, 1715, 1625, 1587 cm^{-1}: ^{1}H NMR (300.13 MHz, DMSO- d₆, δ/ppm): 1.07 (t, *J*=7.18 Hz , 3H, CH₃), 2.24 (s, 3H, CH₃), 3.75 (q, *J*=7.2, Hz, 2H, CH₂), 6.02 (s, H, CH), 6.9-7.42 (m, 4H, Ar-H), 7.98 (s, 1H, NH), 8.88 (s, 1H, NH); ^{13}C NMR (75 MHz, DMSO-d₆, δ/ppm): 16.56, 17.34, 56.43, 60.65, 103.38, 123.43, 126.66, 127.70, 128.67, 132.77, 143.36, 150.14, 160.65, 166.72; MS(ESI): *m/z* 295 (M+H)$^+$; Anal. Calcd for C₁₄H₁₅ClN₂O₃: C, 57.14; H, 5.10; N, 9.52; Found: C, 56.88; H, 5.00; N, 9.46.

5-Ethoxycarbonyl-4-(3-fluorophenyl)-6-methyl-3,4-dihydropyrimidin-2(1H)-one **(5h).** White solid; yield 95%; mp 182–184°C; IR (KBr, v_{max}, cm^{-1}): 3423, 3242, 2880, 1722, 1656, 1605 cm^{-1}: ^{1}H NMR (300.13 MHz, DMSO- d₆, δ/ppm): 1.14 (t, *J*=7.4 Hz , 3H, CH₃), 2.15 (s, 3H, CH₃), 3.71 (q, *J*=7.4, Hz, 2H, CH₂), 5.78 (s, H, CH), 6.93-7.72 (m, 4H, Ar-H), 7.92 (s, 1H, NH), 9.10 (s, 1H, NH)); ^{13}C NMR (75 MHz, DMSO-d₆, δ/ppm): 16.33, 18.78, 57.15, 60.24, 102.56, 121.23, 125.54, 126.87, 127.13, 130.48, 140.79, 156.36, 163.62, 165.47; MS(ESI): *m/z* 279 (M+H)$^+$; Anal. Calcd for C₁₄H₁₅FN₂O₃: C, 60.43; H, 5.39; N, 10.07; Found: C, 60.30; H, 5.28; N, 10.10.

5-Ethoxycarbonyl-4-(4-fluorophenyl)-6-methyl-3,4-dihydropyrimidin-2(1H)-one **(5i).** White solid; yield 92%; mp 185–188°C; IR (KBr, v_{max}, cm^{-1}): 3420, 3217, 2874, 1708, 1635, 1580 cm^{-1}: ^{1}H NMR (300.13 MHz, DMSO- d₆, δ/ppm): 1.16 (t, *J*=7.12 Hz , 3H, CH₃), 2.34 (s, 3H, CH₃), 3.83 (q, *J*=7.12 Hz, 2H, CH₂), 6.05 (s, H, CH), 6.85-7.40 (m, 4H, Ar-H), 8.10 (s, 1H, NH), 9.03 (s, 1H, NH); ^{13}C NMR (75 MHz, DMSO-d₆, δ/ppm): 18.62, 18.14, 54.46, 64.67, 102.85, 123.75, 128.23, 138.11, 143.91, 154.46, 159.35, 167.42; MS(ESI): *m/z* 279 (M+H)$^+$; Anal. Calcd for C₁₄H₁₅FN₂O₃: C, 60.43; H, 5.39; N, 10.07; Found: C, 60.33; H, 5.30; N, 10.04.

5-Ethoxycarbonyl-4-(4-tolyl)-6-methyl-3,4-dihydropyrimidin-2(1H)-one **(5j).** White solid; yield 97%; mp 250–252 °C; IR (KBr, v_{max}, cm^{-1}): 3227, 3220, 2982, 1695, 1666, 1582, cm^{-1}; ^{1}H NMR (300.13 MHz, DMSO- d₆, δ/ppm): 1.11 (t, *J*=7.25 Hz , 3H, CH₃), 1.92 (s, 3H, CH₃), 2.42 (s, 3H, CH₃), 3.65 (q, *J*=7.25 Hz, 2H, CH₂), 6.14 (s, H, CH), 7.05-7.68 (m, 4H, Ar-H), 8.38 (s, 1H, NH), 9.20 (s, 1H, NH);); ^{13}C NMR (75 MHz, DMSO-d₆, δ/ppm): 18.78, 19.37, 23.1, 59.04, 64.91, 105.15, 1

22.37, 125.48, 128.57, 138.44, 152.19, 160.48, 164.38; MS(ESI): *m/z* 275 (M+H)$^+$; Anal. Calcd. for $C_{15}H_{18}N_2O_3$: C, 65.68; H, 6.61; N, 10.21; Found C, 65.60; H, 6.55; N, 10.15.

RESULTS AND DISCUSSION

The development of new nanocatalysts has emerged as an available field for research and innovation. Nanotechnology enhances catalytic activity and the inexpensive nanocatalysts replace expensive catalysts. The advantage of nano-$BBr_3.SiO_2$ over bulk catalysts may be attributed to the higher surface area of nanocatalysts and the increased catalytic activity. This is assumed to be due to morphological differences, as shown in the SEM and TEM images and the XRD pattern. According to the SEM and TEM images and the XRD pattern, the particle size of nano-$BBr_3.SiO_2$ is 40 nm (Figure 1).

Nano-$BBr_3.SiO_2$ can be used as a catalyst in the synthesis of organic compounds. Features of this catalyst that are of interest include: easy separation, environmental friendliness, reusability, cleanness, and economy. The mechanism of formation of dihydropyrimidines using nano-$BBr_3.SiO_2$ as a catalyst is shown in Scheme. 2. Most of the catalysts used for preparation of dihydropyrimidinones are halogen-containing Lewis acids. The present results indicate that the halide present in the catalyst may be playing a crucial role in these transformations and may be the cause of the large number of publications which have appeared recently on the synthesis of dihydropyrimidinones by modified Biginelli reactions using halide catalysts. Nano-$BBr_3.SiO_2$ acts as a Lewis base by interaction with the electrophilic carbon of the aldehyde.
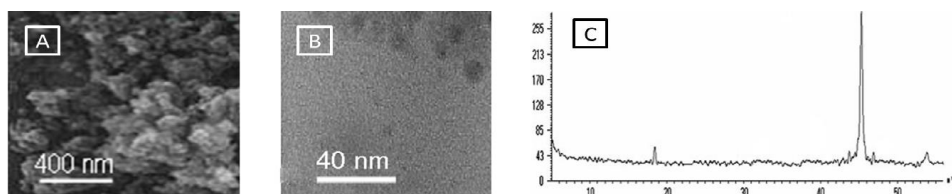
Fig 1. SEM (A) image, TEM (B) image and XRD (C) pattern of nano-$BBr_3.SiO_2$.
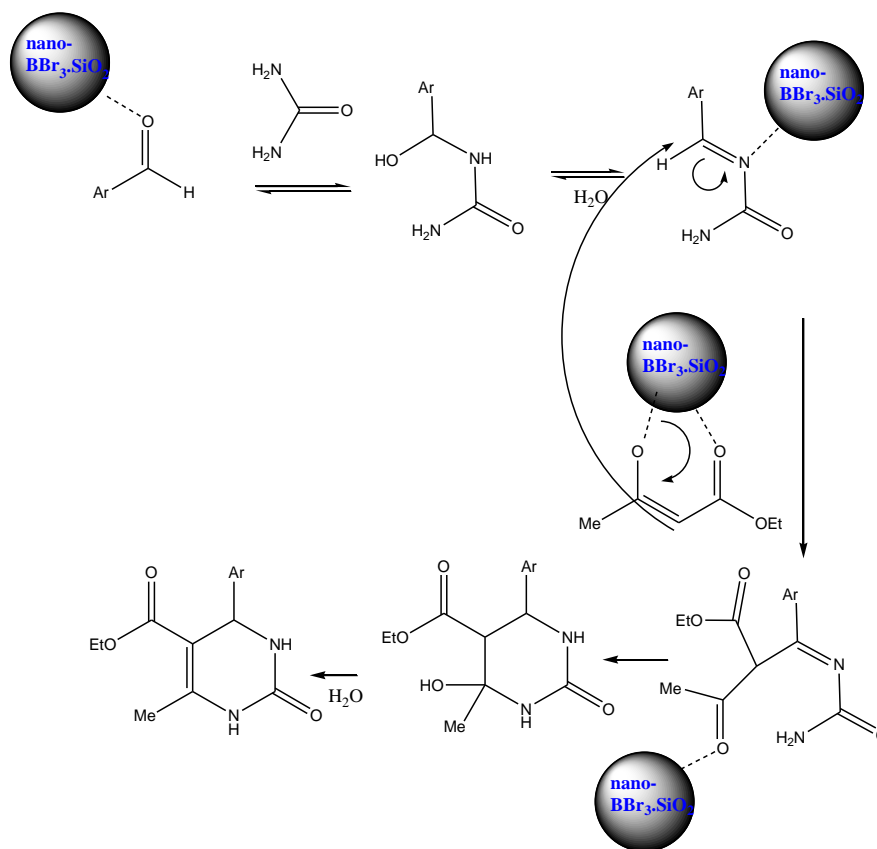
Scheme 2. Mechanism of the synthesis of 3,4-dihydropyrimidin-2-(1H)-one catalyzed by nano-$BBr_3.SiO_2$.

Dihydropyrimidines exhibit a wide range of biological activities. We are interested in studying the mechanism of the Biginelli reaction in order to develop a simple method for the synthesis of DHPMs. Urea is not sufficiently nucleophilic to react directly with aldehydes. However, nano-$BBr_3.SiO_2$ as a Lewis acid causes the reaction to occur by coordination at the carbonyl oxygen, activating the carbonyl group to nucleophilic attack.

We started our study of one-pot, three-component Biginelli condensation using nano-$BBr_3.SiO_2$ as a catalyst (Scheme 2) and carrying out reactions using benzaldehyde, ethyl acetoacetate, and urea to create corresponding DHPM products. As the model reaction the synthesis of compound 5a was selected to determine suitable reaction conditions in the presence of nano-$BBr_3.SiO_2$ with various amounts of catalyst (Table 1). We found that yield was strongly affected by the amount of catalyst and the temperature. Best results were obtained (Entry 8) in the presence of 0.05 g catalyst under reflux conditions for 1 h (Table 1).

We have successfully synthesized many 3,4-dihydropyrimidin-2(1H)-one derivatives from aldehydes, ethyl acetoacetate and urea using nano-$BBr_3.SiO_2$. Several aromatic aldehydes were condensed with ethyl acetoacetate and urea as shown in Scheme. 1. These results are shown in Table 2. Nano-$BBr_3.SiO_2$ as a catalyst significantly increases the reaction rate and is easily separated and reused (Table 2). All reactions were monitored by TLC and carried forward to maximum atom utilization. All compounds were characterized using melting point, IR, ¹H NMR, ¹³C NMR, and CHN techniques. All of our results were in agreement with the cited literature. It was noted that aldehydes that had electron donating/withdrawing substituents reacted within the reaction time to give DHPMs with very good to excellent isolated yields.

The structures of products 5a–5j were characterized based on their ¹H and ¹³C NMR, IR and CHN data. The ¹H NMR spectrum of compound 5a in DMSO-d6 shows a singlet at 5.42 ppm, which is related to H-4, whereas the two separated methyl groups resonate at 1.10 (t, J=7.10 Hz, 3H, CH_3) and 2.26 (s, 3H, CH_3) ppm. In the ¹³C NMR spectrum of compound 5a, the peak at 58.63 ppm is related to C-4 (sp3), which confirms the formation of a product. The two different carbonyl groups resonate at 158.3 and 166.7 ppm. In the ¹H NMR spectra of 5a and 5b, H-4 resonates at 5.42 and 5.27 ppm, respectively.

Finally, the reusability of the nano-$BBr_3.SiO_2$ catalyst was investigated in subsequent reactions, using benzaldehyde, ethyl acetoacetate, and urea to afford the corresponding DHPM product 5a as a model reaction. Comparison of reaction conditions and product yield (5a) between previously reported methods and the present method is shown in Table 3. The catalyst was easily recovered by simple filtration after dilution of the reaction mixture with ethyl acetate and was reused after being vacuum dried. Nano-$BBr_3.SiO_2$ was reused for four runs without significant loss of activity (run 1: 87%; run 2: 84%; run 3: 80%; run 4: 75%).

Table 1. Nano-$BBr_3.SiO_2$ catalyzed synthesis of 5–(ethoxycarbonyl)–6–methyl–4–phenyl–3,4–dihydropyrimidin–2(1H)–one (1) at various temperatures and various amounts of the catalyst [a]

Entry	Catalyst (mol%)	Temp. (°C)	Yield (%)[b]
1	0.03	70	66
2	0.03	80	76
3	0.03	90	78
4	0.04	70	80
5	0.04	80	84
6	0.04	90	85
7	0.05	70	87
8	0.05	80	95
9	0.05	90	94
10	0.06	70	78
11	0.06	80	84
12	0.06	90	85
13	-	70	30
14	-	80	32
15	-	90	35
16	0.05	-	18

[a] Reaction conditions: benzaldehyde (1 mmol), ethyl acetoacetate (1 mmol), urea (1.2 mmol) and nano-$BBr_3.SiO_2$ as a catalyst for 1 h under reflux conditions;
[b] Isolated yield.

Table 2. Nano-BBr$_3$.SiO$_2$ catalyzed synthesis of 3,4-dihydropyrimidinone derivatives[a]

Entry	Product	RCHO	Yield (%)[b]	MP (°C) Found	MP (°C) Reported (Ref.)
1	5a	C$_6$H$_5$CHO	95	203–205	201–203[11]
2	5b	4-ClC$_6$H$_4$CHO	95	213–215	212-214[11]
3	5c	4-HOC$_6$H$_4$CHO	91	231-233	231-233[12]
4	5d	4-CH$_3$OC6H4CHO	94	202–203	203-204[11]
5	5e	3-BrC$_6$H$_4$CHO	95	183–185	182–184[12]
6	5f	2-HOC$_6$H$_4$CHO	91	209–211	210–212[30]
7	5g	2-ClC$_6$H$_4$CHO	93	204–206	206–208[29]
8	5h	3-FC$_6$H$_4$CHO	95	182–184	180-182[30]
9	5i	4-FC$_6$H$_4$CHO	92	185–188	186–188[30]
10	5j	4-CH$_3$C$_6$H$_4$CHO	97	250-252	49–251[31]

[a]Reaction conditions: aldehyde (1 mmol), β-ketoester (1 mmol), urea (1.2 mmol), nano-BBr$_3$.SiO$_2$ (0.05 g) under reflux conditions;

[b]Isolated yield.

Table 3. Comparison of reaction conditions and yield of product (1) of reported methods [32-35] *versus* the present method.

Entry	Catalyst	Condition	Time	Yield (%)
1	Methanesulfonic acid	Ethanol, reflux	60 min	95
2	P$_2$O$_5$	Ethanol, reflux	240 min	91
3	Chlorosulfonic acid	Solvent free, 60°C	30 min	93
4	P$_2$O$_5$/SiO$_2$	Solvent free, 85°C	120 min	95
5	ZnCl$_2$	Solvent free, 80°C	20 min	90
6	I$_2$	Solvent free, 90°C	15 min	86
7	CF$_3$COONH$_4$	Solvent free, 80°C	10 min	98
8	1:10 P$_2$O$_5$/MeSO$_3$H	Solvent free, r.t.	5 min	94
Present method	Nano-BBr$_3$.SiO$_2$	Ethanol, reflux	60 min	95

CONCLUSION

In conclusion, we have demonstrated a novel catalyst nano-BBr$_3$.SiO$_2$ for the synthesis of substituted dihydropyrimidinones. The advantages of this method using nano-BBr$_3$.SiO$_2$ include: high yields, reasonable time, one-pot procedure, experimental simplicity, environmental friendliness and easy separation with reuse of this catalyst.

REFERENCES

1. A. Debache, B. Boumoud, M. Amimour, A. Belfaitah, S. Rhouati, B. Carboni, *Tetrahedron Lett.*, **49**, 6119 (2008).
2. D. Shobha, M. A. Chari, A. Mano, S. T. Selvan, K. Mukkanti, A. Vinu. *Tetrahedron*, **65**, 10608 (2009).
3. S. Tu, F. Fang, C. Miao, H. Jiang, Y. Feng, D. Shi, X.S. Wang, *Tetrahedron Lett.*, **44**, 6153 (2003).
4. P. Biginelli, *Gazz. Chim. Ital.*, **23**, 360 (1893).
5. B. K. Banik, A. T. Reddy, A. Datta, C. Mukhopadhyay, *Tetrahedron Lett.*, **48**, 7392 (2007).
6. J. T. Li, J. F. Han, J. H. Yang, T. S. Li, *Ultrason. Sonochem.* **10**, 119 (2003).
7. A. N. Dadhania, V. K. Patel, D. K. Raval, *J. Braz. Chem. Soc.*, **22(3)**, 511 (2011).
8. J. J. Peng, Y. Q. Deng, *Tetrahedron Lett.*, **42**, 5917 (2001).
9. Y. Ma, C. Qian, L. Wang, M. Yang, *J. Org. Chem.*, **65**, 3864 (2000).
10. P. Salehi, M. Dabiri, M. A. Zolfigol, M.A.B. Fard, *Tetrahedron Lett.*, **44**, 2889 (2003).
11. J. Cheng, D. Y. Qi, *Chin. Chem. Lett.*, **18**, 647 (2007).
12. C. J. Liu, J. D. Wang, *Molecules*, **14**, 763 (2009).
13. D. Abdelmadjid, C. Louisa, C. Bertrand, B. Raouf, *The Open Organic Chemistry Journal*, **6**, 12 (2012).
14. R. Tayebee, N. Abdollahi, M. Ghadamgahi, *J. Chin. Chem. Society*, **60**, 1014 (2013).
15. S. Agarwal, U. Aware, A. Patil, et al. *Bulletin of Korean Chemical Society*, **33**, 377 (2012).
16. J. A. Kumar, C. Shanmugam, P. H. Babu, *Der Pharma Chemica*, **3**, 292 (2011).
17. M. Z. Kassaee, H. Masrouri, F. Movahedi, R. Mohammadi, *Helvetica Chimica Acta*, **93**, 261 (2010).
18. X. Caia, H. Guob, B. Xie, *Jordan Journal of Chemistry*, **6**, 17 (2011).
19. N. B. Reddy, U.M. Rao Kunda, C. S. Sundar, S. K. Nayak, S. Reddy, *Heterocyclic Communications*, **18,** 53 (2012).
20. F. Shirini, K. Marjani, H. Taherpour Nahzomi, *Arkivoc*, **I**, 51 (2007).

21. E. Abbaspour-Gilandeh, et al, *RSC Advances*. **4**, 54854 (2014).
22. C. Liu, et al, *Molecules*. **20**, 3811 (2015).
23. E. Abbasi, F. Hatamjafari, *Oriental Journal of Chemistry*, **29**, 731 (2013).
24. F. Hatamjafari, F. Germani Nezhad, *Orient. J. Chem.* **30,** 355 (2014).
25. F. Hatamjafari*, Organic Chemistry International,* Article ID 761209, 5 pages (2014).
26. S. K. Pasha, V. S. V. Satyanarayana, A. Sivakumar, K. Chidambaram, L. J. Kennedy, *Chin. Chem. Lett.* **22(8)**, 891 (2011).
27. W. Bytyn, M. Baerns, *Appl. Catal.* **28**, 199 (1986).
28. A. V. Borhade, B. K. Uphade, D. R. Tope, *J. Chem. Sci.* **125(3)**, 583 (2013).
29. H. N. Karade, M. Sathe, M. P. Kaushik, *Molecules*, **12**, 1341 (2007).
30. S. Tu, F. Fang, S. Zhu, T. Li, X. Zhang, Q. Zhuang, *Synlett.*, 537 (2004).
31. S. Tu, F. Fang, S. Zhu, T. Li, X. Zhang, Q. Zhuang, *J. Heterocyclic Chem.*, **41**, 253 (2004).
32. A. Borse, M. Patil, N. Patil, R. Shinde, *ISRN Organic Chemistry*, doi:10.5402/2012/415645 (2012).
33. S. Sheik Mansoor, S. Syed Shafi, S. Zaheer Ahmed, *Arabian Journal of Chemistry*, DOI:10.1016/j.arabjc. 09.018 (2011).
34. J. Safari, S. Gandomi-Ravandi, *Journal of Molecular Catalysis A: Chemical*, http://dx.doi.org/doi: 10.1016/j. molcata. 02.02 (2013).
35. H. Slimi, Y. Moussaoui, R. B. Salem, *Arabian Journal of Chemistry*, http://dx.doi.org/ 10.1016/j.arabjc.2011.06.010 (2011).

НАНО-BBr₃.SiO₂: НОВ ВИСОКОЕФЕКТИВЕН КАТАЛИЗАТОР ЗА ЕДНОСТАДИЙНА ХЕТЕРОГЕННА СИНТЕЗА НА ПРОИЗВОДНИ НА 3,4-ДИХИДРОПИРИМИДИН-2-(1H)-ОН

Ф. Хатамджафари

Департамент по химия, Научен факултет, Ислямски университет „Азад", клон Тонекабон, П.К. 46841-61167, Тонекабон, ИР Иран

(Резюме)

В тази статия се описва прост протокол за ефективна синтеза производни на 3,4-дихидропиримидин-2(1H)-он, използвайки ароматни алдехиди, етил ацет-ацетат и карбамид в присътствие на нано-BBr₃.SiO₂ като катализатор**.** Структурата на синтезираните съединения е охарактеризирана чрез точката на топене, ИЧ, МС, ¹Н ЯМР, ¹³С ЯМР and CHN-елементен анализ. Ние синтезирахме за първи път нано-BBr₃.SiO₂ като нано-катализатор и охарактеризирахме чрез XRD, SEM и ТЕМ-техниките. Високи добиви, меки условия, лесна достъпност, повторна употреба и „зелени" условия са някои от предимствата на използвания катализатор.

Removal of mercury from contaminated water by activated carbon produced from waste coal and biomass materials

I. G. Stoycheva[1]*, B.N. Petrova[1], B.G. Tsyntsarski[1], T.K. Budinova[1], N.V. Petrov[1], B. Nagel[2], U. Szeluga[2], S. Pusz[2], S. Chajkowska[2], B. Trzebicka[2]

[1]Lab. Chemistry of Solid Fuels, Institute of Organic Chemistry with Centre of Phytochemistry, Bulgarian Academy of Sciences, Acad.G.Bonchev Str., Block 9, 1113 Sofia Bulgaria
[2]Center of Polymer and Carbon Materials, Polish Academy of Sciences, M. Sklodowskiej-Curie 34, 41-819 Zabrze, Poland

Adsorption of mercury ions on activated carbons - oxidized and non-oxidized - prepared by hydro-carbonization from mixture of coal tar pitch and furfural, was investigated. The structure and surface properties of the samples were characterized by N_2 adsorption, IR spectroscopy and surface oxygen groups determination. The activated carbon, obtained from a mixture of furfural and coal tar pitch, and oxidized cabon demonstrate high adsorption ability towards mercury ions (149 and 136 mg/g, respectively). The relative part of the surface occupied by mercury ions is higher for the oxidized carbon. It was found that Hg (II) uptake increases with increasing pH.

Key words: activated carbon, coal tar pitch, furfural, mercury, adsorption

INTRODUCTION

The rapid urbanization and the extensive development of agriculture and tourism during the last decades have intensified the use of underground and surface waters. So there appears the issue of water contamination. The strive for alignment to standard legislation norms requires development of efficient methods for purification of waste and potable waters. Water pollution is a big problem for the modern world and it inflicted a lot of investigations, dedicated to protection of environment and living organisms. Metals such as Hg, Cd, Ni, As, Pb, etc. are highly toxic and carcinogenic, they have irreversible harmful, even lethal effect on human physiology and other biological systems. In order to ensure consistent protection of surface waters, the European Parliament and the Council of the European Union have announced Directives on the Environmental Quality Standards in the field of water policy. The European Environmental Agency (EEA) has included different heavy metal ions in the List of Priority Pollutants to be monitored in industrial effluents [1].

Mercury is generally considered to be one of the most toxic metals found in the environment. The major sources of mercury pollution in the aquatic environment are industries such as chloralkali, pulp paper, paint industry, rubber processing, oil refining, electrical power and fertilizer productions [2,3]. Numerous methods are available for removal of mercury, including membrane separation [4,5], chemical precipitation [6,7], coagulation [8], photodegradation [9], reverse osmosis [10], biodegradation [11-13]. These methods are associated, however, with high operational costs and incomplete removal, and they require large amounts of energy and chemicals.

Adsorption is a suitable purification process, but the high price of commercial activated carbon decreases the economical efficiency of pollutant removal. Therefore it is very important to find new effective adsorbents. Nowadays the researchers are focused on the preparation of low-cost activated carbons from different waste materials for the treatment of drinking and waste waters. Activated carbons can be produced from a large variety of precursors - bituminous coal, wood, peat, petroleum pitch, polymer and biomass [14-16]. Preparation of activated carbons from waste materials and industrial by-products, like coal tar pitch and furfural (contained in waste products from treatment of biomass), reveals a possibility for their appropriate utilization.

This work presents the results from the investigation of the adsorption activity of activated carbon, obtained from coal by-product (coal tar pitch) and furfural (waste material from pyrolysis of biomass), towards Hg (II) ions.

* To whom all correspondence should be sent:
E-mail: racheva89@abv.bg

EXPERIMENTAL

A mixture of coal tar pitch and furfural (45:55 wt.%) was treated with concentrated H_2SO_4 added dropwise under continuous stirring at 120 °C until solidification. The obtained solid product was heated at 600 °C in a covered silica crucible at a heating rate of 10 °C min^{-1} in nitrogen atmosphere. The carbonized solid product was further submitted to steam activation at 800°C for 1 h (carbon A).

The synthesized material was oxidized in order to incorporate more oxygen functionalities. For this purpose, carbon A sample was oxidized with HNO_3. The oxidation treatment with HNO_3 was performed according to the following procedure: about 10 g of the sample was treated with 100 cm^3 10% HNO_3 and boiled for 1 h. After that the sample was washed with distilled water, dried at 105°C and kept in a desiccator until use. The oxidized carbon was labeled as carbon B.

The nanotexture of the synthesized carbon materials was characterized by N_2 adsorption at -196°C, carried out in an automatic volumetric apparatus (ASAP 2010 from Micromeritics). Before the experiments, the samples were outgassed under vacuum at 300°C for overnight. The isotherms were used to calculate specific surface area S_{BET}, total pore volume V_T, micropore volume W_o. The samples were further characterized by elemental analysis and Boehm titration to determine the amount of oxygen, incorporated after oxidation treatment, and the nature of the appeared surface functionalities. FTIR experiments were performed on a spectrometer IFS 113V using KBr pellets.

The pH of the carbons was measured according to the following procedure: 4.0 g of carbon was weighed into a 250 cm^3 beaker, and 100 cm^3 of water was added. The beaker was covered with a watch glass, and the mixture was boiled for 5 min. The suspension was set aside, and the supernatant liquid was poured off at 60 °C. The decanted portion was cooled down to ambient temperature and pH was measured to the nearest 0.1 pH unit.

Batch adsorption studies were carried out with 10 mg of adsorbent and 50 cm^3 of Hg (II) solution with the desired concentration at pH 5.5 in 100 cm^3 conical flasks. The amount of Hg (II) in the final volume of 25 cm^3 was determined spectrophotometrically on a Pfaro 300 UV-Vis spectrometer. Rhodamine 6G and potassium iodide were used to obtain a pink-colored solution in the presence of Hg (II). The reaction occurs immediately in the pH range 1-7, when the system is stabilized with gelatin. The absorbance at 575 nm remains unchanged for at least 24 h. The pH values are adjusted with dilute solutions of hydrochloric acid.

RESULTS AND DISCUSSION

Characterization of carbon adsorbents from coal tar pitch and furfural

Furfural resin is a suitable oxygen-containing raw material for the production of carbon adsorbents with insignificant ash and sulphur content. There are many sources of furfural, because most agricultural wastes contain sufficient quantities of pentosans allowing industrial exploration by a well-established technique. The elemental analysis of coal tar pitch shows that the amount of oxygen containing structures is not high, whereas the high C/H ratio indicates the presence of a considerable amount of aromatic species in the pitch (Table 1).

Table 1. Chemical composition of the samples (wt.%).

	Ash	C	H	N	S	O	C/H
Coal tar pitch	-	90.90	4.95	0.90	0.50	2.75	1.53
Carbon A	0.8	90.81	0.82	0.75	0.51	7.11	9.23
Carbon B	1.5	86.77	1.02	1.30	0.56	10.35	7.09

Table 2. Quantification and identification of the oxygen surface groups [meq g^{-1}].

	Carboxylic	Lactonic	Phenolic	Carbonyl	Basic groups	pH
Carbon A	BDL	BDL	0.210	1.356	0.78	8.1
Carbon B	0.109	0.239	0.456	1.767	0.330	3.7

BDL – below detection limits

The content of surface oxygen-containing functional groups in carbon has a significant effect on metal ion adsorption on carbon. The results from Boehm titration of surface groups (Table 2) show that carbon A and carbon B are characterized with the presence of different oxygen-containing surface functionalities. The presence of surface oxygen groups is also confirmed by IR spectroscopy (Fig. 1). The band at 1704 cm^{-1} could be related to the stretching of C=O in aliphatic aldehydes, ketones and carboxyls. The bands around 1600 cm^{-1} cannot be unequivocally interpreted. They could be due to: i) aromatic ring stretching couples to highly conjugated carbonyl groups (C=O); ii) stretch vibrations of C=C bonds in aromatic structures; iii) OH groups. The bands in the region of 1360-1150 cm^{-1} are due to C=O in complex ethers and ring structures. [17-19].
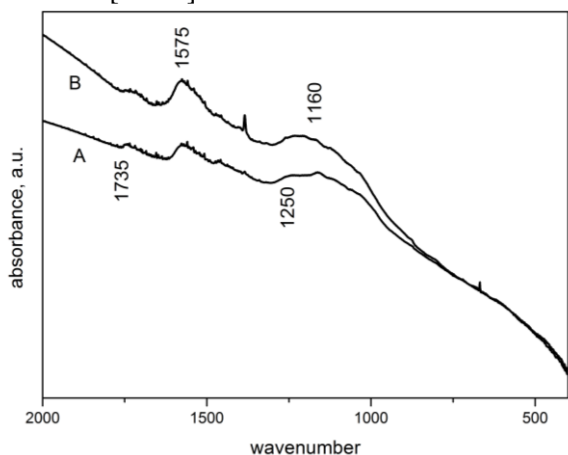
Fig. 1. IR spectra of the samples (A – Carbon A; B – Carbon B).

We have observed that the furfural content has a strong effect on the porosity of the resulting carbons. Lower proportions of furfural leads to synthesis of activated carbons with a narrow microporosity. With rising the furfural content this microporosity is gradually opened in favor of appearance of large micropores and mesopores. Carbon A was prepared with a moderate proportion of furfural in the precursor mixture (45 wt.%), and as a result it is characterized by a moderate BET surface area and well developed microporosity (Table 3 and Figure 2).

Table 3. Surface characteristics of the samples.

Sample	S_{BET} m^2/g	V_{tot}* cm^3/g	V_{micro}**. cm^3/g	V_{meso}** cm^3/g
Carbon A	678	0.316	0.216	0.030
Carbon B	487	0.217	0.113	0.010

* evaluated at p/p$_0$~0.99
** evaluated from DFT applied to N$_2$ adsorption data

The nitrogen adsorption/desorption isotherms of the carbon samples are shown in Fig.2. It can be seen that the adsorption isotherms are of type I, indicating a microporous material. These porous features should be ideally adapted for the removal of aromatics from aqueous phase. Oxidation brought about a slight decrease in the porous features of the carbon (likely due to the boiling step during oxidation), although the fall in the micropore volume accounts for only 16 %.
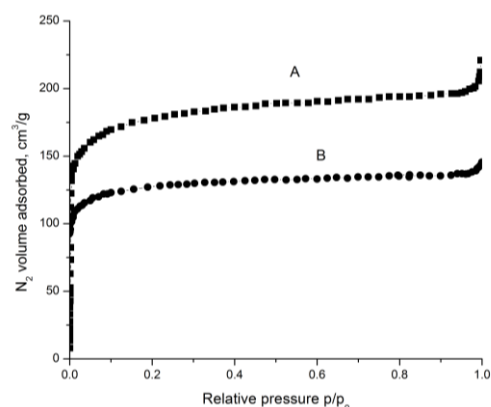
Fig. 2. N$_2$ adsorption isotherms at -196 ℃ of the samples (A-Carbon A; B-Carbon B).

Adsorption measurements

The equilibrium adsorption isotherms of Hg (II) on activated carbons are presented on Fig. 3. The adsorption isotherms belong to the L(2)-type according to the Giles classification [20, 21] showing a steep initial rise and a concave curvature at low equilibrium concentrations, followed by a plateau, i.e. saturation limit. L-type isotherms reflect adsorption at higher contaminant concentrations, corresponding to the completion of a monolayer in the experimental range.

The adsorption capacity, Q_o, was calculated from the linearized Langmuir plot [22]:

$$C_e/q_e = 1/Q_ob + C_e/Q_o \qquad (1),$$

where C_e is the equilibrium concentration (mg/L); q_e is the amount of Hg (II) adsorbed at equilibrium (mg/g) and Q_o and b are the characteristic Langmuir parameters related to the maximum adsorption capacity and intensity of adsorption, respectively. The model is frequently used for adsorption from dilute solutions. The value Q_o gives the saturation limit for adsorption from solution and b can be considered as a measure of the adsorption energy [22]. The Q_o values determined for synthetic (carbon A) and oxidized activated carbon (carbon B) are 149 and 136 mg/g, respectively (Table 4).

615
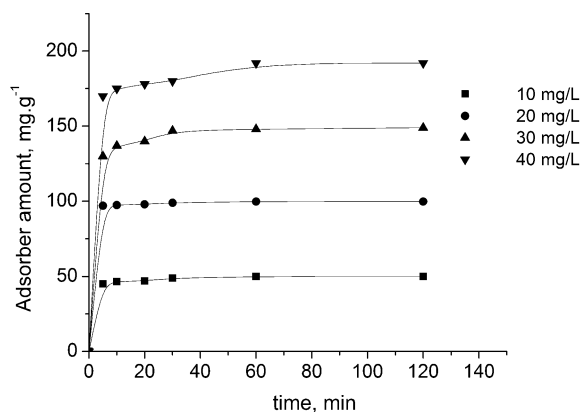
Fig. 3. Adsorption isotherms of Hg (II) ions on the different activated carbons. Conditions: C_o 10-40 mg/dm^3; pH =5.5; τ 60 min; carbon amount, 10 mg/50 cm^3.

Table 4. Data for mercury ion adsorption obtained from the Langmuir plot.

Sample	Q_o mg/g	B L/mg	S_m^{2-} m^2/g	S_m^{2-}/S_{tot} %
Carbon A	149	1.17	20.64	3.04
Carbon B	136	1.39	20.64	4.24

Some theoretical parameters in the Langmuir equation were calculated from the experimental data and are presented in Table 4. The surface area S_m covered by Hg (II) ions was calculated on the basis of the Goldschmidt ionic radius, which is 0.112 nm [23]. Metal ions with amphoteric character are adsorbed to a considerably greater degree by activated carbons *via* alkaline reaction. The increased porosity and specific surface area after activation with water vapor leads to increased uptake of mercury ions. The water steam-activated carbon adsorbs Hg ions to a lower extent than the oxidized carbon, due to the fact that part of the surface of the former is inaccessible to mercury ions.

The investigation of the effect of pH on the adsorption activity of different carbons is very important. In the case of mercury (II) solutions, most of the mercury exists in the form of complexes, which can be positive, neutral or negative, depending on the composition and pH. Appropriate amounts of hydrochloric acid and sodium hydroxide were added in order to obtain solutions with different pH values. The adsorption capacities of the carbon were studied at different pH values and a maximum was established near pH 6.0 for all samples. The metal uptake increases in the range of pH values from 2 to 5.5, and stays constant above pH 6 for all carbons. The effect of the pH on mercury ion adsorption for the studied samples is illustrated in Fig. 4 (for initial concentration of 40 mg/dm^3).

Bearing in mind that activated carbon A has

higher pore volume and total surface area than carbon B, it is evident that the removal efficiency is not directly related to these values. Most probably removal efficiency could be related to differences in the pore size distribution and the surface chemistry of the carbons.
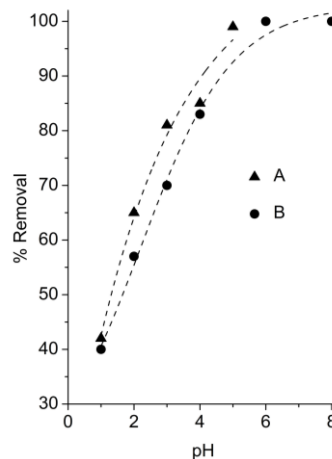
Fig. 4. Influence of pH on the adsorption equilibrium of mercury (II) ions on carbon A and carbon B. Conditions: τ, 60 min, carbon concentration, 10 mg/dm^3.

It can be shown by stability constant calculations that, in the presence of Cl$^-$, the predominant form at pH > 4.0 is Hg(OH)$_2$, and at pH < 4, the predominant form is HgCl$_2$ [24]. The dominant form in the range of highest sorption efficiency is Hg(OH)$_2$. When the pH drops, various chloride species, especially HgCl$_2$(aq), appear, however they are poorly adsorbed. It was assumed that, in addition to the different oxygen-containing groups, C_xSO_3H groups are present on the carbon surface as a result of effect of H_2SO_4 in the process of activated carbon preparation.

We suggest that following complexes could be formed:

$$2C_xOH + Hg^{2+} \rightarrow (C_xO)Hg^{2+} + 2H^+$$
$$2C_xOOH + Hg^{2+} \rightarrow (C_xCOO)_2Hg^{2+} + 2H^+$$
$$2C_xSO_3H + Hg^{2+} \rightarrow (C_xSO_3)Hg^{2+} + 2H^+$$
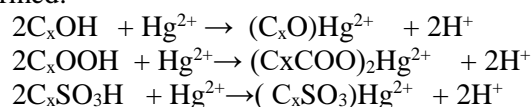
CONCLUSIONS

Activated carbons with good adsorptive properties were synthesized from biomass and coal waste materials, and were applied for removal of mercury ions from aqueous solutions. The obtained activated carbons exhibited very good ability to adsorb mercury ions from aqueous solution, oxidized carbon (136 mg/g) having lower adsorption capacity than the non-oxidized sample (149 mg/g). The relative part of the surface occupied by mercury ions is greater for the oxidized activated carbon. Stable chemical bonds (chemisorption) are formed between Hg (II) ions and oxygen-containing groups present on the carbon surface.

REFERENCES

1. Directive 2008/105/EC Environmental quality standards for priority substances and certain other pollutants, 16 December 2008.
2. O. Rodriguez, I. Padilla, H. Tayibi, A. Lopez-Delgado, *Journal of Environmental Management*, **101,** 197 (2012).
3. F. Di Natale, A. Lancia, A. Molino, M. Di Natale, D. Karatza, D. Musmarra, *Journal of Hazardous Materials,* **132,** 220 (2006).
4. H. Bessbousse, T. Rhlalou, J.F. Verchere, L. Lebrun, *Chem. Eng. J.* , **164,** 37 (2010) .
5. K. Chakrabarty, P. Saha, A.K. Ghoshal, *J.Membr. Sci.,* **346,** 37 (2010) .
6. J. Esalah, M.M. Husein, *Sep. Sci. Technol.* , **43,** 3461 (2008) .
7. A. Essa, L. Macaskie, N. Brown, *Biotechnol. Lett.* **27,** 1649 (2005).
8. C.P. Nanseu-Njiki, S.R. Tchamango, P.C. Ngom, A. Darchen, E. Ngameni, *J. Hazard. Mater.,* **168,** 1430 (2009).
9. L.R. Skubal. N.K. Meshkov*, J. Photochem. Photobiol.*, A, **148,** 211 (2002).
10. M. Mullett, L. Mohamed, Removal of mercury from solution using reverse osmosis filtration, in: Proc. 37th Chemeca 2009 - Engineering Our Future: Are We up to the Challenge, 27 - 30 September 2009, Burswood Entertainment Complex, Perth W.A., Barton, ACT: Engineers Australia, 2009 , p. 2207.
11. H.R. Dash, S. Das, *International Biodeterioration and Biodegradation* ,**75,** 207 (2012) 3
12. D. Jaysankar, N. Ramaiah and L. Vardanyan, Detoxification of toxic heavy metals by marine bacteria highly resistant to mercury, *Marine Biotechnology*, **10** , 471 (2008) .
13. L. Svecova, M. Spanelova, M. Kubal, E. Guibal, Cadmium, lead and mercury biosorption on waste fungal biomass issued from fermentation industry. I. Equilibrium studies, *Separation and Purification Technology,* **52,** 142 (2006).
14. T.J Bandosz, Activated carbon surface in environmental remediation, In: T.J.Bandosz (Editor) Interface Science and Technology Series, Elsevier, New York, 2006.
15. D. Savova, E. Apak, E. Ekinci, F. Yardim, N. Petrov, T. Budinova, M. Razvigorova, V. Minkova, Biomass conversion to carbon adsorbents and gas. *Biomass and Bioenergy* **21**, 133 (2001).
16. N. Petrov, T. Budinova, M. Razvigorova, J.B. Parra, P. Galiatsatou, Conversion of olive wastes to volatiles and carbon adsorbents. *Biomass Bioenergy,* **32**, 1303 (2008).
17. G. Socrates, Infrared and Raman Characteristic Group Frequencies – Tables and Charts, 3rd ed., John Wiley & Sons Ltd., England, 2001.
18. J. Zawadzki, B. Azambre, O. Heintz, A. Krzton, J. Weber, IR study of the adsorption and decomposition of methanol on carbon surfaces and carbon-supported catalysts, *Carbon,* **38**, 509 (2000).
19. J. Zawadzki, M. Wisniewski, J. Weber, O. Heintz, B. Azambre, IR study of adsorption and decomposition of propan-2-ol on carbon and carbon-supported catalysts, *Carbon* , **39**, 187 (2001).
20. F. Rouquerol, J. Rouquerol, K. Sing, In: Adsorption by powders and porous solids. Principles, methodology and applications, Academic Press: London, 1999.
21. C.H. Giles, T.H. MacEwan, S.N. Nakhwa, D. Smith, Studies in adsorption. Part XI. A system of classification of solutions adsorption isotherms, and its use in diagnosis of adsorption mechanisms and in measurement of specific surface areas of solids. *J. Chem. Soc.,* 3973 (1960).
22. I. Langmuir, The constitution and fundamental properties of solids and liquids, Part I Solids. *J. Am. Chem. Soc.*, **38**, 2221 (1916).
23. A.F. Holleman, E. Wiberg, Lehrbuch der Anorganischen Chemie, Walter de Gruyter, Berlin, 1995.
24. W.R. Knocke, L.H. Hemphill, *Water Res.*, **15**, 275 (1981).

ПРЕЧИСТВАНЕ НА ОТПАДНИ ВОДИ ОТ ЖИВАК ПОСРЕДСТВОМ АКТИВЕН ВЪГЛЕН, ПОЛУЧЕН ОТ ОТПАДНИ СУРОВИНИ ОТ ВЪГЛИЩА И БИОМАСА

И. Г. Стойчева[1]*, Б. Н. Петрова[1], Б. Г. Цинцарски[1], Т. К. Будинова[1], Н. В. Петров[1], Б. Нагел[2], У. Шелуга[2], С. Пуш[2], С. Чайковска[2], Б. Тржебицка[2]

[1]*Лаб. Химия на твърдите горива, Институт по органична химия с Център по фитохимия, Българска Академия на Науките, ул. Акад. Г. Бончев, бл.9,1113 София, България*
[2]*Център за полимерни и въглеродни материали към Полската Академия на Науките, ул. Мария Склодовска-Кюри 34,41-819 Забже, Полша*

(Резюме)

Изследвана бе адсорбцията на живачни йони върху окислени и неокислени проби активен въглен, получени чрез хидро-пиролиз от смес от каменовъглен пек и фурфурол. Структурата и повърхностните свойства на пробите бяха характеризирани чрез азотна физисорбция, ИЧ спектроскопия и бе определена концентрацията на повърхностните кислородни групи. Активният въглен, получени от смес от каменовъглен пек и фурфурол, и окисленият въглен демонстрират висока адсорбционна способност спрямо живачните йони (съответно 149 и 136 мг/г). Частта от повърхността, заета от живачни йони е по-висока за окисления въглен, в сравнение с неокисления. Бе установено, че отстраняването на Hg (II) се увеличава с увеличаване на pH на разтвора.

A facile solvent-free route for the one-pot multicomponent synthesis of benzylpyrazolyl coumarins catalyzed by FeCl₃.SiO₂ nanoparticles

Z. Piruzmand, J. Safaei-Ghomi[*], M. A. Ghasemzadeh

Department of Chemistry, Qom Branch, Islamic Azad University, Qom, I. R. Iran

The synthesis of benzylpyrazolyl coumarin derivatives is achieved by the four-component reaction of arylhydrazine/hydrazine hydrate, ethyl acetoacetate, aromatic aldehydes and 4-hydroxycoumarin. FeCl₃/SiO₂ nanoparticles are used as an efficient and green catalyst for the present research work. This method is fast and affords high yields. It is also clean, safe, cost-effective and importantly, the FeCl₃/SiO₂ nanocatalyst is easily recovered and reused for at least five cycles, which confirms its good stability.

Keywords: FeCl₃/SiO₂ nanoparticles, multicomponent, solvent-free, pyrazolone.

INTRODUCTION

Compounds containing the pyrazolone ring system have received considerable attention due to the attractive pharmacological properties associated with this heterocyclic moiety. Since many of these heterocycles like phenazone, propyphenazone, ampyrone (Fig. 1a) exhibit biological activities such as anti-inflammatory, postmenopausal, anti-osteoporosis, angiotensin antagonist, and anticoagulant activities [1-3], these derivatives have become an integral part of pharmacologically important heterocyclic compounds. 3-Substituted 4-hydroxycoumarins, particularly 3-benzylsubstituted 4-hydroxycoumarin derivatives are of much importance because they are present in many natural products.
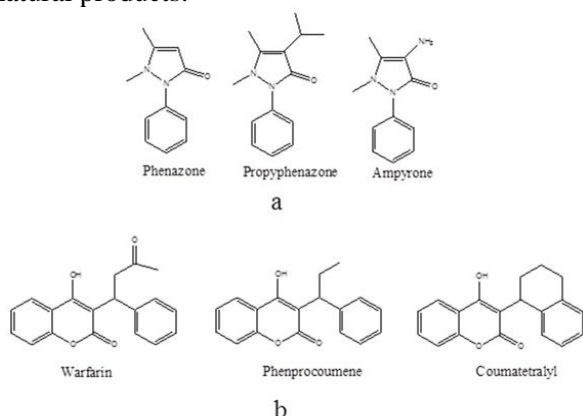
Fig. 1. (a) Bio-active pyrazolone moieties; (b) Some biologically active 3-substituted coumarins.

It is also established that these compounds show a wide range of biological activities due to their abundance in medicinal scaffolds, namely warfarin, phenprocoumon, coumatetralyl (Fig. 1b) offering antibacterial, anti-HIV [4], antiviral [5], anticoagulant [6], antioxidant [7] and anticancer activities [8].

Multicomponent reactions (MCRs) are a promising and vital field of chemistry because the synthesis of complicated molecules can be achieved in a very fast, efficient, and time saving manner without the isolation of any intermediate. Multicomponent reactions are some of the most important protocols in organic synthesis and medicinal chemistry [9,10].

Heterogeneous supported catalysts have gained an important role in organic synthesis due to high activity and selectivity, available active sites, easy catalyst separation, long catalytic life, thermal stability, easy handling and reusability [11,12]. Therefore, the use of supported and recoverable catalysts in organic transformations has economical and environmental benefits [13-18]. Among various silica-based heterogeneous catalysts, FeCl₃–SiO₂ has the advantages of low cost, ease of preparation and recyclability [19-21].

In this work, which is a continuation of our studies of catalytic multicomponent reactions using inorganic solids as heterogeneous catalysts [22-24], we describe the preparation of benzylpyrazolyl coumarin derivatives in the presence of FeCl₃–SiO₂ nanoparticles (NPs) under solvent-free conditions (Scheme 1).
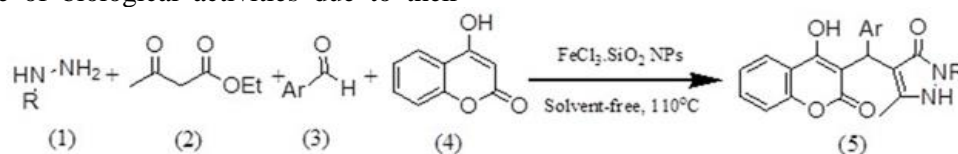
Scheme 1. Synthesis of benzylpyrazolyl coumarin derivatives.

* To whom all correspondence should be sent:
E-mail: safaei@kashanu.ac.ir

EXPERIMENTAL

General

All reagents were purchased from Merck and Aldrich and were used without further purification. The reaction was monitored by TLC using 0.2 mm Merck silica gel 60 F254 pre-coated plates, which were visualized with UV light. Melting points were measured on an Electrothermal 9200 apparatus. The IR spectra were recorded on a FT-IR Magna 550 apparatus using KBr discs. The ^{1}H-NMR and ^{13}C-NMR spectra were recorded on a Bruker Avance DRX-400 MHz instrument using TMS as the internal standard. The elemental analyses (C, H, N) were obtained from a Carlo ERBA Model EA 1108 analyzer. Microscopic morphology of products was visualized by SEM (LEO 1455VP).

General procedure for the preparation of nano-silica-supported ferric chloride

In a 100-cm^3 flask, 25 g nano silica gel and 2 g FeCl$_3$.6H$_2$O (8 % of the weight of nano-SiO$_2$) were vigorously stirred under solvent-free conditions at room temperature for 24 h to achieve homogeneous adsorption. A yellow powder was obtained. This powder was heated for 1 h at 100ºC to give a brownish powder ("active" FeCl$_3$/nano-SiO$_2$ reagent).

General procedure for the preparation of benzylpyrazolyl coumarin derivatives

A mixture of 0.05 g FeCl$_3$/SiO$_2$ NPs, hydrazine 1 (1 mmol), ethyl acetoacetate 2 (1 mmol), aromatic aldehyde 3 (1 mmol) and 4-hydroxycoumarin 4 (1 mmol) was finely ground with a mortar and pestle and then heated in a flask under stirring at 110ºC in an oil bath. After completion of the reaction (indicated by TLC), the reaction mixture was dissolved in hot ethanol, and the mixture was stirred for 5 min. The reaction mixture was filtered, and the heterogeneous catalyst was recovered. Then the product was recrystallized from ethanol to get the pure compounds as white or pale yellow crystals. The isolated compounds were characterized by IR, ^{1}H NMR and ^{13}C NMR.

Spectral data of 5a, 5e, 5h and 5k compounds

1,2-Dihydro-4-((4-hydroxy-2-oxo-2H-chromen-3-yl)(3-nitrophenyl)methyl)-5-methyl-2-phenylpyrazol-3-one (5a): Pale yellow crystalline solid; mp 241-243 °C, IR (KBr, cm^{-1}): ν_{max} 3074, 1649, 1609, 1560, 1525, 1179, 1103, 749; ^{1}H NMR (400 MHz, CDCl$_3$): δ 2.38 (3H, s), 5.79 (1H, s), 7.10-7.21 (3H, m), 7.32-7.44 (4H, m), 7.54-7.59 (3H, m), 7.74-7.76 (2H, d, J=7.8 Hz),

7.92-7.98(2H, m), 12.07 (1H, s, OH); ^{13}C NMR (100 MHz, CDCl$_3$): δ 10.8, 34.2, 105.5, 106.5, 115.9, 118.4, 121.2, 121.3, 122.1,123.7, 124.4, 126.9, 129.2, 131.8, 133.7, 135.3, 142.1, 147.1, 148.36, 152.5, 162.6, 164.6, 165.1. Anal. Calcd. for C$_{26}$H$_{19}$N$_3$O$_6$: C 66.48, H 4.07, N 8.93, Found: C 66.50, H 4.08, N 8.92.

1,2-Dihydro-4-((4-hydroxy-2-oxo-2H-chromen-3-yl)(4-methoxyphenyl)methyl)-5-methyl-2-phenylpyrazol-3-one (5e): White crystalline solid; mp 207-209 °C, IR (KBr, cm^{-1}): ν_{max} 3072, 1645, 1606, 1563, 1522, 1174, 1103, 746; ^{1}H NMR (400 MHz, CDCl$_3$): δ 2.34 (3H, s), 3.61 (3H, s), 5.76 (1H, s), 7.08-7.25 (3H, m), 7.30-7.42 (4H, m), 7.52-7.58 (3H, m), 7.75-7.78 (2H, d, J=7.8 Hz), 7.92-7.98(2H, m), 12.08 (1H, s, OH); ^{13}C NMR (100 MHz, CDCl$_3$): δ 10.7, 34.5, 105.2, 106.4, 115.7, 118.8, 121.1, 121.3, 122.1,123.4, 124.4, 126.8, 129.2, 131.6, 133.5, 135.5, 142.6, 147.1, 148.42, 152.5, 162.5, 164.4, 165.5. Anal. Calcd. for C$_{27}$H$_{22}$N$_2$O$_4$: C 71.35, H 4.88, N 6.16, Found: C 71.37, H 4.90, N 6.19.

1,2-Dihydro-4-((4-hydroxy-2-oxo-2H-chromen-3-yl)(4-bromophenyl)methyl)-5-methyl-2-phenylpyrazol-3-one (5h): Cream crystalline solid; mp 244-246 °C, IR (KBr, cm^{-1}): ν_{max} 3068, 1641, 1606, 1562, 1520, 1177, 1103, 747; ^{1}H NMR (400 MHz, CDCl$_3$): δ 2.34 (3H, s), 5.76 (1H, s), 7.09-7.25 (3H, m), 7.31-7.43 (4H, m), 7.50-7.58 (3H, m), 7.73-7.78 (2H, d, J=7.8 Hz), 7.91-7.97(2H, m), 12.06 (1H, s, OH); ^{13}C NMR (100 MHz, CDCl$_3$): δ 10.5, 34.6, 105.1, 106.6, 115.6, 118.8, 121.2, 121.6, 122.1,123.6, 124.4, 126.9, 129.2, 131.5, 133.5, 135.5, 142.8, 147.1, 148.42, 152.5, 162.8, 164.3, 165.7. Anal. Calcd. for C$_{26}$H$_{19}$N$_2$O$_4$Br: C 62.15, H 3.78, N 5.57, Found: C 62.18, H 3.80, N 5.54.

4-((4-Hydroxy-2-oxo-2H-chromen-3-yl)(4-methylphenyl) methyl)-5-methyl-3H-pyrazol-3-one (5k): Cream crystalline solid; mp 226-228 °C, IR (KBr, cm^{-1}): ν_{max} 3083, 1613, 1527, 1347, 1186, 1038, 758; ^{1}H NMR (400 MHz, CDCl$_3$): δ 2.18 (3H, s), 2.37 (3H, s), 5.75 (1H, s), 7.09-7.23 (3H, m), 7.30-7.44 (4H, m), 7.49-7.59 (3H, m), 7.73-7.79 (2H, d, J=7.8 Hz), 7.90-7.99 (2H, m), 12.06 (1H, s, OH); ^{13}C NMR (100 MHz, CDCl$_3$): δ 10.6, 20.9, 33.8, 105.3, 106.7, 115.8, 119.7, 123.3, 124.4, 125.8, 127.1, 128.0, 131.2, 140.7, 144.7, 152.6, 163.3, 165.8. Anal. Calcd. for C$_{21}$H$_{17}$N$_2$O$_4$: C 69.80, H 4.70, N 7.75, Found: C 69.82, H 4.72, N 7.73.

RESULTS AND DISCUSSION

In our initial studies, we attempted to optimize the reaction conditions for the multicomponent

reaction between 3-nitrobenzaldehyde, phenylhydrazine hydrate, ethyl acetoacetate and 4-hydroxycoumarin as model substrates. Since solvent-free syntheses [25] have gathered much interest, so we decided to compare this reaction under solvent-free conditions and in different solvents (Table 1). It was observed that the reaction afforded high yields under solvent-free conditions, but poor yields in solvents.

Table 1. The model reaction using different solvents.

Entry	Solvent	Time (min)	Yield[a] (%)
1	EtOH (reflux)	50	89
2	H_2O (reflux)	120	10
3	CH_2Cl_2	60	50
4	Solvent-free	10	95

[a] Isolated yield.

Then we focused on the systematic evaluation of different catalysts for the model reaction under solvent-free conditions. A wide variety of catalysts including $FeCl_3$, SiO_2, nano SiO_2, $FeCl_3/SiO_2$ and $FeCl_3/SiO_2$ NPs were employed to test their efficacy for the specific synthesis of benzylpyrazolyl coumarins (Table 2).

Table 2. The model reaction carried out in the presence of various catalysts.[a]

Entry	Catalyst (g)	Time (min)	Yield of 5a (%)[b]
1	Without catalyst	210	Trace
2	$FeCl_3$ (0.05)	160	35
3	SiO_2 (0.05)	160	27
4	nano SiO_2 (0.05)	120	60
5	$FeCl_3/SiO_2$ (0.05)	100	70
6	$FeCl_3/SiO_2$ NPs (0.01)	20	79
7	$FeCl_3/SiO_2$ NPs (0.03)	10	85
8	$FeCl_3/SiO_2$ NPs (0.05)	10	95
9	$FeCl_3/SiO_2$ NPs (0.1)	10	95

[a] phenylhydrazine hydrate (1 mmol), ethyl acetoacetate (1 mmol), 3-nitrobenzaldehyde (1 mmol) and 4-hydroxycoumarin (1 mmol).
[b] Isolated yield.

The results presented in Table 2 show that in presence of $FeCl_3/SiO_2$ NPs, the desired product

was obtained in 95% yield within 10 min. Therefore, this catalyst appears to be superior to any of the other catalysts tested. This also checked that the quantity of the catalyst can play a vital role in realizing the optimal product yield. An increase in the amount of $FeCl_3/SiO_2$ NPs from 0.01 to 0.05 g increased the yield of the desired product to a great extent.

During the optimization of the reaction conditions, the effect of temperature was monitored (Fig. 2). At 110 °C the maximum yield of the product was obtained. The yield of the reaction was very poor at a temperature below 110 °C and at a higher temperature there might be some sort of polymerization of the Knoevenagel condensation product which lowers the yield of the desired product.
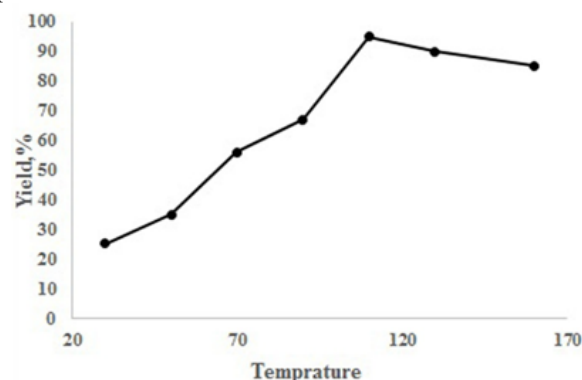
Fig. 2. Effect of temperature on the synthesis of benzylpyrazolyl coumarins.

On the basis of the above results during the optimization of solvent, catalyst and temperature, we then devised to employ a wide range of aldehydes with 4-hydroxycoumarin, arylhydrazine/ hydrazine hydrate and ethyl acetoacetate. As can be seen from Table 3 (following Scheme 1), the reaction proceeded smoothly with unsubstituted benzaldehyde, electron-withdrawing, and electron-releasing para-substituted benzaldehydes.

Table 3. Synthesis of benzylpyrazolyl coumarins.

Entry	Hydrazine (R)	Aldehyde (Ar)	Product	Time (min)	Yield[a] (%)	M.p. [ref]
1	C_6H_5	$3-NO_2C_6H_4$	5a	10	95	241-243[26]
2	C_6H_5	$4-ClC_6H_4$	5b	12	94	225-227[26]
3	C_6H_5	$4-NO_2C_6H_4$	5c	15	93	247-249[26]
4	C_6H_5	C_6H_5	5d	18	91	233-235[26]
5	C_6H_5	$4-OMeC_6H_4$	5e	20	89	207-209[26]
6	C_6H_5	$4-MeC_6H_4$	5f	20	92	223-225[26]
7	C_6H_5	$4-FC_6H_4$	5g	16	93	241-243[26]
8	C_6H_5	$4-BrC_6H_4$	5h	17	91	244-246
9	H	$3-NO_2C_6H_4$	5i	9	91	205-207[26]
10	H	$4-OMeC_6H_4$	5j	10	90	201-203[26]
11	H	$4-MeC_6H_4$	5k	10	90	226-228
12	H	C_6H_5	5l	12	92	232-234[26]

[a] Isolated yield.

In order to investigate the morphology and particle size of FeCl$_3$/SiO$_2$ NPs, a SEM image of FeCl$_3$/SiO$_2$ NPs was recorded (Fig. 3). As can be seen, the sample shows a nanocrystalline structure. The reusability of the catalyst in the model reaction was studied. The separated catalyst was collected and washed several times with acetone to remove all organic substances. It was then dried at 100°C and was recycled five consecutive times with almost unaltered catalytic activity (Table 4).
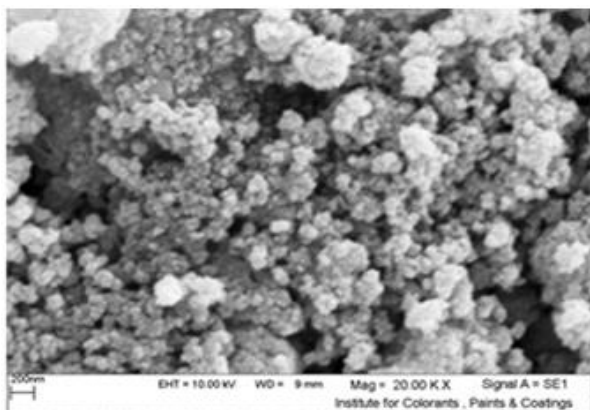
Fig 3. SEM image of FeCl$_3$/SiO$_2$ NPs.

Table 4. Catalyst reusability for the synthesis of benzylpyrazolyl coumarins.

Entry	Cycle	Yield[a], %
1	Fresh	95
2	1	95
3	2	94
4	3	94
5	4	94
6	5	93

[a] Isolated yield.

In view of these results, we offer a mechanistic scheme for this reaction which involves Knoevenagel condensation, Michael addition, and cyclization catalyzed by FeCl$_3$/SiO$_2$ NPs as presented in Scheme 2. There are two paths for this reaction: path (a) and path (b). Initially, aryl hydrazine/hydrazine hydrate (1) reacts with ethyl acetoacetate (2) to generate the pyrazolone ring (I). In path (a) Knoevenagel reaction between pyrazolone ring (I) and aromatic aldehyde (3) takes place to form the intermediate (II) and then condensation of this intermediate with 4-hydroxycoumarin (4) affords the desired product (5). In another path, Knoevenagel reaction between 4-hydroxycoumarin (4) and aromatic aldehyde (3) takes place to form the Knoevenagel product (III). Subsequently, during the Michael addition step, nucleophilic attack on (III) by the pyrazolone (I) affords the desired product (5).
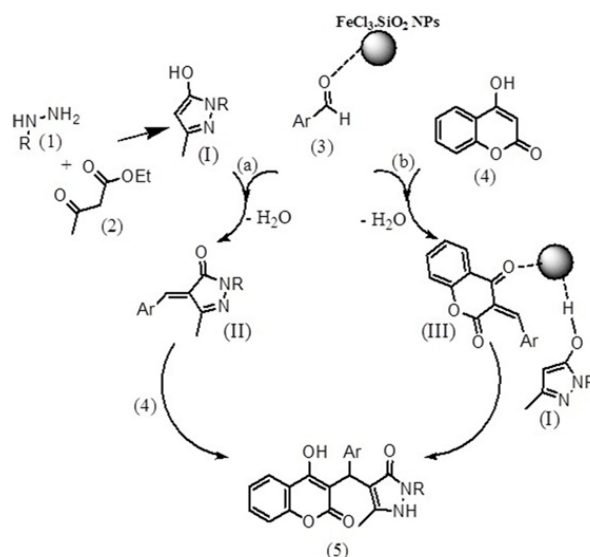
Scheme 2. Plausible mechanism for the formation of benzylpyrazolylcoumarins.

CONCLUSIONS

In conclusion, a simple and convenient method was developed for the synthesis of benzylpyrazolyl coumarins by the reaction of arylhydrazine/hydrazine hydrate, ethyl acetoacetate, aromatic aldehydes and 4-hydroxycoumarin using FeCl$_3$/SiO$_2$ NPs as a catalyst under solvent free conditions. The attractive features of this protocol are: simple reaction procedure, short reaction time, easy product separation and purification, reusability of FeCl$_3$/SiO$_2$ NPs and its high adaptability to the synthesis of a broad spectrum of benzylpyrazolyl coumarin derivatives in good to excellent yields.

REFERENCES

1. P. Francisco, A.M.O. de Retana, P.A. Jaiore, *Tetrahedron*, **55**, 14451 (1999).
2. K.Y. Lee, J. M. Kim, J.N. Kim, *Tetrahedron Lett.*, **44**, 6737 (2003).
3. J. Jiaz, Y. Wu, W. Hung, P. Zhang, Y. Song, J. Woolfrey, U. Sinha, A. E. Arfsten, S.T. Edwards, A. Hutchaleelaha, S. J. Hollennbach, J.L. Lambing, R.M. Scarborough, B.Y. Zhu, *Bioorg. Med. Chem. Lett.*, **14**, 1229 (2004).
4. S. Hesse, G. Kirsch, *Tetrahedron Lett.*, **43**, 1213 (2002).
5. B. H. Lee, M. F. Clothier, F. E. Dutton, G. A. Conder, S.S. Johnson, *Bioorg. Med. Chem. Lett.*, **8**, 3317 (1998).
6. J. C. Jung, Y. J. Jung, O. S. Park, *Synth. Commun.*, **31**, 1195 (2001).

7. G. Melagraki, A. Afantitis, O. Igglessi-Markopoulou, A. Detsi, M. Koufaki, C. Kontogiorgis, D. J. Hadjipavlou-Litina, *Eur. J. Med. Chem.*, **44**, 3020 (2009).

8. J. C. Jung, J. H. Lee, S. Oh, J. G. Lee, and O. S. Park, *Bioorg. Med. Chem. Lett.*, **14**, 5527 (2004).

9. (a) Multicomponent Reactions, eds. J. Zhu, and H. Bienayme, Wiley-VCH, Weinheim, Germany, 2005. For some recent reviews on MCRs, see: A. Domling, *Chem. Rev.*, **106**, 17 (2006); (b) J. Zhu, *Eur. J. Org. Chem.*, 1133 (2003); (c) R. V. Orru, and M. De. Greef, *Synthesis*. 1471 (2003); (d) D. J. Ramon, and M. Yus, *Angew. Chem., Int. Ed.*, **44**, 1602 (2005).

10. (a) A. Pinto, L. Neuville, and J. Zhu, *Angew. Chem., Int. Ed.*, **46**, 3291 (2007); (b) M. R. M. Huettl, *Angew. Chem., Int. Ed.*, **46**, 1570 (2007); (c) L. F. Tietze, *Chem. Rev.* **96**, 115 (1996); (d) P. Arya, R. Joseph, D. T. H. Chou, *Chem. Biol.*, **9**, 145 (2002).

11. B. S. Kwak, *Catal. Surv. Asia.*, **9**, 103 (2005).

12. M. J. Climent, A. Corma, S. Iborra, *Chem. Rev.*, **111**, 1072 (2011).

13. A. Corma, *Chem. Rev.*, **95**, 559 (1995).

14. K. Wilson, J.H. Clark, *Pure Appl. Chem.*, **72**, 1313 (2000).

15. T. Okuhara, *Chem. Rev.*, **102**, 3641 (2002).

16. J.H. Clark, *Acc. Chem. Res.*, **35**, 791 (2002).

17. A. Corma, H. Garcia, *Chem. Rev.,* **103**, 4307 (2003).

18. G. Sartori, R. Ballini, F. Bigi, G. Bosica, R. Maggi, P. Righi, *Chem. Rev.*, **104**, 199 (2004).

19. (a) N. J. Ahmed, E. Van Lier, *Tetrahedron Lett.*, **47**, 2725 (2006); (b) M. Bandini, R. Luque, V. Budarin, D. J. Macquarrie, *Tetrahedron*, **61**, 9860 (2005); (c) C. Ramesh, G. Mahender, N. Ravindranath, B. Das, *Tetrahedron Lett*. **44**, 1465 (2003).

20. (a) M. A. Chari, D. Shobha, K. Mukkanti, *Catal. Commun*. **6**, 787 (2007); (b) Q. Dang, B.S. Brown, M. D. Erion, *Tetrahedron Lett.*, **41**, 6559 (2000); (c) P. Morys, T. Schlieper, J. *Mol. Catal. A: Chem.*, **95**, 27 (

21. 1995); (d) A. Hosseini, M. R. Halvagar, M. A. Khalilzadeh, E. Alaee, M. Tajbakhsh, *J. Chem. Res.*, **48**, 2005 (2005); (f) C. Wang, M. Li, *Synth. Commun.*, **32**, 3469 (2002); (g) Z. Ma, W. H. Sun, N. Zhu, Z. Li, C. Shao, Y. Hu, *Polym. Int.*, **51**, 349 (2002); (h) Z. Ma, Y. Ke, H. Wang, C. Guo, M. Zhang, W. H. Sun, Y. Hu, *J. Appl. Polym. Sci.*, **88**, 466 (2003); (i) A. Fadel, J. Salaün, *Tetrahedron*, **41**, 413 (1985); (j) A. Fadel, J. Salaün, *Tetrahedron*, **41**, 1267 (1985); (k) D. M. Tal, E. Keinan, Y. Mazur, *Tetrahedron*, **31**, 4327 (1981); (l) H. K. Patney, *Tetrahedron Lett*. **32**, 2259 (1991).

22. A. R. Modarresi-Alam, F. Khamooshi, M. Nasrollahzadeh, H. A. Amirazizi, *Tetrahedron,* **63**, 8723 (2007).

23. J. Safaei-Ghomi, A. Ziarati, S. Zahedi, *J. Chem. Sci.*, **124**, 933 (2012).

24. J. Safaei-Ghomi, A. Ziarati, *J. Iran. Chem. Soc.*, **10**, 135 (2013).

25. J. Safaei-Ghomi, M. A. Ghasemzadeh, *Chin. Chem. Lett.*, **23**, 1225 (2012).

26. (a) K. Tanaka, F. Toda, *Chem. Rev.* **100**, 1025 (2000); (b) J. O. Metzger, *Angew. Chem., Int. Ed.*, **37**, 2975 (1998); (c) M. A. P. Martins, C. P. Frizzo, D. N. Moreira, L. Buriol, P. Machado, *Chem. Rev.*, **109**, 4140 (2009).

27. P. P. Ghosh, G. Pal, S. Paul, A. R. Das, *Green Chem*. **14**, 2691 (2012).

ПРОСТ МЕТОД ЗА ЕДНОСТАДИЙНА СИНТЕЗА НА БЕНЗИЛ-ПИРАЗОЛИЛОВИ КУМАРИНИ, КАТАЛИЗИРАНА ОТ НАНОЧАСТИЦИ ОТ FeCl₃.SiO₂ БЕЗ РАЗТВОРИТЕЛ

З. Пирузманд, Дж. Сафаеи-Гоми*, М.А. Гасемзаде

¹*Департамент по химия, Ислямски университет „Азад", Клон Кум, Кум, Иран*

(Резюме)

Постигната е синтеза на бензил-пиразолил-кумаринови производни чрез четири-компонентна реакция на арил-хидразин/хидразин-хидрат, етилацето-ацетат, ароматни алдехиди и 4–хидроксикумарин. Използвани са наночастици от FeCl₃/SiO₂ като катализатор като ефективен и „зелен" катализатор. Методът е бърз и позволява високи добиви. Освен това той е чист, безопасен, евтин и което е важно, катализаторът лесно се оползотворява и използва петкратно.

Comparative analysis of some physico-chemical properties of the glassy systems (GeSe₅)₁₀₀₋ₓInₓ and (GeTe₅)₁₀₀₋ₓInₓ

Y. N. Trifonova, V. C. Ivanova, A. A. Stoilova, V. D. Lilova*

Department of Physics, University of Chemical Technology and Metallurgy, 8, Kl. Ohridski blvd, 1756 Sofia, Bulgaria

Our study concerns the two glassy systems $(GeSe_5)_{100-x}In_x$ and $(GeTe_5)_{100-x}In_x$ which contain different chalcogen elements. Se and Te rich glasses are interesting in view of the possibility of their application in switching and memory devices. They show, however, high values of electrical resistance implying certain limitations as short lifetime and low sensitivity. To eliminate these limitations we added In as a third element into the Ge-Se (Te) matrix. As a result of the addition of In new properties are expected, which can be related with structural transformation. The investigation of the physico-chemical properties gives useful information about the real structure of the glasses.

In this paper some physico-chemical properties of the glasses were studied, such as density, compactness, molar volume, number of constraints per atom and overall mean bond energy. The correlations between the composition and the properties of the glasses were discussed in terms of the supposed structural changes that occur in the investigated chalcogenide materials.

Key words: chalcogenide glasses, physico-chemical properties, structure

INTRODUCTION

The physico-chemical properties of chalcogenide semiconducting glasses are strongly dependent on their composition. Normally, control of the properties and expansion of the scope of applications of two-component systems is achieved through introduction of a third component. The addition of a third component expands the glass-forming area and also creates compositional and configurational disorder. Thus, the addition of In in the binary systems Ge-Se and Ge-Te is expected to affect some of their physico-chemical properties [1]. The chosen concentration ratio of the investigated glasses provides good flexibility of the structure, which facilitates the photoinduced changes in these materials.

In this paper we report the results of the studies of some physico-chemical properties as density, compactness, molar volume, number of constraints per atom and overall mean bond energy of these glasses and the results are discussed in respect to the composition of the glasses. The relation between chemical bonding and basic physico-chemical properties of the glasses (transformation temperature, density) is an essential feature of any comprehensive theory relating their structure and properties [2, 3].

EXPERIMENTAL

Bulk samples with composition $(GeSe_5)_{100-x}In_x$ and $(GeTe_5)_{100-x}In_x$, x = 0, 5mol% were prepared by melt-quenched technique [4]. The initial elements Ge, Se (Te) and In were used with 4N purity elements. The respective amounts of the initial elements were evacuated in quartz ampoules with a residual pressure 1.33×10^{-3}Pa. The synthesis was carried out in furnace „Firemagic FM4 Plus" with a constant rate of 5×10^{-2}K/s up to final temperature 1300K. Glasses were obtained after quenching in a mixture of water and ice with quenching rate of 1×10^{2}K/s.

The density of the bulk samples was measured by the pycnometer method with an accuracy of $\pm0.5\%$.

The compactness was calculated using the formula [5]:

$$\delta = \frac{\sum_i \frac{c_i A_i}{\rho_i} - \sum_i \frac{c_i A_i}{\rho}}{\sum_i \frac{c_i A_i}{\rho}}, \qquad (1)$$

where c_i is the atomic fraction, A_i – the atomic weight, ρ_i – the density of the components and ρ is the measured density of the bulk sample.

The molar volume was determined from the density data by the equation:

$$V_m = \frac{1}{\rho}\sum_i c_i A_i . \qquad (2)$$

The average coordination number was estimated according to [3] as:

$$Z_{glass} = 4x + 2y + 3z, \qquad (3)$$

where x, y and z are the atomic fractions of Ge, Se (Te) and In, respectively.

* To whom all correspondence should be sent:
E-mail: vanya_di@yahoo.com

The number of constraints per atom can be calculated by theoretical arguments according to the Phillips model [6]:

$$N_{co} = N_d ,$$ (4)

i. e. the number of the topological constraint N_{co}, evaluated for an atom, is equal to the number of degrees of freedom N_d. N_{co} is defined by the formula:

$$N_{co}(Z_{glass}) = N_a + N_b = \frac{Z_{glass}}{2} + (2Z_{glass} - 3) ,$$ (5)

where N_a and N_b are the radial and axial bond strengths, respectively.

Using the correlation proposed by Tichy *et al.* [7] for chalcogenide-rich systems we could determine the values of the overall mean bond energy:

$$< E > = \overline{E}_c + \overline{E}_{rm} ,$$ (6)

where $\overline{E}_c$ is the average heteropolar bond energy and $\overline{E}_{rm}$ is the average homopolar bond energy.

RESULTS AND DISCUSSION

The results obtained for the density of the bulk samples from the system Ge-Se-In (Table 1) show that the density increases after indium addition. It is known that the variation of the density is related to the atomic weight and to the atomic volume of the chemical elements contained in the chalcogenide glassy system. The atomic weight of Se and In is $A_{Se}=7.9 \times 10^{-2}$ kg/mol and $A_{In}=11.5 \times 10^{-2}$ kg/mol, respectively, i.e. the atomic weight of In is higher and by replacement of Se atoms with In atoms (increasing content of indium) the density increases. In the system Ge-Te-In, with increasing the In content the values of the density decrease. The Te atomic weight is $A_{Te}=12.6 \times 10^{-2}$ kg/mol, i. e. the atomic weight of In is lower than that of Te and by replacing tellurium with indium atoms (increasing of In content) the value of the density decreases. The compositions containing Te are denser than the compositions containing Se due to the higher atomic weight of Te.

The strength of the chemical bond is associated with the compactness of the material, i. e. with the "free volume" or it can be related to the density of defect states in the samples [8]. The dependence of the compactness on the In content for both systems is the same as the compositional dependence of the density (Table 1). The Te containing compositions show lower values of compactness than the Se containing compositions, i. e. bigger structural changes would be expected for the Te containing compositions.

The compositional dependence of the molar volume also repeats the compositional dependence of the density (Table 1).

The dependence of the physico-chemical properties on the composition could be investigated based on the expected chemical bonds in the glasses. The first approximation consists of ignorance of the unstable chemical bonds and the weak van der Waals forces. It is assumed that atoms predominantly combine with atoms of different types than of the same kind in chalcogenide glasses [9], i. e. chemical bond between atoms from the same kind will only occur, if there is an excess of these atoms. Furthermore, the bonds are formed in sequence of increasing bond energies until all available valences of the atoms are saturated. In the investigated chalcogenide glassy systems Ge-Se-In and Ge-Te-In, which are enriched in Se, or Te, respectively, the homopolar Se bonds or Te bonds are formed in the presence of unsaturated valences of Se or Te atoms after all heteropolar bonds are created. By In addition the number of the homopolar selenium, respectively tellurium bonds decreases and the number of degrees of freedom per atom increases (Table 1), which leads to an increase in the stability of the glassy systems (the number of degrees of freedom for an atom moving in a 3-dimensional space is $N_d=3$, and for the ideal glass $N_{co}=3$ [10], with an optimum mechanical stability of the network).

The physico-chemical properties of the chalcogenide glasses are related to their mean bond energy, which is a function of the average coordination number and of the bond type and bond energy between the atoms of the glass components. According to [6], the structure of the glassy system Ge-Se-In is realized by a network composed of tetrahedral $GeSe_2$ structural units and pyramidal In_2Se_3 structural units. Based on the model of the chemically ordered covalent random network [11] they are combined with the additional Se atoms. The remaining Se atoms are combined in chains. The structure of the glassy system Ge-Te-In is also realized by a network composed of tetrahedral $GeTe_2$ structural units and pyramidal In_2Te_3 structural units. They are also combined with the additional Te atoms, and the remaining Te atoms are combined in chains. No formation of Ge-Ge bonds at a Ge content up to 33mol% is expected [12].

Table 1. Composition and physico-chemical properties of the investigated samples.

Composition, mol%	Z_{glass}	Density, 10^3kg/m^3	Compactness, 10^{-2}	Molar volume, 10^{-5}m^3/mol	N_{co}	$<E>$,10^{-19}J
Ge$_{17}$Se$_{83}$	2.34	4.34	-3.95	1.80	2.85	3.58
Ge$_{16}$Se$_{79}$In$_5$	2.37	4.54	-0.09	1.75	2.93	3.61
Ge$_{17}$Te$_{83}$	2.34	5.86	-4.86	2.02	2.85	3.62
Ge$_{16}$Te$_{79}$In$_5$	2.37	5.55	-12.61	2.12	2.93	4.18

The value of the In-Se bond energy (4.27×10^{-19}J) [13] is higher than that of the Ge-Se bond energy (3.39×10^{-19}J) [14], and the value of the In-Te bond energy (3.60×10^{-19}J) [15] is higher than that of the Ge-Te bond energy (3.32×10^{-19}J) [15], i. e. the overall mean bond energy increases by indium addition (Table 1) and the bonds between atoms of the glass components become more stable. The formation of stronger bonds could be responsible for the variations in their physico-chemical properties. Te containing compositions possess higher overall mean bond energy than Se containing compositions because of the higher value of the Te-Te bond energy (3.24×10^{-19}J) [15] in comparison to that of the Se-Se bond energy (2.82×10^{-19}J) [14].

CONCLUSIONS

The values of the density of the compositions containing Te are higher than the values of the density of the compositions containing Se. The increase in the In content leads to variation of the density in both investigated systems Ge-Se-In and Ge-Te-In in a different way.

Because of their lower compactness, more structural changes would be expected in the compositions containing Te.

The compositional dependence of the molar volume repeats the compositional dependence of the density.

The increase in the number of degrees of freedom with addition of In leads to an increase in the sustainability of the glassy system.

The overall mean bond energy of the glassy alloys containing Te is higher than the overall mean bond energy of the glassy alloys containing Se. By In addition the bonds between the atoms of the glass components become more stable.

REFERENCES

1. E. Abd El-Wahabb, M. Abd El-Aziz, M. Fadel, *Vacuum*, **57,** 365 (2000).
2. J. Cheng, W. Chen, D. Ye, *J. Non-Cryst. Sol.*, **184**, 124 (1995).
3. S. Elliott, (ed.), Physics of Amorphous Materials, Pitman Press Ltd, Bath, 2000.
4. V. Vassilev, Z. Boncheva-Mladenova, Physical Chemistry of Semiconducting materials, Ministry of Education, Sofia, 1991.
5. L. Pauling, ed., The Nature of Chemical Bond, Cornell Univ. Press, New York, 1967.
6. J. Philips, *J. Non-Cryst. Sol.*, **34**, 153 (1972).
7. L. Tichý, H. Tichá, *J. Non-Cryst. Sol.*, **189**, 141 (1995).
8. K. Tanaka, *Phys. Rev. Lett.*, **B 39**, 1270 (1989).
9. S. Found, *Phys. B*, **270**, 360 (1999).
10. A. Giridhar, S. Mahadevan, *J. Non-Cryst. Sol.*, **134**, 94 (1991).
11. G. Lucovsky, F. Galeener, R. Keezer, R. Geils, H. Six, *Phys. Rev*, **B10**, 5134 (1974).
12. H. Trodahl, *Sol. State Comm.*, **44**, 319 (1982).
13. M. Thobega, S. Sathiaraj, K. Maabong, C. Muiva, *Advances in Applied Science Research*, **4**(6), 6 (2013).
14. A. Ibanez, P. Armand, E. Philippot, *Sol. State Ionics*, **59**, 157 (1993).
15. D. Lide (ed.), CRC Handbook of Chemistry and Physics, CRC Press, Boca Raton, Florida, USA, 2010.

СРАВНИТЕЛЕН АНАЛИЗ НА НЯКОИ ФИЗИКО-ХИМИЧНИ СВОЙСТВА НА СТЪКЛОВИДНИТЕ СИСТЕМИ $(GeSe_5)_{100-x}In_x$ И $(GeTe_5)_{100-x}In_x$

Й. Н. Трифонова, В. Х. Иванова, А. А. Стоилова, В. Д. Лилова*

Катедра „Физика", Химикотехнологичен и металургичен университет, бул. „Климент Охридски" № 8,

1756 София, България

(Резюме)

Изследвани са системите $(GeSe_5)_{100-x}In_x$ и $(GeTe_5)_{100-x}In_x$, съдържащи различни халкогенни елементи. Стъклата, обогатени на Se и Te, са интересни от гледна точка на възможността за приложението им в превключващи устройства и памети. Но те притежават високи стойности на електрическо съпротивление, което предполага някои ограничения като кратко време на живот и ниска чувствителност. За подобряване на качествата на тези материали е добавен трети елемент In в Ge-Se (Te) матрицата. Добавянето на In може да бъде свързано със структурни промени в стъклата и се очаква те да проявят нови свойства. Изследването на физико-химичните свойства дава полезна информация за реалната структура на стъклата.

Настоящата работа е свързана с определянето някои физико-химични свойства на стъклата като плътност, компактност, моларен обем, брой връзки на атом и пълна средна енергия на връзките. Зависимостите на свойствата на изследваните халкогенидни материали от техния състав са дискутирани от гледна точка на възникването на структурни промени в тях.

Kinetic and thermodynamic investigations on the electrocoagulation of methyl orange from aqueous solution using aluminum electrodes

M.R. Majdi, I. Danaee*, S. Nikmanesh

Abadan Faculty of Petroleum Engineering, Petroleum University of Technology, Abadan, Iran

The removal of color from solutions containing methyl orange (MO) was experimentally investigated using direct current electrocoagulation (EC) on aluminum electrodes. The experimental results suggested that electrocoagulation was an effective method in MO removal. Metal hydroxides generated during EC were used to remove MO from aqueous solution. The influence of operational parameters such as electrolysis time, applied constant potential, initial dye concentration, temperature and solution conductivity on color removal efficiency was explored. Thermodynamic parameters, including Gibbs free energy, enthalpy, and entropy were calculated for adsorption of MO on metal hydroxides. Thermodynamic parameters indicated that MO adsorption on metal hydroxides was feasible, spontaneous and endothermic in the temperature range from 298 K to 358 K. The adsorption of MO preferably fitted the Langmuir adsorption isotherm suggesting monolayer coverage of adsorbed molecules. In addition, the adsorption kinetic studies showed that the first-order rate equation provided the best correlation for the removal rate of MO.

Keywords: Electrocoagulation; Methyl orange; Aluminum; Langmuir, Adsorption isotherm.

INTRODUCTION

Textile and printing industry are regarded as some of the most polluting sectors due to their high discharge volume of dye-containing wastewater. Among these dyes, azo dyes are some of the most important kinds since they constitute about 50–70% of the world dye production [1,2]. Such kinds of dye effluents are characterized by intense color, high organic content and stable chemical structure due to the existence of azo groups. Moreover, they are toxic and recalcitrant to biodegradation. Therefore, they have caused serious risks for environmental pollution [3,4]. Hence, the removal of dyes during processing of waste effluents becomes environmentally important. Methyl orange (MO) is an azo compound, which is commonly used as a coloring agent in several applications, such as textile, paint, ink, plastic, and cosmetic industries. The release of this coloring agent into wastewater definitely causes a severe environmental problem. Several techniques have been developed to treat wastewaters containing dye pollutants [5-9].

There are many processes to remove dyes from colored effluents such as adsorption, precipitation, chemical degradation, photodegradation, biodegradation, chemical coagulation and electrocoagulation. When chemical coagulation is used to treat dyed wastewater, pollution may be caused by the chemical substances added at a high concentration [10,11]. The adsorption process is one of the effective methods used to remove dyes from aqueous solutions. Activated carbon is the most widely used adsorbent for dye removal, but it is too expensive [12]. Photooxidation by UV/H_2O_2 or UV/TiO_2 and Fenton oxidation needs additional chemicals [13], and therefore cause secondary pollution. Biological methods are generally cheap and simple to apply and are currently used to remove organics and color from dyed and textile wastewater. However, biological methods are less effective because of the toxicity of dyes that has an inhibiting effect on the bacterial development [14]. This dyed wastewater cannot be readily degraded by conventional biological processes, because the structures of most commercial dye compounds are generally very complex and many dyes are non-biodegradable due to their chemical nature, molecular size, which results in sludge bulking [15].

Electrochemical process is more effective for dye removal [16]. Electrocoagulation (EC) as an electrochemical method was developed to overcome the drawbacks of conventional decolorization technologies. EC is an attractive alternative for the treatment of textile dyes [17-18]. EC process provides a simple, reliable and cost-effective method for the treatment of wastewater without any need for additional chemicals, and thus secondary pollution. It also decreases the amount of sludge, which needs to be disposed. EC is a process consisting of creating a floc of metallic hydroxides within the effluent to be cleaned by electrodissolution of soluble anodes. Iron and

* To whom all correspondence should be sent:
E-mail: danaee@put.ac.ir

aluminum are generally used as sacrificial anodes. The dye in dye-containing wastewater is coagulated by iron (II) and aluminum hydrates or hydroxides produced from the sacrificial anode [19-20].

For aluminum electrodes, the electrolytic dissolution of the aluminum anode produces Al^{3+}ions, which are initially transformed into $Al(OH)_3$ and finally polymerized to $Al_n(OH)_{3n}$. The main reactions occurring in the anodic compartment are as follows [19,20].

$$Al \rightarrow Al^{3+} + 3e \ , \tag{1}$$
$$Al^{3+} + H_2O \rightarrow Al(OH)_3 + 3H^+, \tag{2}$$
$$nAl(OH)_3 \rightarrow Al_n(OH)_{3n}, \tag{3}$$
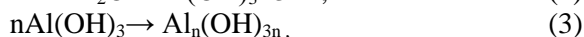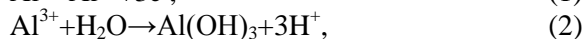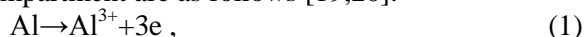
The main reaction in the cathodic compartment is:

$$2H_2O + 2e \rightarrow H_2 + OH^- \ , \tag{4}$$

In recent years, different methods have been developed to treat wastewaters containing methyl orange. Saldan˜a-Robles *et al.* investigated the decolorization of methyl orange using the Fenton oxidation process and adsorption on vegetal carbon. and removal efficiency lower than 85% was obtained. Ling et al. [21] studied repeated oxidative degradation of methyl orange through bio-electro-Fenton in bioelectrochemical system and decolorization efficiency lower than 86% was obtained. In addition, EC has been successfully tested to treat decolorization of methyl orange from waste water [23-25]. Zhang *et al.* [24] investigated the decolorization of methyl orange by electrocoagulation with Fe electrodes and the effect of different operation parameters was studied. Pi *et al.* [25] studied the electrocoagulation of methyl orange from synthetic waste water with periodic reversal of the electrodes technique. Different experimental conditions such as cell voltage, current density, and initial concentration were investigated. Under optimum conditions, a color removal efficiency of 97 % was obtained [25].

The purpose of this investigation was to study the high-efficiency decolorization of methyl orange from aqueous solution in a very short time by an electrocoagulation process. In this method, aluminum electrodes were used as a simple instrument under applied direct constant current and voltage. The effects of constant applied potential, initial MO concentration, and solution temperature on the color removal were investigated. In addition, the adsorption thermodynamics, isotherms, and kinetic characteristics involved in the MO removal from aqueous solution were studied in order to lay a theoretical foundation for the adsorption of MO from aqueous solutions onto aluminum hydroxides.

EXPERIMENTAL

All chemicals were of analytical grade from Merck and were used without further purification. The schematic structure of MO is shown in Fig. 1. Working solutions were prepared by suitable dilution of the stock solutions. All solutions were prepared in doubly distilled water.
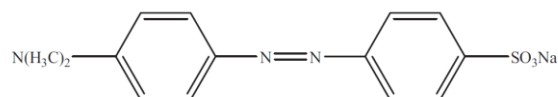
Fig. 1. Chemical structure of methyl orange.

In order to increase the conductivity of the solution, NaCl was added before injecting the solution into the apparatus. The chloride salt added to the solution prevents the formation of an oxide layer on the anode and decreases in this way the passivation problem of the electrodes.

The schematic diagram of the experimental apparatus is shown in Fig 2. The EC unit consists of an electrochemical cell, a D.C. power supply and aluminum electrodes. The aluminum cathode and aluminum anode consist of pieces of aluminum sheet separated by a space of 1 cm dipped in the wastewater. The electrodes were placed in aqueous dye solutions in a cylindrical glass cell. There were two electrodes connected in a monopolar mode in the electrochemical cell, each one with dimensions of $15 \times 5.5 \times 0.2$ cm^3.
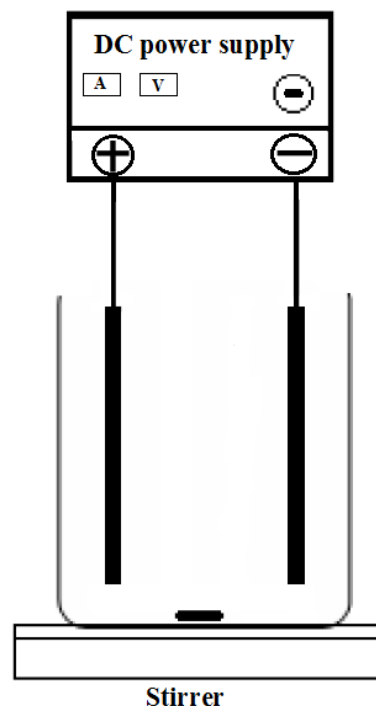
Fig. 2. Schematic diagram of the electrocoagulation equipment.

The stirrer was used in the electrochemical cell to maintain an unchanged composition and avoid the association of the flocs in the solution. The D.C. source was used through a power supply system with 0-24 V and 0-10 A. Electrodes were washed with dilute HCl between the experiments.

The dye concentration was measured using a UV/Vis spectrophotometer model Shimadzu UV1600, Japan at a wave-length corresponding to the maximum absorbance of the dye (λ_{max}=463 nm). The color removal efficiency, CR (%), was calculated using:

$$CR\% = \frac{A_0 - A_i}{A_0} \times 100 \qquad (5)$$

where A_0 and A_i are the absorbance values of the dye solution before and after treatment.

RESULTS AND DISCUSSION

Effect of applied potential

It is well-known that electrical potential and current not only determine the coagulant dosage rate but also the bubble production rate and size and the floc growth, [26,27] which can influence the treatment efficiency of the electrocoagulation. Therefore, the effect of applied potential on the MO removal efficiency was investigated. Fig. 3 illustrates the comparative removal efficiency at different applied potentials with an initial MO concentration of 4 mg l^{-1}.
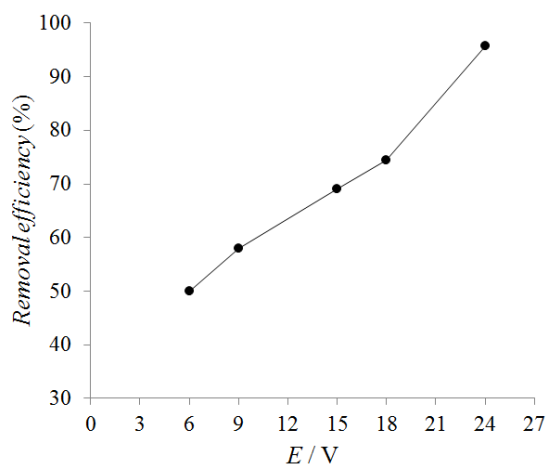
Fig. 3. Effect of applied potential on the removal efficiency of MO(C$_0$=4 mg l-1, t=30 min; C$_{NaCl}$=0.5 gl^{-1}).

For a given time, the removal efficiency increases significantly with increasing in current density. This is ascribed to the fact that at higher applied potential, the amount of aluminum oxidized increases, which results in a greater amount of precipitate for the removal of pollutants. In addition, the bubbles density increases and their size decreases with increasing current density [28-

630

30] leads to a greater upwards flux and a faster removal of pollutants and sludge flotation. As the current decreases, the time needed to achieve similar efficiencies increases. However, the cost of the process is determined by the consumption of the sacrificial electrode and the electrical energy which increases in higher applied potentials. The removal efficiency reaches to 96% by applying constant potential 24 V in 30 min.

To observe the effect of initial dye concentration on the dye removal efficiency by EC, the experiments were carried out in different dye concentrations with constant applied potential of 18 V for 30 min. Fig. 4 shows the percentage removal for different initial dye concentrations. As the results indicated, the dye removal efficiency decreases when the dye concentration increases from 7 to 15 mg L^{-1}. It is due to the fact that at constant applied potential, current density and time, the same amount of aluminum hydroxide complexes generates in all the dye solutions. Consequently, the same amount of flocs would be produced in the solutions. As a result, the flocs produced at high dye concentration are insufficient to adsorb all of the dye molecules of the solution. In very low concentration of dye, below 7 mg L^{-1}, access to the MO molecule and adsorption decreases which lead to decreasing removal efficiencies.
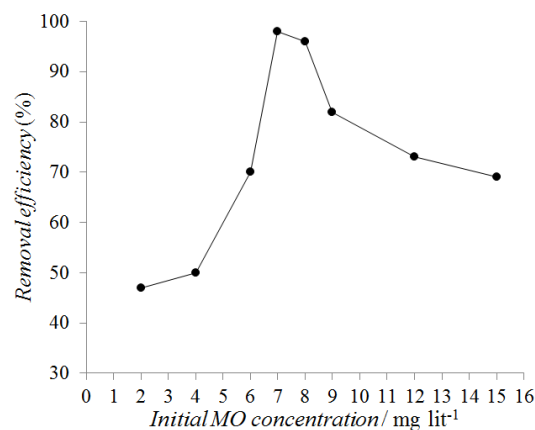
Fig. 4. Effect of initial concentration of MO on the removal efficiency (applied potential= 18 V, t=30 min, C$_{NaCl}$=0.5 g l^{-1}).

Effect of NaCl concentration

Solution conductivity affects the current efficiency, cell potential and consumption of electrical energy in electrolytic cells. The conductivity of the wastewater was adjusted to the desired levels by adding appropriate amounts of NaCl. The effect of NaCl concentration on the removal efficiency is shown in Fig. 5. Both the conductivity of the solution and the current density

increase when the salt concentration in solution increases.
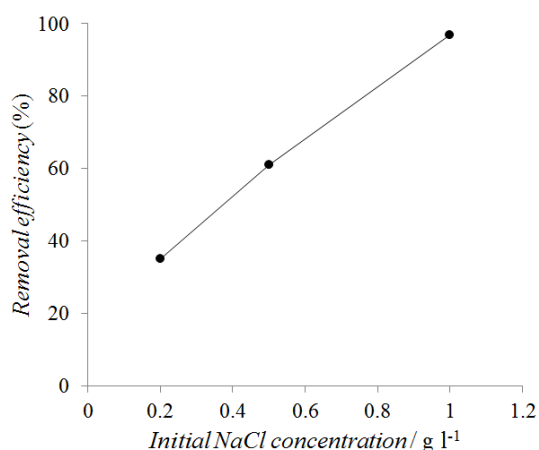
Fig. 5. Effect of NaCl concentration on the removal efficiency of MO (applied potential = 18 V, t=15 min, C_0 =8 mg l^{-1}).

The higher ionic strength generally causes an increase in the current density at the same cell potential or, equivalently, the cell potential decreases with increasing wastewater conductivity at a constant current density. Consequently, the necessary potential to attain a certain current density will be diminished and the consumed electrical energy will be decreased [31-33]. From Fig. 5, it was found that raising the conductivity of dye solutions has a considerable effect on color removal efficiency. At NaCl concentrations higher than 4 g l^{-1}, the removal efficiency approaches a constant value due to the constant electric conductivity of the solution.

Effect of temperature on MO removal

The effect of temperature on the MO removal efficiency obtained at 298, 318, 338, and 358 K is shown in Fig. 6. After 15 min of electrolysis, the MO removal efficiencies increase with increasing temperature. The electrochemical reaction rate increases with increasing solution temperature. The temperature influence can be attributed to an improved destruction of the aluminum oxide film on the anode surface and an increase in the rate of all reactions involved in the process according to the Arrhenius equation [33]. Also, the higher temperature promotes the generation of aluminum hydroxides formed in the EC process, which leads to a higher concentration and thus more frequent collisions of MO and aluminum hydroxides, resulting in an increase in the reaction rate of pollutant adsorption [34].
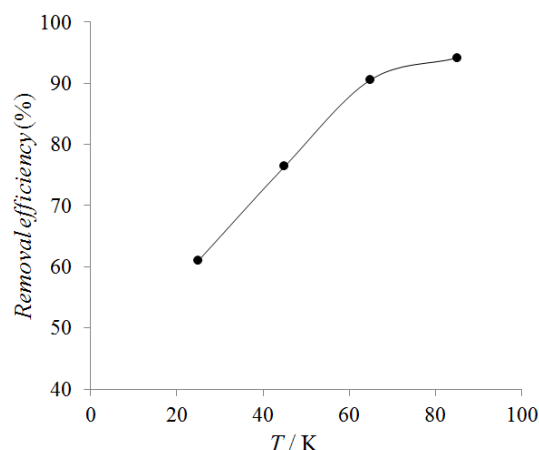
Fig. 6. Effect of temperature on the removal of MO (C_0=8 mg l^{-1}, applied current=0.9 A, C_{NaCl}=0.5 g/L).

Effect of temperature on thermodynamic adsorption parameters

Thermodynamic parameters, including Gibbs free energy ΔG^0, enthalpy ΔH^0, and entropy change ΔS^0, were calculated and used to determine the adsorption behavior of MO. The ΔG^0 was calculated by the following equation:

$$\Delta G^0 = -RT \ln K_d \tag{6}$$

where R is the universal gas constant (8.314 J mol^{-1} K^{-1}), T is the temperature (K), and K_d is the distribution coefficient (l g^{-1}). The K_d value is calculated using the following equation [35]:

$$K_d = \frac{q_e}{C_e} \tag{7}$$

where q_e and C_e are the equilibrium concentrations of MO for the adsorbent (mg g^{-1}) and the solution (mg l^{-1}), respectively. The relationship between ΔG^0, ΔH^0, and ΔS^0 can be expressed by the following equation:

$$\Delta G^0 = \Delta H^0 - T\Delta S^0 \tag{8}$$

The combination of Eqs. (6) and (8) leads to:

$$\ln K_d = \frac{\Delta S^0}{R} - \frac{\Delta H^0}{RT} \tag{9}$$

The effect of temperature on the adsorption efficiency of MO from aqueous solution was evaluated at different temperatures ranging from 298 K to 358 K. At each temperature, the corresponding C_e values at different fixed values of q_e were calculated. The thermodynamic parameters of ΔH^0 and ΔS^0 were obtained from the slope and intercept of the lnK_d versus T^{-1} plot. The Gibbs free energies at different temperatures were calculated from Eq. (8). The values of ΔG^0, ΔH^0 and ΔS^0 for MO adsorption onto aluminum hydroxides at different temperatures are given in Table 1. At all temperatures, ΔG^0 is negative which indicates the feasibility of the process and the spontaneous

nature of the adsorption of MO on aluminum hydroxides. The increase in the absolute magnitude of ΔG^0 with increasing temperature indicates that these processes are favored at high temperatures. The positive value of ΔH^0 indicates that the adsorption process is endothermic. In addition, the positive value of ΔS^0 suggests that randomness at the solid–solution interface increases during MO adsorption onto aluminum hydroxides. While the adsorption process is endothermic under these conditions, it is spontaneous due to the positive entropy change.

Adsorption isotherms

The pollutant is generally adsorbed on the surface of the metal hydroxides generated during the EC process. Thus the removal of pollutant is similar to conventional adsorption, except for coagulants generated. In order to identify the mechanism of the adsorption process, it is important to establish the most appropriate correlation for the equilibrium curves. Different adsorption isotherms were applied to establish the relationship between the amounts of MO adsorbed onto the aluminum hydroxides and its equilibrium concentration in the aqueous solution. Among them, Langmuir and Freundlich adsorption isotherms show higher correlation coefficients for MO adsorption onto the aluminum hydroxides.

The Langmuir model is originally developed for a set of well-defined localized adsorption sites with the same adsorption energy, independent of the surface coverage, and with no interaction between adsorbed molecules. This model assumes a monolayer deposition on a surface with a finite number of identical sites. It is well known that the Langmuir equation is valid for a homogeneous surface. The mathematical expression for the Langmuir isotherm is [36]:

$$q_e = \frac{\alpha_L K_L C_e}{1 + K_L C_e} \ , \tag{10}$$

where α_L (mg g^{-1}) is a constant related to the area occupied by a monolayer of adsorbate, reflecting the maximum adsorption capacity, C_e (mg l^{-1}) is the equilibrium liquid-phase concentration, K_L (l mg^{-1}) is a direct measure of the intensity of adsorption, and q_e (mg g^{-1}) is the amount adsorbed at equilibrium. K_L and α_L can be determined from the slope and intercept of the straight line in the plot of q_e^{-1} versus Ce^{-1}. Fig. 7 shows the linearized Langmuir absorption isotherm plot with experimental data.
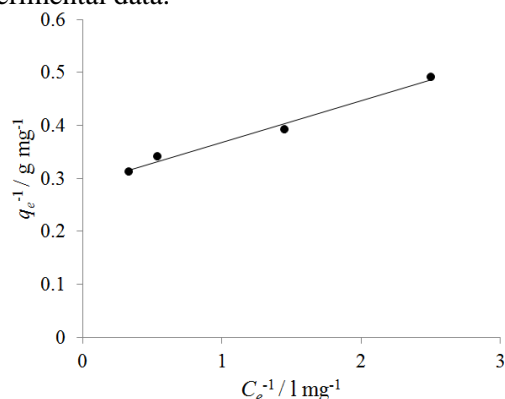
Fig. 7. Linearized Langmuir adsorption isotherms MO (C_0=8 mg l^{-1}, applied current=0.9 A, C_{NaCl}=0.5 g/L).

The Freundlich adsorption isotherm typically fits experimental data over a wide range of concentrations. This empirical model includes considerations of surface heterogeneity and exponential distribution of the active sites and their energies. The isotherm is adopted to describe reversible adsorption and is not restricted to monolayer formation. The mathematical expression for the Freundlich mode is [36]:

$$q_e = K_f C_e^{1/n} \ , \tag{11}$$

where K_f ((mg g^{-1}) (l mg^{-1})$^{1/n}$) and n (dimensionless) are constants that account for all factors affecting the adsorption process, such as adsorption capacity and intensity.

Table 1. Thermodynamic parameters of MO adsorption onto aluminum hydroxides at different temperatures.

T / K	Thermodynamic equilibrium constant (K_d)	ΔG^0 / kJ mol^{-1}	ΔS^0 / J mol^{-1} K^{-1}	ΔH^0 / kJ mol^{-1}
298	1.075	-0.18	81.8	24.389
318	1.569	-1.19		
338	3.706	-3.681		
358	5.075	-4.834		

Table 2. Langmuir and Freundlich constants for the adsorption of salicylic acid onto aluminum hydroxides.

Langmuir			Freundlich		
K_L /l mg^{-1}	α_L / mg g^{-1}	R^2	K_f / (mg g^{-1}) (l mg^{-1})$^{1/n}$	n	R^2
3.68	3.46	0.98	2.58	4.78	0.93

The Freundlich constants K_f and $1/n$ are determined from the intercept and slope, respectively, of the linear plot of log q_e vs. log C_e. Fig. 8 shows the linearized Freundlich adsorption isotherm plot with the experimental data.
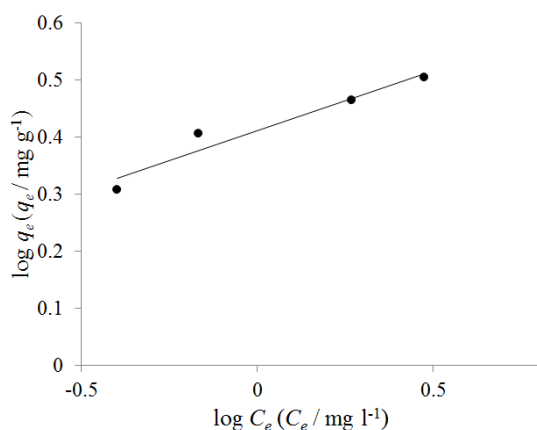
Fig. 8. Linearized Freundlich adsorption isotherms MO (C_0=8 mg l^{-1}, applied current=0.9 A, C_{NaCl}=0.5 g/L).
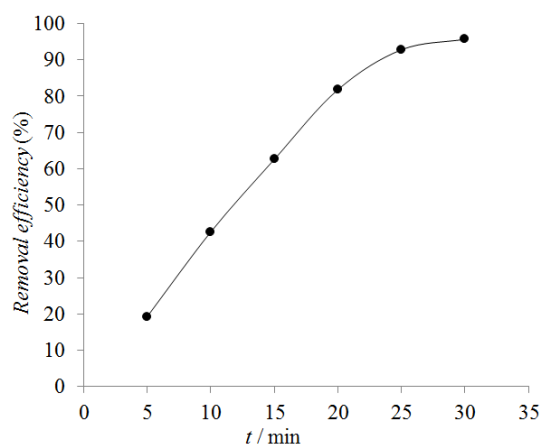
Fig. 9. Effect of electrocoagulation time on the removal efficiency (C_0 =4 mg l^{-1}, applied potential = 24 V, C_{NaCl}=0.5 g l^{-1}).

The applicability of the two isotherm equations is compared using the correlation coefficient R^2. The Langmuir and Freundlich constants for the adsorption of MO onto aluminum hydroxides are presented in Table 2. The value of the correlation coefficient R^2 is found to be 0.98 for Langmuir isotherm and 0.93 for Freundlich isotherm. However, the Langmuir isotherm model provides a better fit compared to Freundlich isotherm model. This can be due to the monolayer adsorption of MO onto aluminum hydroxides and the low interaction between the adsorbed MO molecules on the surface. Methyl orange has functional groups for adsorption which lead to strong interaction with aluminum hydroxides and increase the tendency for monolayer formation.
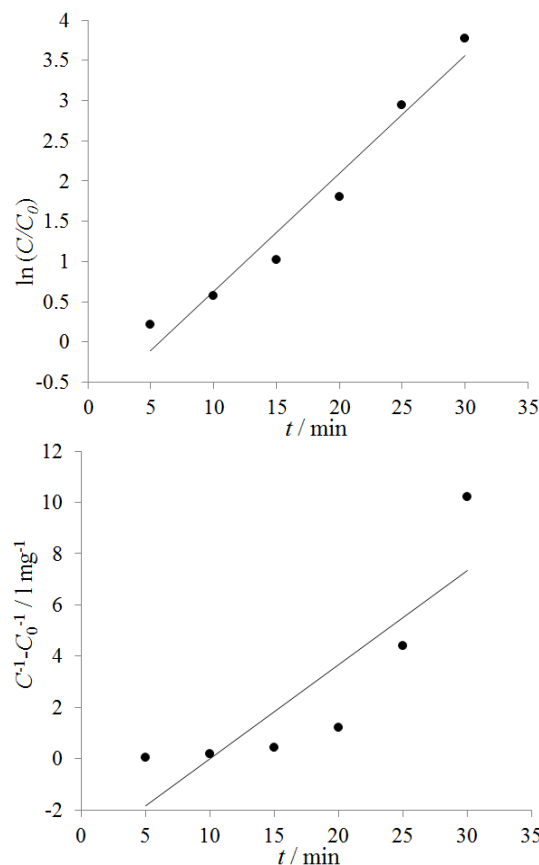
Fig. 10. Plot of (a) first-order and (b) second-order equation for the removal kinetics of MO. (C_0 =4 mg l^{-1}, applied potential = 24 V, C_{NaCl}=0.5 g l^{-1}).

Effect of electrocoagulation time

Fig. 9 shows the effect of electrocoagulation time on the removal efficiency at a constant applied potential. As can be seen, with increasing electrocoagulation time, comparable changes in the removal efficiency of MO are observed. The color removal efficiency directly depends on the concentration of hydroxyl and metal ions produced on the electrodes. The color of the dye solution decreases as a function of elapsed time. After 30 min of electrolysis, the color removal efficiency reaches a maximum value at 24 V applied potential. The rate of removal of MO can be presented by the following first-order reaction kinetics:

$$\frac{dC}{dt} = -k_1 C^m \qquad (12)$$

where C represents the MO concentration, m the order of reaction, k the reaction rate coefficient and t is the time. For a first-order reaction, the above equation becomes

$$\ln\left(\frac{C}{C_0}\right) = -k_1 t \qquad (13)$$

where C_0 is the initial MO concentration.

According to the above equation, a plot of ln (C_0 C^{-1}) against t yields a straight line with a slope of k_1.

For a second-order reaction, the above equation becomes:

$$\frac{1}{C} - \frac{1}{C_0} = -k_2 t \qquad (14)$$

The slope of the plot of $C^{-1} - C_0^{-1}$ versus time gives the value of the rate constant k_2.

Fig. 10 reveals the reasonably good fit of first-order kinetic model to the observed data. The conformity between experimental data and the model values was evaluated by the values of the correlation coefficient (R^2). The correlation coefficient R^2 for the first-order model is 0.96 which is relatively higher than that for the second-order model (0.73). The rate coefficient for a first-order removal rate of MO was obtained as 0.1468 min^{-1}.

CONCLUSION

Electrocoagulation was used to remove color from dye solutions containing MO. The effect of various operational parameters on color removal efficiency was investigated. The results indicated that EC was a promising treatment for the removal of MO from aqueous solutions. The experiments showed the feasibility of removing MO by adsorption and co-precipitation with aluminum hydroxides. The removal efficiencies increased in the presence of higher supporting electrolyte concentration. The effect of different applied constant potentials was checked and the removal efficiencies increased with increasing applied potential.

In addition, with increasing temperature, the MO removal efficiencies increased and the thermodynamic parameters were determined in different temperatures. Their values indicated that the adsorption process was favorable and spontaneous. As the temperature increased from 298 K to 358 K, ΔG^0 became further negative, indicating a stronger driving force, resulting in a greater adsorption capacity at higher temperatures. The positive value of ΔH^0 confirmed that the process was endothermic, meaning that the reaction consumed energy. The positive value of ΔS^0 suggested that the higher randomness at the solid–solution interface occurred during the MO adsorption from the aqueous solution onto aluminum hydroxides. The metal hydroxides generated by EC can efficiently remove MO by adsorption, and the EC process was modeled using adsorption isotherm models. The MO adsorption was best fitted by the Langmuir adsorption

isotherm, and the results were in good agreement with the experimental data. Decolorization of MO wastewater was described well by a first-order reaction equation and the rate constant was obtained to be 0.1468 min^{-1}.

REFERENCES

1. D. P. Ilieva, L. L. Nedelchev, D. I. Nazarova, *Bulgarian Chemical Communications*, **45**, 137 (2013).
2. J. Dikova, S. Kitova, D. Stoyanova, A.Vasilev, T. Deligeorgiev, S. Angelova, *Bulgarian Chemical Communications*, 45,SI B, **175** (2013).
3. K. I. Milenova, A. E. Eliyas, V. N. Blaskov, I. A. Avramova, I. D. Stambolova, Y. G. Karakirova, S. V. Vassilev, P. M. Nikolov, N. A. Kasabova, S. K. Rakovsky, *Bulgarian Chemical Communications,* **47**, 336 (2015).
4. M. P. Tsvetkov, K. L. Zaharieva, Z. P. Cherkezova-Zheleva, M. M. Milanova, I. G. Mitov, *Bulgarian Chemical Communications,* **47**, 354 (2015).
5. [5] B. Zhang, Z. Wang, X. Zhou, C. Shi, H. Guo, C. Feng, *Bioresource Technol.*, **181**, 360 (2015).
6. G. Wei, L. Zhang, T. Wei, Q. Luo , Z. Tong, *Environmen. Technol.* **33**, 1589 (2012).
7. P. He, L. Wang, J. Xue, Z. Cao, *Environmen. Technol.* **31**, 417 (2010).
8. W. Shi, Q. Cheng, P. Zhang, Y. Ding, H. Dong, L. Duan, X. Li, A. Xu, A. *Catal. Commun.*, **56**, 32 (2014).
9. J. Zou, J. Ma, X. Zhang, P. Xie, *Chem. Eng. J.*, **34**, 253 (2014).
10. V.N. Blaskov, I.D. Stambolova, S.V. Vassilev, C.D. Dushkin, *Bulgarian Chemical Communications*, **45**, 263 (2013).
11. M. T. Baei, H. Mohammadian, S. Hashemian, *Bulgarian Chemical Communications*, **46**, 735 (2014).
12. B. G. Tsyntsarski, B. N. Petrova, T. K. Budinova, N. V. Petrov, D. K. Teodosiev, *Bulgarian Chemical Communications*, **46**, 353, (2014).
13. N. Kaneva, A. Bojinova, K. Papazova, D. Dimitrov, *Bulgarian Chemical Communications,* **47**, 402 (2015).
14. R. Boukoureshtlieva, S. Yankova, V. Beschkov, J. Milusheva, G. Naydenova, L. Popova, G. Yotov, S. Hristov, *Bulgarian Chemical Communications,* **45**, SI A, 129 (2013).
15. S. Hamid, W. Bae, S. Kim, M. T. Amin, *Environmen. Technol.* **35**, 1470 (2014).
16. O. Tünay, M. Şimşeker, I. Kabdaşlı, T. Ölmez-Hancı, *Environmen. Technol.* **35**, 1577 (2014).
17. D. R. Manenti, A. N. Módenes, P. A. Soares, R. A. R. Boaventura, S. M. Palácio, F. H. Borba, F. R. Espinoza-Quiñones, R. Bergamasco, V. J. P. Vilar, *Environmen. Technol.* **36**, 496 (2015).
18. M. Kobya, M. Bayramoglu, M. Eyvaz, *J. Hazard. Mater. B* **148**, 311 (2007).
19. I. A. Şengil, M. Özacar, B. Öműrlű, *Chem. Biochem. Eng. Q.* **18**, 391 (2004).
20. C. Y. Hu, S. L. Lo, W. H. Kuan, Y. D. Lee, *Water Research*, **39**, 895 (2005).

21. T. Ling, B. Huang, M. Zhao, Q. Yan, W. Shen, *Bioresource Technology* **203**, 89 (2016).
22. A. Saldana-Robles, R. Guerra-Sanchez, M. I. Maldonado-Rubio, J. M. Peralta-Hernandez, *J. Ind. Eng. Chem.* **20**, 848 (2014).
23. Y. Zhang , Y. Q. Cong , Q. Wang, *Environ. Eng. Manag.* J., **12**, 517 (2013).
24. Y. Zhang, Y. Cong, P. Sun, *CIESC J.*, **60**, 2345 (2009).
25. K. W. Pi, Q. Xiao, H. Q. Zhang, M. Xia, A. R. Gerson, *Process Saf. Environ.*, **92**, 796 (2014).
26. R. D. Letterman, A. Amirtharajah, C. R. O'Melia, Chapter 6, Coagulation and flocculation, in, Water quality and treatment, 5th. ed., AWWA, McGraw-Hill., New York, 1999.
27. P. H. Holt, G. W. Barton, M. Wark, A. A. Mitchell, *Colloids Surf. A: Physicochem. Eng. Aspects*, **211**, 233 (2002).
28. E. Bazrafshan, A. H. Mahvi, S. Nasseri, M. Shaighi, *Iran. J. Environ. Health. Sci. Eng.*, **4**, 127 (2007).
29. E. Bazrafshan, A. H. Mahvi, S. Naseri, A. R. Mesdaghinia, *Turkish J. Eng. Environ. Sci.*, **32**, 59 (2008).
30. N. K. Khosla, S. Venkatachalam, P. Somasundaran, *J. Appl. Electrochem.*, **21**, 986 (1991).
31. M. Y. A. Mollah, R. Schennach, J. R. Parga, D. L. Cocke, *J. Hazard. Mater. B* **84**, 29 (2001).
32. M. Y. A. Mollah, P. Morkovsky, J. A. G. Gomes, M. Kesmez, J. Parga, D. L. Cocke, *J. Hazard. Mater. B* **114**, 199 (2004).
33. G. Chen, *Sep. Purif. Technol.* **38**, 11 (2004).
34. E. S. Z. El-Ashtoukhy, N. K. Amin, O. Abdelwahab, *Chem. Eng. J.* **146**, 205 (2009).
35. [35] E. I. Unuabonah, K. O. Adebowale, B. I. Olu-Owolabi, *J. Hazard. Mater.* **144**, 386 (2007).
36. J. Walter, J. Weber, Physicochemical Processes for Water Quality Control, Wiley Interscience, Canada, 1972.

КИНЕТИКА И ТЕРМОДИНАМИЧНО ИЗСЛЕДВАНЕ НА ЕЛЕКТРО-КОАГУЛАЦИЯТА НА МЕТИЛОРАНЖ ОТ ВОДЕН РАЗТВОР С АЛУМИНИЕВИ ЕЛЕКТРОДИ

М.Р. Маджди, И. Данае*, С. Никманеш

Факултет по нефтоинженерство, Нефто-технологичен университет, Абадан, Иран

(Резюме)

Опитно е изследвано отстраняването на оцветяването на разтвори, съдържащи метилоранж (МО) с помощта на правотокова електро-коагулация с алуминиеви електроди. Опитните резултати показват, че това е ефективен метод за отстраняването на МО, което става поради образуването на метални хидроксиди . изследването на влиянието на работните параметри, като времето за електролизата, прилаганият потенциал, началната концентрация на багрилото, температурата и проводимостта на разтвора върху ефективността на обезцветяването. Термодинамичните параметри, включително свободната енергия, енталпията и ентропията са изчислени за адсорбцията на МО върху металните хидроксиди и показват, че тя е спонтанна и ендотермична за температури в интервала от 298 до 358 K. Адсорбцията се описва добре с изотермата на Лангмюир, което предполага мономолекулен слой на покритието. Освен това, кинетиката на адсорбция на МО е на реакция от първи порядък.

Effects of drought stress on the components of the essential oil of evening primrose (*Oenothera macrocarpa)* and determination of the biological activities of its extracts

M. Kolivand, Z. Aghajani[*]

Department of Chemistry, Qom Branch, Islamic Azad University, Qom, Iran

In this study, the essential oil of *Oenothera macrocarpa* belonging to *Onagraceae* family, subjected to drought stress, was studied. First, the plants were grown in three irrigation conditions, including 80% field capacity (control), 60% field capacity (mild stress) and 40% field capacity (intense drought stress). Then, the antioxidant properties of aqueous and ethanolic extracts were evaluated *via* DPPH radical scavenging and beta-carotene bleaching assays. Total phenolic content of the extracts was assessed using the Folin-Ciocalteu reagent.

Results demonstrated that the main components of the plant's essential oil were alkanes and terpene compounds. The antioxidant potency of the ethanolic extract increased by increasing the drought stress.

Keywords: *Oenothera macrocarpa*, Essential oil, Antioxidant, Total phenol

INTRODUCTION

Plants can be considered as the foundation of traditional medicine, the base of phytochemistry and pharmacology; they are the source of unique flavors in the fostod industries and are the exclusive factor of perfumes in the healthcare industries.

By having rapid advancements in science on one hand and economic issues on the other hand, application of medicinal plants has gradually been decreased and industrial drugs have replaced them in the majority of cases. History of treating some diseases with medicinal plants dates back to early humans. By gaining experience and creating science, humans have learned to treat themselves with medicinal plants [1-3].

The extracts of evening primrose are rich in gamma-linoleic and gamma-linolenic acids and are antihypertensive, anti-inflammatory, antispasmodic, antitussive and thrombolytic, having been widely used for treating everything from hang nails to terminal cancer [5].

To the best of our knowledge, all studies on *Oenothera* species have only been performed on their seeds [5-7].

In Italy, Lotti *et al*. (1984), showed that the level of gamma-linoleic acid in the seeds of *Oenothera biennis* grown in the spring seeding, is lower than in those grown in autumn [8]. Levy *et al.* (2002) illustrated that precocious samples of *Oenothera lamarckiana* can be planted successfully in warm zones [9]. Effects of different nitrogen doses demonstrated that the optimum nitrogen doses and row spacing applications for the highest yield and quality were 120 kg ha^{-1} and 40 cm, respectively.

However, increasing nitrogen doses negatively affected the gamma-linolenic acid content of evening primrose oil [10].

Mardani *et al*. (2012), reported that the acetone extract of evening primrose flowers (*Oenothera biennis)* has higher level of phenolic and flavonoid compounds and better extraction efficiency in comparison with ethanolic and methanolic extracts. Moreover, the extracts also showed good antibacterial activity against all tested microorganisms [11].

Evening primrose (*Oenothera biennis*) oil has a high GLA content that promotes healthy skin and skin repair. It is usually yellow in color and soothes skin problems and inflammation, making it a good choice for people with eczema, psoriasis, or any type of dermatitis. Evening primrose skin oil helps dry skin conditions and avoids premature aging of the skin [12].

According to our research, two scientific papers had been published on the seeds of *O. macrocarpa*; one is the analysis of the triglycerides of the seeds of *O.macrocarpa* published in 1965 [13] and the other is about the hydrocarbon compounds of its seed reported in 1975 [14].

Here we report the effects of drought stress on the composition of the essential oil of *O. macrocarpa* and investigate the biological activities of its extracts.

MATERIAL AND METHODS

Plant materials

The seeds of *O. macrocarpa* were cultured using the method of Completely Randomized Design (CRD), in 3 replicates (pots) and 3 irrigation conditions including: 80% field capacity (control),

---

* To whom all correspondence should be sent:
Email: haj_aghajani@yahoo.com

60% field capacity (mild stress) and 40% field capacity (intense drought stress) in Qom's Agricultural Research Station of Medicinal Plants.

Essential oil extraction

To extract essential oils, distillations were performed using the Clevenger apparatus. The duration of the extraction procedure was 3 hours, after which samples were collected and sodium sulfate was added to them to absorb their probable water content. The samples were kept in a refrigerator.

Gas chromatographic analysis

Analytical gas chromatography of the essential oils was carried out using a Hewlett-Packard 5975B series gas chromatograph with Agilent HP-5 capillary column (30 m×0.25 mm, f.t. 0.25 µm); carrier gas, He; split ratio, 1:10, using a flame ionization detector. The column temperature was adjusted at 50°C which was unchanged for 10 min. It was programmed to rise up to 240°C at the rate of 4°C/min and then stay constant at that temperature for 15 min. GC/MS was performed on an HP 5975B instrument with a Hewlett–Packard 5973 quadruple detector, on a capillary column HP-**5** (30 m×0.25 mm; f.t 0.25 µm). The MS was operated at 70 eV ionization energy. Retention indices were calculated using the retention times of n-alkanes that were injected after the essential oil at the same chromatographic conditions. Quantitative data were obtained from the electronic integration of the FID peak areas. Acquisition mass range was 40-400 m/z.

The components of the oils were identified by comparing their mass spectra and kovats indexes with Wiley library and published books, data bases available and credible websites [15].

Preparation of extracts

Powdered dehydrated flowering branches and leaves of the plant were used for extraction. First, the reflux system was assembled. Then, the cartouche was twice filled with plant samples, put in place and then the extraction took place using two solvents separately: ethanol and water. Finally, ethanol and water extracts that had a blackish green color and contained a lot of solvent were obtained. These solutions were concentrated using a rotary evaporator.

Evaluation of antioxidant activity

DPPH radical assay. Radical-scavenging activities of the plant extracts were determined using a published DPPH radical scavenging activity

assaying method with minor modifications [16-17]. Briefly, stock solutions (10 mg/ml each) of the extracts and the synthetic standard antioxidant BHT were prepared in methanol. Dilutions were made to obtain concentrations ranging from 0.8 to 5×10^{-4} mg/ml. Dilute solutions (1 ml each) were mixed with 1 ml of a freshly prepared 1 mg/ml DPPH radical methanol solution and were kept in the dark at room temperature, for 30 min, in order to let the desired reactions to take place. Absorbance values of these solutions were recorded on an UV–Vis spectrometer at 517 nm using a blank containing the same concentration of the extract or BHT without DPPH radicals. Inhibition of DPPH radical in percentage (I %) was calculated as follows:

$$I\% = [(A_{blank} - A_{sample}) / A_{blank}]\times100$$

where A_{blank} is the absorbance value of the control reaction (containing all reagents except the test compound) and A_{sample} is the absorbance value of the test compound. The sample's concentration is expressed in terms of IC_{50}, which was calculated by drawing the chart of inhibitory percentages against concentrations of the sample. All the tests were carried out in triplicate and IC_{50} values were reported as means ± SD.

β-carotene /linoleic acid bleaching assay. In the β-carotene/linoleic acid test, the antioxidant competes with β-carotene for transferring hydrogen atoms to the proxy radicals (R1R2HCOO.) formed from the oxidation of linoleic acid in the presence of molecular oxygen (O_2) and converts them to hydroperoxides (R1R2HCOOH), leaving the β-carotene molecules intact [18]. Assaying the remaining β-carotene gives an estimation of the antioxidant potential of the sample. A mixture of β-carotene and linoleic acid was prepared by adding 0.5 mg of β-carotene to 1 ml of chloroform (HPLC grade), 50 mg of linoleic acid and 200 mg of Tween 40. The chloroform was then completely evaporated under vacuum and 100 ml of oxygenated distilled water were subsequently added to the residue and mixed gently to form a clear yellowish emulsion. The extract and BHT (positive control) were individually dissolved in methanol (2 g/l) and 350 µl of each of them were added to 2.5 ml of the above-mentioned emulsion in the test tubes and were mixed thoroughly. The test tubes were incubated in a water bath at 50 °C for 2 h together with a negative control (blank) that contained the same volume of methanol instead of the extracts. The absorbance values were measured at 470 nm on an UV–Vis spectrometer. Antioxidant activities (inhibition percentages, I %) of the

samples were calculated using the following equation:

$$I\% = (A_{\beta\text{-carotene after 2 h assay}}/ A_{\text{initial }\beta\text{-carotene}}) \times 100$$

where $A_{\beta\text{-carotene after 2 h assay}}$ is the absorbance value of β-carotene after 2 h assay remaining in the samples and $A_{\text{initial }\beta\text{-carotene}}$ is the absorbance value of β-carotene at the beginning of the experiments. All tests were carried out in triplicate and inhibition percentages were reported as means ± SD of triplicates.

Total phenol assay. Total phenolic constituents of the extracts of *O. macrocarpa* were determined by literature methods involving the Folin–Ciocalteu phenol reagent and the gallic acid standard [19]. A solution of the extract (0.1 ml) containing 1000 µg of the extract was pipetted into a 50 ml volumetric flask, then 46 ml of distilled water and 1 ml of Folin–Ciocalteu phenol reagent were added to it, and the flask was shaken thoroughly. After 3 min, 3 ml of 2% Na_2CO_3 solution were added and the mixture was allowed to stay for 2 h with intermittent shaking. Absorbance values were measured at 760 nm. The same procedure was performed for all standard gallic acid solutions (0–1000 µg /1 ml) and a standard curve was obtained from the following equation:

$$\text{Absorbance} = 0.0012 \times \text{gallic acid (µg)} + 0.0033$$

Total phenols of the extracts, as gallic acid equivalents, were determined using the absorbance values of the extracts measured at 760 nm as the input for the standard curve and the equation. The tests were carried out in triplicate and the gallic acid equivalent values were reported as means ± SD of triplicate.

RESULTS AND DISCUSSION

Chemical composition of the essential oils

The essential oils of the aerial parts of *O. macrocarpa* subjected to three irrigation regimes (80%, 60% and 40% field capacity) were extracted by means of water distillation. Quantitative and qualitative analyses of the plant were performed using the GC-MS method. In the essential oil obtained from the first regime, 23 compounds were recognized, followed by 17 compounds in the second regime and 8 compounds in the third one (Table 1). One interesting point here is that two important compounds in terms of biological activities, thymol and oleic acid, were only observed in the conditions of full irrigation and no drought stress.

ANTIOXIDANT EFFECTS

General results of DPPH experiment on the extracts of O. macrocarpa

In order to investigate the antioxidant activities of the derived extracts, the DPPH method of controlling free radicals and the beta-carotene test were used. The rate of reduction in the absorption of free radicals was measured using a spectrophotometer and the antioxidant activities of aqueous and ethanolic extracts were calculated in different concentrations; also, the IC_{50} level was determined. Among the tested samples that were obtained from the aerial parts of *O. macrocarpa*, the ethanolic extract of the third regime (40% field capacity) and the aqueous extract of the first regime (80% field capacity) had the highest antioxidant activities. Moreover, the beta-carotene test showed that the ethanolic extract of the third regime (40% field capacity) and the aqueous extract of the second regime (60% field capacity) had the highest levels of antioxidant activity.

Determination of total phenolic content

In order to evaluate the phenolic content in the studied extracts, the Folin-Ciocalteu reagent was used with gallic acid as the standard. The aqueous extract of the first regime (80% field capacity) showed the highest level of phenolic compounds, equivalent to 28 µg/mg concentration of gallic acid. The ethanolic extract of the third regime (40% field capacity) showed the highest level of phenolic compounds equivalent to 49 µg/mg concentration of gallic acid (Table 2).

CONCLUSION

Summarizing, from the compounds recognized in the plant's essential oils it can be concluded that most of the compounds are saturated compounds of alkanes and monoterpenes, with a phenolic cycle. By comparing three agricultural capacities, it can be inferred that in 40% field capacity, due to less irrigation, terpene compounds cannot be produced and they were not observed in this stress. Another important point is that the antioxidant potency of ethanolic extract of this plant was increased by increasing the drought stress.

Table 1. Composition of the essential oils of *Oenothera macrocarpa* in 3 irrigation conditions.

No.	Components	A%	B%	C%	RI
1	n-Octane	1.70	20.62	9.61	800
2	Nonane, 5-methyl	-	0.70	-	959
3	Nonane, 3-methyl	-	1.38	-	971
4	1-Hexyl-3-methylcyclopentane	-	1.15	-	991
5	Decane	3.33	36.90	3.36	1004
6	Undecane	-	-	5.63	1108
7	Dodecane	9.06	9.59	-	1206
8	Citral	-	1.29	-	1279
9	2-Undecanone	1.37	0.53	-	1302
10	Thymol	6.81	-	-	1310
11	Guaiene	0.73	-	-	1353
12	Tetradecane	4.43	2.45	19.91	1406
13	n-Decanoic acid	-	-	14.15	1421
14	Caryophyllene	0.87	-	-	1430
15	Nerol acetate	2.75	-	-	1595
16	Phenol,2,5-bis(1-methyl ethyl)	1.08	-	-	1589
17	Hexadecane	1.52	0.64	-	1605
18	2-Ethylhexyl 2-ethylhexanoate	3.03	1.45	13.84	1612
19	2,2-Dimethyl-7-ethoxy-6-methoxy-4-chromanone	11.63	-	-	1734
20	trans-Nuciferol	1.32	-	-	1743
21	Myristic acid	1.59	1.81	-	1789
22	Octadecane	0.41	-	-	1804
23	Phthalic acid	-	0.48	-	1972
24	Dibutyl phthalate	0.89	-	-	1974
25	n-Hexadecanoic acid	6.84	8.91	-	1996
26	Phytol	0.57	-	-	2038
27	9,12,15-Octa decatrien-1-ol	-	2.83	-	2051
28	Oleic acid	15.68	-	-	2052
29	Tricosane	8.84	6.03	18.45	2090
30	Tetracosane	0.55	-	-	2401
31	Pentacosane	6.12	3.23	-	2501
32	Triacontane	-	-	14.99	2970

Category	A%	B%	C%
Oxygenated monoterpenoids	9.56	1.29	-
Non terpenoid oxygenated hydrocarbons	43.45	16.01	27.99
Non terpenoid hydrocarbons	35.96	82.69	71.95
Sesquiterpenoid hydrocarbons	1.60	-	-
Oxygenated diterpene	0.57	-	-

A: Composition of essential oil in non-stress condition; B: Composition of essential oil in mild drought condition;
C: Composition of essential oil in intense drought condition; RI: Relative retention indices to C8–C24 n-alkanes HP-5 MS column.

Table 2. Antioxidant activity of the extracts of *Oenothera macrocarpa* in 3 irrigation conditions

Sample	DPPH (IC$_{50}$μg/ml)	β-Carotene/linoleic acid Inhibition (%)	Folin-Ciocalteu
Aqueous extract FC 40%	40.0 ±.0.9	4.8 ± 0.4	28.0 ± 1.1
Aqueous extract FC 60%	43.0 ± 1.1	15.5 ± 0.6	16.5 ± 0.8
Aqueous extract FC 80%	39.0 ± .0.7	4.6 ± 0.5	28.3 ± 0.9
Ethanolic extract FC 40%	6.1 ± 0.5	49.7 ± 1.1	49.1 ± 1.2
Ethanolic extract FC 60%	14.0 ± 0.3	34.4 ±0.9	41.3 ± 0.7
Ethanolic extract FC 80%	17.0 ± 0.6	44.8 ± 0.8	19.1 ± 0.8
BHT	19.5 ± 0.6	94.2 ± 1.2	–

REFERENCES

1. M. Naseri, *Daneshvar Med.* **11**, **52**, 53 (2004).
2. M.A. Kay, Healing with plants in the American and Mexican West. Tucson: University of Arizona Press. 1996, p. 19.
3. The Cannon of Medicine, 6ᵗʰ ed. Tehran: Sorush Publisher; Avicenna, 2004.
4. B.J.F. Hudson, *J Am Oil Chem Soc.,* **61,** 540 (1984).
5. Mosby's medical dictionary (8th ed.) St. Louis, MO: Mosby/Elsevier 2009.
6. S.A. Balch, C.B. Mckenney, D.L. Auld, *Hort. Science* **38**, 595 (2003).
7. A.K. Kiss, M. Derwinska, S. Granica, *J Food Nutr Sci.* **61,** 109 (2011).
8. G. Lotti, R. Izzo, F. Bottazzi, A. Bellani, *Agrochimica.* **28,** 85 (1984).
9. A. Levy, Z. Yaniv, E. Menagem, M. Barzilai , Proc. of the Workshop on Agricultural and Quality Aspects of Medicinal and Aromatic Plants, Adana, Turkey,2002; p. 1.
10. N. Secroglu, M. Ozguven, *Turk J Agric.* **30,** 125 (2006).
11. V. Mardani, M. Alami, S. Arabshahi, R. Khoda Bakhshi, M. Ghaderi, *Iran Food Sci Technol Res J.* **9,** 182 (2013).
12. R. Wilson, Aromatherapy: Essential Oils for Vibrant Health and Beauty, Part one: The basic principle of aromatherapy. New York: Penguin Putman Inc., 2002.
13. F.D. Gunstone, M. Ilyas-Qureshi, *J Am Oil Chem Soc.* **42,** 961 (1965).
14. S.O. Brown, R.J. Hamilton, S. Shaw, *Phytochemistry*, **14,** 2726 (1975).
15. R.P. Adams, Identification of essential oil components by gas chromatography/mass spectroscopy, Carol Stream IL: Allured Publishing Co., 2001.
16. M.C. Foti, C. Daquino, C. Geraci, *J Org Chem.* **69,** 2309 (2004).
17. Y.D. Garcia, B.S. Valles, A.P. Lobo, *Food Chem.* **117,** 731 (2009).
18. D. Huang, B. Ou, R.L. Prior, *J. Agric. Food Chem.* **53,** 1841 (2005).
19. K. Slinkard, V.L. Singleton, *Am J Enol. Viticult.* **28,** 49 (1977).

ЕФЕКТ НА СТРЕСА ОТ СУША СПРЯМО КОМПОНЕНТИТЕ НА ЕТЕРИЧНО МАСЛО ОТ ВЕЧЕРНА ИГЛИКА (*Oenothera macrocarpa)* И ОПРЕДЕЛЯНЕ НА БИЛОГИЧНАТА АКТИВНОСТ НА ЕКСТРАКТИ ОТ НЕЯ

М. Коливанд, З. Агаджани[*]

Департамент по химия, Ислямски университет „Азад", Клон Кум, Иран

(Резюме)

В тази работа е изследвано етеричното масло от *Oenothera macrocarpa,* принадлежаща към семейство *Onagraceae*, подложена на стрес от суша. Най-напред растението е отглеждано при три условия на напояване, включващи 80% полеви капацитет (контрола), 60% (умерен стрес) and 40% (интензивен стрес). След това са оценени анти-оксидантниет свойства на спиртните екстракти от маслата с помощта на DPPH-метода за отстраняване на радикали и β-каротенови тестове. Общото съдържание на феноли в екстрактите е оценено с реагента на Folin-Ciocalteu.

Резултатите показват, че главните компоненти на етеричното масло са алкани и терпени, като анти-оксидантната активност на спиртните екстракти нараства с нарастването на стреса от суша.

Chemical composition and analgesic activity of the essential oil of *Mentha mozaffarianii* jamzad leaves

H. Sam-Daliri[1], Z. Mousavi[1], N. Naderi[2], J. Asgarpanah[3*]

[1] *Department of Pharmacology & Toxicology, Faculty of Pharmacy, Pharmaceutical Sciences Branch, Islamic Azad University, Tehran - Iran (IAUPS).*

[2] *Department of Pharmacology and Toxicology, Faculty of Pharmacy, ShahidBeheshti University of Medical Sciences, Tehran - Iran.*

[3] *Department of Pharmacognosy, Faculty of Pharmacy, Pharmaceutical Sciences Branch, Islamic Azad University, Tehran - Iran (IAUPS).*

The analgesic property of *Mentha mozaffariani* essential oil was investigated on mice and rats. The analgesic activity of the oil was assessed by acetic acid-induced writhing and formalin-induced paw licking methods. *M. mozaffariani* oil significantly decreased the number of acetic acid-induced writhes in mice compared to animals that received vehicle only. In formalin test, a dose of 100 mg/kg significantly reduced the pain score of first phase in comparison to control ($p<0.05$). The inhibitory activity of *M. mozaffariani* essential oil was found to be very close to that of the standard drug, aspirin (100mg/kg). The studied oil was analyzed by GC and GC–MS and twenty two constituents, representing 99.4 % of the oil, were identified. The major component of the oil was characterized as piperitone (51.0%) which might be responsible for the observed activity. The results suggest that *M. mozaffariani* essential oil possesses biologically active constituent(s) that have significant analgesic effects which support the ethnomedicinal claims of the plant application in the management of pain.

Keywords: Analgesic activity, *Mentha mozaffariani*, Essential oil, Piperitone

INTRODUCTION

The Iranian endemic plant *Mentha mozaffarianii*Jamzad. belongs to the *Lamiaceae* family and is known locally as "Pooneh-Koohi" [1]. Six species and several subspecies of the genus *Mentha* are found in Iran, among which just *M. mozaffarianii* is endemic. It has a limited geographical range in the south of Iran and is found in Siyahoo, Qotb-Abad, Damtang and Sikhoran in Hormozgan Province [2]. The leaves have been commonly used in Iranian traditional medicine as antiseptic, analgesic means,for treating painful menstruation, dyspepsia, arthralgia, fever, headache, common cold and for healing wounds [1-3]. This plant is also among the medicinal plants which have served as natural remedies for Huntington's disease in medieval Persian medicine [4].

Due to the widespread use of *M. mozaffarianii* in Iranian traditional medicine for the relief and treatment of pain, we were prompted to evaluate the analgesic activity of this plant. As the plant's leaves contain high amount of essential oil (2-4% v/w), the analgesic effect of the essential oil extracted from *M. mozaffarianii* leaves was investigated to confirm the pharmacological basis for its folkloric use as a natural pain killer agent. This study explores the analgesic property of *M. mozaffarianii* oil by two standard experimental test models. The oil was also analyzed by GC and GC–MS in order to identify the potentially responsible compounds for the observed property. This is the first attempt addressing such ethnopharmacological properties of *M. mozaffarianii* essential oil in a comprehensive manner.

EXPERIMENTAL

Plant Materials

Leaves of *M. mozaffariani* were collected in March 2014 from Genow protected area, Bandar Abbas, Hormozgan Province, south of Iran. The leaves were identified by R. Asadpour. A voucher specimen has been deposited at the herbarium of the Department of Pharmacognosy, Pharmaceutical Sciences Branch, Islamic Azad University, Tehran, Iran, under code number 1011-AUPF.

Fresh leaves were separately submitted to hydrodistillation in a Clevenger-type apparatus for 3 hours. At the end of distillation the oils were collected, dried with anhydrous Na_2SO_4, measured,

---

transferred to clean glass vials and kept at a temperature of −18°C for further analyses.

Experimental animals

Male NMRI mice (20–25 g) and male Wistar rats (200-250 g) were used throughout this study. Animals were housed separately in groups of 5-6 and were allowed free access to food and water except for the short time that animals were removed from their cages for testing. All experiments were conducted during the period between 10.00 a.m. and 13 p.m. with normal room light (12 h regular light/dark cycle) and temperature (22 ± 1 °C). All procedures were carried out in accordance with the institutional guidelines for animal care and use (ethical approval number: 3183). Each mouse was used only once.

Analgesic activity

Acetic acid-induced writhing in mice

The writhing acetic acid test was performed as originally described by Siegmund*et al.* [5]. This method was employed to preferentially evaluate possible peripheral effects of *M. mozaffarianii* essential oil as an analgesic substance. Four groups of 10 mice were fasted overnight prior to the start of the experiment, while given free access to water. The vehicle, tween 80 (2%, 10 ml/kg), aspirin (100 mg/kg) and the essential oil (50 and 100 mg/kg) were orally administered to the first, second, third and fourth group of mice, respectively, 45 min prior to the injection of acetic acid (1%, 10 ml/kg). Aspirin is a well-known peripheral analgesic drug and it was used as a positive control in the present investigation. The mice were then placed in an observation box, and the number of writhes was counted for 30 min after acetic acid injection [6].

Formalin test in rats

The formalin test differs from most other nociceptive tests as it enables evaluation of analgesic activity towards moderate continuous pain generated by injured tissue [7]. This method was employed to preferentially evaluate possible central effects of *M. mozaffarianii* essential oil as an analgesic substance. Five groups of 6 rats were fasted overnight prior to the start of the experiment, while given free access to water. 30 min after oral administration of the vehicle, tween 80 (2%, 10 ml/kg), aspirin (100 mg/kg) and the essential oil (50, 100 and 200 mg/kg) to the first, second, third, fourth and fifth group of rats, respectively, the right hind paw was subcutaneously injected with 0.05 ml of 5% formalin in saline. Aspirin is a well-known central analgesic drug and it was used as a positive

control in the present investigation. The animals were placed in a transparent polypropylene cage next to a mirror so that they could be observed from all angles. The animals were continuously observed from the time of formalin injection to 60 min. The behaviors were quantified as described by Dubuisson and Dennis [8] as 0 = normal weight bearing on the injected paw, 1=limping during locomotion or resting the paw lightly on the floor, 2=elevation of the injected paw so that at most the nails touch the floor, and 3=licking, biting or shaking the injected paw. Subjects' behaviors were continuously scored in 5 min intervals by a trained observer. The pain score was then calculated for a 5-min interval using the following equation:

$\Sigma n/20$ = average score in 5 min

Subcutaneous formalin injection resulted in a biphasic response of nociceptive behavior in rats. The early phase starts immediately after formalin application, followed by an intermediate phase in which the pain-related behavior was relatively decreased and finally by a more prolonged but delayed phase of increasing pain-related behavior. The area-under-the-curve (AUC) of the pain score of the first 10 min was considered as phase 1 and the AUC of pain scores during 10–60 min after formalin injection was considered as phase 2.

Statistical analysis

The results were presented as mean+SEM. Statistical analysis was performed using Prism 5 (Graphpad Software Inc.). One-way analysis of variance (ANOVA) followed by Dunnett'stests was used and a p-value less than 0.05 was considered as statistically significant.

Analysis of the essential oil

Oil sample analysis was performed on a HP-6890 gas chromatograph (GC) equipped with a FID and a DB-5 capillary column, 30 m × 0.25 mm, 0.25 μm film thickness, temperature programmed as follows: 60°−240°C at 4°C/min. The carrier gas was N_2 at a flow rate of 2.0 ml/min; injector port and detector temperature were 250°C and 300°C, respectively. Sample was injected by splitting and the split ratio was 1:10.

GC/MS analysis was performed on a Hewlett-Packard 6890 /5972 system with a DB-5 capillary column (30 m × 0.25 mm; 0.25 μm film thickness). The operating conditions were as described above but the carrier gas was He. Mass spectra were taken at 70 eV. Scan mass range was 40-400 m/z at a sampling rate of 1.0 scan/s. Quantitative data were obtained from the electronic integration of the FID peak areas. The components of the oils were

identified by their retention times, retention indices, relative to C_9-$C_{28}n$-alkanes, computer matching with the WILEY275.L library and by comparison of their mass spectra with data already available in the literature [9-10]. The percentage composition of the identified compounds was computed from the GC peak areas without any correction factors and was calculated relatively. The result of the oil analysis is the average of three replicates.

RESULTS AND DISCUSSION

In this study, we evaluated the efficacy of the essential oil of *M. mozaffarianii* aerial parts since the volatile constituents comprise the main components of this plant. Oral administration of *M. mozaffarianii* oil (50 and100 mg/kg) decreased the number of acetic acid-induced writhes in mice compared to the animals that received vehicle only (Table 1). The writhe inhibitory effects of the oil ranged from 68 to 78%. The best results were observed by 100 mg/kg dose of the oil. By comparison, 100 mg/kg aspirin produced a little less (i.e. 77.68% effectiveness) analgesia in this nociception model. The analgesic effect induced by *M. mozaffarianii* oil was dose-related.

The effects of the systemic administration of different doses of the oil on the behavioral responses in the first and second phases of formalin test were evaluated (Figure 1. A.). In both phases of the pain, behaviors were separately analyzed as the area under the curve pain score *versus* time. As shown in Figure 1. B, in the first phase of the formalin test 100mg/kg dose of the essential oil reduced the pain score (p<0.05) and aspirin as a standard analgesic drug significantly (p<0.001) reduced pain behavior. Doses of 50, 100 and 200 mg/kg of the essential oil did not affect the area-under-the-curve pain score in the second phase of the formalin test when compared to aspirin as the standard analgesic drug which significantly (p<0.001) reduced pain behavior (Figure 1. C.).

M. mozaffarianii essential oil was analyzed by GC and GC/MS to determine the possible compounds responsible for the observed antinociceptive activity. The hydrodistillation of *M. mozaffarianii* aerial parts gave yellowish oil with a pleasant odor and a yield of 4.3% (v/w). As shown in Table 2, twenty two components were identified in this oil, which represented about 99.4% of the total chromatographic material. The major constituent of the oil was piperitone (51.0%). Different preparations made from *M. mozaffarianii* leaves are commonly used in ethnobotanical practices for the treatment of pain in Iran.
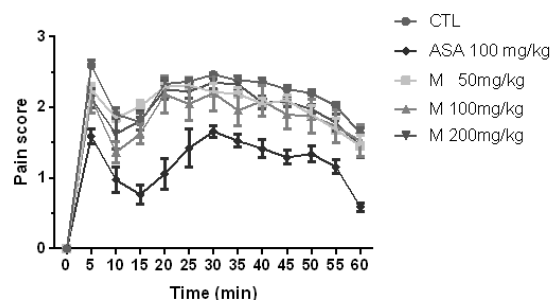
A: Changes in pain scores during 60 min of the observation.
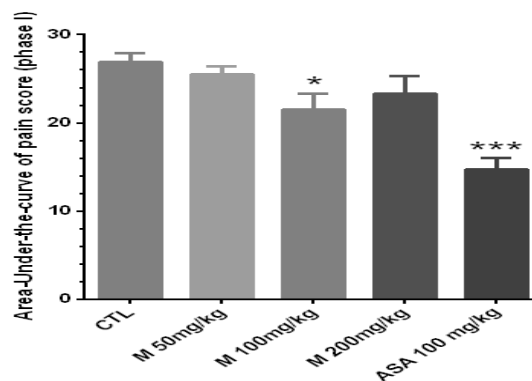
B: Overall changes in pain scores as the area-under-the-curve (AUC) of the first phase of the formalin test.
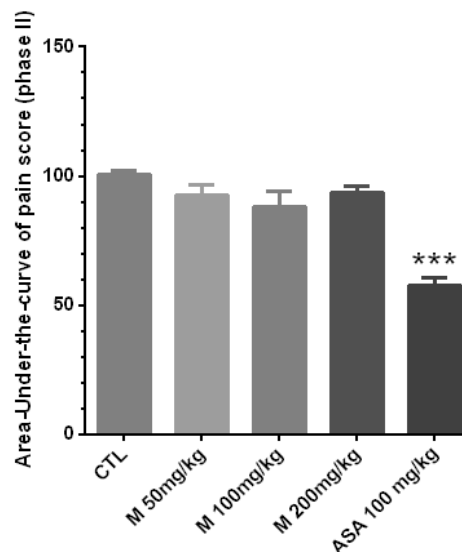
C:Overall changes in pain scores as the area-under-the-curve (AUC) of the second phase of the formalin test.

Fig. 1. Effect of oral administration of *M. mozaffarianii* essential oil (50, 100 and 200 mg/kg) on pain related behavior in formalin test. The oil or its vehicle (control group) was administered 30 min before the formalin test. Data are shown as mean ± SEM (n = 6). *P<0.05, **P<0.01, ***P<0.001 significant difference compared to control group.

Table 1. Effect of *M. mozaffarianii* essential oil on acetic acid-induced writhing in mice.

Group	Dose (mg/kg)	Number of writhings	Inhibition (%)
Control	10	45.71±6.94	-
Essential oil	50	14.50±8.75[*]	68.27
	100	10.12±11.51[**]	77.89
Aspirin	100	10.23±4.57[***]	77.68

Each value represents the mean±S.E.M. of 5 mice. *$P<$ 0.05, **$P<0.01$ and ***$P<0.001$ compared to control group using one way ANOVA followed by Dunnett's multiple comparison test.

Table 2. GC-MS analysis of the essential oil of *M. mozaffariani* aerial parts.

Compound[a]	KI[b]	KI[c]	Percentage
α-Pinene	938	939	0.6
Camphene	952	954	0.2
Sabinene	971	975	0.5
β-Pinene	977	979	1.0
Myrcene	990	991	0.3
Ocymene	998	999	0.6
Limonene	1028	1029	0.4
1,8-Cineol	1033	1031	11.7
Linalool	1097	1097	11.1
Menthone	1149	1153	1.9
δ-Terpineol	1162	1166	0.3
Borneol	1165	1169	1.0
4-Terpineol	1178	1177	0.2
α-Terpineol	1190	1189	3.4
Pulegone	1237	1237	0.3
Piperitone	1251	1253	51.0
Thymol	1290	1290	1.0
Piperitenone	1339	1343	8.6
Piperitenone oxide	1371	1369	2.3
trans-Jasmone	1390	1391	1.9
β-Caryophyllene	1419	1419	0.8
Bicyclogermacrene	1500	1500	0.3
Total			99.4

[a]Compounds listed in order of elution.
[b]KI (Kovats index) measured relative to *n*-alkanes (C$_9$-C$_{28}$) on the non-polar DB-5 column under conditions listed in the experimental section.
[c]KI, (Kovats index) from literature.

Acetic acid-induced and formalin-induced pain models were applied in the present study to evaluate the antinociceptive effect of *M. mozaffarianii* essential oil in experimental mice and rats. The abdominal constriction response induced by acetic acid is a sensitive procedure to evaluate peripherally acting analgesics. In general, acetic acid causes pain by liberating endogenous substances such as serotonin histamine, prostaglandins (PGs), bradykinins and substance P endings. Local peritoneal receptors are postulated to be involved in the abdominal constrictions response. The method has also been associated with prostanoids in general, that is, increased levels of

PGE2 and PGF2α in peritoneal fluids, as well as lipoxygenase products [11]. The formalin test is an important animal model in the study of acute long-lasting pains comprising two distinct phases. The first phase (neurogenic pain) is caused by direct chemical stimulation of nociceptive afferent fibers, predominantly C fibers, which can be suppressed by opiates like morphine. The second phase (inflammatory pain) results from the action of inflammatory mediators such as prostaglandins, serotonin and bradikinin in the peripheral tissues and from functional changes in the spinal dorsal horn. The level of pain in this model is sensitive to both centrally (phase 1 and phase 2) and peripherally (mostly phase 2) acting analgesics [12].

Results obtained in the present study showed it to be the first report describing the antinociceptive activity of *M. mozaffarianii* oil. The results demonstrated that the essential oil decreased the abdominal constriction, indicating the inhibition of the expression of prostaglandin synthesis by cyclooxygenase pathway [13]. The profile of anti-nociceptive activity of the oil identified in these experiments is different from that of aspirin, decrease of pain behavior in the first phase of formalin test but not in the second phase. Perhaps the simplest explanation is that the oil did not show anti-inflammatory effects. According to the phytochemical results, piperitoneconstituted more than half of the oil composition and it could be concluded that the analgesic effects of *M. mozaffarianii* essential oil may be due to the high content of piperitone. As there are no data on the analgesic activity of piperitone, further work to establish the analgesic activity of pure piperitone is currently going on in our laboratory. 1,8-Cineol as the other main compound of *M. mozaffarianii* essential oil comprising 11.7% of the oil could be considered as one of the active components. Several studies have proven the potent analgesic property of this monoterpenoidalcohol [14-16]. Analgesic activity of linalool which comprises 11.1% of the studied oil has been previously examined in two different pain models including the acetic acid-induced writhing response and the hot plate test in mice and since results have shown marked analgesic activity, it could be concluded that the observed analgesic activity of the studied oil could be also related to the linalool content [17]. These results justified the use of *M. mozaffarianii* in traditional medicine and the plant essential oil could be a potential candidate as an analgesic agent.

REFERENCES

1.   V. Mozaffarian, A Dictionary of Iranian Plant Names. Farhang Moaser Press, Tehran, Iran, 2006.
2.   M. A. Soltanipour, *Iran J. Med. Aroma. Plant Res.*, **20**, 547 (2005).
3.   M. Arman, M. Yousefzadi, S. Z. Khademi, *J. Essent. Oil Bear Plns.*,**14**, 131 (2011).
4.   M.R. Sailani, Z. Hojati, M. Amiri, L. Lachinani, *Iran J. Parmacol. Ther.*,**6**, 229 (2007).
5.   E. Siegmund, R. Cadnus, G. Lu, *Proc. Soc. Exp. Biol.*, **95**, 729 (1957).
6.   C.A. Winter, E.A. Risley, G.W. Nuss, *Proc. Soc. Exp. Biol. Med.*, **111**, 544 (1962).
7.   C.J. Meunier, J. Burton, J. Cumps, R.K. Verbeeck, *Europ. J. Pharm. Sci.*, **6**, 307 (1998).
8.   D. Dubuisson, S.G. Dennis, *Pain*, **4**, 161 (1978).
9.   A.A. Swigar, R.M. Silverstein, Monoterpenes. WI: Aldrich Chemical Company Publ., Milwaukee, USA, 1981.
10.   R.P. Adams, Identification of essential oil components by gas chromatography/mass spectroscopy. Allured publishing Co. Carol Stream, Illinois, 1995.
11.   M.N. Manjavachi, N.L. Quintao, M.M. Campos, I.K. Deschamps, R.A. Yunes, R.J. Nunes, P.C. Leal, J.B. Calixto, *Eur. J. Pain*, **14**, 23 (2009).
12.   A.J. Reeve, A.H. Dickenson, *Braz. J. Pharmacol.*, **116**, 222 (1995).
13.   I.D. G. Duarte, M. Nakamura, S.H. Ferreira, *Braz. J. Med. Biol. Res.*,**21**, 341 (1988).
14.   F.A. Santos, V.S. Rao, *Phytother. Res.*, **14**, 240 (2000).
15.   Z.K. Asanova, E.M. Suleimenov, G.A. Atazhanova, A.D. Dembitskii, R.N. Pak, A. Dar, S.M. Adekenov, *Pharm. Chem. J.*, **37**, 30 (2003).
16.   R.C. Silveira e Sá, L.N. Andrade, D. Pergentino de Sousa, *Mol.*, **18**, 1227 (2013).
17.   A.T. Peana, P.S. D'Aquila, M. L. Chessa, M. D. Moretti, G. Serra, P. Pippia, *Europ. J. Pharmacol.*, **460**, 37 (2013).

ХИМИЧЕН СЪСТАВ И АНАЛГЕТИЧНО ДЕЙСТВИЕ НА ЕСЕНЦИАЛНО МАСЛО ОТ ЛИСТА НА *Mentha mozaffarianii*

Х. Сам-Далири[1], З. Мусави[1], Н. Надери[2], Дж. Асгарпанах[3*]

[1]*Департамент по фармакология и токсикология, Факултет по фармация, Фармацевтичен научен клон, Ислямски университет „Азад“, Техеран, Иран*
[2]*Департамент по фармакология и токсикология, Факултет по фармация, Медицински университет "ШахидБехещи", Техеран, Иран*
[3]*Департамент по фармакогнозия, Факултет по фармация, Фармацевтичен научен клон, Ислямски университет „Азад“, Техеран, Иран*

Аналгетичните свойства на есенциалното масло от *Mentha mozaffariani* са изследвани върху мишки и плъхове.Аналгетичната активност е оценена чрез гърчове, предизвикани от оцетна киселина и близане на лапа, индуцирано от формалин. Маслото от *M. mozaffariani* значително намалява гърчовете от оцетна киселина, в сравнение с контролни животни. Във формалиновия тест дозата от 100 mg/kg значително намалява болките в сравнение с контрола (p<0.05). Инхибиторната активност на маслото от *M. mozaffariani* essential е много близка до стандартно лекарство - аспирин (100 mg/kg). Изследваното масло е изследван аналитично с GC и GC–MS, като са идентифицирани 22 съставки, представляващи 99.4 % от маслото.Главна компонента на маслото е пиперитонът (51.0%), който може би е отговорен за наблюдаваната активност. Резултатите показват, че есенциалното масло от *M. mozaffariani* притежава биологично активни компоненти със значителен аналгетичен ефект, което обяснява медицинските му приложения, установени от народната медицинска практика.

Assessment of the water quality of Lumbardhi river, Prizren (Kosovo)

F. Faiku, A. Haziri[*]

Department of Chemistry, Faculty of Natural Sciences,
University of Prishtina, 10000, George Bush Street, p.n., Kosovo

The surface waters in Kosovo are predominantly polluted, and there are still no plants for the treatment of domestic or industrial wastewaters in any of the cities in Kosovo. The main goal of this research is to analyze some environmentally toxic elements downstream the river where they end up as natural recipients. The sampling sites are geographically positioned using GIS (Geographic Information System). The results were interpreted using modern statistical methods used to locate polluted regions with abnormal concentration values. Values of selected elements were evaluated by Pearson's factor statistical analysis to identify their correlation. Concentrations of some toxic elements are as follows: Cu (1.4-4.4 µg dm^{-3}), Zn (3.2-9.4 µg dm^{-3}), Pb (1.03-2.58 µg dm^{-3}), Cd (0.03-0.13 µg dm^{-3}), Mn (10.6 -59.6 µg dm^{-3}), As (0.43-28.5 µg dm^{-3}), Cr (0.6-1.0 µg dm^{-3}), Fe (80-570 µg dm^{-3}), Ni (0.6-2.5 µg dm^{-3}), Sb (0.02-0.07 µg dm^{-3}), Al (58-195 µg dm^{-3}). The results obtained were compared with WHO and EU standards for drinking water. Even though there is no legislative convent in Kosovo for allowed concentrations of toxic metals in natural water resources, the results from this study are a small contribution to gain a clear overview of the state in this field of environmental quality assurance.

Keywords: Lumbardhi river, pollution assessment, heavy metals, physico-chemical parameters, ICP/MS, FIMS.

INTRODUCTION

Kosovo is regarded as a place with developed river network. Its small territory and dynamic topography have not created circumstances to form any major river flows. Kosovo has no navigable river but existing rivers have been the deciding factor for the development of life, the establishment of settlements and communication links through their valleys.

Scarcity and misuse of fresh water pose a serious and growing threat to sustainable development and protection of the environment. Human health and welfare, food security, industrial development and the ecosystems on which they depend, are all at risk, unless water and land resources are managed more effectively in the present decade than they have been in the past [1].

Overexploitation of nature and uncontrolled use of natural resources, including inadequate processing of industrial wastes have caused large contamination of world ecosystems by toxic metals (Hg, Pb, Cd, Cu, Zn, Ni, Mn). The major contaminants are metals and metalloids [2, 3]. They have the ability to bioaccumulate in organisms living in the water systems [4-6]. Studies on toxic metals and metalloids in lakes, rivers, groundwater and fish have been the main environmental focal spots, particularly over the last decade [7-10].

Nowadays, qualitative and quantitative determination of total metals and distribution of all their physical and chemical species in trace amounts (speciation) in natural water resources is to be considered as the main challenge for most scientists [11]. Based on the results of such studies it will be possible in the future to propose protection and detoxification measures of affected river waters and general protection and remediation of ecosystems. This work is a continuation of earlier studies of surface waters in Kosovo [12-17].
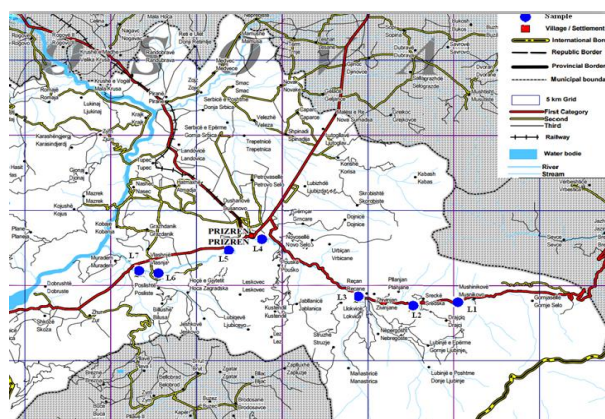
Fig. 1. Study area with sampling stations

The aim of this paper is to study the watershed of Lumbardhi river in Prizren, which belongs to the basin of Drini Bardhë, the richest basin with an annual flow of 2.200.00 million m³ and with the longest surface of 4.622 km² in the territory of the republic of Kosovo. The Lumbardhi river, Prizren has its origins from Sharr Mountains [18].

* To whom all correspondence should be sent:
E-mail: arben.haziri@uni-pr.edu

MATERIALS AND METHODS

Samples were taken along the banks of the sampling stations in April 2013. Sampling tools were washed with water and dried before the next sample was collected. Water samples were collected from surface waters below 10 cm [19]. The collected samples were stored in polythene plastic containers. Weather was cloudy and rainy, with middle water levels, which was very suitable for sampling. Sample preparation was done according to standard methods for surface water analysis [20, 21]. The study area with the sampling locations is shown in Figure 1 and the details about all sampling sites are presented in Table 1. Geographical positions were determined by GPS, using model "geko 201, 12 channel". The number of sampling spots was 7 and at every sampling spot samples were taken in order to determine the chemical parameters. The sampling spots of water in the river of Lumbardhi Prizren, were marked by codes L_1, L_2, L_3, L_4, L_5, L_6 and L_7.

Determination of physico-chemical parameters

For determination of the quality parameters of the water we have used standard methods for water analysis including classical and modern methods. Temperature of water was measured immediately after sampling, using a digital thermometer, model "Quick 63142". Measurements of pH were performed immediately after sampling using a pH/ion-meter, model "Hanna Instruments, pH & EC". Electric conductivity was measured by a "HANNA Instrument HI 8424" conductivity meter. Total hardness of water was determined by EDTA titration using Mercurochrome black T indicator and chemicals of p.a. purity. Chlorides were determined using argentometric methods. Some physico-chemical parameters (NH_4^+, NO_3^-, PO_4^{3-}) were determined by UV-VIS spectrometry. "WTW S12 photometer", "SECOMAM Prim Light spectrophotometer" and "SECOMAM Pastel UV RS232 spectrophotometer" were used with a monochromatic irradiation in the spectral range of 190-1100 nm. The measurement region, in a cuvette of 10 mm, was 340-800 nm, for the analysis of drinking waters, discharged and sea water.

Determination of elements

We used ICP/MS (inductively coupled plasma mass spectrometry) to determine the concentration of the target elements. Hg was determined by FIMS (flow injection Hg analysis).

Statistical analysis

Program Statistica 6.0 [22] was used in the statistical calculations of this work, such as: determination of basic statistical parameters and two-dimensional box plot diagrams for the determination of anomalies (extremes and outliers) for solution data.

Table1. Sampling stations with detailed locality description

Sample	Locality	Coordinates	Possible pollution sources
L_1	Mushnikovë	$42^0 10^{'} 23.75^{''}$N $20^0 53^{'} 3.67^{''}$E	Throwing rubbish, Wastewater
L_2	Sredskë	$42^0 10^{'} 15.47^{''}$N $20^0 51^{'} 5.88^{''}$E	Throwing rubbish, Wastewater
L_3	Reçan	$42^0 12^{'} 34.76^{''}$N $20^0 44^{'} 56.25^{''}$E	Factory Fruti
L_4	Marash	$42^0 12^{'} 44.78^{''}$N $20^0 44^{'} 40.65^{''}$E	Throwing rubbish, Traffic
L_5	Prizren	$42^0 12^{'} 35.53^{''}$N $20^0 44^{'} 11.34^{''}$E	Throwing rubbish, Traffic
L_6	Poslisht	$42^0 11^{'} 5.31^{''}$E $20^0 40^{'} 11.31^{''}$E	Throwing rubbish
L_7	Vlashne	$42^0 11^{''} 57.87^{''}$N $20^0 39^{'} 47.31^{''}$E	Throwing rubbish, Wastewater

Table 2. Physico-chemical parameters determined in river waters: air temperature, water temperature, pH, total solids, electrical conductivity (EC), dissolved oxygen, BOD_5, total hardness, content of sulfates, nitrites, ammonium and phosphates

Parameters	Sampling station						
	L_1	L_2	L_3	L_4	L_5	L_6	L_7
Water temp./ ^0C	12.08	13.5	20.3	15.6	15.0	14.9	17.4
Air temp./ ^0C	9.8	10.3	11.1	11.4	11.9	11.7	15.7
pH	8.25	8.49	8.51	8.38	8.37	8.10	8.12
TS/ mg dm^{-3}	100	200	200	190	560	360	960
EC/μS cm^{-1}	126	159	188	178	190	226	280
DO/ mg dm^{-3}	7.7	8.2	10.5	10.0	9.8	8.5	9.1
BOD_5/ mg dm^{-3}	5.0	4.2	0.5	4.8	6.1	5.5	6.74
Total hardness / ^0D	6.72	11.2	7.84	7.89	6.72	16.8	26.88
SO_4^{2-}/ mg dm^{-3}	15	17	12	22	20	25	27
NO_3^-/ mg dm^{-3}	0.04	0.025	0.08	0.15	0.18	0.20	0.28
NH_4^+/ mg dm^{-3}	0.25	0.3	0.4	0.8	0.9	1.2	2.2
PO_4^{3-}/ mg dm^{-3}	0.11	0.15	0.2	0.55	0.7	0.65	0.8
Cl^-/ mg dm^{-3}	5.01	4.30	3.58	2.66	1.43	3.94	4.85

RESULTS AND DISCUSSION
Physico-chemical parameters

Table 2 shows several physico-chemical parameters measured in the water of Lumbardhi river, Prizren: air temperature, water temperature, pH, electrical conductivity (EC), dissolved oxygen, BOD_5, total hardness, content of sulfates, nitrites, ammonium and phosphates.

Temperature is a biologically significant factor which plays an important role in the metabolic activities of organisms. It is also an important parameter in determining water quality, as it influences pH, alkalinity, acidity and dissolved oxygen (DO). The temperature values recorded in the water samples from the study area range between 12.08 ^0C (L_1) and 20.3 ^0C (L_3), as summarized in Table 2 with a mean temperature of 15.54 ^0C. The recorded temperature values were within the WHO standard for drinking water.

The pH is a measure of the acidity or alkalinity and measures the concentration of hydrogen ions in water. Basically, pH is determined by the amount of dissolved carbon dioxide (CO_2) which forms carbonic acid in the water. The pH values of the surface water sampled in the area varied from 8.10 to 8.51 with a mean value of 8.32 (the WHO standard range is 6.50-8.50). From these data we can see that the water of the river Lumbardhi Prizren is slightly basic.

The minimum TS value of 100 mg dm^{-3} was recorded at L_1 while the maximum value of 960 mg dm^{-3} was recorded at L_7. No limit has been set by WHO for drinking water and water for domestic uses but water with values similar to these has previously been described as good [23].

Electrical conductivity (EC) is a measure of water capacity to convey electric current. It is a determination of levels of inorganic constituents in water [24]. EC values obtained for the samples were in the range of 126-280 μS cm^{-1}, which is below the WHO recommended value of 400 μS cm^{-1} indicating a low amount of dissolved inorganic substances in ionized form.

Dissolved oxygen (DO) is an important parameter in water quality assessment and reflects the physical and biological processes prevailing in the water. The DO values indicate the degree of pollution in water bodies. DO values, as shown in Table 2, varied from 7.7 to 10.5 mg dm^{-3}.

The values for biochemical demand shown in Table 2 range from 0.5 to 6.74 mg dm^{-3} with a mean of 4.69 mg dm^{-3}. The values are quite lower than the standard of 10 mg dm^{-3} recommended by WHO.

The total hardness was 6.72 ^0D (sampling spots L_1 and L_5), 11.2 ^0D (sampling spot L_2), 7.84 ^0D (sampling spot L_3), 7.89 ^0D (sampling spot L_4),

16.8 ^{0}D (sampling spot L_6) and 26.88 ^{0}D (sampling spot L_7). The lowest total hardness was observed at L_1 and L_5 spots (6.72 ^{0}D) and a higher value of the hardness was observed at spot L_7 (26.88 ^{0}D).

Sulfate content higher than 100 mg dm^{-3} tends to give water a bitter taste and has a laxative effect on people not adapted to the water [25]. Also ailments like catarrh, dehydration and gastrointestinal irritation have been linked with high sulfate concentration. The results revealed that all analyzed water samples have a low sulfate content ranging from 12 to 27 mg dm^{-3} (Table 2). So, the concentration of sulfates is below the maximum value allowed by the WHO and the EU [23, 26].

Nitrate content in the analyzed water samples ranged from 0.025 mg dm^{-3} in L_2 to 0.28 mg dm^{-3} in L_7. These fall within the allowable value when compared to the WHO recommended guidelines. Nitrate fouls the water system and epidemiological studies have shown that exposure to nitrate causes methemoglobinemia disease [27].

The amounts of Cl$^-$, PO$_4^{3-}$, NH$_4^+$ ions range from 1.43 to 5.01 mg dm^{-3}, 0.11 to 0.8 mg dm^{-3}, and 0.25 to 2.2 mg dm^{-3}, respectively. Table 3 shows the concentrations of 67 elements in the water of river Lumbardhi Prizren.

Concentration of major and trace elements

Cadmium levels in all samples were in the range of 0.03-0.13 µg dm^{-3} with a mean value of 0.061 µg dm^{-3} (Table 4). The relative cadmium concentration for individual samples is indicated in Table 3. L_5 has the lowest cadmium content and L_1 has the highest one. In the case of cadmium, the highest concentration was recorded at the sampling spot L_1 (0.13 µg dm^{-3}), where this high concentration comes from the face of the earth geology. The values are lower than the WHO recommended standard of 3×10^{-3} mg dm^{-3}. Excess cadmium concentration in water is highly toxic and is responsible for adverse renal arterial changes in kidneys [28].

Copper detected in the water samples was very low and far below the recommended limits of 2.0 mg dm^{-3} set by WHO. Copper concentration was found to vary from 1.4 to 4.4 µg dm^{-3} with a mean of 3.029 µg dm^{-3} (Table 4) for all samples.

Most groundwater supplies contain some iron because it is one of the most abundant metals in the earth crust and is essential for plants and human beings. But excess iron in drinking water produces inky taste and muddy smell. The WHO recommends that the iron content of drinking water should not exceed 0.2 mg dm^{-3} because iron in water stains plumbing fixtures, cloths during laundering, incrusts well screens and clogs pipes [29]. Iron concentration was observed to vary from 80-570 µg dm^{-3} with a mean of 230 µg dm^{-3} (Table 4) for all samples. Iron concentrations in the water samples from L_4, L_5 and L_7 were above the EU guideline [26].

Magnesium ions are directly related to hardness. Magnesium content in the investigated water samples was ranging from 2120 to 7730 µg dm^{-3} which were below the WHO guidelines of 200 mg dm^{-3}. It is known that Ca^{2+} and Mg^{2+} ions in water are essential for human health and metabolism [30].

The sodium content ranged from a minimum of 2570 µg dm^{-3} to a maximum of 6750 µg dm^{-3}. The minimum values of the samples can be explained on the basis of lower microbial activity. No limit is established by the WHO for sodium in drinking water but a maximum standard of 100 mg dm^{-3} has been proposed for the general public.

The major source of potassium in natural fresh water is weathering of rocks [31]. Potassium content in the water samples varied from 790 to 1340 µg dm^{-3}. No guide and acceptable limits have been specified for potassium levels in the WHO standards for drinking water.

Aluminum levels in all samples were in the range of 58-195 µg dm^{-3} with a mean value of 126.571 µg dm^{-3} (Table 4). Relative aluminum concentration for individual samples is indicated in Table 3. L_2 has the lowest aluminum content and L_5 has the highest one. The values are lower than the WHO recommended standard of 0.2 mg dm^{-3}.

Arsenic levels in all samples were in the range of 0.43-28.5 µg dm^{-3} with a mean value of 4.487 µg dm^{-3} (Table 4). Relative arsenic concentration for individual samples is indicated in Table 3. L_1 has the lowest arsenic content and L_7 has the highest one. In the case of arsenic the highest concentration was recorded at the sampling spot L_7 - 28.5 µg dm^{-3}. Also from Table 3, we can see that arsenic (28.5 µg dm^{-3}, sample L_7) has higher concentration compared to WHO and EU standards for drinking water.

The WHO recommends that the zinc content of drinking water should not exceed 3 mg dm^{-3}. Zinc concentration was observed to vary from 3.2 to 9.4 µg dm^{-3} with a mean of 5.743 µg dm^{-3} (Table 4) for all samples, which is below the WHO guideline.

Table 3. Concentrations ($\mu g\ dm^{-3}$) of 67 elements in the water of river Lumbardhi Prizren

Element	Sampling station						
($\mu g\ dm^{-3}$)	L_1	L_2	L_3	L_4	L_5	L_6	L_7
Na	2570	2850	3080	2760	3200	6750	4850
Li	<1	<1	1	1	1	1	1
Be	<0.1	<0.1	<0.1	<0.1	<0.1	<0.1	<0.1
Mg	2120	3400	3920	4760	4910	5460	7730
Al	80	58	111	136	195	167	139
Si	2200	2600	2700	3000	3000	3100	2900
K	790	930	1080	1060	1100	1560	1340
Ca	>20000	>20000	>20000	>20000	>20000	>20000	>20000
Sc	1	1	1	1	1	1	1
Ti	2.4	1.5	1.4	1.6	1.9	2.1	1.9
V	0.3	0.2	0.3	0.5	0.6	0.5	0.5
Cr	0.6	<0.5	0.7	0.8	1	0.9	0.7
Mn	10.6	12.3	22.2	31.3	43.2	59.6	24.7
Fe	100	80	130	210	320	200	570
Co	0.182	0.163	0.228	0.35	0.486	0.361	0.305
Ni	0.6	2	1.2	2.2	2.5	0.8	0.9
Cu	1.4	3	2.8	4.4	4	2.8	2.8
Zn	4.3	3.2	3.5	6.1	5.3	8.4	9.4
Ga	0.22	0.15	0.1	0.08	0.07	0.05	<0.01
Ge	<0.1	<0.1	<0.1	<0.1	<0.1	<0.1	<0.1
As	0.43	0.44	0.46	0.45	0.55	0.58	28.5
Se	<0.2	<0.2	<0.2	<0.2	<0.2	0.3	0.3
Br	4	4	5	4	4	6	7
Rb	0.519	0.415	0.476	0.483	0.548	0.884	0.795
Sr	77	88.9	95.4	78.5	80.3	81.3	163
Y	0.121	0.096	0.163	0.272	0.346	0.254	0.214
Zr	0.03	0.02	0.04	0.04	0.04	0.02	0.03
Nb	<0.005	<0.005	<0.005	<0.005	<0.005	<0.005	<0.005
Mo	0.3	0.3	0.2	0.1	0.1	0.1	0.1
Ru	0.01	0.01	0.01	0.02	0.01	0.01	0.01
Pd	0.01	0.01	0.01	0.01	<0.01	0.01	0.01
Ag	<0.2	<0.2	<0.2	<0.2	<0.2	<0.2	<0.2
Cd	0.13	0.05	0.07	0.04	0.03	0.05	0.06
In	<0.001	<0.001	<0.001	<0.001	<0.001	<0.001	<0.001
Sn	<0.1	<0.1	<0.1	<0.1	<0.1	<0.1	<0.1
Sb	0.07	0.21	0.02	0.05	0.03	0.06	0.07
Te	<0.1	<0.1	0.1	<0.1	<0.1	0.1	0.1
I	<0.1	<0.1	<0.1	<0.1	<0.1	1	1
Cs	0.01	0.008	0.009	0.013	0.014	0.014	0.013
Ba	13.7	14	13.7	23.7	24.7	25.7	74.3
La	0.181	0.115	0.145	0.276	0.33	0.228	0.186
Ce	0.474	0.247	0.336	0.653	0.743	0.373	0.332
Pr	0.036	0.027	0.04	0.074	0.084	0.061	0.048
Nd	0.145	0.1	0.157	0.288	0.316	0.255	0.181
Sm	0.028	0.032	0.039	0.072	0.093	0.069	0.047
Eu	<0.001	<0.001	<0.001	<0.001	0.004	<0.001	<0.001
Gd	0.036	0.03	0.046	0.08	0.1	0.066	0.062
Tb	0.004	0.004	0.006	0.011	0.013	0.01	0.008
Dy	0.029	0.019	0.031	0.047	0.071	0.045	0.038
Ho	0.004	0.004	0.005	0.009	0.012	0.008	0.007
Er	0.011	0.011	0.013	0.021	0.029	0.025	0.018
Tm	0.001	<0.001	0.002	0.003	0.004	0.003	0.002
Yb	0.01	0.009	0.014	0.019	0.023	0.018	0.012
Lu	0.002	0.001	0.001	0.003	0.003	0.003	0.002
Hf	0.003	0.003	0.003	0.004	0.001	0.003	0.002

Table 3. continuation.

Element	Sampling station						
(μg dm^{-3})	L$_1$	L$_2$	L$_3$	L$_4$	L$_5$	L$_6$	L$_7$
Ta	<0.001	<0.001	<0.001	<0.001	<0.001	<0.001	<0.001
W	<0.02	<0.02	<0.02	<0.02	<0.02	<0.02	0.02
Re	0.002	0.001	0.001	0.002	0.001	0.002	0.002
Os	<0.002	<0.002	<0.002	<0.002	<0.002	<0.002	<0.002
Pt	<0.3	<0.3	<0.3	<0.3	<0.3	<0.3	<0.3
Au	<0.002	<0.002	<0.002	<0.002	<0.002	<0.002	<0.002
Hg	<0.2	<0.2	<0.2	<0.2	<0.2	<0.2	<0.2
Ti	0.002	0.002	0.002	0.002	0.004	0.003	0.005
Pb	2.58	1.18	1.03	1.54	1.18	1.93	1.42
Bi	<0.3	<0.3	<0.3	<0.3	<0.3	<0.3	<0.3
Th	0.002	0.003	0.003	0.003	0.004	0.002	0.005
U	0.097	0.0184	0.158	0.137	0.148	0.153	0.206
Hg (ng L^{-1})	53	27	24	23	12	<6	<6

Lead levels in all samples were in the range of 1.03-2.58 μg dm^{-3} with a mean value of 1.551 μg dm^{-3} (Table 4). Relative lead concentration for individual samples is also indicated in Table 3. L$_3$ has the lowest lead content and L$_1$ has the highest one. The values are lower than the WHO recommended standard of 0.01 mg dm^{-3}.

Antimony ranges from 0.02 μg dm^{-3} (L$_4$) to 0.07 μg dm^{-3} (L$_1$ and L$_7$); barium ranges from 13.7 μg dm^{-3} (L$_1$ and L$_3$) to 74.3 μg dm^{-3} (L$_7$); bromine ranges from 4 μg dm^{-3} (L$_1$, L$_2$, L$_4$, L$_5$) to 7 μg dm^{-3} (L$_7$); chromium ranges from 0.6 μg dm^{-3} (L$_1$) to 1 μg dm^{-3} (L$_5$); manganese ranges from 10.6 μg dm^{-3} (L$_1$) to 59.6 μg dm^{-3} (L$_6$); mercury ranges from 12 ng dm^{-3} (L$_5$) to 53 ng dm^{-3} (L$_1$); molybdenum ranges from 0.1 μg dm^{-3} (L$_4$, L$_5$, L$_6$ and L$_7$) to 0.3 μg dm^{-3} (L$_1$ and L$_2$), nickel ranges from 0.6 μg dm^{-3} (L$_1$) to 2.5 μg dm^{-3} (L$_5$); uranium ranges from 0.0184 μg dm^{-3} (L$_2$) to 0.206 μg dm^{-3} (L$_7$). So, the concentration of these elements is below the maximum value allowed by the WHO.

The data from Table 3 show that the concentrations of the elements Be, Ge, Nb, Ag, In, Sn, Ta, W, Os, Pt, Au and Bi are below the corresponding limits of detection.

The concentrations of heavy metals are almost within the allowed standard concentrations except for some sampling spots where higher concentrations of some heavy metals were found. Removing heavy metals from surface water is important. Metal ions like Cu^{2+}, Hg^{2+}, Pb^{2+}, Zn^{2+}, Ni^{2+}, Cd^{2+} represent harmful and noxious water pollutants for human and animal consumption, mostly due to their tendency to accumulate in the food chain. Their removal can be done by chemical precipitation, coagulation and flocculation, adsorption onto plant wastes and special treatments, as nanofiltration or reverse osmosis.

So, before human utilization, this kind of waters must be subjected to intensive physical and chemical treatment, extended treatment and disinfection, e.g., chlorination to break-point, coagulation, flocculation, decantation, filtration, adsorption (activated carbon), disinfection (ozone, final chlorination). The vulnerability of water quality is followed by serious changes of its properties resulting in undesirable effects like: lack of oxygen, reduction in pH value, increase of heavy metal complexation capacity, increase of toxicity and accumulation of hazardous substances in the food chain. Water resources in Kosovo are limited and the major ingredients of surface water are rivers except for some artificial accumulation lakes.

Global concern for environment, in spite of the fact that efforts were done and are being done to overcome pollution, permanent monitoring of polluted waters now and in the future will be a big challenge for us and all scientific institutions in entire Kosovo. Water like a natural resource of general interest should be rationally used and protected from eventual degradation.

Statistical Analysis

Determination of basic statistical parameters

Table 4 presents the basic statistical parameters for 67 elements in four samples, which can be considered as preliminary values until a larger data set will be compiled. For each element, the values are given as arithmetic mean, geometric mean, median, minimal and maximal concentration, variance and standard deviation. From the experimental data (Table 3) and the box plot approach of Tukey [32], we have determined the abnormal data (extremes and outliers) for some elements in the river Lumbardhi Prizren.

Table 4. Basic statistical parameters for four major and 67 minor elements in samples of river Lumbardhi Prizren

Variables	Descriptive Statistics (Spreadsheet1)						
	Mean	Geom. Mean	Median	Minimum	Maximum	Variance	Std. Dev.
Na	3722.857	3506.865	3080.000	2570.000	6750.000	2356457	1535.076
Li	29.571	3.738	1.000	1.000	101.000	2381	48.795
Mg	4614.286	4315.420	4760.000	2120.000	7730.000	3118262	1765.860
Al	126.571	117.921	136.000	58.000	195.000	2279	47.738
Si	2785.714	2769.457	2900.000	2200.000	3100.000	98095	313.202
K	1122.857	1098.811	1080.000	790.000	1560.000	65424	255.781
Sc	1.000	1.000	1.000	1.000	1.000	0	0.000
Ti	1.829	1.800	1.900	1.400	2.400	0	0.355
V	0.414	0.389	0.500	0.200	0.600	0	0.146
Cr	15.100	1.549	0.800	0.600	101.000	1435	37.879
Mn	34.029	28.079	31.300	10.600	59.600	422	20.534
Fe	230.000	186.903	200.000	80.000	570.000	29067	170.489
Co	0.296	0.277	0.305	0.163	0.486	0	0.114
Ni	1.457	1.282	1.200	0.600	2.500	1	0.761
Cu	3.029	2.875	2.800	1.400	4.400	1	0.969
Zn	5.743	5.335	5.300	3.200	9.400	6	2.392
Ga	14.524	0.266	0.100	0.050	101.000	1454	38.132
Ge	86.573	27.057	101.000	0.010	101.000	1457	38.171
As	4.487	0.863	0.460	0.430	28.500	112	10.589
Se	72.229	19.154	101.000	0.300	101.000	2414	49.137
Br	4.857	4.740	4.000	4.000	7.000	1	1.215
Rb	0.577	0.559	0.519	0.415	0.884	0	0.165
Sr	94.914	91.707	81.300	77.000	163.000	944	30.717
Y	0.209	0.192	0.214	0.096	0.346	0	0.089
Zr	0.031	0.030	0.030	0.020	0.040	0	0.009
Mo	0.171	0.151	0.100	0.100	0.300	0	0.095
Ru	0.011	0.011	0.010	0.010	0.020	0	0.004
Pd	14.437	0.037	0.010	0.010	101.000	1457	38.171
Cd	0.061	0.056	0.050	0.030	0.130	0	0.033
Sb	0.073	0.057	0.060	0.020	0.210	0	0.063
Te	57.757	5.209	101.000	0.100	101.000	2909	53.933
I	72.429	27.018	101.000	1.000	101.000	2381	48.795
Cs	0.012	0.011	0.013	0.008	0.014	0	0.003
Ba	27.114	22.520	23.700	13.700	74.300	463	21.517
La	0.209	0.197	0.186	0.115	0.330	0	0.075
Ce	0.471	0.443	0.474	0.247	0.743	0	0.176
Pr	0.053	0.049	0.048	0.027	0.084	0	0.021
Nd	0.206	0.192	0.181	0.100	0.316	0	0.081
Sm	0.054	0.050	0.047	0.028	0.093	0	0.024
Eu	86.572	23.737	101.000	0.004	101.000	1457	38.173
Gd	0.060	0.056	0.062	0.030	0.100	0	0.025
Tb	0.008	0.007	0.008	0.004	0.013	0	0.004

Table 4 continuation.

Variables	Descriptive Statistics (Spreadsheet1)						
	Mean	Geom. Mean	Median	Minimum	Maximum	Variance	Std. Dev.
Dy	0.040	0.037	0.038	0.019	0.071	0	0.017
Ho	0.007	0.006	0.007	0.004	0.012	0	0.003
Er	0.018	0.017	0.018	0.011	0.029	0	0.007
Tm	14.431	0.011	0.003	0.001	101.000	1457	38.173
Yb	0.015	0.014	0.014	0.009	0.023	0	0.005
Lu	0.002	0.002	0.002	0.001	0.003	0	0.001
Hf	0.003	0.003	0.003	0.001	0.004	0	0.001
Ta	101.000	101.000	101.000	101.000	101.000	0	0.000
W	86.574	29.873	101.000	0.020	101.000	1457	38.167
Re	0.002	0.001	0.002	0.001	0.002	0	0.001
Tl	0.003	0.003	0.002	0.002	0.005	0	0.001
Pb	1.551	1.481	1.420	1.030	2.580	0	0.543
Th	0.003	0.003	0.003	0.002	0.005	0	0.001
U	0.155	0.151	0.153	0.097	0.206	0	0.035
Hg	48.714	37.097	27.000	12.000	101.000	1430	37.810

Frequency histograms and two-dimensional scatter with plot diagrams of 12 measured elements are presented in Figures 2 and 3. Using experimental data and the box plot approach of Tukey [32], anomalous values (extremes and outliers) of some elements were determined (Table 5). It was found that cadmium shows an outlier (L_1), arsenic - an extreme (L_7) and antimony - an extreme (L_2).

Table 5. Anomalous values (extremes and outliers) of concentrations for particular elements ($\mu g\ dm^{-3}$).

Sample	Extremes of elements (*)	Outliers of elements (o)
L_1	-	Cd (0.13 $\mu g\ dm^{-3}$)
L_2	Sb (0.21 $\mu g\ dm^{-3}$)	-
L_3	-	-
L_4	-	-
L_5	-	-
L_6	-	-
L_7	As (28.5 $\mu g\ dm^{-3}$)	-

The results from Pearson's correlation factors displayed in Table 6 for some elements as sodium show an excellent and very high positive relationship (>0.65) compared with K, Mn, Zn and Br but it is in high negative relationship with Hg (-0.69). Magnesium is in excellent and very high positive relationship compared with K, Mn, Fe, Zn, As, Br, Sr, Ba, Th and U but is in very high negative relationship with Hg (-0.87). The concentration of aluminum in water samples is in excellent correlation and in very high positive relationship with V, Cr, Mn, and Co. No correlations were found for Sb and Hg.

As it belongs, the concentration of chromium in the same samples is in excellent and very high positive relationship with Co (0.96) but in high negative relationship with Sb (-0.69). The calculated iron concentration from the program data is in excellent and very high positive relationship with Zn, As, Sr, Ba and Th, but no correlation with the concentration of Hg was found. The results from the correlation factors displayed on Table 6 for the concentration of nickel are in excellent and very high positive relationship with Cu (0.85), but in very high negative relationship with Cd (-0.72). It is worth mentioning that the manganese concentration is in high positive relationship with Fe (0.77), Co (0.70), Zn (0.92) and Br (0.76) but in very high negative relationship with Hg (-0.88).

Discussing the arsenic concentration from the program data it is evident that it is in excellent and very high positive relationship with Br, Sr, Ba and Th. Finally, the cobalt concentration is in very positive relationship with Cu (0.67). No correlation with concentrations of Cd (-0.65) and Hg (-0.66) was found.
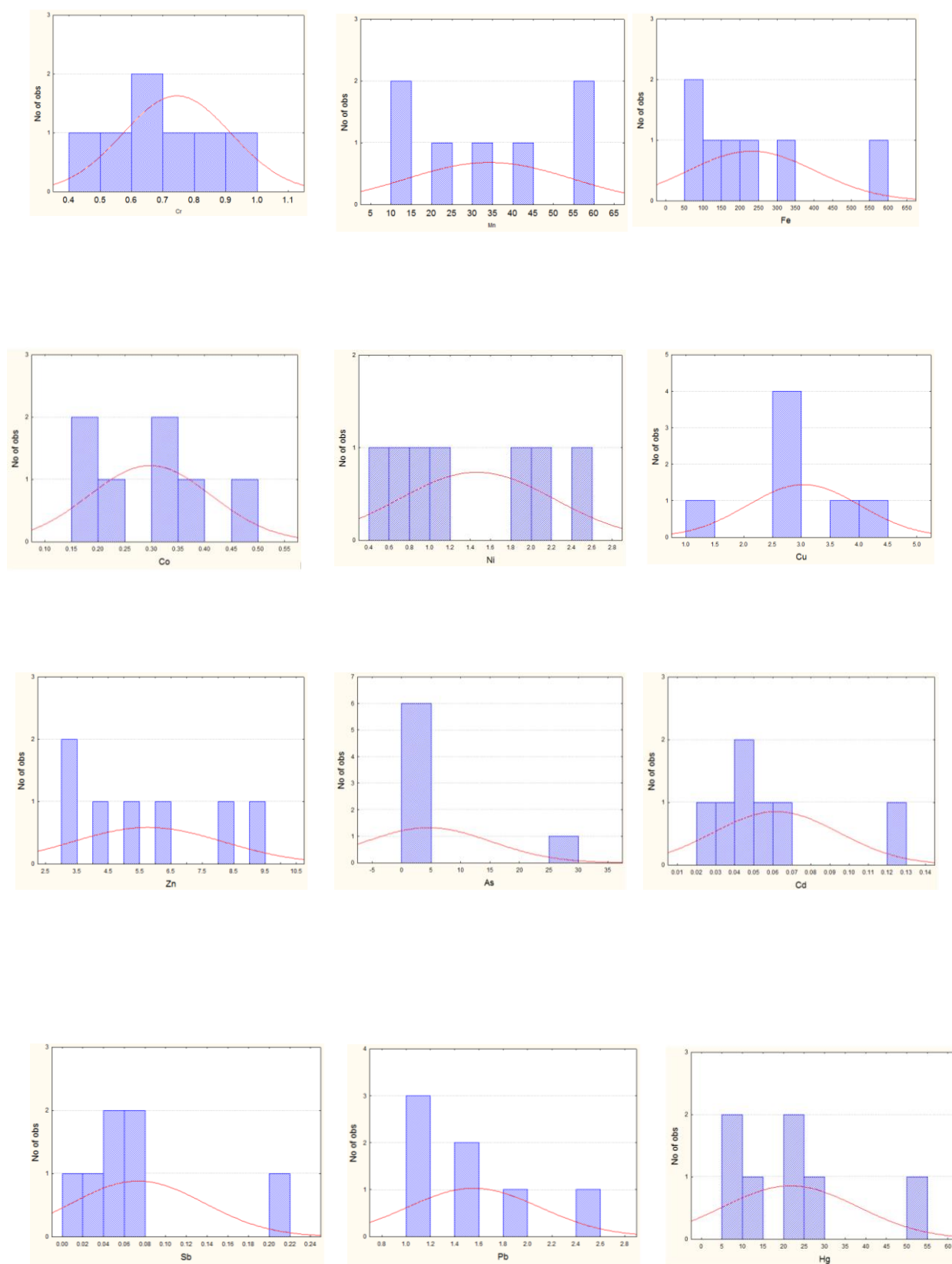
Fig. 2. Frequency histograms of 12 measured elements.
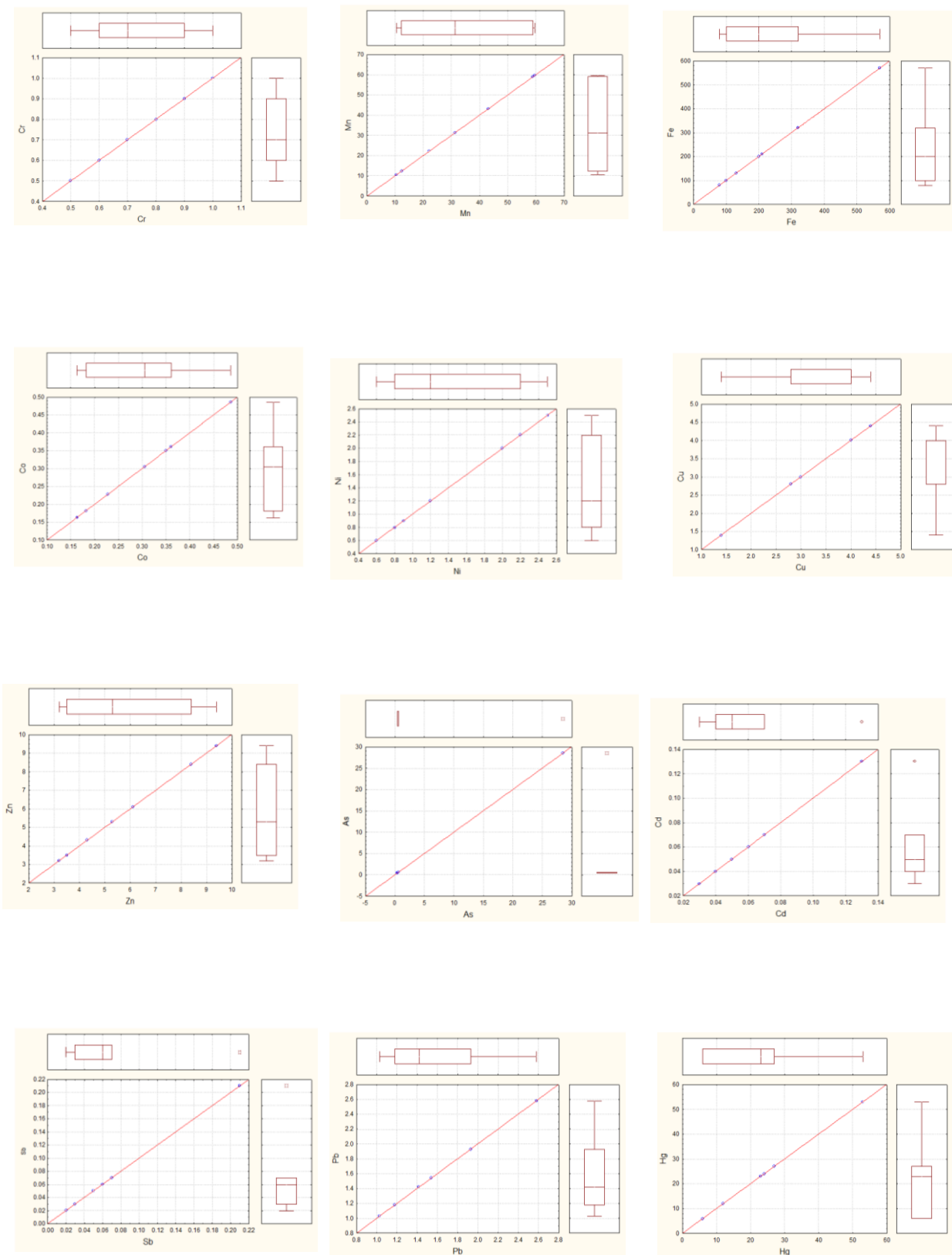
Fig. 3. Scatter box plot diagrams of 12 measured elements.

Table 6. Correlation factors for 23 elements ($\mu g\ dm^{-3}$) in 7 water samples.

Correlations Case 1I=7

Variable	Na	Mg	Al	K	Ti	V	Cr	Mn	Fe	Co	Ni	Cu	Zn	As	Br	Sr	Cd	Sb	Ba	Pb	Th	U	Hg
Na	1.00																						
Mg	0.62	1.00																					
Al	0.49	0.60	1.00																				
K	0.94	0.78	0.65	1.00																			
Ti	0.30	-0.08	0.17	0.07	1.00																		
V	0.42	0.67	0.95	0.58	0.25	1.00																	
Cr	0.41	0.42	0.97	0.55	0.17	0.90	1.00																
Mn	0.83	0.90	0.80	0.92	0.20	0.80	0.67	1.00															
Fe	0.39	0.90	0.55	0.52	0.12	0.67	0.35	0.77	1.00														
Co	0.33	0.53	0.97	0.51	0.11	0.95	0.96	0.70	0.50	1.00													
Ni	-0.46	-0.08	0.24	-0.25	-0.54	0.25	0.30	-0.13	-0.04	0.45	1.00												
Cu	-0.08	0.37	0.54	0.20	-0.56	0.56	0.55	-0.39	0.23	0.67	0.85	1.00											
Zn	0.79	0.86	0.59	0.82	0.36	0.69	0.44	0.92	0.78	0.48	-0.32	0.11	1.00										
As	0.33	0.78	0.12	0.38	0.09	0.26	-0.11	0.54	0.88	0.04	-0.32	-0.10	0.68	1.00									
Br	0.79	0.80	0.29	0.80	0.13	0.29	0.11	0.76	0.69	0.10	-0.58	-0.19	0.81	0.78	1.00								
Sr	0.30	0.75	0.04	0.37	-0.07	0.14	-0.18	0.48	0.82	-0.05	-0.32	-0.11	0.57	0.98	0.79	1.00							
Cd	-0.24	-0.54	-0.57	-0.48	0.55	-0.52	-0.54	-0.50	-0.32	-0.65	-0.72	-0.89	-0.25	-0.02	-0.08	-0.05	1.00						
Sb	-0.14	-0.24	-0.67	-0.28	-0.19	-0.62	-0.69	-0.39	-0.29	-0.56	0.13	-0.15	-0.29	-0.02	-0.19	0.02	-0.02	1.00					
Ba	0.45	0.89	0.34	0.53	0.13	0.48	0.12	0.71	0.95	0.26	-0.23	0.06	0.81	0.97	0.80	0.92	-0.19	-0.12	1.00				
Pb	0.14	-0.34	-0.17	-0.12	0.87	-0.06	-0.12	-0.10	-0.21	-0.22	-0.61	-0.63	0.17	-0.11	-0.04	-0.25	0.73	-0.07	-0.11	1.00			
Th	-0.01	0.72	0.32	0.19	-0.28	0.41	0.14	0.43	0.85	0.35	0.30	0.38	0.37	0.77	0.40	0.78	-0.48	-0.08	0.77	-0.59	1.00		
U	0.35	0.71	0.06	0.47	-0.51	0.05	-0.12	0.45	0.57	0.02	0.11	0.25	0.36	0.65	0.61	0.75	-0.55	0.35	0.64	-0.68	0.70	1.00	
Hg	-0.69	-0.87	-0.71	-0.86	0.25	-0.65	-0.60	-0.88	-0.65	-0.66	-0.20	-0.55	-0.67	-0.42	-0.63	-0.44	0.80	0.18	-0.58	0.54	-0.54	-0.70	1.00

Table 7. Classification of the water of Lumbardhi river, Prizren based on some trace metals as pollution indicators

Element	Water class				
(μg dm^{-3})	I	II	III	IV	V
	<2	2 – 10	10 – 15	15 – 20	>20
Cu	L_1	$L_2 – L_7$			
	<50	50 – 80	80 – 100	100 – 200	>200
Zn	$L_1 – L_7$				
	<0.1	0.1 – 2.0	2.0 – 5.0	5.0 – 80	>80
Pb		$L_2 – L_7$	L_1		
	<0.1	0.1 – 0.5	0.5 – 2.0	2.0 – 5.0	>5.0
Cd	$L_2 – L_7$	L_1			

In Kosovo there are no standards for water quality yet, that is why we decided to use the Croatian standards to classify the water quality of the Lumbardhi river, Prizren [33]. Table 7 shows the classification of the water samples of the Lumbardhi river, Prizren, based on the concentrations of toxic metals.

Based on Croatian standards for drinking water, the water from the Lumbardhi river, Prizren is classified in first class (no anthropogenic pollutions) according to the concentrations of zinc. Based on lead the samples L_2- L_7 are in second class (the concentrations of toxic metals are higher than their natural concentrations) and L_1 in third class (the toxic metal concentrations are lower than their permanent levels). Based on copper the sample L_1 is classified in first class and L_2-L_7 in second class. Based on cadmium the samples L_2-L_7 are classified in first class and L_1 in second class.

CONCLUSIONS

Based on our results we can conclude:
- Our analyses of the water of the river Lumbardhi of Prizren relate the water quality as good except for some spots where anthropogenic pollutants probably appear.
- Results of heavy metals show that their concentrations are within the standard concentrations except for some spots where higher concentrations of some heavy metals are observed.
- According to pH the water is basic (pH=8.10-8.51).
- Based on Croatian standards for drinking water the Lumbardhi water was classifed in the first class according to the concentration of zinc.
- Based on Croatian standards for drinking water the Lumbardhi water was classified in the second and third class according to the concentration of lead.
- Based on Croatian standards for drinking water, the Lumbardhi water was classified in the first and second class according to the concentrations of copper and cadmium.
- Although Kosovo has no legislative prohibition for exceeded concentrations of toxic metals in the natural water resources until now, the results from this study represent a small contribution to gain a clear overview of the state in this field of environmental quality assurance.
- We have thus concluded that water resources of Kosovo's are put at risk by anthropogenic pollution. As a first step further forward, surface water pollution has to be prevented, managed and its condition continually improved.

REFERENCES

1. Agenda 21, Governments at the United Nations Conference on Environment and Development (UNCED), Rio de Janeiro,1997.
2. P. Censi, S. Spoto, F. Saiano, M. Sprovieri, S. Mazzola, G. Nardone, S. Di Geronimo, R. Punturo, D. Ottonello, *Chemosphere*, **64**, 1167 (2006).
3. C. Fernandes, A. Fontaínhas-Fernandes, D. Cabral, M. Salgado, *Environmental Monitoring and Assessment*, **136**, 267 (2008).
4. M. B. Arain, T. G. Kazi, M. K. Jamali, N. Jalbani, H. I. Afridi, A. Shah, *Chemosphere*, **70**, 1845 (2008).
5. G. G. Pyle, J. W. Rajotte, P. Couture, *Ecotoxicology and Environmental Safety*, **61**, 287 (2005).
6. A. Szymanowska, A. Samecka-Cymerman, A. Kempers, *Ecotoxicology and Environmental Safety*, **43**, 21 (1999).
7. A. M. Christensen, F. Nakajima, A. Baun, *Environmental Pollution*, **144**, 621 (2006).
8. K. Peng, C. Luo, L. Lou, X. Li, Z. Shen, *Science of The Total Environment*, **39**, 22 (2008).
9. R. Sadiq, T. Husain, B. Bose, B. Veitch, *Environmental Modelling & Software*, **18**, 451 (2003).
10. Y. Issa, A. Elewa, M. Rizk, A. Hassouna, *Journal of Agricultural Research*, **21**, 733 (1996).
11. R. Kestner, Chemical speciation in sea water, in: E. D. Goldberg (Ur.), The nature of sea water, Dahlem Konfernzen, Berlin, 1975, p.172.
12. F. Gashi, N. Troni, R. Hoti, F. Faiku, R. Ibrahimi, F. Laha, K. Kurteshi, S. Osmani F. Hoti, *Fresenius Environmental Bulletin*, **23**, 91 (2014).
13. F. Gashi, S. Frančišković-Bilinski, H. Bilinski, *Fresenius Environmental Bulletin*, **18**, 1462 (2009).
14. F. Gashi, S. Frančišković-Bilinski, H. Bilinski, N. Troni, M. Bacaj, F. Jusufi, *Environ. Monit. Assess.*, **175**, 279 (2011).
15. F. Gashi, N. Troni, F. Faiku, F. Laha, A. Haziri, I. Kastrati, E. Beshtica, *American Journal of Environmental Science*, **9**, 142 (2013)..

16. F. Faiku, E. Rysheni, S. Abazi, A. Haziri, *Journal International Environmental Application Science*, **6**, 417 (2011).

17. F. Faiku, A. Haziri, M. Kryeziu, I. Haziri, *Bulletin of Environment, Pharmacology and Life Sciences*, **3**, 242 (2014).

18. S. Fazliu, *Journal of Environmental Science and Engineering* A, **1**, 1173 (2012).

19. P. K. Gupta, Methods in Environmental Analysis. Water, Soil and Air. 1st ed., Agrobios, India, 2009, 79.

20. B. Alper, K. Abidin, K. Yuksel, *Water, Air & Soil Pollution*, **149**, 93 (1998).

21. APHA, AWWA, WEF, Standard methods for the examination of water and wastewater (20th ed.) Washington DC, 1998.

22. Stat Soft, Inc., Statistica (data analysis software system), version 6. 2001. http://www.statsoft.com.

23. World Health Organization, WHO, Guidelines for Drinking Water Quality. World Health Organization, Geneva, Switzerland, 1993.

24. O. R. Awofolu, R. Du Plessis, I. Rampedi, *African Journal of Biotechnology*, **6**, 2251 (2007).

25. S. I. Ibrahim, L. T. Ajibade, *Transnational Journal of Science and Technology*, **12**, 63 (2012).

26. EU's drinking water standards, Council Directive 98/83/EC on the quality of water intended for human consumption, 1998.

27. O. K. Adeyemo, I. O. Ayodeji, C. O. Aiki-Raji, *African Journal Biomedical Research*, **5**, 51 (2002).

28. M. L. Sanjoy, K. H. Rakesh, *International Journal Environmental Sciences*, **3**, 1857 (2013).

29. B. Maureen, N. Anttoniette, J. Afolayan, *Advances in Applied Science Research*, **3**, 2549 (2012).

30. B. K. Kortatsi, *West African Journal Applied Ecology*, **11**, 1 (2007).

31. P. Narayan, P. Kumar, G. Caravello, *Journal of Water Resource and Protection*, **5**, 761 (2013).

32. J. W. Tukey, Exploratory Data Analysis. Addison-Wesley, Reading, MA., 1977.

33. Narodne Novine 107/95, Directive about water classification (in Croatian, legislative act), 1998.(№37 in original)

ОЦЕНЯВАНЕ НА КАЧЕСТВОТО НА ВОДИТЕ НА РЕКА ЛУМБАРДИ, ПРИЗРЕН, КОСОВО

Ф. Файку[*], А. Хазири

Департамент по химия, Факултет по природни науки, Университет в Прищина, Косово

(Резюме)

Повърхностните води в Косово са предимно замърсени, като все още няма пречиствателни станции за битови и промишлени води. Главната цел на настоящето изследване е да се анализира съдържанието на някои токсични елементи по течението на реката. Местата за пробовзимане са разположени спрямо географска информационна система(GIS). Резултатите са интерпретирани с помощта на съвременни методи за локализирането на замърсените райони с повишени концентрации. Стойностите на подбраните елементи са оценени с факторен статистически анализ по Pearson за намирането на корелации. Концентрациите на токсичните елементи са както следва: Cu (1.4-4.4 µg dm^{-3}), Zn (3.2-9.4 µg dm^{-3}), Pb (1.03-2.58 µg dm^{-3}), Cd (0.03-0.13 µg dm^{-3}), Mn (10.6 -59.6 µg dm^{-3}), As (0.43-28.5 µg dm^{-3}), Cr (0.6-1.0 µg dm^{-3}), Fe (80-570 µg dm^{-3}), Ni (0.6-2.5 µg dm^{-3}), Sb (0.02-0.07 µg dm^{-3}), Al (58-195 µg dm^{-3}). Получените резултати са сравнени със стандартите на Световата здравна организаия (WHO) и на Европейския съюз за питейна вода. Въпреки, че в Косово няма законови ограничения за допусими концентрации на токсични метали в природните води, настоящите резултати са скромен принос към получаването на ясен поглед състоянието на околната среда и нейното подобряване.

Hall effects on MHD natural convection flow with heat and mass transfer of heat absorbing and chemically reacting fluid past a vertical plate with ramped temperature and ramped surface concentration

S. M. Hussain[1]*, J. Jain[2], G. S. Seth[3]

[1]Department of Mathematics, O. P. Jindal University, Raigarh, India
[2]Department of Applied Mathematics, Government Engineering College, Bastar, India
[3]Department of Applied Mathematics, Indian Institute of Technology (ISM), Dhanbad, India

This paper is concerned with studying the influence of Hall current on the unsteady hydromagnetic natural convection flow with heat and mass transfer of an electrically conducting, viscous, incompressible, temperature dependent heat absorbing and chemically reacting fluid past an accelerated moving vertical plate with ramped temperature and ramped surface concentration through a porous medium. The governing non-dimensional equations are solved analytically in closed form by Laplace Transform Technique. The expressions for skin friction, Nusselt number and Sherwood number are also derived. The variations in fluid velocity, fluid temperature and species concentration are displayed graphically, whereas numerical values of skin friction, Nusselt number and Sherwood number are presented in tabular form for various values of pertinent flow parameters. Numerical results of natural convection flow near a ramped temperature plate with ramped surface concentration are also compared with the corresponding flow near an isothermal plate with uniform surface concentration.

INTRODUCTION

Hydromagnetic natural convection flows in porous and non-porous media have been studied extensively due to the widespread applications abound in many areas of science and technology including fusion processes in electrical furnaces, problems of boundary layer control in the field of aerodynamics, geothermal energy extraction, metallurgy, plasma studies, mineral and petroleum engineering, etc. In addition to it, the Magnetohydrodynamic (MHD) natural convection flow of an electrically conducting fluid in a fluid saturated porous medium has also been successfully exploited in crystal formation. Oreper and Szekely [1] observed that the presence of magnetic field can suppress natural convection currents and the strength of magnetic field is one of the important factors in reducing non-uniform composition thereby enhancing quality of crystal. Following this, several researchers investigated the unsteady hydromagnetic natural convection flow of an electrically conducting fluid past bodies with different geometries under various initial and boundary conditions. Mention may be made of the research studies of Raptis and Kafousias [2], Raptis [3], Chamkha [4], Aldoss *et al*. [5], Helmy [6], Kim [7], Chaudhary and Jain [8], Rashidi *et al*. [9-10],

Seth *et al*. [11-12] and Makinde and Tshehla [13].

The study of hydromagnetic natural convection flow with heat and mass transfer, induced due to a moving surface with a uniform or non-uniform velocity, has drawn considerable attention of several researchers owing to its vast applications in numerous manufacturing processes in industry, which include boundary layer flow along with material handling conveyers, cooling of an infinite metallic plate in a cooling bath, extrusion of plastic sheets, distribution of temperature and moisture over agricultural fields and groves of trees, continuous casting and levitation, glass blowing, design of chemical processing equipments, formation and dispersion of fog, damage of crops due to freezing, common industrial sight, especially in power plants, etc. Keeping in view the significance of such study, Jha [14] investigated hydromagnetic natural convection and mass transfer flow past a uniformly accelerated moving vertical plate through a porous medium. Ibrahim *et al*. [15] examined the unsteady hydromagnetic natural convection flow of a micro-polar fluid and heat transfer past a vertical porous plate through a porous medium in the presence of thermal and mass diffusion with a constant heat source. Makinde and Sibanda [16] analyzed the hydromagnetic mixed convective flow with heat and mass transfer past a vertical plate embedded in a porous medium with constant wall suction. Makinde [17] studied the

hydromagnetic mixed convection flow and mass transfer over a vertical porous plate with constant heat flux embedded in a porous medium. Makinde [18] also studied the hydromagnetic boundary layer flow with heat and mass transfer over a moving vertical plate under convective surface boundary conditions. Poonia and Chaudhary [19] investigated a unsteady two-dimensional hydromagnetic laminar mixed convective boundary layer flow with heat and mass transfer of a viscous, incompressible and electrically conducting fluid along an infinite vertical plate embedded in a porous medium. Eldabe *et al*. [20] analyzed the unsteady hydromagnetic convection flow of a viscous and incompressible fluid with heat and mass transfer in a porous medium near a moving vertical plate with time-dependent velocity. Prakash *et al*. [21] studied the diffusion-thermo and radiation effects on a unsteady hydromagnetic natural convection flow in a porous medium past an impulsively started infinite vertical plate with variable temperature and uniform mass diffusion.

The effect of heat absorption/generation on the hydromagnetic natural convection flow of a viscous, incompressible and electrically conducting fluid has a significant effect on heat transfer characteristics in numerous physical problems of practical interest such as fluids undergoing exothermic and/or endothermic chemical reaction [22], convection in Earth's mantle [23], post accident heat removal [24], fire and combustion modeling [25], development of metal waste from spent nuclear fuel [26], etc. This encouraged several researchers to undertake the study of a hydromagnetic natural convection flow in the presence of heat absorption/generation of a viscous, incompressible and electrically conducting fluid past bodies with various geometries. Kamel [27] investigated unsteady hydromagnetic convection flow due to heat and mass transfer through a porous medium bounded by an infinite vertical porous plate with temperature dependent heat sources and sinks. Chamkha [28] examined the unsteady hydromagnetic two-dimensional convective laminar boundary layer flow with heat and mass transfer of a viscous, incompressible, electrically conducting and temperature dependent heat absorbing fluid along a semi-infinite vertical permeable moving plate in the presence of a uniform transverse magnetic field. Makinde [29] analyzed heat and mass transfer by a hydromagnetic mixed convection stagnation point flow toward a vertical plate embedded in a highly porous medium with radiation and internal heat generation. In all these investigations, numerical/analytical solutions were

obtained by assuming simplified conditions that the velocity and temperature at the plate are uniform, continuous and well defined. However, the majority of problems of practical interest require the velocity and temperature to satisfy non-uniform, discontinuous or arbitrary conditions at the plate. Due to this fact, several researchers investigated the natural convection flow from a vertical plate with discontinuities in the surface temperature considering different aspects of the problem. Mention may be made of the research studies by Hayday *et al*. [30], Kelleher [31], Kao [32], Lee and Yovanovich [33] and Chandran *et al*. [34]. The effect of radiation on the natural convection flow of a viscous and incompressible fluid near a vertical flat plate with ramped temperature was investigated by Patra *et al*. [35]. They compared the effects of radiative heat transfer on the natural convection flow near a ramped temperature plate with the flow near an isothermal plate. Seth and Ansari [36] studied the unsteady hydromagnetic natural convection flow of a viscous, incompressible, electrically conducting and temperature dependent heat absorbing fluid past an impulsively moving vertical plate with ramped temperature in a porous medium taking into account the effects of thermal diffusion. Subsequently, Seth *et al*. [37] extended the problem studied by Seth and Ansari [36] to consider the effects of rotation on flow-field. Seth *et al*. [38] analyzed the hydromagnetic natural convection flow past an accelerated moving vertical plate with ramped temperature in a porous medium with thermal diffusion and heat absorption.

The practical applications of a hydromagnetic convection flow with heat and mass transfer in the presence of chemically reactive species showed its importance in different areas of science and engineering. In many chemical engineering processes, there occurs a chemical reaction between a foreign mass and fluid. Classically, chemical reactions encompass changes that strictly involve the motion of electrons in forming and breaking of chemical bonds, although the general concept of a chemical reaction is applicable to transformations of elementary particles, as well as to nuclear reactions. Chemical reactions can be classified as either heterogeneous or homogeneous processes depending on, whether they occur at an interface or as a single-phase volume reaction. These processes take place in numerous industrial applications, *viz.* curing of plastics, cleaning and chemical processing of materials, manufacturing of pulp and insulated cables, polymer production, manufacturing of ceramics or glassware, food processing, etc. Keeping into consideration such study, Afify [39]

investigated the effect of radiation on the natural convection flow and mass transfer past a vertical isothermal cone surface with chemical reaction in the presence of a transverse magnetic field. Muthucumaraswamy and Chandrakala [40] studied radiative heat and mass transfer effects on a moving isothermal vertical plate in the presence of chemical reaction. Zueco and Ahmed [41] analyzed the combined heat and mass transfer by a mixed convection hydromagnetic flow along a porous plate with chemical reaction in the presence of heat source. Suneetha and Reddy [42] investigated radiation and Darcy effects on the unsteady hydromagnetic heat and mass transfer flow of a chemically reacting fluid past an impulsively started vertical plate with heat generation. Chamkha *et al*. [43] discussed the effects of Joule heating, chemical reaction and thermal radiation on the unsteady hydromagnetic natural convection boundary layer flow with heat and mass transfer of a micro polar fluid from a semi-infinite heated vertical porous plate in the presence of a uniform transverse magnetic field. Bhattacharya and Layek [44] obtained a similarity solution of MHD boundary layer flow with mass diffusion and chemical reaction over a porous flat plate with suction/blowing. Mohamed *et al*. [45] investigated the unsteady MHD natural convection heat and mass transfer boundary layer flow of a viscous, incompressible, optically thick and electrically conducting fluid through a porous medium along an impulsively moving hot vertical plate in the presence of homogeneous chemical reaction of first order and temperature-dependent heat sink. They obtained analytical solution of the governing equations in closed form by the Laplace transform technique. Hernandez and Zueco [46] studied the unsteady hydromagnetic free convection by a laminar, viscous, electrically conducting and heat generating/absorbing fluid on a continuously moving vertical permeable surface in the presence of radiation effect, chemical reaction and mass flux. Nandkyeolyar *et al*. [47] analyzed the unsteady hydromagnetic heat and mass transfer flow of a radiating and chemically reactive fluid past a flat porous plate with ramped wall temperature.

It is found that, when the density of an electrically conducting fluid is low and/or the applied magnetic field is strong, a current is induced in a direction which is normal to both the electric and magnetic fields. Thus, if an electric field be applied at the right angle to the magnetic field, the total current will not flow along the electric field. This tendency of the electric current to flow across an electric field in the presence of a magnetic field is called Hall effect and the resulting current is known as Hall current which reduces the electrical conductivity normal to the lines of force so that the electrical conductivity becomes anisotropic [48]. One of the important characteristics of Hall current is to induce a secondary flow in the flow-field. Hall effects are significant in science and engineering, namely, MHD power generation, nuclear power reactors, Hall current accelerator, magnetometers, underground energy storage system, Hall effect sensors and spacecraft population and in several areas of astrophysics and geophysics. Taking into consideration this fact, Takhar and Ram [49] studied the effects of Hall current on the hydromagnetic free convection boundary layer flow of a heat generating fluid past an infinite plate in a porous medium using harmonic analysis. Aboeldahab and Elbarbary [50] analyzed the influence of Hall current on a MHD natural convection flow with heat and mass transfer over a vertical plate in the presence of a strong external magnetic field. Seth *et al*. [51] considered the Hall effects on a hydromagnetic natural convection flow past an impulsively moving vertical plate with ramped temperature taking into account thermal diffusion and heat absorption.

Keeping in view the above literature survey, our objective is to study the effects of Hall current on a unsteady hydromagnetic natural convection flow with heat and mass transfer of a viscous, incompressible, electrically conducting, heat absorbing and chemically reacting fluid past an accelerated moving vertical plate with ramped temperature and ramped surface concentration through a porous medium. To the best of our knowledge, this problem has not yet received any attention from the researchers despite having its applications in the recovery of petroleum products and gases (e.g. CBM: Coal Bed Methane and UCG: Underground Coal Gasification), fire dynamics in insulations, solar collection systems, nuclear waste repositories, geothermal energy systems, catalytic reactors, etc.

PROBLEM FORMULATION AND ITS SOLUTION

Consider the unsteady hydromagnetic natural convection flow with heat and mass transfer of an electrically conducting, viscous, incompressible, temperature dependent heat absorbing and chemically reacting fluid past an accelerated moving vertical plate through a porous medium taking into account Hall effects. The flow is assumed to be in the x' direction, which is taken

along the length of the plate in upward direction, y' -axis is normal to it and z' -axis is perpendicular to the $x'y'$-plane. A uniform transverse magnetic field B_0 is taken to be acting along the y' -axis. Firstly, i.e. at time $t' \leq 0$, both the fluid and plate are at rest and maintain uniform temperature T'_∞ and uniform surface concentration C'_∞. At time $t' > 0$, the plate begins to move in the x' direction against the gravitational field with time dependent velocity $U(t')$. Instantaneously, the temperature of the plate is raised or lowered to $T'_\infty + (T'_w - T'_\infty)t'/t_0$ and the level of concentration at the surface of the plate is raised or lowered to $C'_\infty + (C'_w - C'_\infty)t'/t_0$ when $0 < t' \leq t_0$. Thereafter, i.e. at time $t' > t_0$, the plate is maintained at uniform temperature T'_w and the level of concentration at surface of the plate is preserved at uniform concentration C'_w. A homogeneous chemical reaction of first order with constant rate K'_2 is supposed to exist between the diffusing species and the fluid. Physical model of the problem is shown in Figure 1. It is assumed that the plate is of infinite extent in x' and z' directions and is electrically non-conducting, all quantities except pressure are functions of y' and t' only. For liquid metals and partially ionized fluid, the magnetic Reynolds number is very small and hence the induced magnetic field produced by the fluid motion is negligible in comparison to the applied one [52] so that the magnetic field $B = (0, B_0, 0)$. Also the effect of polarization of fluid is negligible when no external electric field is applied [52]; that is $E = (0,0,0)$. This corresponds to the case where no energy is added or extracted from the fluid by electrical means.

Owing to the above mentioned assumptions, the governing equations for the unsteady hydromagnetic natural convection flow with heat and mass transfer of an electrically conducting, viscous, incompressible and temperature dependent heat absorbing and chemically reacting fluid through a porous medium taking Hall effects into account, under Boussinesq approximation, are reduce to

$$\frac{\partial u'}{\partial t'} = \upsilon \frac{\partial^2 u'}{\partial y'^2} - \frac{\sigma B_0^2}{\rho}\left(\frac{u' + mw'}{1 + m^2}\right) - \frac{\upsilon}{K'_1}u'$$

$$+ g\beta'(T' - T'_\infty) + g\beta^*(C' - C'_\infty), \dots \quad (1)$$

$$\frac{\partial w'}{\partial t'} = \upsilon \frac{\partial^2 w'}{\partial y'^2} + \frac{\sigma B_0^2}{\rho}\left(\frac{mu' - w'}{1 + m^2}\right) - \frac{\upsilon}{K'_1}w', \quad (2)$$

$$\frac{\partial T'}{\partial t'} = \alpha'\frac{\partial^2 T'}{\partial y'^2} - \frac{Q_0}{\rho C_p}(T' - T'_\infty), \quad \dots\dots\dots (3)$$

$$\frac{\partial C'}{\partial t'} = D\frac{\partial^2 C'}{\partial y'^2} - K'_2(C' - C'_\infty), \quad \dots\dots\dots (4)$$

where
u', w', T', C', v, σ, ρ, K'_1, g, β', β^*, α', Q_0, D, ω_e, τ_e and $m = \omega_e\tau_e$ are, respectively, fluid velocity in x' direction, fluid velocity along z' direction, fluid temperature, species concentration, kinematic coefficient of viscosity, electrical conductivity, fluid density, permeability of porous medium, acceleration due to gravity, coefficient of thermal expansion, volumetric coefficient of expansion, thermal diffusivity, heat absorption coefficient, chemical molecular diffusivity, cyclotron frequency, electron collision time and Hall current parameter.
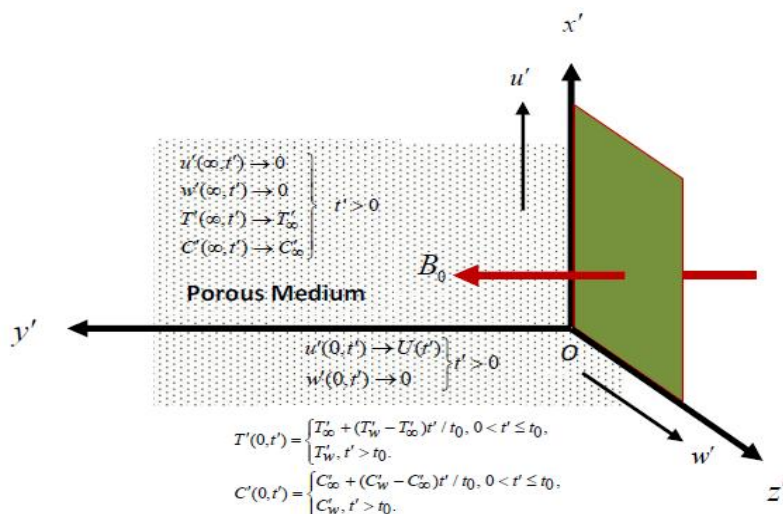
Fig.1. Physical model of the problem.

Initial and boundary conditions for fluid velocity, fluid temperature and species concentration for the model are

$$
\left.
\begin{array}{l}
u' = 0,\ w' = 0,\ T' = T'_\infty,\ C' = C'_\infty \text{ for } y' \ge 0 \text{ and } t' \le 0, \\
u' = U(t'),\ w' = 0 \text{ at } y' = 0 \text{ for } t' > 0, \\
T' = T'_\infty + (T'_w - T'_\infty)t'/t_0,\ C' = C'_\infty + (C'_w - C'_\infty)t'/t_0 \\
\quad \text{at } y' = 0 \text{ for } 0 < t' \le t_0, \\
T' = T'_w,\ C' = C'_w \text{ at } y' = 0 \text{ for } t' > t_0, \\
u' \to 0,\ w' \to 0,\ T' \to T'_\infty,\ C' \to C'_\infty \text{ as } y' \to \infty \text{ for } t' > 0.
\end{array}
\right\} \quad (5)
$$

In order to convert Eqn. (1) to (4) along with the initial and boundary conditions in non-dimensional form, the following non-dimensional quantities and parameters are introduced

$$
\left.
\begin{array}{l}
y = y'/U_0 t_0,\ u = u'/U_0,\ w = w'/U_0\ t = t'/t_0, \\
T = (T' - T'_\infty)/(T'_w - T'_\infty),\ C = (C' - C'_\infty)/(C'_w - C'_\infty), \\
G_r = \upsilon g \beta'(T'_w - T'_\infty)/U_0^3,\ G_c = \upsilon g \beta^*(C'_w - C'_\infty)/U_0^3, \\
M = \sigma B_0^2 \upsilon / \rho U_0^2,\ K_1 = K_1' U_0^2 / \upsilon^2,\ P_r = \upsilon / \alpha', \\
S_c = \upsilon / D,\ K_2 = \upsilon K_2' / U_0^2 \text{ and } \phi = \upsilon Q_0 / \rho C_p U_0^2,
\end{array}
\right\} \quad (6)
$$

where $G_r,\ G_c,\ M,\ K_1,\ P_r,\ S_c,\ K_2$ and ϕ are respectively, thermal Grashof number, solutal Grashof number, magnetic parameter, permeability parameter, Prandtl number, Schmidt number, chemical reaction parameter and heat absorption parameter.

The governing equations (1) to (4), in non-dimensional form, become

$$
\frac{\partial u}{\partial t} = \frac{\partial^2 u}{\partial y^2} - M\left(\frac{u + mw}{1 + m^2}\right) - \frac{u}{K_1} + G_r T + G_c C, \quad (7)
$$

$$
\frac{\partial w}{\partial t} = \frac{\partial^2 w}{\partial y^2} + M\left(\frac{mu - w}{1 + m^2}\right) - \frac{w}{K_1}, \quad \ldots\ldots\ldots\ldots \quad (8)
$$

$$
\frac{\partial T}{\partial t} = \frac{1}{P_r}\frac{\partial^2 T}{\partial y^2} - \phi T, \quad \ldots\ldots\ldots\ldots\ldots\ldots \quad (9)
$$

$$
\frac{\partial C}{\partial t} = \frac{1}{S_c}\frac{\partial^2 C}{\partial y^2} - K_2 C. \quad (10)
$$

It may be noted that the characteristic time t_0 may be defined according to the non-dimensional process mentioned above, i.e.

$$
t_0 = \upsilon / U_0^2,
$$

where U_0 is the characteristic velocity.
The initial and boundary conditions in non-dimensional form are

$$
\left.
\begin{array}{l}
u = 0,\ w = 0,\ T = 0,\ C = 0 \text{ for } y \ge 0 \text{ and } t \le 0, \\
u = G(t),\ w = 0 \text{ at } y = 0 \text{ for } t > 0, \\
T = t,\ C = t \text{ at } y = 0 \text{ for } 0 < t \le 1, \\
T = 1,\ C = 1 \text{ at } y = 0 \text{ for } t > 1, \\
u \to 0,\ w \to 0,\ T \to 0,\ C \to 0 \text{ as } y \to \infty \text{ for } t > 0,
\end{array}
\right\} \quad (11)
$$

where $G(t) = U(t')/U_0$.

The equations (7) to (10) subject to initial and boundary conditions (11) showing fluid flow, are quite general. We now take a particular case of interest, namely, uniformly accelerated movement of the plate, i.e. $G(t) = Rt$ where R is a non-dimensional constant, to explore the flow features of the fluid flow.

Eqns. (7) and (8) are presented in compact form as

$$
\frac{\partial F}{\partial t} = \frac{\partial^2 F}{\partial y^2} - \lambda F + G_r T + G_c C, \quad (12)
$$

where

$$
F = u + iw \text{ and } \lambda = M(1 - im)/(1 + m^2) + 1/K_1.
$$

Initial and boundary conditions (11) in compact form become

$$
\left.
\begin{array}{l}
F = 0,\ T = 0,\ C = 0 \text{ for } y \ge 0 \text{ and } t \le 0, \\
F = Rt \text{ at } y = 0 \text{ for } t > 0, \\
T = t,\ C = t \text{ at } y = 0 \text{ for } 0 < t \le 1, \\
T = 1,\ C = 1 \text{ at } y = 0 \text{ for } t > 1, \\
F \to 0,\ T \to 0,\ C \to 0 \text{ as } y \to \infty \text{ for } t > 0.
\end{array}
\right\} \quad (13)
$$

The exact solutions for fluid velocity $F(y,t)$, fluid temperature $T(y,t)$ and species concentration $C(y,t)$ are obtained by using Laplace transform technique, which are expressed in the following form after simplification

$$
F(y,t) = Rf_1(y,1,\lambda,t) + \frac{a_1}{b_1^2}\{F_1(y,t) - H(t-1)F_1(y,t-1)\}
$$

$$
\quad - \frac{a_2}{b_2^2}\{G_1(y,t) - H(t-1)G_2(y,t-1)\}, \quad (14)
$$

$$
T(y,t) = f_1(y,P_r,\phi,t) - H(t-1)f_1(y,P_r,\phi,t-1), \quad (15)
$$

$$
C(y,t) = f_1(y,S_c,K_2,t) - H(t-1)f_1(y,S_c,K_2,t-1), \quad (16)
$$

where

$$
F_1(y,t) = e^{b_1 t}\{f_2(y,P_r,\phi,b_1,t) - f_2(y,1,\lambda,b_1,t)\}
$$

$$
\quad + b_1\{f_3(y,P_r,\phi,b_1,t) - f_3(y,1,\lambda,b_1,t)\},
$$

$$
G_1(y,t) = e^{b_2 t}\{f_2(y,S_c,K_2,b_2,t) - f_2(y,1,\lambda,b_2,t)\}
$$

$$
\quad + b_2\{f_3(y,S_c,K_2,b_2,t) - f_3(y,1,\lambda,b_2,t)\},
$$

$$
a_1 = G_r/(1 - P_r),\ a_2 = G_c/(1 - S_c),\ b_1 = (P_r\phi - \lambda)/(1 - P_r)
$$

and $b_2 = (S_c K_2 - \lambda)/(1 - S_c)$.

The expressions for $f_i\ (i = 1, 2, 3)$ are given in the Appendix A.

SOLUTION WHEN THE FLUID IS IN CONTACT WITH AN ISOTHERMAL PLATE WITH UNIFORM SURFACE CONCENTRATION

In order to put emphasis on the influence of ramped temperature and ramped surface concentration on the flow-field, it may be justified to compare such a flow with the one near an accelerated moving vertical isothermal plate with uniform surface concentration. Keeping in view the assumptions made in this paper, the solutions for fluid velocity, fluid temperature and species concentration for a natural convection flow past an accelerated moving vertical isothermal plate with uniform surface concentration are obtained and are presented in the following form

$$F(y,t) = \left(\frac{a_1}{b_1} + \frac{a_2}{b_2}\right) f_2(y,1,\lambda,0,t) + R f_1(y,1,\lambda,t)$$

$$+ \frac{a_1}{b_1}\left[e^{b_1 t}\left\{ f_2(y,P_r,\phi,b_1,t) - f_2(y,1,\lambda,b_1,t)\right\} - \right.$$

$$\left. f_2(y,P_r,\phi,0,t)\right] + \frac{a_2}{b_2}\left[e^{b_2 t}\left\{ f_2(y,S_c,K_2,b_2,t)\right.\right.$$

$$\left.\left. - f_2(y,1,\lambda,b_2,t)\right\} - f_2(y,S_c,K_2,0,t)\right], \dots \dots (17)$$

$$T(y,t) = f_2(y,P_r,\phi,0,t), \dots \dots \dots (18)$$

$$C(y,t) = f_2(y,S_c,K_2,0,t) \dots \dots \dots (19)$$

SKIN FRICTION, NUSSELT NUMBER AND SHERWOOD NUMBER

The expressions for primary skin friction τ_x, secondary skin friction τ_z which are measures of the shear stress at the plate due to primary flow, shear stress at the plate due to secondary flow, the Nusselt number N_u, which measures the rate of heat transfer at the plate and the Sherwood number S_h, which measures the rate of mass transfer at the plate, are presented in the following form for a ramped temperature plate with ramped surface concentration and an isothermal plate with uniform surface concentration:

For the plate with ramped temperature and ramped surface concentration

$$\tau = \tau_x + i\tau_z = R\left[\left(t\sqrt{\lambda} + \frac{1}{2\sqrt{\lambda}}\right)\left\{erfc\left(\sqrt{\lambda t}\right) - 1\right\} - \sqrt{\frac{t}{\pi}} e^{-\lambda t}\right]$$

$$+ \frac{a_1}{b_1^2}\left[F_2(0,t) - H(t-1)F_2(0,t-1)\right] + \frac{a_2}{b_2^2}\left[G_2(0,t)\right.$$

$$\left. - H(t-1)G_2(0,t-1)\right], \tag{20}$$

$$N_u = f_6(P_r,\phi,t) - H(t-1)f_6(P_r,\phi,t-1), \tag{21}$$

$$S_h = f_6(S_c,K_2,t) - H(t-1)f_6(S_c,K_2,t-1), \tag{22}$$

where

$$F_2(0,t) = e^{b_1 t}\left\{ f_4(P_r,\phi,b_1,t) - f_4(1,\lambda,b_1,t)\right\}$$

$$- b_1\left\{ f_5(P_r,\phi,b_1,t) - f_5(1,\lambda,b_1,t)\right\},$$

$$G_2(0,t) = e^{b_2 t}\left\{ f_4(S_c,K_2,b_2,t) - f_4(1,\lambda,b_2,t)\right\}$$

$$- b_1\left\{ f_5(S_c,K_2,b_2,t) - f_5(1,\lambda,b_2,t)\right\},$$

and for the isothermal plate with uniform surface concentration

$$\tau = \tau_x + i\tau_z = \left\{\left(\frac{a_1}{b_1} + \frac{a_2}{b_2} + Rt\right)\sqrt{\lambda} + \frac{R}{2\sqrt{\lambda}}\right\}\left\{erfc\left(\sqrt{\lambda t}\right) - 1\right\}$$

$$- \left(\frac{a_1}{b_1} + \frac{a_2}{b_2} + Rt\right)\frac{e^{-\lambda t}}{\sqrt{t\pi}} + \frac{a_1}{b_1}\left[e^{b_1 t}\left\{ f_4(P_r,\phi,b_1,t) - \right.\right.$$

$$\left. f_4(1,\lambda,b_1,t)\right\} - f_4(P_r,\phi,0,t)\right] + \frac{a_2}{b_2}\left[e^{b_2 t}\left\{ f_4(S_c,K_2,b_2,t)\right\}\right.$$

$$\left. - f_4(1,\lambda,b_2,t)\right\} - f_4(S_c,K_2,0,t)\right],$$

$$\tag{23}$$

$$N_u = f_4(P_r,\phi,0,t), \tag{24}$$

$$S_h = f_4(S_c,K_2,0,t). \tag{25}$$

Expressions for $f_i(i = 4,5,6)$ are provided in the Appendix A.

RESULTS AND DISCUSSION

In order to analyze the effects of Hall current, thermal buoyancy force, solutal buoyancy force, field, heat absorption, chemical reaction and time on the flow-field, the numerical values of primary and secondary fluid velocities in the boundary layer region, computed from the analytical solutions reported in the previous sections, are displayed graphically versus boundary layer coordinate y in Figures 2-13 for various values of Hall current parameter m, thermal Grashof number G_r, solutal Grashof number G_c, heat absorption parameter ϕ, chemical reaction parameter K_2 and time t taking magnetic parameter $M = 10$, permeability parameter $K_1 = 0.5$, Prandtl number $P_r = 0.71$ (ionized air), Schmidt number $S_c = 0.22$ and $R = 1$. It is noticed from Figures 2-13 that, for both ramped temperature plate with ramped surface concentration and isothermal plate with uniform surface concentration, the primary fluid velocity u and the secondary fluid velocity w attain a maximum distinctive value near the surface of the plate and then decrease properly on increasing the boundary layer coordinate y to approach the free stream value. Also the primary and secondary fluid velocities are faster in case of isothermal plate with uniform surface concentration than those of ramped temperature plate with ramped surface concentration. Figures 2-7 reveal the influence of

Hall current, thermal and solutal buoyancy forces on the primary and secondary fluid velocities u and w, respectively.
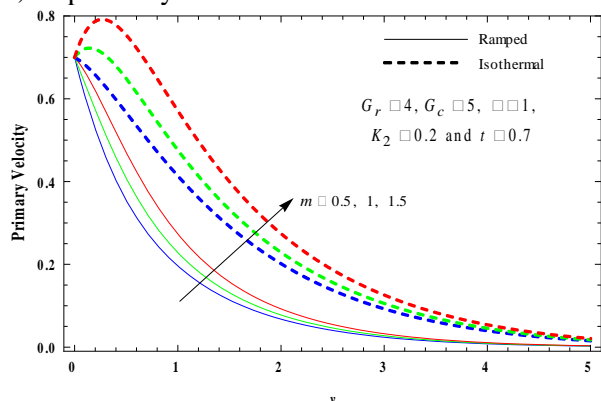
Fig. 2. Primary velocity for varying m.
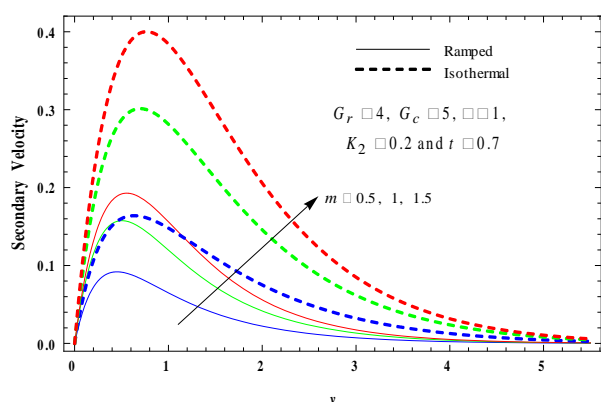
Fig.3. Secondary velocity profiles for varying m.
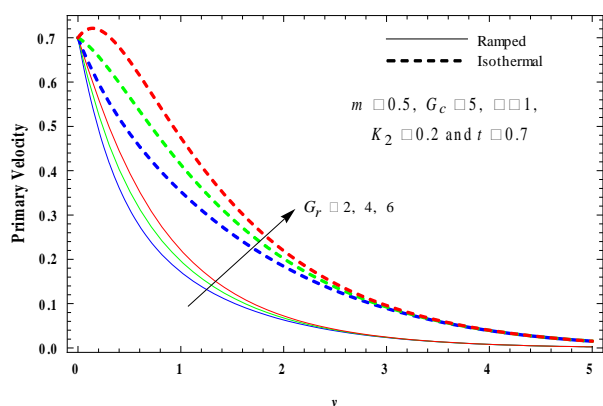
Fig. 4. Primary velocity profiles for varying G_r.
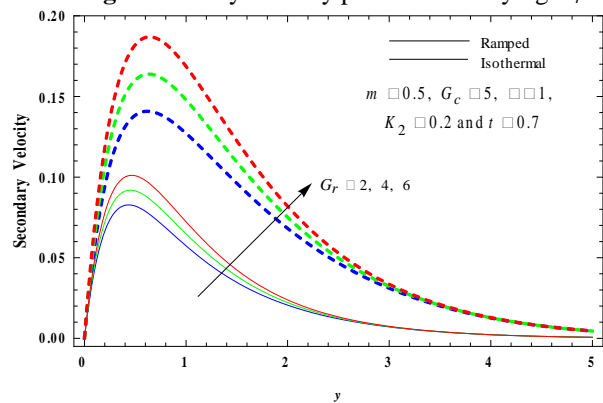
Fig. 5. Secondary velocity profiles for varying G_r.
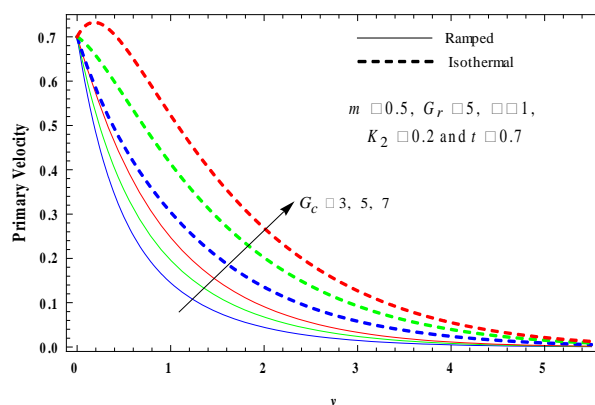
Fig. 6. Primary velocity profiles for varying G_c.
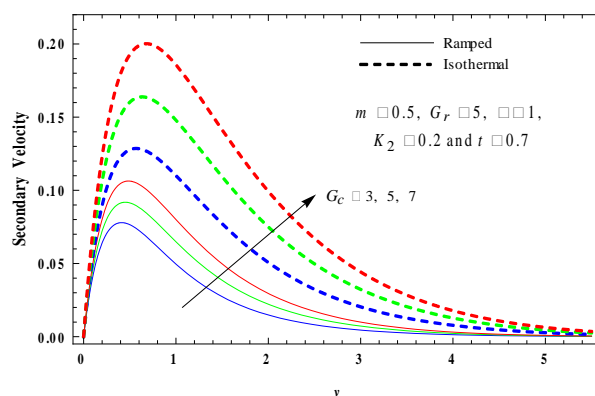
Fig. 7. Secondary velocity profiles for varying G_c.

The thermal Grashof number G_r signifies the relative effect of the thermal buoyancy force to the viscous hydrodynamic force. The solutal Grashof number G_c characterizes the ratio of the solutal buoyancy force and viscous hydrodynamic force. As expected, it is noticed from Figures 2-7 that, for both ramped temperature plate with ramped surface concentration and isothermal plate with uniform surface concentration, u and w increase with the increase in either Hall current parameter m, Grashof number G_r or solutal Grashof number G_c. This implies that Hall current, thermal and solutal buoyancy forces tend to accelerate primary and secondary fluid velocities for both ramped temperature plate with ramped surface concentration and isothermal plate with uniform surface concentration. Figures 8-11 depict the effects of heat absorption and chemical reaction on the primary and secondary fluid velocities. It is observed from Figures 8-11 that, for both ramped temperature plate with ramped surface concentration and isothermal plate with uniform surface concentration, u and w decrease with the increase in either heat absorption parameter ϕ or chemical reaction parameter K_2. This implies that heat absorption and chemical reaction have the retarding influence on the primary and secondary fluid velocities for both ramped temperature plate

665
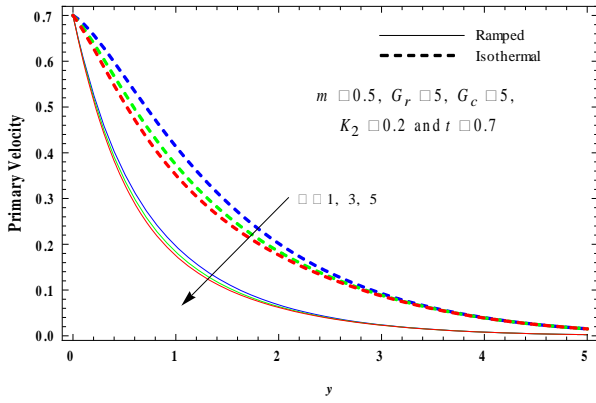
Fig. 8. Primary velocity profiles for varying ϕ.
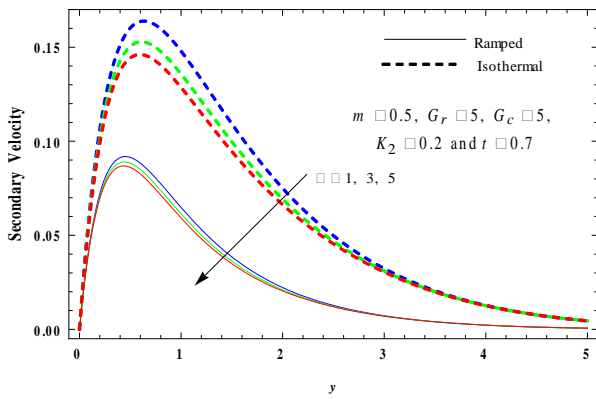
Fig. 9. Secondary velocity profiles for varying ϕ.
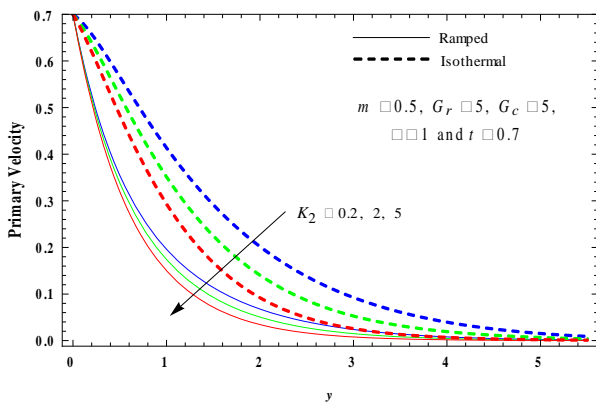
Fig. 10. Primary velocity profiles for varying K_2.
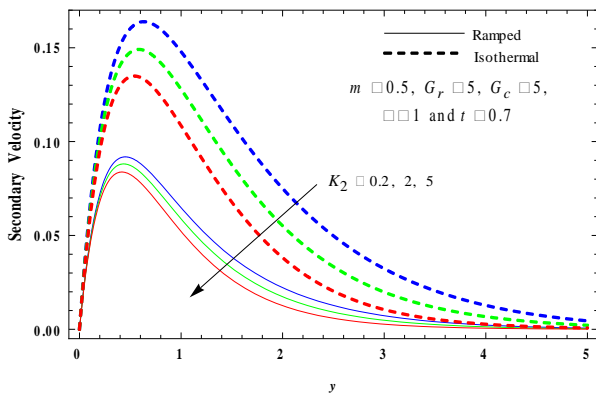
Fig. 11. Secondary velocity profiles for varying K_2.

with ramped surface concentration and isothermal plate with uniform surface concentration. This may be attributed to the fact that the tendency of heat absorption (thermal sink) is to reduce the fluid temperature which causes the strength of thermal buoyancy force to decrease resulting in a net reduction in the fluid velocity. Figures 12 and 13 demonstrate the effects of time on the primary and secondary fluid velocities. It is evident from Figures 12 and 13 that, for both ramped temperature plate with ramped surface concentration and isothermal plate with uniform surface concentration, u and w increase on increasing time t. This implies that there is enrichment in the primary and secondary fluid velocities for both ramped temperature plate with ramped surface concentration and isothermal plate with uniform surface concentration with the progress of time.
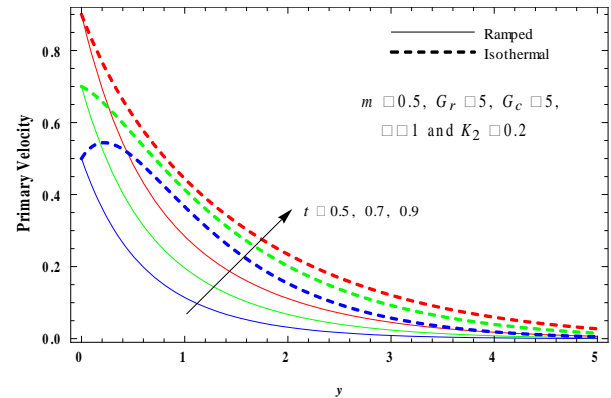
Fig. 12. Primary velocity profiles for varying t.
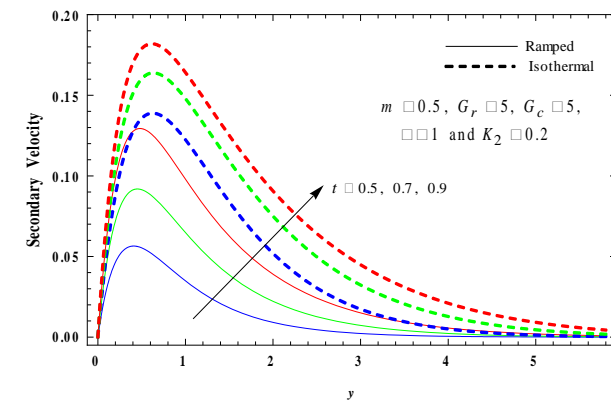
Fig. 13. Secondary velocity profiles for varying t.

The numerical values of species concentration C, computed from the analytical solution mentioned in the previous sections, are depicted graphically versus the boundary layer coordinate y in Figures 14-16 for various values of the chemical reaction parameter K_2, Schmidt number S_c and time t. It is observed in Figures 14-16 that, for both ramped temperature plate with ramped surface concentration and isothermal plate with uniform surface concentration, species concentration

decreases on increasing either K_2 or S_c, whereas it increases on increasing time t. Since the Schmidt number S_c is the ratio of momentum diffusivity to mass diffusivity, an increase in S_c implies a decrease in the mass diffusion rate. This implies that, for both ramped temperature plate with ramped surface concentration and isothermal plate with uniform surface concentration, chemical reaction tends to reduce species concentration, whereas mass diffusion has a reverse effect on it and there is an enhancement in the species concentration with the progress of time throughout the boundary layer region. It is also noticed from Figures 14-16 that species concentration is maximal at the surface of the plate and decreases properly with the increase of boundary layer coordinate y to approach free stream value.
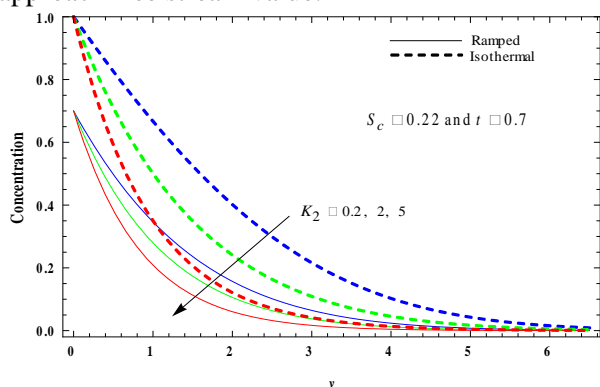
Fig. 14. Concentration profiles for varying K_2.
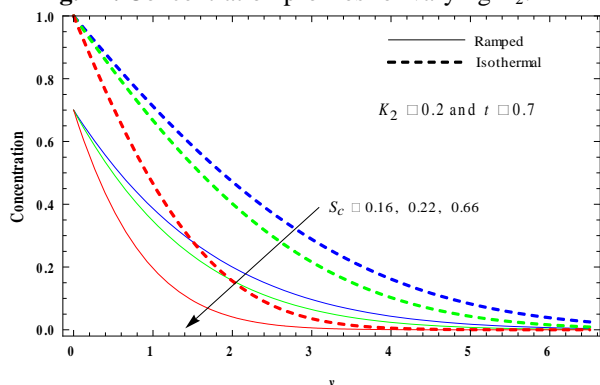
Fig.15. Concentration profiles for varying S_c.
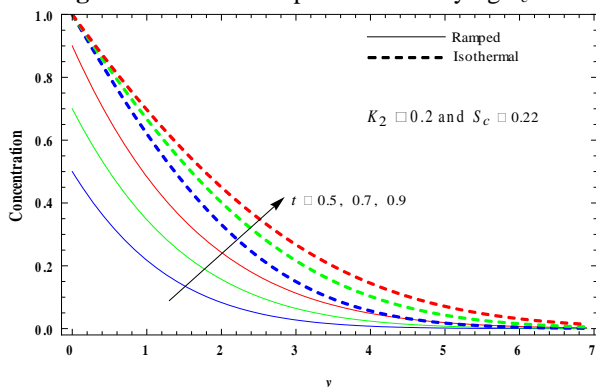
Fig. 16. Concentration profiles for varying t.

The numerical values of non-dimensional skin frictions τ_x and τ_z due to primary and secondary flows, respectively, for both ramped temperature plate with ramped surface concentration and isothermal plate with uniform surface concentration, computed from the analytical expressions reported in the paper, are presented in tabular form in Tables 1 to 6 for various values of m, ϕ, G_r, G_c, K_2 and t taking $R = 1$, $M = 10$, $K_1 = 0.5$, $P_r = 0.71$ and $S_c = 0.22$ whereas those of Sherwood number S_h, calculated from the analytical expressions presented in the paper, are exhibited in tabular form in Table 7 for different values of K_2 and t.

It is observed from Tables 1 to 6 that, for both ramped temperature plate with ramped surface concentration and isothermal plate with uniform surface concentration, primary skin friction $-\tau_x$ increases on increasing either ϕ or K_2 or t and it decreases on increasing either m or G_r or G_c whereas secondary skin friction τ_z increases on increasing either m or G_r or G_c or t and it decreases on increasing either ϕ or K_2. This implies that, for both ramped temperature plate with ramped surface concentration and isothermal plate with uniform surface concentration, heat absorption and chemical reaction have a tendency to enhance primary skin friction whereas Hall current, thermal and solutal buoyancy forces have the reverse effect on it. Hall current, thermal and solutal buoyancy forces have a tendency to enhance secondary skin friction, whereas heat absorption and chemical reaction have the reverse effect on it, for both ramped temperature plate with ramped surface concentration and isothermal plate with uniform surface concentration. Both the primary and secondary skin frictions are getting enhanced with the progress of time, for both ramped temperature plate with ramped surface concentration and isothermal plate with uniform surface concentration.

It is found from Table 7 that, for both ramped temperature plate with ramped surface concentration and isothermal plate with uniform surface concentration, Sherwood number S_h increases on increasing K_2. On increasing time t, S_h increases for the ramped temperature plate with ramped surface concentration, whereas it decreases for the isothermal plate with uniform surface concentration. This implies that, for both ramped

Table 1. Primary skin friction $-\tau_x$ when $K_2 = 0.2, G_r = 4, G_c = 5$ and $t = 0.7$

$\phi \downarrow m \rightarrow$	Ramped			Isothermal		
	0.5	**1.0**	**1.5**	**0.5**	**1.0**	**1.5**
1	1.01741	0.622583	0.278910	0.154959	0.144327	0.100579
3	1.05740	0.667453	0.329253	0.249978	0.236641	0.176908
5	1.08762	0.701253	0.367049	0.293849	0.264610	0.194591

Table 2. Secondary skin friction τ_z when $K_2 = 0.2, G_r = 4, G_c = 5$ and $t = 0.7$

$\phi \downarrow m \rightarrow$	Ramped			Isothermal		
	0.5	**1.0**	**1.5**	**0.5**	**1.0**	**1.5**
1	0.579536	0.862241	0.931667	0.760465	1.19187	1.3681
3	0.571497	0.848668	0.915488	0.736848	1.14988	1.3150
5	0.565602	0.838733	0.903647	0.721472	1.12255	1.2803

Table 3. Primary skin friction $-\tau_x$ when $m = 0.5, K_2 = 0.2, \phi = 1$ and $t = 0.7$

$G_r \downarrow G_c \rightarrow$	Ramped			Isothermal		
	3	**5**	**7**	**3**	**5**	**7**
2	1.62883	1.29846	0.968091	1.13613	0.599886	0.463638
4	1.34778	1.01741	0.687043	0.67120	0.434959	0.401288
6	1.06673	0.73636	0.405995	0.40628	0.329967	0.266214

Table 4. Secondary skin friction τ_z when $m = 0.5, K_2 = 0.2, \phi = 1$ and $t = 0.7$

$G_r \downarrow G_c \rightarrow$	Ramped			Isothermal		
	3	**5**	**7**	**3**	**5**	**7**
2	0.503644	0.547908	0.592173	0.60533	0.69448	0.78363
4	0.535271	0.579536	0.623800	0.67131	0.76046	0.84961
6	0.566899	0.611163	0.655428	0.73730	0.82645	0.91560

Table 5. Primary skin friction $-\tau_x$ when $m = 0.5, G_r = 4, G_c = 5$ and $\phi = 1$

$t \downarrow K_2 \rightarrow$	Ramped			Isothermal		
	0.2	**2**	**5**	**0.2**	**2**	**5**
0.5	0.82261	0.84418	0.87252	0.129931	0.181550	0.289501
0.7	1.01741	1.05636	1.10406	0.134959	0.229325	0.329780
0.9	1.20486	1.26388	1.33210	0.752093	0.857801	0.962095

Table 6. Secondary skin friction τ_z when $m = 0.5, G_r = 4, G_c = 5$ and $\phi = 1$

$t \downarrow K_2 \rightarrow$	Ramped			Isothermal		
	0.2	**2**	**5**	**0.2**	**2**	**5**
0.5	0.386746	0.382209	0.376293	0.610284	0.589456	0.564859
0.7	0.579536	0.570093	0.558730	0.760465	0.732626	0.703327
0.9	0.776110	0.760566	0.743094	0.898134	0.865231	0.833698

Table 7. Sherwood number $-S_h$ when $S_c = 0.22$

$K_2 \downarrow t \rightarrow$	Ramped			Isothermal		
	0.5	**0.7**	**0.9**	**0.5**	**0.7**	**0.9**
0.2	0.386593	0.463189	0.531694	0.428415	0.379505	0.349641
2	0.488076	0.625355	0.760246	0.785973	0.757863	0.738408
5	0.628694	0.838894	1.04877	1.12945	1.09522	1.07538

temperature plate with ramped surface concentration and isothermal plate with uniform surface concentration, chemical reaction tends to enhance the rate of mass transfer at the plate. For the ramped temperature plate with ramped surface concentration, the rate of mass transfer at the plate is getting enhanced, whereas for the isothermal plate with uniform surface concentration it is getting reduced with the progress of time.

CONCLUSIONS

The present study brings out the following significant findings of the effects of Hall current on the unsteady hydromagnetic natural convection flow with heat and mass transfer of a viscous, incompressible, electrically conducting, temperature dependent heat absorbing and chemically reacting fluid past an accelerated moving vertical plate with ramped temperature and ramped surface concentration through a porous medium:

1. For both ramped temperature plate with ramped surface concentration and isothermal plate with uniform surface concentration.

Hall current, thermal and solutal buoyancy forces tend to accelerate primary and secondary fluid velocities whereas heat absorption and chemical reaction have a reverse effect on it. There is enrichment in the primary and secondary fluid velocities with the progress of time. Chemical reaction tends to reduce species concentration whereas mass diffusion has a reverse effect on it and there is an enhancement in the species concentration with the progress of time throughout the boundary layer region. Heat absorption and chemical reaction have a tendency to enhance primary skin friction, whereas Hall current, thermal and solutal buoyancy forces have a reverse effect on it. Hall current, thermal and solutal buoyancy forces have a tendency to enhance secondary skin friction, whereas chemical reaction has a reverse effect on it. Both the primary and secondary skin frictions are getting enhanced with the progress of time. Chemical reaction tends to enhance the rate of mass transfer at the plate.

2. For a ramped temperature plate with ramped surface concentration, the rate of mass transfer at the plate is getting enhanced, whereas for an isothermal plate with uniform surface concentration, it is getting reduced with the progress of time.

REFERENCES

1. G. M. Oreper, J. Szekely, *J. Crystal Growth*, **64**, 505 (1983).
2. A. Raptis, N. Kafousias, *Int. J. Energy Res.*, **6**, 241(1982).
3. A. Raptis, *Int. J. Energy Res.*, **10**, 97(1986).
4. A. J. Chamkha, *Int. J. Eng. Sci.*, **35**, 975(1997).
5. T. K. Aldoss, M. A. Al-Nimr, M. A. Jarrah, B. J. Al-Shaer, *Num. Heat Transf.*, **28**, 635 (1995).
6. K. A. Helmy, *J. Appl. Math. Mech. (ZAMM)*, **78**, 255 (1998).
7. Y. J. Kim, *Int. J. Eng. Sci.*, **38**, 833 (2000).
8. R. C. Chaudhary, A. Jain, *Turkish J. Eng. Env. Sci.*, **32**, 13 (2008).
9. M. M. Rashidi, T. Hayat, A. B. Parsa, *Heat Transf.—Asian Res.*, **40** (8), 677 (2011).
10. M. M. Rashidi, M. Ferdows, A. B. Parsa, S. Abelman, *Abs. Appl. Anal.*, Article ID 923487, 10 pages (2014).
11. G. S. Seth, S. M. Hussain, S. Sarkar, *J. Porous Media*, **17**, 67 (2014).
12. G. S. Seth, R. Nandkeolyar, Md. S. Ansari, *J. Appl. Fluid Mech.*, **6**, 27 (2013).
13. O. D. Makinde, M. S. Tshehla, *Adv. Math. Phys.*, Article ID 973593, 10 pages (2014).
14. B. K. Jha, *Astrophys. Space Sci.*, **175**, 283 (1991).
15. F. S. Ibrahim, I. A. Hassanien, A. A. Bakr, *Canad. J. Phys.*, **82**, 775 (2004).
16. O. D. Makinde, P. Sibanda, *J. Heat Transf.*, **130**, 1 (2008).
17. O. D. Makinde, *Int. J. Num. Methods Heat Fluid Flow*, **19**, 546 (2009).
18. O. D. Makinde, *Canad. J. Chem. Eng.*, **88**, 983 (2010).
19. H. Poonia, R. C. Chaudhary, *Theo. Appl. Mech.*, **37**, 263 (2010).
20. N. T. M. Eldabe, E. M. A. Elbashbeshy, W. S. A. Hasanin, E. M. Elsaid, *Int. J. Energy & Tech.*, **3**, 1 (2011).
21. J. Prakash, D. Bhanumathi, A. G. V. Kumar, S. V. K. Verma, *Trans. Porous Media*, **96**, 135 (2013).
22. K. Vajravelu, J. Nayfeh, *Int. Comm. Heat Mass Transf.*, **19**, 701 (1992).
23. D. P. MaKenzie, J. M. Roberts, N. O. Weiss, *J. Fluid Mech.*, **62**, 465 (1974).
24. I. Baker, R. F. Faw, A. Kulacki, *Nucl. Sci. Eng.*, **61**, 222 (1976).
25. M. A. Delichatsios, The SFPA handbook of fire protection engineering. NFPA publications, M. A. Quincy, pp. 306, 1988.
26. B. R. Westphal, D. D. Keiser, R. H. Rigg, D. V. Laug, Production of metal waste forms from spent nuclear fuel treatment, *DOE Spent Nuclear Fuel Conference*, Salt Lake City, UT, pp. 288 (1994).
27. M . H. Kamel, *Energy Conversion Manag.*, **42**, 393 (2001).
28. A. J. Chamkha, *Int. J. Eng. Sci.*, **42**, 217 (2004).
29. O. D. Makinde, *Meccanica*, **47**, 1173 (2012).
30. A. A. Hayday, D. A. Bowlus, R. A. McGraw, *ASME J. Heat Transf.*, **89**, 244 (1967).
31. M. Kelleher, *ASME J. Heat Transf.*, **93**, 349 (1971).
32. T. T. Kao, *Letters Heat Mass Transf.*, **2**, 419 (1975).
33. S. Lee, M. M. Yovanovich, *ASME J. Heat Transf.*, **113**, 501 (1991).
34. P. Chandran, N. C. Sacheti, A. K. Singh, *Heat Mass Transf.*, **41**, 459 (2005).
35. R. R. Patra, S. Das, R. N. Jana, S. K. Ghosh, *J. Appl. Fluid Mech.*, **5**, 9 (2012).
36. G. S. Seth, Md. S. Ansari, *Int. J. Appl. Mech. Eng.*, **15**, 199 (2010).
37. G. S. Seth, R. Nandkeolyar, Md. S. Ansari, *Int. J. Appl. Math. Mech.*, **7**, 52 (2011).
38. G. S. Seth, S. M. Hussain, S. Sarkar, *J. Nature Sci. Sustainable Tech.*, **7**(3), 207 (2013).
39. A. A. Afify, *Canad. J. Phys.*, **82**, 447 (2004).
40. R. Muthucumaraswamy, P. Chandrakala, *Int. J. Appl. Mech. Eng.*, **11**, 639 (2006).
41. J. Zueco, S. Ahmed, *Appl. Math. Mech.-Eng. Ed.*, **31**(10), 1217 (2010).
42. S. Suneetha, N. B. Reddy, *Int. J. Appl. Math. Mech.*, **7**(7), 1 (2011).
43. A. J. Chamkha, R. A. Mohamed, S. E. Ahmed, *Meccanica*, **46**, 399 (2011).
44. K. Bhattacharyya, G. C. Layek, *Meccanica*, **47**, 1043 (2012).
45. R. A. Mohamed, A-N. A. Osman, S. M. Abo-Dahab, *Meccanica*, **48**, 931 (2013).

46. V. R. Hernandez, J. Zueco, *Int. J. Heat Mass Transf.*, **64**, 375 (2013).
47. R. Nandkeoylyar, M. Das, P. Sibanda, *Math. Prob. Eng.*, Article ID 381806, 12 Pages (2013).
48. G. W. Sutton, A. Sherman, Engineering Magnetohydrodynamics. McGraw-Hill, New York, 1965.
49. H. S. Takhar, P. C. Ram, *Astrophys. Space Sci.*, **183**, 193 (1991).
50. E. M. Aboeldahab, E. M. E. Elbarbary, *Int. J. Eng. Sci.*, **39**, 1641 (2001).
51. G. S. Seth, G. K. Mahato, S. Sarkar, Md. S. Ansari, *Int. J. Appl. Math. Res.*, **1**(4), 462 (2012).
52. K. R. Cramer, S. I. Pai, Magnetofluid dynamics for engineers and applied physicists. McGraw Hill Book Company, New York, USA, 1973.

APPENDIX A

$$f_1(x_1,x_2,x_3,x_4) = \frac{1}{2}\left[\left(x_4 + \frac{x_1}{2}\sqrt{\frac{x_2}{x_3}}\right)e^{x_1\sqrt{x_2 x_3}}erfc\left(\sqrt{x_3 x_4} + \frac{x_1}{2}\sqrt{\frac{x_2}{x_4}}\right) + \left(x_4 - \frac{x_1}{2}\sqrt{\frac{x_2}{x_3}}\right)e^{-x_1\sqrt{x_2 x_3}} \times \right.$$
$$\left. erfc\left(-\sqrt{x_3 x_4} + \frac{x_1}{2}\sqrt{\frac{x_2}{x_4}}\right)\right],$$

$$f_2(x_1,x_2,x_3,x_4,x_5) = \frac{1}{2}\left[e^{x_1\sqrt{x_2(x_3+x_4)}}erfc\left(\sqrt{(x_3+x_4)x_5} + \frac{x_1}{2}\sqrt{\frac{x_2}{x_5}}\right) + e^{-x_1\sqrt{x_2(x_3+x_4)}} \times \right.$$
$$\left. erfc\left(-\sqrt{(x_3+x_4)x_5} + \frac{x_1}{2}\sqrt{\frac{x_2}{x_5}}\right)\right],$$

$$f_3(x_1,x_2,x_3,x_4,x_5) = \frac{1}{2}\left[\left(x_5 + \frac{1}{x_4} + \frac{x_1}{2}\sqrt{\frac{x_2}{x_3}}\right)e^{x_1\sqrt{x_2 x_3}}erfc\left(\sqrt{x_3 x_5} + \frac{x_1}{2}\sqrt{\frac{x_2}{x_5}}\right) + \left(x_5 + \frac{1}{x_4} - \frac{x_1}{2}\sqrt{\frac{x_2}{x_3}}\right) \times \right.$$
$$\left. e^{-x_1\sqrt{x_2 x_3}}erfc\left(-\sqrt{x_3 x_5} + \frac{x_1}{2}\sqrt{\frac{x_2}{x_5}}\right)\right],$$

$$f_4(x_1,x_2,x_3,x_4) = \left[\sqrt{x_1(x_2+x_3)}\left\{erfc\left(\sqrt{(x_2+x_3)x_4}\right) - 1\right\} - \sqrt{\frac{x_1}{\pi x_4}}e^{-(x_2+x_3)x_4}\right],$$

$$f_5(x_1,x_2,x_3,x_4) = \left[\left\{\frac{1}{2}\sqrt{\frac{x_1}{x_2}} + \left(x_4 + \frac{1}{x_3}\right)\sqrt{x_1 x_2}\right\}\left\{erfc\left(\sqrt{x_2 x_4}\right) - 1\right\} - \left(x_4 + \frac{1}{x_3}\right)\sqrt{\frac{x_1}{\pi x_4}}e^{-x_2 x_4}\right],$$

$$f_6(x_1,x_2,x_3) = \frac{1}{2}\left[\left(\sqrt{\frac{x_1}{x_2}} + 2x_3\sqrt{x_1 x_2}\right)\left\{erfc\left(\sqrt{x_2 x_3}\right) - 1\right\} - 2x_3\sqrt{\frac{x_1}{\pi x_3}}e^{-x_2 x_3}\right].$$

ЕФЕКТ НА ХОЛ ПРИ ЕСТЕСТВЕНА КОНВЕКЦИЯ ПРИ МАГНИТО-ХИДРОДИНАМИЧЕН ПОТОК С ТОПЛО–МАСОПРЕНАСЯНЕ ЗАД ВЕРТИКАЛНА ПЛОСКОСТ ПРИ ПРОМЕНЛИВИ ПОВЪРХНОСТНИ ТЕМПЕРАТУРА И КОНЦЕНТРАЦИЯ С ОТНЕМАНЕ НА ТОПЛИНА И ХИМИЧЕСКИ РЕАГИРАЩ ФЛУИД

С. М. Хусаин[1]*, Дж. Джаин[1], Г.С. Сетх[2]

[1]*Департамент по математика, Университет „О.П. Джиндал“, Райгарг, Индия*
[2]*Департамент по приложна математика, Държавен колеж по инженерство, Бастар, Индия*
[3]*Департамент по приложна математика, Индийски технологичен институт, Дханбад, Индия*

(Резюме)

В тази работа се изследва влиянието на ефекта на Хол върху нестационарна естествена конвекция при магнито-хидродинамично течение с топло и масопренасяне в електропроводяща, вискозна и несвиваема течност. Разглежда се температурно зависимо поглъщане на топлина и химична реакция във флуида зад вертикална подвижна плоскост с променливи температура и концентрации на повърхността й. Водещите безизмерни уравнения са решавани аналитично с решения в затворена форма чрез Лапласова трансформация. Получени са зависимости за числата на Нуселт и Шервуд. Измененията на скоростта на флуида, температурата му и концентрацията на пренасяното вещество са представени графично, докато коефициентът на триене и числата на Нуселт и Шервуд са представени таблично за различни стойности на параметрите на течението. Числените резултати са сравнени с тези за подобно течение в близост до изотермична плоскост с постоянна повърхностна концентрация.

Mechanistic insight into the oxidation of atropine sulfate monohydrate with aqueous acidic chloramine-T: Design of kinetic modeling

Nirmala Vaz [1]*. A. S. Manjunatha[2], Puttaswamy[2]

[1] Department of Chemistry, Jyoti Nivas College Autonomous, Bangalore-560 095, India.
[2] Department of Chemistry, Central College Campus, Bangalore University, Bangalore- 560 001, India

Atropine sulfate monohydrate (ASM), with the chemical name (RS)-(1R,3r,5S)-3-tropoyloxytropanium sulfate monohydrate, is a prominent anticholinergic drug. The kinetic study of its oxidation is of great significance in understanding the mechanistic chemistry of this drug in redox reactions. For this reason, the kinetics and mechanism of the reaction of ASM with chloramine-T (CAT) in $HClO_4$ medium were investigated at 303 K. The reaction exhibits a first-order dependence of the rate on $[CAT]_o$ and a fractional-order dependence on both $[ASM]_o$ and $[HClO_4]$. The effects of added *p*-toluenesulfonamide and chloride ion, and varying ionic strength and dielectric constant of the medium on the rate of the reaction were studied. The reaction was carried out at different temperatures and activation parameters were determined from the Arrhenius plot. Absence of any polymerization of acrylonitrile added to the reaction mixture indicated a non-radical pathway. The stoichiometry of the reaction gave a mole ratio of 1:1 and the oxidation product was identified as atropine *N*-oxide. The protonated conjugated acid ($CH_3C_6H_4SO_2N^+H_2Cl$) was postulated as the reactive oxidizing species in the acid accelerating step. The mechanistic pathways and kinetic modeling for this redox system were computed.

Keywords: atropine sulfate mo

nohydrate; chloramine-T; oxidation-kinetics; acid medium

INTRODUCTION

The chemical name of atropine sulfate monohydrate (ASM) is (RS)-(1R,3r,5S)-3-tropoyloxytropanium sulfate monohydrate. It is a potent anticholinergic, antispasmodic and antimuscarinic drug [1]. Due to its therapeutical and pharmacological relevance, a lot of attention has been paid on the determination of ASM [2-6], but a very limited number of kinetic and mechanistic investigations on the oxidation of this drug have appeared in the literature. Up to now, ASM has been oxidized by Chimatadar *et al.* [7-9] using a number of oxidizing agents under various experimental conditions. Surprisingly, no such information is available with +1 oxidants. This gave us an interest to investigate the title reaction.

N-haloamines contain a halogen in +1 oxidation state and the chemistry of these compounds is of great significance due to their diverse behavior [10]. Their versatile nature is due to the ability of these compounds to act as sources of halonium cations, hypohalite species, and nitrogen anions, which act both as bases and nucleophiles [10]. The important chlorine compound of this class is chloramine-T (CAT: *p*-$CH_3C_6H_4SO_2NClNa. 3H_2O$), which is a well-known oxidizing/ chlorinating reagent. This reagent has been exploited as an oxidant for diverse substrates in both acidic and alkaline media [11-20] and their mechanisms have been kinetically

investigated. CAT is commercially available, cost-effective, water-tolerant and relatively non-toxic [21]. Our preliminary kinetic studies revealed that ASM drug oxidation with CAT is most favorable in acidic conditions. It is for these reasons that CAT has been opted as an oxidizing agent in the present redox system.

In view of the above facts, and as a part of our on-going research on the kinetic and mechanistic investigations of oxidation of pharmaceuticals using CAT, we report herein for the first time the results obtained on the kinetics and mechanism of oxidation of ASM with CAT in $HClO_4$ medium. This research program was designed with the following objectives: (i) to accumulate all possible kinetic data, (ii) to formulate the plausible mechanism, (iii) to design the rigorous kinetic rate law, (iv) to deduce thermodynamic parameters, (v) to ascertain the reactive species and, (vi) to identify the reaction stoichiometry and oxidation products.

Further, it is well known that hypochlorous acid (HOCl) is a biologically relevant oxidant. It is also reported that CAT resembles HOCl in its oxidative-mechanistic behavior [10]. Moreover, both CAT and HOCl contain chlorine in +1 oxidation state. Hence, the current research knowledge is very beneficial for kineticists who are working on the kinetics and mechanistic aspects of ASM drug in redox chemistry, as well as in biological processes.

MATERIALS AND METHODS

Materials

The drug atropine sulfate monohydrate of analytical grade purity was purchased from Rolex Chem. Ind., Mumbai, India and was used as received. An aqueous solution of ASM was freshly prepared whenever required. Chloramine-T was obtained from Merck and was purified by the method of Morris *et al.* [22]. An aqueous solution of CAT was periodically prepared and standardized by the iodometric method. CAT solution was stored in brown bottles to prevent photochemical deterioration. All other chemicals used were of Analar grade. Double distilled water was used throughout the study.

Kinetic procedure

Detailed kinetic runs were performed under pseudo-first-order conditions with a known excess of $[ASM]_o$ over $[CAT]_o$ at 303 K. Detailed kinetic procedure was followed by an iodometric method, which is similar to that reported earlier [16]. The course of the reaction was studied for at least two half-lives. Plots of log [CAT] *vs.* time were made to evaluate the pseudo-first-order rate constants (k/s^{-1}). All kinetic runs were carried out twice and were found to be reproducible within $\pm$ 3-6%. The regression coefficients (R^2) of the linear plots were obtained using an fx-100Z scientific calculator.

Reaction stoichiometry

Reaction mixtures containing varying proportions of CAT to ASM in the presence of 0.5×10^{-3} mol dm^{-3} of HClO$_4$ were equilibrated at 303 K for 24 h. Determination of residual CAT by iodometric method showed that one mole of ASM consumed one mole of CAT. The stoichiometry obtained can be formulated as Eq. (1):

Product analysis

The reaction mixture of ASM and CAT in HClO$_4$ solution was stirred for 24 h at 303 K. After completion of the reaction (monitored by TLC), the reaction mixture was neutralized with dilute NaOH and the products were extracted twice with ethyl acetate. The organic products were subjected to spot tests and chromatographic analysis (TLC technique), which revealed the formation of atropine *N*-oxide as the oxidation product of ASM and *p*-toluenesulfonamide as the reduction product of CAT. These products were separated by column chromatography on silica gel (60-120 mesh) using dichloromethane and petroleum ether (3:5 v/v) as the mobile phase. Further, atropine N-oxide was confirmed by GC-MS analysis. The GC-MS data were obtained by an Agilent technologies mass spectrometer. The mass spectrum showed a molecular ion peak at 306 (M+1) amu clearly confirming atropine *N*-oxide. (Figure 1)
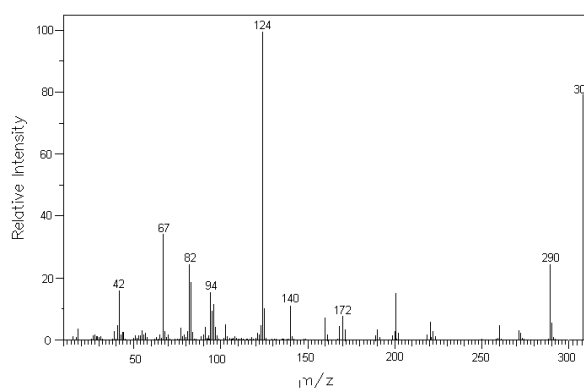
Fig. 1. Mass spectrum of atropine *N*-oxide with its molecular ion peak at m/z 306 (M+1) amu.

(1)
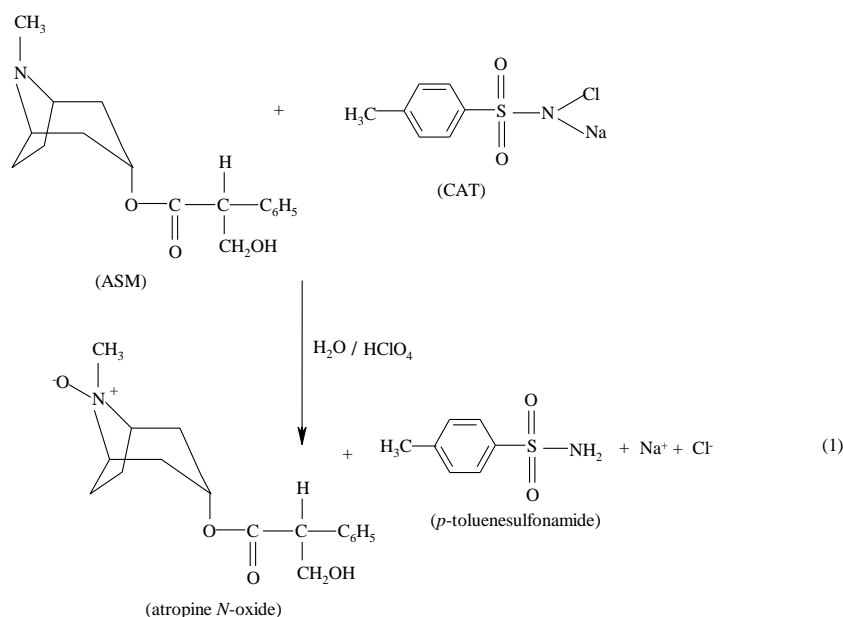
All other peaks observed in GC-MS were interpreted in accordance with the observed structure. It was also observed that there was no further oxidation of these products under the prevailing experimental conditions. *p*-toluenesulfonamide (TsNH$_2$), the reduction product of CAT, was extracted with ethyl acetate and identified by paper chromatography [20]. Benzyl alcohol saturated with water as a solvent with 0.5% vanillin in 1% HCl solution in ethanol was used as a spray reagent (R_f = 0.905). The R_f determined agrees well with the literature value (R_f = 0.905) [20].

RESULTS AND DISCUSSION

The oxidation of atropine sulfate by CAT was kinetically investigated at different initial concentrations of the reactants in HClO$_4$ medium at 303 K. Under pseudo-first-order conditions of [ASM]$_o$ >> [CAT]$_o$ and at constant [ASM]$_o$, [HClO$_4$] and temperature, plots of log [CAT] *vs.* time are linear (R^2 > 0.9986), indicating a first-order dependence of the rate on [CAT]$_o$. The pseudo-first-order rate constants (k' s^{-1}) are listed in Table 1.

Table 1. Effect of varying oxidant, substrate and acid concentrations on the rate of reaction at 303 K.

10^4 [CAT] (mol dm^{-3})	10^2 [ASM] (mol dm^{-3})	10^3 [HClO$_4$] (mol dm^{-3})	10^4 k' (s^{-1})
1.0	2.0	0.5	2.70
2.0	2.0	0.5	2.83
4.0	2.0	0.5	2.70
6.0	2.0	0.5	2.68
8.0	2.0	0.5	2.75
4.0	0.5	0.5	1.12
4.0	1.0	0.5	1.91
4.0	2.0	0.5	2.70
4.0	3.0	0.5	3.90
4.0	4.0	0.5	4.94
4.0	2.0	0.1	1.50
4.0	2.0	0.2	2.19
4.0	2.0	0.5	2.70
4.0	2.0	1.0	3.28
4.0	2.0	2.0	4.35

Further, the values of k' remained unaltered with variation of [CAT]$_o$, confirming the first-order dependence of the rate on [CAT]$_o$. Under the same experimental conditions, an increase in [ASM]$_o$ increased the rate (Table 1). The plot of log k' *vs.* log [ASM] is linear (R^2 = 0.9959) with a slope of 0.72, indicating a fractional-order dependence of the rate on [ASM]$_o$. Further, the plot of k' *vs.* [ASM]$_o$ is a straight line (R^2 = 0.9974) with a y-intercept confirming a fractional-order dependence of the rate on [ASM]$_o$. Increase in [HClO$_4$] increased the reaction rate (Table 1) and the log-log plot of k' *vs.*

[HClO$_4$] is linear (R^2 = 0.9897) with a slope of 0.35, suggesting a fractional-order dependence of the rate on [HClO$_4$].

Rate studies were carried out in MeOH-H$_2$O mixtures of different compositions (0-15% v/v), thereby varying the dielectric constant (D) of the solvent medium. The rate was found to increase with the increase in MeOH content (Table 2). The plot of log k' *vs.* 1/D was linear (R^2 = 0.9995) with a positive slope. The values of the dielectric constant of MeOH-H$_2$O mixtures reported in the literature [23] were employed. It was further noticed that no reaction of the dielectric with the oxidant took place under the experimental conditions employed.

Table 2. Effect of varying dielectric constant of the medium on the rate of reaction at 303 K.

% MeOH v/v	D	10^4 k' (s^{-1})
0	76.73	2.70
5	74.50	3.02
10	72.37	3.39
15	69.75	3.98

Experimental conditions: [CAT]$_o$ = 4.0×10^{-4} mol dm^{-3}, [ASM]$_o$ = 2.0×10^{-2} mol dm^{-3}, [HClO$_4$] = 0.5×10^{-3} mol dm^{-3}.

Addition of 5.0×10^{-4} mol dm^{-3} of *p*-toluenesulfonamide (PTS or TsNH$_2$) to the reaction mixture has no pronounced effect on the reaction rate. This signifies that PTS is not involved in any step prior to the rate-determining step (rds) in the reaction scheme proposed.

The effect of ionic strength of the medium on the reaction rate was studied in presence of 0.2 mol dm^{-3} NaClO$_4$ solution, keeping other experimental conditions constant. It was found that addition of NaClO$_4$ had a negligible effect on the reaction rate, indicating the involvement of non-ionic species in the reaction scheme. Hence, the ionic strength was not a fixed constant for all kinetic runs studied. Addition of NaCl (5.0×10^{-4} mol dm^{-3}) to the reaction mixture had no effect on the rate, suggesting that no free chlorine is formed in the reaction sequence. The reaction rates were determined at 293, 298, 303, 308 and 313 K, keeping the other experimental conditions constant. Based on the Arrhenius plot of log k' *vs.* 1/T (R^2 = 0.9961) the activation parameters (Ea, $\Delta H^{\neq}$, $\Delta G^{\neq}$, $\Delta S^{\neq}$ and log A) for the overall reaction were computed. These results are summarized in Table 3. Addition of an aqueous solution of acrylamide to the reaction mixture did not initiate polymerization. This suggests non-involvement of free radicals during the oxidation. Appropriate controlled experiments were simultaneously run.

Table 3. Effect of varying temperature on the rate of reaction and activation parameters for the oxidation of ASM with CAT in acid medium.

Temperature (K)	$10^4 k^{/}$ (s^{-1})
293	1.17
298	1.80
303	2.70
308	3.62
313	5.70
E_a(kJ mol^{-1})	59.0
$\Delta H^{\neq}$ (kJ mol^{-1})	56.3
$\Delta G^{\neq}$ (kJ mol^{-1})	95.2
$\Delta S^{\neq}$(JK^{-1}mol^{-1})	-122
Log A	9.80

Experimental conditions: [CAT]$_o$= 4.0×10^{-4} mol dm^{-3}, [ASM]$_o$ = 2.0×10^{-2} mol dm^{-3}, [HClO$_4$] = 0.5×10^{-3} mol dm^{-3}.

Reactive species of CAT

Chloramine-T acts as a mild oxidant in both acidic and alkaline media, with a two electron change per mole, giving PTS and NaCl [24]. The oxidation potential of the CAT-PTS redox system varies with pH of the medium [25], having values of 1.139V at pH 0.65, 1.778V at pH 7.0 and 0.614V at pH 9.7. It behaves like a strong electrolyte [25] in aqueous solutions, and depending on pH of the medium it furnishes different equilibria in aqueous solutions [10, 25-26].

The possible oxidizing species in acidified CAT solutions are TsNHCl, TsNCl$_2$, HOCl and possibly H$_2$O$^+$Cl. From these four possibilities, the reactive species of CAT can be selected based on the observed kinetic results. If TsNCl$_2$ were to be the reactive species, then the rate law would predict a second-order dependence of the rate on [CAT]$_o$, which is contrary to the experimental results. If HOCl were primarily involved, a first-order retardation of the rate by adding PTS or TsNH$_2$ would be expected. Since no such effects were observed, both TsNCl$_2$ and HOCl could be ruled out as the oxidizing species. Hardy and Johnston [26], who have studied the pH dependent relative concentrations of the species present in acidified CAT solutions of comparable molarities, have shown that TsNHCl is the likely oxidizing species in acid medium. Further, formation of doubly protonated species TsN$^+$H$_2$Cl in acidic solutions is reported by Narayanan and Rao [27], with a value of 1.02×10^2 at 25°C for the second protonation constant. In the present case, acceleration of the rate by [H$^+$] indicates that TsN$^+$H$_2$Cl is the most active oxidizing species and hence we believe that it is involved in the present reaction.

Reactive species of ASM

Under acidic conditions, the drug ASM may get protonated and exist in the following equilibrium form:

(unprotonated ASM)   (protonated ASM)
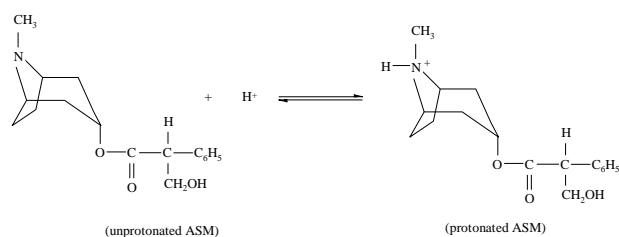
Unprotonated form of atropine sulfate monohydrate is involved in the present reaction

Reaction Scheme

In the light of the above facts, a detailed mechanism (Scheme 1) is suggested for the oxidation of ASM with CAT in acid medium. In the fast rate accelerating step (step(i)) of Scheme 1, the conjugated acid TsNHCl accepts a proton to give a diprotonated species TsN$^+$H$_2$Cl. In the next fast step (step (ii)), TsN$^+$H$_2$Cl reacts with the substrate ASM forming an intermediate complex-I with the elimination of TsNH$_2$. In the next slow and rate determining step (step (iii)), complex-I hydrolyses to complex-II with the elimination of a molecule of HCl. Finally, complex-II loses a proton to yield the ultimate product atropine *N*-oxide.

Kinetic rate law

If [CAT]$_t$ is the total effective concentration of CAT, then

$$[CAT]_t = [TsNHCl] + [TsN^+H_2Cl] + [Complex\text{-}I] \quad (2)$$

Finding the values of [TsNHCl] and [TsN$^+$H$_2$Cl] from steps (i) and (ii) of Scheme 1, and solving for [Complex-I], we get

$$[Complex\text{-}I] = \frac{K_1K_2[CAT][ASM][H^+]}{1+K_1[H^+] + K_1 K_2 [ASM][H^+]} \quad (3)$$

From the slow and rds of Scheme 1,

$$Rate = k_3 [Complex\text{-}I] \quad (4)$$

By substituting for [Complex-I] from Eq. (3) into Eq. (4), the following rate law is obtained.

$$Rate= \frac{K_1K_2k_3[CAT][ASM][H^+]}{1+K_1[H^+]+K_1K_2[ASM][H^+]} \quad (5)$$

This rate law is in complete agreement with the experimental results. Since the rate = k$^{/}$ [CAT], under pseudo-first-order conditions of [CAT]$_o$<<[ASM]$_o$,

$$k^{/}= \frac{K_1K_2k_3[ASM][H^+]}{1+K_1[H^+]+K_1K_2[ASM][H^+]} \quad (6)$$

or

i) $TsNHCl + H^+ \underset{(fast)}{\overset{K_1}{\rightleftharpoons}} TsN^+H_2Cl$

ii)

(ASM)　　　　　(Complex-I)

iii)

(Complex-I)　　　　　(Complex-II)

iv)

(Complex-II)　　　　　(atropine *N*-oxide)
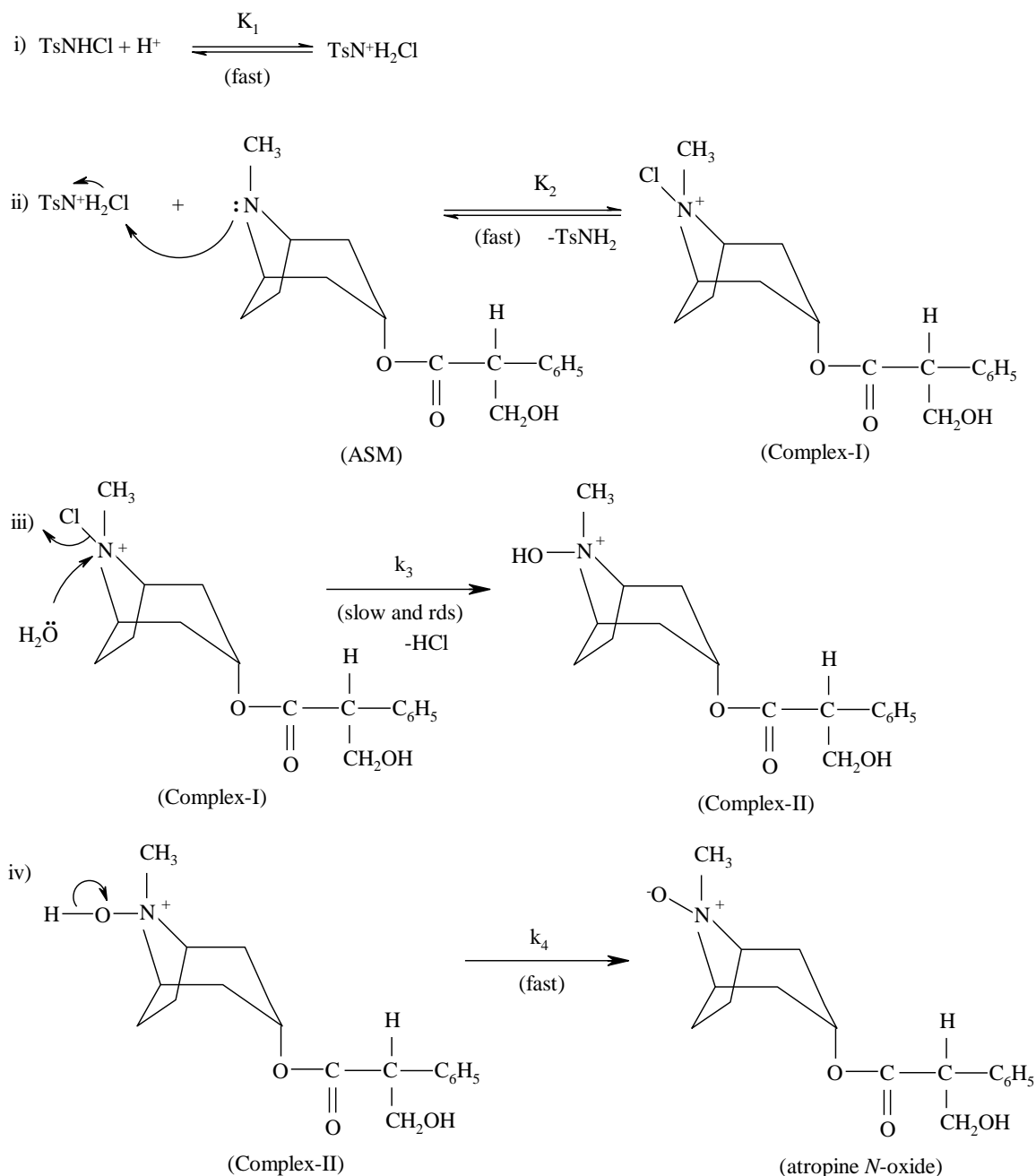
Scheme 1. Detailed mechanistic scheme for the oxidation of atropine by CAT in acid medium.

$$\frac{1}{k'} = \frac{1}{K_1 K_2 k_3 [ASM][H^+]} + \frac{1}{K_2 k_3 [ASM]} + \frac{1}{k_3} \quad (7)$$

or

$$\frac{1}{k'} = \frac{1}{[ASM]} \left\{ \frac{1}{K_1 K_2 k_3 [H^+]} + \frac{1}{K_2 k_3} \right\} + \frac{1}{k_3} \quad (8)$$

A double reciprocal plot of $1/k'$ *vs.* $1/[H^+]$ from Eq. (7) yields:

$$slope = \frac{1}{K_1 K_2 k_3 [ASM]} \text{ and an intercept} = \left\{ \frac{1}{K_2 k_3 [ASM]} + \frac{1}{k_3} \right\}$$

Similarly, a double reciprocal plot of $1/k'$ *vs.* $1/[ASM]$ from Eq. (8) gives:

$$slope = \left\{ \frac{1}{K_1 K_2 k_3 [H^+]} + \frac{1}{K_2 k_3} \right\} \text{ and an intercept} = \frac{1}{k_3}$$

From the slopes and intercepts of Eqs. (7) and (8), the values of the equilibrium constants K_1 and K_2, and the decomposition constant k_3 were calculated for the standard run. The values obtained are $K_1 = 9.0 \times 10^5$ dm^3 mol^{-1}, $K_2 = 22.2$ dm^3 mol^{-1} and $k_3 = 1.25 \times 10^{-3}$ s^{-1}. The proposed reaction scheme and the derived rate law are also evinced by the following experimental findings.

The proposed mechanism is evinced by the observed effect of ionic strength on the rate of the reaction. The primary salt effect on the reaction rate was described by the Brønsted and Bjerrum theory

[28]. According to this concept, the effect of ionic strength on the rate of a reaction involving two ions depends on the charges of the ions. When the ions are of the same charge, an increase in the ionic strength increases the reaction rate because the solvated ions change the dielectric behavior of the solution so that ions of like charge do not repel each other as greatly. If the reacting ions are oppositely charged, raising ionic strength reduces the effective rate constant because the ions are shielded from each other to a greater extent. For the reactions that involve uncharged (neutral) reactants, the rate constant is expected to be independent of the ionic strength of the solution. In the present case, a neutral molecule and a positive ion are involved in the rate-determining step (step (iii) of Scheme 1). Hence, the variation of the ionic strength of the medium does not alter the rate, which clearly confirms the above theory [28].

Several approaches [29-32] have been made to qualitatively explain the effect of dielectric constant of the medium on the reaction rates in solutions. A change in the solvent composition by varying the methanol content in methanol-water affects the reaction rate. For the limiting case of zero angle of approach between two dipoles or an ion-dipole system, Amis [32] has shown that a plot of log k' vs. $1/D$ gives a straight line, with a negative slope for a reaction between a negative ion and a dipole or between the dipoles, while a positive slope indicates a reaction between a positive ion and a dipole. The positive dielectric effect on the rate of the reaction observed in the present case is in agreement with the positive ion – dipole nature of the rate determining step in the proposed reaction scheme (step (iii) of Scheme 1) and a reaction pathway was suggested to the kinetic results.

The proposed reaction mechanism and the derived rate law are also supported by the moderate value of the energy of activation and other thermodynamic parameters (Table 3). The positive values of free energy and enthalpy of activation indicate that the transition state is highly solvated and enthalpy controlled. The observed large negative entropy of activation may be interpreted in a way that some collisions become more stringent and form a rigid associative activated complex with less degrees of freedom. Hence, decomposition of the activated complex is quite a slow process. The values of the frequency factor (A) specify the frequency of collisions and the orientation of reacting molecules. The negligible effects of PTS and NaCl on the reaction rate also confirm the proposed reaction mechanism and kinetic rate law.

CONCLUSIONS

From the present research, the following conclusions are drawn. The kinetics of oxidation of ASM with CAT in $HClO_4$ medium obeys the rate law: Rate = k $[CAT]^1[ASM]^{0.72}[HClO_4]^{0.35}$. The stoichiometry of the reaction was found to be 1:1 and atropine *N*-oxide was characterized as the oxidation product of ASM by GC-MS analysis. Activation parameters were determined. The protonated conjugated acid ($CH_3C_6H_4SO_2N^+H_2Cl$) is postulated as the reactive oxidizing species in the acid-accelerated step. The observed experimental results were explained by an elegant mechanism and the relevant rate law was formulated.

REFERENCES

1. The British Pharmacopoeia, 383, The pharmaceutical Press, London, 1963, p.64.
2. N.B. Brown, H.K. Sleeman, *J. Chromat; A.,* **150**(11), 225 (1978).
3. G. Santoni, A. Tonsini, P. Gratteri, P. Mura, S. Furlanetto, S. Pinza, *Int. J. Pharmac.,* **93**(1-3), 239 (1993).
4. T. Ceyhan, M. Kartal, M. L. Altun, F. Tulemis, S. Cevheroglu, *J Pharmac and Biomed Anal.,* **25**(3-4), 399 (2001).
5. P.A.Greenwood, C. Merrin, T. McCreedy. G. M. Greenway, *Talanta*, **56**(3), 539 (2002).
6. S. Sun, J. Lu, *Anal. Chimica. Acta*, **580**(1), 9 (2008).
7. B.S. Kirthi, H.V. Rajeshwari, S.T. Nandibewoor, S.A. Chimatadar, *Zeischr. fuer. Phys. Chemie*, **226**(3), 233 (2012).
8. B.S. Kirthi, S.T. Nandibewoor, S.A. Chimatadar, *Acta. Chemie.* **60**(3), 617 (2013).
9. M.D. Meti, S.T. Nandibewoor, S.A. Chimatadar, *Synth. React. Inorg. Metal-Org Nano-Metal. Chem.* **44**(2), 263 (2014).
10. M.M. Campbell, G. Johnson, *Chem. Rev.,* **78**, 65 (1978).
11. K.K. Banerji, B. Jayaram, D.S. Mahadevappa, *J. Scient. Ind. Res.*, **46,** 65 (1987).
12. M.C. Agarwal, S.K. Upadhyay, *J. Scient. Ind. Res.,* **49,** 13 (1990).
13. E. Kolvari, A. Ghorbani-Choghamarani, P. Salehi, F. Shirini, M.A. Zolfigol, *J. Iran. Chem. Soc.,* **4(2),** 126 (2007).
14. R.V. Jagadeesh, Puttaswamy. Chloramine-T: Second update, Encyclopedia of Reagents for Organic Synthesis RC0569, Wiley online 2013.

15. D.S. Mahadevappa, K.S. Rangappa, N.M.M. Gowda, B.T. Gowda, *J. Phys. Chem.,* **85,** 3651 (1981).
16. Puttaswamy, R.V. Jagadeesh, Nirmala Vaz; A. Radhakrishna, *J. Mole. Catal: A Chem*, **229,** 211 (2005).
17. Puttaswamy, Nirmala Vaz, R.V. Jagadeesh, *Chinese. J. Chem.*, **26**(3), 536 (2008).
18. K.N. Vinod, Puttaswamy, K.N.N. Gowda, *Inorg. Chim. Acta*, **362**, 2044 (2009).
19. Puttaswamy, Anu Sukhdev, J.P. Subha, *J. Mole. Catal.: A Chem.*, **332,** 113 (2010).
20. Puttaswamy, S. Dakshayani, A.S. Manjunatha, *J. Catalyst and Catalysis,* **1(1),** 39 (2014).
21. G. Agnihotri, *Synlett.*, **18,** 2857 (2005).
22. J.C. Morris, J.A. Salazar, M.A. Wineman, *J. Am. Chem. Soc.* **70**, 2036 (1948).
23. G. Akerloff, *Am. Chem. Soc.*, **54,** 4125 (1932).
24. A.R.V. Murthy, B.S. Rao, *Proc. Indian. Acad. Sci.,* **35**, 69 (1952).
25. E. Bishop, V.J. Jennings, *Talanta*, **1,** 197 (1958).
26. F.F. Hardy, J.P. Johnston, *J. Chem. Soc. Perkin Trans. II*, 742 (1973).
27. S.S. Narayanan, V.R.S. Rao, *Radiochim. Acta*, **32,** 211 (1983).
28. K.S. Laidler, *Chemical Kinetics*, 3rd ed. Harper and Row Publishers, Inc. New York, 1987.
29. S.W. Benson, *The Formulations of Chemical Kinetics and Mechanism*. Mcgraw-Hill, New York. 1960.
30. A.A. Frost. R.G. Pearson, *Kinetics and Mechanism.* 2nd edn. Wiley, New York, 1961.
31. S.G. Entelis, R.P. Tiger. *Reaction Kinetics in the Liquid Phase;* Wiley: New York, 1976.
32. E.S. Amis. *Solvent Effects on Reaction Rates and Mechanisms*. Academic Press, New York, 1976.

МЕХАНИСТИЧЕН ПОГЛЕД ВЪРХУ ОКИСЛЕНИЕТО НА АТРОПИН СУЛФАТ МОНОХИДРАТ С ХЛОРАМИН-Т В КИСЕЛА ВОДНА СРЕДА: ДИЗАЙН И КИНЕТИЧНО МОДЕЛИРАНЕ

Нирмала Ваз[1]*. А.С. Манджунатха[2], Путтасвами[2]

[1] Департамент по химия, Автономен колеж „Джоти Нивас",Бангалор-560 095, Индия
[2] Департамент по химия, Централен колеж, Университет в Бангалор, Бангалор-560001, Индия

(Резюме)

Химическото съединение (RS)-(1R,3r,5S)-3-тропоил-окситропаниум сулфат монохидрат с търговско наименование атропин сулфат монохидрат (ASM) е разпространено анти-холинергично лекарство. Изследването на кинетиката на окислението му е от голямо значение за механистичното разбиране на редокс-реакциите в които то участва. Изследвани са кинетиката и механизма на реакцията на ASM с хлорамин -Т (CAT) в среда на $HClO_4$ при 303 K. Реакцията е от първи порядък по отношение на $[CAT]_o$ и частично от първи порядък по отношение а $[ASM]_o$ и перхлорната киселина. Изучен е и ефекта на добавения *p*-толуенсулфонамид и хлорните йони, йонната сила и диелектричната константа на средата. Реакцията е провеждана при различни температури и активиращата енергия е определена по уравнението на Арениус. Отсъствието на полимеризация при добавянето на акрилонитрил свидетелства за не-радикалов механизъм. Стехиометрията на реакцията дава моларно отношение 1:1, а продуктът окисление е идентифициран като атропин *N*-оксид. Протонираната спрегната киселина ($CH_3C_6H_4SO_2N^+H_2Cl$) е постулирана като реактивно окисляващ компонент в етапа на киселинн ускоряване на реакцията. Направени се изчиления и моделиране на тази редокс-система.

Chemical compositions and antimicrobial activities of oregano and thyme essential oils

D. Pecarski[1], S. Ketin*[2], I. Omerovic[3], M. Mirkovic[4], Z. Jugovic[1], R. Biocanin[3]

[1]*Medical High School, Belgrade, Serbia*
[2]*University of Novi Sad, Novi Sad, Serbia*
[3]*University of Novi Pazar, Serbia*
[4]*Security and Information Agency of Serbia, Novi Pazar, Serbia*

The aim of this study was to evaluate the chemical composition and antimicrobial activity of essential oils of thyme and oregano. Gas chromatography with mass spectrometry (GC-MS) was used to determine the chemical structure of essential oils and their dominant components. Antimicrobial activity of essential oils was tested against standardized bacterial and fungal cultures: *Staphylococcus aureus* ATCC 25923, *Escherichia coli* ATCC 25922, *Candida albicans* ATCC 24433, *Enterococcus faecalis* ATCC 25929, using the agar diffusion method with wells. Minimum inhibitory concentration (MIC) for essential oils determined by the broth dilution method and valued in the range of 3 - 5 μl/ml, depends on the essential oil and bacteria and *C.albicans* tested. Both essential oils provided strong antibacterial activity for the tested microorganisms. The essential oil of thyme was especially recognized. These experiments aimed at showing the *in vitro* antimicrobial activity of the selected essential oils in order to find out the most potential essential oil that would be an objective in further investigation on chitosan drug delivery system with controlled release of antimicrobial essential oil.

Key words: essential oils, antimicrobial activity, oregano, thyme

INTRODUCTION

There is an increasing interest in the examination of the antimicrobial activity of phyto-therapeutics in the past few years, especially considering the increased bacteria resistance to implemented antibiotics, which becomes a global problem.

Among all alternative natural antimicrobial agents, essential oils display significant antimicrobial activity. It is important to note that no resistance or tolerance to essential oils has been discovered yet. This can be explained by the great complexity of their structure which allows the essential oils to act on several target places at the same time, rather than convential antibiotics, which act on one specific target place. Essential oils are secondary metabolites of plants. They are defined as complex mixtures of lipophilic liquid, fragrant and volatile components included in the secretory structures of aromatic plants. Main active components of essential oils are terpenoids (dominant and economically most significant components), aliphatic volatile components and substances which include nitrogen and sulfur [1]. Numerous studies of the antimicrobial activity and the mechanisms of essential oils action argued that resistance does occur due to the large number of different compounds with ultimate strong antimicrobial action. However, specifity of their synergistic effects is very important. These effects actually prevent emergence of resistance [2].

As hydrophobic substances, essential oils have high affinity for the lipids of bacterial cell membranes and their antibacterial effect is mostly related to their lypophilic property [3]. Such strong antimicrobial activity of essential oils against pathogenic bacteria is based on the high level of phenol components such as carvacrol, eugenol (2-methoxy-4-(2-propenyl) phenol) and thymol (4-6).

However, despite numerous studies of the antimicrobial activity of the natural products, the number of tested microorganisms is relatively small and it does not include newer multiple resistant species. Nowadays, aromatic plants from the *Lamiaceae* family present very important sources of biologically and pharmacologically active substances which are widely used and whose effects are very well documented. Antioxidant and antimicrobial activity of 100 volatile components of essential oils from *Lamiaceae* species, especially thyme and oregano, showed that these essential oils are very important for regulation of oxido-reduction potential and normal bacterial flora [7].There is a great number of studies which confirmed the strong antibacterial effect of essential oils of thyme and oregano [8-12].

The objective of this study was to prove the antimicrobial effect of thyme and oregano essential

* To whom all correspondence should be sent:
E-mail: ketin.sonja@gmail.com

oils in order to select the essential oil with the strongest antibacterial effect. The selected essential oil would be the subject of subsequent investigations on designing an adequate *drug delivery* system based on chitosan particles with encapsulated essential oil in them. The chitosan particles with essential oil would be an optimal solution for therapeutic purposes of these phyto-antibiotics by keeping the pharmacological properties of the volatile and photosensitive essential oils and enhancing their therapeutic effect.

MATERIAL AND METHODS

Plant material

Leaves of thyme and oregano were obtained from the Institute for the Study of Medicinal Herbs "Dr. Josif Pančić" in Belgrade in 2010. The plant material was kept in double paper bags in a dark and dry place until hydrodistillation. Immediately prior to hydrodistillation, the fruits of thyme (*Thimis vulgaris*) and oregano (*Origanum vulgare*) were chopped to the size of 0.75[13].

Hydrodistillation (HD)

The essential oils were isolated through hydrodistillation as per Ph. Eur. IV, with *n*-hexane as the collective solvent. An amount of 500 ml of distilled water was poured over the plant material (100 g). The obtained essential oils (EO) were initially dried over anhydrous Na_2SO_4 for 24 h, and then the drying process continued in a desiccator for another hour. The n-hexane was removed in a rotational vacuum-boiler, the obtained EO was measured three times and its quantity was expressed as per mass of dry plant material (g/100 g). Dried oils were preserved in cuvettes with Teflon stoppers at +4°C until use.

Gas chromatography with mass spectrometry (GC-MS)

Gas-chromatographic analysis of essential oils was conducted in a Hewlett Packard 5973-689 GC-MS system in EI mode on 70 eV with spectrometric mass detection (GC-MS). Initial temperature of the capillary column HP 5MS (30 m × 0.25 mm; film thickness 0.25 μm) was 60°C. Using a heating speed of 3°C/min, it was heated to 280°C. Helium was the gas carrier at a flow of 1 ml/min. An amount of 1 μl of each investigated sample was injected in the GC column in proportion of 1:10.

Identification of components was based on calculated retention indexes (RI) [14] and mass spectra compared with standard substances and/or with NIS/NBS Wiley library of mass spectra, including literature data or data from the free database (http//www. flavornet.org/iowtv. pherobase.com) [15]. Experimental values of retention indexes were defined using "calibrated Automated Mass Spectral Deconvolution and Identification System software" (AMDIS ver.2.1., DTRA/NIST, 2002). Results were compared with retention indexes from literature data and internet available database.

The microorganism cultures

For the purpose of *in vitro* testing of the antimicrobial activity of the thyme and oregano essential oils, the following standardized bacterial cultures were used (ATCC – American Type Culture Collection): *Staphylococcus aureus* ATCC 25923, *Escherichia coli* ATCC 25922, *Candida albicans* ATCC 24433, *Enterococcus faecalis* ATCC 29212. These microorganism cultures were supplied from the Collection of bacteria cultures of the Department for Microbiology at the Faculty of Technology, Belgrade, and the bacteria cultures – from the Institute of Virology and Immunology, Torlak.

Determination of antimicrobial activity

Antibacterial activity was determined by the agar well diffusion method and the agar dilution method.

Agar well diffusion method was employed for the determination of the antimicrobial activity of the essential oils. Tubules with diameter of 6 mm were placed on Petri plates with prepared sterile Miller-Hinton TSA (tryptonesoyagar-Torlak) surface, impregnated with soft agar (0.60 % of agar) with the same surface, inoculated with indicator pathogenic strain (0.2 ml of 24-h broth culture for 6 ml of soft agar). After firming of the agar, the tubules were removed and each of the formed wells was filled with 20 μl of the investigated essential oil. Plates were incubated at 37°C for 24 h. In the study of the antimicrobial activity of essential oils, the antimicrobial activity of lactic acid (20 μl) and that of the individual essential oil and lactic acid was investigated in order to determine their synergistic effect (the compound included 50 ppm of lactic acid for 20 μl of essential oil). As a positive control of antibacterial activity the standard antibiotic – clyndamicin (10 μg/ml) and the antimycotic nystatine (30 μg/ml) were taken.

Antimicrobial activity of essential oils was present all over the inhibition zone, measured and expressed in mm.

Minimum inhibitory concentration (MIC) evaluation using the agar dilution method

For determining the minimal inhibitory concentration (MIC) of the tested bacterial strains, the agar dilution method was performed in a Mueller Hinton broth. Each test tube with 2.997 ml of base was filled with 3 µl of essential oil. Due to the difference in antimicrobial activity by applying the agar dilution method, concentrations of 10, 30, 50 and 100 µl/ml were used for essential oils of thyme and oregano. Indicator breeds of microorganism (1% of inoculum) were inoculated in the prepared test tubes with diluted essential oils and in the control test tube. The tubes were incubated at 37 °C.

At certain time intervals, after 1, 3, 8, 16 and 24 h, the change in optic density (OD) was followed on a colorimeter (MA 9504. Metrix), using a yellow filter (575 nm). Increasing of optic density or blurring was observed on increasing the microorganism biomass in the liquid base. MIC is defined as the first concentration of essential oil with no visible growth of bacteria registered.

RESULTS

Results on the qualitative and quantitative analysis of the chemical composition of essential oils of thyme and oregano are presented in Table 1. Chemical profile of essential oils is presented by names of the components while amounts of these components are presented in percentages (%).

GC-MS analysis conducted for essential oils of thyme and oregano provided definition of 25 compounds or 94.53% for thyme oil and 41 compounds or 97.98% of oregano oil (Table 1, Figure 1). Essential oil of thyme mostly includes monoterpenes (94.08%), especially oxidized monoterpenes (55.86%). There are hydrocarbon monoterpenes (38.67%) as well. The amount of sesquiterpenes is much lower.

Table 1. Chemical composition of essential oils of thyme and oregano.

Component	Oregano	Thyme
Monoterpenic hydrocarbons	**9.40**	**15.38**
Pinene	0.31	1.2
Phellandrene	0.27	0.08
Terpinene	0.88	1.75
Pinene	1.54	0.39
Camphene	0.2	2.09
Carene	-	-
Terpinene	4.64	6.98
Limonene	0.69	0.7
Myrcene	0.53	1.64
Sabinene	-	-

Table 1. continuation

Component	Oregano	Thyme
Terpinolene	0.12	0.46
L-Fenchone	-	-
Elemene	0.22	-
Pseudolimonene	-	0.09
Aromatic monoterpene hydrocarbons	**9.66**	**21.15**
p-Cymene	5.02	21.15
p-Anisaldehyde	-	-
-Caryophyllene	4.38	-
o-Cymene	-	-
Cuminaldehyde	0.26	-
Oxidized monoterpenes	**75.76**	**53.51**
Terpineol	1.04	0.95
Camphor	0.39	-
Eucalyptol	1.59	4.74
Isopropenyltoluene	-	-
Linalol	2.69	5.9
3-Octanol	0.1	-
3-Octanone	0.2	-
4-Carvomenthenol	1.47	0.61
4-Thujanol, stereoisomer	0.07	-
Copaene	0.17	-
-ELEMENE	0.03	-
Fenchyl alcohol	0.38	-
Carvacrol	59.03	2.34
CARVACROL METHYL ETHER	0.63	-
Carvone	0.11	-
Eugenol	0.42	-
Isoborneol (Isomer 2)	1.67	0.96
p-Isopropenyl toluene	0.08	-
Thymol	5.69	36.12
Isoborneol (isomer 1)	-	0.58
Menthone	-	-
Geraniol	-	0.32
Geranyl acetate	-	0.69
Nerol	-	0.3
Monocyclic sesquiterpenes	**2.72**	**4.41**
Amorphene	0.22	-
Humulene	1.34	0.44
Bisabolene	0.29	-
Cadinene	0.5	-
Humulene Oxide	0.07	-
Isoledene	0.08	-
Naphthalene, 1,2,3,4,6,8a--hexahydro-1-isopropyl-4,7-dimethyl-CADINA-1,4-DIENE	0.09	
Caryophyllene	-	3.38
Caryophyllene oxide	-	0.59
Bornyl acetate		
Valencene	0.13	-
Bicyclic sesquiterpenes	**0.44**	**0.00**
Caryophyllene oxide	0.38	-
-Cadinene	0.06	-
Tricyclic sesquiterpene	**0.00**	**0.08**
-Copaene	-	0.08
TOTAL:	**97.98**	**94.53**

More than half of the amount of thyme essential oil consists of 6 dominant compounds. Oxidized monoterpene thymol (36.12%) and monoterpene hydrocarbon p-cymene (21.15%) are mostly included. Other dominant components of this essential oil are -terpinene (6.98%), linalool (5.90%), carvacrol (4.54 %) and eucalyptol (4.74%). (Figure 1).
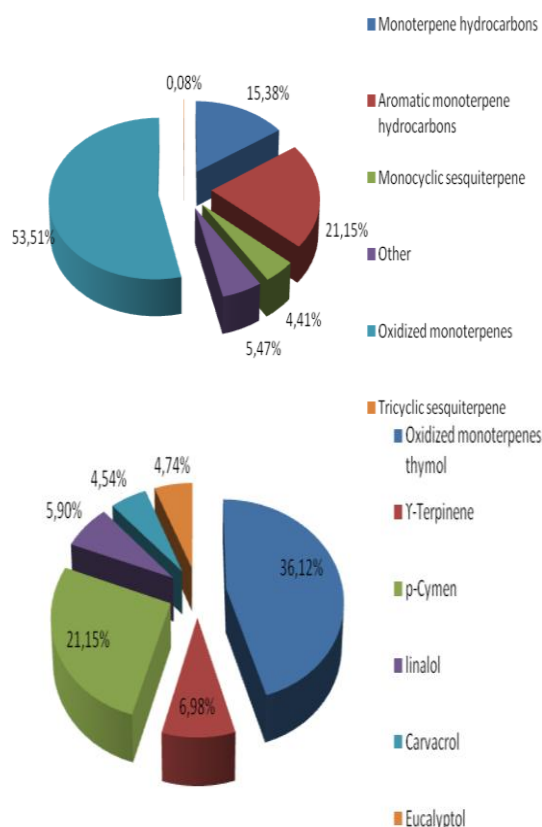
Fig. 1. Main classes of compounds (%) in the essential oil of thyme.

More than half of the total amount of essential oil of oregano consists of oxidized monoterpene carvacrol (59.03%); significantly lower amount of thymol (5.69%) and monoterpene hydrocarbons p-cymene (5.02%) and-terpinene (4.64 %). There is a large number of sesquiterpenes but their quantity is significantly lower (Figure 2).

Antimicrobial activity of essential oils

Results of the study of essential oil activity using the disk diffusion method are presented in Table 2 as inhibition zone diameter (mm) and decrease in bacterial growth (Figure 3).
According to the results of the bacteriological analysis *S.aureus* (11-12 mm) showed higher sensitivity towards Gram-positive bacteria than *E. faecalis* (0.5-0.8 mm). Slightly lower sensitivity was noted in Gram-negative bacteria *E. coli* ATCC 25922 (8 mm).
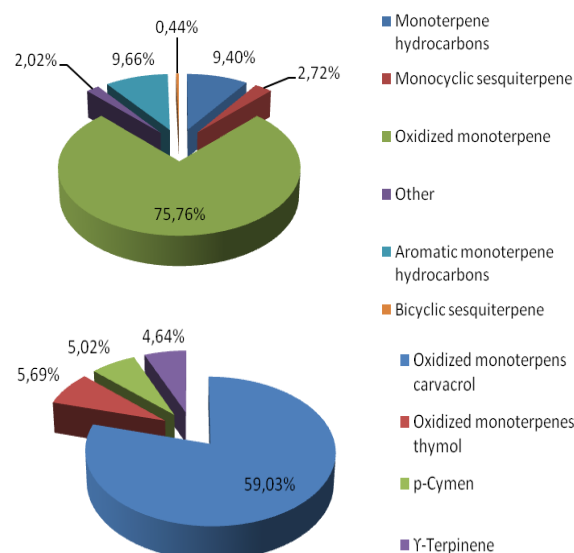
Fig. 2. Main classes of compounds (%) in the essential oil of oregano
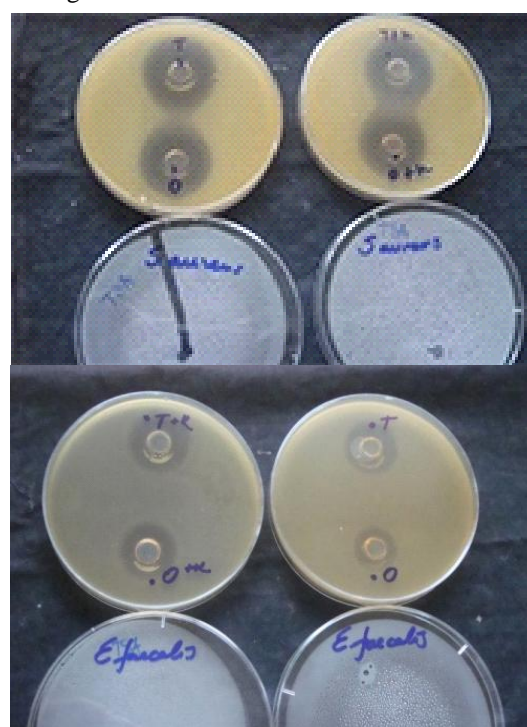
Fig. 3. Antibacterial effect of thyme (T), oregano (O) to *S. aureus* and *E. faecalis*

Table 2. Antimicrobial activity of thyme and oregano, combination of essential oils and lactic acid, clindamycin and nystatin towards investigated bacteria

Essential Oil	Inhibition zone diameter, mm			
	S. aureus	*E. coli*	*C. albicans*	*E. faecalis*
Oregano	11	8	1	0.5
Thyme	12	8	1	0.8
Oregano+acid	11	10	1.25	0.7
Thyme+acid	13	10	1.3	0.9
Acid	-	-	-	-
Nystatin (30μl/ml)	-	-	4	-
Clindamycin (30μl/ml)*	2	2	-	2.5

681

Results obtained by the dilution method for determination of MIC values showed that essential oils of oregano and thyme in concentrations of 1 to 5 µl/ml act bacteriostatic and bactericidal.

DISCUSSION

The main components of thyme and oregano essential oils detected by GC-MS analyses are phenolic compounds, thymol and carvacrol, which define the biological and pharmacologic properties of these oils. Therefore, the ratio between chemical composition and antimicrobial activity will be crucial for the antibacterial effect of the essential oil. Regarding the strength of antibacterial effect of phenolic compounds, hydroxyl groups have no important role, as expected. This was proven by the similar antibacterial effect of carvacrol and thymol to *S.aureus* and *P.aeruginosa* [5]. The importance of phenolic ring (system of destabilized electrons) can be observed in the significantly lower activity of menthol relating to carvacrol [1]. There are many earlier studies that confirmed the antibacterial activity of the main constituents of thyme and oregano essential oils [4, 6-8].

Low sensitivity of Gram-negative bacteria in the antimicrobial analyses of the tested essential oils can be a consequence of the construction of their cell wall which includes an additional outer membrane around the peptidoglycan layer [16]. It decreases the diffusion of hydrophobic components through their lipopolysaccharide cover [17].

Although both essential oils include the strongest antimicrobial components thymol and carvacrol, thyme oil contains 36.12% of thymolol and 2.34% of carvacrol while oregano oil – 59.63% of carvacrol and 5,69% of thymolol. The antibacterial effect of thyme oil is stronger than the effect of oregano oil. This is aligned with data on the higher activity of thymol relating to carvacrol [4] and the fact that antimicrobial activity is affected by the amount of certain components in the oil and their synergistic action. Both oils showed antimycotic activity to *C.albicans*. The strong antimicrobial effect of the tested essential oils is also explained by the fact that the zones of inhibition for the tested antibiotics are significantly smaller relating to the essential oils of thyme and oregano.

Also, significant synergism between the essential oil of thyme and lactic acid can be noted. This is aligned with literature data on the antimicrobial effect of lactic acid [18]. It is very significant from the aspect of formulation of mycoadhesive products of essential oils in chitosan particles whose optimal effect necessarily includes acid medium.

Significant inhibition of the growth of bacteria *E. coli* was shown in concentrations of 5 µl/ml for oregano, which can be taken as its MIC value. There is no significant difference in the antimicrobial action of the two oils to *E. coli*. The antimicrobial effect of the essential oils of oregano and thyme at the investigated concentrations of 1, 3, 5 and 10 µl/ml is sufficient for efficient inhibition of the growth of *E. faecalis*. MIC value for thyme is 1 µl/ml. Thyme acts bactericidal relating to oregano which acts bacteriostatic with a MIC value of 3 µl/ml.

Significant antimicrobial action of the essential oils of oregano and thyme can be observed for the species of *S. aureus* where the MIC values for oregano and thyme are 3 µl/ml.

The essential oils of thyme and oregano display a lower antimicrobial effect to the pathogenic fungi *C.albicans* in the applied concentrations. However, thyme oil showed a slightly better effect, decreasing the development of cells of *C.albicans* to 50% at a concentration of 10 µl/ml (MIC$_{50}$ value).

Summarizing, one can imply that the results of these investigations are aligned with those of preliminary investigations on the antimicrobial effect of essential oils using the disk diffusion method in wells [9-11]. These results are partially expected having in mind the preliminary results of inhibition zones of the tested microorganisms.

CONCLUSIONS

According to the obtained results of chemical and microbiological analysis, aligned with literature data, the essential oil of thyme showed a stronger antibacterial effect to the tested bacteria and *C.albicans*. Regarding the natural origin, numerous biochemical and pharmacologic investigations and wide antibacterial spectrum of thyme, the possibility of production and use of antimicrobial phyto-products for therapeutic and prophylactic purposes is taken into account. This biologically active natural product would be an ideal replacement for conventional antimicrobial products, especially if we consider the increasing resistance to implemented antibiotics.

REFERENCES

1. R. Croteau, T.M. Kutchan, N.G. Lewis, Natural products (secondary metabolites). Biochemistry and Molecular Biology of Plants. American Society of Plant Biologists, Rockville, MD, 2000, p. 1250.

2. S. Prabuseenivasan, M. Jayakumar, S. Ignacimuthu, *Compl. Altern. Med.,* **12**, 6 (2006).

3. Tacamovic, J.D.Brooker, Proceedings of the Nutrition Society, **64**, 403 (2005).

4. R. J. W. Lambert, P. N. Skandamis, P. J. Coote, G.-J.E. Nychas, *Journal of Applied Microbiology* , **91**, 453 (2001).

5. A. Ultee, M. H. Bennik, R. Moezelaar, *Appl Environ Microbiol.,* **68**: 1561 (2002).

6. A. Sivropoulou, E. Papanikolaou, C. Nikolaou, S. Kokkini, *Journal of Agricultural and Food Chemistry*, **44**: 1202 (1996).

7. M. Marino, C. Bersani, G. Comi, *International Journal of Food Microbiology*, **67**, 187 (2001).

8. S. Cosentino, C. I. G. Tuberoso, B. Pisano, M. Satta, V. Mascia, E. Arzedi, *Letters in Applied Microbiology*, **29**: 130 (1999).

9. M. Marino, C. Bersani, G. Comi, *Journal of Food Protection,* **62**: 1017 (1999).

10. C. Juliano, A. Mattana, M. Usai, *Journal of Essential Oil Research,* **12**: 516 (2000).

11. C. F. Bagamboula, M. Uyttendaele, J. Debevere, *Food Microbiol,* **21**: 33 (2004).

12. H.J. D. Dorman, S F. Deans, *J. Appl. Microbiol.* , **88**, 308 (2000).

13. Pharmacopoea Jugoslavica IV, The Federal Institute for Health Protection, Belgrade, 1984.

14. H. Van den Dool, D. P. A. Kratz, *J. Chromatograph,* **11**, 463 (1963).

15. R.P. Adams, Identification of Essential Oil Component by Gas Chromatography/Quadrupole Mass Spectrometry, Allured Publishing Corporation, Carol Stream: IL, 2007.

16. C. Ratledge, S.G. Wilkinson, An overview of microbial lipids. In: Ratledge, C.,Wilkinson, S.G. (Eds.), Microbial Lipids, vol. 1. Academic Press, London, 1988, p. 3.

17. A. Salam, S.A. Ibrahima, H.Y. Chung, W. Seoa, *Food Chemistry*, **109**: 137 (2008).

18. V. Dodane, V. D. Vilivalam, *Pharm. Sci. Technol. Today,* **1**, 246 (1998).

ХИМИЧЕСКИ СЪСТАВ И АНТИМИКРОБНИ ДЕЙНОСТИ НА РИГАН И МАЩЕРКА ЕТЕРИЧНИ МАСЛА

Д. Пекарски[1], С. Кетин*[2], И. Омерович[3], М. Миркович[4], З. Югович[1], Р. Биочанин[3]

[1]Медицински гимназия, Белград, Сърбия
[2]Университета на Нови Сад, Нови Сад, Сърбия
[3]Университета на Нови Пазар, Сърбия
[4]Сръбска агенция „Сигурност и информация", Нови Пазар, Сърбия

(Резюме)

Целта на това проучване е да се оцени химичен състав и antimicrobal активност на етерични масла от мащерка и риган. Газова хроматография с мас спектрометрия (GC-MS) се използва за определяне на химическата структура на етерични масла и техните доминиращи елементи. Antimicrobal активност на етерични масла е тествана срещу стандартизирани и Fungy бактериални култури: *Staphylococcus aureus* ATCC 25923, E *Esherichia coli* ATCC 25922, *Candida Albicans* ATCC 24433, *Enterococcus faecalis* видове ATCC 25929., използвайки метода на дифузия в агар с кладенци. Минималната инхибираща концентрация (MIC) за етерични масла е била определена по метода на разреждане на бульон и ценен в диапазон от 3 µL/ml -. 5 µL/ml, Зависи от етерично масло и бактерии и тествани за *C.albicans*. И двете етерични масла, предвидени силна антибактериална активност за изследваните микроорганизми, а етеричното масло от мащерка е особено признат. Тези експерименти запишат гол на които е показано ин витро антимикробна активност на подбрани етерични масла направи подбор на най-голям потенциал етерично масло, че ще бъде обективен и по-нататъшно разследване и хитозан система за доставка на наркотици с контролирано освобождаване на антимикробната етерично. масло.

Chemometric expertise of Bulgarian mineral, spring and table waters

A. K. Detcheva[1]*, V. D. Simeonov[2], E. H. Ivanova[1]

[1]*Institute of General and Inorganic Chemistry, Bulgarian Academy of Sciences, Acad. G. Bonchev Str. Bl.11, 1113 Sofia, Bulgaria*
[2]*Faculty of Chemistry and Pharmacy, Sofia University "St. Kliment Ohridski", J. Bourchier Blvd. No 1, 1164 Sofia, Bulgaria*

Ten brands of Bulgarian bottled mineral, spring and table waters were subjected to chemometric expertise using cluster analysis and principal components analysis. The waters were classified into several patterns depending on their microelement composition. Groups of similarity between the chemical components of the potable waters were found and the specific indicators for the separate groups of waters were determined. The separation is obviously related to the specificity of the local origin of the waters, e.g. crustal and soil properties and composition. It is of interest to note that the chemical composition of spring waters strongly differs from that of the mineral waters from the same locations. The obtained results point to the stability of the chemical composition and lack of contamination of the bottled mineral waters in examination over a prolonged period of storage (up to 2.5 years after bottling).

Keywords: Bulgarian bottled potable waters; chemometric expertise; cluster analysis; principal components analysis

INTRODUCTION

Bulgaria is one of the countries in the world richest in mineral waters (more than 850 springs and boreholes), as well against its surface area, as *per capita* [1]. This natural richness has been known and exploited since antiquity. Nowadays, more than 50 brands of bottled mineral and spring waters are offered on the Bulgarian market. The major components of bottled Bulgarian drinking waters, such as K, Na, Ca, Mg, and Fe are monitored in accordance with European legislation [2,3], whereas only limited data are available about their trace element content. Information on the location, physico-chemical characteristics, element content, and medical applications of Bulgarian mineral and spring waters are reported by Pentcheva *et al.* [1], Vladeva and Kostadinov [4,5] and Vladeva *et al.* [6]. The quality of the waters, including their macro- and microelement content, as well as their stability during storage, is of paramount importance for the consumers.

The great variety of mineral water springs with respect to their location and chemical composition often requires a specific approach for expert assessment of mineral water origin and quality. Since careful monitoring of the chemical content of different mineral, spring and table waters creates large data sets, chemometric data classification, modelling and interpretation seems to be the most reliable assessment procedure [7-10].

Subject of the present work was the chemometric assessment of Bulgarian potable waters of the following ten brands: „Gorna Banya" mineral, „Bankya" mineral, „Kom" mineral, „Thorn Springs" mineral, „Hissar" mineral, „Devin" mineral and spring, „Mihalkovo" mineral and spring and „Savina" table using cluster analysis and principal components analysis. The „Savina" table water was added to the sample list in order to assess the efficiency of the demineralization processing of this water prior to bottling. It was also of substantial interest to assess the water quality during a prolonged period after bottling.

Typical representatives of mineral waters of Southern and Western Bulgaria were selected for analysis among Bulgarian natural mineral waters recognised by the EC [11]. Commercial drinking waters in standard PET bottles of 0.5 L were subjected to chemical analysis. The microelement composition of the waters was determined in former works of the authors [12,13] using total reflection X-ray fluorescence spectrometry (Tables 1 and 2). The data for the microelement composition of the waters were treated in the present chemometric study in order to:

- find out groups of similarity between the chemical components of the waters, to which the local specificity of the potable waters may be related;
- find out groups of similarity between the different types of potable waters;
- find out the specific indicators for the separate groups of waters.

Two chemometric methods were employed in the study – cluster analysis and principal

---

* To whom all correspondence should be sent:
E-mail: albena@svr.igic.bas.bg

Table 1. Microelement content in bottled mineral waters analyzed in the year of bottling (samples C_1 - C_5) and about 2.5 years after bottling (samples C_6 – C_10), reported by Georgieva *et al.* (2013, 2014).

Element	"Gorna Banya"		"Kom"		"Thorn Spring"		"Devin"		"Mihalkovo"	
	(C_1)	(C_6)	(C_2)	(C_7)	(C_3)	(C_8)	(C_4)	(C_9)	(C_5)	(C_10)
S, mg L^{-1}	7.9 ± 0.4	6.4 ± 0.5	8.9 ± 0.2	8.8 ± 0.3	2.8 ± 0.4	2.2 ± 0.3	5.1 ± 0.8	4.5 ± 0.4	123 ± 13	96 ± 6
Cl, mg L^{-1}	2.4 ± 0.2	1.8 ± 0.2	1.2 ± 0.1	0.9 ± 0.1	2.9 ± 0.4	2.2 ± 0.3	3.4 ± 0.2	3.1 ± 0.2	47 ± 7	45 ± 7
K, mg L^{-1}	0.3 ± 0.1	0.3 ± 0.1	1.3 ± 0.2	1.0 ± 0.1	1.2 ± 0.2	1.5 ± 0.2	0.6 ± 0.1	0.6 ± 0.1	48 ± 7	46 ± 6
Ca, mg L^{-1}	1.3 ± 0.2	1.5 ± 0.2	1.4 ± 0.2	1.7 ± 0.2	78 ± 8	80 ± 6	1.5 ± 0.1	1.3 ± 0.1	215 ± 25	217 ± 29
Mn, µg L^{-1}	< 2	< 2	< 2	< 2	< 2	< 2	< 2	< 2	48 ± 7	38 ± 5
Fe, µg L^{-1}	25 ± 4	24 ± 3	10 ± 1	7.9 ± 1.0	6.8 ± 0.8	8.0 ± 1.0	15 ± 2	13 ± 2	15 ± 2	15 ± 2
Ni, µg L^{-1}	3.0 ± 0.5	< 1	12 ± 1	10 ± 1	5.0 ± 0.8	4.0 ±0.5	4.0 ± 0.5	3.0 ± 0.5	14 ± 2	13 ± 2
Cu, µg L^{-1}	6.0 ± 0.5	4.8 ± 0.5	6.0 ± 0.5	4.8 ± 0.1	< 2	< 2	3.0 ± 0.5	3.0 ± 0.5	< 10	< 10
Zn, µg L^{-1}	6.0 ± 0.5	4.9 ± 0.5	47 ± 4	50 ± 4	10 ± 1	13 ± 2	< 2	3.0 ± 0.5	< 9	< 9
As, µg L^{-1}	3.0 ± 0.5	3.0 ± 0.5	12 ± 2	9.0 ± 1.0	2.5 ± 0.2	< 1	< 1	< 1	< 7	< 7
Br, µg L^{-1}	8.0 ± 1.0	6.5 ± 1.0	37 ± 5	32 ± 3	5 ± 2	13 ± 2	6.0 ± 0.5	6.0 ± 0.5	400 ± 50	350 ± 50
Rb, µg L^{-1}	5.0 ± 0.5	4.0 ± 0.5	4.0 ± 0.5	4.0 ± 0.5	< 1	< 1	< 1	< 1	163 ± 25	160 ± 25
Ba, µg L^{-1}	45 ± 7	36 ± 1	30 ± 5	26 ± 4	8 ± 4	23 ± 2	38 ± 5	35 ± 2	< 100	< 100

Table 2. Microelement content in bottled table, mineral and spring waters analyzed in the year of bottling, reported by Georgieva *et al.* (2014).

Element	"Savina" table (C_11)	"Hissar" mineral (C_12)	"Bankya" mineral (C_13)	"Devin" spring (C_14)	"Mihalkovo" spring (C_15)
S, mg L^{-1}	0.20 ± 0.01	6.3 ± 1.1	14 ± 1	0.80 ± 0.05	2.6 ± 0.4
Cl, mg L^{-1}	2.2 ± 0.2	6.2 ± 0.8	9.8 ± 1.2	1.2 ± 0.2	1.4 ± 0.2
K, mg L^{-1}	1.1 ± 0.1	1.7 ± 0.1	0.7 ± 0.1	1.5 ± 0.2	10.6 ± 0.3
Ca, mg L^{-1}	6.1 ± 0.5	3. 6 ± 0.2	6.1 ± 0.7	7.9 ± 1.3	5.7 ± 0.8
Mn, µg L^{-1}	< 2	< 2	< 2	< 2	< 2
Fe, µg L^{-1}	18 ± 3	19 ± 1	20 ± 3	15 ± 2	16 ± 2
Ni, µg L^{-1}	< 1	< 1	< 1	< 1	< 1
Cu, µg L^{-1}	12 ± 2	19 ± 2	9 ± 1	8 ± 1	7 ± 1
Zn, µg L^{-1}	15 ± 2	29 ± 2	9 ± 1	9 ± 1	12 ± 2
As, µg L^{-1}	< 1	< 1	< 1	< 1	< 1
Br, µg L^{-1}	6 ± 1	30 ± 3	76 ± 6	9 ± 1	9 ± 1
Rb, µg L^{-1}	< 1	19 ± 1	< 1	< 1	< 1
Ba, µg L^{-1}	< 14	< 14	< 14	< 14	< 14

components analysis [14,15]. Both methods are well documented and find wide application.

Cluster analysis is a well-known and widely used classification approach for environmetric purposes with its hierarchical and non-hierarchical algorithms. In order to cluster objects characterized by a set of variables, one has to determine their similarity. The representation of the results of the cluster analysis is performed either by a tree-like scheme called dendrogram comprising a hierarchic structure (large groups are divided into small ones) or by tables containing different possible clusterings. *Principal components analysis (PCA)* is a typical display method which allows estimating the internal relations in the data set. There are different variants of PCA but basically, their common feature is that they produce linear combinations of the original columns in the data matrix (data set) responsible for the description of the variables characterizing the objects of observation. These linear combinations represent a type of abstract measurements (factors, principal components) being better descriptors of the data structure (data pattern) than the original (chemical or physical) measurements.

RESULTS AND DISCUSSION

Two data sets were treated: [10×12] including the mineral waters „Gorna Banya" (samples C_1, C_6), „Kom" (samples C_2, C_7), „Thorn Springs" (samples C_3, C_8), „Devin" (samples C_4, C_9), and „Mihalkovo" (samples C_5, C_10), analyzed in the year of bottling and 2.5 years after bottling for 12 chemical parameters (As, Zn, Cu, Ba, Fe, Ni, Ca, Br, Mn, Rb, K, Cl), and [5×12] including the waters „Savina" table (sample C_11), „Bankya" mineral (sample C_12), „Hissar" mineral (sample C_13), „Devin" spring (sample C_14), and „Mihalkovo" spring (sample C_15), analyzed in the year of bottling for the same chemical parameters.

Data set [10×12]

Figure 1 presents the hierarchic dendrogram for clustering of the 12 variables from the data set [10×12]. As can be seen, three clusters are formed at the significance level of 33.3 % D_{max}:

K1 (As, Zn)
K2 (Cu, Ba, Fe)
K3 (Ni, Ca, Br, Mn, Rb, K, Cl)
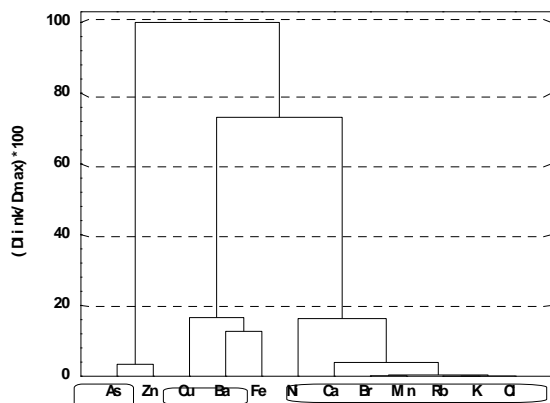
Fig. 1. Hierarchic diagram for clustering of 12 variables.

It follows from the results shown on Figure 1 that three main sources form the composition of all examined waters of the first data set, two of them being related to the microcomponents in the mineral waters (**К1** and **К2**), and the third one (**К3**) – mainly to the major components and the microcomponents Mn, Rb, Br, and Ni. This data structure is confirmed by the principal components (PC) analysis, where three latent factors appear to be responsible for the structure (Table 3). The first latent factor (PC1) is connected with all major components, while the other two (PC2 and PC3) – with characteristic combinations of microcomponents. Conditionally, one could define three latent factors responsible for the data structure: "soil mineral" factor, "strong As-Zn specific" factor and "rock mineral" factor.

Table 3. Factor loads for the data matrix [10×12].

Variables	PC1	PC2	PC3
Cl	0.99	0.06	0.14
K	0.99	0.02	0.13
Ca	0.96	0.15	-0.13
Mn	0.98	0.02	0.14
Fe	-0.06	0.29	0.94
Ni	0.76	-0.62	-0.12
Cu	0.20	-0.58	0.78
Zn	-0.23	-0.93	-0.26
As	-0.02	-0.99	0.04
Br	0.99	-0.04	0.12
Rb	0.98	0.01	0.16
Ba	0.67	0.21	0.68
Explained variance (%)	58	23	18

Figure 2 presents the hierarchic dendrogram for clustering of the mineral waters (firstly in the year of bottling and secondly – about 2.5 years later). Three clusters can be distinguished; there is a good correlation (grouping) between the results in the year of bottling and those about 2.5 years after bottling (samples 1 and 6, 2 and 7, 3 and 8, 4 and 9 and 5 and 10, respectively). This is an indication of the stability of the chemical composition and lack of contamination of all examined mineral waters even 2.5 years after bottling.
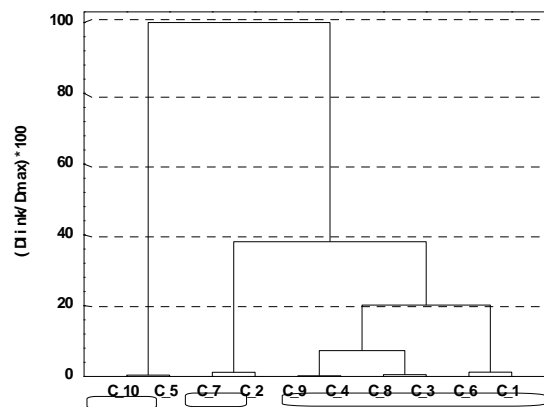
Fig. 2. Hierarchic dendrogram for clustering of the types of mineral waters analyzed in the year of bottling (samples C_1 - C_5) and about 2.5 years after bottling (samples C_6 – C_10).

On Figure 3 the diagram for the factor score is presented. The five brands of mineral waters included in the data set [10×12] ("Gorna Banya", "Kom", "Thorn Spring", "Devin" and "Mihalkovo") form three groups of similarity and the pairs (at the year of bottling and ~2.5 years after bottling) are very well distinguished. The three groups of similarity are described as follows:
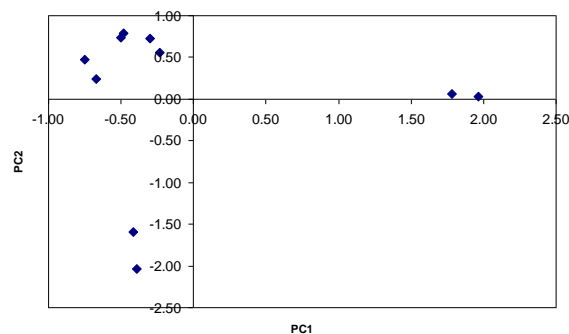
Fig. 3. Diagram for the factor scores (PC1 vs. PC2) for the data matrix [10×12].

• **„Mihalkovo"**: highest values of all major components (strong mineralization) and of the microcomponents manganese, nickel, copper, bromine and rubidium.

- **„Kom"**: highest values of zinc and arsenic (specific As-Zn mineralization) and lowest values of chlorides and calcium.
- **„Gorna Banya", „Thorn Spring", „Devin"**: mineral waters with similar chemical composition – lowest potassium content, significant content of calcium and iron.

Data set [5×12]

In this case four chemical variables were eliminated from the set, because they provided no chemical information – equal values were displayed for all examined samples. So the data set was reduced to **[5×8]**, the eliminated variables being the concentrations of manganese, nickel, arsenic and barium. The grouping of the chemical components yields three clusters at the significance level of 66.7% D_{max}, while at 33.3% D_{max} one of the clusters could be separated in two components (Figure 4).

K1 (Rb, Zn, Cu)
K2 (Ca, K) or (Ca) (K)
K3 (Fe, Br, Cl)
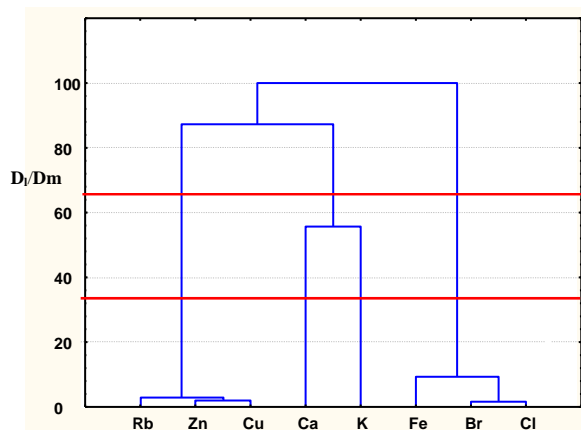
Fig. 4. Hierarchic dendrogram for clustering of 8 variables.

This clustering reveals that the microcomponents form similarity groups, while the major components (except for chloride) are of individual significance. The principal components analysis (Table 4) indicates the same grouping of the variables.

Table 4. Factor loads for the matrix [5×8].

Variables	PC1	PC2
Cl	0.15	0.98
K	-0.24	-0.51
Ca	0.01	-0.26
Fe	0.36	0.84
Cu	0.97	0.17
Zn	0.99	-0.003
Br	-0.10	0.98
Rb	0.94	0.14
Explained variance (%)	38	37

Two latent factors explain 75% of the total variance. Conditionally, they could be named "soil mineral" factor (strong correlations between Zn, Cu, Rb in PC1) and "rock mineral" factor (strong correlation for Cl, Fe, Br in PC2). Owing to their relatively low contents in the second set of water samples, Ca and K play a negligible role for the data structure (non-significant factor loadings).

The clustering of the water types (Figure 5) reveals a strong similarity only between the samples C_14 and C_15 ("Devin" spring and "Mihalkovo" spring), which are typical spring waters and display low concentrations of chlorides, bromides and iron.
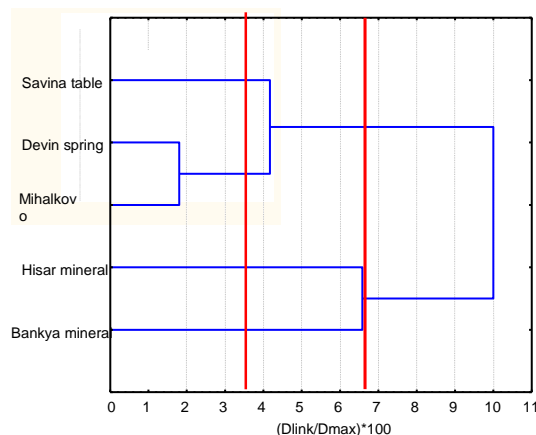
Fig. 5. Clustering of the investigated potable waters (samples C_11 - C_15).

The other three brands of waters differentiate (particularly at the first significance level and to a certain degree – at the second significance level). "Hissar" and "Bankya" form a group of mineralized waters with a high content of chlorides, iron, zinc and copper. The "Savina" table water forms a separate pattern owing to the demineralization processing of this water prior to bottling. However, calcium, iron, copper, and zinc are not removed - their contents are similar to those in the untreated mineral and spring water samples. These conclusions are confirmed by the principal component analysis (factor score diagram presented on Figure 6) where the separation of the five brands of waters can be observed.
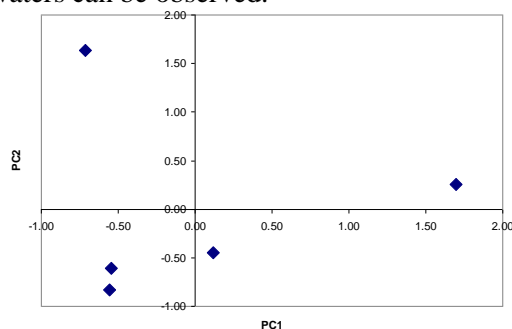
Fig. 6. Diagram for the factor scores (PC1 vs. PC2) for the data matrix [5×8].

CONCLUSIONS

The present study has indicated that the brands of mineral, spring and table waters in consideration could be classified into several patterns depending on their microelement composition. The separation is obviously related to the specificity of the local origin of the waters, e.g. crustal and soil properties and composition. In this relation it is of interest to note that the chemical composition of the spring waters „Devin" and „Mihalkovo" strongly differs from that of the mineral waters from the same locations. The separate pattern formed by the „Savina" table water may be related to the additional demineralization processing of this water prior to bottling. The results of the cluster analysis point to the stability of the chemical composition and lack of contamination of the bottled mineral waters even for a prolonged period of storage (2.5 years after bottling).

REFERENCES

1. E. N. Pentcheva, L. Van't dack, E. Veldeman, V. Hristov, R. Gijbels, Hydrogeochemical characteristics of geothermal systems in South Bulgaria. Universiteit Antwerpen (UIA), Antwerpen, 1997.
2. Bulgarian Governmental Standard BDS 14947 Natural Potable Mineral Waters (1980) (in Bulgarian).
3. DIN 38406 1982); DIN 38405 (1988); DIN 38405 (1989).
4. L. Vladeva, D. Kostadinov, Bulgarian mineral potable waters. Part 1. M-8-M Publ. House, Sofia, 1996 (in Bulgarian).
5. L. Vladeva, D. Kostadinov, Bulgarian mineral potable waters. Part 2. M-8-M Publ. House, Sofia, 2007 (in Bulgarian).
6. L. Vladeva, D. Krasteva, J. Jordanov, D. Kostadinov, Guide on Bulgarian Mineral Waters. Nauka i Technika Publ. House, Stara Zagora, 2000 (in Bulgarian).
7. K. Snuderl, M. Simonovic, J. Mocak, D. Brodnjak-Voncina, *Acta Chim Slov*, **54**, 33 (2007).
8. A. Mustapha, A. Z. Aris, *Pol J Environ Stud* **21**, 1359 (2012).
9. S. Oyebog, A. Ako, G. Nkeng, E. Suh, *J Geochem Explor,* **112,** 118 (2012).
10. A. Z. Aris, R. C. Y. Kam, A. Phing Lim, S. Praveena, *Appl Water Sci,* **3**, 67 (2013).
11. Directive 2009/54/EC (2009).
12. R. Georgieva, A. Detcheva, M. Karadjov, J. Jordanov, E. Ivanova, *Intern J Environ Anal Chem* **93**, 1043 (2013).
13. R. H. Georgieva, A. K. Detcheva, M. G. Karadjov, S. E. Mitsiev, J. H. Jordanov, E. H. Ivanova, *Bulg Chem Commun*, **46**, 840 (2014).
14. D. L. Massart, L. Kaufman, The interpretation of analytical chemical data by the use of cluster analysis, Wiley, New York, 1983.
15. B, Vandeginste, D. L. Massart, L. Buydens, S. De Jong, P. Lewi, J. Smeyers-Verbeke, Handbook of chemometrics and qualimetrics, Elsevier, Amsterdam, 1998.

ХЕМОМЕТРИЧНА ЕКСПЕРТИЗА НА БЪЛГАРСКИ МИНЕРАЛНИ, ИЗВОРНИ И ТРАПЕЗНИ ВОДИ

А. К. Дечева[1]*, В. Д. Симеонов[2], Е. Х. Иванова[1]

[1]Институт по обща и неорганична химия, Българска академия на науките, ул. Акад. Г. Бончев, бл.11, 1113 София, България
[2]Факултет по химия и фармация, Софийски университет "Св. Климент Охридски", бул. Дж. Баучер № 1, 1164 София, България

(Резюме)

Десет вида бутилирани български минерални, изворни и трапезни води са изследвани хемометрично с помощта на кластерен анализ и анализ на главни компоненти. Водите са класифицирани в няколко категории в зависимост от елементния им състав. Намерени са групи на подобие между химичните компоненти на питейните води и са определени специфичните индикатори за отделните групи води. Това разделение очевидно се дължи на специфичността на локалните водни източници, като например свойствата и състава на земната кора и почвата. Интересно е да се отбележи, че химичният състав на изворните води се различава съществено от този на минералните води от същия район. Получените резултати свидетелстват за стабилността на химичния състав, както и за липсата на замърсяване на изследваните води за продължителен период на съхранение (до 2.5 години след бутилирането).

Quartz crystal microbalance-based unlabeled immunosensor for the determination of aflatoxin B1

M. P. Slavova [1,2*], R. T. Georgieva-Nikolova[3], M. M. Nikolova[4], R. K. Hadjiolova[5]

[1]*Institute of Electrochemistry and Energy Sources, Bulgarian Academy of Sciences, Sofia, Bulgaria*
[2] *Department of Machine Elements and Chemistry, Faculty of Transport Management, Todor Kableshkov University of Transport, Sofia, Bulgaria*
[3] *Department of Inorganic Chemistry and Chemical Education, Faculty of Natural Sciences, Shumen University "Konstantin Preslavski", Shumen, Bulgaria*
[4] *Middlesex University, School of Health and Education − London, United Kingdom*
[5] *Department of Pathophysiology, Faculty of Medicine, Medical University of Sofia, Sofia, Bulgaria*

The aim of this work is to describe our first results obtained by a quartz crystal microbalance (QCM)-based unlabeled immunosensor for quantification of afllatoxins. Aflatoxins are natural mycotoxins that enter the food chain by contamination of crops and nuts, potentially posing carcinogenic risks to animal and human health. On choosing aflatoxin B1, immuno-QCM approaches were examined including sandwich assays with monoclonal antibodies. The immuno-QCM assay leads to the sensitive detection and quantification of aflatoxin B1 down to 0.01 ng/ml. The approach discussed here is used as a model system that could easily be adapted for aflatoxin detection in a variety of food or animal feed samples using a simple methanol/water solution as an extraction solvent.

Keywords: immune-quartz crystal microbalance, immunosensor, aflatoxin B1.

INTRODUCTION

Aflatoxins are natural mycotoxins that enter the food chain by contamination of crops and nuts, potentially posing carcinogenic risks to animal and human health. In fact, the European Committee Regulation (ECR) has established the maximum acceptable level of AFB1 in cereals, peanuts and dried fruits for direct human consumption: 4 ng/g for total aflatoxins (AFB1, AFG1, AFB2, AFG2) and 2 ng/g for AFB1 alone [1]. Aflatoxin B1 (AFB1) is the most common mycotoxin produced by strains of *Aspergillus flavus* and *Aspergillus parasiticus* that grow on food crops during their production and storage. It exhibits carcinogenic, teratogenic, mutagenic and immunosuppressive properties and has been regarded as a human carcinogen by the International Agency for Research on Cancer [2].

Analytical methodology must allow the determination of aflatoxins at least below the specific regulatory levels [3]. The measurement of antibody or antigen concentrations based on biospecific recognition interactions such as immunoassay and biosensors, has been considered a major analytical method used in clinical diagnosis, environment, and biochemical studies and has generated much interest due to its cost-effectiveness, sensitivity and specificity [4].

Immunosensing is a very active research field. The inherent combination of the exquisite molecular recognition ability of antibodies and the philosophy of rapid, continuous, reversible and automatic analysis of chemical sensors utilized in immunosensors is very useful in many fields [5]. In this sense, batch immunoassays can solve analytical problems that require a high number of determinations, while immunosensing is the better choice when automation and rapid results are needed [6].

The general strategy for immunosensor construction is to place the biological material in close contact with the transducer in order to obtain high sensitivity and to minimise the time of measurement. In a sandwich assay, after interaction between immobilised antibodies (Ab) and free antigens (Ag), second antibodies (Ab*), directed toward a second binding site of the Ag are added; at this point, Ag is "sandwiched" between two antibodies (Ab and Ab*). Transducers, such as piezoelectric sensors (quartz crystal microbalance, QCM) allow label-free detection with a direct quantification of the immunocomplex (Ab–Ag). For QCM, only a few examples are based on the use of a direct assay (not to be confused with the direct competitive assay) where the simple binding between an antigen and an antibody is detected. In fact, for low-molecular weight analytes such as aflatoxins the sensitivity of QCM is usually not sufficient when a direct antibody/antigen

---

interaction is adopted. For this reason competitive and sandwich formats (without any labeled molecules) are highly preferred [7]. Quartz crystal microbalance (QCM) has been extensively investigated as a transducer in chemical and biological sensing [8, 9]. A unique feature of QCM is that it can be designed as an immunosensor for directly detecting biomolecules [10, 11]. The QCM immunosensors measure the resonant frequency (F_0) using the standard oscillator technique, and the frequency change (ΔF) is usually explained by Sauerbrey equation, which states that the decrease in F_0 ($-\Delta F$) is linearly proportional to the increase in surface mass loading of QCM [12]. One of the biggest challenges for the development of QCM immunosensor devices for the antigen–antibody interaction is to understand the interaction process on the probe surface [13-15]. Thus, the surface properties of the immobilized antibody should be reproducible, stable, and selective to a corresponding antigen [16, 17].

The aim of this work is to describe the observation of a quartz crystal microbalance (QCM)-based unlabeled immunosensor for quantification of toxins suspended in methanol/water solution that can also serve as an extraction solvent (Figure 1). These are the first results of this kind of observation.
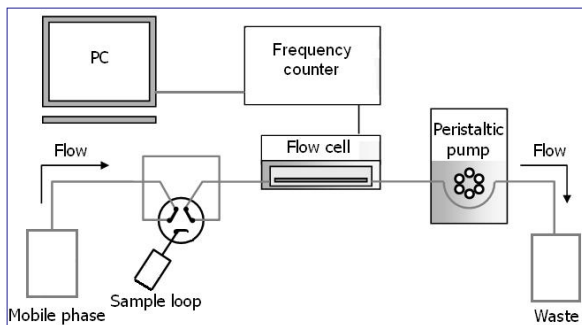
Fig. 1. Quartz crystal microbalance technology

MATERIALS AND METHODS

Aflatoxin B_1, the monoclonal antibodies against AFB_1 from rabbit (r-anti-AFB1) and the monoclonal antibodies against AFB_1 from mouse (m-anti-AFB1) were purchased from Sigma (St Louis, MO, USA). All chemicals and solvents used were of analytical grade and were used without further proceeding.

Aflatoxin B1 standards

Aflatoxin B1 analytical standard containing 5 µg AFB1 was solved in 1 ml of 100% methanol. A main stock of 100 ppb was prepared in 60:40 methanol/water solvent and used to prepare several standards by diluting the main stock in the same

690

solvent. Considering our objective of quantifying low aflatoxin concentrations (less than 100 ppb), a narrow 2-fold dilution range of aflatoxin standards was prepared [18].

Obtaining of polymer layer of polyacrylonitrile-polyacrylamide over QCM-resonator

The particles of the polyacrylonitrile-polyacrylamide copolymer were obtained according to the method used in [19]. Then 0.100 g of the obtained copolymer was diluted in 1 mL dimethylformamide (DMF) and the solution was stirred for 15 min on a magnetic stirrer. After 1:1 dilution with anizol the prepared polymer solution was cast as a thin layer over the QCM- resonator using spin coating (Figure 2).
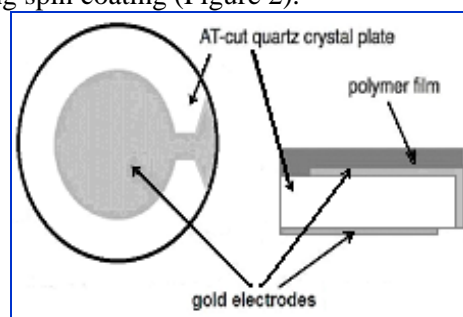
Fig. 2. Quartz crystal resonator with thin polymer layer

Method of oxidation of anti-aflatoxin B1 antibody

The working concentration of monoclonal m-anti-AFB1 was 0.67 mg/mL Oxidation of the carbohydrate moieties of the antibody with periodic acid (0.04 mmol/L in 0.05 mmol/L acetate buffer, pH 5.0) was performed according to Zabrosky and Ogletree. The unreacted periodic acid was removed with 0.025 mmol/l ethylene glycol. The oxidized antibody was dialyzed against 50 mmol/l phosphate buffer with pH 6.0 for 18-24 h [19].

Covalent immobilization of oxidized m-anti-AFB1 on polymer film over QCM-resonator

The immobilization of m-anti-AFB1 was performed in the following manner: 5 mL of oxidized dialytic solution of antibody was added to a resonator. The process was implemented for 24 hours at t = 4°C in dark.

QCM-based immunosensor for aflatoxin B1 using sandwich immunoassay

Saline was used as a basic solution for QCM (0.9% sodium chloride solution). Different dilutions of aflatoxin B1 prepared using 60:40 methanol/water solvent in separate 1 ml microcentrifuge tubes (100 µl of each standard) were added with 1 µg (5 µl) of r-anti-AFB1. Toxin

capture was performed by gently shaking the tubes at room temperature.

All solutions of AFB1 were previously incubated with r-anti-AFB1 to avoid unspecific adsorption onto the polymer layer. Including one of the AFB1 solutions in the system causes a decrease in the frequency of oscillation of the resonator due to the formation of a sandwich between the antibodies and AFB1 (Figure 3).
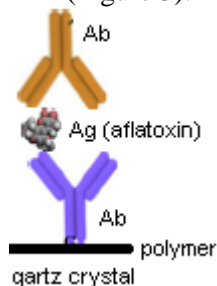
Fig. 3. QSM-immunosensor

Recovery of immunosensor

After 20 min treating with citrate-phosphate buffer (containing 4.7 g/l citric acid and 9.2 g/l dibasic sodium phosphate (Na_2HPO_4) anhydrous) at pH 5.0 the sandwich is destroyed and the sensor is regenerated.

Modified Lowry method

The protein content was measured using a modified Lowry method [20]. The principle behind the Lowry method for determining protein concentrations lies in the reactivity of the peptide nitrogens with the copper [II] ions under alkaline conditions, and the subsequent reduction of the Folin-Ciocalteu phosphomolybdic phosphotungstic acid to heteropolymolybdenum blue by the copper-catalyzed oxidation of aromatic acids.

First, reagent A: 2% Na_2CO_3 in 0,1N NaOH, reagent B: 1% $CuSO_4.5H_2O$ and reagent C: 2% sodium tartrate, were prepared. Reagent D was prepared by mixing reagents B and C at a ratio of 1:1. Reagent D was prepared just prior to use of reagents A and D at a ratio of 1:50.

After immobilization, the QCM-resonator was put into 1 ml of distilled water. Thereafter 5 ml of reagent D were added, and the solution was left for 160 min with occasional stirring. Then, 0.5 ml of 1N Folin-Ciocalteu reagent (phosphomolybdotungstate) were added. After 45 min, the absorbance was measured at 750 nm against a control that contained the same components, but without the immobilized QCM-resonator. The amount of protein was determined by the standard. As a reference a solution of m-anti-AFB1 was used.

RESULTS AND DISCUSSION

100 μl solution of 0,01 ng/ml AFB1 decreased the signal by 175Hz due to the accumulation of mass on the resonator. The increased amount of mass can be attributed to the formation of the sandwich assay or a non-specific binding of the components of the solution with the resonator (Figure 4a).
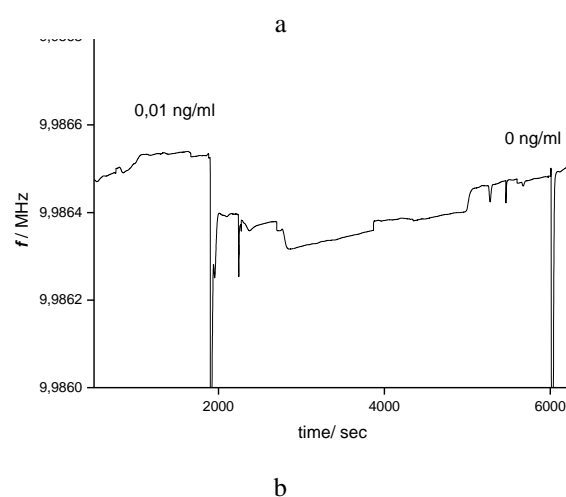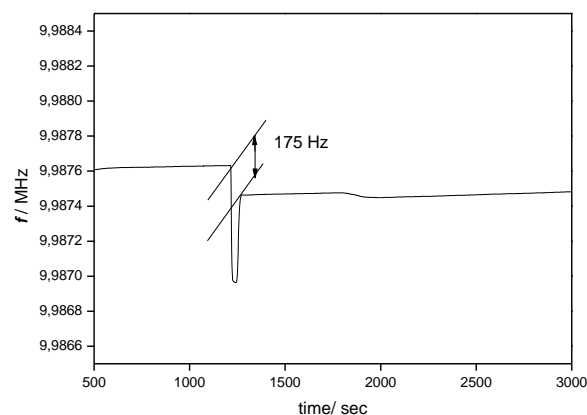
Fig. 4. Frequency dependence of the QCM-resonator: a) 100 μl 0,01 ng/ml AFB1; b) 100 μl r-anti-AFB1 without AFB1 after regeneration

The vibration frequency of the QCM-resonator is inversely proportional to the mass that has been deposited on it. Since the mass of AFB1 is very small, we increased it multifold by adding in advance r-anti-AFB1 to the primary solution containing the toxin. This method makes possible the determination of very small concentrations of AFB1.

After the regeneration of the sensor, the acid buffer was replaced with saline. The solution flow containing 100 μl of r-anti-AFB1 without AFB1 did not change the frequency of the resonator, which indicated that there was no non-specific binding (Figure 4b).

Table 1. Standard solutions for determination of protein according to the Lowry method

Solution	Control	1	2	3	4	5	6	7	8	9
1 mg/ml mouse IgG	-	0.1 ml	0.15 ml	0.2 ml	0.25 ml	0.3 ml	0.35 ml	0.4 ml	0.45 ml	0.5 ml
Dist. H$_2$O	1 ml	0.9 ml	0.85 ml	0.8 ml	0.75 ml	0.7 ml	0.65 ml	0.6 ml	0.55 ml	0.5 ml

The calibration curve was prepared by the Lowry method, using an m-anti-AFB1 solution at 1 mg/ml concentration as a standard protein solution. Out of the solution, the following solutions were prepared (Table 1):

To each tube 5 ml of reagent D were added and after stirring for 10 min at room temperature, to each tube 0,5 ml 1N solution of Folin-Ciocalteu were added. After 45 min, the solutions were tested by photometry at 750 nm against a control (Figure 5).
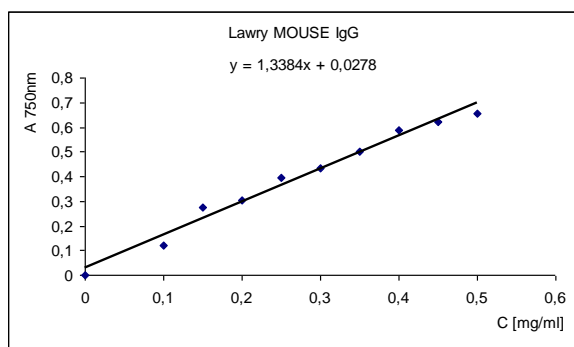
Fig. 5. Calibration Lawry curve

The quantity of immobilized antibodies on the QCM-resonator was 0.094 mg, entirely consisting of covalent immobilized immunoglobulin.

CONCLUSIONS

This method combined the sandwich competitive immunoassay with the amplification method of covalent immobilization onto the QCM-surface for AFB1 detection. The immuno-QCM assay leads to a sensitive detection and quantification of aflatoxin B1 from 100 down to 0.01 ng/ml. The approach discussed here is used as a model system that could easily be adapted for aflatoxin detection in a variety of food or animal feed samples using a simple methanol/water solution as an extraction solvent.

REFERENCES

1. European Commission. Commission Regulation no. 472/2002 of 12 March 2002 and no. 123/2005 of 26 January 2005 setting maximum limit for certain contaminants in food stuff, *The Official Journal of the European Union,* **L 77**, p 1.
2. A. P. Wacoo, D. Wendiro, P. C. Vuzi, J. F. Hawumba, *Journal of Applied Chemistry*, **2014**, 1 (2014).
3. A. Sharma, Z. Matharu, G. Sumana, P. R. Solanki, C. G. Kim, B. D. Malhotra, *Thin Solid Films*, **519**, 1213 (2010).
4. J. Zhang, J. Wang, J. Zhu, J. Xu, H. Chen, D. Xu, *Microchim Acta*, **163**, 63 (2008).
5. S. Shastry, *IJFAS*, **2-3**, 59 (2013).
6. M. A. González-Martínez, R. Puchades, A. Maquieira, *Analytical and Bioanalytical Chemistry*, **387**, 205 (2007).
7. F. Ricci, G. Volpe, L. Micheli, G. Palleschi, *Analytica Chimica Acta*, **605**, 111 (2007).
8. X. Mao, L. Yang, X. Su, Y. Li, *Biosens. Bioelectron.*, **21**, 1178 (2006).
9. A. Gerdon, D. Wright, D. Cliffel, *Anal. Chem*, **77**, 304 (2005).
10. Q. Zhang, Y. Huang, R. Zhao, G. Liu, Y. Chen, *Journal of Colloid and Interface Science*, 319, 94 (2008).
11. A. Palanianppan, S. Moochhala, F. Tay, X. Su, N. Phua, *Sensors and Actuators B: Chemica,* 129, 184 (2008).
12. S. J. Martin, V. E. Granstaff, G. C. Frye, *Analytical Chemistry*, **63**, 2272 (1991).
13. P. Luppa, L. Sokoll, D. Chan, *Clinica Chimica Acta*, **314**, 1 (2001).
14. T. Deng, J. Li, H. Wang, G. Sheng, R. Yu, *Journal of Immunological Methods*, **299**, 1 (2005).
15. D. Tang, R. Yuan, Y. Chai, H. An, *Advanced Functional Materials*, **17**, 976 (2007).
16. B. Pejcic, R. Marco, *Electrochimica Acta*, 51, 6217 (2006).
17. Li Wang, Xian-Xue Gan. *Bioprocess and Biosystems Engineering*, **32**, 109 (2009).
18. D. Babu, D. Muriana, *Toxins (Basel)*, 6, 3223 (2014).
19. L. Yotova, S. Yaneva, *Bulgarian Chemical Communications*, 45, 516 (2013).
20. A. L. Winters, F. R. Minchin *Analytical Biochemistry*, **346**, 43 (2005).

ИМУНОСЕНЗОР ЗА ОПРЕДЕЛЯНЕ НА АФЛАТОКСИН В1

М.П. Славова [1,2*], Р.Т. Георгиева-Николова [3], М.М. Николова [4], Р.К. Хаджийолова [5]

[1] *Институт по електрохимия и енергийни източници, Българска академия на науките, София, България*
[2] *Катедра Машинни елементи, Материалознание и Химия, Висше Транспортно Училище „Т. Каблешков"-София, България*
[3] *Катедра по Химия и Биохимия, Медицински Факултет, Медицински Университет-София, София, България*
[4] *Университет Мидълсекс, Училище за здравно образование − Лондон, Великобритания*
[5] *. Катедра по Патофизиология, Медицински Факултет, Медицински Университет-София, България*

(Резюме)

Настоящото проучване представя нашите първи резултати, получени с имуносензор базиран на кварцова кристална микровезна (QCM) за количествено определяне на афлатоксини. Афлатоксините са природни микотоксини, които постъпват в храната от замърсени зърна и ядки. Те са причина за канцерогенни заболявания при човека и животните. Афлатоксин В1 е избран за изследване с имуно-QCM сандвич метод с моноклонални антитела. Анализът показва добра чувствителност на откриване и количествено определяне на афлатоксин В1 до 0.01 нг/мл. Подходът, обсъден тук, се използва като моделна система, която лесно може да се адаптира за откриване на афлатоксин в различни проби от храни и фуражи, използвайки разтвор метанол/ вода като екстракционен разтворител.

Preparation of α-benzylamino coumarin derivatives using oxalic acid in aqueous media

M. Ghashang[1]*, M.R.M. Shafiee[1], S. Delzendeh[1], A. Fazlinia[2], H. Esfandiari[2], M.N. Biregan[1], N. Heydari[1]

[1]Department of Chemistry, Faculty of Sciences, Najafabad Branch, Islamic Azad University, Najafabad, Esfahan, Iran; P.O. Box: 517.
[2]Department of Chemistry, Neyriz Branch, Islamic Azad University, P.O. Box:74915-311, Neyriz, Iran

A simple and efficient preparative approach for the synthesis of different α-benzylamino coumarins catalyzed by oxalic acid is developed which involves three-component reaction of 4-hydroxycoumarin, aromatic aldehydes and secondary amines under ambient conditions in aqueous media. The salient features of this protocol are aerobic conditions, short reaction time, and mild reaction conditions without additives.

Keywords: Oxalic acid, 3-substituted coumarin, Mannich type reaction, α-benzylamino coumarin

INTRODUCTION

There is a great deal of interest in finding environmentally friendly solvents for synthesis. The use of water as a solvent in organic synthesis leads to a clean and economical technology. With water as a solvent the safety is largely increased, work-up is considerably simplified and cost is reduced [1,2]. The use of water as a solvent coupled with high yields and short reaction times makes synthetic procedures very attractive. The rates of the multicomponent reactions (MCRs) can increase when carried out in water [3]. MCRs have the advantages of high atom economy, structural diversity, operational simplicity, and lack of waste products in multistep reactions. The use of efficient and eco-friendly MCRs for construction of carbon-carbon and carbon-nitrogen bonds is a continued issue in organic synthesis [4-10].

3-Benzylcoumarin and its derivatives are an important class of heterocyclic compounds that have attracted much attention because of their diverse therapeutic and pharmacological activities such as anti-HIV, anti-malarial, anticoagulant, antibacterial, insecticide, antioxidant and antiviral [14-16]. The existence of coumarin derivatives in natural products is also of interest. Some analogues of coumarin have been isolated from sweet clover, bison grass and woodruff and are used to prevent clotting of blood in the veins, lungs or heart [17-20].

Mannich reaction is one of the most important C-C bond formation methods in organic synthesis, and its products (Mannich bases) are of considerable importance in industry, natural products chemistry, and pharmacy [21]. The classical Mannich reaction has limited applications, and many attempts have been made to extend this reaction [22]. The first report of Mannich type reaction was done by Robertson and Link [23] to prepare a range of benzyl amino coumarins at the mid of the 20th century. Thereafter, numerous modifications of this reaction surfaced and several methods have been developed for the preparation of 3-(benzyl)-substituted coumarins by using various catalysts, including triton X-100 as a non-ionic surfactant [24], nano crystalline ZnO [25] and InCl$_3$ [26].

Based on the above informations and due to our interest in developiing synthetic strategies for the construction of heterocyclic compounds, herein we report a facile methodology for the multicomponent condensation reaction of 4-hydroxycoumarin, aromatic aldehydes and secondary amines (Scheme 1).
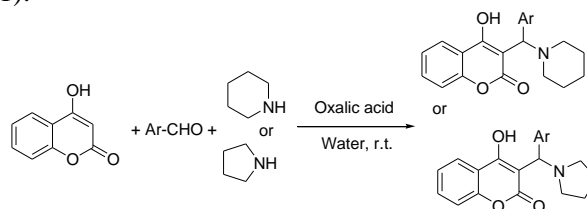
Scheme 1. Preparation of 3-(benzyl) amino coumarins.

EXPERIMENTAL

All reagents were purchased from Merck and Aldrich and used without further purification. All yields refer to isolated products after purification. The NMR spectra were recorded on a Bruker Avance DPX 400 MHz instrument. The spectra

* To whom all correspondence should be sent:
E-mail: ghashangmajid@gmail.com

were measured in DMSO-d_6 relative to TMS (0.00 ppm). Elemental analysis was performed on a Heraeus CHN-O-Rapid analyzer. Melting points were determined in open capillaries with a BUCHI 510 melting point apparatus. TLC was performed on silica gel polygram SIL G/UV 254 plates.

General procedure

To a mixture of 4-hydroxycoumarin (1.0 mmol), aromatic aldehyde (1.2 mmol) and secondary amine (1.2 mmol) in water (3 mL), oxalic acid (0.28 mmol) was added as the catalyst, and the mixture was stirred for an appropriate time at room temperature. After the reaction was completed, the solid compound obtained was filtered off and the crude products were purified by recrystallization from EtOH.

Selected data

3-((4-*tert*-Butylphenyl)(piperidin-1-yl)methyl)-4-hydroxy-2*H*-chromen-2-one (g): ^{1}H-NMR (400 MHz, DMSO-d_6): 1.28 (s, 9H), 1.73-1.94 (m, 6H), 2.22-2.26 (m, 2H), 3.09-3.12 (m, 2H), 5.29 (s, 1H), 7.11-7.27 (m, 4H), 7.43 (t, J = 7.7 Hz, 1H), 7.50 (t, J = 7.7 Hz, 1H), 7.82(d, J = 7.7Hz, 1H), 7.89 (d, J = 7.7 Hz, 1H), ppm; ^{13}C-NMR (100 MHz, DMSO-d_6): 19.9, 20.3, 22.8, 34.5, 35.7, 52.7, 67.9, 103.4, 115.9, 122.6, 123.9, 124.5, 128.7, 131.4, 135.9, 152.7, 153.6, 163.3, 164.7, 172.7 ppm; Found: C, 76.77; H, 7.56; N, 3.66; $C_{25}H_{29}NO_3$; requires: C, 76.70; H, 7.47; N, 3.58%.

4-Hydroxy-3-((3-nitrophenyl)(piperidin-1-yl)methyl)-2*H*-chromen-2-one (h): ^{1}H-NMR (400 MHz, DMSO-d_6): 1.70-1.93 (m, 6H), 2.21-2.25 (m, 2H), 3.12-3.14 (m, 2H), 5.59 (s, 1H), 7.10-7.16 (m, 2H), 7.43-7.48 (m, 2H), 7.49-7.53 (m, 2H), 7.82(d, J = 7.7Hz, 1H), 7.90 (d, J = 7.7 Hz, 1H), 8.08 (s, 1H) ppm; ^{13}C-NMR (100 MHz, DMSO-d_6): 20.3, 22.8, 34.5, 52.7, 103.6, 116.3, 121.6, 122.9, 123.7, 124.5, 128.9, 130.3, 133.9, 144.7, 148.3, 153.6, 166.3, 165.7, 172.3 ppm; Found: C, 66.39; H, 5.38; N, 7.44; $C_{21}H_{20}N_2O_5$; requires: C, 66.31; H, 5.30; N, 7.36%.

4-Hydroxy-3-((9-methyl-9H-carbazol-2-yl)(piperidin-1-yl)methyl)-2H-chromen-2-one (q): ^{1}H-NMR (400 MHz, DMSO-d_6): 1.66-1.91 (m, 6H), 2.35-3.71 (m, 4H), 3.79 (s, 3H, CH$_3$), 5.23 (s, 1H), 7.19-7.72 (m, 9H), 7.84 (s, 1H), 7.95 (d, J = 8.0 Hz, 1H) ppm; ^{13}C-NMR (100 MHz, DMSO-d_6): 23.7, 26.3, 29.7, 50.9, 54.3, 107.8, 116.4, 116.6, 116.9, 120.7, 120.9, 121.6, 122.2, 123.7, 124.5, 126.4, 127.7, 128.0, 129.5, 131.6, 139.7, 140.3, 142.6, 153.7, 165.3, 173.1 ppm; Found: C, 76.86; H, 6.21; N, 6.54; $C_{28}H_{26}N_2O_3$; requires: C, 76.69; H, 5.98; N, 6.39%.

4-Hydroxy-3-((9-methyl-9H-carbazol-2-yl)(pyrrolidin-1-yl)methyl)-2H-chromen-2-one (r): ^{1}H-NMR (400 MHz, DMSO-d_6): 1.89-1.96 (m, 4H), 3.02-3.11 (m, 4H), 3.79 (s, 3H, CH$_3$), 5.25 (s, 1H), 7.20-7.71 (m, 9H), 7.84 (s, 1H), 7.96 (d, J = 8.1 Hz, 1H) ppm; ^{13}C-NMR (100 MHz, DMSO-d_6): 24.2, 29.9, 50.3, 54.2, 107.6, 116.3, 116.7, 116.9, 120.6, 120.9, 121.7, 122.3, 123.7, 124.4, 126.5, 127.6, 127.8, 129.5, 131.6, 139.5, 142.7, 140.4, 153.6, 165.1, 173.3 ppm; Found: C, 76.56; H, 5.84; N, 6.78; $C_{27}H_{24}N_2O_3$; requires: C, 76.39; H, 5.70; N, 6.60%.

RESULTS AND DISCUSSION

Initial investigations were carried out using benzaldehyde (1.2 mmol), 4-hydroxycoumarin (1 mmol) and piperidine (1.2 mmol) as reactants in order to assess the suitability of oxalic acid as a catalyst (Scheme 2) and to optimize the reaction conditions. The results are presented in Table 1.

Scheme 2. synthesis of 4-hydroxy-3-(phenyl(piperidin-1-yl)methyl)-2H-chromen-2-one

As shown in Table 1, a variety of polar and non-polar solvents like CH$_2$Cl$_2$, ethanol, methanol, *n*-hexane, ethyl acetate, diethyl ether and water were examined. Under solvent-free conditions the product was obtained in a low yield. It was noticed that the polar protic solvents afforded better yields than other solvents and the best catalytic activity of oxalic acid (0.56 mmol) was observed in aqueous medium (Table 1).

To find out the optimial amount of barium chloride, the reaction was carried out by varying the quantity of catalyst (Table 1, entries 7, 9-11). The maximum yield was obtained using 0.28 mmol of catalyst (Table 1, entry 10). Further increase in the amount of oxalic acid in the mentioned reaction had no significant effect on the product yield.

With the successful optimization of the synthesis of 4-hydroxy-3-(phenyl(piperidin-1-yl)methyl)-2*H*-chromen-2-one we further studied the reactions of various aromatic aldehydes, piperidine/pyrrolidine and 4-hydroxy coumarin under similar conditions (Table 2, products **a-p**). A wide range of aromatic aldehydes was investigated under the optimal conditions.

The electron-donating groups attached to the phenyl rings of aldehydes decreased the reactivity (Table 2, entries 5-7,). However, the electron withdrawing groups (Table 2, entry 8) exhibited good reactivity.

Table 1. Optimization of the reaction conditions in the synthesis of 4-hydroxy-3-(phenyl(piperidin-1-yl)methyl)-2H-chromen-2-one (Scheme 2)

Entry	Catalyst (mmol)	Temperature	Solvent (5 mL)	Yield (%)[a]
1	0.56	r.t.	*n*-Hexane	-
2	0.56	r.t.	CH_2Cl_2	-
3	0.56	r.t.	Et_2O	5
4	0.56	r.t.	EtOAc	20
5	0.56	r.t.	EtOH	40
6	0.56	r.t.	MeOH	40
7	0.56	r.t.	H_2O	80
8	0.56	r.t.	-	10
9	1	r.t.	H_2O	85
10	0.28	r.t.	H_2O	89
11	0.14	r.t.	H_2O	50

[a] Isolated yields, reaction time: 2 h

Table 2. Synthesis of α-benzylamino coumarin derivatives

Entry	Aldehyde	Amine	Product	Time (h)	Yield (%)[a]
1	Benzaldehyde	piperidine	**a**	2	89
2	2-Chlorobenzaldehyde	piperidine	**b**	3	87
3	4-Chlorobenzaldehyde	piperidine	**c**	2	74
4	2-Methylbenzaldehyde	piperidine	**d**	4	80
5	4-Methylbenzaldehyde	piperidine	**e**	3	86
6	4-Methoxybenzaldehyde	piperidine	**f**	3	77
7	4-*tert*-Butylbenzaldehyde	piperidine	**g**	3	85
8	3-Nitrobenzaldehyde	piperidine	**h**	2	95
9	2,4-Dichlorobenzaldehyde	piperidine	**i**	3	60
10	4-Bromobenzaldehyde	piperidine	**j**	2	93
11	Benzaldehyde	pyrrolidine	**k**	2	90
12	2-Chlorobenzaldehyde	pyrrolidine	**l**	2	94
13	4-Chlorobenzaldehyde	pyrrolidine	**m**	3	95
14	2-Methylbenzaldehyde	pyrrolidine	**n**	2	80
15	4-Methylbenzaldehyde	pyrrolidine	**o**	2	90
16	3-Nitrobenzaldehyde	pyrrolidine	**p**	2	92
17	9-Methyl-9H-carbazole-2-carbaldehyde	piperidine	**q**	5	85
18	9-Methyl-9H-carbazole-2-carbaldehyde	pyrrolidine	**r**	5	87

[a] Isolated yields. All products have been reported previously in the literature and were characterized by comparison of NMR spectra with authentic samples [20-22].

CONCLUSION

In conclusion, a one-pot three-component reaction of aromatic aldehydes, piperidine/pyrrolidine and 4-hydroxycoumarin was described and an efficient procedure for the synthesis of a variety of α-benzylamino coumarins was found. Prominent among the advantages of this method are: easy workup procedure, operational simplicity and excellent yields of products in short reaction times.

696

REFERENCES

1. C-J. Li, T-H. Chan, Comprehensive Organic Reactions in Aqueous Media, 2nd ed., John Wiley & Sons, Inc., Hoboken, New Jersey, 2007.
2. C-J. Li, L. Chen, *Chem. Soc. Rev.,* **35,** 68 (2006).
3. M..C Pirrung, K.D. Sarma, *J. Am. Chem. Soc.,* **126,** 444 (2004).
4. J. Zhu, H. Bienaym, Multicomponent Reactions, John Wiley & Sons, Weinheim, 2006.
5. M. Ghashang *Curr. Org. Synth.,* **9,** 727 (2012).
6. M, Ghashang, *Lett. Org. Chem.* **9,** 497 (2012).
7. M.R.M. Shafiee, M. Ghashang, A. Fazlinia, *Curr. Nanosci.,* **9,** 197 (2013).
8. M. Ghashang, *Res. Chem. Intermed.,* **39,** 2187 (2013).

9. M. Ghashang, *Res. Chem. Intermed.* **39,** 2837 (2013).
10. M. Dehbashi, M. Aliahmad, M.R.M. Shafiee, M. Ghashang, *Synth. React. Inorg. Met. Org. Chem.,* **43,** 1301 (2013).
11. S. Hesse, G. Kirsch, *Tetrahedron Lett.,* **43,** 1213 (2002).
12. B.H. Lee, M.F. Clothier, F.E. Dutton, G.A. Conder, S.S Johnson, *Bioorg. Med. Chem. Lett.,* **8,** 3317 (1998).
13. J-C. Jung, Y-J. Jung, O-S. Park, *Synth. Commun.* **31,** 1195 (2001).
14. G. Melagraki, A. Afantitis, O. Igglessi-Markopoulou, A. Detsi, M. Koufaki, C. Kontogiorgis, D.J. Hadjipavlou-Litina, *Eur. J. Med. Chem.,* **44** , 3020. (2009).
15. J-C. Jung, J-H. Lee, S. Oh, J-G. Lee, O-S. Park, *Bioorg. Med. Chem. Lett.* , **14,** 5527 (2004).
16. C. Gleye, G. Lewin, A. Laurens, J. Jullian, P. Loiseau, C. Bories, R. Hocquemiller, *J. Nat. Prod.,* **66,** 690 (2003).
17. A. Bye, H.K. King, *Biochem. J.,* **117**, 23 (1970).
18. S. Thaisrivongs, P.K Tomich, K.D Watenpaugh, K. Chong, W. Howe, C. Yang, J. Strohbach, S. Tureer, J. McGrath, M. Bohanon, J. Lynn, A. Mulichak, P. Spinelli, R. Hinshaw, P. Pagano, J. Moon, M. Ruwart, K. Wilkinson, B. Rush, G. Zipp, R. Dalga, F. Schwende, G. Howard, G. Padbury, L. Toth, Z. Zhao, K. Koeplinger, T. Kakuk, S. Cole, R. Zaya, R. Piper, P. Jeffrey, *J. Med. Chem.,* **37,** 3200 (1994).
19. R.G. Bell, P.T. Caldwell, *Biochemistry,* **12,** 1759 (1973).
20. E.F. Kleinman, In: Comprehensive Organic Synthesis, B.M. Trost, I. Fleming (eds.), Pergamon Press, Oxford, 1991, p. 893.
21. H. Heaney, In Comprehensive Organic Synthesis, B.M. Trost, I. Fleming (eds.); Pergamon Press: Oxford. 1991, p. 953.
22. N.D. Robertson, P.K. Link, *J. Am. Chem. Soc.,* **75** 1883 (1953).
23. A. Kumar, M.K. Gupta, M. Kumar *Tetrahedron Lett.,* **52,** 4521 (2011).
24. P.P. Ghosh, A.R. Das, *Tetrahedron Lett.,* **53,** 3140 (2012).
25. P. Rao, S. Konda, J. Iqbal, S. Oruganti, *Tetrahedron Lett.,* **53,** 5314 (2012).

ПРИГОТВЯНЕ НА ПРОИЗВОДНИ НА α-БЕНЗИЛАМИНОКУМАРИН С ИЗПОЛЗВАНЕТО НА ОКСАЛОВА КИСЕЛИНА ВЪВ ВОДНА СРЕДА

М. Гашанг[1]*, М.Р.М. Шафие[1], С. Делзенде[1], А. Фазлина[2], Х. Есфандиари[2], М.Н. Биреган[1], Н. Хейдари[1]

[1]*Департамент по химия, Ислямски университет „Азад", Клон Наджафабад, Наджафабад, Есфахан, Иран*
[2] *Департамент по химия, Ислямски университет „Азад",Клон Нейриз, Нейриз, Иран*

(Резюме)

Разработен е прост и ефикасен препаративен подход за синтезата на различни производни на α-бензиламинокумарин при катализатор оксалова киселина, който включва три-компонентна реакция на 4-хидроксикумарин, ароматни алдехиди и вторични амини във водна среда. Характерни особености на този протокол са аеробни условия, кратко реакционно време и меки условия, без добавки.

Tin electrodeposition in the presence of *Linseed* essential oil

A. Benabida*, M. Cherkaoui

Laboratory of Materials, Electrochemistry and Environment, Faculty of Science, Ibn Tofail University, PB 133-14050 Kénitra, Morocco

In the present study, a tin deposit was elaborated electrolytically at different temperatures on an ordinary steel substrate in an H_2SO_4 based electrolyte for different linseed essential oil (LSEO) concentrations. The effect of this additive on the electrochemical properties of the coating was investigated using both the stationary and chronopotentiometry method. Thermodynamic parameters such as Ea, Δ*G, Δ*H and Δ*S have been evaluated in accordance with the Arrhenius theory and it has been found that the sorption process is non-spontaneous and endothermic in nature. The surface state of the deposit obtained was characterized by electron microscopy (SEM). The results have shown an approving surface quality of the deposit involved with the addition of an optimum concentration of LSEO in the electrolyte.

Keywords: Electrodeposition, Thermodynamic parameters, additive, kinetic, linseed essential oil, Tin, chronopotentiometry.

INTRODUCTION

Tin and its alloys are utilized in a large range of industrial applications pertaining to light engineering and electronics. An increasing interest of their investigation has been manifest in recent years because of the health and environmental concerns, particularly in the electronics industry, likewise in the automotive industry and in decorative plating,where the coatings types are mentioned as ecological alternatives to replace lead based soldering or nickel-chromium decorative coatings [1-3].

In tin plating baths including no organic additives, the tin is massively deposited under a low polarization. The deposit obtained is then porous, less adherent and dendritic with the formation of tin whiskers that spontaneously extend on the tin surface, which may cause a short circuit between the anode and the cathode [4-6].

To remedy or minimize this problem, it is essential to modify the kinetics of deposition. Several authors have proposed the addition of an organic compound into the bath, which can slow the deposition rate. First of all, marked efforts have been made in order to promote adequate additives and then to determine their intervention modes in both the mechanism and the kinetics of the deposit and hence their effect on the coating structure [7, 8]. The advantage in using natural organic compounds is due to theiraccessibility, cost and effect on the environment [9-12]. They pose no detrimental effects on the environment or risk to human health. A number of natural organic compounds have been recognized as good brightening actors in tin electroplating. A sample of these substances is *linseed* essential oil (LSEO). These classes of organic compounds are biodegradable and non-toxic.

Linseed oil is yellowish oil,also known as flax seed oil,extracted from the dried ripe seeds of the flax plant (Linumusitatissimum, Linaceae). As a renewable resource for agriculture, the application knowledge of the *linseed* essential oil as an industrial product has acquired much consideration. In 1965, the triglyceride composition of *linseed* essential oil was assured by a combination of several chromatographic techniques [13]. After that, the oxidation of *linseed* essential oil was reported by different groups [14,15]. Then, the drying operation was investigated with different methods and influencing factors [16-19]. More complex systems of *linseed* essential oil were also applied in concrete penetration [20], characterized by spectroscopy [21]. The recent interest in materials science, focusing on producing environmentally friendly products that substitute the oleo-chemical derived ones, point out a new way to the area of technical significance for *linseed* essential oil [22].

EXPERIMENTAL METHODS

Linseed oil is pressed from the seeds of the flax plant, Linumusitatissum, grown in temperate and cold climates such as Morocco. The essential oil was acquired by hydrodistillation and analyzed by Gas chromatography (GC) and Gas

---

* To whom all correspondence should be sent:
E-mail: benabida2000@hotmail.com

chromatography mass spectrometry (GC-MS) techniques as described in our earlier work [23, 24]. The chemical structure of the linseed essential oil is presented in Fig. 1. The major constituents of linseed essential oil are α-linolenic acid (60%), linoleic acid (29%), and oleic acid (27%). Linseed oil, which contains 60% α-linolenic acid, is an example of non-conjugated oil and it is rich in polyunsaturated fatty acids [23]. Oxygen atoms are present in their molecular structures and in addition, linolenic and linoleic acids include double bonds, which form potential adsorption sites on the mild steel surface by the donation of electrons to the empty d-orbital of Iron.
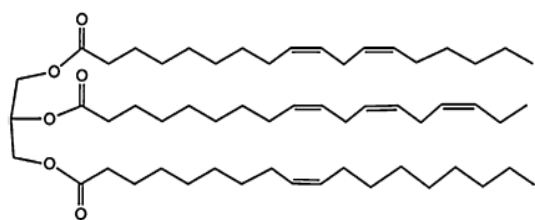
Fig. 1. The chemical structure of *linseed* essential oil additive.

The solution of tin sulfate and sulfuric acid were prepared using analytical grade chemicals. The pH is around 1 as in industrial applications and the temperature was varied as (25, 35, 45, and 55)°C using a hotplate stirrer. Table 1 contains the electrolytes used.

Table 1. Compositionofthestudiedbaths.

Electrolytes	$SnSO_4$ (M)	H_2SO_4 (M)	LSEO (ppm)
a	0	0.56	0
b	0	0	20
c	0	0.56	20
d	0.14	0.56	0
e	0.14	0.56	10
f	0.14	0.56	20
g	0.14	0.56	30

A 200ml cell was used. The gravimetric method is used to evaluate the electrodeposition efficiency, in the basic solutions without and with an *LSEO* additive, using rectangular mild steel coupons having the same purity as for mild steel rods. The substrates were iron plates (1cm^2), mechanically polished down to 1200by SiC paper, degreased in ethanol, etched in dilute sulfuric acid and rinsed with distilled water prior experiment initiation. The electrochemical measurements were executed with

a potentiostat (VoltaLab model PGZ100). A platinum electrode was used as the counter electrode and a silver/silver chloride (Ag/AgCl) as the reference electrode with all potentials referred. The surface of the deposits was examined by scanning electron microscopy (SEM) to confirm the results obtained.

RESULTS AND DISCUSSIONS

Cathodic Polarization curves

This study was carried out for the first time to explore the effect of LSEO on the cathodic polarization without tin in a cathodic polarization sweepin the potential range from -0.35V to -1.2V. The results foundfrom the three basic solutions (table 1) are shown in Fig.2.
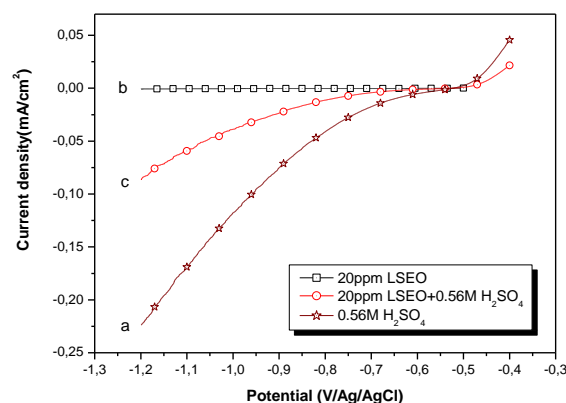
Fig. 2. Linear sweep polarizations in the tin-free electrolyte. (a) 0.56M H2SO4. (b) 10 ppm LSEO. (c) 0.56M H2SO4 + 10 ppm LSEO. at 25◦C andscanrateof 10 mv.s^{-1}

When the cathodic sweep takes place in the sulfuric acid electrolyte alone, there is a high hydrogen evolution reaction (HER) that appears rapidly when LSEO is added to the electrolyte. The process reduction changes concretely, such that the HER reaction is delayed until a higher potential is reached. Increasing the LSEO concentration in the electrolyte inhibits the HER more. On the other hand it can be inferred that this electrolyte is not electroactivein the zone of the potential studied:

$$2H^+ + 2é = H_2, \qquad (1)$$

The cathode polarizations were measured in the basic solution (Table 1) in the presence of the tin electrolyte, at different *LSEO* concentrationsand under the scan rate of 5mV/s presented in Fig. 3. The results show that this additive significantly decreases simultaneously with the current densities and the peak of tin reduction (2) at a disposed potential. This can be explained by the adsorption of the additive on the surface of the electrode [25, 26]. On the other hand, the hydrogen gas evolution

699

(1) is more impeded whenever the LSEO concentrations increase[27].

$$Sn^{2+} + 2e^- \rightarrow Sn, \qquad (2)$$
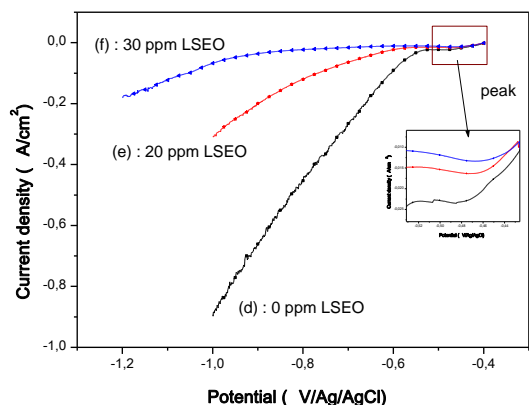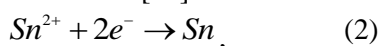
Fig. 3. Linear sweep polarizations in the presence of tin in the electrolyte. (d) 0.14M $SnSO_4$ + 0.56M H_2SO_4. (e) 0.14M $SnSO_4$ + 0.56M H_2SO_4 + 10 ppm LSEO. (f) 00.14M $SnSO_4$ + 0.56M H_2SO_4 + 20 ppm LSEO. at $25°C$ and a scan rate of 10 mv.s^{-1}

Chronopotentiometry

The transitory curves E=f(t) plot, for different current densities in baths from (d) to (g) (Fig. 4) show that the potential of stabilization is affected by the presence of *linseed* essential oil for different chosen current densities, as well as there is an overvoltage occurs when increasing the current density due 10 mA/cm^2 to 20 mA/cm^2, for all baths studied. These results show that the additive studied has a considerable effect on tin electrodeposition on the substrate. This potential drop after the addition of *LSEO* may be attributed to a partial blockage of the surface by adsorption of the additive [28]. Furthermore, the cathodic overvoltage increases as the concentration of the additive rises, as may be expected if the inert film behaves as a physical barrier [29].

In view of the galvanostatic curves shown above (Fig.4), the lowest overpotential is obtained in the absence of an LSEO additive,when the voltage increases gradually as a function of the LSEO concentration.Therefore, it is obvious that the increase in the concentration of LSEO would significantly affect the electrochemical properties of Sn. The highest overpotential is obtained as the structure becomes more compact and uniform (Fig.10).

Fig. 4. Potentiostatic current-time transients during tin deposition in the absence and in the presence of different LSEO concentrations (d):0ppm; (e): 10ppm; (f): 20ppm; (g): 30ppm.

700

Electrodeposition efficiency

The amount of tin deposited at the working electrode surface can be expressed using the electrodeposition efficiency (CE) that may be calculated from the Faraday's law (3) :

$$CE = \frac{m_{exp}}{m_{theor}} x100, \qquad (3)$$

Where m_{exp} is the weight of the deposit obtained experimentally and m_{theor} the theoretical mass m_{theor} of the deposit calculated theoretically according to Faraday's law[30].

Fig. 5 presents the electrodeposition efficiency with different LSEO concentrations as a function of various current densities. It is noticeable that the CE increases in general with an elevation of the current density.
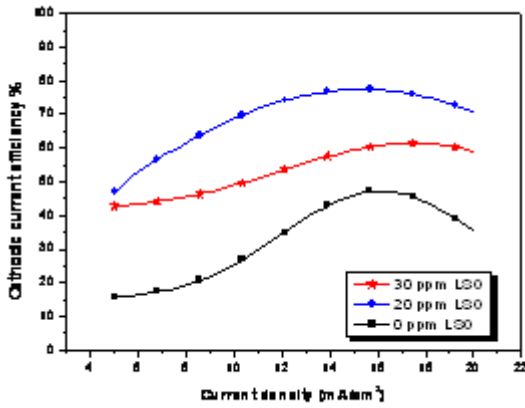
Fig. 5. Effect of the current density on the cathodic electrodeposition efficiency for various LSEO concentrations at 25°C.
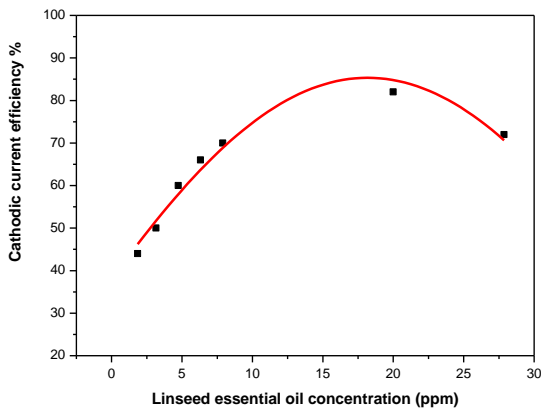
Fig. 6. Effect of the LSEO concentration on the cathodic electrodeposition efficiency at 25°C and 15mA/cm^2.

Furthermore, the presence of the LSEO significantly improves the electrodeposition efficiency, which may be explained by the fact that the stannous ions when they arrived on the substrate they attach themselves better than in the case of the absence of an additive, which results in the absence of whiskers during electrodeposition [27]. On the other hand, it is noticeable that the obtained results (Fig. 6) show that the CE varies in accordance with the different concentrations and the highest value is obtained when we choose a concentration of 20ppm. This result is confirmed in the curve of Fig.4f by the drop of the voltage for this value of the concentration. The decrease in the CE at a high concentration may lead to a decrease in the number of catalytic sites on the metal surface because of the formation of a thin film of adsorbed LSEO on top of the active surface [31].

Thermodynamic parameters

A thermochemical study of the temperature effects on the tin electrodeposition system by means of potential–current density is presented in Fig.7 to understand the effect of temperature on the deposition mechanism. These studies have been completed by activation parameters calculation at different temperatures between room temperature and 55°C.

The Arrhenius equation provides a mathematical dependency between the reaction rates (the time limiting current density) and temperature as follows:

$$\log I_\ell = \log A - E_a / 2.3R.T \quad (4)$$

Where I_ℓ is the limiting current density. A is the Arrhenius pre-exponential constant. R is the molar gas constant and T is the absolute temperature. A plot of log I versus 1/T produces straight lines (fig. 8) with a slope as ($-Ea/2.3R$) and an intercept at log A. The activation parameters calculated from the plot are displayed in table 2. The transition state equation (18) afforded thermodynamic parameters (table 2) such as the enthalpy change $\Delta*H$ and entropy change $\Delta*S$ from a plot of log I_ℓ/T versus 1/T as shown in Fig. 9.

$$I_\ell = \frac{RT}{Nh} \exp\left(\frac{\Delta*S}{R}\right) \exp-\left(\frac{\Delta*H}{RT}\right)$$

where N is Avogadro's number and h is Plank's constant. The enthalpy was calculated from the slope (-$\Delta*H$/2.3R) while the entropy was calculated from the intercept { ln(R/Nh)+ ($\Delta*S$/2.3R) of the plot. Therefore $\Delta*G$is calculated from equation (4):

$$\Delta*G = \Delta*H - T\Delta*S , \qquad (4)$$

The activation energies of the tin deposition with and without LSEO are calculated in accordance with the Arrhenius equation (4). The results obtained (Table 2) reveal that the higher

values of Ea obtained for the deposition of tin containing LSEO may be attributed to the blockage of the surface of the working electrode by molecules of the additive [32].
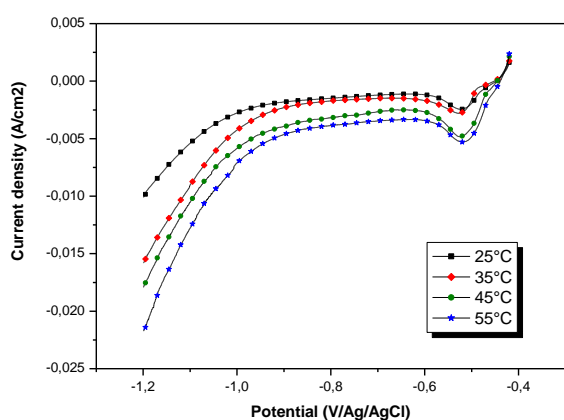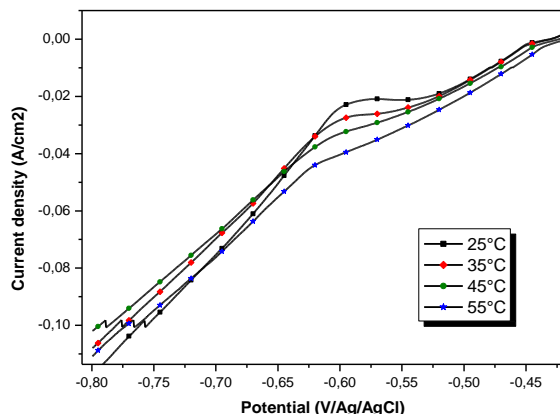
Fig. 7. Linear sweep polarizations recorded at various temperatures and a scan rate of 10 mV.s^{-1}for the electrolyte ; (a) without an additive, (b) with 20 ppm of LSEO.

Like Ea, the Δ*H increases in the presence of the additive. The positive values of Δ*G are a sign of the non-spontaneous process as expected. The process was endothermic due to the positive values of Δ*H. Therefore, the entropy Δ*S was negative and decreased gradually with the presence of the LSEO compared to that of the LSEO - free solution, meaning that the formation of the new tin layer with LSEO is less disordered[33].

Fig. 8. Thelogarithmofthe currentdensityversus T^{-1}forthelinearsweeppolarizationsat a potentialof −570 mV ;(a) 0.14M SnSO$_4$ + 0.56M H$_2$SO$_4$, (b) 0.14M SnSO$_4$ + 0.56M H$_2$SO$_4$ + 20 ppm LSEO. Data takenfromFig. 7.
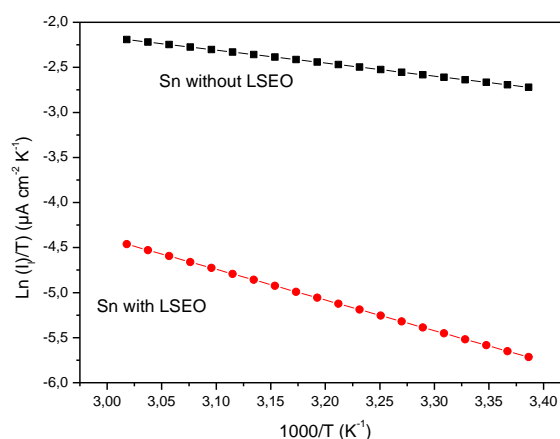
Fig. 9. Transition state plots for tin reduction on mild steel;(a) 0.14M SnSO$_4$ + 0.56M H$_2$SO$_4$. (b) 0.14M SnSO$_4$ + 0.56M H$_2$SO$_4$ + 20 ppm LSEO.

Surface morphology of deposits

The surface morphology of tin deposits was studied in the absence and in the presence of LSEO using scanning electron microscopy (SEM) and is given in Fig.10a and Fig.10b. It is remarked that the tin deposit in the absence of LSEO was rough and porous.

Table 2. The thermodynamic parameters for tin electrodeposition in 0.56 M H$_2$SO$_4$, in the absence and presence of 20 ppm LSEO.

Surfactant	Linear regression coefficient (r)	E$_a$ (kJ/mol)	Δ*H (kJ/mol)	Δ*S (J/mol)	Δ*G (kJ/mol)
Without additive	0.99964	14.54	11.957	-122.29	48.399
In the presence of LSEO	0.99877	30.92	28.315	-185.34	86.153
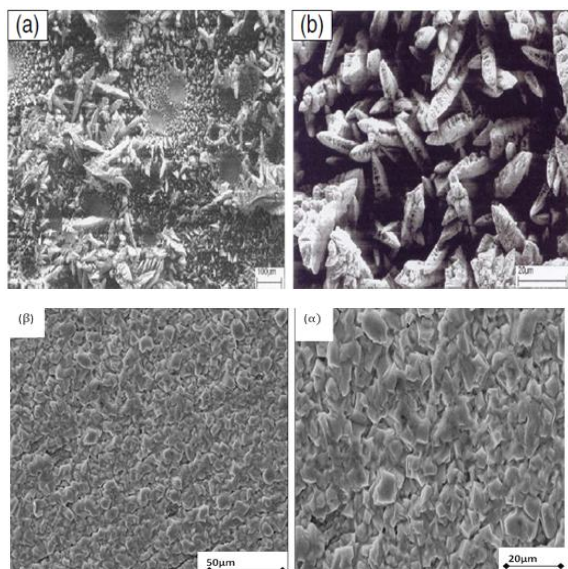
Fig. 10. (a and b) SEM images of tin deposits obtained at 25°C from the additive-free bath under the current density of 15 mA/cm^2. (α and β) SEM images of tin deposits obtained at 25°C at 20 ppm of LSEO under the current density of 15 mA/cm^2.

However, the tin deposit became compact and the roughness was decreased in the presence of LSEO as shown in Fig.10α and Fig.10β. It is noted that the grain size was clearly decreased with LSEO addition. Thus, it is found that the deposits with fine grains have a relatively large resistivity [34]. Also, the color of the deposits is modified from dark brown to bright with the presence of LSEO. This bright appearance of the deposits generally manifests better mechanical and electrical properties.

CONCLUSION

The electrochemical behavior of Sn (II) was studied in the sulphuric acid bath where *linseed* essential oil is an additive at different temperatures between room temperature and 55°C, using a mild steel working electrode. The insertion of *LSEO* into the base electrolyte of a tin deposit containing SnSO$_4$ and sulfuric acid leads to an improvement of the coating quality. Thus, the coating is more homogeneous more regular and less burnt than the one obtained from the base bath. This improvement may be attributed to a slowdown in the process of tin reduction by adsorption of this additive on the surface blocking a part of the actives sites. The thermodynamic parameters (Ea. Δ*G. Δ*H and Δ*S) showed that the adsorption process is non-spontaneous and endothermic in nature. In addition,*linseed* essential oil can be efficiently used as a low-cost and eco-friendly alternative as an organic compound in the bath.

REFERENCES

1. C.Han, Q.Liu, D. G. Ivey., *Electrochim. Acta,* **54**, 3419 (2009).
2. J.A. Jaen, M.I. Varsanyi, H. Csontos, A. Vertes, *Hyperfine Interact*, **66**, 101 (1991).
3. M.S. Jellesen, P. Miller., *Plat. Surf. Finish,* **92**, 36 (2005).
4. E. Chason, N. Jadhav, F. Pei, E. Buchovecky, A. Bower., *Progress in Surf. Sci*, **88**, 103 (2013).
5. S. Bakkali, T. Jazouli, M. Cherkaoui, M.E. Touhami, N. El-Hajjaji, E. Chassaing, *Plat. Surf. Finish*, **90**, 46 (2003).
6. G.S. Tzeng, S.H. Lin, Y.Y. Wang, C.C. Wan, *J. of Electroanal. Chem*, **26**, 419 (1996).
7. A. Aragon, M.G. Figueroa, R.E. Gana, J.J.H. Zagal, *Appl.Electrochem*, **22**, 558.
8. C.T.J. Low, F.C. Walsh., *J. Electroanal. Chem*, **615**, 2 (2008).
9. B.C. Tripathy, P. Singh, D.M. Muir, S.C. Das, *J. Appl. Electrochem*, **31**, 301 (2001).
10. A.Loto, I. Olefjord., *Corros. Prevent. Contr*, **39**, 149 (1992).
11. C. A.Loto, *Discov. Innovat*, **5**, 253 (1993).
12. C.A. Loto , I. Olefjord, H. Mattson., *Corros. Prevent. Contr*, **39**, 885 (1991).
13. A.G. Vereshchagin, G.V. Novitskaya., *Journal of the American Oil Chemists' Society,* **42**, 970 (1965).
14. P.S. Hess, *Industrial and Engineering Chemistry*, **42**, 1424 (1950).
15. C. Nunn, A.I. Smedley-Maclean, *Biochemical Journal,* **32**, 1974 (1938).
16. S.Tuman, J.Chamberlain, D. Scholsky, K.M. Soucek, M.D, *Progress in Organic Coatings, 28*, 251 (1996).
17. M.Lazzar, O.Chiantore, *Polymer Degradation and Stability,* **65**, 303 (1999).
18. J. Mallégol, J. Lemaire, J.L. Gardette, *Progress in Organic Coatings,* **39**, 107 (2000).
19. C. Stenberg, M. Svensson, M. Johansson, *Industrial Crops and Products*, **21**, 263(2005).
20. P. Blankenhorn, R. Barnes, D. Gowen, W. Kline, P. D.D.E. Cady, *Cement and Concrete Research*, **9**, 353 (1979).
21. V. Sharma, J.S. Banait, P.P. Kundu, *Polymer Testing,* **27**, 916 (2008).
22. Y.Xiaohong, L. Jing., *Industrial Crops and Products*, **41**, 437 (2013).
23. D. Rashmita, B. Sudip, R. Bandyopadhyay, P. Panchanan, *Sensors and Actuators B: Chemical*, **185**, 293 (2013).
24. D.M. Kasote, Y. S. Badhe, M. V. Hegde, *Industrial Crops and Products,* **42**, 10 (2013)
25. E.Rudnik., *Ionics,* **19**, 1047 (2013).
26. F.J. Barry, V.J. Cunnane, *J. Electroanal. Chem,* **537**, 151 (2002).
27. A. Benabida, M. Galai, A. Zarrouk, *Der Pharma Chemica,* **6**, 285 (2014).
28. S. Cherrouf, Y. Salhi, A. Benabida, H. Elgrini, M. Cherkaoui, L. Lakhrissi, B. Lakhrissi., *J. Chem.,* **2**, 175 (2014).

29. M. Moussa, A. El-Far., A. El-Shafei., *Materials chemistry and physics,* **105**, 105 (2007).
30. N.V. Sotskaya, O.V. Dolgikh, *Protection of Metals*, **44**, 479 (2008).
31. J. Huh, *Corros. Sci. Soc. Korea*, **29**, 46 (2000).
32. M. Charrouf, S. Bakkali, M. Cherkaoui, M. Amrani, *Journal of the Serbian Chemical Society,* **71**, 661 (2006).
33. A.I. Rasheed, *J. For Pure & Appl. Sci.,***24,** 10 (2011).
34. W. Sha, X. Wu, K.G. Keong, Electroless copper and nickel–phosphorus plating, processing, characterization and modeling, first ed., Woodhead Publishing Limited, New Delhi, 2011.

ЕЛЕКТРООТГАЛАНЕ НА КАЛАЙ В ПРИСЪСТВИЕ НА ЕСЕНЦИАЛНО МАСЛО ОТ ЛЕНЕНО СЕМЕ

А. Бенабида*, М. Черкауи

Лаборатория по материалознание, електрохимия и околна среда, Научен факултет, Университет Ибн Тофайл, Кенитра, Мароко

(Резюме)

В настоящата работа електролитное отлаган калай при различни температури на обикновен стоманен субстратв H_2SO_4 базирани електролит за различни концентрациина ленено етерично масло (LSEO). Изследван е ефекта на тази добавка върху електрохимичните свойства на покритието,както при стационарни, така и при хроно-потенциометрични методи. Определени се термодинамични параметри, като Ea, Δ*G, Δ*H и Δ*S в съгласие на теорията на Арениус и е установено, че адсорбцията е ендотермичен и неспонтанен процес. Повърхностното състояние на отлагането е охарактеризирано с електронна микроскопия. Резултатите показват, че подобрените повърхностни качества на покритието се дължат на оптималната концентрация на LSEO в електролита.

Three component condensation of a Betti-type – efficient tool for synthesis of chiral naphthoxazines and aminobenzylnaphthols for enantioselective diethylzinc addition to aldehydes

M. Tavlinova-Kirilova, M. Marinova, P. Angelova, M. Kamenova-Nacheva, K. Kostova[*], V. Dimitrov[*]

Institute of Organic Chemistry with Center of Phytochemistry, Bulgarian Academy of Sciences, Acad. G. Bonchev 9, Sofia 1113, Bulgaria

2-Naphthol, formaldehyde and chiral amines have been applied in three component Betti-type condensation to provide chiral 1,3-naphthoxazines in excellent yields. The latter have been easily transformed to chiral N-methyl aminobenzylnaphthols through reaction with lithium aluminum hydride. The chiral aminobenzylnaphthols are active catalyst (ligands) for enantioselective diethylzinc addition to aldehydes providing secondary alcohols in good yields only up to a moderate degree of enantioselectivity.

Keywords: oxazines, aminobenzylnaphthols, diethylzinc, enantioselectivity

INTRODUCTION

The three component condensation of 2-naphthol (**1**), benzaldehyde (**2**) and ammonia (**3**) was first realized by Mario Betti [1] and has been forgotten for a long time until the finding in recent years that the replacement of the ammonia used with chiral amines leads to a very potent approach for the synthesis of chiral aminobenzylnaphthols (Scheme 1). This relatively simple reaction, often referred to as modified Mannich condensation, forms in a first step equilibrating mixture of an imine **A** and 1,3-naphthoxazine **B**. Upon treatment with hydrochloric acid the aminonaphthol salt **4** is formed which treatment with sodium hydroxide then leads to aminonaphthol **5** (the so called "Betti base"). In recent years there is a growing interest in the synthesis of "Betti bases" due to the application of chiral analogues in asymmetric synthesis [2, 3]. The scope of the current knowledge about the synthesis and application of aminobenzylnaphthols of type "Betti base" has recently been demonstrated in review articles [4-6]. The most important achievement in the recent history of the "Betti bases" is the condensation of enantiopure amines with 2-naphthol and aldehydes leading to aminobenzylnaphthols of type **5** (Scheme 1) formed in high to excellent diastereoselectivity [7-10]. The aminonaphthols of type **5** form readily 1,3-oxazines with aldehydes, including formaldehyde [11-13].

Surprisingly, little attention has been directed to the condensation of 2-naphthol, formaldehyde and amines for the synthesis of 1,3-naphthoxazines [14-16]. There is only one report describing the synthesis of enantiopure 1,3-naphthoxazine by using formaldehyde and chiral amine [17].

The aim of the current work is the realization of three component condensation of 2-naphthol, formaldehyde and chiral amines with the purpose of using the targeted 1,3-naphthoxazines for further transformations to chiral aminobenzylnaphthols. The latter compounds can be applied as precatalysts in the enantioselective addition of diethylzinc to aldehydes.
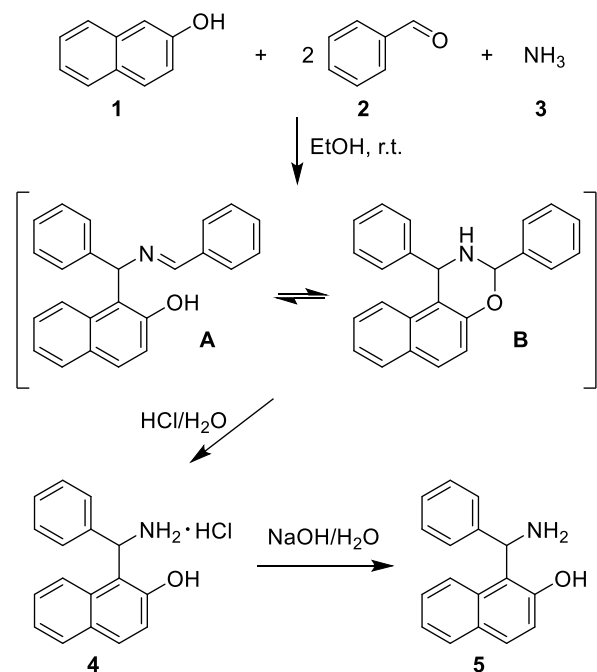
Scheme 1. Condensation of 2-naphthol, benzaldehyde and ammonia (Betti condensation).

EXPERIMENTAL

General

The reagents were commercial grade and used without further purification. Thin layer chromatography (TLC) was performed on aluminum sheets pre-coated with silica gel 60 F$_{254}$ (Merck). Flash column chromatography was carried out using silica gel 60 (230-400 mesh, Merck). Optical rotations ($[\alpha]_D^{20}$) were measured on a Perkin Elmer 241 polarimeter. The NMR spectra were recorded on a Bruker Avance II+ 600 spectrometer (600.13 MHz for ^{1}H, 150.92 MHz for ^{13}C NMR) in CDCl$_3$ with TMS as the internal standard for chemical shifts (δ, ppm). ^{1}H and ^{13}C NMR data are reported as follows: chemical shift, multiplicity (s = singlet, d = doublet, t = triplet, q = quartet, br = broad, m = multiplet), coupling constants (Hz), integration and identification. The assignment of the ^{1}H and ^{13}C NMR spectra was made on the basis of DEPT, COSY, HSQC, HMBC and NOESY experiments. All assignments marked with an asterisk are tentative. Mass spectra (MS) were recorded on a Thermo Scientific High Resolution Magnetic Sector MS DFS by electrospray ionization (ESI) and are reported as fragmentation in *m/z* with relative intensities (%) in parentheses. Gas chromatography (GC) was performed with a Shimadzu GC-17A. Elemental analyses were performed at the Microanalytical Service Laboratory of the Institute of Organic Chemistry, Bulgarian Academy of Sciences.

(S)-2-(1-phenylethyl)-2,3-dihydro-1H-naphtho[1,2-e][1,3]oxazine 11

To a mixture of 2-naphthol (**1**) (0.100 g, 0.694 mmol) and S-(-)-1-phenylethylamine (**6**) (0.088 g, 0.728 mmol) in EtOH (3 ml) 37% aq solution of formaldehyde (calculated to provide 3 equiv of formaldehyde) was added. The mixture was stirred at 50°C for 2h. After evaporation of the solvent, the crude product was chromatographed (petroleum ether/MTBE = 20:1) to give 0.192 g (96%) of **11**. $[\alpha]_D^{20}$ = +66 (c 1.04, CHCl$_3$). ^{1}H NMR: δ 1.50 (d, $J_{H,H}$ = 6.6 Hz, 3H, H-14), 4.04 (q, $J_{H,H}$ = 6.6 Hz, 1H, H-13), 4.17 (d, $J_{H,H}$ = 16.7 Hz, 1H, H-11), 4.41 (d, $J_{H,H}$ = 16.8 Hz, 1H, H-11), 4.92 (d, $J_{H,H}$ = 10.1 Hz, 1H, H-21), 5.17 (dd, $J_{H,H}$ = 10.1, 1.0 Hz, 1H, H-21), 7.05 (d, $J_{H,H}$ = 8.9 Hz, 1H, H-3), 7.25-7.29 (m, 1H, H-18), 7.30-7.37 (m, 5H, H-16, H-17, H-7, H-19, H-20), 7.38-7.42 (m, 1H, H-8), 7.46 (d, $J_{H,H}$ = 8.4 Hz, 1H, H-9), 7.64 (d, $J_{H,H}$ = 8.9 Hz, 1H, H-4), 7.76 (d, $J_{H,H}$ = 8.1 Hz, 1H, H-6) ppm. ^{13}C NMR: δ 21.62 (q, C-14), 46.12 (t, C-11), 58.21 (d, C-13),

79.91 (t, C-21), 112.14 (s, C-1), 118.48 (d, C-3), 121.03 (d, C-9), 123.34 (d, C-7), 126.39 (d, C-8), 127.23 (d, C-18), 127.30 (2d, C-16, C-20), 127.85 (d, C-4), 128.53 (2d, C-17, C-19), 128.57 (d, C-6), 128.90 (s, C-5), 131.82 (s, C-10), 144.70 (s, C-15), 152.55 (s, C-2) ppm. MS (ESI) *m/z* (rel int.) = 290 (100, [M+H]$^+$), 157 (17), 152 (10), 128 (30), 104 (40). Anal. Calcd for C$_{20}$H$_{19}$NO (289.37): C 83.01, H 6.62, N 4.84; Found: C 83.24, H 6.54, N, 4.71.

(S)-2-(1,2,3,4-tetrahydronaphthalen-1-yl)-2,3-dihydro-1H-naphtho[1,2-e][1,3]oxazine 12

To a mixture of 2-naphthol (**1**) (0.100 g, 0.694 mmol) and S-(+)-1,2,3,4-tetrahydro-1-naphthylamine (**7**) (0.107 g, 0.728 mmol) in EtOH (3 ml) 37% aq solution of formaldehyde (calculated to provide 3 equiv of formaldehyde) was added. The mixture was stirred at 50°C for 2h. After evaporation of the solvent, the crude product was chromatographed (petroleum ether/MTBE = 10:1) to give 0.209 g (95%) of **12**. $[\alpha]_D^{20}$ = +34.4 (c 0.975, CHCl$_3$). ^{1}H NMR: δ 1.63-1.73 (m, 2H, H-14, H-15), 1.87 (m, 1H, H-15), 2.07 (dt, $J_{H,H}$ = 11.4, 5.6, 1H, H-14), 2.65-2.78 (m, 2H, H-16), 4.12 (d, $J_{H,H}$ = 17.0 Hz, 1H, H-11), 4.28 (dd, $J_{H,H}$ = 8.8, 4.90, Hz, 1H, H-13), 4.38 (d, $J_{H,H}$ = 17.0 Hz, 1H, H-11), 5.05 (dd, $J_{H,H}$ = 10.0, 1.35, Hz, 1H, H-23), 5.14 (d, $J_{H,H}$ = 10.0 Hz, 1H, H-23), 7.04 (d, $J_{H,H}$ = 8.88 Hz, 1H, H-3), 7.07-7.11 (m, 1H, H-18), 7.16-7.22 (m, 2H, H-19, H-20), 7.30-7.35 (m, 1H, H-7), 7.39-7.43 (m, 1H, H-8), 7.53 (d, $J_{H,H}$ = 8.40 Hz, 1H, H-9), 7.63 (d, $J_{H,H}$ = 8.89 Hz, 1H, H-4), 7.66-7.69 (m, 1H, H-21), 7.75 (d, $J_{H,H}$ = 8.04 Hz, 1H, H-6) ppm. ^{13}C NMR: δ 21.25 (t, C-15), 27.91 (t, C-14), 29.19 (t, C-16), 43.58 (t, C-11), 62.64 (d, C-13), 82.35 (t, C-23), 114.38 (s, C-1), 118.99 (d, C-3), 121.14 (d, C-9), 123.32 (d, C-7), 125.81 (d, C-20), 126.33 (d, C-8), 126.80 (d, C-19), 127.66 (d, C-4), 128.39 (d, C-21), 128.54 (d, C-6), 128.74 (s, C-5), 129.10 (d, C-18), 131.16 (s, C-10), 137.48 (s, C-22), 138.44 (s, C-17), 152.96 (s, C-2) ppm. MS (ESI) *m/z* (rel int.) = 316 (100, [M+H]$^+$), 186.4(15), 157.4 (17), 131.1 (33). Anal. Calcd for C$_{22}$H$_{21}$NO (315.41): C 83.78, H 6.71, N, 4.44; Found: C 83.82, H 6.82, N, 4.52.

(S)-2-(1-(naphthalen-1-yl)ethyl)-2,3-dihydro-1H-naphtho[1,2-e][1,3]oxazine 13

To a mixture of 2-naphthol (**1**) (0.200 g, 1.387 mmol) and S-(-)-1-(1-naphthyl)-ethylamine (**8**) (0.249 g, 1.456 mmol) in EtOH (3 ml) paraformaldehyde (0.104 g) was added. The mixture was stirred at 50°C for 4h. After evaporation of the solvent, the crude product was chromatographed (petroleum ether/MTBE = 10:1)

to give 0.461 g (98%) of **13**. $[\alpha]_D^{20}$ = + 104 (c 1.00, CHCl$_3$). ^{1}H NMR: δ 1.64 (d, $J_{H,H}$ = 6.7 Hz, 3H, H-14), 4.18 (d, $J_{H,H}$ = 16.9 Hz, 1H, H-11), 4.52 (d, $J_{H,H}$ = 16.9 Hz, 1H, H-11), 4.86 (q, $J_{H,H}$ = 6.6, Hz, 1H, H-13), 5.02 (d, $J_{H,H}$ = 10.2 Hz, 1H, H-25), 5.26 (dd, $J_{H,H}$ = 10.2, 1.4 Hz, 1H, H-25), 7.08 (d, $J_{H,H}$ = 8.9 Hz, 1H, H-3), 7.28-7.31 (m, 1H, H-7), 7.32-7.35 (m, 1H, H-8), 7.37-7.41 (m, 2H, H-9, H-19), 7.42-7.45 (m, 1H, H-18), 7.46-7.50 (m, 1H, H-23), 7.66 (d, $J_{H,H}$ = 8.9 Hz, 1H, H-4), 7.72-7.76 (m, 2H, H-6, H-24), 7.78 (d, $J_{H,H}$ =8.17 Hz, 1H, H-22), 7.86 (d, $J_{H,H}$ = 8.04 Hz, 1H, H-17), 8.17 (d, $J_{H,H}$ = 7.58 Hz, 1H, H-20) ppm. ^{13}C NMR: δ 20.69 (q, C-14, CH$_3$), 46.42 (t, C-11), 55.18 (d, C-13), 80.03 (t, C-25), 112.46 (s, C-1), 118.57 (d, C-3), 121.09 (d, C-9), 123.33 (d, C-7), 123.69 (d, C-20), 124.62 (d, C-24), 125.39 (d, C-18), 125.63 (d, C-23), 125.72 (d, C-19), 126.33 (d, C-8), 127.69 (d, C-22), 127.83 (d, C-4), 128.53 (d, C-6), 128.81 (d, C-17), 128.91 (s, C-5), 131.33 (s, C-16), 131.82 (s, C-10), 134.08 (s, C-21), 140.14 (s, C-15), 152.70 (s, C-2) ppm. MS (ESI) *m/z* (rel int.) = 340 (100, [M+H]$^+$), 155 (73). Anal. Calcd for C$_{24}$H$_{21}$NO (339.43): C 84.92, H 6.24, N, 4.13; Found: C 85.19, H 6.17, N, 4.09.

*(S)-2-(1-(naphthalen-2-yl)ethyl)-2,3-dihydro-1H-naphtho[1,2-e][1,3]oxazine **14***

To a mixture of 2-naphthol (**1**) (0.200 g, 1.387 mmol) and *S*-(-)-1-(2-naphthyl)-ethylamine (**9**) (0.249 g, 1.456 mmol) in EtOH (3 ml) paraformaldehyde (0.104 g) was added. The mixture was stirred at 50°C for 3h. After evaporation of the solvent, the crude product was chromatographed (petroleum ether/MTBE = 10:1) to give 0.466 g (99%) of **14**. $[\alpha]_D^{20}$ = +25.6 (c 1.02, CHCl$_3$). ^{1}H NMR: δ 1.57 (d, $J_{H,H}$ = 6.6 Hz, 3H, H-14), 4.16-4.23 (m, 2H, H-11, H-13), 4.44 (d, $J_{H,H}$ = 16.9 Hz, 1H, H-11), 4.98 (d, $J_{H,H}$ = 10.1 Hz, 1H, H-25), 5.23 (dd, $J_{H,H}$ = 10.1, 1.30, Hz, 1H, H-25), 7.07 (d, $J_{H,H}$ = 8.9 Hz, 1H, H-3), 7.31 (ddd, $J_{H,H}$ = 10.2, 5.7, 2.4, Hz, 1H, H-7), 7.35 (ddd, $J_{H,H}$ = 8.3, 6.8, 1.4, Hz, 1H, H-8), 7.42 (d, $J_{H,H}$ = 8.3 Hz, 1H, H-9), 7.44-7.48 (m, 2H, H-19, H-20), 7.56 (dd, $J_{H,H}$ = 8.5, 1.64, Hz, 1H, H-24), 7.66 (d, $J_{H,H}$ = 8.9 Hz, 1H, H-4), 7.73-7.79 (m, 3H, H-6, H-16, H-18), 7.82-7.86 (m, 2H, H-23, H-21) ppm. ^{13}C NMR: δ 21.62 (q, C-14), 46.21 (t, C-11), 58.33 (d, C-13), 79.89 (t, C-25), 112.18 (s, C-1), 118.51 (d, C-3), 121.09 (d, C-9), 123.36 (d, C-7), 125.44 (d, C-24), 125.64* (d, C-19), 125.94* (d, C-20), 125.99* (d, C-16), 126.41 (d, C-8), 127.63* (d, C-18), 127.83 (d, C-4), 127.86* (d, C-21), 128.36* (d, C-23), 128.55 (d, C-6), 128.91 (s, C-5), 131.84 (s, C-10), 132.91 (s, C-22), 133.41 (s, C-17), 142.28 (s, C-15) 152.61 (s,

C-2) ppm. MS (ESI) *m/z* (rel int.) = 340 (100, [M+H]$^+$), 155 (40). Anal. Calcd for C$_{24}$H$_{21}$NO (339.43): C 84.92, H 6.24, N 4.13; Found: C 85.19, H 6.18, N, 4.05.

*(S)-2-(3,3-dimethylbutan-2-yl)-2,3-dihydro-1H-naphtho[1,2-e][1,3]oxazine **15***

To a mixture of 2-naphthol (**1**) (0.200 g, 1.387 mmol) and *S*-(+)-3,3-dimethyl-2-butylamine (**10**) (0.147 g, 1.456 mmol) in EtOH (3 ml) paraformaldehyde (0.104 g) was added. The mixture was stirred at 50°C for 4h. After evaporation of the solvent, the crude product was chromatographed (petroleum ether/MTBE = 10:1) to give 0.329 g (88%) of **15**. $[\alpha]_D^{20}$ = −109.1 (c 1.00, CHCl$_3$). ^{1}H NMR: δ 0.95 (s, 9H, H-16, H-17, H-18), 1.00 (d, $J_{H,H}$ = 7.1 Hz, 3H, H-14), 2.81 (q, $J_{H,H}$ = 7.1 Hz, 1H, H-13), 4.29 (d, $J_{H,H}$ = 17.0 Hz, 1H, H-11), 4.40 (d, $J_{H,H}$ = 17.0 Hz, 1H, H-11), 4.91 (dd, $J_{H,H}$ = 10.0, 1.52 Hz, 1H, H-19), 5.02 (d, $J_{H,H}$ = 10.0 Hz, 1H, H-19), 7.00 (d, $J_{H,H}$ = 8.9 Hz, 1H, H-3), 7.31-7.36 (m, 1H, H-7), 7.46 (ddd, $J_{H,H}$ = 8.3, 6.9, 1.3 Hz, 1H, H-8), 7.62 (d, $J_{H,H}$ = 7.9 Hz, 1H, H-6), 7.61 (d, $J_{H,H}$ = 8.6 Hz, 1H, H-4), 7.75 (d, $J_{H,H}$ = 8.2 Hz 1H, H-9) ppm. ^{13}C NMR: δ 12.78 (q, C-14), 26.69 (3q, C-16, C-17, C-18), 36.59 (s, C-15), 45.61 (t, C-11), 67.25 (d, C-13), 84.83 (t, C-19), 114.96 (s, C-1), 119.07 (d, C-3), 120.88 (d, C-6), 123.22 (d, C-7), 126.33 (d, C-8), 127.56 (d, C-4), 128.59 (d, C-9), 128.67 (s, C-5), 131.11 (s, C-10), 153.20 (s, C-2) ppm. Anal. Calcd for C$_{18}$H$_{23}$NO (269.38): C 80.26, H 8.61, N, 5.20; Found: C 80.18, H 8.75, N, 4.95.

General procedure for the reduction of the naphthoxazines with LiAlH$_4$

To a solution of the corresponding naphthoxazine (1 equiv) in dry THF (4 ml), LiAlH$_4$ (2.5 equiv) was added portion wise at 0°C and the mixture was stirred at rt for 3 h. The reaction mixture was quenched with water and the suspension was filtered through celite. The water phase was extracted with EtOAc and the organic phase was dried over Na$_2$SO$_4$. After evaporation of the solvent, the crude product was purified by column chromatography (petroleum ether/MTBE = 5:1).

*(S)-1-((methyl(1-phenylethyl)amino)methyl)-naphthalene-2-ol **16***

According to the GP the reduction of **11** (0.160 g, 0.553 mmol) with LiAlH$_4$ (0.031 g, 0.830 mmol) afforded after column chromatography 0.126 g (78%) of **16**. $[\alpha]_D^{20}$ = -11 (c 1.00, CHCl$_3$). ^{1}H NMR:

δ 1.55 (d, $J_{H,H}$ = 6.9 Hz, 3H, H-14), 2.28 (s, 3H, H-21), 3.86 (q, $J_{H,H}$ = 6.9 Hz, 1H, H-13), 4.14 (br s, 2H, H-11), 7.10 (d, $J_{H,H}$ = 8.8 Hz, 1H, H-3), 7.26 (ddd, $J_{H,H}$ = 7.9, 6.8, 0.9 Hz, 1H, H-7), 7.28-7.31 (m, 1H, H-18), 7.33 (d, $J_{H,H}$ = 7.2 Hz, 2H, H-16, H-20), 7.35-7.38 (m, 2H, H-17, H-19), 7.38-7.42 (m, 1H, H-8), 7.67 (d, $J_{H,H}$ = 8.8, Hz, 1H, H-4), 7.71-7.76 (m, 2H, H-9, H-6) ppm. ^{13}C NMR: δ 17.68 (q, C-14), 37.61 (q, C-21), 53.29 (t, C-11), 62.79 (d, C-13), 111.26 (s, C-1), 119.14, (d, C-3), 120.87 (d, C-9), 122.29 (d, C-7), 126.19 (d, C-8), 127.69 (d, C-18), 128.06 (2d, C-16, C-20), 128.42 (s, C-5), 128.55 (2d, C-17, C-19), 128.85 (d, C-6), 129.01 (d, C-4), 132.49 (s, C-10), 140.42 (s, C-15) 156.72 (s, C-2) ppm. MS (ESI) *m/z* (rel int.) = 292 (70 [M+H]$^+$), 157 (73), 136 (32), 129 (93), 105 (100), 102 (18). Anal. Calcd for C$_{20}$H$_{21}$NO (291.39): C 82.44, H 7.26, N 4.81; Found: C 82.23, H 7.35, N 4.58.

1-((methyl(1,2,3,4-tetrahydronaphthalen-1-yl)amino)methyl)naphthalene-2-ol 17

According to the GP the reduction of **12** (0.185 g, 0.587 mmol) with LiAlH$_4$ (0.056 g, 1.466 mmol) afforded after column chromatography 0.130 g (70%) of **17**. $[\alpha]_D^{20}$ = -23 (c 1.00, CHCl$_3$). ^{1}H NMR: δ 1.66-1.75 (m, 1H, H-15), 1.92-1.99 (m, 1H, H-14), 2.05 (m, 1H, H-15), 2.14 (m, 1H, H-14), 2.24 (s, 3H, H-23), 2.74 (dt, $J_{H,H}$ = 16.4, 4.5 Hz, 1H, H-16), 2.82 (m, 1H, H-16), 4.21 (dd, $J_{H,H}$ = 8.7, 6.5 Hz, 1H, H-13), 4.32-4.40 (m, 2H, H-11), 7.10 (d, $J_{H,H}$ = 7.5 Hz, 1H, H-18), 7.13 (d, $J_{H,H}$ = 8.8 Hz, 1H, H-3), 7.17 (t, $J_{H,H}$ =7.38, 1H, H-19), 7.23-7.26 (m, 1H, H-20), 7.28 (dd, $J_{H,H}$ = 7.9, 7.0 Hz, 1H, H-7), 7.43-7.46 (m, 1H, H-8), 7.53 (d, $J_{H,H}$ = 7.8 Hz, 1H, H-21), 7.69 (d, $J_{H,H}$ = 8.8 Hz, 1H, H-4), 7.76 (d, $J_{H,H}$ = 8.1 Hz, 1H, H-6), 7.86 (d, $J_{H,H}$ = 8.6 Hz, 1H, H-9) ppm. ^{13}C NMR: δ 21.07 (t, C-14), 21.51 (t, C-15), 29.82 (t, C-16), 35.86 (q, C-23), 52.84 (t, C-11), 61.04 (d, C-13), 111.18 (s, C-1), 119.00 (d, C-3), 120.81 (d, C-9), 122.31 (d, C-7), 126.28 (d, C-8), 126.48 (d, C-20), 126.90 (d, C-19), 128.12 (d, C-21), 128.46 (s, C-5), 128.93 (d, C-6), 129.19 (2d, C-4, C-18), 132.63 (s, C-10), 135.97 (s, C-22), 138.75(s, C-17), 156.76 (s, C-2). MS (ESI) *m/z* (rel int.) = 318 (43 [M+H]$^+$), 157 (70), 131 (100), 129 (55). Anal. Calcd for C$_{22}$H$_{23}$NO (317.43): C 83.24, H 7.30, N 4.41; Found: C 83.10, H 7.21, N 4.33.

(S)-1-((methyl(1-(naphthalen-1-yl)ethyl)amino)methyl)naphtalen-2-ol 18

According to the GP the reduction of **13** (0.140 g, 0.410 mmol) with LiAlH$_4$ (0.040 g, 1.031 mmol) afforded after column chromatography 0.106 g (75%) of **18**. $[\alpha]_D^{20}$ = +187 (c 1.00, CHCl$_3$). ^{1}H NMR: δ 1.71 (d, $J_{H,H}$ = 6.7 Hz, 3H, H-14), 2.38 (s, 3H, H-25), 4.22 (d, $J_{H,H}$ =14.4, 1H, H-11), 4.29 (d, $J_{H,H}$ =14.5, 1H, H-11), 4.70-4.78 (m, 1H, H-13), 7.04 (d, $J_{H,H}$ = 8.8 Hz, 1H, H-3), 7.25 (dd, $J_{H,H}$ = 9.2, 5.6 Hz, 1H, H-7), 7.36-7.41 (m, 1H, H-8), 7.50 (d, $J_{H,H}$ = 8.6, Hz, 1H, H-19), 7.53 (d, $J_{H,H}$ = 8.5, Hz, 1H, H-23), 7.59 (t, $J_{H,H}$ = 7.6 Hz, 1H, H-18), 7.63 (d, $J_{H,H}$ = 8.8, 1H, H-4), 7.66 (d, $J_{H,H}$ = 7.2 Hz, 1H, H-24), 7.72 (d, $J_{H,H}$ = 8.1 Hz, 1H, H-6), 7.74 (d, $J_{H,H}$ = 8.5 Hz, 1H, H-9), 7.81 (d, $J_{H,H}$ = 8.1 Hz, 1H, H-22), 7.89 (d, $J_{H,H}$ = 8.1 Hz, 1H, H-20), 8.20 (d, $J_{H,H}$ = 8.53 Hz, 1H, H-17) ppm. ^{13}C NMR δ 16.51 (q, C-14), 38.71 (q, C-25), 53.42 (d, C-13), 59.14 (t, C-11), 111.24 (s, C-1), 119.11 (d, C-3), 120.89 (d, C-9), 122.30 (d, C-7), 122.81 (d, C-17), 124.69 (d, C-24), 125.33 (d, C-23), 125.75 (d, C-19), 126.15 (d, C-8), 126.46 (d, C-18), 128.26 (d, C-22), 128.41 (s, C-5), 128.82 (d, C-6), 128.96 (d, C-4), 129.14 (d, C-20), 131.51 (s, C-16), 132.54 (s, C-10), 134.07 (s, C-21), 137.73 (s, C-15), 156.24 (s, C-2) ppm. MS (ESI) *m/z* (rel int.) = 342 (10, [M+H]$^+$), 186 (40), 155 (100). Anal. Calcd for C$_{24}$H$_{23}$NO (341.45): C 84.42, H 6.79, N 4.10; Found: C 84.24, H 6.52, N 4.29.

(S)-1-((methyl(1-naphthalen-2-yl)ethyl)amino)methyl)naphtalen-2-ol 19

According to the GP the reduction of **14** (0.190 g, 0.560 mmol) with LiAlH$_4$ (0.053 g, 1.40 mmol) afforded after column chromatography 0.150 g (79%) of **19**. $[\alpha]_D^{20}$ = -49.3 (c 1.00, CHCl$_3$) ^{1}H NMR: δ 1.65 (d, $J_{H,H}$ = 6.8 Hz, 3H, H-14), 2.33 (s, 3H, H-25), 4.03 (q, $J_{H,H}$ = 6.8 Hz, 1H, H-13), 4.11-4.30 (m, 2H, H-11), 7.12 (d, $J_{H,H}$ = 8.8 Hz, 1H, H-3), 7.27 (t, $J_{H,H}$ = 7.4 Hz, 1H, H-7), 7.38-7.43 (m, 1H, H-8), 7.45-7.54 (m, 3H, H-19, H-20, H-24), 7.68 (d, $J_{H,H}$ = 8.8 Hz, 1H, H-4), 7.71 (s, 1H, H-16), 7.72-7.76 (m, 2H, H-6, H-9), 7.80-7.85 (m, 2H, H-21, H-18), 7.87 (d, $J_{H,H}$ = 8.5 Hz, 1H, H-23) ppm. ^{13}C NMR: δ 17.7 (q, C-14), 37.71 (q, C-25), 53.31 (t, C-11), 62.73 (d, C-13), 111.31 (s, C-1), 119.14 (d, C-3), 120.95 (d, C-9), 122.34 (d, C-7), 125.84 (d, C-20)*, 126.04 (d, C-19)*, 126.21 (d, C-24)*, 126.25 (d, C-8), 127.16 (d, C-16), 127.63 (d, C-18)*, 127.89 (d, C-21)*, 128.41 (d, C-23), 128.46 (s, C-5), 128.87 (d, C-6), 129.08 (d, C-4), 132.49 (s, C-10), 132.90 (s, C-22), 133.13 (s, C-17), 137.8 (s, C-15) 156.74 (s, C-2) ppm. MS (ESI) *m/z* (rel int.) = 342 (43, [M+H]$^+$), 155 (100), 153 (43), 129 (40). Anal. Calcd for C$_{24}$H$_{23}$NO (341.45): C 84.42, H 6.79, N 4.10; Found: C 84.56, H 6.85, N 3.98.

(S)-1-(((3,3-dimethylbutan-2-yl)(methyl)amino)methyl)naphthalene-2-ol 20

According to the GP the reduction of **15** (0.306 g, 1.136 mmol) with LiAlH₄ (0.108 g, 2.840 mmol) afforded after column chromatography 0.170 g (55%) of **20**. ^{1}H NMR: δ 1.04 (s, 9H, H-16, H-17, H-18), 1.17 (d, $J_{H,H}$ = 7.0 Hz, 3H, H-14), 2.30 (s, 3H, H-19), 2.69 (q, $J_{H,H}$ = 7.0 Hz, 1H, H-13), 4.06 (d, $J_{H,H}$ = 14.6 Hz, 1H, H-11), 4.35 (d, $J_{H,H}$ = 14.6 Hz, 1H, H-11), 7.09 (d, $J_{H,H}$ = 8.8, 1H, H-3), 7.21-7.32 (m, 1H, H-7), 7.42 (ddd, $J_{H,H}$ = 8.5, 6.8, 1.5 Hz, 1H, H-8), 7.67(d, $J_{H,H}$ = 8.8 Hz, 1H, H-4), 7.71-7.81 (m, 2H, H-6, H-9) ppm. ^{13}C NMR: δ 6.83 (q, C-14), 27.84 (3q, C-16, C-17, C-18), 35.50 (d, C-13), 55.22 (t, C-11), 68.29 (q, C-19), 110.91 (s, C-1), 119.16 (d, C-3), 120.71 (d, C-9), 122.21 (d, C-7), 126.19 (d, C-8), 128.38 (s, C-15), 128.57 (s, C-5), 128.90 (d, C-4), 129.04 (d, C-6), 132.70 (s, C-10), 156.73 (s, C-2) ppm.

General procedure for enantioselective addition of diethylzinc to aldehydes

To a solution of the corresponding ligand **16-20** (3 mol %) in hexane or toluene (4 ml) Et₂Zn (1.7 mmol, 1M solution in hexane) was added dropwise at 0°C in an Ar atmosphere. The mixture was stirred for 30 min at 0°C and then the corresponding aldehyde (1.0 mmol) was added at -20°C. The reaction mixture was stirred at 20°C and monitored by TLC (petroleum ether/MTBE = 5:1) until the aldehyde was consumed. The mixture was quenched (aq. NH₄Cl), extracted with Et₂O, and dried (Na₂SO₄). After evaporation of the solvent, the crude product was purified by column chromatography (petroleum ether/MTBE = 5:1).
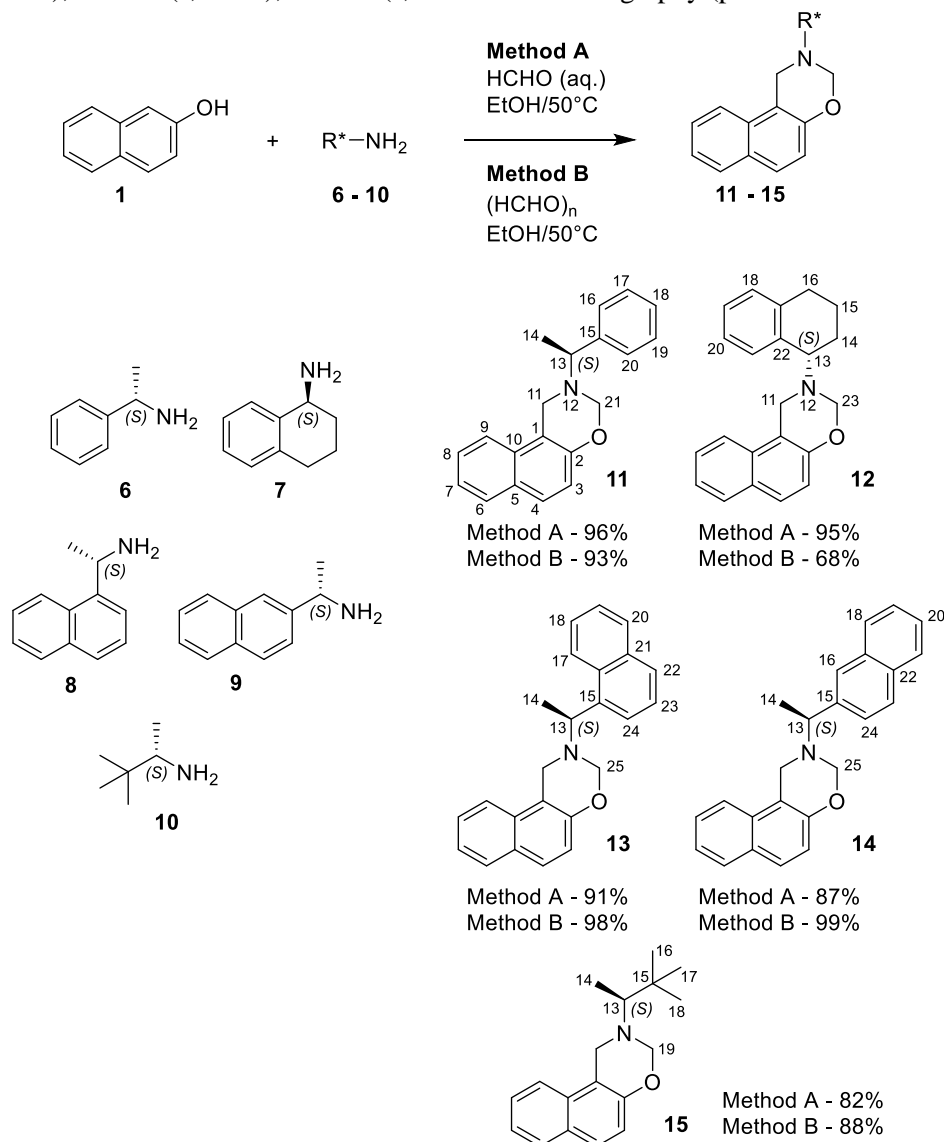
Scheme 2. Three component condensation of 2-naphthol, formaldehyde and chiral amines (the numbering of the C-atoms is presented to support the assignment of the NMR spectra.
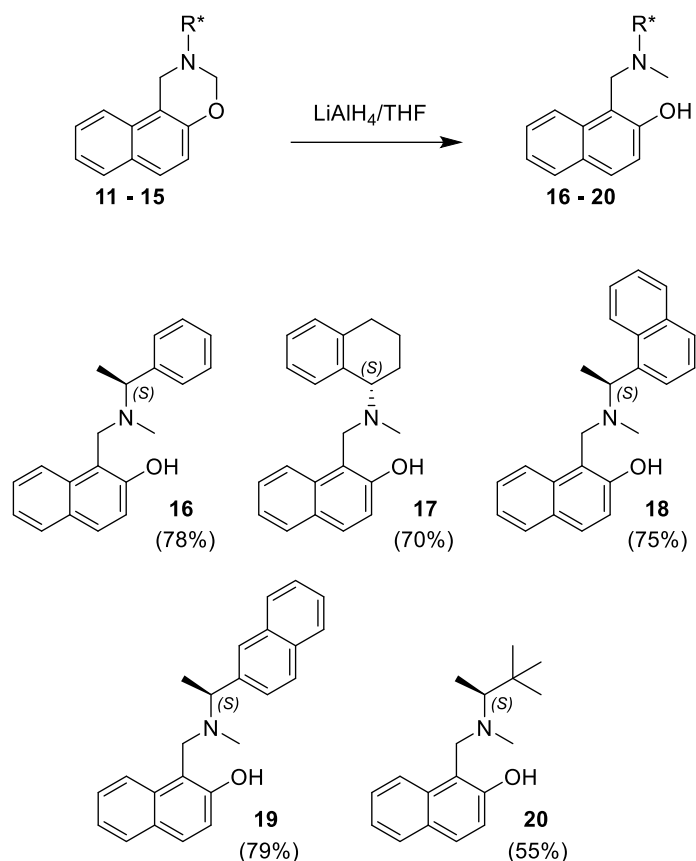
Scheme 3. Reduction of the 1,3-oxazines **11-15** to the N-methyl derivatives **16-20**.

Table 1. Enantioselective addition of Et_2Zn to *o*-methoxybenzaldehyde (**21**) and 1-naphthaldehyde (**22**) catalyzed by chiral ligands **16-20**.
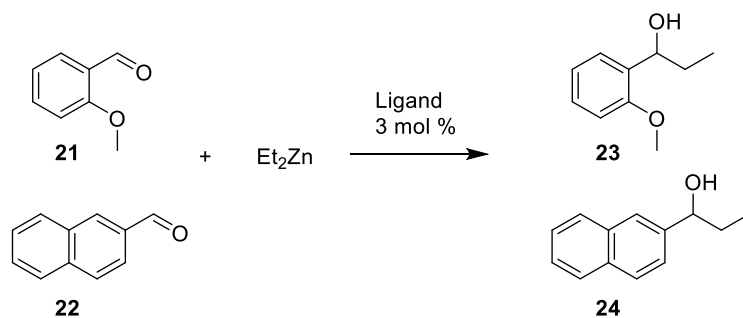
Ligand	Product **23**		Product **24**	
	Yield[a] %	ee %, (config.)[b]	Yield[a] %	ee %, (config.)[c]
16	68	0	54	3 *R*
17	69	14 *R*	34	0
18	86	47 *R*	57	2 *R*
19	64	24 *R*	36	14 *R*
20	56	8 *R*	56	3 *R*

[a]Isolated pure products after column chromatography; [b]Enantiomeric excess (ee) determined by GC analysis (FS-Cyclodex beta-I/P, 150 °C isothermal, 1 ml/min He, split 21:1, T_{det} = 230 °C, T_{inj} = 220 °C; retention time t_{minor} = 9.6 min, t_{major} = 10.1 min.); [c](FS-Cyclodex beta-I/P, 160 °C isothermal, 1 ml/min He, split 21:1, T_{det} = 230 °C, T_{inj} = 220 °C; retention time t_{minor} = 29.2 min, t_{major} = 30.0 min.).

RESULTS AND DISCUSSION

The condensation of 2-naphthol (**1**), formaldehyde and chiral amines was performed in ethanol at 50°C whereupon the formaldehyde was applied as formalin (37% aq. solution) or as paraformaldehyde, methods **A** or **B**, respectively (Scheme 2). Compounds **6**-**10**, were used as chiral amines that are readily available and relatively inexpensive. The yields of 1,3-naphthoxazines **11**-**15** were slightly better due to the use of Method **B** with the exception of product **12** (Method **A** provided better results). With respect to all the other reaction conditions results obtained, both methods are equally efficient. Naphthoxazines **11**-**15** are colorless amorphous solids, which are not stable when standing for long periods at room temperature. It seems that the compounds **11**, **13** and **14** bearing the aromatic amino moiety are somewhat more stable. For longer periods of time oxazines can be stored in flasks in an inert atmosphere in the refrigerator.

The naphthoxazines synthesized were reduced with lithium aluminum hydride in tetrahydrofuran as a solvent providing the N-methyl aminobenzylnaphthols **16**-**20** in good yields (Scheme 3). Aminobenzylnapthols **16**-**19** were stable while standing at room temperature for a couple of days in contrast to compound **20** which decomposes fast within hours after purification by column chromatography. This might be the reason for the lower yield of **20**.

With the aminobenzylnaphthols in hand we performed additional reactions of diethylzinc to the aromatic aldehydes **21** and **22** to test the activity of compounds **16**-**20** (3 mol %) as precatalysts (ligands). In all the cases the ligands studied were active catalysts that provide the additional reaction in relatively good yields. However, the enantioselectivity observed was very low. In some cases there was no selectivity or selectivity in error in the range (0 to 2 or 3% ee). Only in the case of ligand **18** a moderate enantioselectivity of product **23** formation could be realized. Comparing these result with our previous studies [11] and literature data [3, 7, 18] it is clear that an efficient ligand of the presented structural type would need substitution at the CH$_2$-carbon atom next to the nitrogen.

CONCLUSIONS

Efficient synthesis of 1,3-naphthoxazines applying three component Betti-type condensation of 2-naphthol, formaldehyde and chiral amines was demonstrated. The lithium aluminum hydride reduction of the naphthoxazines obtained provides chiral aminobenzylnaphthols, which were tested as precatalysts (ligands) for enantioselective addition of diethylzinc to aldehydes realizing good yields of secondary alcohols with low to moderate enantioselectivity. The synthesis of the chiral naphthoxazines and aminobenzylnaphthols could be extended to the synthesis of a structurally diverse series of analogues, which is important as these compounds are expected to possess biological activity.

REFERENCES

1. M. Betti, *Gazz. Chim. Ital.* **30**, 310 (1900).
2. C. Cardellicchio, G. Ciccarella, F. Naso, E. Schingaro, F. Scordari, *Tetrahedron: Asymmetry* **9**, 3667 (1998).
3. C. Cardellicchio, G. Ciccarella, F. Naso, F. Perna, P. Tortorella, *Tetrahedron* **55**, 14685, (1999).
4. I. Szatmári, F. Fülöp, *Curr. Org. Synth.* **01**, 155 (2004).
5. C. Cardellicchio, M. A. M. Capozzi, F. Naso, *Tetrahedron: Asymmetry*, **21**, 507 (2010).
6. I. Szatmári, F. Fülöp, *Tetrahedron*, **69**, 1255 (2013).
7. G. Palmieri, G. *Tetrahedron: Asymmetry* **11**, 3361 (2000).
8. C. Cimarelli, A. Mazzanti, G. Palmieri, E. Volpini, *J. Org. Chem.* **66**, 4759 (2001).
9. C. Cimarelli, D. Fratoni, A. Mazzanti, G. Palmieri, *Tetrahedron: Asymmetry*, **22**, 591 (2011).
10. L. Cappannini, C. Cimarelli, S. Giuli, G. Palmieri, M. Petrini, *Tetrahedron: Asymmetry* **18**, 1022 (2007).
11. M. Marinova, K. Kostova, P. Tzvetkova, M. Tavlinova-Kirilova, A. Chimov, R. Nikolova, B. Shivachev, V. Dimitrov, *Tetrahedron: Asymmetry* **24**, 1453 (2013).
12. Y. Wang, X. Li, K. Ding, *Tetrahedron: Asymmetry* **13**, 1291 (2002).
13. E. Rajanarendar, D. Nagaraju, S. Ramakrishna, B. Kishore, *Indian J. Chem.* **53B**, 412 (2014).
14. S. Ganesan, N. Rajendran, S. Sundarakumar, A. Ganesan, B. Pemiah, *Synthesis* **45**, 1564 (2013).
15. D. Vaughan, A. B. Naidu, A. Jha, *Curr. Org. Synth.* **09**, 613 (2012).
16. S. A. Sadaphal, S. S. Sonar, B. B. Shingate, M. S. Shingare, *Green Chem. Lett. Rev.* **3**, 213 (2010).
17. H. R. Talele, A. V. Bedekar, *Org. Biomol. Chem.* **10**, 8579 (2012).
18. D.-X. Liu, L.-C. Zhang, Q. Wang, C.-S. Da, Z.-Q. Xin, R. Wang, M. C. K. Choi, A. S. C. Chan, *Org. Lett.* **3**, 2733 (2001).

ТРИ КОМПОНЕНТНА КОНДЕНЗАЦИЯ ОТ БЕТИ ТИП – ЕФЕКТИВЕН ИНСТРУМЕНТ ЗА СИНТЕЗ НА ХИРАЛНИ НАФТОКСАЗИНИ И АМИНОБЕНЗИЛНАФТОЛИ ЗА ЕНАНТИОСЕЛЕКТИВНО ДИЕТИЛ ЦИНК ПРИСЪЕДИНЯВАНЕ КЪМ АЛДЕХИДИ

М. Тавлинова-Кирилова, М. Маринова, П. Ангелова, М. Каменова-Начева, К. Костова, В. Димитров

Институт по Органична химия с Център по Фитохимия, ул. Акад. Г. Бончев, бл.9, София 1113, България

(Резюме)

2-Нафтол, формалдехид и хирални амини са приложени в трикомпонентна кондензация от Бети тип за получаване на 1,3-нафтоксазини с отлични добиви. Последните са трансформирани лесно до хирални N-метил аминобензилнафтоли посредством реакция с литиевоалуминиев хидрид. Хиралните аминобензилнафтоли са активни катализатори (лиганди) за енантиоселективно диетил цинк присъединяване към алдехиди и получаване на вторични алкохоли с добри добиви с достигане на умерена енантиоселективност.

Modified multi-population genetic algorithms for parameter identification of yeast fed-batch cultivation

T. K. Pencheva*, M. K. Angelova

Institute of Biophysics and Biomedical Engineering, Bulgarian Academy of Sciences
105 Acad. Georgi Bonchev Str., 1113 Sofia, Bulgaria

In this investigation two new modifications of the standard multi-population genetic algorithm have been developed. Modifications differ from each other in the sequence of implementation of main genetic operators selection, crossover and mutation. The main idea of newly developed modifications is the operator selection to be executed between the operators crossover and mutation, no matter their order. Both modifications, together with the standard one multi-population genetic algorithm, have been investigated for parameter identification of yeast fed-batch cultivation. The obtained results have been compared and the newly proposed modifications have been shown to be as accurate as the standard multi-population genetic algorithms and proven to be even faster.

INTRODUCTION

Fermentation processes (FP) as representatives of biotechnological processes attract sustained interest due to the fact that they are an indigenous part of many industries such as industrial biotechnology, microbiology and the pharmaceutical industry. FP combine the dynamics of both biological and non-biological processes but their specific peculiarities are predominantly determined by the characteristics of live microorganisms. Since FP are complex dynamic systems with interdependent and time-varying process variables, their modeling, optimization and future high quality control is a real challenge. Adequate modeling of the non-linear FP significantly depends on the choice of a certain optimization procedure for model parameter identification. Conventional optimization methods usually fail in leading to a satisfactory solution [1]. This fact provokes the idea to apply stochastic algorithms, i.e. genetic algorithms (GA). GA are known as a quite promising stochastic global optimization method and have been widely applied to solve different complicated engineering problems [2-5]. Among a number of searching techniques, GA are representatives of the methods inspired by biological evolution and the principle of Darwin's theory of "survival of the fittest". GA are a feature of hard problem solving, tolerant to noise, easy to interface and hybridize. All these properties make GA convenient and more workable for different optimization problems, among them parameter identification and optimization of fermentation processes [6-9].

The standard simple genetic algorithm (SGA) [10] imitates the processes that occur in nature and searches for a global optimum solution using three main genetic operators implementing them in a sequence selection, crossover and mutation. SGA works with "chromosomes" (coded parameters) and starts with a selection of such chromosomes that represent better possible solutions according to their objective function values. Then a new offspring is formed applying the crossover operator. Finally, mutation is applied with deterministic probability, aiming to prevent the failing of all the solutions into a local optimum of the solved problem.

If there are many populations (called subpopulations), that evolve independently from each other, the single-population GA is converted to a multi-population GA (MpGA) [10]. This feature presents MpGA as more similar to nature than SGA. After the isolation time (a certain number of generations), part of the individuals "migrate" – they are distributed between the subpopulations. Similar to SGA, the standard MpGA as originally presented in [10], implements the three main genetic operators in a sequence selection, crossover and mutation. In this investigation this algorithm will be denoted as MpGA_SCM, coming from selection, crossover and mutation. According to [10, 11] the working principle of MpGA_SCM can be shortly presented as shown in Fig. 1.

To imitate the mechanics of natural selection and genetics is enshrined in the "philosophy" of GA. Thus one can make an analogy with the processes occurring in nature and to speculate that

---

* To whom all correspondence should be sent:
E-mail: tania.pencheva@biomed.bas.bg

for the probability mutation to come first and then crossover it is comparable that both processes occur in reverse order; or perform selection after crossover and mutation, no matter their order. Following this idea altogether five modifications of MpGA_SCM, differing in the sequence of implementation of the main genetic operators, have been developed [12, 13]. They all aim to improve the model accuracy and the algorithm convergence time for the purposes of parameter identification of fed-batch cultivation of *S. cerevisiae*. Table 1 lists the order of the steps to create a new population for five of the developed up to the moment modifications of MpGA_SCM.

As seen from Table 1, there are two modifications of MpGA_SCM that have not yet been considered, namely MpGA_CSM (crossover, selection, mutation) and MpGA_MSC (mutation, selection, crossover).

The aim of the present investigation is two modifications of MpGA, namely MpGA_CSM and MpGA_MSC, to be developed and to be applied for parameter identification of *S. cerevisiae* fed-batch cultivation. Moreover, the influence of the most important GA parameters, namely the generation gap and rates of crossover, mutation, insertion and migration are going to be investigated towards model accuracy, presented by the optimization criterion, and algorithms convergence time.

MATHEMATICAL MODEL OF *S. CEREVISIAE* FED-BATCH CULTIVATION

The cultivation of the yeast *S. cerevisiae* is performed in the Institute of Technical Chemistry – University of Hannover, Germany. The cultivation conditions and full process description details can be found in [1]. The fed-batch cultivation of *S. cerevisiae* considered here corresponds to the so called *mixed oxidative state* according to the functional state modeling approach [1].

```
1. [Start]
   Generate k random subpopulations each of them with n chromosomes
2. [Object function]
   Evaluate the object function of each chromosome n in the
   subpopulations
3. [Fitness function]
   Evaluate the fitness function of each chromosome n in the
   subpopulations
4. [New population]
   Create a new population by repeating following steps:
   4.1. [Selection]
        Select parent chromosomes from the subpopulation according to
        their fitness function
   4.2. [Crossover]
        Cross over the parents to form new offspring with a crossover
        probability
   4.3. [Mutation]
        Mutate new offspring at each locus with a mutation probability
5. [Accepting]
   Place new offspring in a new population
6. [Replace]
   Use new generated population for a further run of the algorithm
7. [Migration]
   Migration of individuals between the subpopulations after
   following isolation time
8. [Test]
   If the end condition is satisfied, stop and return the best
   solution in current population, else move to Loop step
9. [Loop]
   Go to Fitness step.
```

Fig. 1. Structure of the standard MpGA

Table 1. Sequence of algorithm steps implemented in MpGA

MpGA	Algorithm steps
MpGA_CMS (crossover, mutation, selection) [12]	1, 2, 3, *4.2, 4.3, 4.1*, 5, 6, 7, 8, 9
MpGA_SMC (selection, mutation, crossover) [12]	1, 2, 3, *4.1, 4.3, 4.2*, 5, 6, 7, 8, 9
MpGA_MCS (mutation, crossover, selection) [12]	1, 2, 3, *4.3, 4.2, 4.1*, 5, 6, 7, 8, 9
MpGA_SC (selection, crossover) [13]	1, 2, 3, *4.1, 4.2*, 5, 6, 7, 8, 9
MpGA_CS (crossover, selection) [13]	1, 2, 3, *4.2, 4.1*, 5, 6, 7, 8, 9

Particularly for this specific functional state, mathematical model of *S. cerevisiae* fed-batch cultivation is described as follows [1]:

$$\frac{dX}{dt} = \left(\mu_{2S} \frac{S}{S+k_S} + \mu_{2E} \frac{E}{E+k_E} \right) X - \frac{F}{V} X, \quad (1)$$

$$\frac{dS}{dt} = -\frac{\mu_{2S}}{Y_{SX}} \frac{S}{S+k_S} X + \frac{F}{V} (S_{in} - S), \quad (2)$$

$$\frac{dE}{dt} = -\frac{\mu_{2E}}{Y_{EX}} \frac{E}{E+k_E} X - \frac{F}{V} E, \quad (3)$$

$$\frac{dO_2}{dt} = \left(\frac{\mu_{2E}}{Y_{EX}} \frac{E}{E+k_E} Y_{OE} - \frac{\mu_{2S}}{Y_{SX}} \frac{S}{S+k_S} Y_{OS} \right) X + k_L^{O_2} a (O_2^* - O_2), \quad (4)$$

$$\frac{dV}{dt} = F, \quad (5)$$

where *X, S, E, O₂* are respectively the concentrations of biomass, [g/l], substrate (glucose), [g/l], ethanol, [g/l], and dissolved oxygen, [%]; O_2^* – dissolved oxygen saturation concentration, [%]; *F* – feeding rate, [l/h]; *V* – volume of the bioreactor, [l]; $k_L^{O_2} a$ – volumetric oxygen transfer coefficient, [1/h]; S_{in} – initial glucose concentration in the feeding solution, [g/l]; μ_{2S}, μ_{2E} – maximum growth rates of the substrate and ethanol, [1/h]; k_S, k_E – saturation constants of the substrate and ethanol, [g/l]; Y_{ij} – yield coefficients, [g/g]. All the functions are continuous and differentiable and all the model parameters fulfill the non-zero division requirement.

The mean square deviation between the model output and the experimental data obtained during cultivation has been chosen as an optimization criterion:

$$J = \sum (Y - Y*)^2 \rightarrow min, \qquad .. \quad (6)$$

where *Y* is the experimental data, *Y** – the model predicted data, *Y* = [*X, S, E, O₂*].

MODIFIED MPGA FOR PARAMETER IDENTIFICATION OF *S. CEREVISIAE* FED-BATCH CULTIVATION

This investigation aims to present the development of two modifications of MpGA in which the selection operator is performed between crossover and mutation, namely MpGA_CSM and MpGA_MSC. They are both going to be compared to the standard MpGA_SCM. Table 2 lists the order of the steps to create a new population only for the three kinds of MpGA considered here.

Many operators, functions, parameters and settings in GA can be improved or implemented specifically solving various problems [10]. In this study five of the main GA parameters, namely generation gap (GGAP), and rates of crossover

(XOVR), mutation (MUTR), insertion (INSR) and migration (MIGR) have been investigated.

Table 2. Sequence of algorithm steps implemented in MpGA modifications considered here

MpGA	Algorithm steps
MpGA-SCM	1, 2, 3, *4.1, 4.2, 4.3*, 5, 6, 7, 8, 9
MpGA-CSM	1, 2, 3, *4.2, 4.1, 4.3*, 5, 6, 7, 8, 9
MpGA-MSC	1, 2, 3, *4.3, 4.1, 4.2*, 5, 6, 7, 8, 9

Higher values of GGAP do not improve the GA performance, especially when aiming to find a faster solution. Usually mutation is applied randomly, with a low probability – typically varying between 0.01 and 0.1. Higher XOVR leads to quicker introduction of new strings into the population, while a low XOVR may cause stagnation due to the lower exploration rate. INSR determines how many of the produced population individuals are inserted into the new generation. Each MIGR characterized the number of exchanged individuals. According to some statements [14], the range of the main GA parameters investigated here are as follows: GGAP = {0.5, 0.67, 0.8, 0.9}, XOVR = {0.65, 0.75, 0.85, 0.95}, MUTR = {0.02, 0.04, 0.06, 0.08, 0.1}, INSR = {0.5, 0.6, 0.8, 0.9, 1} and MIGR = {0.1, 0.2, 0.4, 0.6, 0.8}. When one of the parameters considered here GGAP, XOVR, MUTR, INSR or MIGR is investigated according to the values mentioned above, the basic values for the other four parameters are chosen as follows: GGAP = 0.8, XOVR = 0.95, MUTR = 0.05, INSR = 0.95 and MIGR = 0.2, hereafter termed as referent points.

The values of the rest GA parameters, type of genetic operators in considered here and MpGA modifications are tuned according to [12]. The values of the GA parameters except the ones investigated here have been accepted as follows: number of variables (NVAR) = 9; precision of binary representation (PRECI) = 20; number of individuals (NIND) = 20; maximum number of generations (MAXGEN) = 100; number of subpopulations (SUBPOP) = 5; number of generation, after which migration takes place between subpopulations (MIGGEN) = 20. The following types of genetic operators are chosen: encoding – binary; reinsertion – fitness-based; crossover – double point; mutation – bit inversion; selection – roulette wheel selection; and, fitness function – linear ranking.

Following model (1)-(5) of *S. cerevisiae* fed-batch cultivation, nine model parameters have to be estimated altogether. All three kinds of MpGA have been consequently applied for the purposes of parameter identification of *S. cerevisiae* fed-batch

cultivation. All the computations are performed in a *Matlab 7* environment using the *Genetic Algorithm Toolbox* [15] on a PC Intel Pentium 4 (2.4 GHz) platform running *Windows XP*. All three kinds of GA are terminated when a certain number of generations (in this case 100) are fulfilled. The scalar relative error tolerance *RelTol* is set to $1e^{-4}$, while the vector of absolute error tolerances (all components) *AbsTol* is set to $1e^{-5}$.

The influence of the main GA parameters, namely GGAP, XOVR, MUTR, INSR and MIGR has been investigated for all three kinds of MpGA – two newly developed modifications MpGA_CSM and MpGA_MSC, as well as for the standard MpGA_SCM as a referent point. The investigation is performed in relation to model accuracy and convergence time. Tables 3 and 4 demonstrate the results obtained with respect to GGAP, XOVR, MUTR, INSR and MIGR. Because of the stochastic nature of GA, thirty runs have been performed for each GA parameter value and each algorithm in order for representative results to be achieved. Presented here are the average values obtained.

None of the three MpGA algorithms considered here are preferred towards time convergence. When investigating different GA operators, different MpGA modifications perform the best: i.e. MpGA_CSM is the fastest one at GGAP, XOVR and INSR, while MpGA_MSC is the "winner" at MUTR, and MpGA_SCM – at MIGR.

RESULTS AND DISCUSSION

As seen from Tables 3 and 4, the optimization criterion values obtained with three kinds of MpGA are very similar, varying between 0.0220 and 0.0222 which means less then 1% divergence. This result is very promising due to the fact that newly developed modifications do not cause a loss in accuracy. It is worth to note that with very few exceptions MpGA_CSM and MpGA_MSC lead to a decrease of the convergence time compared to the standard MpGA_SCM. As such, it can be speculated that processing the selection operator between crossover and mutation (no matter their order) needs much less computational time.

Table 3. Influence of GGAP, XOVR and MUTR on the model accuracy and convergence time

		MpGA_SCM		MpGA_CSM		MpGA_MSC	
		J	*t*, [s]	*J*	*t*, [s]	*J*	*t*, [s]
GGAP	0.5	0.0220	100.8910	**0.0221**	**97.6870**	0.0220	98.2970
	0.67	0.0221	112.1720	0.0221	128.8750	0.0221	121.8600
	0.8	0.0221	155.4680	0.0221	163.8590	0.0220	145.6710
	0.9	0.0220	170.2660	0.0221	165.6720	0.0220	166.0150
XOVR	0.65	0.0221	166.2500	**0.0221**	**143.4060**	0.0221	144.6570
	0.75	0.0221	151.1100	0.0222	149.6720	0.0220	153.6870
	0.85	0.0221	154.7660	0.0220	144.8750	0.0220	144.7340
	0.95	0.0221	166.7970	0.0221	149.7810	0.0221	149.7810
MUTR	0.02	0.0221	144.1880	0.0221	140.0000	**0.0221**	**122.0660**
	0.04	0.0221	140.4690	0.0220	145.8910	0.0220	150.4680
	0.06	0.0221	162.0940	0.0221	160.6870	0.0221	159.7660
	0.08	0.0221	156.0940	0.0221	155.9370	0.0221	142.4530
	0.1	0.0221	162.2970	0.0221	147.9060	0.0220	156.3280

Table 4. Influence of INSR and MIGR on the model accuracy and convergence time

		MpGA_SCM		MpGA_CSM		MpGA_MSC	
		J	*t*, [s]	*J*	*t*, [s]	*J*	*t*, [s]
INSR	0.5	0.0221	177.0310	0.0222	159.2970	0.0220	144.9530
	0.6	0.0221	174.2030	0.0221	146.2810	0.0220	149.7650
	0.8	0.0221	185.9530	0.0220	145.5160	0.0220	151.2810
	0.9	0.0221	157.1250	**0.0221**	**142.0310**	0.0220	150.4060
	1	0.0220	169.1410	0.0221	146.7820	0.0221	151.4060
MIGR	0.1	**0.0221**	**143.7190**	0.0221	146.4690	0.0220	147.2500
	0.2	0.0221	163.6880	0.0221	154.4530	0.0221	146.0320
	0.4	0.0221	174.0310	0.0222	149.6250	0.0221	146.6410
	0.6	0.0221	175.6250	0.0222	143.7960	0.0221	155.5310
	0.8	0.0221	181.2970	0.0221	157.4060	0.0220	147.7340

It should be noted that in this investigation the GGAP is the most sensitive of the five investigated parameters toward a convergence time. Considering three kinds of MpGA at GGAP = 0.8 (used as a referent value), there is no significant decrease of the convergence time. But, using GGAP = 0.5 instead of GGAP = 0.8 leads to the fastest performance of all the considered here three kinds of MpGA for all the values of the investigated parameters. The fastest algorithm is MpGA_CSM, while the other two are a bit more accurate. Comparing both MpGA modifications implemented at GGAP = 0.5 towards the standard one MpGA_SCM at GGAP = 0.8 (used as a referent value), MpGA_CSM appears as 1.59, while MpGA_MCS − as 1.58 times faster than MpGA_SCM. Thus, GGAP = 0.5 is chosen as the most appropriate one.

Considering XOVR, the biggest decrease in the convergence time is observed when using XOVR = 0.65 instead of XOVR = 0.95 (used as a referent value) in both MpGA modifications, respectively 14% when applying MpGA_CSM, and 13% for MpGA_MCS in a comparison to the standard MpGA_SCM at XOVR = 0.95. For these two out of three algorithms, XOVR = 0.65 leads to the fastest performances and as such this value is chosen as the most appropriate one.

Considering MUTR, using MUTR = 0.02 instead of MUTR = 0.04 or MUTR = 0.06 (closest to the used as a referent value MUTR = 0.05) leads to decrease of convergence time, respectively, of about 13% towards MUTR = 0.04 and about 25% towards MUTR = 0.06, both achieved when newly presented modification MpGA_MSC is applied and compared to the standard MpGA_SCM. In this case, two out of three algorithms lead to the fastest performances, and as such MUTR = 0.02 is chosen as the most appropriate value.

Respectively almost 16 and 11% of the convergence time can be saved using INSR = 0.9 instead of INSR = 1 (the closest to the used as a referent value INSR = 0.95) when applying MpGA_CSM and MpGA_MSC. In this case again two out of three algorithms, INSR = 0.9 leads to the fastest performances − the standard MpGA_SCM and MpGA_CSM, and as such this value is chosen as the most appropriate one.

Some very promising results are obtained when MIGR is investigated. Again about 10-11% decrease of convergence time is observed when using MIGR = 0.1 instead of MIGR = 0.2 (used as a referent value) in the case of presented MpGA modifications towards the standard MpGA_SCM at MIGR = 0.2. As it can be seen from Table 4, in this case the standard MpGA_SCM is the fastest one. For MIGR the value of 0.1 is chosen, although not all of the algorithms perform the best at this value, but the obtained results are very close to the best results achieved.

As a summary of the detailed analysis presented above, the following values of the GA parameters have been chosen as the most promising ones: GGAP = 0.5, XOVR = 0.65, MUTR = 0.02, INSR = 0.9 and MIGR = 0.1. Developed here are two MpGA modifications that lead to a decrease of the convergence time: MpGA_CSM is the fastest one for three of the GA parameters – GGAP, XOVR and INSR, while another modification of MpGA_MSC is the fastest one for MUTR. Only considering MIGR, the fastest algorithm is the standard one – MpGA_SCM, but two modifications are with very close results with about a 2% bigger convergence time. Finally, if one compares the fastest algorithm, which in this investigation is MpGA_CSM at GGAP = 0.5, to the slowest one, which in this investigation is MpGA_SCM at MIGR = 0.8, it is 1.90 times faster, yielding almost the highest model accuracy.

Distinguished as the fastest, the newly developed and presented algorithm, MpGA_CSM is applied for parameter identification of *S. cerevisiae* fed-batch cultivation. The identification procedure is performed with the values chosen due to five GA parameters investigated here and Table 5 lists the evaluated model parameters.

Fig. 2 shows the results from the experimental data and the model prediction, respectively, for biomass, ethanol, substrate and dissolved oxygen when MpGA_CSM is applied.

The results presented in Fig. 2 demonstrate the workability and efficacy of MpGA_CSM as one of the two newly elaborated modifications of MpGA presented here.

Table 5. Results from parameter identification when MpGA_CSM is applied.

Parameter	J	t	μ_{2S}	μ_{2E}	k_S	k_E	Y_{SX}	Y_{EX}	$k_L a$	Y_{OS}	Y_{OE}
Value	0.0221	97.5940	0.90	0.12	0.15	0.80	0.41	1.64	65.20	509.82	360.17

a) biomass

b) ethanol

c) substrate

d) dissolved oxygen
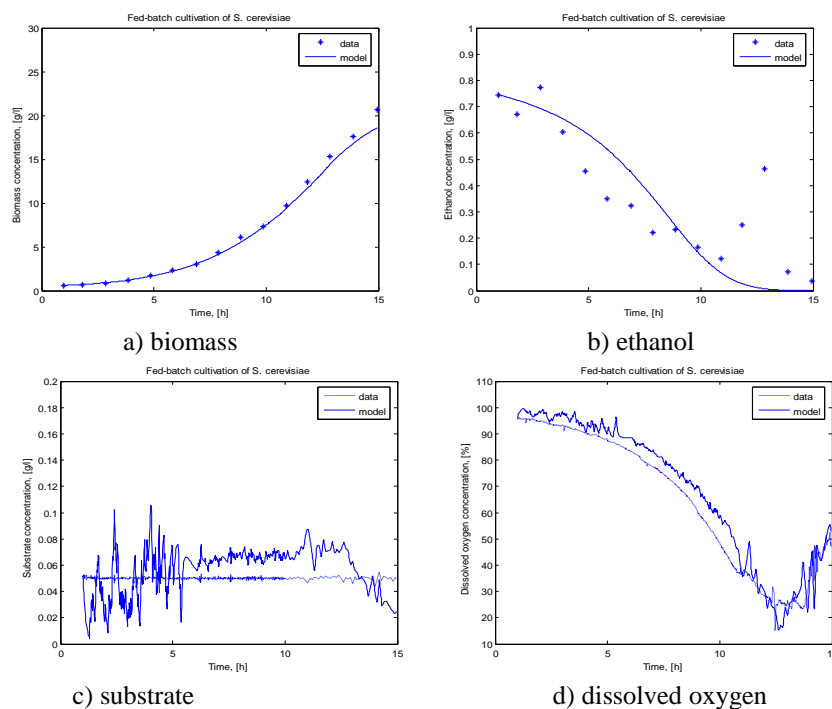
Fig. 2. Model prediction compared to experimental data when MpGA_CSM is applied.

CONCLUSIONS

In this investigation two newly developed modifications of the standard MpGA are presented. In both modifications, MpGA_CSM and MpGA_MSC, the operator selection is executed between crossover and mutation, no matter their order. The workability and efficacy of the newly elaborated modifications have been demonstrated, together with the standard MpGA_SCM, for the purposes of parameter identification of fed-batch cultivation of *S. cerevisiae*. The investigation of the influence of the most important GA parameters with respect to the convergence time and generation gap have been recognized as the most sensitive among the five parameters examined. About 45% of the convergence time can be saved using GGAP = 0.5 instead of the referent value of GGAP = 0.8 in both MpGA_CSM and MpGA_MSC without a loss in accuracy.

As a whole, newly proposed modifications of MpGA have been shown to be as accurate and effective as the standard one even proved to be faster.

It is noteworthy that the proposed two modifications of MpGA, as representatives of the global search optimization technique, might be considered convenient for model parameter identification in different branches of GA implementations.

REFERENCES

1. T. Pencheva, O. Roeva, I. Hristozov, Functional State Approach to Fermentation Processes Modelling, Prof. Marin Drinov Academic Publishing House, Sofia, 2006.
2. O. Cordon, F. Herrera, *Fuzzy Sets Syst.*, **118**, 235 (2001).
3. R. Kuo, C. Chen, Y. Hwang, *Fuzzy Sets Syst.*, **118**, 21 (2001).
4. G. Carrillo-Ureta, P. Roberts, V. Becerra, *IEEE Int. Symp. Intell. Control (2001)*, Mexico City, 2001, p. 391.
5. P. Vasant, N. Barsoum, *Eng. Appl. Artif. Intell.*, **22**, 767 (2009).
6. M. Ranganath, S. Renganathan, C. Gokulnath, *Bioprocess Eng.*, **21**, 123 (1999).
7. J. Adeyemo, A. Mehablia, *Sci. Res. and Essays*, **6**(7), 1464 (2011).
8. M. Angelova, P. Melo-Pinto, T. Pencheva, *WSEAS Trans. Syst.*, **11**(7), 256 (2012).
9. M. Angelova, T. Pencheva, *C. R. de l'Acad. Bulg. Scie.*, **65**(3), 299 (2012).
10. D. E. Goldberg, Genetic Algorithms in Search, Optimization and Machine Learning, Wiley, Massachusetts, (1989).
11. D. Gupta, S. Ghafir, *Int. J. Emerg. Techn. Adv. Eng.*, **2**(5), 56 (2012).
12. M. Angelova, S. Tzonkov, T. Pencheva, *Lect. Notes Comput. Scie.*, **6046**, 224 (2011).

13. M. Angelova, T. Pencheva, Improvement of Multi-population Genetic Algorithm Convergence Time, Chapter in: *Sabelfeld K. K., I. Dimov (Eds.)*, *Monte Carlo Methods and Applications*, 2013, 1-9, De Gruyter, Berlin, Germany, eBook ISBN: 9783110293586,

14. K. Schuegerl, K.-H. Bellgardt (Eds.), Bioreaction Engineering, Modeling and Control, Springer-Verlag, Berlin Heidelberg New York, 2000.

15. A. Chipperfield, P. Fleming, H. Pohlheim, C. Fonseca, Genetic Algorithm Toolbox for Use with MATLAB, User's guide, version 1.2., UK, 1994.

МОДИФИЦИРАНИ ГЕНЕТИЧНИ АЛГОРИТМИ ЗА ПАРАМЕТРИЧНА ИДЕНТИФИКАЦИЯ НА ПОЛУПЕРИОДИЧНА КУЛТИВАЦИЯ НА ДРОЖДИ

Т. К. Пенчева, М. К. Ангелова

Институт по биофизика и биомедицинско инженерство, Българска академия на науките
ул. Акад. Георги Бончев, бл. 105, София 1113, България

(Резюме)

В настоящото изследване са разработени две нови модификации на стандартните мултипопулационни генетични алгоритми. Модификациите се различават една от друга по реда на изпълнение на основните генетични оператори селекция, кръстосване и мутация. Основната идея на новоразработените модификации е операторът селекция да бъде изпълняван между операторите кръстосване и мутация, без значение от техния ред. Двете модификации, заедно със стандартния мултипопулационен генетичен алгоритъм, са изследвани при параметрична идентификация на полупериодична култивация на дрожди. Получените резултати са сравнени и новопредложените модификации са демонстрирани като също толкова точни, колкото и стандартния мултипопулационен генетичен алгоритъм, но с доказана по-добра сходимост.

In Vitro effects of pesticide exposure on Bovine liver catalase activity

H. Paluzar*[1], A. Sagiroglu[2]

[1]Trakya University, Arda Vocational High School, Edirne, Turkey
[2]Department of Chemistry, Faculty of Science, Trakya University, Edirne, Turkey

In this work we investigated the inhibitory effect of Deltamethrin, Dichlorvos, Malathion and Lambda-cyhalothrin on bovine liver catalase (CAT) activity. We observed that the inhibition of enzyme increased with increasing concentrations of the pesticides from 0 to 250 ppm. The Kinetics conformed to the Michaelis-Menten model and a Lineweaver-Burk graph of CAT was drawn. To identify the inhibition type, Vmax and Km were calculated at different concentrations of Deltamethrin, Dichlorvos, Malathion and Lambda-cyhalothrin. It was documented that dichlorvos and malathion inhibited CAT competitively, whereas deltamethrin and Lambda-cyhalothrin inhibition over CAT were non-competitive.

Keywords: deltamethrin; dichlorvos; lambda-cyhalothrin; malathion; catalase; inhibition; pesticide

INTRODUCTION

Catalase (CAT, EC 1.11.1.6) is an important antioxidant enzyme in organisms which can catalyze H_2O_2 to H_2O and O_2 to maintain the redox balance. Catalase has one of the highest turnover rates of all enzymes; one molecule of catalase can convert millions of molecules of hydrogen peroxide to water and oxygen [1]. The intake of pollutants might change the activity of CAT due to the co-effects of oxidative stress or damages on enzyme structure and function caused by direct binding [2].

Dichlorvos is a highly volatile organophosphate that is extensively used as an insecticide to control household pests, in public health and to protect stored products from insects. Additionally, dichlorvos damages the DNA of insects [3].

Deltamethrin is a pyrethroid and a broad-spectrum insecticide. Deltamethrin is registered for use on various crops including cotton, corn, cereals, soybeans and vegetables for pests such as mites, ants, weevils and beetles [4].

Malathion is an organophosphate parasympathomimetic which binds irreversibly to cholinesterase. Malathion is an insecticide of relatively low human toxicity. Malathion is widely used in agriculture, residential landscaping, public recreation areas and in public health pest control programs such as mosquito eradication [5].

Lambda-cyhalothrin is an insecticide that belongs to the pyrethroid chemical class of pesticides. It is a mixture of highly active isomers of cyhalothrine and is used to control a wide range of pests in a variety of applications [6].

In this study the inhibition of CAT by deltamethrin, dichlorvos, malathion and Lambda-cyhalothrin was observed.

EXPERIMENTAL

Catalase from bovine liver (lyophilized powder, ≥10,000 units/mg protein), deltamethrin, dichlorvos, malathion, lambda-cyhalothrin and all reagents and chemicals were purchased from Sigma-Aldrich and were prepared analytically.

CAT activity measurement

CAT activity was measured in accordance with the method of Aebi [7]. The principle of the assay is based on the determination of the rate constant (s^{-1}, k) of hydrogen peroxide decomposition by the CAT enzyme at 240nm.

Protein measurement

The protein concentration was determined using the method of Lowry et al. [8].

Effects of pesticides on enzyme activity

All pesticides were dissolved in ethyl alcohol. Stock pesticide solutions were arranged to match 0, 50, 100 and 250 ppm and then each of these was mixed with a 750 µl enzyme solution. The final volume of the mixture was 1 ml. The mixture was incubated at room temperature for 30 min and then the activities of CAT were measured.

* To whom all correspondence should be sent:
E-mail: hatice_paluzar@hotmail.com

RESULTS AND DISCUSSION

Inhibition type of deltamethrin to CAT

The activities of CAT were measured in the presence of different concentrations of *deltamethrin* (0, 50, 100 and 250 ppm) for different substrate concentrations of H_2O_2 (5, 10, 15, 20, 25 and 30 mM)(n=3). The activity of CAT decreased with increasing concentrations of *deltamethrin*. The Kinetics conformed to the Michaelis-Menten model and a Lineweaver-Burk graph of CAT was drawn by using the obtained results (Figure 1).

To identify the inhibition type, according to Figure 1, Vmax and Km were calculated at different concentrations of *deltamethrin* and are shown in

Table 1. From the Lineweaver-Burk graph, we determined that the Km values were close to each other but we found that the Vmax values decreased. Thus, we suggest that *deltamethrin* inhibited CAT non - competitively.

Inhibition type of lambda-cyhalothrin to CAT

The activities of CAT were measured in the presence of different concentrations of Lambda-cyhalothrin (0, 50, 100 and 250 ppm) for different substrate concentrations of H_2O_2 (5, 10, 15, 20, 25 and 30 mM)(n=3). The activity of CAT decreased with the increasing concentrations of lambda-cyhalothrin.

.
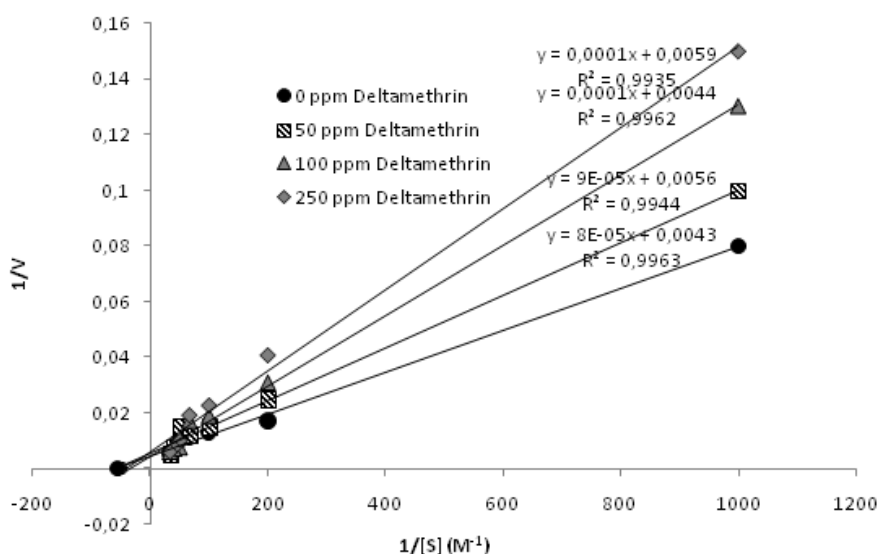
Fig 1. Lineweaver-Burk graph of CAT treated with deltamethrin.

Table 1. Effects of deltamethrin, lambda-cyhalothrin, dichlorvos and malathion on the kinetic parameters of CAT.

Concentrations of Pesticides	V_{max} (U/mg)	K_m (M H_2O_2)
0ppm Deltametrin	222.22	0.0181
50ppm Deltametrin	178.57	0.0161
100ppm Deltametrin	227.27	0.0227
250ppm Deltametrin	169.49	0.0169
0ppm Lambda-cyhalothrin	222.22	0.0181
50ppm Lambda-cyhalothrin	256.41	0.026
100ppm Lambda-cyhalothrin	238.09	0.0238
250ppm Lambda-cyhalothrin	181.81	0.036
0ppm Dichlorvos	222.22	0.0181
50ppm Dichlorvos	238.09	0.0238
100ppm Dichlorvos	250.00	0.05
250ppm Dichlorvos	285.71	0.0571
0ppm Malathion	222.22	0.0181
50ppm Malathion	250.00	0.025
100ppm Malathion	208.33	0.021
250ppm Malathion	227.27	0.045

The Kinetics conformed to the Michaelis-Menten model and a Lineweaver-Burk graph of CAT was drawn by using the obtained results (Figure 2).

To identify the inhibition type, according to Figure 2, Vmax and Km were calculated at different concentrations of lambda-cyhalothrin and are shown in Table 1. From the Lineweaver-Burk graph, we determined that the Km values are close to each other but we found decreased Vmax values. Thus, we suggest that lambda-cyhalothrin inhibited CAT non-competitively.

Inhibition type of dichlorvos to CAT

The activities of CAT were measured in the presence of different concentrations of dichlorvos (0,

50, 100 and 250 ppm) for different substrate concentrations of H_2O_2 (5, 10, 15, 20, 25 and 30mM)(n=3). The activity of CAT decreased with the increasing concentrations of dichlorvos. The Kinetics conformed to the Michaelis-Menten model and a Lineweaver-Burk graph of CAT was drawn by using the obtained results (Figure 3).

To identify the inhibition type, according to Figure 3, Vmax and Km were calculated at different concentrations of dichlorvos and are shown in Table 1. From the Lineweaver-Burk graph, we determined that the Vmax values are close to each other but we found increased Km values. Thus, we suggest that dichlorvos inhibits CAT competitively.
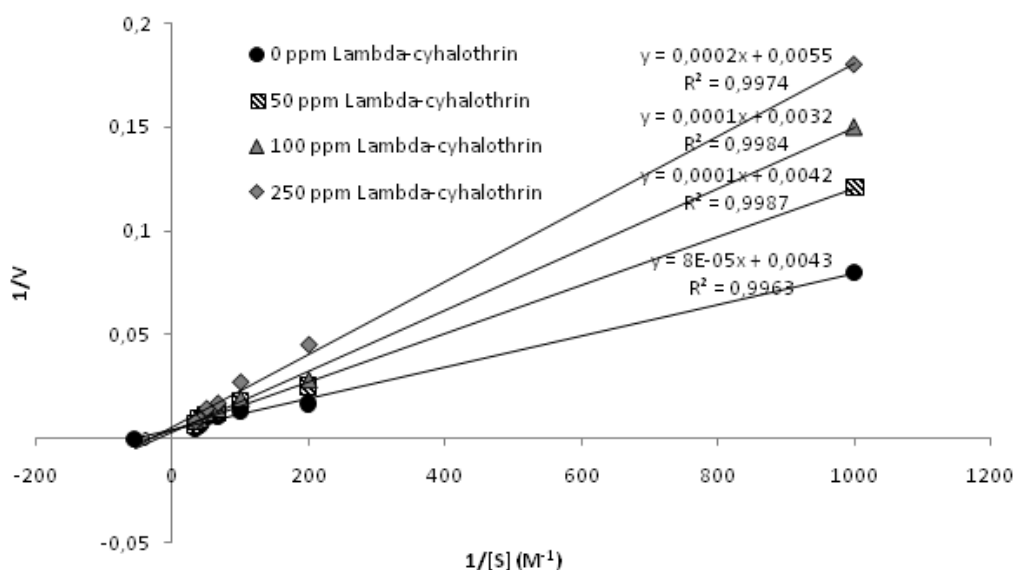
Fig 2. Lineweaver-Burk graph of CAT treated with lambda-cyhalothrin
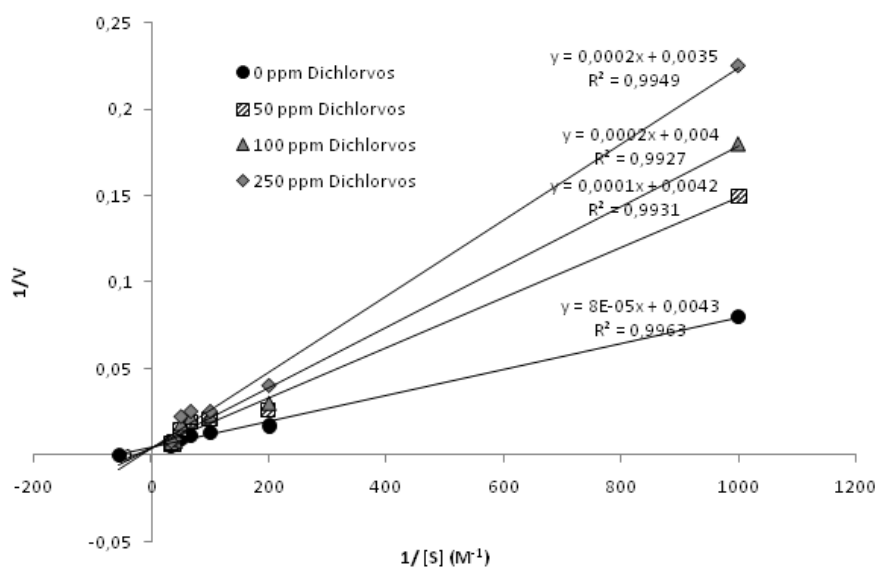
Fig 3. Lineweaver-Burk graph of CAT treated with dichlorvos
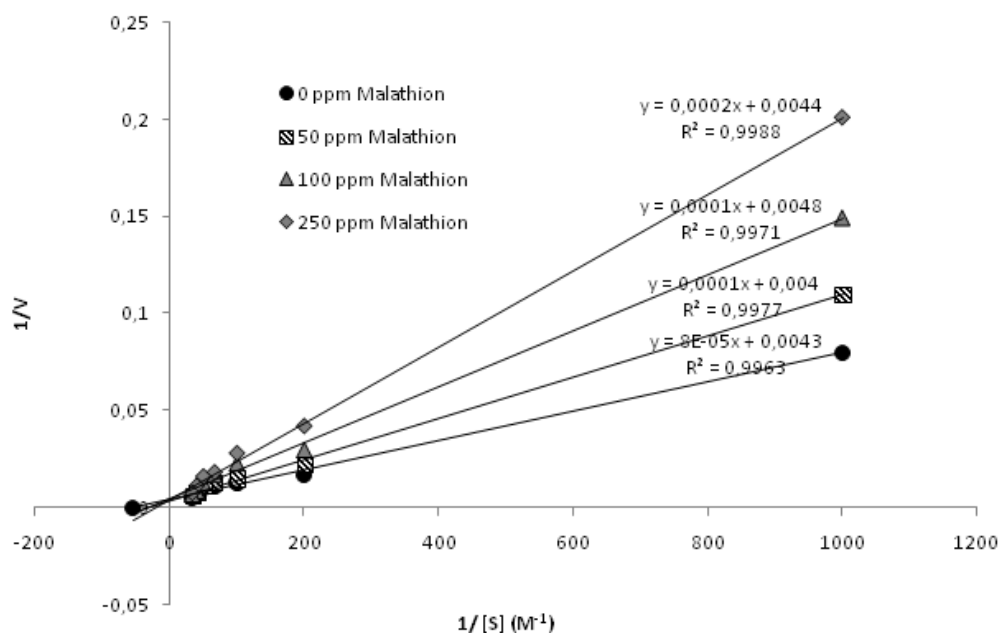
Fig 4. Lineweaver-Burk graph of CAT treated with malathion.

Inhibition type of malathion to CAT

The activities of CAT were measured in the presence of different concentrations of malathion (0, 50, 100 and 250 ppm) for different substrate concentrations of H_2O_2 (5, 10, 15, 20, 25 and 30 mM)(n=3). The activity of CAT decreased with increasing concentrations of malathion. The Kinetics conformed the Michaelis-Menten model and a Lineweaver-Burk graph of CAT was drawn by using the obtained results (Figure4).

To identify the inhibition type in accordance with Figure 4, Vmax and Km were calculated at different concentrations of malathion and are shown in Table 1. From the Lineweaver-Burk graph, we determined that the Vmax values are close to each other but we found increased Km values. Thus, we suggest that malathion inhibits CAT competitively.

The effects of different chemical substances, drugs, metal ions and anions on CAT have been investigated in many *in vitro* and *in vivo* studies, performed with various organisms.

T. Hamers et. al. observed that Dichlorvos at low concentrations inhibited acetylcholinesterase (AChE) competively [9]. M. A. Kamal observed malathion inhibited AChE non-competitively [10]. They reported similar results for AChE but there isn't any kinetic study for CAT inhibition by these pesticides. In addition to this, other studies also examined the inhibition of CAT by pesticides.

D. Julka et. al. [11] observed that treatment by dichlorvos resulted in significant decreases in the activities of the antioxidant enzymes SOD and CAT which were accompanied by a decrease in the values of lipid peroxidation. B. Mazmancı et. al. [12] and M. Berköz et. al. [13] have reported deltamethrin to cause a decrease in the activities of CAT, SOD and GPx.

E. Büyükgüzel [14] observed that treatment by malathion resulted in decreases of the activities of CAT and GPx. H. Fetoui et. al. [15] have reported the activities of CAT, SOD, GPx, glutathione reductase (GR) and glutathione-S-transferase (GST) were significantly decreased due to lambda-cyhalothrine exposure. We obtained similar results in the present study.

CONCLUSION

In this study we wanted to elucidate the kinetic parameters of H_2O_2 as a substrate and some pesticides as inhibitors, as well as the inhibition type. Kinetic studies were performed at very low concentrations of H_2O_2 and very short reaction times. The results showed that bovine liver catalases are inhibited by malathion, dichlorvos, lambda cyhalothrin and deltamethrin *in vitro*. It was shown that the catalytic degradation of H_2O_2 is inhibited competitively by malathion and dichlorvos but non-competitively by deltamethrin and lambda cyhalothrin.

REFERENCES

1. M. A. Ibrahim, A. H. M. Ghazy, H. M. M. Masoud, *Biochemistry and Biophysics Reports*, **4**, 411 (2015).
2. V .I. Lushchak, *Aquat. Toxicol*., **101**, 13(2011).
3. S. Patel, M. Bajpayee, A.K. Pandey, D. Parmar, A. Dhawan, *Toxicol. in vitro*. **21**, 1409 (2007).
4. S. Manna, D. Bhattacharyya, T.K. Mandal, S. Das, *Indian J. Pharmacol*., **37**, 160 (2005).
5. L. G. Costa, The Basic Science of Poisons, 7th ed.; Klaassen, C. D.,Ed.; McGraw Hill Medical: New York. 2008, p.883.
6. B. K. Cebeci, Z. Alım, Ş. Beydemir, *Turkish Journal of Chemistry*, **38**, 512 (2014).
7. H. Aebi, *Methods in Enzymology*, **105**,121 (1984).
8. O. H. Lowry, N .J. Rosebrough, N. J. Farra, R. J. Randall, *J Biol Chem*., **193**, 265 (1951).
9. T. Hamers, K. R. J. Molin, J.H. Koeman, A.J. Murk, *Toxicol Sci.*, **58**, 60 (2000).
10. M. A. Kamal, *Biochemistry And Molecular Biology Internationa*., **43**, 89 (1997).
11. D. Julka, R. Pal, K.D. Gill, *Experimental and Molecular Pathology*., **56**, 144 (1992).
12. B. Mazmancı, M.A. Mazmanci, A. Unyayar, S. Unyayar, F.O. Cekic, A. Guzel Deger, S. Yalin, U. Comelekoglu, *Food Chemistry*, **125,** 1037 (2011).
13. M. Berköz, S. Yalın, Ü. Çömelekoğlu, B. Mazmancı, M.A. Mazmancı, A. Ünyayar, P. Eroğlu, *Mersin Üni. Sağlık Bilimleri Enstitüsü Dergisi*, **3**, 1 (2010)**.**
14. E. Büyükgüzel**,** *J. Econ. Entomol*., **102,** 152 (2009)**.**
15. H. Fetoui, M. Makni, E. M. Garoui, N. Zeghal,Experimental and ToxicologicPathology, **62**, 593 (2010).

In vitro ЕФЕКТ НА ПЕСТИЦИДИ ВЪРХУ АКТИВНОСТТА НА КАТАЛАЗА ОТ ГОВЕЖДИ ЧЕРЕН ДРОБ

Х. Палузар*[1], А. Сагироглу[2]

[1]*Тракийски университет, Професионално висше училище "Арда", Одрин, Турция*
[2]*Департамент по химия, Научен факултет, Тракийски университет Одрин, Турция*

(Резюме)

В тази работа е изследван инхибиращия ефект на пестицидите делтаметрин, малатион, дихлорвос и ламбда-цихалотрин върху активността на каталаза (САТ), изолирана от говежди чер дроб. Забелязахме, че инхибирането на ензима нараства с нарастването на концентрациите на пестицидите от 0 до 250 ppm. Кинетиката е в съгласие с уравнението на Михаелис-Ментен, което е потвърдено в координатите на Lineweaver-Burk. Характерът на инхибирането е различен, като при дихлорвосът и малатионът са конкурентни инхибитори, а делтаметринът и ламбда-цихалотринът - неконкурентни.

Synthesis of 2-(substituted)-3*H*-benzimidazole-5-carboxylic acids and 2-(substituted)-3*H*-imidazo[4,5-b]pyridine-5-carboxylic acids: synthons for fluorescent Hx and *aza*-Hx amides

V.S. Satam[1], P.C. Patil[1], B. Babu[1], K.A. Brien[1], M. Gregory[1], M. Bowerman[1], J. Sweers[1],

A. Mepham[1], M. Lee[1,2]∗

[1]Department of Chemistry, Hope College, Holland, Michigan, USA;
[2]Department of Chemistry, Georgia State University, Atlanta, Georgia, USA

The syntheses of fifteen fluorescent 2-(substituted)benzimidazole-5- (Hx) and 2-(substituted)imidazopyridine-5- (*aza*-Hx) carboxylic acids are reported. These are key moieties of Hx- and *aza*-Hx amides, which bind DNA at specific sequences in the minor groove. Condensation of methyl 3, 4-diaminobenzoate **10a** or methyl 5,6-diaminopyridine-2-carboxylate **10b** with the appropriate aryl- or heteroarylaldehyde **9** produced the desired Hx (**7a-k**) and *aza*-Hx esters (**8l-o**) in 31-88% and 18-70% yields, respectively. Hydrolysis of esters **7a-k** and **8l-o** gave the corresponding Hx (**5a-k**) and *aza*-Hx acids (**6l-o**) in 66-93% and 64-85% yields, respectively. Hx acids **5d**, **5e**, **5g**, and **5k**, and *aza*-Hx acids **6m-o** are novel compounds.

Keywords: polyamides; fluorescence; benzimidazole; imidazopyridine; DNA binding; sequence specificity

INTRODUCTION

Pyrrole (Py)- and imidazole (Im)-containing analogs of distamycin (**1**, Figure 1) are polyamides (PAs) that bind in the minor-groove of DNA in a stacked fashion at specific DNA sequences[1]. These PAs, such as **2** (Figure 1), can potentially be designed to target specific sequences and modulate the expression of genes, including those associated with cancer cell growth [2-7]. Recently, our group demonstrated the usefulness of PAs by reporting a new class of compounds called Hx amides [8]. These amides (**3**, Figure 1) contain the fluorescent 2-(4-methoxyphenyl)benzimidazole or Hx moiety at the *N*-terminus. Mimicking the fluorescent and DNA binding properties of Hoechst, a stacked Hx motif behaves as a Py-Py unit; thus, a stacked Hx/PP unit recognizes two A/T base pairs [8a] and a stacked Hx/II unit recognizes CC/GG [8b]. The important feature of Hx amides is their ability to fluoresce which enables tracking of these molecules in cells and in animals [9]. The success of Hx amides has led to the design and synthesis of *aza*-Hx amides **4** (Figure 1), which contains a fluorescent 2-(4-methoxyphenyl)-3*H*-imidazo[4,5-b]pyridine (*aza*-Hx) moiety [10]. Our group has recently reported that *aza*-Hx mimics a Py-Im unit; thus, when stacked with Im-Py the the stacked dimer binds preferentially to CG/GC. *Aza*-Hx amide **4** can also be tracked in cells by means of fluorescence [10].

In our pursuit of Hx and *aza*-Hx amides, we have synthesized a variety of analogs with the intention of affecting their DNA binding properties. Hx analogs that contain substituents such as 4-fluorophenyl, 4-(*N*,*N*-dimethyl)phenyl, 4-methoxy-3-nitrophenyl, pyridin-4-yl, indol-3-yl, or 7-(*N*,*N*-diethylamino) coumarin-3-yl in place of 4-methoxyphenyl were synthesized to mimic a Py-Py unit. However, replacing 4-methoxyphenyl in Hx with 6-methoxypyridin-2-yl, 6-methoxypyridin-3-yl, furan-2-yl, or benzofuran-2-yl could potentially mimic an Im-Py unit. Furthermore, replacing 4-methoxyphenyl in *aza*-Hx with 6-methoxypyridin-2-yl, 6-methoxypyridin-3-yl, or furan-2-yl could potentially provide analogs that mimic an Im-Im unit. The synthesis of Hx and *aza*-Hx amides is challenging due to the susceptibility of *N*-methylpyrrole-2-carbonyl chloride to undergo polymerization [11], the instability of the polyamide amines [6-10,12] and the lack of access to key Hx acids (**5a-k**) and *aza*-Hx acids (**6l-o**). Table 1 depicts fifteen Hx and *aza*-Hx acids synthesized in this study. Hx acids **5a** [13,14], **5b** [14,15], **5c** [14,16], **5h**[14,17] and **5j** [14,18] were previously reported and are commercially available. Hx acids **5f** and **5i** are commercially available [14], and *aza*-Hx acid **6l** was preliminarily reported by our group [10] but no experimental or characterization data was published. The synthesis and characterization data for the novel Hx and *aza*-Hx acids (**5d**, **5e**, **5g**, **5k**, and **6n-o**) are reported herein, along with *aza*-Hx acid **6l**.
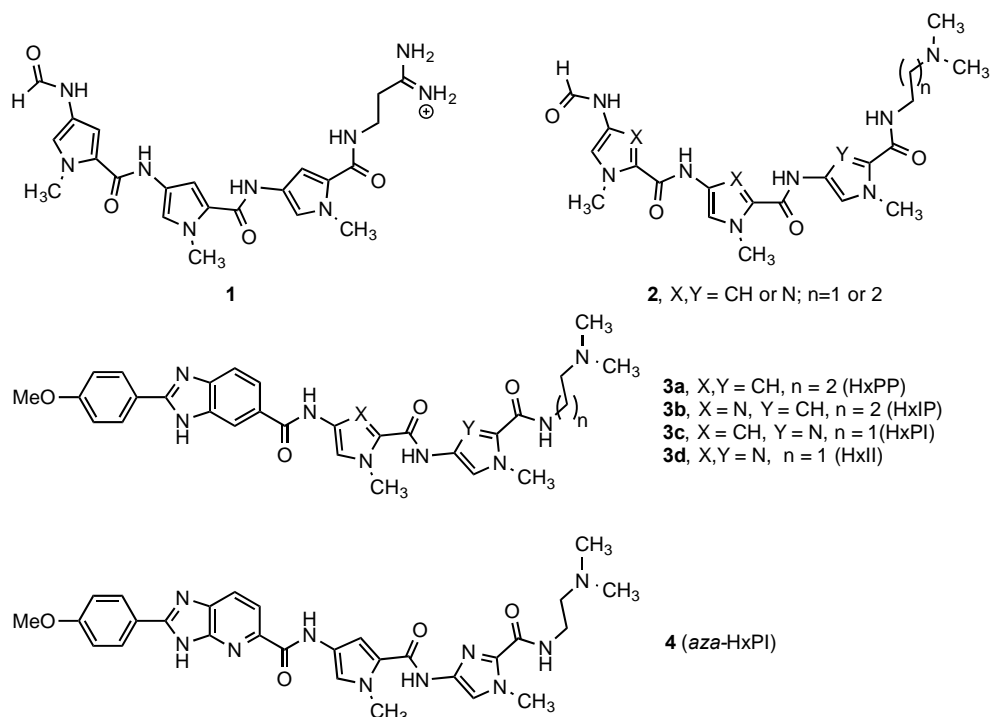
Fig. 1. Structures of distamycin **1**, *N*-formamido polyamide **2**, Hx amide **3,** and an *aza*-Hx amide **4 .**
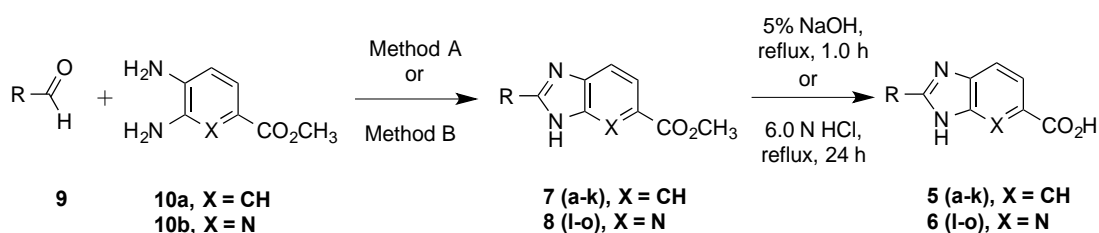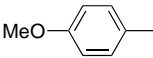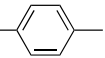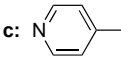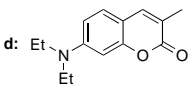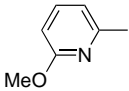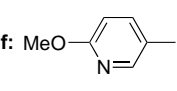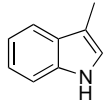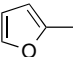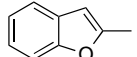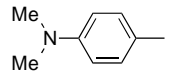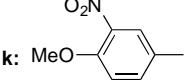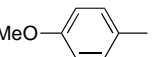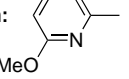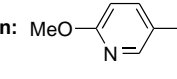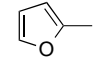
Scheme 1. Synthesis of Hx acids (**5a-k**) and *aza*-Hx acids (**6l-o**). Method A: nitrobenzene, 150-155 °C, 16 h; Method B: DMSO, 120-125 °C, 12 h.

RESULTS AND DISCUSSION

Hx acids (**5a-k**) and *aza*-Hx acids (**6l-o**) were prepared by hydrolysis of their corresponding esters **7a-k** and **8l-o**, respectively (Scheme1). Even though there are various methods for synthesizing benzimidazoles [19], the approach taken by our group is oxidative condensation of a substituted 1,2-diaminobenzene and a substituted benzaldehyde. In Method A, an appropriate aryl- or heteroarylaldehyde **9** (R groups are defined in Table 1) reacts with methyl 3,4-diaminobenzoate **10a** in nitrobenzene at 150-155 °C for 16 h to produce benzimidazole esters **7a-d** in modest to high yields (44-88%). However, using Method A, Hx esters **7e-7i**, were obtained in poor yields and methyl 5,6-diaminopyridine-2-carboxylate **10b** reacted with the aldehydes to generate diimino products. To

overcome these challenges, we discovered that reaction of methyl 3,4-diaminobenzoate **10a** or methyl 5,6-diaminopyridine-2-carboxylate **10b** with an appropriate aryl- or heteroarylaldehyde **9** in DMSO at 120-125 °C proceeded smoothly in 12 h to give the desired products. Esters **7e-k** and **8l-o** were produced in low to good yields (18-84%). All the esters except compound **7d** were hydrolyzed using 5% aqueous sodium hydroxide at reflux to afford the corresponding carboxylic acids **5** and **6** in good to high yields (64-93%). The coumarin compound **7d** was hydrolyzed using 6.0 M hydrochloric acid - because the lactone framework was susceptible to hydrolysis under basic conditions to obtain Hx acid **5d** at a 79% yield. All the compounds were characterized by ^{1}H-NMR, IR spectroscopy, and mass spectrometry but only those for the novel compounds and acid **6l** are reported.

Table 1. Percent yields of Hx (**7**) and *aza*-Hx esters (**8**), as well as Hx (**5**) and *aza*-Hx acids (**6**) prepared in this study

R =	7 (%)	5 (%)	R =	7 (%)	5 (%)	R =	7 (%)	5 (%)
a: MeO-C6H4-	88	93	b: F-C6H4-	47	87	c: pyridyl	69	89
d: diethylamino-coumarin	44	79	e: MeO-pyridyl	50	75	f: MeO-pyridyl	55	88
g: methylindole	46	91	h: furyl	31	81	i: benzofuran	51	88
j: Me2N-C6H4-	84	66	k: O2N, MeO-C6H3-	33	70			

R =	8 (%)	6 (%)	R =	8 (%)	6 (%)	R =	8 (%)	6 (%)
l: MeO-C6H4-	61	81	m: MeO-pyridyl	49	83	n: MeO-pyridyl	70	85
o: furyl	18	64						

EXPERIMENTAL

The solvents and reagents were purchased from Aldrich or Fisher and were used without further purification. The Melting points (Mp) were determined using a Mel-temp instrument and uncorrected. Infrared spectra were recorded on either a Midac FT-IR or Bruker Alpha-P spectrophotometer. ^{1}H-NMR spectra were obtained using a Bruker AVANCE III 400 MHz instrument with TMS as the internal standard. High-resolution mass spectra (HRMS) and low-resolution mass spectra (LRMS) were measured in the Mass Spectrometry Laboratory at the University of South Carolina, Columbia, USA.

Method A: Synthesis of methyl 2-(substituted)-3H-benzimidazole-5-carboxylates (7a-d)

Methyl 3,4-diaminobenzoate **10a** (3.0 mmol) and the appropriate aryl- or heteroarylaldehyde **9** (3.0 mmol) were dissolved in nitrobenzene (4.0 ml). The reaction mixture was heated at 150-155°C for 16 h. The reaction mixture was cooled to room temperature, the solvent was removed under reduced pressure and the crude product was purified by silica gel column chromatography. Compounds **7b** and **7d** precipitated upon cooling the reaction mixture. The products were filtered, washed with toluene followed by hexane and dried under vacuum at 45°C. The esters were directly hydrolyzed to obtain the corresponding carboxylic acids.**7a**: Pale brown solid

(0.80 g); Mp 210-212°C.**7b**: White solid (0.37 g); Mp 196-200°C.**7c**: White solid (0.50 g); Mp 204-207°C.

Methyl 2-(7-(diethylamino)-2H-coumarin-3-yl)-3H-benzimidazole-5-carboxylate (**7d**): Yellow solid (0.35g, 44%); Mp >210°C; R$_f$ 0.58 [ethyl acetate:hexane(5:5)]; IR (KBr): 3400, 2980, 2856, 1709, 1612, 1580, 1523, 1426, 1348, 1293, 1229, 1129, 777, 744, 689cm^{-1}. ^{1}H-NMR (CDCl$_3$): δ 11.41 (s br, 1H,), 8.95 (d, *J*=4.0 Hz, 1H), 8.35 (m, 1H), 8.00 (dd, *J*=4.0 Hz, 8.0 Hz, 1H), 7.50 (m, 2H), 6.70 (dd, *J*=4.0 Hz, 8.0 Hz, 1H), 6.57 (s, 1H), 3.95 (s, 3H), 3.48 (q, *J*=8.0 Hz, 4H), 1.26 (t, *J*=8.0 Hz, 6H); LRMS: (EI) *m/z* 391 (M$^+$, 100%).

Method B: Synthesis of methyl 2-(substituted)-3H-benzimidazole-5-carboxylates (7e-k) and methyl 2-(substituted)-3H-imidazo[4,5-b]pyridine-5-carboxylates (8l-o)

Methyl 3,4-diaminobenzoate **10a** or methyl 5,6-diaminopyridine-2-carboxylate **10b** (3.0 mmol) and the appropriate aryl- or heteroarylaldehyde **9** (3.0 mmol) were dissolved in DMSO (4.0 ml). The reaction mixture was heated at 120-125°C for 12 h. The removal of the solvent under reduced pressure was followed by purification of the residue by silica gel column chromatography yielding esters **7e-k** and **8l-o**, which were directly hydrolyzed to obtain the corresponding carboxylic acids. **7f**: White solid (0.69 g); Mp 198-202°C. **7h**: White solid (0.45 g);

Mp 129-131°C.**7i**: Yellow solid (0.45 g); Mp>210°C. **7j**: White solid (0.60 g); Mp 198-202°C.

Methyl 2-(6-methoxypyridin-2-yl)-3H-benzimidazole-5-carboxylate(**7e**): White solid (0.43 g); Mp200-204°C; R$_f$ 0.44 [ethyl acetate:hexane (4.5:5.5)]; IR (KBr): 3385, 3041, 2956, 2860, 1694, 1599, 1573, 1535, 1471, 1430, 1408, 1319, 1290, 1227, 1152, 1028, 883, 774, 665cm^{-1}; ^{1}H-NMR: (CDCl$_3$) δ 8.30 (s, 1H), 7.93 (d, *J*=8.0Hz, 1H), 7.90 (dd, *J*=4.0Hz, 8.0Hz, 1H), 7.62 (m, 1H), 7.57 (d, *J*=8.0Hz, 1H), 6.74 (d, *J*=8.0Hz, 1H), 3.89 (s, 3H), 3.85 (s, 3H); LRMS: (EI) *m/z* 283 (M$^+$, 100%).

Methyl 2-(indol-3-yl)-3H-benzimidazole-5-carboxylate (**7g**): Off-white solid (0.56 g, 46%); Mp 238-242°C; R$_f$ 0.62 [methanol:chloroform (2:8)];IR (KBr): 3264, 3224, 3198, 3119, 2953, 2948, 1684, 1621, 1590, 1573, 1500, 1458, 1388, 1312, 1182, 1087, 1036, 880, 772, 692 cm^{-1};^{1}H-NMR (DMSO-d$_6$): δ 12.86 (s, 1H), 11.75 (s, 1H), 8.49 (d, *J*=8.0Hz, 1H), 8.20 (s, 1H), 8.13 (s, 1H), 7.81 (d, *J*=8.0Hz, 1H), 7.62 (d, *J*=8.0Hz, 1H), 7.52 (d, *J*=4.0Hz, 1H), 7.23 (d, *J*=1.5Hz, 2H), 3.88 (s, 3H); LRMS: (EI) *m/z* 291 (M$^+$, 100%).

Methyl 2-(3-nitro-4-methoxyphenyl)-3H-benzimidazole-6-carboxylate (**7k**): White solid (0.30 g); Mp 185-189°C; R$_f$ 0.27[ethyl acetate:hexane (1:1)]; IR (KBr): 1713, 1621, 1530, 1449, 1433, 1350, 1334, 1274, 1265, 1233, 1186, 1162, 1119, 1085, 1069, 1012, 973, 827 cm^{-1};^{1}H-NMR(DMSO-d$_6$): δ13.40 (s, 1H), 8.70 (d, *J*=2.0Hz, 1H), 8.47 (dd, *J*=4.0Hz, 8.0Hz, 1H), 8.18 (d, *J*=12.0Hz, 1H), 7.86 (d, *J*=8.0Hz, 1H), 7.70 (s, 1H), 7.61 (d, *J*=12.0Hz, 1H), 4.03 (s, 3H), 3.88 (s, 3H); LRMS: (EI) *m/z* 327 (M$^+$, 100%); HRMS: calc. for *m/z* C$_{16}$H$_{13}$N$_3$O$_5$327.0855, found 327.0860.

Methyl 2-(4-methoxyphenyl)-3H-imidazo[4,5-b]pyridine-5-carboxylate (**8l**): White solid (0.52 g); Mp 238-241°C; R$_f$ 0.45 [ethyl acetate:hexane (4:6)]; IR (KBr): 3047, 3006, 2949, 1728, 1717, 1607, 1494, 1461, 1443, 1413, 1397, 1279, 1028, 947, 838, 788, 740, 641 cm^{-1}; ^{1}H-NMR (DMSO-d$_6$): δ 13.87 (s, 1H), 8.20 (d, *J*=8.0Hz, 2H), 8.08 (d, *J*=8.0Hz, 1H), 7.97 (d, *J*=8.0Hz, 1H), 7.16 (d, *J*=8.0Hz, 2H), 3.90 (s, 3H), 3.86 (s, 3H); LRMS: (EI) *m/z* 283 (M$^+$, 100%).

Methyl 2-(6-methoxypyridin-2-yl)-3H-imidazo[4,5-b]pyridine-5-carboxylate (**8m**):White solid (0.42 g); Mp 204-206°C; R$_f$ 0.49 [methanol:chloroform (0.5:9.5)]; IR (KBr): 3040, 2920, 2856, 1719, 1571, 1473, 1394, 1272, 1220, 1122, 1027, 821, 763 cm^{-1}; ^{1}H-NMR (CDCl$_3$): δ 10.81 (s, 1H), 8.15 (d, 1H), 8.00 (dd, *J*=4.0Hz, 8.0Hz, 1H), 7.75 (d, *J*=8.0Hz, 1H), 7.73 (d, *J*=8.0Hz, 1H), 6.88 (dd, *J*=4.0Hz, 8.0Hz, 1H), 4.01 (s, 3H), 3.99 (s, 3H); LRMS: (EI) *m/z* 284 (M$^+$, 40%).

Methyl 2-(6-methoxypyridin-3-yl)-3H-imidazo[4,5-b]pyridine-5-carboxylate (**8n**): White solid (0.64 g); Mp>260 °C; R$_f$ 0.41 [ethyl acetate:hexane (4:6)]; IR (KBr): 3050, 2948, 2870, 1720, 1601, 1475, 1401, 1360, 1274, 1228, 1132, 1019, 832, 761, 666 cm^{-1};^{1}H-NMR(DMSO-d6): δ 13.93 (s, 1H); 9.09 (d, *J*=4.0Hz, 1H), 8.53 (dd, *J*=4.0Hz, 12.0Hz, 1H), 8.19 (d, *J*=8.0Hz, 1H), 8.05 (d, *J*=8.0Hz, 1H), 7.11 (d, *J*=12.0Hz, 1H), 4.02 (s, 3H), 3.97 (s, 3H); LRMS: (EI) *m/z* 284 (M$^+$, 100%).

Methyl 2-(furan-2-yl)-3H-imidazo[4,5-b]pyridine-5-carboxylate (**8o**):Light brown solid (0.10 g); Mp 204-207°C (dec); R$_f$0.5 [methanol:chloroform (2.5:7.5)];IR (KBr): 3040, 2981, 2926, 2883, 1763, 1716, 1603, 1574, 1519, 1504, 1489, 1475, 1412, 1391, 1276, 1107, 1017, 960, 884, 757, 745 cm^{-1}; ^{1}H-NMR (CDCl$_3$): δ 10.12 (s br, 1H), 8.18 (d, *J*=12.0Hz, 1H), 8.12 (d, *J*=8.0Hz, 1H), 7.66 (d, *J*=2.0Hz, 1H), 7.36 (d, *J*=4.0Hz, 1H), 6.67 (dd, *J*=4.0Hz, 1H), 4.02 (s, 3H); LRMS: (EI) *m/z* 243 (M$^+$, 100%).

Synthesis of 2-(substituted)-3H-benzo[d]imidazole-5-carboxylic acids (**5a-c, e-k**) and 2-(substituted)-3H-imidazo[4,5-b]pyridine-5-carboxylic acids(**6l-o**).

The appropriate Hx ester (**7a-c**, 7**e-k**, and **8l-o**) (2.0 mmol) was added to an aqueous solution of sodium hydroxide (5%, 10 ml) and the reaction mixture was heated to reflux for 1.0 h. The reaction mixture was cooled to ambient temperature and acidified to pH of 3-4 with concentrated hydrochloric acid. The precipitate was filtered, washed with water and dried under vacuum at 50°C.**5a**: Tan solid (1.10 g); Mp 253°C [13,14]. **5b**: White solid (0.41 g); Mp 204-208°C [14,15]. **5c:** White solid (0.42 g); Mp >250°C [14,16]. **5f**: White solid (0.42 g); Mp >210°C [14]. **5h**: Off-white solid (0.44 g); Mp 245°C [14,17]. **5i**: White solid (0.42 g); Mp 201-205°C [14]. **5j**: Off-white solid (0.38 g); Mp 220-222°C [14,18].

2-(6-Methoxypyridin-2-yl)-3H-benzimidazole-5-carboxylic acid (**5e**): White solid (0.36 g); Mp 157-159°C; R$_f$ 0.28 [ethyl acetate:hexane (4:6)]; IR (KBr): 3082, 2984, 2949, 1691, 1599, 1536, 1474, 1409, 1328, 1296, 1272, 1243, 1152, 1120, 1073, 1028, 769, 678, 617 cm^{-1}; ^{1}H-NMR (DMSO-d6): δ 13.00 (s br, 1H), 8.27 (s, 1H), 7.93 (m, 3H), 7.72 (s, 1H), 6.98 (d, *J*=4.0Hz, 1H), 4.10 (s, 3H); LRMS: (EI) *m/z* 269 (M$^+$, 100%); HRMS: calc. for *m/z* C$_{14}$H$_{11}$N$_3$O$_3$ 269.0800, found 269.0792.

2-(Indolyl-3-yl)-3H-benzimidazole-5-carboxylic acid (**5g**): Light orange solid (0.55 g); Mp 250-252°C(dec); R$_f$ 0.25 [methanol:chloroform (2:8)];IR (KBr): 3275, 3184, 3113, 3065, 1630,

1587, 1557, 1499, 1446, 1373, 1312, 1226, 1178, 1086, 745, 678 cm^{-1};^{1}H-NMR (DMSO-d6): δ 12.72 (s, 1H), 11.73 (s, 1H), 8.51 (d, *J*=4.0Hz, 1H), 8.21 (s, 1H), 8.10 (s, 1H), 7.78 (d, *J*=8.0Hz, 1H), 7.49 (d, *J*=4.0Hz, 2H), 7.20 (m, 3H); LRMS: (EI) *m/z* 277 (M$^+$, 100%); HRMS: calc. for *m/z* C$_{16}$H$_{11}$N$_3$O$_2$ 277.0851, found 277.0854.

2-(3-Nitro-4-methoxyphenyl)-3H-benzimidazole-6-carboxylic acid (**5k**): Light yellow solid (0.20 g); Mp >250°C; R$_f$ 0.20 [methanol:chloroform (0.5:9.5)]; IR (KBr): 1706, 1695, 1685, 1629, 1530, 1509, 1484, 1426, 1387, 1349, 1335, 1294, 1214, 1126, 1091, 1060, 984, 890 cm^{-1}; ^{1}H-NMR (DMSO-d6): δ 8.80 (s, 1H), 8.61 (d, *J*=12.0Hz, 1H), 8.20 (s, 1H), 7.87 (d, *J*=8.0 Hz, 1H), 7.68 (d, *J*=12.0Hz, 1H), 7.62 (d, *J*=8.0Hz, 1H), 4.03 (s, 3H); LRMS: (ES$^+$, TOF) *m/z* 314 (M+H$^+$, 100%); HRMS: calc. for *m/z* C$_{16}$H$_{13}$N$_3$O$_5$ 314.0777, found 314.0781.

2-(4-Methoxyphenyl)-3H-imidazo[4,5-b]pyridine-5-carboxylic acid(**6l**): White solid (0.38 g); Mp >250°C; R$_f$ 0.4 [methanol:chloroform (0.5:9.5)]; IR (KBr): 3065, 2961, 2836, 1706, 1607, 1575, 1492, 1441, 1397, 1363, 1250, 1176, 1024, 829, 763, 692, 675 cm^{-1}; ^{1}H-NMR (DMSO-d6): δ 8.22 (d, *J*=8.0Hz, 2H), 8.05 (d, *J*=8.0Hz, 1H), 7.97 (d, *J*=8.0Hz, 1H), 7.15 (d, *J*=8.0Hz, 2H), 3.86 (s, 3H);LRMS: (ES$^+$, TOF) *m/z* 270 (M+H$^+$ 100%); HRMS: calc. for *m/z* C$_{14}$H$_{11}$N$_3$O$_3$ 270.0878, found 270.0870.

2-(6-Methoxypyridin-2-yl)-3H-imidazo[4,5-b]pyridine-5-carboxylic acid (**6m**): White solid (0.30 g); Mp >250°C (dec); R$_f$0.23 [methanol:chloroform (1:9)]; IR (KBr): 3200, 3050, 2982, 2943, 1763, 1714, 1603, 1573, 1557, 1504, 1475, 1463, 1412, 1366, 1351, 1321, 1305, 1269, 1204, 1097, 1074, 895, 762, 735, 669 cm^{-1}; ^{1}H-NMR (DMSO-d6): δ 8.17 (d, *J*=8.0Hz, 1H), 8.04 (d, *J*=12.0Hz, 1H), 7.99 (d, *J*=8.0Hz, 1H), 7.94 (t, *J*=8.0Hz, 1H), 7.02 (d, *J*=8.0Hz, 1H), 4.09 (s, 3H);LRMS: (EI) *m/z* 270 (M$^+$, 67%); HRMS: calc. for *m/z* C$_{13}$H$_{10}$N$_4$O$_3$ 270.0753, found 270.0757.

2-(6-Methoxypyridin-3-yl)-3H-imidazo[4,5-b]pyridine-5-carboxylic acid (**6n**): White solid (0.40g); Mp 251-253°C; R$_f$ 0.38 [methanol:chloroform (0.5:9.5)]; IR (KBr): 3050, 2946, 1602, 1466, 1373, 1283, 1019, 767, 664 cm^{-1}; ^{1}H-NMR (DMSO-d6, two drops D$_2$O): δ 8.95 (s, 1H), 8.42 (d, *J*=8.0Hz, 1H), 7.97 (d, *J*=8.0Hz, 1H), 7.91 (d, *J*=8.0Hz, 1H), 7.02 (d, *J*=8.0Hz, 1H), 3.92 (s, 3H); LRMS: (EI)*m/z* 270 (M$^+$ 100%); HRMS calc. for *m/z* C$_{13}$H$_{10}$N$_4$O$_3$ 270.0753, found 270.0754.

2-(Furan-2-yl)-3H-imidazo[4,5-b]pyridine-5-carboxylic acid (**6o**): Light brown solid (0.24 g); Mp 245-247°C (dec); R$_f$ 0.12 [methanol:chloroform

(2.5:7.5)]; IR (KBr): 3250, 3110, 3069, 1702, 1620, 1523, 1471, 1399, 1294, 1254, 1230, 1172, 1081, 1022, 890, 797, 699, 679, 634 cm^{-1}; ^{1}H-NMR (CD$_3$OD): δ 8.05 (d, *J*=8.0Hz, 1H), 7.97 (d, *J*=8.0Hz, 1H), 7.77 (d, *J*=2.0Hz, 1H), 7.30 (d, *J*=4.0Hz, 1H), 6.65 (dd, *J*=4.0Hz, 1H); LRMS: (EI) *m/z* 229 (M$^+$ 100%); HRMS: calc. for *m/z* C$_{12}$H$_7$N$_3$O$_3$ 229.0487, found 229.0483.

2-(7-(Diethylamino)-2H-coumarin-3-yl)-benzoimidazole-5-carboxylic acid (**5d**):Hx ester**7d** (782 mg, 2.0 mmol) was added to a solution of hydrochloric acid (6.0 M, 15 ml) and the reaction mixture was heated to reflux for 24 h. The reaction mixture was cooled to 10-15°C and neutralized using 10% aqueous sodium hydroxide solution. The precipitate obtained was filtered, washed with water and dried. The crude product was purified by silica gel column chromatography using 10% methanol in chloroform as the eluent system to afford the desired Hx acid **5d** as a yellow solid (597 mg); Mp >210°C; R$_f$ 0.52 [methanol:chloroform (2:8)]; IR (KBr): 3294, 2970, 2860, 1701, 1619, 1586, 1526, 1432, 1353, 1295, 1233, 1182, 1134, 1073, 848, 799, 744 cm^{-1};^{1}H-NMR (DMSO-d6): δ 12.70 (s, 1H), 8.98 (s, 2H), 8.25 (s, 1H), 7.84 (d, *J*=12.0Hz, 1H), 7.75 (d, *J*=8.0Hz, 1H), 7.68 (d, *J*=8.0Hz, 1H), 6.85 (dd, *J*=4.0Hz, 8.0Hz, 1H), 6.70 (s, 1H), 3.52 (q, *J*=8.0Hz, 4H), 1.18 (t, *J*=8.0Hz, 6H); LRMS: (ES$^+$, TOF) *m/z* 378 (M+H$^+$, 100%); HRMS: calc. for *m/z* C$_{21}$H$_{19}$N$_3$O$_4$ 378.1454, found 378.1447.

REFERENCES

1. (a) S. N. Mitra, M. C. Wahl, M. Sundaralingam, *Acta Crystallogr. Sect. D,* **55**, 602 (1999); (b) J. G. Pelton, D. E. Wemmer, *Proc. Natl. Acad. Sci.*, **86**, 5723 (1989); (c) J. G. Pelton, D. E Wemmer, *J. Am. Chem. Soc.*, **112**, 1393 (1990).

2. (a) C. J. Chou, M. E. Farkas, S. M. Tsai, D. Alvarez, P. B. Dervan, J. M. Gottesfeld, *Mol. Cancer Ther.*, **7**, 769 (2008); (b) B. H. Geierstanger, M. Mrksich, P. B. Dervan, D. E. Wemmer, *Nat. Struct. Biol.*, **3**, 321 (1996); (c) D. M. Chenoweth, P. B. Dervan, *Proc. Natl. Acad. Sci.*, **106**, 13175 (2009).

3. (a) D. Hochhauser, M. Kotecha, C. O'Hare, P. J. Morris, J. M. Hartley, Z. Taherbhai, D. Harris, C. Forni, R. Mantovani, M. Lee, J. A. Hartley, *Mol. Cancer Ther.*, **6**, 346 (2007); (b) T. J. Dwyer, B. H. Geierstanger, Y. Bathini, J. W. Lown, D. E. Wemmer, *J. Am. Chem. Soc.*, **114**, 5911 (1992).

4. (a) K. Shinohara, T. Bando, H. Sugiyama, *Anticancer Drugs,***21**, 228 (2010); (b) M. Minoshima, T. Bando, K. Shinohara, H. Sugiyama, *Nucl. Acids Symp. Ser.*, **53**, 69 (2009); (c) S. Borman, *Chem. Eng. News,* **88**, 50 (2010).

5. (a) P. B. Dervan, B. S. Edelson, *Curr. Opin. Struc. Biol.,* **13**, 284 (2003); (b) M. A. Marques, R. M. Doss, A. R. Urbach, P. B. Dervan, *Helv. Chim. Acta,* 85, 4485 (2002); (c) P. B. Dervan, *Bioorg. Med. Chem.,* **9**, 2215 (2001).

6. (a) X.-L. Yang, R. B. Hubbard IV, M. Lee, Z.-H. Tao, H. Sugiyama, A. H.-J. Wang, *Nucl. Acids Res.*, 27, 4183 (1999); (b) E. R. Lacy, K. K. Cox, W. D. Wilson, M. Lee, *Nucl. Acids Res.,* 30, 1834 (2002); (c) E. R. Lacy, B. Nguyen, M. Le, K. K. Cox, C. O'hare, J. A. Hartley, M. Lee, W. D. Wilson, *Nucl. Acids Res.,* 32, 2000 (2004); (d) V. C. Rucker, S. Foister, C. Melander, P. B. Dervan, *J. Am. Chem. Soc.,***125**, 1195 (2003); (e) X.-L. Yang, C. Kaenzig, M. Lee, A. H.-J. Wang, *Eur. J. Biochem.*, **263**, 646 (1999).

7. (a) K. L. Buchmueller, A. M. Staples, C. M. Howard, S. M. Horick, P. B. Uthe, N. M. Le, K. K. Cox, B. Nguyen, K. A. O. Pacheco, W. D. Wilson, M. Lee, *J. Am. Chem. Soc.,* **127**, 742 (2005); (b) K. L. Buchmueller, S. L. Bailey, D. A. Matthews, Z. T. Taherbhai, J. K. Register, Z. S. Davis, C. D. Bruce, C. O'Hare, J. A. Hartley, M. Lee, *Biochemisry,* **45**, 13551 (2006); (c) B. Babu, Y. Liu, A. Plaunt, C. Riddering, R. Ogilvie, L. Westrate, R. Davis, A. Ferguson, H. Mackay, T. Rice, S. Chavda, D. Wilson, S. Lin, K. Kiakos, J. A. Hartley, M. Lee, *Biochem. Biophys. Res. Commun.*, **404**, 848 (2011); (d) V. Satam, B. Babu, A. Porte, M. Savagian, Y. Liu, M. Lee, J. Ramos, W. D. Wilson, S. Lin, K. Kiakos, J. A. Hartley, M. Lee, *Bioorg. Med. Chem. Lett.*, **22**, 5898 (2012).

8. (a) S. Chavda, Y. Liu, B. Babu, R. Davis, A. Sielaff, J. Ruprich, L. Westrate, C. Tronrud, A. Ferguson, A. Franks, S. Tzou, C. Adkins, T. Rice, H. Mackay, J. Kluza, S. A. Tahir, S. Lin, K. Kiakos, C. D. Bruce, W. D. Wilson, J. A. Hartley, M. Lee, *Biochemistry,* 50, 3127 (2011); (b) V. Satam, P. Patil, B. Babu, M. Gregory, M. Bowerman, M. Savagian, M. Lee, S. Tzou, K. Olson, Y. Liu, J. Ramos, W. D. Wilson, J. P. Bingham, K. Kiakos, J. A.

Hartley, M. Lee, *Bioorg. Med. Chem. Lett.,* **23**, 1699 (2013).

9. (a) K. Kiakos, J. Ruprich, R. Davis, A. Sielaff, L. Westrate, C. Tronrud, A. Ferguson, T. Brown, H. Mackay, M. Lee, Y. Liu, D. Wilson, D. Hochhauser, J. A. Hartley, *Proc. Am. Assoc. Cancer Res.*, abstract 3521 (2010); (b) K. Kiakos, L. Pett, V. Satam, P. Patil, D. Hochhauser, M. Lee, J. A. Hartley, *Chem. & Biol.*, **22**, 862 (2015).

10. V. Satam, B. Babu, P. Patil, K. A. Brien, K. Olson, M. Savagian, M. Lee, A. Mepham, L. B. Jobe, J. P. Bingham, L. Pett, S. Wang, M. Ferrara, C. D. Bruce, W. D. Wilson, M. Lee, J. A. Hartley, K. Kiakos, *Bioorg. Med. Chem. Lett.*, **25**, 3681 (2015).

11. M. Thomas, U. Varshney, S. Bhattacharya, *Eur. J. Org. Chem.*, 3604 (2002).

12. H. Mackay, T. Brown, M. Lee, in: Synthetic and Biophysical Studies of DNA binding Compounds, M. Lee, L. Strekowski (eds), Transworld Research Network, India, 2007, p. 67.

13. C. Cong, H. Wang, Y. Hu, C. Liu, S. Ma, X. Li, J. Cao, S. Ma, *Eur. J. Med. Chem.,* **46**, 3105 (2011).

14. These compounds are commercially available according to a SciFinder search on December 26, 2015.

15. L. Yurttas, Y. Ozkay, H. Karaca, Y. Tunali, Z. A. Kaplancıkli, *Lett. Drug Design & Discovery,* **10**, 486 (2013).

16. R. Wubulikasimu, Y. Yang, F. Xue, X. Luo, D. Shao, Y. Li, R. Gao, W. Ye, *Bull. Korean Chem. Soc.,* **34**, 2297 (2013).

17. H. Göker, E. Tebrizli, U. Abbasoglu, *Famaco,* **51**, 53 (1996).

18. S. Manoharan, S. Anandan, *Dyes & Pigments,* **105**, 223 (2014).

19. Y. Kim, M. R. Kumar, N. Park, Y. Heo, S. Lee, *J. Org. Chem.*, **76**, 9577 (2011), and references given therein.

СИНТЕЗА НА 2-(ЗАМЕСТЕН)-3*H*-БЕНЗИМИДАЗОЛ-5-КАРБОКСИЛНА КИСЕЛИНА И 2-(ЗАМЕСТЕН)-3*H*-ИМИДАЗО[4,5-b]ПИРИДИН-5-КАРБОКСИЛНИ КИСЕЛИНИ: СИНТОНИ ЗА ФЛУОРЕСЦЕНТНИ Hx И *aza*-Hx АМИДИ

В.С. Сатам[1], П.К. Патил[1], Б. Бабу[1], К.А. Брайън[1], М. Грегори[1], М. Бауъмен[1], Дж. Суирз[1], А. Мефам[1], М. Лии[1,2]*

[1]Департамент по химия, Хоуп Колидж, Холанд, Мичиган, САЩ
[2]Департамент по химия, Щатски университет в Джорджия, Атланта, Джорджия, САЩ

(Резюме)

Съобщава се за синтезите на 15 флуоресцентни 2-(заместен)бензимидазол-5-(Hx) и 2-(заместен) имидазопиридин-5-(*aza*-Hx) карбоксилни киселини. Ключови са половините на Hx- и *aza*-Hx амидите, които свързват ДНК в специфични секвенции. Кондензацията на метил 3, 4-диаминобензоат **10a** или метил 5,6-диаминопиридин-2-карбоксилат **10b** с подходящи арил- или хетероарил-алдехиди **9** дава желаните Hx (**7a-k**) и *aza*-Hx естери (**8l-o**) с добиви съответно 31-88% и 18-70%. Хидролизата на естерите **7a-k** и **8l-o** дава съответните Hx (**5a-k**) и *aza*-Hx киселиини (**6l-o**) с добиви съответно от 66-93% и 64-85%. Hx - киселините **5d**, **5e**, **5g** и **5k**, както и *aza*-Hx киселините **6m-o** са нови съединения.

Thermosensitive flocculation of aqueous suspension using a UCST polymer

W. Bogacz[1], M. Lemanowicz[1], A. Gierczycki[1]*, W. Kuźnik[1,2]

[1]*Silesian University of Technology, Faculty of Chemistry, Department of Chemical Engineering and Process Design, ul. ks. M. Strzody 7, 44-100 Gliwice, Poland*
[2]*Technical University of Czestochowa, Faculty of Electrical Engineering, al. Armii Krajowej 17, 42-200 Czestochowa*

In this work the thermosensitive aggregation and breakage of a model TiO_2 suspension in water in the presence of poly(acrylic acid) – a polymer characterized by Upper Critical Solution Temperature (USCT) behavior, is presented. Contrary to the Lower Critical Solution Temperature (LCST) polymer flocculation, in this case the suspension is stable at higher temperatures and the particles aggregate upon cooling. In the experiments the suspension was destabilized in a baffled mixing tank equipped with a mechanical stirrer and thermostating jacket. Due to the extremely high sensitivity of the system to the change of any of the process parameters the aggregation process was investigated via digital analysis of the microscopic photographs. The UCST thermo-sensitive flocculation in an aqueous environment was found to be reversible and as such suitable to be used in processing run under a cyclic regime.

Keywords: aggregation, thermosensitive polymers, poly(acrylic acid), Lower Critical   Solution Temperature (LCST), Upper Critical Solution Temperature (UCST)

INTRODUCTION

Nowadays extensive research is dedicated to the novel approaches to aggregation phenomenon [1]. For example, *N*-isopropylacrylamide is known for its Lower Critical Solution Temperature (LCST), *i.e.* the polymer is hydrophilic below LCST and becomes hydrophobic above this temperature, this process is reversible and can be run repeatedly [2]. When derivatives of such polymers are used as flocculants the temperature greatly influences the particle size distribution [3 − 5] or sediment volume [6, 7]. Moreover, they can be used simultaneously in flotation due to their hydrophobic nature [8, 9]. Thermosensitive aggregation has two significant advantages over the conventional process. First, it can be triggered and reversed on demand and therefore the aggregation and breakage phenomena may be repeated in a cyclic manner. Second, thermo-sensitive polymers can be tailor made to show affinity to chosen substances, thus stimuli-controlled processes may be realized in a new way.

In general Upper Critical Solution Temperature (UCST) polymers have attracted only a small fraction of the attention devoted to their LCST counterparts, most likely because the UCST transition is usually less drastic (the UCST is a wider range of temperature than the sharp LCST of PNIPAM) and very strongly dependent on the solution pH and salinity in the suspending media

[10]. To the best of our knowledge there have been no reports of UCST flocculation of solid dispersions in water, even though the most popular UCST polymer – poly(acrylic acid) (PAA) is easily available commercially. In this paper the results of flocculation of a model TiO_2 aqueous suspension with a UCST polymer are presented. To the best of our knowledge UCST flocculation of water-dispersed solid suspensions has not been studied up to the present.

EXPERIMENTAL

A model suspension of TiO_2 particles (Avantor Performance Materials Poland S.A.) in reverse osmosis water was used. The solid particles in the form of white powder were weighted on an analytical balance and transferred to a small beaker. Subsequently a dense sludge was created by the addition of a small portion of RO water. Poly(acrylic acid) was used as the flocculating agent. It was received in the form of 25% w/w water solution (Avantor Performance Materials Poland S.A., molecular weight equal to 240 000 g/mol). In order to enable the hydrophilic-hydrophobic transition the addition of salt was required. For this purpose potassium chloride was used (pure for analysis, Avantor Performance Materials Poland S.A.).

In order to verify the polymer dosage impact on the flocculation performance three different dosages were investigated, *i.e.* 10 mg/g, 100 mg/g and 1000 mg/g. Unfortunately the natural

---

consequence of different polymeric acid concentrations was a change of the solution's pH. This in turn influenced the location of the UCST point. During thermo-sensitive aggregation the driving force of flocs creation results from the hydrophobic interactions between the solid particles. The magnitude of these interactions depends directly on the temperature. Therefore, it was decided that in all the experiments a constant UCST value will be preserved at the expense of a pH value change (Table 1). Contrary to the standard flocculation experiments in which the flocculation performance is investigated from the moment of polymer addition, in the presented cases the polymer solution with a strictly determined UCST point had to be prepared before the aggregation experiments. Next, the solid particles in the form of a dense sludge were introduced to the mixing tank and the observations initiated. The final concentration of solid particles during all the experiments was equal to $12 \ g/dm^3$.

The flocculation experiments were performed in a thermostated mixing tank equipped with 4 baffles and a mechanical 3-blade marine propeller (400 RPM). The key dimensions of the laboratory setup are presented in Fig. 1. During solution preparation it was found that the value of the UCST depends on a very delicate balance between the component concentrations. Even a small change in the salt concentration or pH value influenced the UCST substantially.

Therefore, it was decided to analyze the UCST flocculation on the basis of microscopic photographs. The authors of this work were aware that a large part of the suspension particle population of submicron size were not visible on the photographs. However, the proposed approach yielded results which proved the scientific goal of this work. It has to be emphasized that the biggest disadvantage of laser sizer measurements of particle size distribution is the possibility of sample contamination by residuals left in the sample circulation loop of the apparatus.
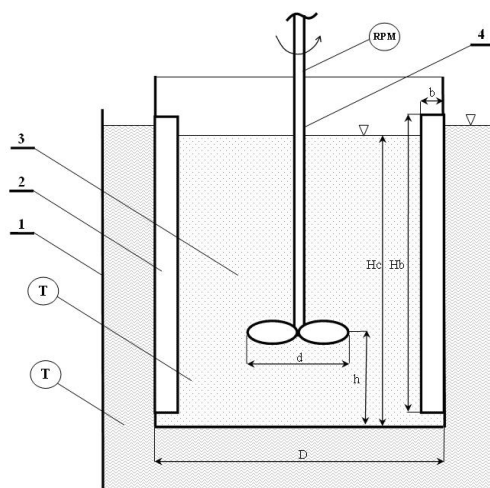
Fig. 1. Mixing tank scheme: 1) thermostated jacket, 2) baffle, 3) mixing tank, 4) propeller. Dimensions: D = 0.098 mm, d = 0.038 m, b = 0.01 m, H_c = D, H_b = D, h = ⅓H_c.

The measurements were made as follows. First, the polymer solution, together with salt addition, was heated to 318 K. Next, the titanium oxide sludge was transferred into the tank. From that moment the suspension was mixed for 10 minutes. After this period of time a sample was taken using a preheated plastic pipette with a wide end and transferred on to a custom-made thermostated microscope slide. The photographs of the aggregates were taken using a biological Olympus CH30 microscope with a CMOS camera. 10 samples in total were collected for each polymer dose. 10 photographs were taken of each sample.

Next, the temperature was decreased to 298 K and once again after 10 minutes 10 samples were taken. The time needed to investigate one sample (taking a sample using a pipette, placing it on the microscope slide and taking 10 photographs) was equal to approximately 20 seconds. The measurements were repeated several times in order to prove their repeatability.

During the next step the photographs were digitally processed using MultiScanBase software. First, all the photographs were converted into grayscale. Second, for each photograph different

Table 1. Experimental data for the polymer solutions.

Polymer dose [mg·g⁻¹ TiO₂]	Polymer concentration [% w/w]	pH	Salt concentration [M]	UCST [K]
1000	1	2.42	1.50	308
100	0.1	3.11	0.43	309
10	0.01	3.88	0.55	310

kinds of anomalies were manually removed (e.g. noises etc.) using a set of filters (median filter for noise reduction, averaging background brightness filter and sharpening filter - if necessary). Subsequently, they were transformed into black and white figures. The number and size of the aggregates were determined using a dedicated algorithm included in the software. Finally, the fractal dimension of the aggregates was determined using the same figures. For this purpose HarFA 5.4 (Harmonic and Fractal Analyzer) software was used [11] which employs a box counting method (2D fractal dimension).

RESULTS AND DISCUSSION

Regardless of the polymer dosage all the polymer-treated TiO$_2$ suspensions behaved similarly at temperature above the UCST (Fig. 2).
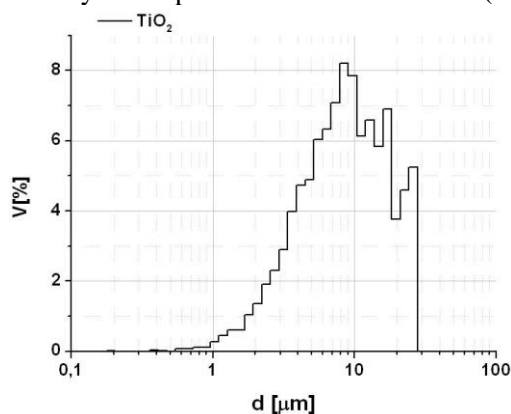
Fig. 2. Particle Size Distribution of the TiO$_2$ suspension in water without polymer addition.

The primary suspension had the Sauter diameter equal to 6.11 μm. The fractal dimensions of the particles were equal to 1.87 (std. dev. 0.05). The diluted suspension of TiO$_2$ has a positive zeta potential at low pH values [12]. Therefore, after addition of PAA some aggregation is present for all the dosages due to charge neutralization and bridging (compare Fig. 2, 3 and 4).

The particle size distribution is only slightly dependent on the dosage which clearly indicates that poly(acrylic acid) has a limited flocculation ability at elevated temperatures. The Sauter diameters were equal to 47.44 (fractal dimension equal to 1.53, std. dev. 0.10), 41.91 μm (fractal dimension equal to 1.57, std. dev. 0.12) and 67.17 μm (fractal dimension equal to 1.81, std. dev. 0.11) for 10 mg/g, 100 mg/g and 1000 mg/g dosages, respectively.

When the temperature was reduced to 25°C (below the polymer's UCST) the aggregation could be seen with the naked eye for the two highest
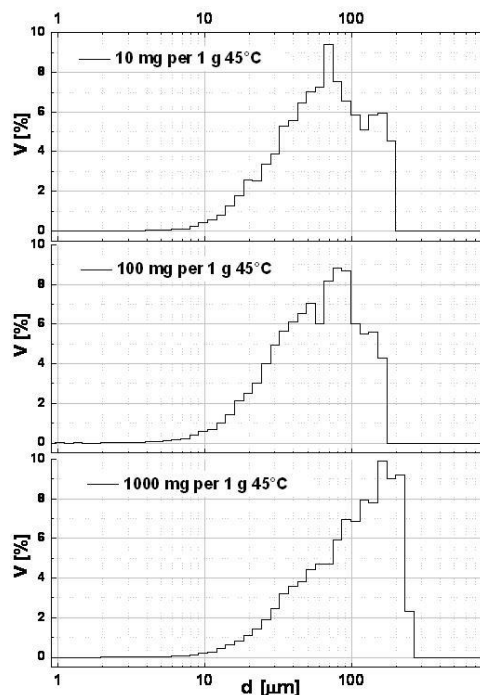
Fig. 3. Particles Size Distribution of TiO$_2$ with different PAA dosage. At 45°C (above the UCST) the polymer is in the hydrophilic form.
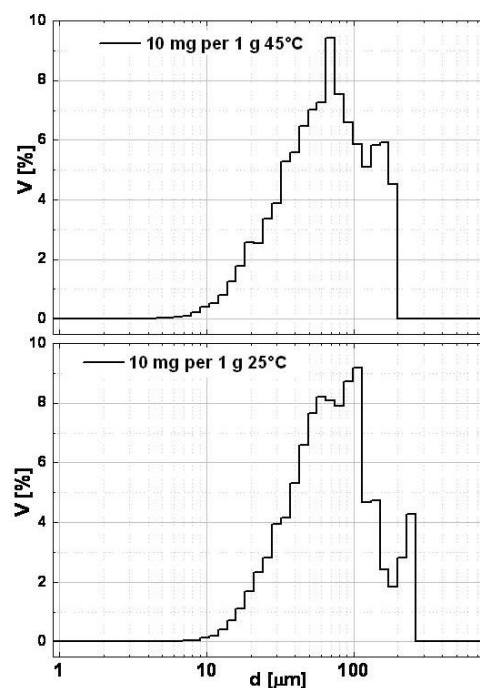
Fig. 4. Particle size distribution of TiO$_2$ with PAA (10 mg/1g dose) at 45°C (top panel) and 25°C (bottom).

polymer doses. In the case of a 10 mg/g dosage a shift in Particle Size Distribution can be observed upon cooling (Fig. 4).

The mean diameter achieved a value equal to 54.81 μm (fractal dimension equal to 1.70, std. dev. 0.08). In the case of higher PAA dosages (100 mg/g and 1000 mg/g) the formation of very large aggregates (Fig. 5) clearly indicates that the

733

polymer starts to act as a very effective flocculant after cooling below the UCST. The PSD (as well as the mean diameter and fractal dimension) at 25°C for these dosages are not presented because with such large aggregates (exceeding the size of the camera frame) it was not possible to obtain images allowing for a meaningful analysis. However, it has to be emphasized that one can easily find aggregates larger than 1 mm.
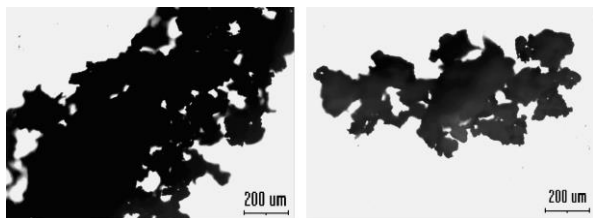
Fig. 5. Aggregates observed at 25°C with a 100 mg/1g PAA dosage.
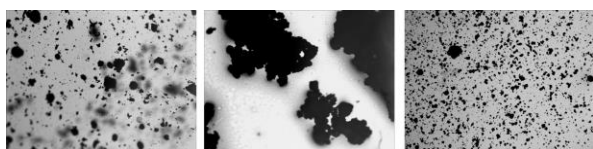
Fig. 6. Reversibility of the thermoresponsive UCST flocculation: TiO_2 suspension with 1000 mg/g of poly(acrylic acid) at 45°C (left), 25°C (middle) and after heating back to 45°C (right).

After cooling the suspension obtained with 1000 mg/g PAA the sludge was heated back to 45°C. The large aggregates present at 25°C are absent from the images taken after heating, proving the reversibility of the UCST-type thermoresponsive flocculation which is crucial from the point of view of the potential practical applications (Fig. 6).

CONCLUSIONS

A reversible flocculation process was demonstrated on a UCST polymer – poly(acrylic acid) and TiO_2 solid aqueous suspension. For all the studied polymer dosages (10, 100 and 1000 mg/1g of TiO_2) the suspension was stable at a temperature above the polymer's UCST (45°C) and

aggregation was observed in all the samples upon cooling to 25°C (below the UCST). In the case of medium and high polymer dosage very large (> 2 mm) aggregates were formed. Breakage of the aggregates was observed after heating the sediment providing a clear proof of the process reversibility. The experimental results presented herein show that UCST-type thermosensitive polymers can be used as flocculating agents in analogy with their more popular LCST counterparts which imply possible applications in separation, process control and catalysis.

REFERENCES

1. L. Ghimici, M. Constantin, G. Fundueanu, *J. Hazard. Mater.*, **181**, 351 (2010).
2. I. Dimitrov, B. Trzebicka, A. Müller, A. Dworak, C. Tsvetanov, *Prog. Polym. Sci.*, **32**, 1275 (2007).
3. E. Burdukova, N. Ishida, T. Shaddick, G. Franks, *J. Colloid Interf. Sci.*, **354**, 82 (2011).
4. W. Kuźnik, M. Lemanowicz, A. Kuś, M. Gibas, A. Gierczycki, *Powder Technol.*, **201**, 1 (2010).
5. M. Lemanowicz, W. Kuźnik, M. Gibas, G. Dzido, A. Gierczycki, *Water Res.*, **46**, 4091 (2012).
6. G. Franks, *J. Colloid Interf. Sci,.* **292**, 598 (2005).
7. G. Franks, H. Li, J. O`Shea, G. Qiao, *Adv. Powder Technol.*, **20**, 273 (2009).
8. E. Burdukova, H. Li, D. Bradshaw, G. Franks, *Miner. Eng.*, **23**, 921 (2010).
9. E. Forbes, D. Bradshaw, G. Franks, *Miner. Eng.*, **24**, 772 (2011).
10. J. Seuring, S. Agarwal, *Macromol. Rapid Commun.*, **33**, 1898 (2012).
11. http://www.fch.vut.cz/lectures/imagesci/ (page access 24th April 2016).
12. D. Deng, V. Boyko, S.M. Pancera, T. Tadros, *Colloid. Surface. A*, **389**, 149 (2011).

ТЕРМОЧУВСТВИТЕЛНА ФЛОКУЛАЦИЯ НА ВОДНИ СУСПЕНЗИИ С ИЗПОЛЗВАНЕТО НА UCST ПОЛИМЕР

В. Богач[1], М. Леманович[1], А. Гиерчицки[1]*, В. Кужник[1,2]

[1]*Силезийски технологичен университет, Факултет по химия, Департамент по химично инженерство и проектиране, 44-100 Гливице, Полша*
[2]*Технически университетв Ченстохова, Факултет по електроинженерство, 42-200 Ченстохова, Полша*

(Резюме)

В тази работа се изследва термочуствителното агрегиране и разпадане на моделна суспензия от TiO_2 във вода в присъствие на поли-акрилова киселина – полимер с висока критична температура на разтворимост (USCT). Противно на флокулацията при ниска критична температура на разтворимост (LCST), в разглеждания случай суспензията е стабилна при висока температура и частиците се агрегират при охлаждане. При проведените експерименти суспензията се дестабилизира в смесителен съд с прегради при механично разбъркване и термостатиране. Поради голямата чувствителност на системата агрегирането беше изследвано чрез цифров анализ на микроскопски снимки. Намерено е, че UCST-термочувствителната агрегация във водна среда е обратима и подходяща за работа в цикличен режим.

QSAR analysis of N[1]-substituted 1,2,4-triazoles against *Escherichia coli*

V. Dimova[1]*, I. Jordanov[1], L. Dimitrov[2]

[1]*Faculty of Technology and Metallurgy, University Ss. Cyril and Methodius Rudjer Boskovic 16, 1000 Skopje, Republic of Macedonia*
[2]*Institute of Agriculture, University Ss. Cyril and Methodius, 16ta Makedonska brigada 3a, 1000 Skopje, Republic of Macedonia*

QSAR analysis of a series of previously synthesized N[1]-substituted 1,2,4-triazole derivatives tested for growth inhibitory activity with respect to *Escherichia coli*, was performed using the computer-assisted multiple regression procedure. Using the Hansch and Free Willson approach the activity contribution of the aminomethyl/aminoethyl unit and aromatic/heteroaromatic ring was determined from the correlation equation. In accordance with the statistical parameters ($R=0.8729$; $R^2_{adj}=0.6430$; $Sd=0.2983$; $Q^2=0.7548$ and $PRESS/SSY=0.2452$), the biparametric model which involves R and L, is selected as the best biparametric model, for determing the activity of the chosen triazole derivatives against *E. coli*. Spreading the investigated system: the subset B (aminomethyl unit replaced with the aminoethyl group) and subset C (aromatic replaced with a heteroaromatic ring), statistically significant QSAR models were not obtained.

Keywords: quantitative structure - activity relationships, 1,2,4-triazole, antibacterial activity, Escherichia coli,

INTRODUCTION

The 1,2,4-Triazole system is a structural element of many drugs that have antimycotic activity such as fluconazole, itraconazole, voriconazole [1-3]. Because of the synthetic utility and broad range of pharmacological effects, the 1,2,4-triazole nucleus is an important five member ring, and the interest in the synthesis and microbiology of this pharmacophore continues to be fuelled by its analgetic, antiasthmatic, diuretic, antihypertensive, antibacterial, antifungal and anti-inflammatory properties [4-10].

One of the methods of preparing derivatives of 1,2,4-triazole is the Mannich reaction (aminomethylation), a well know process [11,12]. N-hydroxymethyl derivatives of heterocycles such as: benzotriazoles and benzimidazoles under the influence of amines, can also give corresponding Mannich bases [12-14]. It is also known that some aminomethyl heterocycles, that possess biological and corrosion-inhibition activity can be used as additives in greasy oils as well as photopolymerizing paints to improve adhesion [15,16].

Quantitative structure activity relationships (*QSARs*) are estimation methods developed and used in order to predict certain effects or properties of chemical substances which are primarily based on the structure of the substances. They have been developed on the basis of experimental data on model substances. Today the investigation of the

QSAR of the substances is an important issue in modern chemistry, biochemistry, medicinal chemistry, as well as in drug discovery [17-20].

This information is composed of mathematical equations relating the chemical structure of the compounds to a wide variety of their physical, chemical, biological and technological properties. Once a correlation between the structure and activity/property is found, any number of compounds, including those not yet synthesized, can be readily screened on the computer in order to select the structure with the desired properties. Then, it is possible to select the most promising compounds to synthesize and test in the laboratory.

In the above mentioned contex and in the continuation of the studies of new antimicrobial agents which possess heterocyclic rings in their structure, such as the 1,2,4-triazole, during the last ten years,some new 1,2,4-triazole derivatives [21-24] were synthesized and investigated.

A group of 18 N[1]-aryl/heteroarylamino-/methyl/ethyl-1,2,4-triazole derivatives was synthesized by condensation of the hydroxymethyl derivative of 1,2,4-triazole and the appropriate aromatic/heteroaromatic amines and by the reaction of 1,2,4-triazole, acetaldehyde and a few aromatic/heteroaromatic amines. All the synthesized compounds were screened for their antibacterial activities with respect to *Escherichia coli* [24].

The objective of this investigation was to study the usefulness of QSAR in the prediction of the antibacterial activity of the investigated triazole derivatives with respect to *Escherichia coli*. Multiple linear regression (MLR) models have been

* To whom all correspondence should be sent:
E-mail: vdimova@tmf.ukim.edu.mk

developed as a mathematical equation which correlate the chemical structure to the activity.

EXPERIMENTAL

Materials and methods

All N[1]-aryl/heteroarylamino/methyl/ethyl-1,2,4-triazole derivatives (1-18), (Table1), used in this study were previously synthesized and reported elsewhere [24].

Antibacterial Investigation

All 1,2,4-triazole derivatives were tested for their *in vitro* growth inhibitory activity against *Escherichia coli*. The antimicrobial activity of the investigated compounds were tested by the filter paper disc method [25], using standard conditions in a Mueller-Hinton agar medium, inoculated with 0.5 mL of the 24 h liquid cultures containing 10^7 microorganisms/mL.

Stock solutions of the compounds were prepared in DMSO, as an inert medium in 3 concentrations: 1 mg/mL; 5 mg/mL and 10 mg/mL DMSO (Figure 1). Filter paper discs (5 mm diameter) saturated with each compound solution were placed on the indicated agar mediums. The incubation time was 24 h at 37^0C. A control disc using DMSO without any

test compound was included. There was no inhibitory activity in those disks. The diameter of the zone inhibition (mm) was measured. The MIC values of the triazoles tested were obtained as µg/mL (Table 1). Every test was done in triplicate to confirm the findings.

Multiple Linear Regression
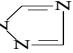
The mathematical foundation of the quantitative structure – activity relationship is based on the principle of polylinearity. Multiple linear regression is a common method used in QSAR studies. The QSAR equations were obtained by the multilinear forms:

$$\log 1/c = a_0 + a_1D_1 + a_2D_2 + a_3D_3 + \ldots + a_nD_n, \quad (1)$$

where D_1, D_2, D_3 and D_n are descriptors, n is the number of desriptors. The intercept (a_0) and regression coefficient of the descriptors were determined using the least squares method.

The MVA (multi variable analysis) approach in *QSAR* analysis has been most widely and effectively used for theoretical drug design due to various physicochemical (electronic, steric and hydrophobic) parameters and structural indicator parameters used together (*Hansch* and *Free Willson* approach) [26,27].

Table 1. Calculated $\log 1/c_{MIC}$ values; logP values and matrix of the Free Willson approach for N[1]-aryl/heteroarylaminomethyl/ethyl-1,2,4-triazole derivatives (1-18)

Comp.	R	Ar	$\log 1/c_{MIC}$	$logP^a$	I_H	$I_{=CH-}$
1	H	$-C_6H_4-COOC_2H_5$ (*p*)	5.3914	1.2981	1	1
2	H	$-C_6H_4-COOH$(*p*)	4.3388	0.4579	1	1
3	H	$-C_6H_4-COOH$(*o*)	4.3388	1.4690	1	1
4	H	$-C_6H_4-Cl$(*p*)	5.3194	1.2210	1	1
5	H	$-C_6H_4-Br$(*p*)	5.4034	1.4665	1	1
6	H	$-C_6H_4-CH_3$ (*p*)	5.2747	1.1238	1	1
7	H	$-C_6H_4-C_6H_5$ (*p*)	5.3985	2.3405	1	1
8	H	$-C_6N_4-NH-CH_2-$N⟨⟩N	4.7328	-1.6900	1	1
9	CH_3	$-C_6H_4-COOC_2H_5$ (*p*)	5.4156	1.7157	0	1
10	CH_3	$-C_6H_4-NO_2$ (*p*)	4.3678	1.3895	0	1
11	H	2-Pyridyl-	5.2435	0.0301	1	0
12	H	4-Methyl-2- pyridyl -	5.2769	0.5774	1	0
13	H	6- Methyl-2- pyridyl -	5.2769	0.5774	1	0
14	H	5-Chloro-2-pyridyl-	-	0.6746	1	0
15	H	2-Pyrimidyl-	-	-1.4763	1	0
16	H	1,2,4-Triazole-4-yl	4.5189	-2.1800	1	0
17	CH_3	6-Methyl-2-pyridyl-	-	0.9950	0	0
18	CH_3	2-Thiazolyl-	-	0.7441	0	0

^{a}*Ref. [28].*

a

b
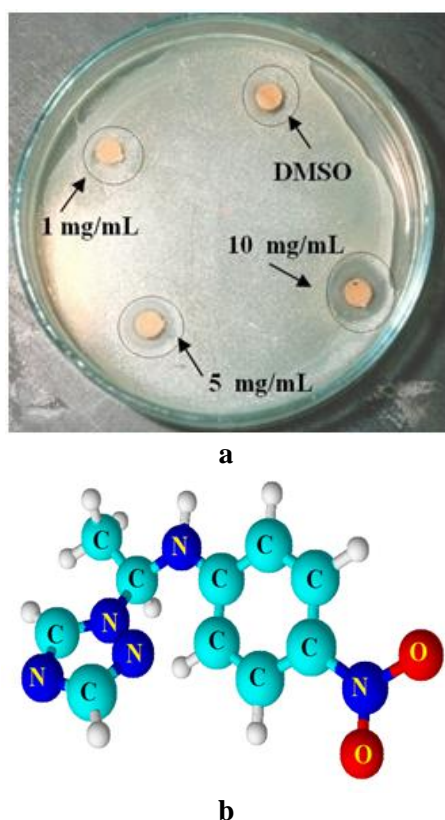
Fig. 1. a) Filter paper discs saturated with compound (10) solution (1 mg/mL; 5 mg/mL and 10 mg/mL DMSO) and b) optimized geometry of the compound (10)

The assumption can be formulated as given in the following equation (*Hansch* approach):

$$\log 1/c = A_1 x + A_2 y + A_3 z + b, \qquad (2)$$

where *x, y* and *z* are the molecular properties and log1/c are the desired biological activities.

From the values of linear slopes A_1, A_2, A_3 we can see the correlation of the particular molecular properties with the activity of the investigated compounds. Applying the same chosen descriptors in *Free Willson* analysis, the activity contributions of either methyl- or substituted heterocyclic ring systems were determined from the correlation equation:

$$\log 1/c = \Sigma a_i I_i + \Sigma b_i x_i + b \qquad (3)$$

where I_i is the structural indicator parameter.

Descriptors

The variables used as descriptors in the analysis are electronic, steric and structural parameters (Tables 1 and 2). The physicochemical parameters taken into consideration in the *QSAR* study are: σ, π, MR, F, R, L and logP (Table 2). For each compound the partition coefficient logP has been calculated (Table 1) [28].

The *Hammett* constant σ is an electronic substituent constant reflecting the electron-donating or electron-withdrawing properties of a substituent. It thus serves as a quantitative measure of the change in the electronic density of the reaction center caused by the introduced substituent. Positive σ values are defined to represent the residues that unfold an electron-withdrawing effect stronger thanthe hydrogen present in the unsubstituted derivative, negative σ values vice versa. It is possible to express the electronic effect of a substituent in terms of non-resonance and resonance capability. The parameter σ_m describes the inductive effect on the electron density present in the reaction center, hence emphasizing the non-resonance capability. The mesomeric effect on the electron density is characterized by σ_p, putting an emphasis on the resonance capability. As resonance conjugation cannot be performed from the *meta*-position, σ_R contributes indirectly to σ_m. A distinction between the non-resonance and resonance capability can also be made by employing the parameters F and R, which are the field (F) and resonance (R) constants calculated by *Swain* and *Lupton* from the *Hammett* σ_m and σ_p values. *Swain* and *Lupton* claim the descriptors F and R "to be more accurately defined and more physically significant independent variables for correlating or predicting substituent effects" than any other pair of *Hammett* values. F and R are supposed to be independent of the performed reaction, of the solvent, and of the temperature. *Hansch* attests the field and resonance constants a remarkable orthogonality and thus theavoidance of the common problem of multi-collinearity. The empirical weighting factors *f* and *r* are independent of the substituent but different for each substituent constant (i.e., σ_m, σ_p):

$$\sigma = f F + r R \qquad (4)$$

where σ is the *Hammett* constant, *f* the field weighting factor, F the field constant, *r* the resonance weighting factor and R is the resonance constant.

A parameter readily available for each substituent is the molar refractivity (MR), described as the molar volume of the substituent, corrected by the refractive index. The refractive index being a part of the definition hints a contribution of the polarizability of the substituent to the MR value which must be regarded as an electronic contribution:

$$MR = \frac{M(n^2 - 1)}{d(n^2 + 2)} \qquad (5)$$

where MR is the molar refractivity of the substituent, M is the molecular weight of the substituent, dis the

density of the substituent, and n is the refractive index, measured at 20 °C.

A purely geometrical definition of the size of a substituent is provided by *Verloop* who thereby wanted to overcome the problem of asymmetry of the substituents. In order to be able to describe the substituents deviating from a spherical shape, a set of five parameters was developed. The length parameter L and the four width parameters B1-4, represent the four rectangular directions perpendicular to the axis describing the length.

The partition coefficient, referred to as logP, represents a parameter expressing the hydrophobicity of the molecule as a whole. The logP value of a compound is commonly determined by measuring the distribution behavior in a biphasic system consisting of 1-octanol, representing the lipid phase, and water:

$$P = \frac{c_{(lipid\,phase)}}{c_{(water\,phase)}} \qquad (6)$$

where P is the partition coefficient of the compound, $c_{(lipid\,phase)}$ is the concentration of the compound present in the lipid phase, and $c_{(water\,phase)}$ is the concentration of the compound present in the water phase.

The *Hansch* constant π describes the contribution of a substituent to the lipophilicity of a compound. The π values are usually derived from the benzene solute system, that is, by partitioning substituted benzene derivatives between 1-octanol and water. Subtraction of the logP value of the unsubstituted benzene from the logP value of the substituted compound yields the π value of the appropriate substituent. Positive π values represent an amplification of the lipophilic character caused by the substituent; negative π values that symbolize an increase in hydrophilicity:

$$\pi_x = logP_{R-X} - logP_{R-H} \qquad (7)$$

where π_X is the Hansch constant characteristic of the substituent X, P_{R-X} is the partition coefficient of the X-substituted benzene, and P_{R-H} is the Partition coefficient of the unsubstituted benzene.

Applying the *Free Willson* analysis, in the first step, the structural variable indicator I_H expresses the replacement of the hydrogen atom with a methyl group in an aminomethyl unit. I_H is defined as 1 for the N^1-aryl/heteroarylaminomethyl-1,2,4-triazoles (1-8, 11-16), and 0 for N^1-aryl/heteroarylaminoethyl-1,2,4-triazole derivatives (9,10,17,18). In the second step, the other indicator $I_{=CH-}$ is defined as 1 for compounds with =CH- in six

membered ring (1-10) and 0 for compounds with –N- replacement (11-18) (Table 1).

Statistical analysis

The statistical evaluation of the data was performed using the STATISTICA program package [31]. To test the quality of the regression models, the following statistical parameters were used:

o **Correlation coefficient (R)** - measures the degree to which the dependent variable is linearly related to the explanatory variables.

o **Standard deviation of the estimate (Sd)** - defined as the square root of the variance represents the most commonly used measure of the spread. Sd expresses the degree of deviation of the calculated biological activity from the experimentally determined biological activity.

o **Fisher test for singnificance of the equation (F-test)** mirrors the ratio of the variance, which is a measure of the spread of data, that is explained by the established regression equation to the variance not explained, taking the degrees of freedom into account. The F-distribution can be regarded as a measure of significance of the established regression equation as a whole.

o **Adjusted $R^2(R^2_{adj})$** an adjusted version of R:

$$R^2_{adj} = 1 - R^2((n-1)/(n-p-1)) \qquad (8)$$

where *n* is the number of compounds and *p* is the number of independent parameters.

o **Predictive residual error Sum of Squares (PRESS)** and **Sum of squares of deviation of the experimental values from their mean (SSY)**:

$$PRESS = \Sigma(Y_{pred}-Y_{exp})^2 \quad and$$
$$SSY = \Sigma\,(Y_{exp}-Y_{mean})^2 \qquad (9)$$

where Y_{pred}-predicted, Y_{exp}-experimental and Y_{mean}-mean are the values of the target property; in our case the (log1/C) values respectively. PRESS appears to be an important cross-validation parameter accounting for a good estimate of the real predictive error of the model. Its value less than SSY (PRESS<<SSY) indicates that the model predicts better than chance and can be consided statistically significant. If the sum of the squared deviations of the calculated values from the observed values (PRESS) is larger than the sum of the squared deviations of the observed values from the mean experimental value (SSY), Q^2 adopts a negative value. This implies that the proposed regression equation does not provide reasonable predictions.

Table 2. Physicochemical parameters of the triazole derivatives studied [a]Ref. [29]; [b]Ref. [30]

Substituent	σ^a	π^a	MR^a	F^a	R^a	L^a
p-COOC$_2$H$_5$	0.45	0.51	17.47	0.33	0.15	5.96
p-COOH	0.45	-0.32	6.93	0.33	0.15	3.91
o-COOH	1.2^b	-0.32	6.93	0.33	0.15	3.91
p-Cl	0.23	0.71	6.03	0.41	-0.15	3.52
p-Br	0.23	0.86	8.88	0.44	-0.17	3.83
p-CH$_3$	-0.17	0.56	5.65	-0.04	-0.13	2.87
p-C$_6$H$_5$	-0.01	1.96	25.36	0.08	-0.08	6.28
p-NO$_2$	0.78	-0.28	7.36	0.67	0.16	3.44

o **Cross-validation squared correlation coefficient (Q^2)** is widely adopted to quantitatively express the predictive power of a correlation and can by calculated by equation:

$$Q^2 = 1 - PRESS/SSY \quad (10)$$

o **Quality factor (Q)** can be calculated by equations:

$$Q = R/Sd \quad (11)$$

A higher value of Q indicates a better prediction of the model.

o **Uncertainty of Prediction (S_{PRESS})** and **Predictive Square Error (PSE)** can by calculated by equations:

$$S_{PRESS} = \sqrt{\frac{PRESS}{(N - p - 1)}}$$

$$PSE = \sqrt{\frac{PRESS}{N}} \quad (12)$$

The lower values of S_{PRESS} and PSE indicate a better model.

o **Variance inflation factor (VIF)** is defined as:

$$VIF = 1/(1 - R_i^2) \quad (13)$$

where R_i is the multiple correlation coefficient of the i-th independent variable on all of the other independent variables.

RESULTS AND DISCUSSION

The series of 18 substiuted 1,2,4-triazole derivatives may be organized in 3 subsets:

Subset A - structurally identical compounds (1-8);

Subset B - compounds with structural changes (*aminomethyl* unit replaced with the *aminoethyl* group) (1-10) and

Subset C - compounds with ring changes (the aromatic ring has been replaced with a heteroaromatic one) (1-18).

In this work QSAR analyses were made between selected physicochemical properties and experimentally obtained values for antimicrobial activities with respect to *Escherichia coli*, applying the general *Hansch* equation for **subset A**, *Free-Wilson* approach for **subset B** and extend *Free-Wilson* equation for **subset C**.

It is well known that there are three important phases in any QSAR study:

  i. *development of the models;*
  ii. *statistical validation of the obtained models and*
  iii. *utility of the developed models.*

In the first step for the development of QSAR models, the selected 1,2,4-triazoles were evaluated for *in vitro* antibacterial activity against *Escherichia coli*. After applying the filter paper disc method, the compounds 14, 15, 17 and 18 do not inhibit the growth of the test strain [24]. In the second step, efforts were focused on developing the QSAR models of compounds with antibacterial activity. Inhibitory activity data determined as µg/mL were first transformed to the negative logarithms of molar MICs (log1/c_{MIC}), (Tab. 2) which were used as a dependent variable in the QSAR study.

In accordance with the calculated values, log1/C_{MIC} is lowest for *orto/para* COOH substituted 1,2,4-triazoles (**2** and **3**). Following the sequence of antibacterial activity the values observed were:

2 = 3 < 10 < 16 < 8 < 11 < 6 < 12 = 13 < 4 < 1 < 7 < 5 < 9

Since the previous work descriptors such as: surface tension, molar refraction, molar volumen, parachor, index of refractivity, density and polarizability were used [23], in the present study different electronic, steric and structural descriptors (σ, π, MR, F, R, L, logP) and structural variable indicators (I_H and $I_{=CH-}$) (Tables 1 and 2), were used as an independent variable and were correlated with antibacterial activity (log1/c_{MIC}).

One-variable model. The relatively good monoparametric model was obtained only for π

indicating the importance of the descriptor in contribution to the inhibitory activity (**Model 1**; Figure 2a).

Model 1 $\quad$ log $1/c_{MIC}$ = 4.7747($\pm$0.1569) + 0.5156($\pm$0.1714)π
R=0.8025 $\quad$ R^2_{adj}=0.5779 $\quad$ F=9.0471
Sd=0.3263 $\quad$ p<0.2983

Furthermore, the data shows that some of the chosen descriptors such as σ (R=0.7235) and R (R=0.6926) correlate median with the activity. A statistically unreliable model was obtained for the following descriptors: logP, MR, F and L (R<0.4).

From this it was concluded that no single variable model is capable of good modelling of activity and that the refereed descriptors should be combined to obtain a statistically significant multiparametric model for modelling the activity.

Two-variable models. In bivariate correlation analysis, by applying a stepwise multiple linear regression method, 21 models were obtained. Among them a few best models were selected for the futher discussion (**Models 2-9**). The selection was based on the statistical quality of the models (R; Sd; F-test; R^2_{adj}; p-level).

Model 2 $\quad$ log $1/c_{MIC}$ = 4.9839($\pm$0.2837) - 0.3745($\pm$0.4194)σ + 0.3710($\pm$0.2383)π

R=0.8385 $\quad$ R^2_{adj}=0.5548 $\quad$ F=4.7391
Sd=0.3331 $\quad$ p<0.0881

Model 3 $\quad$ log $1/c_{MIC}$ = 4.8484($\pm$0.4007) - 0.7481($\pm$0.3259)σ + 0.3526($\pm$0.2575)logP
R=0.8219 $\quad$ R^2_{adj}=0.5132 $\quad$ F=4.1639
Sd=0.3483 $\quad$ p<0.1052

Model 4 $\quad$ log $1/c_{MIC}$ = 5.1377($\pm$0.4425) + 0.7216($\pm$0.2925)π- 0.3579($\pm$0.4067)logP
R=0.8377 $\quad$ R^2_{adj}=0.5527 $\quad$ F=4.7069
Sd=0.3339 $\quad$ p<0.0889

Model 5 $\quad$ log $1/c_{MIC}$ = 4.9288($\pm$0.2491) + 0.6698($\pm$0.2593)π -0.0218($\pm$0.0268)MR
R=0.8335 $\quad$ R^2_{adj}=0.5422 $\quad$ F=4.5533
Sd=0.3378 $\quad$ p<0.0931

Model 6 $\quad$ log $1/c_{MIC}$ = 4.8340($\pm$0.1755) + 0.3907($\pm$0.2288)π- 0.9911($\pm$1.1590)R

R=0.8361 $\quad$ R^2_{adj}=0.5486 $\quad$ F=4.6460
Sd=0.3354 $\quad$ p<0.0905

Model 7 $\quad$ log $1/c_{MIC}$ = 5.0401($\pm$0.5498) + 0.5747($\pm$0.2192)π- 0.0688($\pm$0.1355)L

R=0.8158 $\quad$ R^2_{adj}=0.4984 $\quad$ F=3.9809
Sd=0.3536 $\quad$ p<0.1118

Model 8 $\quad$ log $1/c_{MIC}$ = 4.6927($\pm$0.2371) + 0.0314($\pm$0.0181)MR - 2.3438($\pm$0.8880)R

R=0.8384 $\quad$ R^2_{adj}=0.5545 $\quad$ F=4.7343
Sd=0.3332 $\quad$ p<0.0882

Model 9 $\quad$ log $1/c_{MIC}$ = 4.0750($\pm$0.4575) - 2.7899($\pm$0.8309)R + 0.2208($\pm$0.1014)L
R=0.8729 $\quad$ R^2_{adj}=0.6430 $\quad$ F=6.4038
Sd=0.2983 $\quad$ p<0.0566

Three-variable models. In the next step an attempt was made for finding the triparametic correlation analysis, involving some of the parameters. Only **Model 10** and **11** gave relatively statistically good results.

Model 10 log $1/c_{MIC}$ = 4.8897($\pm$0.4245) - 0.2822($\pm$0.4814)logP+0.0474($\pm$0.0337)MR -2.7389($\pm$1.1823)R
R=0.8565 $\quad$ R^2_{adj}=0.46708 $\quad$ F=2.7529
Sd=0.3654 $\quad$ p<0.2138

Model 11 $\quad$ log $1/c_{MIC}$ = 4.6032($\pm$0.4202) + 0.0332($\pm$0.0216)MR + 0.2578($\pm$0.9266)F - 2.4082($\pm$1.0385)R
R=0.8429 $\quad$ R^2_{adj}=0.4097 F=2.4541
Sd=0.3790 $\quad$ p<0.2401

Models 10 and **11** indicate that logP and R negatively contribute to the biological activities, opposite to MR and F.

Model with structural variable indicators. The aminoalkyl linker between the triazole and substituted aromatic core was also investigated (Subset B). The extension of the alkyl chain (methyl) by one carbon (ethyl) led to the statistically realable regression **model 12**:

Model 12 $\quad$ log $1/c_{MIC}$ = 4.8251($\pm$0.4245) + 0.5799($\pm$0.1748)π - 0.0866($\pm$0.2889)I_H
R=0.8095 $\quad$ R^2_{adj}=0.5403 $\quad$ F=5.7024 $\quad$ Sd=0.3467
p<0.0410
where I_H is a structural indicator parameter representing -CH_2- group as 1 and CH_3-CH- group as 0.

Model with heteroaromatic unit. Further modification of the investigated triazole set whenthe aromatic was replaced with a heteroaromatic core (subset C), led to a reduction in activity. After applying an extend *Free – Wilson* equation for such a structured group of compoundsthe following model was obtained:

Model 13 log $1/c_{MIC}$=5.1300($\pm$0.2110)+ 0.2051($\pm$0.1057)logP-0.3532($\pm$0.2849) $I_{=CH-}$
R=0.5101 $\quad$ R^2_{adj}=0.1257 $\quad$ F=1.9345 $\quad$ Sd=0.4189
p<0.1905

A good correlation was not obtained, indicating that another type of heteroaromatic core must be chosen to be a part of the system investigated.

Occurrence of colinearity

At this step, it is worth examining the occurrence or otherwise of colinearity in the proposed models. The best candidates for this purpose would obviously be the two-parametric models. We can do this in two different ways: (*i*) by examining the correlation matrices for used descriptors and (*ii*) by statistical evaluation - calculation of the additional statistical parameters: PRESS/SSY; Q^2; PSE; SPRESS and Q.

a

b
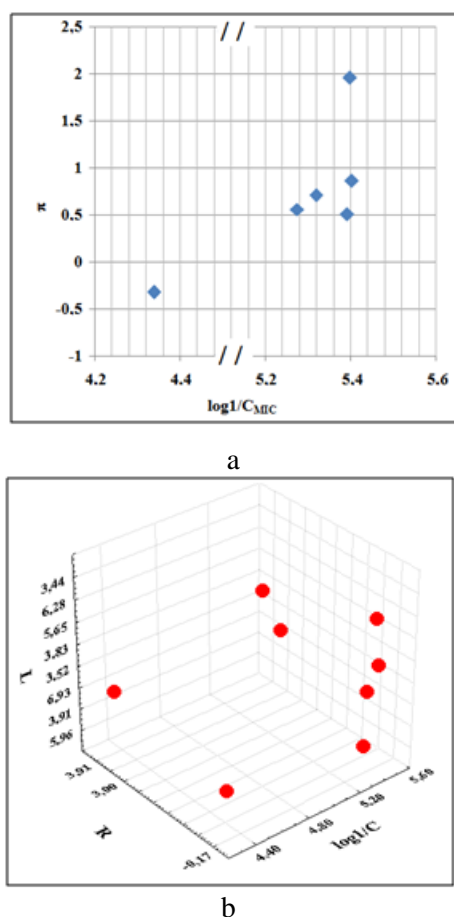
Fig. 2. a) Linear correlation between log $1/c_{MIC}$ and π (**model 1**) b) 3D Scatterplot of correlation between log $1/c_{MIC}$, R and L (**model 9**)

Correlation matrix. It was important for further analysis to find the correlation matrix for used descriptors and their correlation with the activity (Table 3). The results show mutual correlation between some of the used descriptors. So, if a combination of them is present in the regression expression, then the model may suffer from the defect due to collinearly. Also, it may result in a change in signs of the coefficients, a change in the values of the previous coefficient, a change of a significant variable into an insignificant one or an increase in the standard error of the estimate in the addition of an additional parameter to the model.

In accordance with Table 3, **models 2, 4** and **5** were excluded from further statistical analysis, although those models had relatively well correlated coefficients and a standard deviation (R>0.83; Sd<0.34). In the statistically best regression **model 9**, descriptor L has the positive effect on the $log1/c_{MIC}$ value, but its influence is not significant compared with the influence of the descriptor R (Figure 2b). The descriptor R receives a relatively large negative coefficient (-2.7899), indicating that this descriptor leads to a lower log $1/c_{MIC}$ value.

Taking into consideration the above mentioned and preliminary conclusions of the statistical evaluation of the quality of all the models (R, R^2_{adj}; F; Sd, p), only **models 9** and **10** can be used as relatively statistically significant.

Finally, in order to confirm these findings, the antimicrobial activity with respect to *Escherichia coli* (log $1/c_{MIC}$) as predicted by **models 9** and **10** was compared with the corresponding observed values reported in Table 1. Within experimental error, the values agree well.

Also, the predictive correlation coefficient (R_{pre}^2) has been calculated, (Table 4). The obtained predictive correlation coefficient (R_{pre}>0.8) confirms our conclusion. The values R_{pre} are found >0.8, respectively, for the **models 9** and **10**. Correlation between the observed log $1/c_{MIC}$ and predicted $log1/c_{MIC}$ values and for all active compounds, calculated by: *(i)* **model 9** and *(ii)* **model 10**, are presented in Figure 3.

Table 3. Correlation matrix for the chosen electronic, steric and hydrophobic parameters.

	σ	π	logP	MR	F	R	L
σ	**1.0000**	*-0.7226*	-0.1338	-0.2845	0.6140	*0.7557*	-0.1180
π		**1.0000**	*0.7255*	*0.7325*	-0.5044	-0.6925	0.5748
logP			**1.0000**	*0.7202*	-0.1879	-0.2990	0.5669
MR				**1.0000**	-0.3256	-0.0191	*0.9540*
F					**1.0000**	0.3934	-0.2317
R						**1.0000**	0.1589
L							**1.0000**

Table 4. Calculated predictive correlation coefficient (R_{pre}) for **models 9** and **10**.

Model	Correlation: log1/C_{model} with log1/C_{exp}	R_{pre}^2	Sd
9	log1/ $c_{model\ 9}$= 1.3505 +0.7334 log1/$c_{exp.}$	0.8565	0.2417
10	log1/ $c_{model\ 10}$=1.4669 +0.7105 log1/$c_{exp.}$	0.8429	0.2482

Table 5. Cross-validation parameters (Q^2, PRESS/SSY, S_{PRESS}, PSE and Q) calculated for **models 9** and **10**.

Model	Parameters	Q^2	PRESS/SSY	S_{PRESS}	PSE	Q
9	R; L	0.7548	0.2452	0.271	0.214	2.926
10	logP; MR; R	0.7335	0.2665	0.283	0.223	2.328
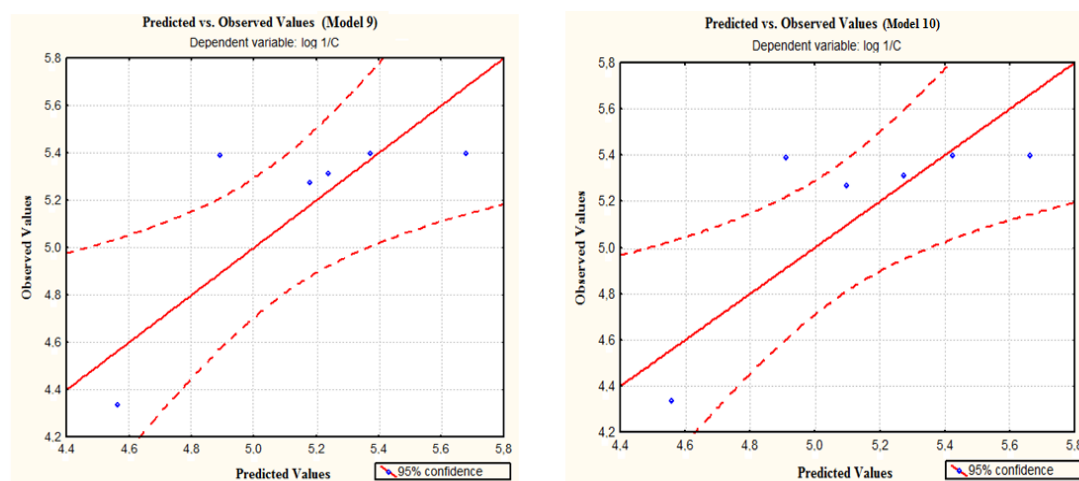
Fig. 3. Plot between the observed and predicted log 1/c_{MIC} values for a) **model 9** and b) **model 10**

Validation

Performing the multiple linear regression of a dependent variable (y; log 1/c_{MIC}) offers the possibility of choosing a large number of explanatory variables (x) and thus raises the question of significance in an acute form. Statistical quantities need to be calculated in order to assess the success of the correlation. Validation is a crucial aspect of any QSAR analysis and a cross-validation methodology was undergoing for deciding the predictive power of the proposed models. This is needed because a model with good statistics may not have a good predictive potential. The predictivity of each model was measured by several cross-validation parameters: Q^2, PRESS/SSY; S_{PRESS}; *PSE* and *Q*.

For a reasonable QSAR model, PRESS/SSY should be smaller than 0.4 [32]. In our case the ratio PRESS/SSY<0.27 indicates that the proposed models are reliable QSPR models (Tab. 5). Good Q^2, S_{PRESS} and *PSE* values, were also obtained: (Q^2>0.73; S_{PRESS} and *PSE*<0.3)(Tab. 5),confirming the assumption that these models can be used as a tool for predicting the inhibition of *E. coli* [33]. But, the lowest value for S_{PRESS} and *PSE*, for **model 9**, compared to other models, supports its highest

predictive potential. An additional requirement should be fulfilled, the difference between R^2 and Q^2 should not be more than 0.3 [33].

The predictive power, determined by the Pogliani Q parameter [34] for **model 9** (Q=2.926) confirms that this model has excellent statistics as well as excellent predictive power, compared with the other model (Tab. 5). In our study, since the previous data are ofa similar ranking, Q is taken as proof of the high predictive ability of the QSAR **model 9**.

We also calculated the variance inflation factor (VIF) for each of the parameters in the selected models, as a measure of multicollinearity [35]. A VIF 10 or more (no upper limit is defined) for large data sets indicates a collinearity problem. For small data sets, even VIFs of five or more (here no upper limit is defined as well) can signify collinearity. The variables with a high VIF are candidates for exclusion from the model. First, we calculated VIF values for **model 9** and **10** (as statistically the best models according to the preliminary statistical data) all VIF values are<4 (VIF=1.102 ÷3.269), meaning that these models are free from defects caused by colinearity (Tab.6).

743

Table 6. VIF values for the two- and three-variabel models.

Models	Descriptors	Variance inflation factor (VIF)
9	R	1.102
	L	1.102
	logP	3.269
10	MR	2.902
	R	1.487

In the statistically best regression **model 9**, the descriptor L has a positive effect on the $\log 1/c_{MIC}$ value, but his influence is not significant (7.33%) compared with the influence of descriptor R (92.67%), (Figure 2b). The descriptor R receives a relatively large negative coefficient (-2.7899), indicating that this descriptor leads to a lower log $1/c_{MIC}$ value. In this model, the coefficients of R and L are much higher than their standard deviation, which is another confirmation for the statistical significance of **model 9**.

The statistical evaluation of the data used to test the quality of the obtained models indicated that **model 9** is statistically significant (R=0.8729; R^2_{adj}=0.6430; F=6.4038; Sd=0.2983 p<0.0566; R_{ped}=0.8565; PRESS/SSY=0.2452; Q^2=0.7548; S_{PRESS}=0.271; *PSE*=0.214; Q=2.926), when all the parameters are summarized.

The MLR method can be useful when a relatively small number of descriptors are used. In this case, for the active compounds, the obtained QSAR models with two descriptors can be good in order to avoid a high chance of spurious correlations. Therefore, we selected **model 9** as the best statistically biparametric models, for determing the activity of the chosen triazole derivatives against *E. coli*.

As a result of spreading the investigated system (Subsets B and C) the results showed that statistically significant QSAR models were not obtained. That means that maybe another heterocyclic nucleus (beside those used in this study) may lead to developing a better *QSAR* system.

CONCLUSION

Spurred by the need of new antimicrobial agents and the fact that many effective drugs, insecticides and fungicides possess heterocyclic systems in their structure, such as triazole core, some new 1,2,4-triazole derivatives were synthesized. Form the results and discussion presented in this work, a conclusion can be made that part of the investigated N^I-substituted 1,2,4-triazole derivatives are effective *in vitro* against the tested strain

Escherichia coli. The inhibitor activity of triazoles derivatives were modeled using multi linear models based on the chosen physico - chemical descriptors and structure variable indicators. Analysis of this limited set of substituted 1,2,4-triazole molecules allowed us to build a model of their antimicrobial activity against *E. coli* in which logP, MR, R and L are important factors.

The obtained biparameter models showed a relatively good correlation and predictive ability, in comparison with the monoparametric models. The validity of the models have been established by the determination of suitable statistical parameters such as: R; R^2_{adj}; Sd; F-test; Q^2; PRESS/SSY, S_{PRESS}, *PSE* and Q.

The structural modification which was made of the basic set (Subset A) didn't show any upgrading of the QSAR models. This result is a good base for expanding the 1,2,4-triazole set with new compounds which will have improved characteristics. In consequence this will help the medical and agriculture chemist in their prediction of an increasing activity and thus the synthesis of new triazoles exhibiting better activities than those reported in this paper.

REFERENCES

1. J. K. Sahu, S. Ganguly, A. Kaushik, *J App Pharm Sci.*, **4**, 81 (2014).
2. N. Chaudharya, R. Dubeyb, H. Panwar, *Der Pharma Chemica,* **6**, 115 (2014).
3. Z. Li, Y. Cao, P. Zhan, C. Pannecouque, J. Balzarini, E. D. Clercq, X. Liu, *Letters in Drug Design & Discovery*, **10**, 27 (2013).
4. K. Rakesh, M. Shahar Yar, B. Srivastava, A. K. Rai, *Der Pharma Chemica*, **6**, 137 (2014).
5. N. S. Dighe, R. B. Saudagar, D. A. Jain, *Bulgarian Chemical Communications,* **46**, 85 (2014).
6. G. R. Kokil, P. V. Rewatkarb, S. Gosainc, S. Aggarwalc, A. Vermac, A. Kalrac, S. Thareja, *Letters in Drug Design & Discovery,* **7**, 46 (2010).
7. A. Martin, R. Martin, *Int. J. Life Sc. Bt & Pharm. Res.*, **3**, 323 (2014).
8. V. N. R Desabattina, R. G. P. Aluru, S. Y. Narasimha, R. R. Dharmapuri, R. L. Rao. *J. App. Pharm.*, **6**, 1 (2014).
9. R. Kumar, M. Shahar Yar, S. Chaturvedi, A.Srivastava, *Int. J. Pharm Tech Res.,* **5**, 1844 (2013).
10. A. Reddy, S. G. Kini, M. Mubeen, *Der Pharma Chemica*, **5**, 259 (2013).
11. B. Andrews, A. Mansur, *Der Pharma Chemica*, **6**, 162 (2014).
12. B. Anil Reddy, *E-Journal of Chemistry*, **7**, 222 (2010).
13. R. Katritzky, S. Rachwal, B. Rachwal, *J. Chem. Soc. Perkin Trans. I.,* **1**, 805 (1987).
14. F. Collino, S. Volpe, *Boll. Chim. Farm.*, **121**, 328 (1982).

15. J. Cruz, E. Gracia-Ochoa, M. Castro, *J. Electrochem. Soc.*,**150**, B26 (2003) .

16. M. A. Quraishi, D. Jamal, *J. Am. Oil Chem. Soc.*,**77,** 1107 (2000).

17. S. S. Panda, S. C. Jain, *Med. Chem. Res.*, **23**, 848 (2014).

18. F. Ding, J. Guo, W. Song, W. Hu, Z. Li, *Chemistry and Ecology*, **27**, 359 (2011).

19. O. Adebimpe, R. C. Dash, M. E. S. Soliman, *Letters in Drug Design & Discovery*, **11**, 618 (2014).

20. M. Polyakova, L. Mei Jin, K. Ho Row, *Bull. Korean Chem. Soc.*, **27**, 211 (2006).

21. V. Dimova, K. Colanceska Ragenovic, V. Kakurinov, *Int. J. Mol. Sci.*, **7**, 119 (2006).

22. V. Dimova, N. Perisic-Janjic, *Organic Chemistry, An Indian Journal,* **3**, 51 (2007).

23. V. Dimova, N. Perisic-Janjic, *Maced. J Chem. Chem. Eng.*, **28**, 79 (2009).

24. V. Dimova, PhD Thesis, University Ss. Cyril and Methodius, Skopje, Macedonia, 2006.

25. S. Rollas, N. Kalyoncuoglu, D. Sür-Altiner,Y. Yegenoglu, *Pharmazie*, **48**, 308 (1993).

26. C. Hansch, A. Leo, Exploring QSAR: Fundamentals and Applications in Chemistry and Biology, American Chemical Society. Washington DC (1995).

27. M. Karelson, V. Lobanov, A. Katritzky, *Chem. Rev.*, **96**, 1027 (1996).

28. http://www.molinspiration.com.

29. R. Todeschini, V. Consonni, Handbook of molecular descriptors, WILEY-VCH Verlag GmbH & Co. KGaA, Weinheim, 2000.

30. T. Sotomatsu, M. Shigemura, *Bull. Chem. Soc. Jpn.*, **65**, 3157 (1992).

31. STATISTICA program package http://www.statsoft.com

32. A. Thakur, *ARKIVOC,* (**xiv**). 49 (2005).

33. R. Veerasamy, H. Rajak, A. Jain, S. Sivadasan, C. P. Varghese, R. K. Agrawal, *International Journal of Drug Design and Discovery*, **2**, 511 (2011).

34. L. Pogliani, *J. Phys. Chem.* **100***,* 18065 (1996).

35. J. Singh, B. Shaik, S. Singh, V. K. Agrawal, P. V. Khadikar, O. Deeb, C. T. Supuran, *Chem. Biol. Drug Des.*, **71**, 244 (2008).

QSAR АНАЛИЗ НА N[1]-ЗАМЕСТЕНИ 1,2,4-ТРИАЗОЛИ СРЕЩУ *Escherichia coli*

В. Димова[1][*,] И. Йорданов[1], Л. Димитров[2]

[1]*Факултет по технология и металургия, Университет „Св. Св. Кирил и Методий", ул. Руджер Бошкович 16, 1000 Скопие, Република Македония*
[2]*Институт по земеделие, Университет „Св. Св. Кирил и Методий", ул. 16-та Македонска бригада 3а, 1000 Скопие, Република Македония*

(Резюме)

Бе направен QSAR анализ на серия от предварително синтезирани N[1]-заместени 1,2,4-триазолови производни тествани за инхибиторна активност по отношение на растеж на *Escherichia coli*, като се използва компютеризирана схема за множествена регресия. Използвайки подхода на Hansch и Free – Willson, приноса за активността на аминометил / аминоетил заместител и ароматен / хетероароматният пръстен се определя от получените корелационни уравнения. В съответствие със статистическите параметри (R = 0,8729; R^2_{adj} = 0.6430; Sd = 0.2983; Q^2 = 0,7548 и PRESS / SSY = 0,2452), двупараметричен модел, който включва R и L, е избран като най-добър, за определяне на активността на избраните триазоловите производни срещу *E. colli*. Разширяването на изследваната система: подмножеството В (аминометилова група заменена с аминоетилова група) и подмножеството С (ароматен пръстен заменен с хетероароматен пръстен), не води до получаване на статистически значими QSAR модели.

Physicochemical characterization and thermal analysis of newly discovered Nigerian coals

B. B. Nyakuma

Centre of Hydrogen Energy, Institute of Future Energy,
Universiti Teknologi Malaysia, 81310 Skudai, Johor Bahru, Malaysia.

The physicochemical properties and thermal degradation behaviour of three newly discovered sources of coals; Afuze, Garin Maiganga and Shankodi-Jangwa from Nigeria were examined. Characterization was performed to determine the rank, classification and quality of the coals using ultimate analysis, proximate analysis and higher heating value (HHV). Ultimate analysis revealed high Carbon (*C*), Hydrogen (*H*) and Oxygen (*O*), but low Nitrogen (*N*) and Sulphur (*S*) content. Proximate analysis demonstrated that the Garin Maiganga (GMG) coal sample exhibited the highest volatile matter (51.16 %) and Moisture (5.28 %) content. The highest ash content 30.99 % was observed in the Afuze coal; whereas the highest FC content was observed in the Shankodi-Jangwa coal sample. The heating values (HHV) of the different samples were; Garin Maiganga (23.74 MJ/kg); Shankodi-Jangwa (27.34 MJ/kg) and Afuze (30.52 MJ/kg) which confirmed Afuze and Shankodi-Jangwa as high rank coals and Garin Maiganga as low rank. Consequently, Afuze coal is classified as Bituminous and NOT Sub-Bituminous as previously reported. The results also demonstrate the reactivity and maturity of the coal samples by increasing order; Garin Maiganga>Shankodi-Jangwa>Afuze. Overall, the physicochemical and low rank properties of GMG coal make it suitable for coal power generation. The high fixed carbon content and thermochemical reactivity of SKJ indicate a good coking potential for steel and cement production. Last, the low moisture content and high carbon and heating values indicate AFZ coal can be utilized for power generation.

Keywords: Physicochemical, Thermogravimetric, Characterization, Low Rank Coal, Nigeria.

INTRODUCTION

Coal is the world's cheapest, most abundant and widely distributed source of energy with a global consumption of 5,544.3 Mtce [1, 2].Consequently, coal is the largest primary source of fossil fuels utilized for electric power generation and the production of chemicals, fuels and steel [3]. Despite the global importance of coal resources, the low cost, sustainable supply and self-sufficient electricity generation in sub-Saharan Africa remains a colossal conundrum.

Nigeria is the largest economy and exporter of crude oil in Africa with estimated crude oil reserves of 35 billion barrels, 187 trillion cubic feet of natural gas, and over 4 billion metric tonnes of coal [4]. In spite of Nigeria's vast energy potential, the country remains perennially plagued by energy crises resulting from low electricity generation, poor distribution and transmission losses [5]. This unfortunate scenario has greatly undermined Nigeria's potential for sustained socioeconomic growth, infrastructural development and energy security. Therefore, there is a critical need for cheap, sustained and consistent electric power supply generated from inexpensive sources of energy such as coal. Nigerian coals are typically low rank sub-bituminous in nature, with deposits located predominantly in the Lower, Middle and Upper Benue Trough of the Nigerian sedimentary basin [6].

Conversely, the search for higher ranked coals has resulted in the discovery of new deposits in Afuze, Garin Maiganga and Shankodi-Jangwa [7]. The Afuze coal is categorised as sub-bituminous with significant deposits located South West of the Benin Flank in the Anambra Basin in Afuze, Edo State [8]. The Shankodi-Jangwa coal is bituminous in nature with deposits situated in the Middle Benue Trough of Obi, Nasarawa state [9]. Last, Garin Maiganga coal is classified as sub-bituminous with deposits in the Akko, Gombe state [10].

However, lack of comprehensive scientific data on Nigerian coal has greatly hampered its utilization for electric power generation and industrial applications [11]. In addition, coal accounts for 37% of global carbon dioxide (CO_2) emissions prompting concerns about the long term socioeconomic and environmental impacts of coal power generation particularly in developing countries like Nigeria. Consequently, clean coal technologies such as underground coal gasification (UCG) [12], carbon capture storage (CCS) [13, 14] and the Integrated Gasification Combined Cycle (IGCC) [15] are currently under investigation for future coal power generation [16-18]. The development and diffusion

---

of these clean coal technologies into the current energy mix of nations around the globe will greatly increase the prospects of cheap, efficient and sustainable energy.

However, the effective application of low-carbon emission techniques for coal power generation in Nigeria will require comprehensive knowledge of the physicochemical and thermal properties of indigenous coal. This is vital for examining the rank classification, environmental impacts and feasibility of the coal feedstocks for future applications [19]. Furthermore, the coal property data will be essential for the engineering design, process optimization and project costing of future energy conversion systems.

Consequently, this study is aimed at describing the physicochemical and thermal properties of the newly discovered Afuze, Garin Maiganga and Shankodi-Jangwa coals from Nigeria. The study presents novel results of the thermal degradation behaviour of the coals using thermogravimetric analysis (TGA) under inert conditions. Finally, the study attempts to propose potential future applications of the newly discovered coals.

EXPERIMENTAL

The coal samples examined in this study were obtained from the Afuze coal field in Afuze, Edo state; the Shankodi-Jangwa coal field in Obi, Nasarawa state and Garin Maiganga coal field in the Akko, Gombe state of Nigeria. The coals were subsequently labelled; AFZ - Afuze coal; SKJ – Shankodi-Jangwa and GMG – Garin Maiganga. The coal mines are all located in various sedimentary basins in Nigeria as illustrated in Figure 1 [21].

The coal samples were subsequently crushed into small particles using a dry miller. Next, the pulverized coal particles were sifted using an analytical sieve (Retsch[TM]250 μm mesh) to obtain homogeneous particles for physicochemical characterization and thermal analysis.

Next, elemental coal analysis was carried out using an EL Vario MICRO Cube Elementar[TM] CHNS analyser in accordance with the specifications of the American Society for Testing and Materials (ASTM) D5291 standard. Proximate analysis was done using ASTM D3173, D3174 and D3175 standard techniques for moisture (M), volatile matter (VM) and ash (AC) content, respectively. The fixed carbon (FC) and Oxygen (O) content were determined by difference. The mineral matter was calculated using the *Parr formula* ($Mm = 1.08A + 0.55S$); where A and S represent the ash and sulphur content, respectively [21].
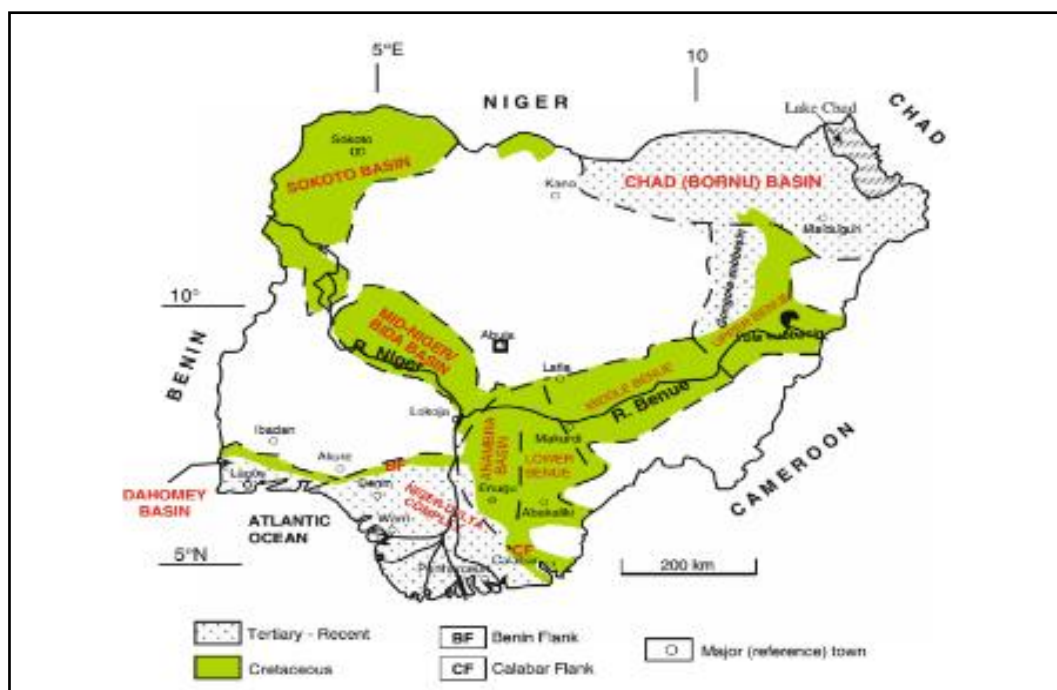
Fig.1. Sedimentary basins of Nigeria [20].

747

Table 1. Physicochemical Properties of Nigerian Coals.

Symbol	C	H	N	S	O	M	VM	A	FC	HHV	Mm
AFZ	72.46	6.07	1.63	1.41	18.43	1.97	45.80	30.99	21.24	30.52	34.24
GMG	61.96	4.42	1.07	0.39	32.16	5.28	51.16	21.05	22.52	23.74	22.95
SKJ	71.46	6.40	1.37	2.03	18.76	5.14	40.73	14.94	39.18	27.34	17.25

The higher heating value (HHV) of the coal samples was determined using bomb calorimetry (IKA C2000 Bomb Calorimeter). All the tests were repeated at least three times to ensure the reliability of the results. It is important to state that the coal samples were not subjected to any thermal or chemical pre-treatment prior to physicochemical and thermal characterization, consequently all the results are presented in *as received* (ar) basis. The rank and agglomeration classification of the coals were examined using the heating value (HHV) as described in the ASTM D388 standard for coal classification [22].

The thermal degradation behaviour of the coal samples was investigated using a Perkin Elmer STA 8000 Simultaneous Thermogravimetric (TG) analyser. About 12-16 mg of each sample was placed in an alumina pan and heated at 25°C/min from 50 to 1000°C to examine the thermal degradation in an inert atmosphere.

The evolved gases from the coals were purged using ultra-pure nitrogen gas at a flow rate 100 mL per min. The resulting thermograms were analysed using the Pyris Thermal Analysis Software (Version 11) to determine the temperature profile characteristics; peak decomposition temperature, T_p, residual mass R_m and total mass of the sample, T_m decomposed during thermal analysis.

RESULTS AND DISCUSSION

Physicochemical properties

The elemental composition, proximate analysis, mineral matter and heating value of the coal samples; Afuze (AFZ), Garin Maiganga (GMG) and Shankodi-Jangwa (SKJ) are presented in Table 1 in *as received* basis (ar) as also reported in the literature [3, 10].

The elemental composition presented in Table 1 indicates that the coal samples possess a high *C* and *H* content but relatively low *O* content. The highest carbon *C* content was observed in AFZ coal, followed by SKJ and GMG. The *H* content of the coal samples was in the range 4.42 to 6.40 % with the highest value observed in SKJ while the lowest value was observed in the GMG coal sample. The *O* content of the coal samples was in the range 18.43 to

32.16 % with GMG exhibiting the highest value. In general, the *C*, *H* and *O* content significantly influences the heating value, maturity and chemical reactivity of the coal [10, 21].

The *N* and *S* content, which serves as a measure of the environmental friendliness of coals, was observed to be low in all samples. The lowest *N* content was observed in GMG coal whereas the values for SKJ and AFZ were 1.37 wt.% and 1.63 wt.%, respectively. Conversely, the lowest *S* content was observed in GMG, whereas the values for SKJ and AFZ were 2.03 wt. % and 1.41 wt. %, respectively. The typical acceptable range for *N* and *S* in coals should not exceed 2.0 % [23] due to the risk of NO_x and SO_x pollutant emissions. Consequently, the high *S* content may hamper the potential application of the coals in steel manufacturing where the limits are 0.8 – 1.0 % [23]. Comparatively, GMG coal showed the lowest *N* and *S* content thereby posing the lowest risk for environmental pollutant emissions. Consequently, GMG may be suitable for cement and steel manufacture, power generation as well as industrial and domestic heating due to its favourable properties [10].

The highest HHV of 30.52 MJ/kg was observed for AFZ coal; whereas SKJ was 27.34 MJ/kg and GMG 23.74 MJ/kg. The observed results are in good agreement with the values for GMG and SKJ reported in the literature [10]. The high heating values of AFZ and SKJ can be attributed to the high *C*, *H* and low *O* content in the elemental composition of the coals. In contrast, the low HHV in GMG is primarily due to its high *O* and low *C* and *H* contents. In addition, with the HHV lower than 24 MJ/kg, the GMG coal can be categorized as low rank (LRC) whereas SKJ and AFZ coals are high rank coals (HRC) [21].

Proximate Analysis

The proximate analysis revealed AFZ coal has the lowest moisture, *M* content 1.97 wt.%, while SKJ was 5.14 wt.% and GMG 5.28 wt.%. Moisture content in coals is undesirable due to its chemical inactivity and tendency to absorb heat during combustion. This typically results in a low heating value and low thermal efficiency during conversion

along with handling and transportation problems [23]. Furthermore, *M* and *VM* content is an index for evaluating the maturity, quality and potential application of coals. Hence, it is fundamentally established that coal rank or maturity increases with decrease in *M* and *VM* content [21, 23]. The highest *VM* content of 51.16 wt.% was observed for GMG, SKJ coal was 40.73 % and AFZ coal recorded as 45.80 %. Consequently, based on *M* and *VM*, the maturity of the coals increases in the order; GMG > SKJ > AFZ on the basis of *M* content; while the order is GMG > AFZ > SKJ based on the *VM* content.

The ash content typically determines the fouling tendency and slagging potential of coals during thermal conversion [21]. Furthermore, ash content can be used to determine the composition, volume and performance of blast furnace coke [10, 24]. The ash analysis results for the coals indicate that the highest ash content of 30.99 % was observed in AFZ coal; compared to 21.05 % for GMG and 14.94 % for SKJ coal. The mineral matter, *Mm*, of the coals also showed a similar trend as observed for ash content. Hence, it can be inferred that the fouling potential of the coals increases in the order; SKJ>GMG>AFZ.

The highest FC content was observed in SKJ coal followed by GMG and AFZ. Since, FC is the solid residue leftover after devolatilization and can be used to estimate the amount of coke obtained from coal carbonization [10, 21]. Therefore, SKJ has the highest coke potential among the coals investigated demonstrating it could be a good source of coking coal required for the manufacture of steel [10].

Coal Rank Classification

The agglomerating or non-agglomerating property of coal samples can be determined from *VM* and HHV, according to the ASTM D388-15 standard [22]. Based on this criteria, the HHV of non-agglomerating coals typically range from 14.7 to 26.7 MJ/kg, however agglomerating coals range from 26.7 to 32.4 MJ/kg [20]. Hence, SKJ with HHV (27.34 MJ/kg) and AFZ (30.52 MJ/kg) can be classified as agglomerating coals while GMG (23.74 MJ/kg) is non-agglomerating.

Furthermore, the coals can be classified into sub groups or ranks based on HHV. The GMG coal can thus be classified as *Sub-Bituminous B coal* with HHV typically from 22.1 to 24.4 MJ/kg [22, 23]. The SKJ coal can be classified as *High Volatile C Bituminous Coal* with an HHV typically from 26.7 to 30.2 MJ/kg [22, 23], which agrees with the Bituminous classification described in the literature by *Ryemshak & Jauro* [10]. Last, the AFZ coal (HHV = 30.52 MJ/kg) can be classified as *High*

Volatile B Bituminous Coal with a typical HHV from 30.2 to 32.6 MJ/kg [22, 23] which distinctly contrasts with the classification widely reported in the literature [4, 8]. Hence, the results indicate that AFZ coal has been hitherto, incorrectly classified or ranked as a *Sub-Bituminous Coal* by the academics and researchers in Nigeria. Consequently, these findings provide not only reference material vital for future studies but also valuable data for the future utilization of AFZ coal in the Nigerian energy industry.

Thermogravimetric (TG) Analysis of Nigerian Coals

The thermogravimetric (TG) curves for the Nigerian coals investigated are presented in Fig. 2. The curves exhibit the slanted *Z*-type downward sloping curves typically observed for thermally degrading materials which demonstrate the effect of increasing temperature on the weight loss characteristics of the coals.
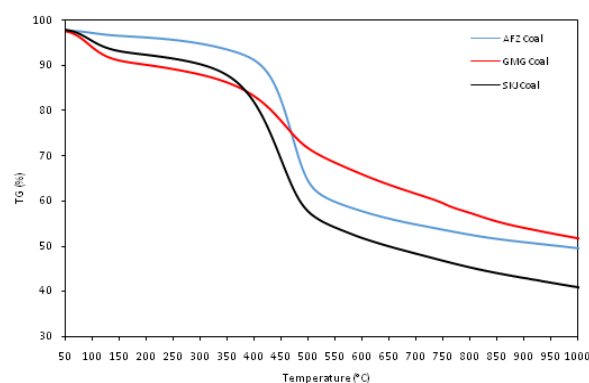
Fig.2. TG curves of Nigerian Coals.

From Fig. 2, it can be observed that the TG curves for AFZ and SKJ are similar in shape and orientation whereas the GMG coal is steeply sloped. This suggests that the reaction mechanisms for the conversion of AFZ and SKJ coal are similar as expected for coals of similar rank, but different from GMG. However, the analysis of the temperature profile characteristics revealed that the ignition temperature, T_i of SKJ coal, 375.74°C is considerably lower than for AFZ, 426.14°C and; GMG coal, 381.36°C. The results indicate that the SKJ is the most reactive while AFZ is the least reactive coal. The observed difference (50.40°C) in the reactivity of SKJ coal and AFZ coal may be due to the ash and mineral matter content of the coal samples. At 30.99 wt.% the AFZ coal has twice the ash content of the SKJ coal (14.94 wt.%). High ash content in coal is known to lower the calorific value, thermal efficiency and results in operational problems such as slagging and agglomeration [21, 23]. Consequently, the lower reactivity of the AFZ

coal relative to SKJ may be due to the difference in ash content which affects the thermal degradation of the samples as observed during thermal analysis.

Derivative Thermogravimetric (DTG) Analysis of Nigerian Coals

The Derivative Thermogravimetric (DTG) curves of the Nigerian coals investigated are presented in Fig. 3. The curves are typically used to examine the devolatilization profiles of the potential solid fuels required for assessing their suitability and potential applications [25, 26]. In addition, the gasification and coking potential of the coals can be examined using DTG curves from the thermal analysis under inert atmosphere [27].

The DTG curves for AFZ and SKJ coals each revealed two peaks within the temperature range 50-200°C and 250-700°C. In contrast, the thermal degradation of the GMG coal revealed three peaks at 50-200°C, 250-700°C and 700-850°C.

The degradation of coals from 50-200°C can be attributed to drying as typically characterised by the loss of chemically bonded water molecules and mineral hydrates [3]. The DTG peaks observed during this stage (50-200°C) are significantly smaller and broader than the DTG peaks between 250-700°C. In particular, the results showed a good correlation between the moisture content and size of the DTG peaks.
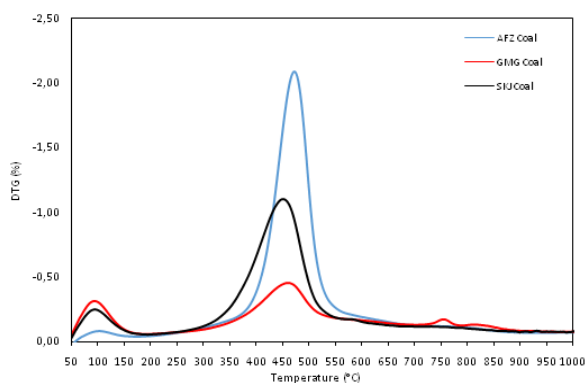
Fig.3. DTG curves of Nigerian Coals.

The weight loss observed from 250-700°C is primarily ascribed to the devolatilization of weakly bonded species into CO_2, CO, CH_4 and other non-condensable gases [27, 28]. The devolatilization of coal typically involves a significant loss of weight, therefore it is termed the active stage of pyrolytic decomposition. For the AFZ coal sample the weight loss observed was 41.58%, while GMG was 28.52% and SKJ 44.09 %. The results for the weight loss during devolatilization the coals confirms the higher reactivity of the SKJ coal compared to the AFZ and GMG coals. Table 2 presents the temperature profile characteristics of the coal samples in terms of the peak decomposition temperatures, T_p, Residual mass, R_m, and total mass D_m, of the sample decomposed during thermal analysis.

The peak decomposition temperature, T_p, is the most significant temperature profile characteristic deduced from DTG. It is used to examine the reactivity, thermal stability and temperature at which the maximum weight loss of the thermally decomposing material occurs. The T_p values for the coals increased in the order SKJ → GMG → AFZ. The low T_p value of SKJ indicates can be easily degraded compared to GMG and AFZ as presented by the results for the total mass decomposed D_m, during TGA. This trend is in good agreement with the results for other Nigerian coals reported in the literature [27].

In addition, the residual mass of the coal samples increased in the order SKJ → AFZ → GMG. The increase in residual mass may be due to the reactivity of the coals based on the high ash and fixed carbon content [29]. However, the effect of ash can be remedied by pre-treatment with additives or co-firing with biomass [30] prior to future application. In general, based on the properties; GMG could be used in domestic heating and power generation while SKJ and AFZ coals for power generation, steel and cement production.

Table 2.Temperature profile characteristics of Nigerian Coals.

Coal Sample	Peak Decomposition (°C) T_p	Residual Mass (%) R_m	Mass Decomposed (%) D_m
AFZ	470.71	49.46	50.54
GMG	459.51	51.74	48.26
SKJ	450.29	40.94	59.06

CONCLUSION

The physicochemical properties and the thermal degradation behaviour of three newly discovered Nigerian coals were examined. The results indicate the coals contain high proportions of C, H, O and low N and S contents. The heating values confirmed the categorization of AFZ and SKJ as high rank coals (HRC) whereas GMG coal is low rank (LRC). Furthermore, the results revealed that AFZ coal is Bituminous NOT Sub-Bituminous as previously presented in the literature. The reactivity and maturity of the coals increased in the order: GMG > SKJ > AFZ. However, based on the devolatilization profile characteristics from thermal analysis, the reactivity of the coals increases in the order SKJ → GMG → AFZ. Additionally, the physicochemical and low rank properties; high moisture, volatile matter yet low Nitrogen and Sulphur content of GMG coal suggest it is suitable for clean coal applications in pyrolysis, gasification and power generation. The high fixed carbon content and thermochemical reactivity of SKJ indicate a good coking potential for application in steel and cement production. Last, the AFZ coal with its low moisture content and high carbon and heating value can be efficiently utilized in thermal conversion technologies for electric power generation.

REFERENCES

1. R. Ye, C. Xiang, J. Lin, Z. Peng, K. Huang, Z. Yan, N. P. Cook, E. L. Samuel, C.-C. Hwang, G. Ruan, *Nature Communications*, **4**, 2943, (2013).
2. OECD Working Paper: in IEA Coal Industry Advisory Board OECD, Paris, 2012.
3. A. Sarwar, M. N. Khan, K. F. Azhar, *Energy Sources, Part A: Recovery, Utilization, and Environmental Effects*, **36**(5), 525, (2014).
4. E. I. Ohimain, *International Journal of Energy and Power Engineering*, **3**(1), 28 (2014).
5. F. Ibitoye, A. Adenikinju, *Applied Energy*, **84**(5), 492-504 (2007).
6. F. B. Fatoye, Y. B. Gideon, *Journal of Environment and Earth Science*, **3**(11), 25 (2013).
7. U. S. Onoduku, *Journal of Geosciences and Geomatics*, **2**(3), 80 (2014).
8. http://www.equatorialmining.com/projects-operations/afuze-coalfields.
9. A. Jauro, N. Obaje, M. Agho, M. Abubakar, A. Tukur, *Fuel*, **86**(4), 520 (2007).
10. A. Ryemshak, A. Jauro, *International Journal of Industrial Chemistry*, **4**(1), 1 (2013).
11. A. Olajire, A. Ameen, M. Abdul-Hammed, F. Adekola, *Journal of Fuel Chemistry and Technology*, **35**(6), 641 (2007).
12. A. W. Bhutto, A. A. Bazmi, G. Zahedi, *Progress in Energy and Combustion Science*, **39**(1), 189 (2013).
13. N. Nakaten, R. Schlüter, R. Azzam, T. Kempka, *Energy*, **66**, 779 (2014).
14. N. Nakaten, R. Azzam, T. Kempka, *International Journal of Greenhouse Gas Control*, **26**, 51 (2014).
15. A. Y. Klimenko, *Energies*, **2**(2), 456 (2009).
16. A. Franco, A. R. Diaz, *Energy*, **34**(3), 348 (2009).
17. Y. Sheng, A. Benderev, D. Bukolska, K. I.-I. Eshiet, C. D. da Gama, T. Gorka, M. Green, N. Hristov, I. Katsimpardi, T. Kempka, *Mitigation and Adaptation Strategies for Global Change*, **1,** 33 (2014).
18. A. N. Khadse, *Fuel*, **142**, 121 (2015).
19. A. Björkman, *Fuel*, **80**(2), 155 (2001).
20. N. G. Obaje, Geology and mineral resources of Nigeria: Springer Science & Business Media, 2009.
21. J. G. Speight, The Chemistry and Technology of Coal: CRC Press, 2012.
22. ASTM D388 Standard:Classification of coals by rank. ASTM International, West Conshohocken, PA, 2015.
23. L. Thomas, Coal Geology: John Wiley & Sons, 2002.
24. N. Obaje, B. Ligouis, *Journal of African Earth Sciences*, **22**(2), 159 (1996).
25. B. B. Nyakuma, A. Johari, A. Ahmad, T. A. T. Abdullah, *Energy Procedia*, **52**, 466 (2014).
26. B. B. Nyakuma, A. Ahmad, A. Johari, T. A. Tuan Abdullah, O. Oladokun, Y. D. Aminu, *Chemical Engineering Transactions*, **45**, 1327 (2015).
27. O. Sonibare, O. Ehinola, R. Egashira, L. KeanGiap, *Journal of Applied Sciences*, **5**(1), 104 (2005).
28. B. K. Saikia, R. K. Boruah, P. K. Gogoi, B. P. Baruah, *Fuel Processing Technology*, **90**(2), 196 (2009).
29. A. K. Sadhukhan, P. Gupta, T. Goyal, R. K. Saha, *Bioresource Technology*, **99**(17), 8022 (2008).
30. D. F. Umar, H. Usui, B. Daulay, *Fuel Processing Technology*, **87**(11), 1007 (2006).

ФИЗИКОХИМИЧНО ОХАРАКТЕРИЗИРАНЕ И ТЕРМИЧЕН АНАЛИЗ НА НОВОТКРИТИ НИГЕРИЙСКИ ВЪГЛИЩА

Б. Б. Някума

Център за водородна енергетика, Институт по енергии на бъдещето, Технологичен университет в Малайзия, 81310 Скудай, Джохор Бахру, Малайзия

(Резюме)

Изследвани са физико-химичните свойства и термичната деградация на каменни въглища от три ново-открити източника (Афузе, Гарин Маинганга и Шанкоди-Джангуа) от Нигерия. Охарактеризирането е проведено с елементен анализ, анализ на химическия състав и на горната калорична стойност, за да се установят степента, класификацията и качеството на въглищата. Анализът на химическия състав показва високо съдържание на летливи вещества (51.16 %) и влага (5.28 %). Най-високо съдържание на пепел се наблюдава в въглищата от Афузе, докато най-високо съдържание на свързан въглерод се забелязва в пробите от Шанкоди-Джангуа. Калоричната стойност (HHV) на различните въглища е: Гарин Маиганга (23.74 MJ/kg); Шанкоди-Джангуа (27.34 MJ/kg) и Афузе (30.52 MJ/kg), което потвърждава въглищата от Афузе и Шанкоди-Джангуа като висококачествени, а Гарин Маиганга – от по-ниско качество. Освен това, въглищата от Афузе са определени като битуминозни, но не суб-битуминозни, акто е било съобщено реди. Резултатите показват реактиво-способност и зрялост в следния възходящ ред: Гарин Майганга >Шанкоди Джангуа >Афуза. Общо взето, физикохимичните свойства и по-ниското качество на въглищата от Гарин Майганга ги правят подходящи за термоцентрали. Високото съдържание на свързан въглерод и термо-реактивоспособността на въглищата от Шанкоди Джангуа ги правят подходящи за коксуване при произдоството на стомана и в циментената промишленост. Накрая, ниското съдържание на влага, високо въглеродно съдържание и калоричност прави въглищата от Афузе подходящи за производство на енергия.

Stabilization of sunflower oil with extracts from fenugreek, mint and liquorice

I. Niamat[1], A.R. Tariq[1], M. Imran[1], F. Kanwal[1], L. Mitu[2]*

[1]Institute of chemistry, University of the Punjab, Lahore-54890, Pakistan
[2]Department of Chemistry, University of Pitesti, Pitesti-110040, Romania

Stabilization studies of sunflower oil were carried out after adding synthetic antioxidants (Butylated hydroxyanisole BHA and Butylated hydroxyltoluene BHT) as well as methanolic extracts of Fenugreek, mint and Liquorice at ambient storage conditions. The antioxidant potential of these methanolic herb extracts was evaluated by PV (peroxide value), FFA (free fatty acid value), IV (iodine value), CD (conjugated diene) and CT (conjugated triene) value determination. These parameters revealed that an appreciably higher concentration (roughly 5 times that of BHA and BHT) of the herb extracts (Liquorice, Mint and Fenugreek) can safely be used to control the rancidity of sunflower oil.

Keywords: Antioxidants, BHA, Lipid peroxidation, Sunflower oil.

INTRODUCTION

Lipid peroxidation is responsible for the development of rancidity causing an unacceptable color, unbearable odor and flavor. This phenomenon may lead to the reduction of the shelf life of oils and eventual economic losses [1]. BHA (butylated hydroxyl anisol), BHT (butylated hydroxyl toluene) and TBHQ (ter-butyl hydroquinone) are some examples of synthetic antioxidants which are most frequently used as potential inhibitors of lipid peroxidation. The use of these synthetic antioxidants has been restricted because of their bad side effects [1]. The addition of antioxidants also prevents deterioration in some other oxidizable products [2]. The concern about these side effects by the consumers diverted the attention of the researchers from the replacement of synthetic by natural antioxidants that may safely be applied for the storage of oils and fats. Some notable related contributions that appeare in the literature are; Jaswir *et al.,* (2000) [3], Badei *et al.,* (2000) [4], Jinyoung *et al.,* (2008) [5], Nedyalka *et al.,* (2006) [6], Burg *et al.,* (2006) [7].

Fenugreek is scientifically named as *Trigonelle foenum-graecum* [8] while locally known as Methi in Pakistan. It's an annual plant and is cultivated worldwide. As a dried or fresh herb it is used as a spice or sometimes directly as food. Mint is locally called Pudina and scientifically named as *Mentha piperita* [9]. It is also called Peppermint in English and has medicinal importance in many Pakistani, Indian and Bangladeshi dishes. Liquorice is Glycyrrhiza glabra L. [10] and called Mulaithi in

Urdu and Sanskrit it is prescribed to treat chronic hepatitis and peptic ulcer. In the present study, we have selected these three locally available herbs (Fenugreek, Mint, Liquorice). The purpose was to evaluate their methanolic extracts for possible antioxidant activities leading to the stabilization of sunflower oil, the most common edible oil.

EXPERIMENTAL

Material and Methods

Reagents and Glassware. The chemicals used such as BHT, iodine monochloride, n−hexane and acetic acid were purchased from BDH Chemical Laboratories; however, ethanol, phenolphthalein and HCl were obtained from Merck. BHA, sodium thiosulphate, potassium iodide, chloroform and carbon tetrachloride were obtained from Fluka Chemicals. Quick fit glassware made of Pyrex was used for in the experiments and was dried at 150°C before use [11]. The herbs (Fenugreek, Mint, Liquorice) were collected from the local market.

Extracts from Herbs. Extracts from these herbs (Fenugreek, Mint, Liquorice) were obtained in 80% of methanol by a previously reported method [8]. The extracts were subjected to evaporation until dry under reduced pressure at 40–45°C and stored at −18°C for further analysis.

Stabilization of sunflower oil and Antioxidant activity testing. Six samples of the sunflower oil (5 g each) were taken for control in 250 ml of glass stoppered flasks. Among these, in two flasks the synthetic antioxidant [BHA (250 ppm), BHT (200 ppm)], in three flasks extracts of Liquorice, Mint and Fenugreek of 200, 500 and 1000 ppm respectively were added. In the last sixth flask no herb extract or synthetic antioxidant was added and was labeled as a control speciment.

* To whom all correspondence should be sent:
E-mail: ktm7ro@yahoo.com

Measurement of peroxide, free fatty, iodine, conjugated diene and conjugated triene values.
The IUPAC standard method [12] as adopted by us in our previous contribution [11] was used for the determination of free fatty acids (FFA), peroxide (PV) and iodine (IV) values during ambient storage of sunflower oil, while the values of the conjugated dienes and trienes were calculated by the method of Xu and Godbaer [13].

RESULTS AND DISCUSSION

Influence of synthetic antioxidants and Herbs extracts on FFA

The changes in free fatty acid value have been noted during ambient storage of sunflower oil after addition of synthetic antioxidants and natural herbs as sources of natural antioxidants. These changes are graphically shown in Fig.(1). The gradual increase in the FFA value was observed after the addition of synthetic antioxidants (BHA and BHT) except a slight decrease in the FFA value by the 15th day. After the 15th day the values gradually increased again. These results argue that the addition of BHA and BHT played a part in the retardation of the rancidity in sunflower oil. The free fatty acids were reduced from 18.8% to 14.2% with BHA and from 18.4% to 14.1% with BHT during 45 days of ambient oil storage. These findings are comparable to the results presented by Kiyomi and Kathy regarding the antioxidant potential of BHA alone or with other antioxidants during ambient storage at both high and ambient temperature [14].
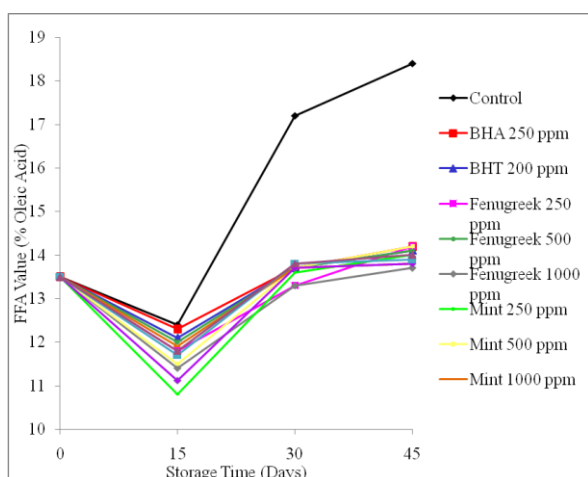
Fig. 1. Influence of storage conditions on the free fatty acid values.

The addition of herb extracts caused a significant reduction in the FFA value at ambient storage of sunflower oil. The FFA value decreased from 18.4% to 13.8% with 1000 ppm mint extracts

and from 18.4% to 13.7% with Fenugreek (1000 ppm) and from 18.4% to 14% with Liquorice (1000 ppm) extracts. A significant difference was observed between the control sample and the samples that were stabilized with herbs. 1000 ppm extracts of Fenugreek and Mint caused more reduction in the FFA than BHA and BHT while the samples stabilized with the same concentration of Liquorice showed parallel potential to that of BHA and BHT. The FFA value of samples stabilized with herb extracts was found to decrease roughly as a function of the increase in concentration of the extracts. The storage period and FFA also possess a direct proportional relationship except for a small deviation of a slight decrease in the FFA value observed at the 15th day which then follows a regular pattern of increase like the synthetic antioxidants.

Influence of synthetic antioxidants and Herb extracts on PV

Peroxide values regarding the control sample and samples stabilized with synthetic as well as extracts were determined and are presented in Fig.(2). This figure shows that PV of the control samples was 146 meq/kg on the day when the analysis was started and after 45 days of storage it was 151 meq/kg. The synthetic antioxidants added to the oil samples caused a gradual increase in PV. A slight decrease in the PV value was observed on the 15th day of storage when the PV was decreased from 151 meq/kg to 148.1 with BHA and from 151 meq/kg to 147.8 meq/kg with BHT.
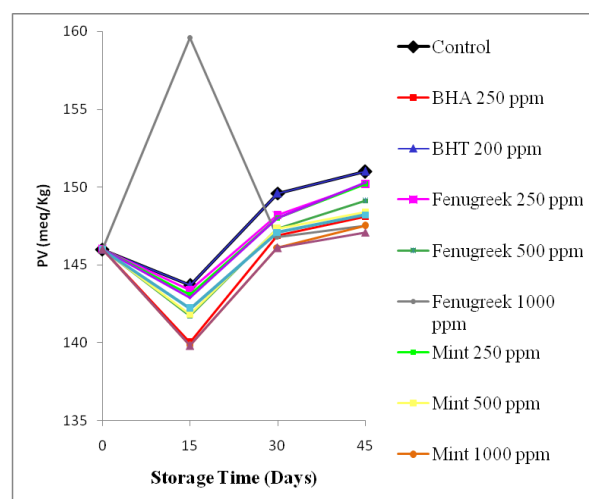
Fig. 2. Influence of the storage conditions on PV.

Fenugreek was reduced from 151 meq/ kg of the control sample to 150.2, 149.1 and 147.5 meq/kg on the 45th day of ambient storage by the addition of its 250, 500 & 1000 ppm methanolic extracts respectively. The PV of the sunflower oil samples

754

stabilized with 250, 500 & 1000 ppm methanolic extracts of Mint also reduced from 151 meq/kg for the control sample to 150.2, 148.4 and 147.5 meq/kg on the 45th day of storage. The addition of 250, 500 & 1000 ppm methanolic extracts of Liquorice also reduced the PV from 151 meq/kg (control) to 150.3, 148.2 and 147.1 meq/kg respectively on the 45th day of storage. As the high value of peroxides attributes to the formation of unstable hydroperoxides that ultimately convert to short chain acids, aldehydes, alcohols and ketones and thus cause flavor and odor changes [15] so the highest PV was observed in control samples which gradually decreased upon addition of varied concentrations (250, 500 and 1000 ppm) of methanolic extracts of herbs (Fenugreek, Mint and Liquorice).

Table 1. Influence of storage conditions on IV.

Herbs	Concentration (ppm)	Days			
		0	15	30	45
Control		100.3	90.4	49.6	47.8
BHT	200	90	95.2	76	62.7
BHA	200	90	97	74	60.1
	250	90.0	90.4	61.6	55.0
Fenugreek	500	90.0	95.7	74.6	61.6
	1000	90.0	100.0	80.0	78.3
	250	90.0	90.4	63.8	53.3
Mint	500	90.0	90.5	74.6	60.0
	1000	90.0	100.0	82.0	80.0
	250	90.0	90.3	61.9	56.9
Liquorice	500	90.0	94.3	74.6	73.0
	1000	90.0	94.0	75.0	63.3

Table 2. Influence of storage conditions on CD content of sunflower oil.

Herbs	Concentration (ppm)	Days			
		0	15	30	45
Control		0.575	0.695	0.459	0.469
	250	0.575	0.728	0.515	0.426
Fenugreek	500	0.575	0.718	0.434	0.408
	1000	0.575	0.687	0.445	0.424
	250	0.575	0.669	0.465	0.406
Mint	500	0.575	0.659	0.4	0.437
	1000	0.575	0.671	0.463	0.422
	250	0.575	0.683	0.425	0.418
Liquorice	500	0.575	0.677	0.434	0.405
	1000	0.575	0.675	0.463	0.428

Table 3. Influence of storage conditions on CT content of sunflower oil.

Herbs	Concentration (ppm)	Days			
		0	15	30	45
Control		0.741	0.752	0.516	0.536
	250	0.741	0.811	0.527	0.488
Fenugreek	500	0.741	0.749	0.475	0.481
	1000	0.741	0.778	0.514	0.494
	250	0.741	0.736	0.485	0.494
Mint	500	0.741	0.767	0.525	0.483
	1000	0.741	0.707	0.522	0.504
	250	0.741	0.759	0.471	0.466
Liquorice	500	0.741	0.777	0.505	0.500
	1000	0.741	0.727	0.486	0.504

The PV of stabilized samples containing the highest concentration (1000 ppm) of extracts from herbs was roughly similar to BHA and BHT proving a good antioxidant potential of herb extracts. Increase in PV follows a regular pattern that is deviated slightly in 15th day of storage probably due to the possibility of initial ultimate capture of previously present oxidants in the oils by strong antioxidants present in the herbs.

Effect of synthetic antioxidant and Herb extracts on IV

The IV of control was 100.3 on the starting day of the analysis which reduced to 47.8 on the 45 day of storage. These results favor the development of rancidity during ambient storage of the refined sunflower oil.

Addition of synthetic (BHA and BHT) and natural (extracts from Fenugreek, Mint and Liquorice) antioxidants retarded this decreasing trend. IV was observed to be 60.1 and 62.7 upon addition of BHA and BHT on the 45th day of storage. Addition of variable concentrations (250, 500 and 1000 ppm) of methanolic extracts of herbs (Fenugreek, Mint and Liquorice) to sunflower oil samples furnished iodine values of 55, 61.6, 78.3, 53.3, 60, 80, 56.9, 73, 63.3 respectively on the 45th day of storage (Table 1). Thus, distinctly higher IV were obtained upon treatment of the antioxidants than the control samples while the IV of stabilized sunflower oil samples treated with 1000 ppm herb extracts were almost comparable to BHA and BHT. Similar to FFA and PV, a slight increase in IV on the 15th day of storage was observed.

Effect of synthetic antioxidant and Herb extracts on Conjugated Dienes and Trienes

CD and CT are usually assessed to estimate the free radical production in order to evaluate the effectiveness of antioxidants in oils by measuring the oxidative deterioration of the oils. Generally, the samples having a higher content of CD and CT have a high intensity of oxidation. CD and CT were observed in control samples after 45 days (0.469 and 0.536 respectively) and were decreased by the incorporation of 250, 500 and 1000 ppm of all three herb extracts (Table 2 and 3). These findings were similar to Sultana et al., [16]. Generally, a non-uniform increase in the values of CD and CT were observed, however all of the stabilized samples exhibited lower values of CD and CT as compared to the control sample.

CONCLUSIONS

The methanolic extracts of Fenugreek, Mint and Liquorice were used to stabilize the samples of sunflower oil during ambient storage that was approximately parallel to the antioxidant activity of BHA and BHT. Therefore, it is suggested that natural antioxidant extracts of Liquorice, Mint and Fenugreek can securely and safely be managed and used as a substitute of synthetic antioxidants to extend or protect the shelf life of fats and oils.

REFERENCES

1. T. Tsuda, M. Wetanabe, K. Ohshima, A. Yamamoto, S. Kawakishi,T. Osawa, *J.Agric.Food Chem.,* **45**, 632 (1998).
2. A. Francisco, M. Silva, F. Borges, M.A. Ferreira, *J. Agric. Food Chem.,* **49**, 3936 (2001).
3. I. Jaswir, Y.B.C. Man, D.D. Kitts, *Food Res.Intl.,* **33**, 501 (2000).
4. A.Z. Badei, H.H. Hemeda, S.A. Hafe, N.H. Hassanen, *Egyp. J. Agric. Res.,* **78**, 321 (2000).
5. L. Jinyoung, L. Yoosung, C. Eunok, *LWT – Food Sci. Tech.,* **41**, 1871 (2008).
6. V.Y. Nedyalka, E. Marinova, J. Pookorny, *Europ. J. Lipid Sci. Tech.,* **108**, 776 (2006).
7. I.H. Burg, H.J.D. Dorman, R. Hiltunen, *J. Food Chem.,* **97**, 122 (2006).
8. P.R. Petit, Y.D. Sauvaire, D.M. Hillaire-Buys, M. Olivier,Y.G. Baissac, G.R. Ponsin, G.R. Ribes, *Steroids,* **60**, 674 (1995).
9. N. Ocak, G. Erener, F. Burak Ak, M. Sungu, A. Altop, A. Ozmen, *Czech J. Anim Sci.,* **53**, 169 (2008).
10. M.A. Hanif, H.N. Bhatti, M.S. Jamil, R.S. Anjum, A. Jamil, M.M. Khan, *Asian J. Chem.,* **22**, 7787 (2010).
11. M.I. Bhanger, S. Iqbal, F. Anwar, M. Imran, M. Akhtar, M. Zia-ul-Haq, *Intl. J. Food Sci. Tech.,* **43**, 779 (2008).
12. International Union of Pure and Applied Chemistry Standard Methods for the Analysis of Oils, Fats and Derivatives, 7th revised and enlarged ed.; Paquot, C., Hautfenne, A., Eds.; Blackwell Scientific Publications, London, U.K, 1987.
13. Z. Xu, J. S. Godber, *J. Agric. Food Chem.,* **47**, 2724 (1999).
14. G. Kathy, B. Randei, T. Peter, C.F. George, *J.Nut.,* **124**, 26835 (1994).
15. G.H. Crapiste, I.V.B. Marta, A.A. Carelli, *J. Am. Oil Chem. Soc.,* **76**, 1437 (1999).
16. B. Sultana, F. Anwar, R. Przybylski, *Food Chem.,* **104**, 997 (2007).

СТАБИЛИЗИРАНЕ НА СЛЪНЧОГЛЕДОВО МАСЛО С ЕКСТРАКТИ ОТ СМИНДУХ, МЕНТА И СЛАДНИК

И. Ниамат[1], А.Р. Тарик[1], М. Имран[1], Ф. Канвал[1], Л. Миту[2]*

[1]Институт по химия, Университет в Пунджаб, Лахор-54890, Пакистан
[2]Департамент по химия, Университет в Питещ, Питещ-110040, Румъния

(Резюме)

Извършени са изследвания по стабилизирането на слънчогледово масло при добавянето на синтетични антиоксиданти (бутилиран хидроксианизол, ВНА и бутилиран хидроксилтолуен, ВНТ), както и метанолови екстракти от сминдух, мента и сладник при стайна температура и влажност. Антиоксидантният потенциал на тези растителни екстракти е оценена с помощта на пероксидното число, съдържанието на свободни мастни киселини, йодното число, спрегнатите двойни връзки (диени и тирени). Тези параметри показват, че значително високи концентрации на екстрактите (грубо до пет пъти над ВНА и ВНТ) може безопасно да се използват за контрола на гранясването на слънчогледовото масло.

A hybrid supercapacitor activated carbon/LiBF₄/activated carbon–biogenic Fe₂O₃ composite

S. K.Veleva[1], L. Z. Stoyanov[1], A. E. Stoyanova[1*], Ch. A. Girginov[2], M. A. Mladenov[1], D. G. Kovacheva[3], R. G. Raicheff[1]

[1]Institute of Electrochemistry and Energy Systems, BAS, 1113 Sofia, Bulgaria
[2]University of Chemical Technology and Metallurgy, 1756 Sofia, Bulgaria
[3]Institute of General and Inorganic Chemistry, BAS, 1113 Sofia, Bulgaria

Two types of electrode material are used in the assembly of supercapacitor cells - activated carbons and electrochemically active α-Fe₂O₃ (hematite). The activated carbon with nanosized particles (specific surface area 1500 m^2g^{-1}) is a product of TDA Research, USA. The nanosized hematite (bio-Fe₂O₃) is produced by thermal treatment (400 ºC/2 h in an argon atmosphere) of biogenic α-FeOOH (goethite) obtained by laboratory cultivated Leptothrix bacteria. The oxide is structurally and morphologically characterized by XRD, SEM, TEM and tested as an electrode material in hybrid lithium battery-double layer supercapacitors. The hybrid cell is assembled from an electrode of activated carbon, a composite electrode with an activated carbon matrix, the addition of 50 % bio-Fe₂O₃ and an organic electrolyte - LiBF₄ with a solvent elthylene carbonate/dimethyl carbonate mixture (EC/DMC) 1:1. A symmetric supercapacitor cell composed of two identical electrodes from activated carbon and the same organic electrolyte is also assembled and tested for comparison. The cells are subjected to galvanostatic charge/discharge cycling at different current loads and both demonstrate a high specific capacity (50 Fg^{-1} for the symmetric and about 50% higher capacity for the hybrid supercapacitor), a high efficiency (above 95%) and stable capacity behavior at prolong cycling. The results prove the possibility of application of bio-Fe₂O₃ as an electrochemically active material for hybrid lithium battery – supercapacitor systems.

Key words: biogenic hematite, electrode materials, hybrid supercapacitors, charge/discharge cycling

INTRODUCTION

The increased interest in electrochemical double-layer capacitors (supercapacitors) is largely stimulated by the growing needs of technology for the storage of energy produced by renewable energy sources, such as solar stations and wind generators, as well as by heeding the advantages of supercapacitors in comparison with conventional electrochemical power sources. As well known, batteries and the fuel cells show a high energy density but they have a low power density and a limited lifecycle. Supercapacitors tend to have a lower energy density compared to batteries, but they can provide a much higher power capability, high efficiency and excellent cycling characteristics [1-3].

The electrochemical double-layer supercapacitors are usually symmetrical with two identical carbon electrodes. In order to improve the energy density while keeping a long lifecycle, hybrid electrochemical systems involving the hybridization of a faradaically rechargeable battery-type electrode with an electrochemical double-layer capacitor-type electrode (e.g. asymmetric supercapacitors), are introduced. Thus, various hybrid capacitor configurations consisting of activated carbon as a positive electrode and a negative electrode based on metal oxides (nickel, lead or manganese oxides) [4–6], conducting polymers [7] or Li intercalation oxides [8, 9], are suggested.

Porous carbons are among the most attractive materials for preparation of electrodes for electrochemical capacitors. The main advantage of these materials is the possibility to produce highly porous structures with a high specific surface area as well as to develop various composite electrodes by adding electrochemically active materials to the carbon matrix [10].

Fe₂O₃ is a promising electrode material for the Li-ion battery because of its low cost, simple manufacturing process, wide range of sources, environmental friendliness and mainly – a large theoretical specific capacity. The cycling performance of this material however is not satisfactory because of the partial destruction of the electrode that may take place upon repetitive cycling reactions between the Fe₂O₃ and Li-ions [11].

---

* To whom all correspondence should be sent:
E-mail: antonia.stoyanova@gmail.com

Our previous studies [12-15] were devoted to the synthesis of activated carbon materials suitable for electrodes for electrochemical double-layer capacitors as well as to the development of carbon-based composite electrodes for hybrid lithium battery-supercapacitor systems. It was shown that nanoporous carbon materials can be synthesized from waste biomass (apricot stones and spent ground coffee) or by carbonization of mixtures of coal tar pitch and furfural with subsequent hydrothermal treatment. The capacitance values of up to 70 Fg^{-1} are obtained for a symmetric carbon-based supercapacitor with Et_4NBF_4 – propylene carbonate electrolyte and about a twice higher capacitance for the asymmetric supercapacitor, composed of an activated graphitized carbon electrode and an activated carbon-$Li_4Ti_5O_{12}$ oxide composite electrode in a $LiPF_6$ – DMC/EC (1:1) electrolyte, with high efficiency and very good cycleability of both supercapacitors.

The objective of the present work is to develop a hybrid lithium battery - supercapacitor using activated carbon and activated carbon-bioFe₂O₃ composite with an organic electrolyte as electrodes, as well as to compare the capacitance behavior of the hybrid supercapacitor with that of a symmetric carbon-based supercapacitor.

EXPERIMENTAL

Synthesis of electrode materials: Two types of electrode materials are used for the assembly of supercapacitor cells - activated carbon (AC) and electrochemically active α-Fe_2O_3 (hematite). The nanosized hematite (bio-Fe₂O₃) is produced by thermal treatment (400ºC for 2 hours in an argon atmosphere) of biogenic iron oxide/hydroxides (goethite) obtained by laboratory cultivated Leptothrix bacteria [15]. The activated carbon with nanosized particles is a product of TDA Research (USA).

Morphological and structural characterization of the electrode materials: The biogenic iron oxide/hydroxide precursor and the obtained oxide material are structurally characterized by X-diffraction (XRD). The powder X-ray diffraction patterns are collected within the range from 5.3 to 80˚ 2θ with a constant step of 0.02˚ 2θ angle on a Bruker D8 Advance diffractometer with Cu Kα radiation and a LynxEye detector. The phase identification was performed with a Diffracplus EVA using the ICDD-PDF2 Database. The mean crystallite size is determined with the Topas-4.2 software package using the fundamental parameters peak shape description including appropriate corrections for the instrumental broadening and the diffractometer geometry.

The morphology of the electrode materials is examined by Transmission electron microscopy (TEM) and Scanning electron microscopy (SEM) using a JEOL Superprobe 733.

The pore structure of the carbon used are investigated by nitrogen gas adsorption [13]. The adsorption isotherm of the sample at −196°C is recorded and used to calculate the specific surface area, pore volumes and pore size distributions.

Electrochemical tests. The activated carbon and bio-Fe₂O₃ materials are used to fabricate electrodes for two types of electrochemical cells for capacity measurements. The first type is a symmetric supercapacitor cell using two identical electrodes from activated carbon and an organic electrolyte - lithium tetrafluoroborate (LiBF₄) with organic solvent - ethylene carbonate and a dimethyl carbonate (EC/DMC) mixture in the ratio 1:1. The symmetric supercapacitor is denoted as AC/(LiBF₄-EC/DMC (1:1))/AC.

The second one is an asymmetric (hybrid) supercapacitor cell with a composite electrode and an activated carbon electrode. The composite (negative) electrode is assembled from an activated carbon matrix with the addition of bio-Fe₂O₃ (50%). The positive electrode is made from the same AC and the same organic electrolyte - LiBF₄-EC/DMC (1:1) as used in the symmetric cell. This asymmetric supercapacitor is denoted as (AC+bio-Fe₂O₃)/(LiBF₄-EC/DMC (1:1))/AC.

By adding a binder - polyvinylidene difluoride (PVDF) to the electrode materials, a paste is formed, which is glued to Cu foil discs (surface area 1,75 cm^2). The formed sheet electrodes are dried at 70 °C for 2 hours and pressed under a pressure of 200 kg cm^{-2}. The electrodes obtained are soaked in organic electrolyte under a vacuum and then mounted in a coin-type cell with a Glassmat separator and filled with an electrolyte in a dry box and argon atmosphere. The capacitor cells were subjected to galvanostatic charge-discharge cycling using an Arbin Instrument System BU-2000 [14, 15]. The test program is carried out at a constant current mode at different current loads (from 10 to 500 mAg^{-1}) at 10 cycles and room temperature. Some cell are subjected to continuous cycling charge/discharge at a current of 60 mAg^{-1} for up to 1000 cycles.

RESULTS AND DISCUSSIONS

Physicochemical characterization of the electrode materials. Fig.1 (a and b) represents the powder X-ray diffraction patterns of the biogenic

FeOOH (goethite) precursor and the α-Fe$_2$O$_3$ oxide phase obtained after thermal treatment. It is seen that the oxide product (bio-Fe$_2$O$_3$) is a single phase hematite with the unit cell parameters: a= 5.0388 Å and c= 13.774 Å. The mean crystallite size of bio-Fe$_2$O$_3$ is estimated to be about 10 nm. The TEM observations have shown that the bio-Fe$_2$O$_3$ particles (cf. Fig.2) are nanosized and form clusters, while the biogenic FeOOH consists of nanotube particles, which cover the bacterium structure in the form of a sheath.
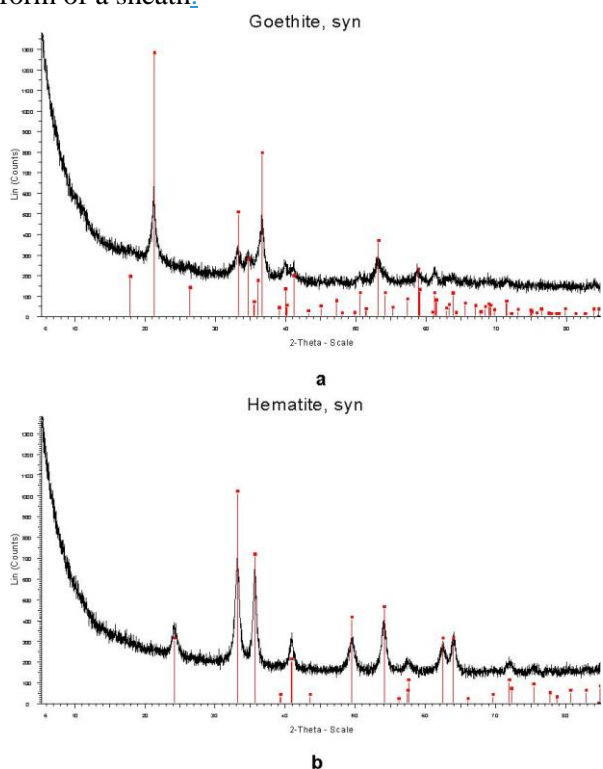
Fig. 1. XRD powder patterns of biogenic FeOOH (a) and bio-Fe$_2$O$_3$ (b).
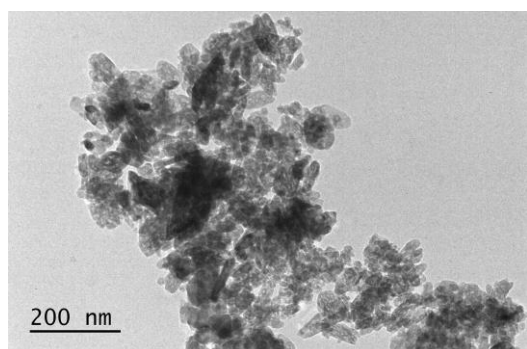
Fig. 2. TEM image of bio-Fe$_2$O$_3$.

The examination of the samples of activated carbon have shown that the specific surface area is 1520 m^{2}g^{-1}, the total volume of the pores is 0,68 cm^{3}g^{-1}, the volume of the micropores - 0,55 cm^{3}g^{-1} (i.e. 80% of the total pore volume) and the volume of the mesopores - 0,13 cm^{3}g^{-1}.

Electrochemical performance of the supercapacitor cells. The electrochemical performance of the two-electrode symmetric and asymmetric (hybrid) capacitor cells are studied by charge-discharge cycling test.
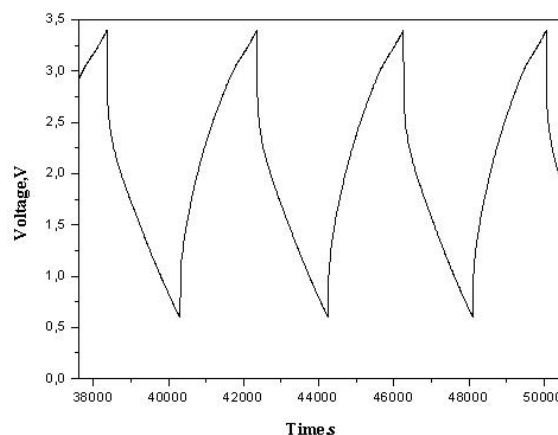
Fig. 3. Charge-discharge behaviuor of a hybrid battery-supercapacitor (AC+bio-Fe$_2$O$_3$)/(LiBF$_4$ - EC/DMC (1:1))/AC at a current load of 60 mAg^{-1}.

Fig. 3 illustrates the charge–discharge behaviuor of a hybrid supercapacitor cell assembled by the composite electrode (AC+bio-Fe$_2$O$_3$), the AC electrode and the electrolyte LiBF$_4$ – EC/DM (1:1) at a current load of 60 mAg^{-1}. As seen the hybrid lithium battery-supercapacitor cell shows a reproducible charge-discharge behavior and indicates very stable and high specific capacity values at a relatively high current load. The processes on the composite anode are obviously lithiation/delithiation of Fe$_2$O$_3$ (i.e. a typical Faradaic process) together with the adsorbtion/desorbtion of the Li-ion on the AC surface of the electrode, while on the AC cathode only the process of electrostatic adsorption/desorption of BF$_4^{-1}$ takes place.
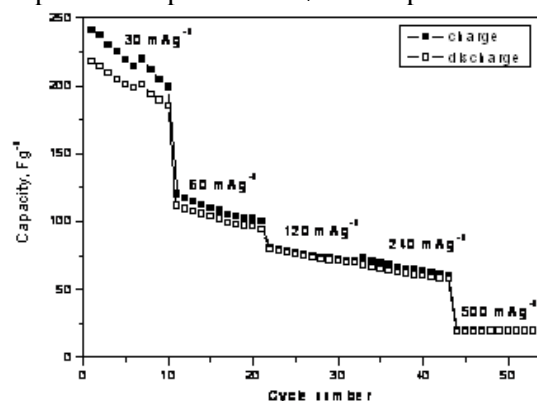
Fig. 4. Dependence of the charge and discharge capacity of hybrid battery-supercapacitor (AC+bio-Fe$_2$O$_3$)/(LiBF$_4$ - EC/ DMC (1:1)) /AC on the number of cycles at different current loads.

The electrochemical test of the hybrid supercapacitor cells includes 10 charge/discharge cycles at each current load – from 30 to 500 mAg^{-1} (Fig. 4). As expected both the charge and discharge capacity decrease with the increase of the current rate but the efficiency of the process (expressed as the ratio of the discharge and charge capacity) increases – from an average of 90% at 30 mAg^{-1} to 98% at 500 mAg^{-1}. It should be noted however that the capacitor cell retains a relatively high specific capacity even at a very high current load (above 100 mAg^{-1}).

Fig. 5 illustrates the dependence of the charge and discharge capacity on the number of cycles for the symmetric and the hybrid supercapacitors at a current load of 60 mAg^{-1} for both the capacitor cells. It is worth noting that the symmetric cell represents typical electric double-layer supercapacitors for energy storage. Both capacitors demonstrate high efficiency (about 95%) and high stability of their capacity during cycling, especially for the symmetric supercapacitor cell. The hybrid supercapacitor shows up to two times higher capacity values than the symmetric one (50 Fg^{-1}).
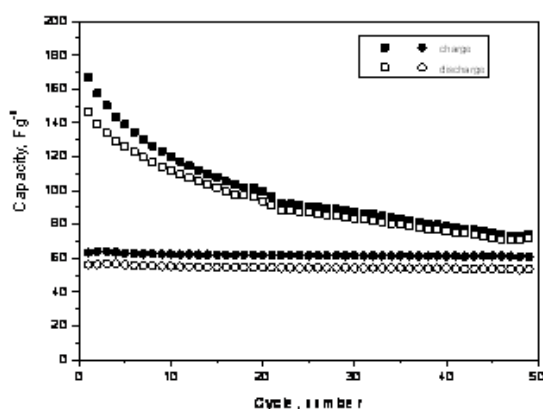
Fig. 5. Dependence of the charge and discharge capacity of hybrid battery- supercapacitor (AC+bio-Fe₂O₃)/(LiBF₄ - EC/ DMC (1:1)) /AC (■, □) and symmetric capacitor AC/(LiBF₄ - EC/ DMC (1:1))/AC (○, ●) on the number of cycles at a current load of 60 mAg^{-1}.

A comparison of the dependence of the discharge capacity on the current load for the symmetric and hybrid supercapacitors is made on Fig. 6. The value of the discharge current affects much more strongly the capacity of the hybrid battery-supercapacitor cell which is obviously related to the much stronger effect of the current on the faradaic reaction on the composite electrode, i.e. on its pseudocapacity. The results illustrate also the higher capacity values of the hybrid supercapacitor, especially at low current loads (below 50 - 100 mAg^{-1}).

In the course of electrochemical testing it is also established that the capacity loss of the hybrid supercapacitor does not exceed 8-10% after prolonged cycling (above 1000 cycles) and the supercapacitor works satisfactorily even at a high current load (above 200 mAg^{-1}).
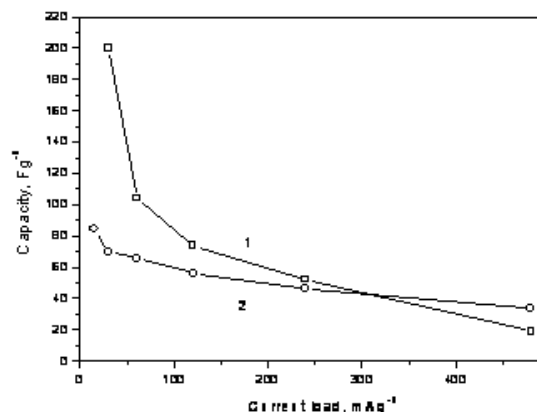
Fig. 6. Dependence of the discharge capacity of a hybrid battery-supercapacitor (AC+bio-Fe₂O₃)/(LiBF₄ - EC/ DMC (1:1)) /AC (1) and a symmetric capacitor AC/(LiBF₄ – EC/ DMC (1:1))/AC (2) on the current load.

The work on the synthesis of activated carbon with an appropriate pore structure and morphology as well as on the optimization of the composition and structure of the composite electrode is in progress and the results will be reported soon.

CONCLUSIONS

On the basis of the results in the present study, the following conclusions are made:

1) Nanosized hematite (bio-Fe₂O₃) can be produced by thermal treatment of biogenic α-FeOOH (goethite), obtained by laboratory cultivated *Leptothrix* bacteria and used as an electrochemically active additive in the composite electrode with an activated carbon matrix for lithium battery - supercapacitor systems.

2) The hybrid supercapacitor thus developed (AC+bio-Fe₂O₃) / (LiBF₄-EC/DMC (1:1)) / AC demonstrates high reproducibility of the charge/discharge processes, a high specific capacity (80 Fg^{-1}), high efficiency (above 95 %) and stable cycleability at prolong cycling.

The results prove the possibility of application of bio-Fe₂O₃ as an electrochemically active material for hybrid lithium battery – supercapacitor systems.

REFERENCES

1. B. E. Conway, Electrochemical Supercapacitors: Scientific Fundamentals and Technological Applications, Kluwer Academic Publ., New York, 1999.
2. V. Khomenko, E. Raymundo-Pinero, F. Beguin, *J. Power Sources,* **177**, 643 (2008).
3. Y. Zhang, H. Feng, X. Wu, L. Wang, A. Zhang, T. Xia, H. Dong, V. Li, L. Zhang, *Intern. J. Hydrogen Energy,* **34**, 4889 (2009).
4. S. Razumov, A. Klementov, S. Letvinenko, A. Beliakov, *US Patent,* #6, 222,723 (2001).
5. W. G. Pell, B. E. Conway, *J. Power Sources,* **136**, 334 (2004).
6. V. Khomenko, E. Raymundo-Pinero, F. Beguin, *J. Power Sources,* **153**, 183 (2006).
7. C.A. Fabio, A. Giorgi, M. Mastragostino, F. Soavi, *J. Electrochem. Soc.,* **148**, A845 (2001).
8. G. G. Amatucci, F. Badway, A. Du Pasquier, T. Zheng, *J. Electrochem Soc.,* **148**, A930 (2001).
9. A. Du Pasquier, I. Blitz, J. Gural, S. Menocal, G. G. Amatucci, *J. Power Sources,* **143**, 62 (2003).
10. R. Kotz, M. Carlen, *Electrochim. Acta* **45**, 2483 (2000).
11. A. Brandt and A. Balducci, *Electrochimica Acta,* **108**, 219 (2013).
12. M. Mladenov, P. Zlatilova, R. Raicheff, S. Vassilev, N. Petrov, K. Belov, V. Trenev, *Bulg. Chem. Commun.,* **40**, 360 (2000).
13. M. Mladenov, N. Petrov, T. Budinova, B. Tsynsarski, T. Petrov, D. Kovacheva, R. Raicheff, *Bulg. Chem. Commun.* **43**, 125 (2011).
14. M. Mladenov, K. Alexandrova, N. Petrov, B. Tsynsarski, D. Kovacheva, N. Saliyski, R. Raicheff, *J. Solid State Electrochem.,* **17**, 2101 (2013).
15. S. Veleva, R. Angelova, L. Stoyanov, V. Grudeva, D, Kovacheva, M. Mladenov, R. Raicheff, Nanoscience and Nanotechnology 14, Eds. E. Balabanova, E. Mileva, Publ. BPC ltd, Sofia, 2014, p.50.

ХИБРИДЕН СУПЕРКОНДЕНЗАТОР - АКТИВЕН ВЪГЛЕН / LiBF₄ / КОМПОЗИТ ОТ АКТИВЕН ВЪГЛЕН И БИОГЕНЕН Fe₂O₃

С. К. Велева[1], Л. З. Стоянов[1], А. Е. Стоянова[1], К. А. Гиргинов[2], М. А. Младенов[1], Д. Г. Ковачева[3], Р. Г. Райчев[1]

[1]Институт по електрохимия и енергийни системи, БАН, 1113 София, България
[2]Химикотехнологичен и металургичен университет, 1756 София, България
[3]Институт по обща и неорганична химия, БАН, 1113 София, България

(Резюме)

Използвани са два вида електродни материали за асамблиране на суперкондензаторни клетки - активен въглен и електрохимично активен α-Fe₂O₃ (хематит). Активният въглен с наноразмерни частици (специфична повърхност 1500 m^2g^{-1}) е търговски продукт на TDA Research, САЩ. Наразмерният хематит (био-Fe₂O₃) е синтезиран чрез термична обработка (400 ° С / 2 ч в атмосфера на аргон) на биогенен α-FeOOH (гьотит), получен чрез лабораторно култивирана *Leptothrix* бактерия. Био-Fe₂O₃ е структурно и морфологично охарактеризиран с помощта на ренгеновата дифракция (XRD), сканираща електронна микроскопия (SEM) и трансмисионна електронна спектроскопия (ТЕМ) и изследван като електроден материал в хибридна литиева батерия-електрохимична суперкондензаторна система. Хибридната клетка е съставена от електрод от активен въглен, композитен електрод с матрица от активен въглен и добавка на 50% био-Fe₂O₃. Използван е органичен електролит LiBF₄, с разтворител смес от етилен карбонат / диметил карбонат (EC/DMC) 1:1. За сравнение е съставена и симетрична суперкондензаторна клетка от два идентични електрода от активен въглен и същият органичен електролит. Клетките са подложени на галваностатични зарядно/разрядни циклични тестове при различно токово натоварване и показват висока специфичен капацитет (50 Fg^{-1} за симетричен и с около 50% по-висок капацитет за хибридния суперкондензатор), висока токова ефективност (над 95%) и стабилен капацитет при продължително циклиране. Резултатите показват възможността за прилагане на био-Fe₂O₃ като електрохимично активен материал за хибридна литиева батерия - суперкондензаторна система.

Corrosion behavior of 316L stainless steel in treated and untreated artificial effluent solutions (AESs)

T. Yetim*

Department of Chemical Engineering, Engineering and Architecture Faculty, Erzurum Technical University, Erzurum, Turkey

Some organic compounds in wastewaters not only pollute the environment but also cause corrosion to the wastewater transportation systems. In this study the corrosion behavior of treated textile wastewater was investigated by using AISI 316L stainless steel. Treatment was done by sonochemical (US), photochemical (UV) and sonophotochemical (US+UV) processing. These processes were used to degrade the dyestuffs which cause the pollution of textile wastewater. Artificial effluent solutions were prepared for use in the treatment processes. The concentrations of the solutions decreased with time for three treatment processes. The most reduced concentration was obtained after sonophotocatalytic treatment and the least was for sonochemical treatment. The OCP curves were found to move away from the noble direction for all the tested samples. The reduction tendency of the potential values for all samples was observed close to each other. The most active OCP values were for US+UV. In polarization results, the US sample showed a lower corrosion potential and higher corrosion current density. The corrosion results of samples tested in treated solutions were better than in untreated solutions. For the sonophotochemical process, stainless steel showed a better corrosion resistance than the others.

Keywords: Sonophotocatalytic process; photochemistry; sonochemistry; dyestuff degradation; pitting corrosion

INTRODUCTION

The textile dyeing and dye production facilities are the most problematic industries as regards releasing the dyes in an effluent form and polluting the environment. If these compounds are released without restraint, they may cause lots of health problems because the chemical and photolytic stability of the textile dyes are highly resistant in a natural environment. It is known that some azo dyes are formed from toxic aromatic amines which are carcinogenic for living organisms [1-4]. Therefore, the discharged effluents from the textile industries are important threats to the environment. About 15% of the total amount of dye produced in the World is lost during the dyeing processing and released to the environment together with textile effluents [1, 5]. The flow of these colorful effluents causes unaesthetic pollution of environment. Also the dyestuffs in the effluent phase can cause dangerous reactions including oxidation, hydrolysis or other chemical reactions [1, 5, 6].

Discharging effluents from textile factories not only pollute the environment but also destroy the pipes that are used to discharge the effluents, due to the impact of corrosion. It is known that corrosion as a phenomenon destroys the materials with time. Because of their high electrochemical reaction tendency, metals are the most common type of corrosion material. The destroyed materials become unused due to inappropriate design. In consequence, the systems of factories which carry the fluids and especially the effluent pipes are exposed to corrosion damage [7, 8].

For this reason the treatment of the effluents is important for the environment and the health of man. At the same time it is financially important to know the working life of the treatment system. The studies of the treatment of fabric effluents have been accelerated in recent years [1, 9]. Among these treatment methods are Advanced Oxidation Processes (AOPs): Fenton and Photo-Fenton catalytic reactions [10, 11], H_2O_2/UV processes [12, 13], Photocatalysis in a TiO_2 medium [1, 14], sonolysis and sonophotochemical treatment [15, 16] have been considered. Recently it was observed that especially the sonolytic and photocatalytic studies are more useful for the treatment of effluents. The treatment of effluents will affect the corrosion in the pipes. In this study, AISI316L stainless steel was used for making a simulation with effluent pipes. The intended use of this material is widespread with many industrial applications, especially chemical processing, the automotive industry and surgical implants. These exhibit a very high corrosion resistance in many aggressive environments [8, 17-18]. Therefore, in this study, the corrosive effect of the effluent including the textile dyes was treated by ultrasound energy (US) and UV irradiationindividually, and also by the application of both processes simultaneously on the pipes was investigated.

* To whom all correspondence should be sent:
E-mail: tuba.yetim@erzurum.edu.tr

EXPERIMENTAL PROCEDURE

The experiments were performed on AISI316L stainless steel, its chemical composition is given in Table 1. The prismatic specimens with dimensions of 25 x 25 x 2 mm^3 were cut from AISI316L stainless steel sheet. The samples were ground by 220–1200 mesh emery paper and then polished with alumina powder with a 1 μm grain size.

All the experiments were performed in artificial effluent solutions (AES) that were prepared with distilled water by using Methylene Blue and Congo Red dyestuffs with a molar concentration ratio of 1:1 uniformly. These were provided by Sigma Aldrich and used as received. The structures of the dyestuffs are shown in Table 2.

These solutions were processed by using ultrasound and UV irradiation before the experiments. For these processes, the parameters were as; 30 ppm of the concentration of the solutions , 30°C of temperature , 132 W/m^2 of light intensity, 50 % of the amplitude of ultrasound energy, 90 min. as the process time And 800 mg/l of TiO$_2$ photocatalyst. In the processes 500 ml of AES were used. Air was blown into the reaction medium by an air pump at a constant flow, to maintain the solution saturated with oxygen during the reaction. The pH was a natural value of the solution. The change in concentration was determined by a UV–vis Thermo Electron Evolution 500 spectrophotometer. First of all the absorbance values of the Methylene Blue and Congo Red were determined as 665 nm and 498 nm, respectively. The concentrations of the dyes were determined by the calibration curve that was a graph of the absorbance versus certain concentration values of the dyes. Also, the calibration graph was obtained with a spectrophotometer. Then the total concentrations of the dyes in the solution were calculated.
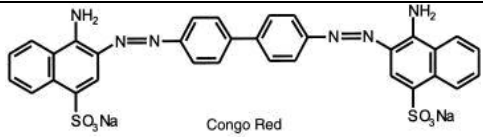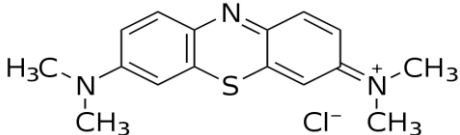
The electrochemical polarization experiments were performed using a GAMRY Series G750™ Potentiostat/Galvanostat/ZRA device. One side of the specimen with an area of approximately 0.38 cm^2 was exposed to the solution. The polarization measurements were carried out in unprocessed and processed AESs with US, UV and US+UV. For the first experiment untreated AES was used. For the second experiment only US was used on the AES, for the third experiment only UV irradiation was used and for the last experiment US and the UV irradiation (US+UV) were applied simultaneously. A stabilization period of 7200 s was employed before starting the measurement. The electrode potential was raised from -0.5V to 1 V compared to OCP with a scanning rate of 1mV/s and a current that flowed through the diffusion layer-substrate system. A three-electrode cell was used for the polarization measurements employing a Ag/AgCl electrode as the reference electrode, a graphite bar as the counter electrode and a working electrode, respectively. The surface morphologies after electrochemical examination were investigated using a scanning electron microscope Zeiss EVO LS 10.

Table 1. *Chemical composition of AISI 316L stainless steel (%)*

C	Si	Cr	Mn	Mo	P	S	Ni
0.016	0.490	16.640	1.820	2	0.030	0.026	10.100

Table 2. *The structures of dyestuffs*

Dyestuff Name	Molecular Formula	Structural Formula
Congo Red	C$_{32}$H$_{22}$N$_6$Na$_2$O$_6$S$_2$	
Methylene Blue	C$_{16}$H$_{18}$N$_3$SCl	

RESULTS AND DISCUSSION

The experiments were repeated three times for each treatment to indicate the reproducibility of the study. First of all the average values of the experimental data as the conversion rate were calculated for each treatment as US, UV and US+ UV. Then the H_0 and H_1 were hypothesized as; H_0: $M_1 = M_2 = M_3$ and H_1: $M_1 \neq M_2 \neq M_3$ where M are the average values of the experimental series. To determine the true hypothesis a statistic test of the variance analysis, which is f-distribution (F), is used. To achieve this goal the calculated F value and the F table values were compared at a 99% level of confidence. In this test, the F values were calculated by ANOVA (Analysis of Variance) tables formed by a MATLAB program for individual treatment. The $F_\alpha(v_1, v_2)$ value is determined from the F table. Here v_1 and v_2 are degrees of freedom and $v_1 = k-1$, $v_2 = k.(n-1)$; k and the n values are 3 and 12 respectively. Where k is the number of repeated experiments for each treatment and n is the number of data for each experiment. For this study the $F_{0.01}(2,33)$ value is 5,31 from the F table [19, 20] which is greater than the calculated F values in the ANOVA tables as shown in Table 3(a) (b) (c). This means that the difference between the averages of the experimental data is accidental and they are from the same population. In other words the H_0 hypothesis is true and this situation proves the reproducibility of the experimental data by using their average values.

The conversion rate versus time graphs of US, UV and US+ UV treatments are given in Figure 1. This figure demonstrates the most effective treatment process for removing the dyes, which are pollutants.
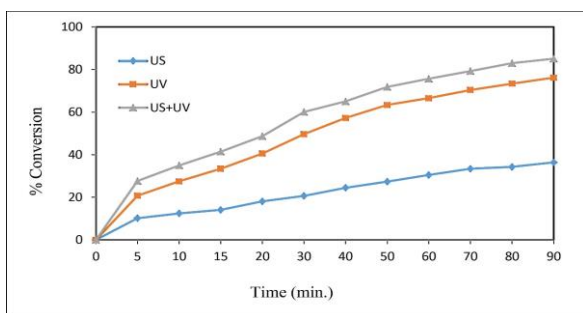
Fig. 1. Conversion rate of US, UV and US+ UV treatments versus time.

This will interrelate with the corrosion behavior of the treatment processes included less corrosive pollutant (dye amount) by identifying the most effective process. As seen in Figure 1, the concentrations of solutions decreased with time after three treatments.

The most reduced value was observed during sonophotocatalytic treatment. On the contrary, the least reduced value was obtained during sonochemical treatment. Also having a glance at the graphic, the conversion ratios of dyestuffs increased with the treatment in time. However, the largest increase was attained by UV+US and the smallest one was by US application. From the results, it can be said that the UV+US is more effective for removing the dyestuffs from the aqueous medium. This is attributed to their synergistic effect. It is known that the main factor for degrading the dyestuffs is forming the OH* radicals in the medium because of their property to destroy as powerful oxidizing agents and attack organic compounds forming intermediates. As more radicals are formed the degradation ratio will increase [13, 20-25]. In US treatment, the ultrasound energy can cause the collapse of the cavitations producehigh transient temperatures and pressures in the aqueous solutions. These lead to the formation of free hydroxyl radicals via the homolysis of water [26, 27]. However, by UV treatment, upon absorption of a photon by TiO_2, an electron is promoted to the conduction band, generating what is commonly referred to as an electron-hole pair [6, 23-25]. The conduction band electron is available for reduction and the valence band hole is available for oxidation. The hole can subsequently react by electron transfer with a substrate to form a radical species or hydroxide (water) to form hydroxyl radicals. In condensed oxygenated aqueous media the surface of TiO_2 is completely hydroxylated and upon photoexcitation it generates hydroxyl radicals in an adsorbed state [7, 9, 28].

For having more OH* radicals these two treatments must be applied simultaneously because of the synergistic effect. During the reaction between these radicals and dyestuffs the intermediates occur. Then these intermediates react with hydroxyl radicals (OH*) to produce final products, such as low molecular weight carboxylic acids, while the hydroxyl radicals can be consumed by inactive species.

Figure 2 showed the open circuit potential (OCP) measurements of the samples tested in the untreated AESs and the treated solutions were obtained after the degradation processes following ultrasound (US), ultraviolet (UV) and ultrasound+ultraviolet (US+UV) applications. The obtained open circuit potential (OCP) curves were found to move away from the noble direction for all

the tested samples. According to the OCP data, it has been observed that the curves of the samples approach a steady state after about 2000 s.As seen in Figure 2, the potential values shift in the negative direction for all samples.That clearly indicates that the surfaces of all the samples were very active to corrosion and there was no protective film formation on the sample surface to prevent the electrochemical dissolution. While the noblest OCP values were observed for the samples tested in the treated AES with US+UV, the most active OCP values were obtained from the samples tested in untreated AES.
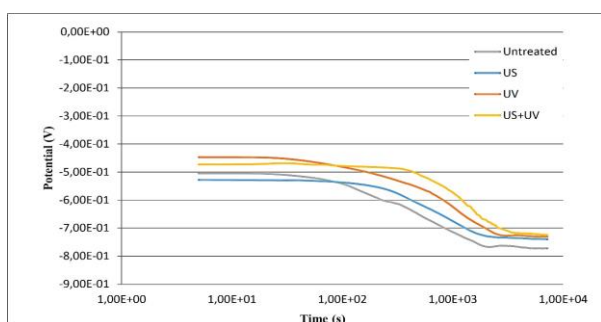
Fig. 2. Change of the OCP potential of samples tested in the AESs that are untreated and treated with US, UV and US+UV energies.

Polarization curves of the samples tested in the AESs that are untreated and treated with US, UV and US+UV processes are given in Figure 3. It was determined that the corrosion results for the samples tested in the solutions after the treatments were better than for the samples tested in untreated solution. A passive and short region was seen at the beginning of the anodic zone of UV treatment. The current values were almost stable while the potential values increased. A sudden and sharp

current increase occurred at the end of this region. This can be attributed to pitting corrosion behavior [29].

The US sample also exhibited similar polarization curves with the UV sample. But, there was no passive pitting corrosion indication for this sample.

On the other hand, the similarity between the polarization curves of the UV and the US+UV samples can be clearly observed in Figure 3. If the corrosion current density and the corrosion potential values are taken into account, the best results have been obtained from the US+UV treatment.

Although the corrosion current density of the US+UV sample was slightly lower than the other samples, previous studies on degradation of dyestuffs indicated that the UV irradiation was more effective than the ultrasound energy [16, 30, 31]. Similar results were obtained from the polarization results. It was found that the US sample showed a lower corrosion potential and a higher corrosion current density. This means that corrosion previously begins for the US sample and then it corrodes more than the UV sample.

The corrosion results for the samples tested in the solutions after treatment were better than the samples tested in untreated solution and depend on the non-destructive products raised from the degradation processes. As known, carboxylic acids occur during the photochemical degradation of dyestuffs and the final products are CO_2 and H_2O at the end of these reactions. As seen in Figure 1, it was thought that carboxylic acids existed in the solution, because of the decrease in dyestuffs' concentration with time.

Table 3. a. ANOVA table of US treatment

'Source'	SS'	'df'	'MS'	F'	Prob>F'
'Columns'	59,70	2	29,85	2,83	0,07340
'Error'	348,12	33	10,55	[]	[]
'Total'	407,82	35	[]	[]	[]

Table 3. b. ANOVA table of UV treatment.

'Source'	'SS'	'df'	'MS'	F'	Prob>F'
'Columns'	86,57682	2	43,28841	0,933111	0,403459
'Error'	1530,92	33	46,39152	[]	[]
'Total'	1617,497	35	[]	[]	[]

Table 3. c. ANOVA table of US+UV treatment

'Source'	'SS'	'df'	'MS'	'F'	'Prob>F'
'Columns'	154,5632	2	77,28159	1,293993	0,287723
'Error'	1970,871	33	59,72336	[]	[]
'Total'	2125,434	35	[]	[]	[]

The carboxylic acids are dissolvable by H_2O and H^+ ions released into the solution. Moreover, before the final products, positive holes (h+) and hydroxyl radicals (OH*) occurr throughout the degradation process and some of them still exist in the solution [21, 32, 33]. It is supposed that the existence of positive holes and H^+ ions may cause a reduction in electron loss from the tested metal samples.

The corroded surfaces of all samples were examined with a SEM and the images are presented in Figure 4.

Intergranular corrosion damages are observed from the surface of the untreated samples in Figure 4a. It can be easily said that the untreated sample surface has undergone more corrosion damage when its surface image is compared to the others. For the treated samples, pitting type corrosion can be seen on their surface images (Figure 4 b, c, d). It was seen that corrosion damage decreased after the degradation processes. The SEM image of the US sample surface after a corrosion test is given in Figure 4b. A spread of many large and deep pits was observed on the sample surface. On the other hand, the surface images of the UV and US+UV samples showed that the pit numbers decreased and thus the corrosion damage was reduced. Moreover, relatively smaller and shallower pits were observed on the UV and US+UV sample surfaces compared to the pits on the untreated and US sample surfaces (Figure 4c and d).
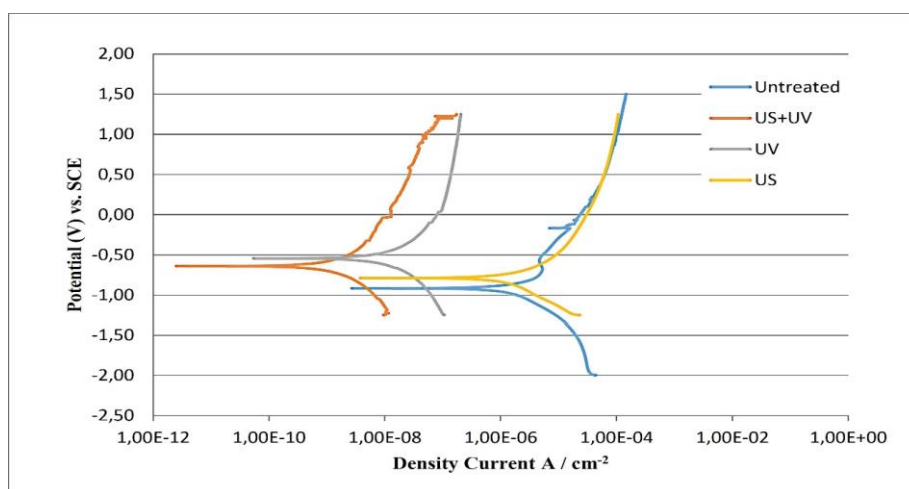
Fig. 3. Polarization curves of untreated and treated samples
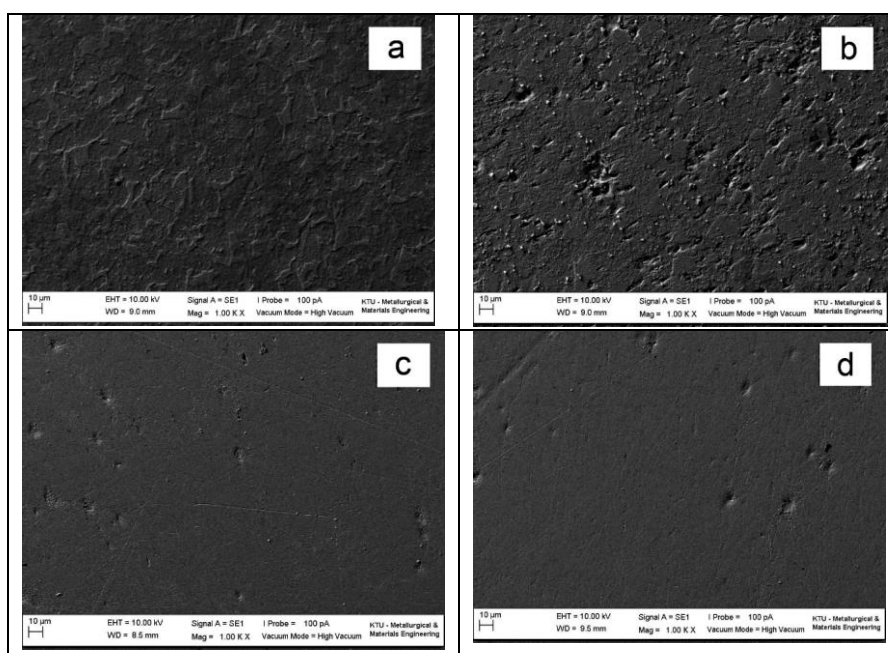
Fig. 4. SEM images of corroded surfaces for **a)** untreated, **b)** US treatment, **c)** UV treatment, **d)** US+UV treatment.

CONCLUSIONS

A solution including dyestuffs was treated with sonochemical, photochemical and sonophotochemical methods. The effects of degradation treatments on the corrosion behavior of 316L stainless steel were investigated in these treated solutions. In the light of these investigations, the following conclusions can be drawn from this study:

- It was seen from the conversion results that the most effective treatment for the degradation of dyestuffs was the US+UV treatment. The conversion rates at 90 minutes were about as 36%, 76% and 85% for US, UV and US+UV treatments, respectively.
- It was determined that the corrosion results of the samples tested in the treated solutions were better than the samples tested in untreated solution.
- Corrosion tests of sonophotochemical treated solution showed better corrosion resistance than the other treatments used in this study.
- While intergranular corrosion damage was seen on the surface of the samples tested in untreated solution, the pitting type of corrosion damage was observed on the samples tested in treated solutions.
- The sample surface tested in the US+UV treated solution showed a smaller amount of pitting and dimensions compared to the treated samples.

REFERENCES

1. S. Kertèsz, J. Cakl, H., Jiránková, *Desalination,* **343,** 106 (2014).
2. N. Kaneva, A. Bojinova, K. Papazova, D. Dimitrov, I. Svinyarov, M. Bogdanov, *Bulg. Chem. Commun.*, **47,** 1, 395 (2015).
3. M. F. Abid, M. Ebrahim, O. Nafi, L. Hussain, N. Maneual, A. Sameer, *Korean J. Chem. Eng.,* **31,** 1194 (2014).
4. S. Wang, D. Li, C. Sun, S. Yang, Y. Guan, H. He, *J. Mol. Catal. A: Chem.*, **383-384,** 128 (2014).
5. K. Golka, S. Kopps, Z.W. Myslak, *Toxicol. Lett.,* **151,** 203 (2004).
6. L. Pereira, A.V. Coelho, C.A. Viegas, M.M. Correia dos Santos, M.P. Robalo, L.O. Martins, *J. Biotechnol.* **139,** 68 (2009).
7. S .A. Nosier, Y.A. Alhamed, *Bulg. Chem. Commun.,* **43,** 3, 401 (2011).
8. T. V. Denisova, M. A. Vyboishchik, T. V. Tetyueva, A. V. Ioffe, *Met. Sci. Heat Treat.,* **54,** 530 (2013).
9. A.K. Verma, R.R. Dash and P. Bhunia, *J. Environ. Manage.* **93,** 154 (2012).
10. S. Kalal, N. P. S. Chauhan, N. Ameta, R. Ameta, S. Kumar, P. B. Punjabi, *Korean J. Chem. Eng.*, **31**, 2183 (2014).
11. S. Kortangsakul, M. Hunsom, *Korean J. Chem. Eng.,* **26**, 1637 (2009).
12. B. Ulusoy, E. Çatalkaya, F. Şengül, *J. Hazard. Mater.,* **114,** 159 (2003).
13. S. Wei, L. Liu, H. Li, J. Shi, Y. Liu, Z. Shao, *Appl. Catal. A-Gen.,* **417-418,** 253 (2012).
14. S. J. Royaee, M. Sohrabi, A. Shafeghat, *Korean J. Chem. Eng.,* **31** (2), 240 (2014).
15. B. Hu, C. Wu, Z. Zhang, L. Wang, *Ceram. Int.,* **40**(5), 7015 (2014).
16. T. Yetim, T. Tekin, *J. Chem. Soc. Pak.,* **34**(6)**,** 1397 (2012) .
17. A.F. Yetim, F. Yildiz, A. Alsaran, A. Celik, *Kovove Mater.*, **46,** 105 (2008).
18. A. Celik, Y. Arslan, A. F. Yetim, I. Efeoglu, *Kovove Mater.,* **45,** 35 (2007).
19. R. Tarı, Ekonometri, Umuttepe Publishers, Kocaeli 2014.
20. D. N. Gujarati, D. C. Porter, Basic Econometrics, McGraw-Hill Irwinp 2009.
21. B. P. Nenavathu, A. V. R. K. Rao, A. Goyal, A. Kapoor, R. K. Dutta, *Appl. Catal.A-Gen.*, **459,** 106 (2013).
22. H. Yang, H. Liu, Z. Hu, J. Liang, H. Pang, B. Yi, *Chem. Eng. J.*, **245,** 24 (2014).
23. T. Fotioua, T.M. Triantisa, T. Kaloudisb, E. Papaconstantinoua, A. Hiskia, *J. Photochem. Photobio. A-Chem.,* **286,** 1 (2014).
24. M. Y. Guo, A. M. Ching Ng, F. Liu, A. B. Djuriˇsi, W. K. Chan, *Appl. Catal. B- Environ.* **107,** 150 (2011).
25. A. Di Paola, M. Bellardita, L. Palmisano, Z. Barbierikova, V. Brezova, *J. Photochem. Photobio., A- Chem.*, **273,** 59 (2014).
26. L. A. Crum, T.J. Mason, J.L. Reisse, K. S. Suslick, *Sonochemistry and Sonoluminescence,* Kluwer Academic, Dordreichtp 1999, p. 363.
27. O. Lavigne, Y. Takeda, T. Shoji, K. Sakaguchi, *Corros. Sci.* **53,** 1079 (2011).
28. T.A. Egerton, H. Purnama, *Dyes Pigments*, **101,** 280 (2014).
29. A.F. Yetim, A. Alsaran, A. Celik, I. Efeoglu, *Corros. Eng. Sci. Technol.*, **46**(4), 439 (2011).
30. C.G. Joseph, G. L. Puma, A. Bono, T. H. Taufiq-Yap, D. Krishnaiah, *Desalination*, **276,** 303 (2011).
31. J. Madhavan, P. S. S. Kumar, S. Anandan, F. Grieser, M. Ashokkumar, *Sep. Purif. Technol.*, **74,** 336 (2010).
32. C. H. Tung, J. H. Chang, Y. H. Hsieh, J. C. Hsu, A. V. Ellis, W. C. Liu, R. H. Yan, *J. Taiwan Inst. Chem. Eng.,* article in press (2014)
33. H. Gao, S. Yan, J. Wang, Z. Zou, *Appl. Catal. B- Environ.,* **158,** 321 (2014)

КОРОЗИОННО ПОВЕДЕНИЕ НА НЕРЪЖДАЕМА СТОМАНА 316L ПРИ ТРЕТИРАНЕ С МОДЕЛНИ ОТПАДЪЧНИ ВОДИ

Т. Йетим

Департамент по инженерна химия, Факултет по инженерство и архитектура, технически университет в Ерзурум, Турция

(Резюме)

Някои органични съединения в отпадъчните води не само замърсяват околната среда, но и причиняват корозия на водните транспортни средства. В тази работа е изследвана корозионната активност на третирани отпадъчни води от текстилната индустрия върху неръждаема стомана AISI 316L. Третирането бе извършено чрез ултразвук (US), фотохимично въздействие (UV) и комбинация от двете (US+UV). Тези процеси бяха използвани за разграждането на багрила, замърсяващи отпадъчните води. Бяха приготвени моделни води. Концентрациите на багрилата се понижаваха с времето при трите изследвани процеса. Най-ниски концентрации бяха постигнати при комбинацията от ултразвуково и фотохимично въздействие, а най-слаб ефект имаше ултразвуковото въздействие. Кривите за потенциала при отворена верига (ОСР) бяха далеч от теоретичното за всички тествани проби. Намаляващата тенденция за стойностите на потенциала бе наблюдавана при всички проби. Най-високи бяха стойностите на ОСР при комбинирано действие. От резултатите при поляризация ултразвуковото въздействие доведе до най-нсък корозионен потенциал и най-висока плътност на тока. Пробите, тествани с третирани разтвори показаха по-добри резултати отколкото без третиране. Неръждаемата стомана показа по-високо съпротивление спрямо корозия след комбинмирано третиране, отколкото при останалите случаи.

An analysis of MHD natural convection heat and mass transfer flow with Hall effects of a heat absorbing, radiating and rotating fluid over an exponentially accelerated moving vertical plate with ramped temperature

G.S. Seth[*], R. Tripathi, R. Sharma

Department of Applied Mathematics, Indian School of Mines, Dhanbad-826004, India

An investigation of unsteady MHD natural convection heat and mass transfer flow with Hall effects and rotation of a viscous, incompressible, electrically conducting, radiating and temperature dependent heat absorbing fluid past an exponentially accelerated moving vertical plate with ramped temperature through a porous medium is carried out. An exact solution for fluid velocity fluid temperature and species concentration is obtained in a closed form by the Laplace transform technique. The expressions for shear stress, rate of heat transfer and rate of mass transfer at the plate are also derived. The numerical values of fluid velocity and fluid temperature are displayed graphically whereas those of shear stress and rate of heat transfer at the plate are presented in tabular form for various values of the pertinent flow parameters.

INTRODUCTION

The effects of thermal radiation and heat generation/absorption on hydromagnetic natural convection flow play a crucial role in controlling the heat transfer and may have promising applications in several physical problems of practical interest viz. convection in the earth's mantle, fire and combustion modeling, fluids undergoing exothermic and/or endothermic chemical reactions, building with buoyancy-driven natural ventilation, radiant ceiling heating systems and floor heating systems. Keeping in view the importance of such a study, Chamkha [1] studied the thermal radiation and buoyancy effects on hydromagnetic flow over an accelerating permeable surface with a heat source or sink. Seddeek [2] investigated the thermal radiation and buoyancy effects on MHD natural convection heat generating fluid flow past an accelerating permeable surface with a temperature-dependent viscosity. Ibrahim *et al*. [3] discussed the effects of radiation and absorption on the unsteady MHD free convection flow past a semi-infinite vertical permeable moving plate with chemical reaction and suction. Mohamed [4] considered chemical reactions and thermal radiation on hydromagnetic free convection flow with heat and mass transfer of a viscous fluid past a semi-infinite vertical moving porous plate embedded in a porous medium in the presence of thermal diffusion and heat generation. Prasad *et al*. [5] investigated the effects of internal heat generation/absorption, thermal radiation, magnetic field and temperature dependent thermal conductivity on the flow and heat transfer characteristics of a Non-Newtonian Maxwell fluid over a stretching sheet.

It is noticed that when the density of an electrically conducting fluid is low and/or the applied magnetic field is strong, Hall current plays a vital role in determining the flow-features of the fluid flow problems because it induces a secondary flow in the flow-field [6]. Taking this fact into account, Aboeldahab and Elbarbary [7] considered the effects of the Hall current on the magnetohydrodynamic free convection flow past a semi-infinite vertical plate with mass transfer. Saha *et al*. [8] discussed the effects of Hall current on the MHD laminar natural convection flow from a vertical permeable flat plate with a uniform surface temperature. Zueco *et al*. [9] made a numerical study of the unsteady MHD free convection flow with the mass transfer taking the Hall current and viscous dissipation into account. Ahmed *et al*. [10] considered the unsteady MHD free convective flow past a vertical porous plate immersed in a porous medium with Hall current, thermal diffusion and a heat source. It is noteworthy that the Hall current induces a secondary flow in the flow-field which is also the characteristics of Coriolis force. Therefore, it is essential to compare and contrast the effects of these two agencies and also to study their combined effects on such fluid flow problems. Considering these two effects, Takhar *et al*. [11] investigated the boundary layer flow of a viscous, incompressible and electrically conducting fluid over a moving surface in a rotating fluid, in the presence of a magnetic field and Hall current with a free moving stream. Recently, Seth *et al*. [12] considered the

* To whom all correspondence should be sent:
E-mail: gsseth_ism@yahoo.com; rajat17@am.ism.ac.in;
rohitsharma@am.ism.ac.in

combined effects of the Hall current, rotation and radiation on natural convection heat and mass transfer flow past a moving vertical plate.

Natural convection flows are generally modeled by researchers under the consideration of uniform surface temperature or a uniform heat flux. However, practical problems often involve non-uniform thermal conditions. Some of the numerous industry based applications considering non-uniform thermal conditions include nuclear heat transfer control, materials processing, turbine blade heat transfer, electronic circuits and sealed gas-filled enclosure heat transfer operations. Keeping this fact in view, several researchers [13-23] investigated natural convection flow from a vertical plate with ramped temperature.

The current study seeks to investigate the effects of Hall current and rotation on unsteady hydromagnetic natural convection heat and mass transfer flow of a viscous, incompressible, electrically conducting, optically thin heat radiating and temperature dependent heat absorbing fluid through a fluid saturated porous medium past an exponentially accelerated vertical plate having the ramped temperature profile. This problem has not yet received attention from the researchers, although natural convection heat and mass transfer flow of a heat absorbing and radiating fluid resulting from such a ramped temperature profile of a plate moving with time dependent velocity may have strong bearings on numerous problems of practical interest where initial temperature profiles are of much significance in the design of hydromagnetic devices and in several industrial processes occurring at high temperatures where the effects of thermal radiation and heat absorption play a vital role in the fluid flow characteristics.

FORMULATION OF THE PROBLEM

Consider unsteady hydromagnetic natural convection flow of viscous, incompressible, electrically conducting, optically thin heat radiating and temperature dependent heat absorbing fluid past an infinite moving vertical plate embedded in a porous medium taking Hall current and rotation into account. The Cartesian co-ordinate system is considered in such a way that the x' – axis is along the length of the plate in the upward direction and the y' − axis is normal to the plane of the plate in the fluid and the z' − axis is perpendicular to the $x'y'$ − plane. The fluid is permeated by a uniform transverse magnetic field B_0 which is applied in a direction parallel to the y' axis. Initially i.e. at time $t' \leq 0$, both the fluid and plate are at rest and at a

uniform temperature T'_∞. Also the species concentration within the fluid is maintained at a uniform concentration C'_∞. At time $t' > 0$, the plate is exponentially accelerated with a velocity $U_0 e^{a't'}$ in the x' – direction and the temperature of the plate is raised or lowered to $T'_\infty + (T'_w - T'_\infty)t' / t_0$ when $t' \leq t_0$ and thereafter at $t' > t_0$, the plate is maintained at a uniform temperature T'_w. a' and U_0 are an arbitrary constant and uniform velocity of the plate (*i.e.* $a' = 0$) respectively. Also at time $t' > 0$, the species concentration at the surface of the plate is raised to a uniform concentration C'_w and this is maintained thereafter. Since the plate is of infinite extent along the x' and z' directions and is electrically non-conducting, all the physical quantities depend only on y' and t'. The geometry of the problem is shown in Figure 1. It is assumed that the induced magnetic field produced by fluid motion is negligible in comparison to the applied one. This assumption is valid for metallic liquids and partially ionized fluids [24]. Also no electric field is applied so the effect of polarization of the fluid is neglected [25].
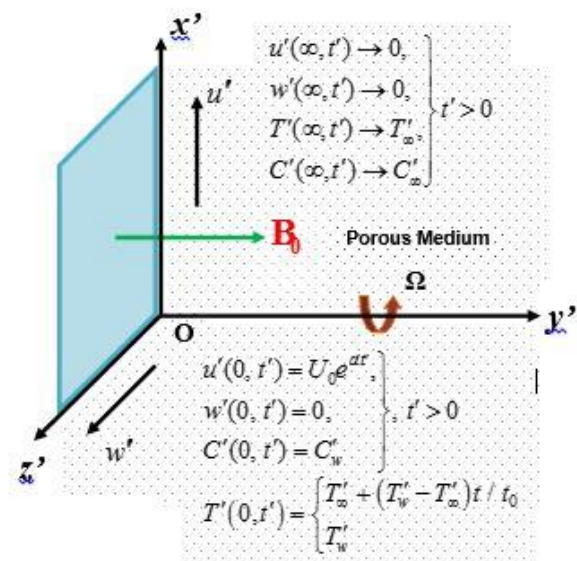
Fig.1. Geometry of the Problem

Keeping in view the assumptions made above, the governing equations for unsteady hydromagnetic natural convection flow of an electrically conducting, viscous, incompressible, temperature dependent heat absorbing and optically thin radiating fluid in a uniform porous medium, under Boussinesq's approximation, taking the Hall current and rotation into account are given by

$$\frac{\partial u'}{\partial t'} + 2\Omega w' = v\frac{\partial^2 u'}{\partial y'^2} - \left(\frac{\sigma B_0^2}{\rho}\right)\frac{(u'+mw')}{(1+m^2)} - v\frac{u'}{K_1'}$$
$$+ g\beta'(T'-T_\infty') + g\beta^*(C'-C_\infty'), \qquad (1)$$

$$\frac{\partial w'}{\partial t'} - 2\Omega u' = v\frac{\partial^2 w'}{\partial y'^2} + \left(\frac{\sigma B_0^2}{\rho}\right)\frac{(mu'-w')}{(1+m^2)} - v\frac{w'}{K_1''}, \quad (2)$$

$$\frac{\partial T'}{\partial t'} = \frac{k}{\rho c_p}\frac{\partial^2 T'}{\partial y'^2} - \frac{Q_0}{\rho c_p}(T'-T_\infty') - \frac{1}{\rho c_p}\frac{\partial q_r'}{\partial y'}, \qquad (3)$$

$$\frac{\partial C'}{\partial t'} = D_M \frac{\partial^2 C'}{\partial y'^2}, \qquad (4)$$

where $m = \omega_e \tau_e$ is the Hall current parameter. $u', w', T', K_1', k, c_p, Q_0, C', D_M, q_r', v, \sigma, \rho, g, \beta', \beta^*,$ ω_e and τ_e are, respectively, fluid velocity in the x'–direction, fluid velocity in the z'–direction, the fluid temperature, permeability of a porous medium, thermal conductivity, specific heat at constant pressure, heat absorption coefficient, species concentration, molecular (mass) diffusivity, radiating flux vector, kinematic coefficient of viscosity, electrical conductivity, fluid density, acceleration due to gravity, coefficient of thermal expansion, coefficient of expansion for species concentration, cyclotron frequency and the electron collision time.

The initial and boundary conditions for the fluid flow problem are

$$u' = w' = 0, T' = T_\infty', C' = C_\infty', \text{ for } y' \geq 0 \text{ and } t' \leq 0, (5a)$$
$$u' = U_0 e^{a't'}, \ w' = 0, \ C' = C_w', \text{ at } y' = 0 \text{ and } t' > 0 \quad (5b)$$
$$T' = T_\infty' + (T_w' - T_\infty')t'/t_0, \text{ at } y' = 0 \text{ and } 0 < t' \leq t_0, (5c)$$
$$T' = T_w', \qquad\qquad \text{ at } y' = 0 \text{ and } t' > t_0, \quad (5d)$$
$$u', w' \to 0, T' \to T_\infty', C' \to C_\infty', \text{ as } y' \to \infty \text{ for } t' > 0 \quad (5e)$$

In the case of an optically thin gray fluid the local radiant absorption is expressed by

$$\frac{\partial q_r'}{\partial y'} = -4a^*\sigma^*\left(T_\infty'^4 - T'^4\right), \qquad (6)$$

where a^* is the absorption coefficient and σ^* is the Stefan-Boltzmann constant.

Assuming a small temperature difference between the fluid temperature T' and the free stream temperature T_∞', T'^4 is expanded in a Taylor series about the free stream temperature T_∞' to linearize equation (6) which, after neglecting the second and higher order terms in $(T'-T_\infty')$, assumes the form

$$T'^4 \cong 4T_\infty'^3 T' - 3T_\infty'^4. \qquad (7)$$

Making use of equations (6) and (7) in equation (3), we obtain

$$\frac{\partial T'}{\partial t'} = \frac{k}{\rho c_p}\frac{\partial^2 T'}{\partial y'^2} - \frac{16a^*\sigma^* T_\infty'^3}{\rho c_p}\left(T'-T_\infty'\right) -$$
$$\frac{Q_0}{\rho c_p}\left(T'-T_\infty'\right). \qquad (8)$$

In order to non-dimensionalize equations (1), (2), (4) and (8), the following non-dimensional variables and parameters are introduced

$$\left.\begin{aligned}
&y = y'/U_0 t_0, \ u = u'/U_0, \ w = w'/U_0, \\
&t = t'/t_0, \ T = (T'-T_\infty')/(T_w'-T_\infty'), \\
&C = (C'-C_\infty')/(C_w'-C_\infty'), a = a'v/U_0^2, \\
&G_r = g\beta'v(T_w'-T_\infty')/U_0^3, \\
&G_c = g\beta^*v(C_w'-C_\infty')/U_0^3, \\
&K^2 = \Omega v/U_0^2, K_1 = K_1'U_0^2/v^2, \\
&M = \sigma B_0^2 v/\rho U_0^2, P_r = v\rho c_p/k, \\
&\phi = vQ_0/\rho c_p U_0^2, R = 16a^*\sigma v T_\infty'^3/U_0^2\rho c_p \\
&\text{and } S_c = v/D_M
\end{aligned}\right\} \quad (9)$$

Equations (1), (2), (4) and (8), in non-dimensional form, are given by

$$\frac{\partial u}{\partial t} + 2K^2 w = \frac{\partial^2 u}{\partial y^2} - \frac{M(u+mw)}{(1+m^2)} - \frac{u}{K_1} + G_r T + G_c C, \qquad (10)$$

$$\frac{\partial w}{\partial t} - 2K^2 u = \frac{\partial^2 w}{\partial y^2} + \frac{M(mu-w)}{(1+m^2)} - \frac{w}{K_1}, \qquad (11)$$

$$\frac{\partial T}{\partial t} = \frac{1}{P_r}\frac{\partial^2 T}{\partial y^2} - RT - \phi T, \qquad (12)$$

$$\frac{\partial C}{\partial t} = \frac{1}{S_c}\frac{\partial^2 C}{\partial y^2}, \qquad (13)$$

where K^2, K_1, M, G_r, G_c, P_r, R, ϕ and S_c are, respectively, the rotation parameter, permeability parameter, magnetic parameter, thermal Grashof number, solution Grashof number, Prandtl number, radiation parameter, heat absorption parameter and Schmidt number.

It may be noted that the characteristic time t_0 is defined according to the non-dimensional process mentioned above, as

$$t_0 = v/U_0^2. \qquad (14)$$

The initial and boundary conditions (5a) to (5e), in non-dimensional form, are given by

$$u = w = 0, T = 0, C = 0, \textbf{for } y \geq 0 \text{ and } t \leq 0, \qquad (15a)$$
$$u = e^{at}, \ w = 0, \ C = 1, \text{ at } y = 0 \text{ and } t > 0, \qquad (15b)$$
$$T = t, \qquad\qquad \text{ at } y = 0 \text{ and } 0 < t \leq 1, \qquad (15c)$$

$T = 1$, at $y = 0$ for $t > 1$, (15d)

$u, w \to 0, T \to 0, C \to 0$, as $y \to \infty$ for $t > 0$, (15e)

where a is the plate acceleration parameter.

Combining equations (10) and (11), we obtain

$$\frac{\partial F}{\partial t} = \frac{\partial^2 F}{\partial y^2} - \left(N + \frac{1}{K_1} - 2iK^2 \right) F + G_r T + G_c C, \quad (16)$$

where $F = u + iw$ and $N = M / (1 + im)$.

The initial and boundary conditions (15a) to (15e), in compact form, are given by

$F = 0, T = 0, C = 0$, for $y \geq 0$ and $t \leq 0$, (17a)

$F = e^{at}, C = 1$, at $y = 0$ for $t > 0$, (17b)

$T = t$, at $y = 0$ for $0 < t \leq 1$, (17c)

$T = 1$, at $y = 0$ and $t > 1$, (17d)

$F \to 0, T \to 0, C \to 0$, as $y \to \infty$ for $t > 0$. (17e)

Equations (12), (13) and (16) are subject to the initial and boundary conditions (17a) to (17e) and are solved by the Laplace transform technique. The exact solutions for the fluid temperature $T(y,t)$, species concentration $C(y,t)$ and fluid velocity $F(y,t)$ are obtained and presented in the following form after simplification

(i) For $P_r \neq 1$ and $S_c \neq 1$

$$T(y,t) = P(y,t) - H(t-1)P(y,t-1), \quad (18)$$

$$C = erfc\left(\frac{y\sqrt{S_c}}{2\sqrt{t}} \right), \quad (19)$$

$$F(y,t) = \left[\frac{e^{at}}{2} f_2(y,1,\beta_1,a,t) + \frac{\gamma}{2b_1} \left[e^{b_1 t} \times \right. \right.$$

$$\{ f_2(y,1,\beta_1,b_1,t) - f_2(y,S_c,0,b_1,t) \} -$$

$$\{ f_2(y,1,\beta_1,0,t) \} - f_2(y,S_c,0,0,t) \} \left. \left. \right] \right]$$

$$+ G(y,t) + H(t-1)G(y,t-1). \quad (20)$$

(ii) For $P_r = S_c = 1$

$$T(y,t) = P_1(y,t) - H(t-1)P_1(y,t-1), \quad (21)$$

$$C(y,t) = erfc\left(\frac{y}{2\sqrt{t}} \right), \quad (22)$$

$$F(y,t) = \frac{e^{at}}{2} \left[f_2(y,1,\beta_1,a,t) \right] + \frac{b_2}{2} \left[f_2(y,1,0,0,t) \right.$$

$$- f_2(y,1,\beta_1,0,t) \right] + G_1(y,t) - H(y,t-1)$$

$$\times G_1(y,t-1), \quad (23)$$

where

$P(y,t) = f_1(y,t,P_r,\beta_2)$,

$P_1(y,t) = f_1(y,t,1,\beta_2)$,

$$G(y,t) = \frac{\alpha}{2a_1^2} \left[e^{at} \{ f_2(y,P_r,\beta_2,a_1,t) - \right.$$

$$- f_2(y,1,\beta_1,a_1,t) \} - a_1 \{ f_3(y,P_r,\beta_2,a_1,t)$$

$$- f_3(y,1,\beta_2,a_1,t) \} \right],$$

$$G_1(y,t) = \frac{a_2}{2} \left[f_2(y,1,\beta_2,0,t) - f_1(y,t,1,\beta_1) \right],$$

$$\beta_1 = N + 1/K_1 - 2iK^2, \quad \beta_2 = R + \phi, \quad a_1 = \frac{(P_r \beta_2 - \beta_1)}{(1 - P_r)},$$

$$b_1 = \beta_1/(S_c - 1), \quad \alpha = G_r/(1 - P_r), \quad a_2 = \frac{G_r}{\beta_1 - \beta_2},$$

$$b_2 = \frac{G_c}{\beta_1} \text{ and } \gamma = G_c/(S_c - 1).$$

$H(t-1)$ and $erfc(x)$ are, respectively, the unit step function and complementary error function. Expressions for f_1, f_2 and f_3 are provided in Appendix-I.

SHEAR STRESS AND RATE OF HEAT TRANSFER AT THE PLATE:

Expressions for the primary shear stress at the plate τ_x, secondary shear stress at the plate τ_z and rate of heat transfer at the plate N_u are obtained and presented in the following form after simplification

$$\tau = \tau_x + i\tau_z = e^{at} \left[f_4(\beta_1,1,a,t) \right] + \frac{\gamma}{b_1} \{ f_4(\beta_1,1,b_1,t)$$

$$- f_4(0,S_c,b_1,t) \} - \{ f_4(\beta_1,1,0,t)$$

$$- \frac{\sqrt{S_c}}{\sqrt{\pi t}} \} + G_2(0,t) + H(t-1)G_2(0,t-1), \quad (24)$$

$$N_u = P_2(0,t) - H(t-1)P_2(0,t-1), \quad (25)$$

where

$$G_2(0,t) = \frac{\alpha}{2a_1^2} \left[e^{a_1 t} \{ f_4(\beta_1,P_r,a_1,t) - f_4(\beta_1,1,a_1,t) \} \right.$$

$$- a_1 \{ f_5(\beta_2,P_r,a_1,t) - f_5(\beta_1,1,a_1,t) \} \right],$$

$$P_2(0,t) = \left(\frac{1}{2} \right) \left[\left(2t\sqrt{P_r\beta_2} + \sqrt{\frac{P_r}{\beta_2}} \right) \left(erfc\left(\sqrt{\beta_2 t} \right) - 1 \right) \right.$$

$$- 2\sqrt{\frac{P_r}{t\pi}} e^{-\beta_2 t} \right].$$

The expressions for f_4 and f_5 are provided in Appendix-I.

Rate of mass transfer at the plate:

The expression for the rate of mass transfer at the plate S_h, is given by

$$S_h = -\sqrt{\frac{S_c}{t\pi}}. \quad (26)$$

Expression (26) reveals that rate of mass transfer at the plate increases on increasing the Schmidt number S_c and decreases on increasing the time. Since S_c presents a relative strength of the viscosity to molecular diffusivity of the fluid, S_c decreases on increasing the molecular diffusivity. This implies that the molecular diffusivity tends to reduce the rate of mass transfer at the plate and there is a reduction in rate of mass transfer at the plate with the progress of time.

RESULTS AND DISCUSSION

In order to analyze the physics of the flow regime, numerical computations from the analytical solutions (18) and (19) for the velocity field and temperature field and from the analytical expressions (24) and (25) for the shear stress and rate of heat transfer at the plate are carried out by assigning some chosen values to different physical parameters. Throughout our investigation, the values of the Prandtl number P_r, magnetic parameter M, permeability parameter K_1 and Schmidt number S_c have been fixed at 0.71, 15, 0.2 and 0.6 respectively as far as the numerical computations are concerned. It is known that $P_r = 0.71$ corresponds to the ionized air and $M = 15$ represents the strong magnetic field. The effects of the pertinent flow parameters on species concentration are already analyzed by Seth *et al.* [22]. Due to this reason, we have omitted the numerical computation for species concentration. The numerical results, computed from analytical solutions and expressions, are illustrated in Figures 2 to 12 along with Tables 1 to 5.

The variation of the primary velocity u and the secondary velocity w, versus the boundary layer co-ordinate y under the influence of the plate acceleration parameter a, Hall current parameter m, rotation parameter K^2, radiation parameter R, heat absorption parameter ϕ, thermal Grashof number G_r, solution Grashof number G_c and time t are depicted graphically in Figures 2 to 9. It is observed from these figures that the secondary velocity w attains a distinctive maximum value in the region near the plate and then decreases properly on increasing the boundary layer coordinate y to approach the free stream value. This may be due to the effects of the Coriolis force and Hall current which induce a secondary flow in the flow field.
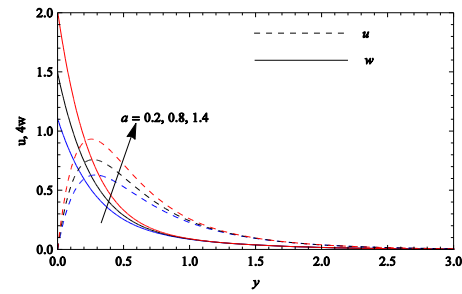
Fig. 2. Velocity profiles when $m = 0.5$, $K^2 = 2$, .

$R = 2, \phi = 3, G_r = 10, G_c = 3, S_c = 0.6$ and $t = 0.5.$
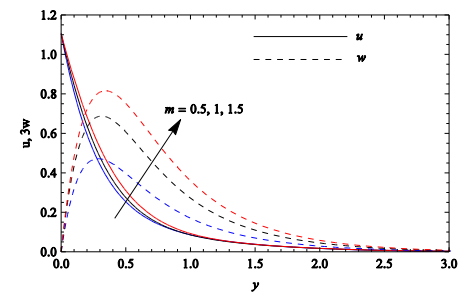
Fig. 3. Velocity profiles when $a = 0.2$, $K^2 = 2$,

$R = 2, \phi = 3, G_r = 10, G_c = 3, S_c = 0.6$ and $t = 0.5.$

It is observed from Figure 2 that, an increase in the plate acceleration parameter a causes u and w to increase in the region near the plate and the effect of the plate acceleration parameter a is almost negligible in the region away from the plate. This observation suggests that the higher plate velocity results in an accelerated fluid motion in the region near the plate. It is inferred from Figure 3 that both u and w are getting accelerated on increasing m. This phenomena is in excellent agreement with the fact that in an electrically conducting fluid whose density is low and/or the applied magnetic field is strong, a current known as the Hall current is induced which moves in a direction normal to both the electric and magnetic field i.e. the total current produced in the flow-field does not move in the direction of the electric field. Thus, the Hall current has a tendency to accelerate both the primary and secondary fluid velocities. It is depicted from Figure 4 that, on increasing K^2, u gets decelerated whilst a reverse pattern occurs for w. This is in agreement with the fact that in a rotating medium, the Coriolis force (which is induced due to rotation) has a tendency to suppress the main flow i.e. the primary flow induces a secondary flow in the flow field. Figures 5 and 6 uniquely establish that there is a fall in the values of u and w for increasing values of R and ϕ. In other words, the primary and secondary velocities for highly radiating and heat absorbing fluids are smaller as compared to those of lesser radiating and heat absorbing fluids which is justified because the fluid temperature is getting reduced on

increasing R and ϕ which is clearly evident from Figures 10 and 11. It is inferred from Figures 7 and 8 that there is a significant increase in the values of u and w due to the increase in G_r and G_c. Since G_r presents the relative strength of the thermal buoyancy force to a viscous force and G_c is a measure of the solution buoyancy force to a viscous force, as G_r and G_c increase, the thermal and solutal buoyancy forces get stronger. This implies that the thermal as well as solution buoyancy forces tend to accelerate both the primary and secondary fluid velocities. It is revealed from Figure 9 that there is an increase in u and w on increasing t. This observation suggests that the primary and secondary fluid velocities are accelerated with the progress of time.

Figures 10 to 12 exhibit how the fluid temperature T is affected by the heat absorption parameter ϕ, radiation parameter R and time t. We see that, an increase in ϕ and R, results in a significant fall in the fluid temperature T. These results are in excellent agreement with the results of Nandkeolyar et al. [15] and Das et al. [20].
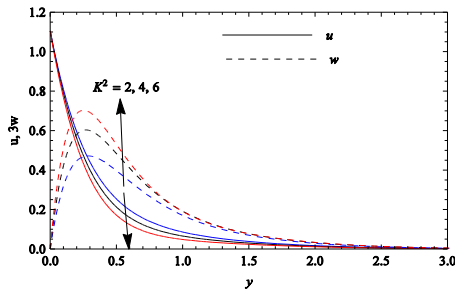
Fig. 4. Velocity profiles when $a = 0.2$, $m = 0.5$, $R = 2, \phi = 3, G_r = 10, G_c = 3, S_c = 0.6$ and $t = 0.5$.
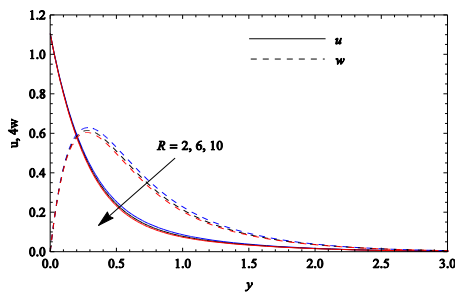
Fig 5. Velocity profiles when $a = 0.2$, $m = 0.5$, $K^2 = 2, \phi = 3, G_r = 10, G_c = 3, S_c = 0.6$ and $t = 0.5$.
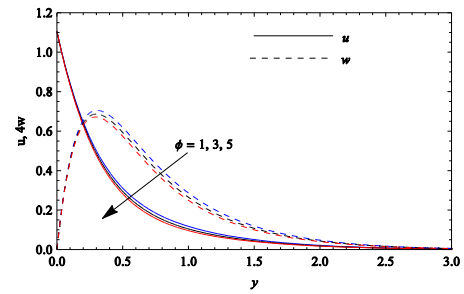
Fig. 6. Velocity profiles when $a = 0.2, m = 0.5$, $K^2 = 2$, $R = 2$, $G_r = 10$, $G_c = 3$, $S_c = 0.6$ and $t = 0.5$
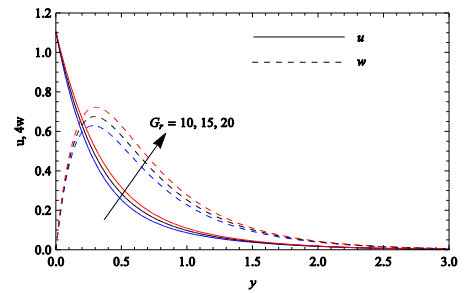
Fig. 7. Velocity profiles when $a = 0.2, m = 0.5$, $K^2 = 2$, $R = 2$, $\phi = 3$, , $G_c = 3$, $S_c = 0.6$ and $t = 0.5$
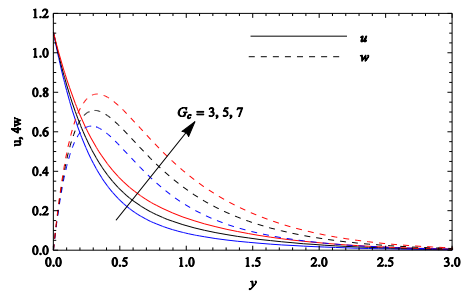
Fig. 8. Velocity profiles when $a = 0.2, m = 0.5$, $K^2 = 2$, $R = 2$, $\phi = 3$, $G_r = 10$, $S_c = 0.6$ and $t = 0.5$
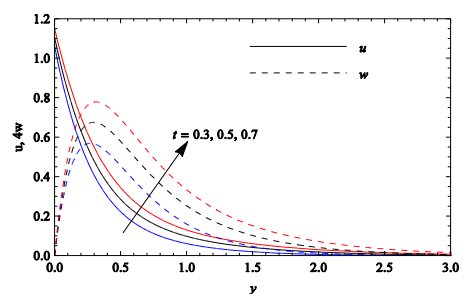
Fig. 9. Velocity profiles when $a = 0.2, m = 0.5$, $K^2 = 2$, $R = 2$, $\phi = 3$, $G_r = 10$, $G_c = 3$ and $S_c = 0.6$
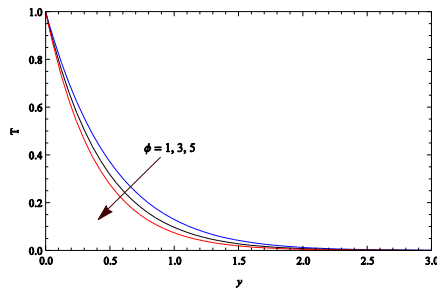
Fig. 10. Temperature profiles when $R = 2$ and $t = 0.5$
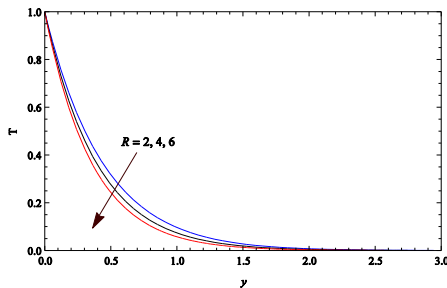
Fig. 11. Temperature profiles when $\phi = 3$ and $t = 0.5$
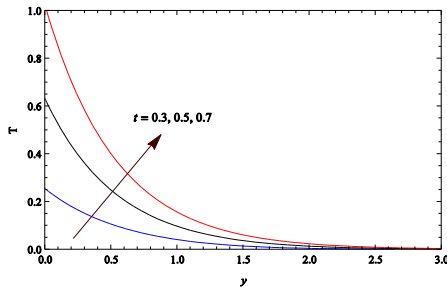
Fig. 12. Temperature profiles when $\phi = 3$ and $R = 2$.

The change in the behavior of the primary shear stress at the plate τ_x and secondary shear stress at the plate τ_z under the influence of K^2, m, G_r, G_c, ϕ, R, a and t, are presented in Tables 1 to 4. It is inferred from Table 1 that the primary shear stress at the plate τ_x increases on increasing K^2 and it decreases on increasing m. The secondary shear stress at the plate τ_z increases on increasing either K^2 or m.

This implies that the rotation tends to enhance the primary as well as secondary shear stress at the plate. The Hall current tends to reduce the primary shear stress at the plate whereas it has a reverse effect on the secondary shear stress at the plate. It is observed from Table 2 that τ_x decreases on increasing either G_c or G_r. τ_z increases on increasing either G_c or G_r. This implies that the thermal and solution buoyancy forces tend to reduce the primary shear stress at the plate whereas these agencies have a reverse effect on the secondary shear stress at the plate. It is evident from Table 3 that τ_x increases on increasing either ϕ or R whereas τ_z is decreased on

increasing either ϕ or R. This implies that, heat absorption and radiation tend to enhance the primary shear stress at the plate whereas these agencies have a reverse effect on the secondary shear stress at the plate. It is clear from Table 4 that, τ_x and τ_z both increase on increasing a. τ_x decreases on increasing t whereas τ_z increases on increasing t.

Table 1. Shear stress at the plate when $G_r = 4$, $G_c = 3$, $\phi = 3$, $R = 2$, $S_c = 0.6$ and $t = 0.5$.

	$K^2 \downarrow$ $m \rightarrow$	0.5	1	1.5
	2	3.4336	2.8786	2.4015
$-\tau_x$	4	3.6436	3.1792	2.7645
	6	3.8789	3.4874	3.1401
	2	1.5472	2.0276	2.1685
τ_z	4	2.0784	2.5658	2.7408
	6	2.5528	3.0234	3.1977

Table 2. Shear stress at the plate when $m = 0.5$, $K^2 = 2$, $\phi = 3$, $R = 2$, $S_c = 0.6$ and $t = 0.5$

	$G_c \downarrow$ $G_r \rightarrow$	10	15	20
	3	3.4336	3.0806	2.7275
$-\tau_x$	5	3.0203	2.6673	2.3143
	7	2.6070	2.2540	1.9010
	3	1.6075	1.6836	1.7597
τ_z	5	1.7225	1.7986	1.8747
	7	1.8375	1.9136	1.9897

Table 3. Shear stress at the plate when $m = 0.5$, $K^2 = 2$, $G_r = 4$, $G_c = 3$, $S_c = 0.6$ and $t = 0.5$.

	$\phi \downarrow$ $R \rightarrow$	2	4	6
	1	3.3646	3.4336	3.4727
$-\tau_x$	3	3.4336	3.4727	3.4986
	5	3.4727	3.4986	3.5181
	1	1.5827	1.5472	1.5280
τ_z	3	1.5472	1.5280	1.5158
	5	1.5280	1.5158	1.5069

Table 4. Shear stress at the plate when $m = 0.5$, $K^2 = 2$, $G_r = 4$, $G_c = 3$, $\phi = 3$ and $R = 2$.

	$a \downarrow$ $t \rightarrow$	0.3	0.5	0.7
	0.2	3.5851	3.4336	3.3053
$-\tau_x$	0.4	3.8923	3.8605	3.7784
	0.6	4.2198	4.1456	4.0517
	0.2	1.4357	1.5472	1.6626
τ_z	0.4	1.5054	1.6750	1.8556
	0.6	1.5791	1.8157	2.0766

Table 5. Rate of heat transfer at the plate

R	ϕ	t	$-N_u$
		0.3	0.8845
2	3	0.5	1.1570
		0.7	1.5122
	1		1.0419
2	3	0.5	1.1570
	5		1.2838
2			1.1570
4	3	0.5	1.2838
6			1.4080

This implies that, both the primary and secondary shear stresses at the plate increase on accelerating the plate. Primary shear stress at the plate is getting reduced whereas secondary shear stress at the plate is getting enhanced with the progress of time. It is noticed from Table 5 that the rate of heat transfer N_u increases on increasing either of R, ϕ and t. This implies radiation and heat absorption tend to enhance the rate of heat transfer at the plate. The rate of heat transfer at the plate is getting enhanced with the progress of time.

CONCLUSION

The noteworthy results are summarized below

- Plate acceleration parameter, Hall current, thermal and solution buoyancy forces tend to accelerate the fluid flow in both the primary and secondary flow direction. Thermal radiation and heat absorption tend to decelerate the fluid flow in both the primary and secondary flow directions. Rotation tends to accelerate the primary fluid velocity whereas it has a reverse effect on the secondary fluid velocity. The primary and secondary fluid velocities get accelerated with the progress in time.
- Heat absorption and thermal radiation tend to reduce the fluid temperature. The fluid temperature is enhanced with the progress in time.
- Rotation, heat absorption, thermal radiation and the plate acceleration parameter tend to enhance the primary shear stress at the plate whereas the Hall current, thermal and solution buoyancy forces tend to reduce the primary shear stress at the plate. The rotation, Hall current, thermal and solution buoyancy forces and plate acceleration parameters tend to enhance the secondary shear stress at the plate whereas the heat absorption and thermal radiation tend to reduce the secondary shear stress at the plate. The primary shear stress at the plate is reduced, whereas the secondary shear stress at the plate is enhanced with the progress of time.

- The rate of heat transfer at the plate is enhanced on increasing either the heat absorption or thermal radiation with the progress of time.

Appendix

$$f_1(c_1,c_2,c_3,c_4) = \left(\frac{1}{2}\right)\left[\left(c_2 + \frac{c_1}{2}\sqrt{\frac{c_3}{c_4}}\right)e^{c_1\sqrt{c_3 c_4}}\right.$$
$$erfc\left(\frac{c_1}{2}\sqrt{\frac{c_3}{c_2}} + \sqrt{c_4 c_2}\right) + \left(c_2 - \frac{c_1}{2}\sqrt{\frac{c_3}{c_4}}\right)\times$$
$$\left. e^{-c_1\sqrt{c_3 c_4}} erf\, c\left(\frac{c_1}{2}\sqrt{\frac{c_3}{c_2}} - \sqrt{c_4 c_2}\right)\right],$$

$$f_2(c_1,c_2,c_3,c_4,c_5) = e^{c_1\sqrt{c_2(c_3+c_4)}}\, erfc\left(\frac{c_1}{2}\sqrt{\frac{c_2}{c_5}}\right.$$
$$\left. + \sqrt{(c_3+c_4)c_5}\right) - e^{-c_1\sqrt{c_2(c_3+c_4)}}\times$$

$$f_3(c_1,c_2,c_3,c_4,c_5) = \left(c_5 + \frac{1}{c_4} + \frac{c_1}{2}\sqrt{\frac{c_2}{c_3}}\right)e^{c_1\sqrt{c_2 c_3}}$$
$$\times erfc\left(\frac{c_1}{2}\sqrt{\frac{c_2}{c_5}} + \sqrt{c_3 c_5}\right) + \left(c_5 + \frac{1}{c_4} - \frac{c_1}{2}\sqrt{\frac{c_2}{c_3}}\right)e^{-c_1\sqrt{c_2 c_3}}\times$$
$$erfc\left(\frac{c_1}{2}\sqrt{\frac{c_2}{c_5}} - \sqrt{c_3 c_5}\right),$$
$$erfc\left(\frac{c_1}{2}\sqrt{\frac{c_2}{c_5}} - \sqrt{(c_3+c_4)c_5}\right),$$

$$f_4(c_1,c_2,c_3,c_4) = e^{-(c_1+c_3)c_4}\sqrt{\frac{c_2}{\pi t}} + \sqrt{(c_1+c_3)c_2}$$
$$\left\{erfc\left(\sqrt{(c_1+c_3)c_4}\right) - 1\right\},$$

$$f_5(c_1,c_2,c_3,c_4) = 2\left\{\sqrt{c_1 c_2}\left(c_4 + \frac{1}{c_3}\right) + \frac{1}{2}\sqrt{\frac{c_2}{c_1}}\times\right.$$
$$\left\{erfc\left(\sqrt{c_1 c_4}\right)\right\} - 1\right\}$$

REFERENCES

1. A.J. Chamkha, *Int. J. Eng. Sci.*, **38**, 1699 (2000).
2. M.A. Seddeek, *Canad. J. Phys.*, **79**, 725 (2001).
3. F.S. Ibrahim, A.M. Elaiw, A.A. Bakr, *Communications in Nonlinear Science and Numerical Simulation*, **13**, 1056 (2008).
4. R.A. Mohamed, *Appl. Math. Sci.*, **3**, 629 (2009).
5. K. V. Prasad, K. Vajravelu, A. Sujatha, *J. Appl. Fluid Mech.*, **6**, 249 (2013).
6. G.W. Sutton, A. Sherman, Engineering Magnetohydrodynamics Mcgraw-Hill, New York, 1965.
7. E.M. Aboeldahab, E.M.E. Elbarbary, *Int. J. Eng. Sci.*, **39**, 1641 (2001).
8. L.K. Saha, M.A. Hossain, R.S.R. Gorla, *Int. J. Thermal Sci.*, **46**, 790 (2007).
9. J. Zueco, P. Eguia, D. Patino, L.M. Lopez-Ochoa, *Int. J. Numer. Meth. Biomed. Engng*, **26**, 1687 (2010).
10. N. Ahmed, H. Kalita, D.P. Barua, *Int. J. Eng., Sci. Tech.*, **2**, 59 (2010).

11. H.S. Takhar, A.J. Chamkha, G. Nath, *Int. J. Eng. Sci.*, **40**, 1511 (2002).
12. G.S. Seth, S. Sarkar, S.M. Hussain, *Ain Shams Engineering Journal*, **5**, 489 (2014).
13. P. Chandran, N.C. Sacheti, A.K. Singh, *Heat Mass Transfer*, **41**, 459 (2005).
14. Samiulhaq, I. Khan, F. Ali, S. Shafie, *J. Phys. Soc. Jpn*, **81**, (2012), DOI: 10.1143/JPSJ.81.044401.
15. R. Nandkeolyar, M. Das, P. Sibanda, *Bound. Value Probl.*, **1**, 247 (2013).
16. A.Q. Mohamad, I. Khan, Z. Ismail, S. Shafie, *AIP Conf. Proc.*, 1605, 398 (2014).
17. V. Rajesh, A.J. Chamkha, *Communications in Numerical Analysis*, **1**, 2014, (2014).
18. P.K. Kundu, K. Das, N. Acharya, *J.Mech.,* **30**, 277 (2014).
19. M. Das, B.K. Mahatha, R. Nandkeolyar, B.K. Mandal, K. Saurabh, *J. Appl. Fluid Mech.*, **7**, 485 (2014).
20. S. Das, S.K. Guchhait, R.N. Jana, *J. Appl. Fluid Mech.*, **7**, 683 (2014).
21. A. Khalid, I. Khan, S. Shafie, *Eur. Phys. J. Plus*, **57**, 130 (2015). DOI: 10.1140/epjp/i2015-15057-9.
22. G.S. Seth, S. Sarkar, S.M. Hussain, G.K. Mahato, *J. Appl. Fluid Mech.*, **8**, 159 (2015).
23. G.S. Seth, S. Sarkar, *Bulg. Chem. Comm.*, **47** (2015).
24. R. Cramer, S. I. Pai,Magnetofluid dynamics for engineers and applied physics. McGraw Hill Book Company, New York. 1973
25. R.C. Meyer, *J. Aero. Science*, **25**, 561 (1958).

АНАЛИЗ НА ЕСТЕСТВЕНА КОНВЕКЦИЯ ПРИ МАГНИТО-ХИДРОДИНАМИЧЕН ПОТОК С ТОПЛО- И МАСОПРЕНАСЯНЕ С ЕФЕКТ НА ХОЛ ПРИ ОТНЕМАНЕ НА ТОПЛИНА И ИЗЛЪЧВАНЕ В РОТИРАЩ ФЛУИД НАД ЕКСПОНЕНЦИАЛНО УСКОРЯВАНА ПОДВИЖНА ПЛОСКОСТ С НЕРАВНОМЕРНО НАГРЯВАНЕ

Г.С. Сетх[*], Р. Трипатхи, Р. Шарма

Департамент по приложна математика, Индийско училище по минно дело, Дханбад, Индия

(Резюме)

Изследвана е нестационарната естествена конвекция при магнитно-хидродинамичен поток с ефект на Хол, придружен с топло- и масопренасяне. Основното течение е ротационно, а флуидът е вискозен, несвиваем, електропроводящ и излъчващ. Течението е в близост до плоска, ускоряваща се стена с неравномерно разпределение на температурата. Точно решение в затворена форма за разпределението на температурата е намерено с помощта на Лапласова трансформация. Изведени са зависимости за срязващото напрежение, скоростта на топлопренасяне и скоростта на масопренасяне от плоскостта. Числените стойности на скоростта на флуида и на температурата са представени графично, докато тези са срязващото напрежение и скоростта на топлопренасяне са в таблична форма за различни управляващи параметри.

Effect of modification of Zeolite A using Poly Vinyl Alcohol (PVA)

S. K. Rout[1]*, P. Padhi[2], D.Panda[2]

[1]Department of Chemistry, Konark Institute of Science & Technology, India
[2]Research and Development Center, Hi-Tech Medical College & Hospital, India

Structural modification of raw zeolite A was carried out at a temperature of 80°C using low and high Poly Vinyl Alcohol (PVA). The product was characterized by X-Ray Diffraction (XRD), Fourier Transform Infrared Spectroscopy (FTIR), Field Emission Scanning Electron Microscopy (FESEM), Energy Dispersive X-ray Spectroscopy (EDS), High Resolution Transmission Electron Microscopy (HRTEM) and Image Analyzer (IA). XRD shows PVA anchored to the faces [6 0 0], [6 2 2], [6 4 2], [6 4 4] resulting in a decrease in the crystallite size of the modified zeolite. But 600°C calcination cannot remove the anchored PVA from the zeolite faces, so calcination does not change the crystallinity. FTIR shows the noise level of the bands in the region 400-420 cm^{-1} decreased in modified zeolite A indicating the raw zeolite surface is smoothened by the application of PVA. From FESEM it is found that the shape of the modified particles changed to slightly spherical with the reduction in size. EDS confirms the oxygen percentage is increasing whereas the Na, Al, and Si percentages are decreasing after modification. HRTEM shows the modification is prominent for zeolite modified with a high PVA and the particle size is reduced to 1.5µm. The particle size analysis shows that after modification with a low and high PVA the maximum particles have the size within the range of 2-2.5 µm (29 % size reduction as compared to raw zeolite A) and 1.5-2 µm (43 % size reduction as compared to raw zeolite A) respectively and there was no significant change in particle size after calcination.

Keywords: Zeolite A, Poly Vinyl Alcohol (PVA), Ultrasonication, Centrifugation and Calcination.

INTRODUCTION

Zeoliteis a crystalline hydrated framework of alumino-silicatehaving group I and II elements, in particular, sodium, potassium, calcium, magnesium, strontium and barium [1, 2]. More than 150 synthetic and 40naturally occurring zeolites are known [3]. Theycan be represented by the empirical formula $M_{2/n}O.Al_2O_3.xSiO_2.yH_2O$. In this oxide formula, x is generally equal to or greater than 2, since tetrahedral AlO_4 joins only tetrahedral SiO_4 and n is the valency of the cation. Natural zeolites wereused initially for different applications, but more recently modified and synthetic forms have been made on an industrial scale giving rise to tailor made zeolites that are highly replicable. Zeolites are highly crystalline due to the well defined structure and enclose the aluminium silicate framework cavities occupied by large ions and water molecules, with the cavities opening ranging from 0.8-1.0 nm in diameter which are the order of the molecular dimensions. The size and shape of these pores determine which molecules enter the cavities and which are excluded. These are called molecular sieves [4]. Cations within the cavities are easily replaced with a large number of different valencycations which exert large electrostatic forces across the small dimension of the cavity, while the introduced cations have separate activities of their own; this facilitates dual function catalysis involving acidity along with other activities [4].

The chemical formula of zeolite A is Na_{12} $[AlO_2.SiO_2]_{12}.27H_2O$. According to the data base for zeolite structure [5], zeolites of type A are classified into three dimensional grades, 3A, 4A and 5A, all of which possess the same general formula but with a different cation type. Zeoliteis commercially produced from sodium aluminate and silicate by hydro gel processes [6]. Faujasite zeolites are obtained from KanKara Kaolin clay [7] and zeolite NaX was synthesized from Kerala Kaolin [8]. Because of the presence of a large volume of micro pores and the high thermal stability of the zeolite, this material is used for purification of waste water, and soil remediation [9-10]. Synthetic zeolites are widely used as industrial adsorbents for various gases and vapours [8] and as catalysts in the petroleum industry [11]. Zeolites have a high tendency to adsorb water and other polar compounds like NH_3, CO_2, H_2S and SO_2 and have a good capacity at very low temperatures compared with other adsorbents. Pressure swing adsorption (PSA) is one of the techniques which can be applied for the removal of CO_2 from gas streams. Zeolite has shown promising results in the separation of CO_2 from gas mixtures and can potentially be used in thePSA process [12-14].

Perfect defect free zeolite crystalline structures are not readily available or easy to prepare. Therefore most of the zeolite material has defects

---

* Towhomall correspondence should be sent:
E-mail: sanjay.tulu@gmail.com

and spaces between the crystals which are larger than the pore sizes in the crystalline structures. To control the pore size different methods have been adopted for modification of zeolite [15-21]. A lot of work has already been done for chemical modification to prepare the composite membranes for gas separation. No extensive work has been done for physical modification of zeolite A. The authors have reported the effect of modification of zeolite A using Carboxy Methyl Cellulose (CMC) [22].

The present study focuses on the physical modification of zeolite A to reduce particle size, as well as to achieve a uniform distribution. There are different types of polymer hydro gels having temperature dependent gelation behavior, i.e.,they convert to gel at an elevated temperature and turn back to solution at room temperature. Poly Vinyl Alcohol (PVA) is a polymerthat is cheap, economical, water soluble, eco-friendly and adheres onto zeolite A. Hence a hydro gel surfactant PVA was used for the modification of zeolite A.

EXPERIMENTAL METHOD

Materials

Raw zeolite A purchased from NALCO, India was used as the starting material for the modification experiments. The chemical composition was determined by Atomic Absorption Spectroscopy (AAS) using Perkin Elmer AAnalyst 200/400, as shown in Table 1. Ignition loss and pH (1% in water) were found to be 21.84% and 10.3, respectively.

Table1. Composition of Zeolite A

Molar composition (Based on chemical analysis)	Average Chemical Composition (%)
1.0 ± 0.2 Na_2O 1.0 Al_2O_3 $1.85 + 0.5$ SiO_2 6.0 (Max.) H_2O	Na_2O 16.5-17.5 Al_2O_3 27.5-28.5 SiO_2 32.5-33.5

PVA was purchased from the Central Drug House (CDH), India with the specification of technical purity (99.5 %).

Modification of zeolite

Zeolite A was modified by using low and high PVA as per the concentration. To modify zeolite using low PVA about 0.17 g of PVA was taken in a beaker, 150 mL of de-ionized water was added and ultrasonic dispersion was carried out in an ultrasonic bath attached to an ultrasonic generator (TPC-15H, Telesonic AG, Switzerland) having a peak power of 150 watt for a period of 5 minutes
780

under a frequency of 30 kHz so as to make a homogeneous solution. Then 9.65 g of zeolite A was added to the solution. Ultrasonic dispersion was carried out for 3 h at 80°C. Finally the zeolite was recovered from the mother liquor by repeated cycles of centrifugation, decanting and ultrasonic redispersion in pure water until PVA was completely washed away (no bubbles observed). Modified zeolite was dried at 100°C for 3 h and calcined for 4 h at 600°C. The same procedure was adopted using 6.5 g of PVA with 5 g of raw zeolite for modification of zeolite using high PVA.

Characterization

The crystalline structure of the modified zeolite A was determined by X-ray diffraction using a PANalytical XPERT-PRO diffractometer with Cu-Kα radiation (λ=1.5406A^0). Diffraction measurements were performed over the 2θ range from 5-80°.

The functional groups present after modification of zeolite A were determined by Fouriertransform infrared spectroscopy (FTIR) using a Perkin Elmer SPECTRUM-GX FTIR spectrometer in the 4000-400 cm^{-1} region using pellets of 0.5 mg powdered samples mixed with 250 mg of KBr.

The microstructure and the morphology of size reduction of the modified zeolite A were examined using field emission scanning electron microscopy (FESEM model ZEISS EM910).

The compositions of the modified zeolite A were examined by energy dispersive X-ray spectroscopy (EDAS model ZEISS EM910).

The particle size of the modified zeolite A was determined using high resolution transmission electron microscopy (HRTEM model ZEISS EM910) operated at 100 Kv, with a 0.4 nm point-to-point resolution side entry goniometer attached to a CCD Mega Vision III image processor.

The particle size distributions were examined by using an image analyzer(IAmodel SAMSUNG SDC-313B) to determine the amount of reduction of the particles and distributions of the particles.

RESULTS AND DISCUSSION

The powder X-ray diffraction patterns of raw, water treated,low and high PVA modified zeolite A are shown in Fig.1(a),(b),(c)and(d) respectively.

The patterns are plots of the X-ray intensity scattered from the sample versus the scattering angle (Bragg angle, 2θ). The positions and intensities of the peaks in the diffraction pattern are a fingerprint of the crystalline components present in the sample. In the samples Na_2O, Al_2O_3 and SiO_2 planes are present in the orthorhombic,

rhombohedral and hexagonal unit cells, respectively. The faces [6 0 0], [6 2 2], [6 4 2], [6 4 4] are with higher intensities than [2 0 0], [2 2 0], [2 2 2], [4 2 0]. When treated with PVA, it anchored to faces [6 0 0], [6 2 2], [6 4 2], [6 4 4]. This is evident from the lowering of the peak intensities. The peaks in the XRD pattern of zeolite A treated with PVA are slightly broadened, as compared to those of raw zeolite A and zeolite A treated with water. This points to a decrease in the crystallite size of the modified zeolite A [15].
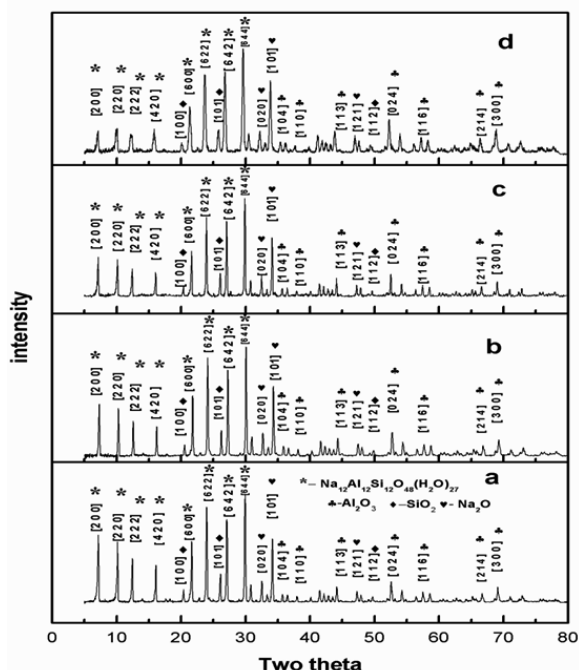
Fig.1. X-ray diffraction patterns of (a) raw zeolite A, (b) zeolite A treated with water, (c) zeolite A modified with low PVA and (d) zeolite A modified with high PVA

During modification, the temperature does not exceed 80°C. It is found that during sonication, the local heat caused by inter-particle collisions (for~10 μm particles) could reach 2600-3400°C [23]. Thus, it is possible that the modification of the supplied zeolite A could take place at a lower macroscopic temperature because of the extremely high local temperatures generated during sonication. It is observed that sub-micron particles cannot be separated by stirring.Sonication is one of the most effective methods for dispersing the particles;whereas due to the cavitation effect the generated micro jet and shock-wave impact on the surface together with the interacting collisions result in particle size reduction;however a stabilization technique like centrifugation must be used to prevent high agglomeration once sonication is stopped. PVA is used as a surfactant, which might cover the zeolite particles to keep them in suspension and to avoid agglomeration. It was also seen that the particle size reduction strongly depends upon the frequency, amount of the sample, power supplied with the processor and time of treatment. Neverthelessthe prolonged ultrasonic treatment increases the structural dis-order of the particle and temperature of the solution [24]. The higher temperature might de-mature the PVA structure and an interaction is prompted at elevated temperatures. That is why we picked up 5 minutes for sonication and 80°C as a reaction temperature well below the boiling point of the solution.Calcinations do not change thecrystallinity and at 600°C calcinations cannot remove the anchored PVA from the zeolite faces, which is evident from the low-intensity peaks [1 0 1], [6 4 4], [6 2 2], [6 4 2], [1 0 1].

The FTIR Spectra of raw, water treated,low and high PVA modified zeolite A are shown in Fig. 2(a),2(b),2(c)and2(d),respectively.Theabsorptionpeaksarediscussed individually.
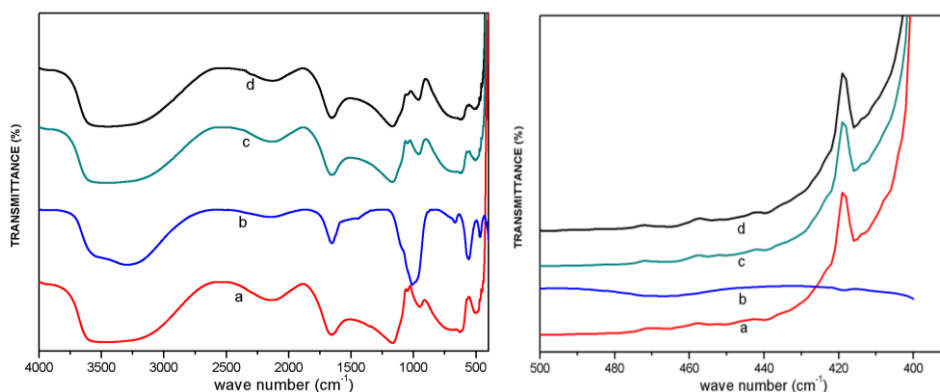
Fig.2. FTIR spectra of (a) raw zeolite A, (b) zeolite A treated with water, (c) zeolite A modified with low PVA and (d) zeolite A modified with high PVA.

A characteristic strong and broad band at 3400 cm^{-1} is seen due to O-H stretching vibrations [25]. The band at 2100 cm^{-1} is due to Si-H stretching vibration [26-27]. The deformation band at 1640 cm^{-1} confirming the presence of bound water [25], pre-dominant in Fig. 2 (b), is related to the (H-O-H) bending vibration of water molecules adsorbed on zeolite. The band at 1150 cm^{-1} appearsbecauseof Si-O-Siasymmetricstretching [28], which is insignificant in Fig. 2(b) due to the presence of excess water molecules in the pores of zeolite A treated with water. The band appearing at 1034 cm^{-1}[29] related to T-O-T (T=Si and/or Al) stretching is more intense in zeolite A treated with water as shown in Fig. 2 (b) because of the excess of water molecules. The asymmetric Al-O stretch of Al$_2$O$_3$ is located at950cm^{-1}[30]. The bands at 557cm^{-1}and 620 cm^{-1}(in the region of 500 - 650 cm^{-1}) are related to the presence of double rings (D4R and D6R) within the framework structure of these zeolites [30]. The band at 557 cm^{-1} also could represent the beginning of the crystallization of a zeolite with double rings [31]. The bands at 420 cm^{-1} and 490 cm^{-1} (in the region of 420-500 cm^{-1}) are related to internal tetrahedral vibrations of Si-O and Al-O in SiO$_2$ and Al$_2$O$_3$ [30]. The two most intense bands of the zeolite usually occur at 860-1230 cm^{-1} and 420-500 cm^{-1}, as shown in Fig.2. The first is assigned to an asymmetric stretching mode and the second one to a bending mode of a T-O bond. All these bands are more or less dependent on the crystal structure. The mid regions of the spectra contain thefundamental framework vibration of Si (Al) O$_4$ groupings [32]. The bands in the region 400-420 cm^{-1} are related to the pore opening or motion of the tetrahedral rings, which form the pore openings of the zeolite [2]. This is shown in the case of raw zeolite A and zeolite treated with PVA but in the case of water-treated zeolite the bands are missing, which is clearly evident from the spectra. The noise level of the bands in the region 400-420 cm^{-1} decreased in the case of zeoliteAmodified with PVA which indicates that the rough zeolite surface is smoothened by the application of PVA.

The FESEM studies of raw, water treated,low and high PVA modified zeolite A are shown in Fig. 3(a),3(b),3(c)and3(d), respectively.Theparticlesizeof the raw zeolite A is in the range of 2.5-3.5 μm with high agglomeration, which remains unchanged in case of zeolite A treated with water.
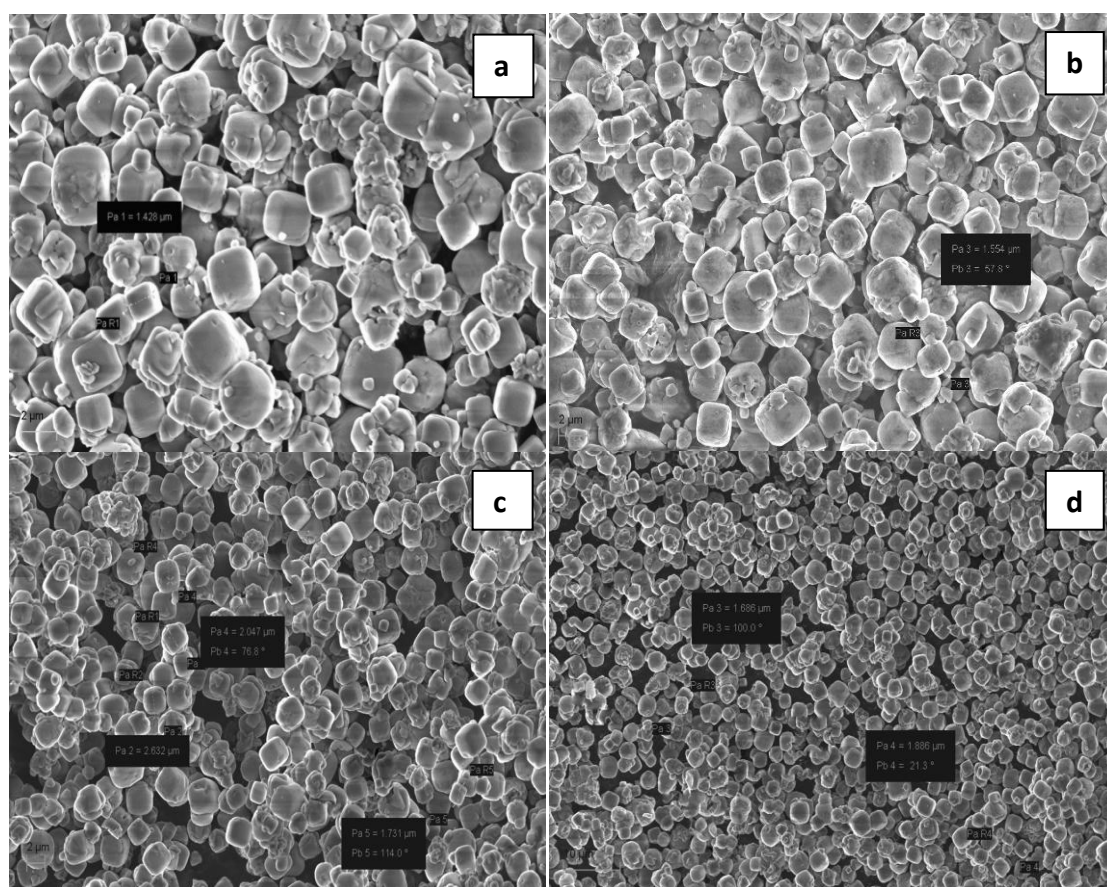
Fig.3. FESEM micrographs of (a) raw zeolite A, (b) zeolite A treated with water, (c) zeolite A modified with low PVA and (d) zeolite A modified with high PVA.

After modification with low and high PVA the particle size was found to decrease to a range of 2-2.5μm and 1.5-2 μm, respectively with better dispersion. The particle size decrease more in case of zeolite A modified with a high PVA possibly due to exploitation of zeolite with ahigh PVA loading.

Theshapeofthe modified particles changed to a slightly spherical one, as observed in Fig. 3 (d). This may be as a result of calcination.

The EDAS studies of raw, water treated, low and high PVA modified zeolite A are shown in Fig. 4 (a), 4 (b), 4 (c) and 4 (d), respectively.

The EDAS is done to determine any change of composition both raw and modified zeolite. It is seen from Table 2 that the composition, weight and atomic percentage are changing slightly. The oxygen percentage is increasing whereas the Na, Al, and Si percentages are decreasing after modification.This may be due to the particle size reduction after modification. Further, it should be noted that in both raw zeolite A and zeolite A treated with water, the distribution of the particles is not uniform,whereas in the modified one, the particle distribution is uniform and with very few agglomerations.

The HRTEM micrograph studies of raw, water treated, low and high PVA modified zeolite A are shown in Fig. 5 (a), 5 (b), 5 (c) and 5 (d), respectively.Itisseenthat the particle size is in the range of 2.5-3.5 μm for zeolite A (as supplied) and remains unchanged in case of zeolite A treated with water. After modification with low and high PVA, the particle size is found to be 2-2.5 μm and 1.5-2 μm, respectively, which confirms the reduction of the size and change in shape of the zeolite.
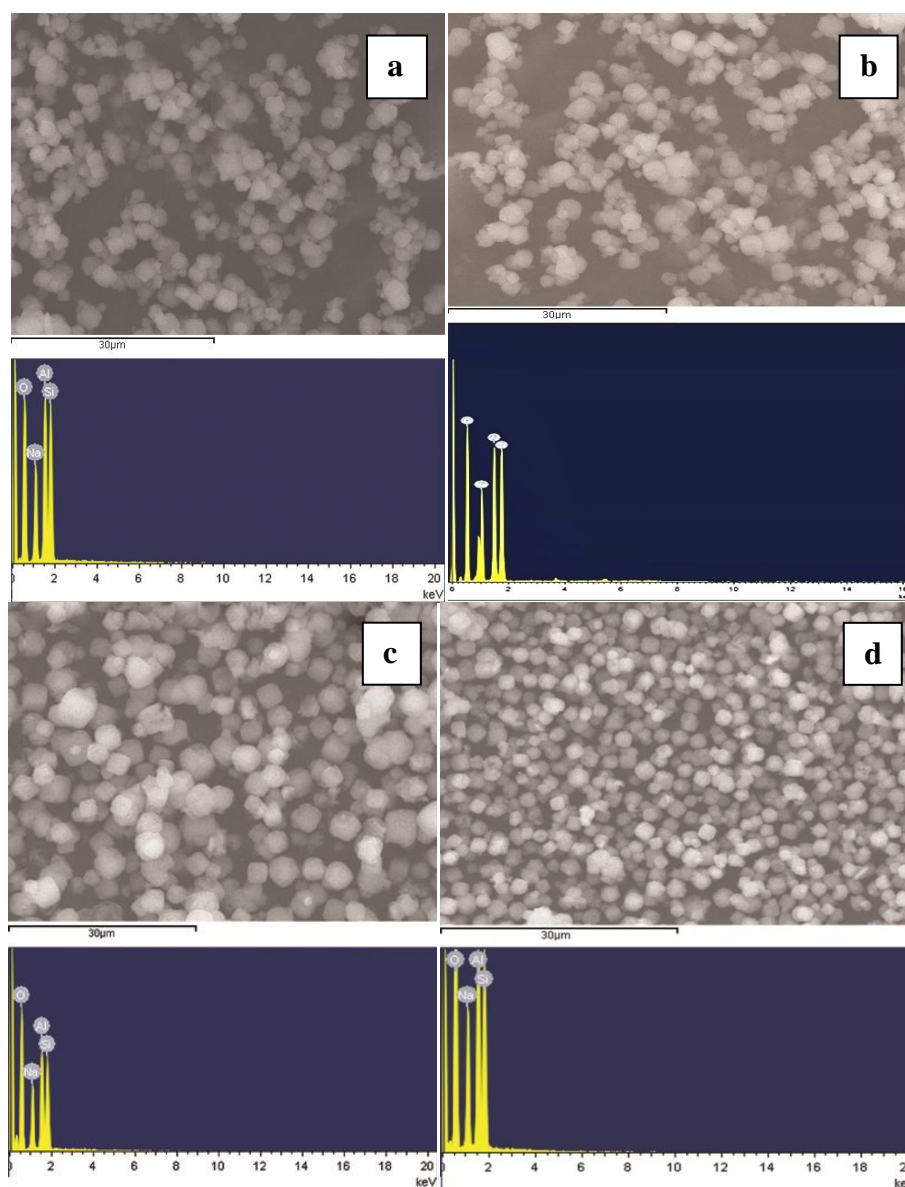
Fig.4. EDAS of (a) raw zeolite A, (b) zeolite A treated with water, (c) zeolite A modified with low PVA and (d) zeolite A modified with high PVA.

Table 2. Elemental Composition of raw, water treated, low and high PVA modified zeolite A.

Elements	Raw Zeolite A		Zeolite A treated with water		Zeolite A modified with low PVA		Zeolite A modified with High PVA	
	Weight %	Atomic %	Weight %	Atomic %	Weight %	Atomic %	Weight %	Atomic %
O	50.01	62.01	51.50	56.98	55.40	66.81	57.35	68.04
Na	14.03	12.10	14.01	12.47	13.99	11.74	12.95	10.84
Al	16.98	12.49	16.97	14.87	14.82	10.60	14.54	10.36
Si	18.98	13.40	17.52	15.68	15.79	10.85	15.16	10.76
Total	100							

| a | b | c | d |
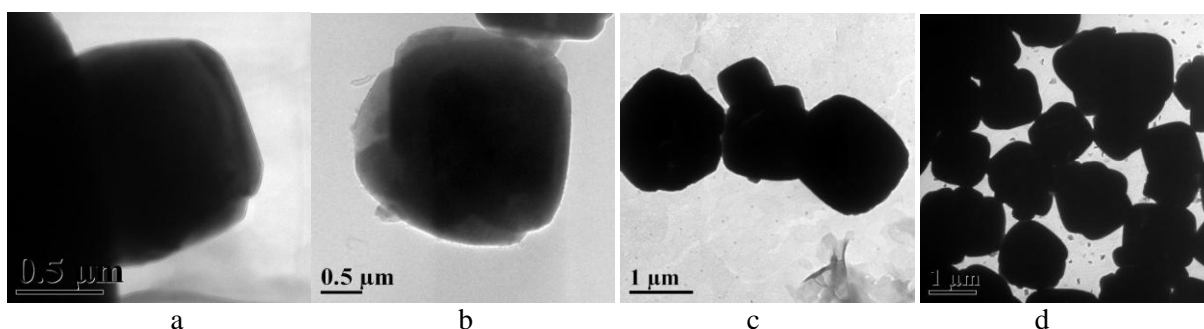
Fig.5. HRTEM micrographs of (a) raw zeolite A, (b) zeolite A treated with water, (c) zeolite A modified with low PVA and (d) zeolite A modified with high PVA.

Particlesizedistributions

The statistical particle size distributionof raw zeolite A (with calcination),zeolite A treated with water (without and with calcination),zeolite A modified with low PVA (without and with calcination)and zeolite A modified with high PVA (without and with calcination)are shown in Fig. 6 (a-g) respectively.

The graph was plotted after statistical image analysis in the frequency and particle size range. It is observed that for rawand water treated zeolite, the distribution of the particles is the highest, nearly within a range of 2.5-3.5 μm, whereas in the case ofmodification with low and high PVA, there is a reduction of the particle size with narrower distribution.After modification with low and high PVA the maximum particles have a size within the range of 2-2.5 μm (29 % size reduction as compared to raw zeolite A) and 1.5-2 μm (43 % size reduction as compared to rawzeoliteA) respectively.Thisindicatesthereduction of the particle size after modification with a high PVA is quite significant. The distribution of theparticlesisquiteuniformasobservedfromFig.6(g). This happens due to a hydrogelsurfactant PVA,which helps to stabilize as well as de

agglomerateanddispersetheparticlesduringsonicatio n.
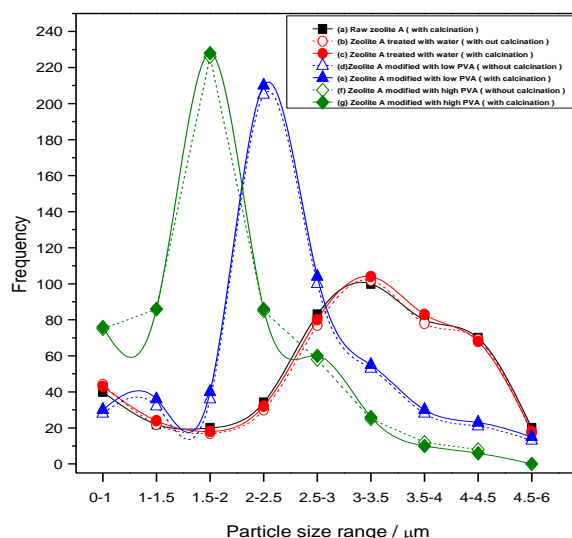
Fig.6. Particle size analysis of(a) raw zeolite A (with calcination), (b) zeolite A treated with water (without calcination), (c) zeolite A treated with water (with calcination),(d)zeolite A modified with low PVA(without calcination),(e) zeolite A modified with low PVA (with calcination),(f) zeolite A modified with high PVA (without calcination) and(g)zeolite A modified with high PVA (with calcination).

From particle size analysis (Fig. 6.), it is found that there was no significant change in theparticlesizeaftercalcination,whichis alsocorrelatedwith the XRD analysis.

CONCLUSIONS

It is found in the present study that the modification of zeolite A using PVA is possible. As a result of PVA modification, the particle size is reduced about 43 % from 3.5 µm to 1.5 µm with better dispersion. The zeolite particles have changed their shape from cubical to slightly spherical by the effect of calcination. Further research should be focussed on the optimisation of the surface modification to raise the zeolite efficiency for various applications. The modified zeolite A may be used for purification of waste water, soil remediation, as a catalyst, molecular sieve, ion exchanger, adsorbent and for the removal of CO_2 from gas streams.

REFERENCES

1. A.Dyer; An Introduction to zeolite Molecular Sieves, John Willey and sons press,1988.
2. D.W.Breck; Zeolite Molecular Sieves: Structure, Chemistry and Uses, John Wiley, New York. 1974.
3. B.K.Marcus,W.E.Cormier,*Chem. Eng. Progress*,**95**, 47 (1999).
4. J.R.Ugal, K.H.Hassan,I.H.Ali,*J. Association of Arab Universities for Basic and Applied Sciences*,**9**, 1 (2010).
5. www.zeolites ethz.ch/zeolites / stdAtlas.htm.
6. R.G.Copperwaite,T.Hutching,M.Vander Riet,*J.Chem Edu*,**7**, 632 (1986).
7. A.Y.Atta, O.A.Ajayi,S.S.Adefila,*J. Appl. Sci. Res*.,**3**, 1017 (2007).
8. S.Chandrasekhar, P.N.Pramada,*J.Porous Mater.*,,**6**, 283 (1999).
9. W.Franus,M.Wdowin, *Min.Res.Manag.***26**,133(2010).
10. A.K.Czurda, R.Haus,*Apply.Clay.Sci.,***21**, 13 (2002).
11. J.G.Speight, The chemistry and technology of petroleum, Marcel Dekker Inc, New York,1999.
12. K.Cheu, K.Jong-Nam, Y.Yun-Jong,C.Soon-Haeng, Fundamentals of Adsorption, Proc. Int.Conf, D.Levan (ed), Klawer Academic Publishers: Boston. MA. 203, 1996.
13. R.V.Siriwardane, M.Shen, E.P.Fisher, J.P.Poston, *Energy Fuels.,***15**, 279 (2001).
14. F.Dong, H.Lou, M.Goto, T.Hirose, *Sep. Purif. Technol.,***15**, 31 (1999).
15. C.Zeng, L.Zhang, X.Cheng, H.Wang,N.Xu, *Sep. Purif. Technol.,* **63**,628 (2008).
16. N. Patdhanagul, K. Rangsriwatananon, K. Siriwong, S. Hengrasmee,*MicroporousMesoporous Mater.* **153**, 30 (2012).
17. S.Khoonsap,P.Khansawai,S.Amnuaypanich,*Adv. Matr. Res.***93-94**, 137(2010).
18. C. Liu, X. Gao, Z. Zhang, H. Zhang, S. Sun, Y. Deng,*Applied Catalysis A,***264**, 225 (2004).
19. L.S.Gadekar, S.S.katkar, K.N.Vidhate, B.R.Arbad,M.K.Lande,*Bull. Cat. Soc. Ind*., **7**, 76 (2008).
20. O.Vassylyev, G.S.Hall, J.G. Khinast,*J.Porous Mater.,* **13**, 5 (2006).
21. C. S. Cundy, *Collect.Czech.Chem.Commun.,***63**, 1699 (1998).
22. P.Padhi, S.K.Rout,D.Panda, *Bulg. Chem. Commun*,**46**(4), 777 (2014).
23. S.J.Doktycz,K.S.Suslick, *Science.* **247**, 1067 (1990).
24. F.Franco, L. A. Perez-Maqueda, J. L. Perez-Rodriguez, *J. Coll. and Inter. Science,***274**, 107 (2004).
25. H.Dogan, N.D. Hilmiglu, *Vacuum.* **84**, 1123 (2010).
26. F.Ruiz, C.V-Lopez, J.G-Hernandz, D.D.Allred, G.R-Paredes, R.P-Sierra, G.T-Delgado, *J.Vaccum Sci. and Technol*.A, **12**, 25 (1994).
27. R.R.Koropecki, R.Arce, *J. Appl. Phys*. **60**, 1802 (1986).
28. K.L.Pong, S.C.Chen,K.W.Cheah, *Solid State Communications*, **99**, 887 (1996).
29. S.S.Rayalu, *Current Science*,**89**, 25 (2005).
30. C.A.Rios, C.D.Williams,M.A.Fullen, *Appl. Clay Sci.* **42**, 446 (2009).
31. M.Alkan, C.Hopa, Z.Yilman, H.Guler, *Microporous Mesoporous Mater.*, **86**, 176 (2005).
32. K.Ojha,N.C.Pradhan, A.N.Samanta, *Bull.Mater .Sci.,***27**,555 (2004).

ЕФЕКТ ОТ МОДИФИКАЦИЯТА НА ЗЕОЛИТ А С ПОМОЩТА НА ПОЛИВИНИЛ-АЛКОХОЛ (PVA)

С.К. Рут[1]*, П. Падхи[2], Д. Панда[2]

[1]*Департамент по химия, научно-технологичен институт, Конарк, Индия*
[2]*Изследователски развоен център, Хай-тек Медицински колеж с болница, Индия*

(Резюме)

Извършена е структурна модификация на суров зеолитА при 80°C с ниско- и високомолекулен поливинилов алкохол (PVA). Продуктът е охарактеризиран чрез рентгеноструктурен анализ (XRD), Фуриерова инфрачервена спектроскопия (FTIR), полево емисионна сканираща електронна микроскопия (FESEM), енергийно дисперсионна рентгенова спектроскопия (EDS), трансмисионна електронна микроскопия с висока резолюция (HRTEM) и образов анализатор (IA). XRD показва, че молекулите на PVA се захващат на стените [6 0 0], [6 2 2], [6 4 2], [6 4 4], което води до намаляване на кристалитните размери на модифираниязеолит. Калцинирането при 600°C не е достатъчно за отстраняването макромолекулите на PVA от стените на заолита. FTIR показва понижени нива на шум в спектралните линии в областта 400-420 cm^{-1} за модифицирания зеолит. Това е индикация за изглаждане на повърхността на суровия зеолит след нанасяне на PVA. Намерено е от FESEM, че формата на модифицираните частици слабо се променя към леко сферични с намаляване на размерите. EDS потвърждава повишаването на съдържанието на кислород, докато съдържанието на Na, Al и Si намаляват след модифицирането. HRTEM показва, че модификацията е значима за зеолити с високомолекулен PVA, а размерът на частиците намалява до 1.5µm. Анализът на размера на частиците показва, че след модификацията с ниско- и високомолекулен PVA най-много частици са с размери в интервала 2-2.5 µm (29 % намаление спрямо суровия зеолитА) и 1.5-2 µm (43 % намаление спрямо зеолитА) и че няма значимо изменение в размерите след калциниране.

Antioxidant activity of secondary metabolites and mycelium extracts of endophytic fungi isolated from *Astragalus monadelphus*

Y. G. Wang[1*], G. R. Yang[1], F. Wang[2], M. J. Yang[1*], J. Li[1], X. F. Liu[1], M. G. Wang[1], X. L. Wang[3]

[1]*School of Life Science and Engineering, Lanzhou University of Technology, 730050, Lanzhou, China*
[2] *Qingdao Institute of Bioenergy and Bioprocess Technology, Chinese Academy of Sciences, 266101, Qingdao, China*
[3]*Lanzhou Institute of Husbandry and Pharmaceutical Sciences of CAAS, 730050, Lanzhou, China*

13 strains of endophytic fungi were isolated from *Astragalus monadelphus*. The radical scavenging activity assay of secondary metabolites and mycelium extracts from these strains were investigated. Results showed that secondary metabolites and mycelium extracts from these strains had significant antioxidant activities. Reducing ability of H401 strain mycelium extracts were stronger than the ethyl acetate extract parts, and its EC_{50} value was 0.0034 mg/mL. Ethyl acetate parts of H802 strain exhibited strong ·OH scavenging effect, the IC_{50} value was 0.0384 mg/mL. the DPPH radical scavenging activity test indicated that endophytic fungi can be a good source of radical scavenger. Besides, the compounds extracted from H401 secondary metabolites belong to β-sitosterol based on the results of NMR analysis and literature data.

INTRODUCTION

Astragalus monadelphus belongs to phylum of Angiospermae, class of Magnoliopsida, order of Fabales, family of Leguminosae sp., genus of *Astragalus*. It grows at a high altitude of 3000-4000 meters in central and southwest of Gansu Province, southeast of Qinghai Province, northwest of Sichuan Province.

Most of researches on the genus *Astragalus* previously focused on the identification of its main chemical compositions. With the development of biology and molecular biological techniques, more and more compounds have been separated. Later, secondary metabolites of genus *Astragalus* callus were studied by some scholars. However, the genus *Astragalus* endophytic fungi was few reported, and the relative researches mainly focused on determination of antimicrobial activities of endophytic fungi. Zhou et al. [1] isolated *Aspergillus fumigatus* from the root of *Astragalus membranaceus*[1], and the ethyl acetate extract of the culture exhibited significant antimicrobial activity. Ma et al. isolated four strains of endophytic fungi (strains 16, 17, 23 and 75) from *A. Mongholicus* [2], but the fourth isolated endophytic fungi did not produce astragalosides I-IV, flavonoids or polysaccharides. Due to rich contents of active constituents such as glucuronic acid, β-sitosterol, astragalosides, isoflavone and asparagines, *Astragalus membranaceus* is recognized one of the most important herbs [3].

Endophytic fungi have been known to be a rich repository of medicinally important compounds since the discovery of penicillin. Some endophytic fungi could produce bioactive compounds the same as their hosts that exemplified by taxol [4], subglutinol A and B [5], and peptide leucinostatin A [6]. By now, few study reported that endophytic fungi isolated from *Astragalus monadelphus* and their secondary metabolites. In this work, isolation, identification and determination of the activities of the endophytic fungi from *Astragalus monadelphus* were investigated.

EXPERIMENTAL

Materials

Plants sample were collected in September 2012 from Longxi County, Gansu Province, China, identified by Yanlin Professor, Lanzhou University of technology, and belonged to *Astragalus Monadelphus*.

Methods

Isolation of endophytic fungi: The endophytic fungi were isolated as described by Fernandes et al.[7]. The growing mycelia were purified on PDA plates and then maintained at 4 ºC on PDA slopes for further study.

Fermentation For coarse screening, the fermentation of endophytic fungi was conducted at 28 ºC for two weeks. Then, the culture broth was centrifuged at 12000 rpm for 10 min. Mycelia were broken down by ultrasound, dried at 50ºC, powdered. And triple volumes of anhydrous ethanol

* To whom all correspondence should be sent:
E-mail: 412316788@163.com; yangmj@lut.cn

was added in, then the system was heated reflux extraction for twice, each time 2 h. The fermentation was successively extracted with the same volume of ethyl acetate and n-butanol for three times, respectively. The above ethyl acetate, n-butanol and ethanol solutions were concentrated in rotary evaporation at 40ºC, 65ºC, and 55ºC to obtain fermentation and mycelia extracts, respectively.

Antioxidant Activity

The total reducing ability assay Total reducing ability was determined according to Scherer's method [8]. 2.5 mL 0.2 mol/L (pH 6.6) phosphate buffer and 2.5 mL 1% potassium ferricyanide solution were in turn added into 2.5 mL different concentrations of samples. The mixed solution was kept at 50 ºC for 20 min, and then cooled rapidly. Then 2.5 mL the supernatant, 2.5 mL distilled water and 0.5 mL 0.1% ferric chloride solution were respectively added into 2.5 mL 10% trichloroacetic acid solution, shook well and stewed for 10 min. The absorbance at 700 nm was measured, with ascorbic acid being the positive control.

Hydroxyl radical scavenging activity assay Hydroxyl radical scavenging activity was measured by the Scherer's method [9]. The reaction mixture containing 1 mL $FeSO_4$ (6 mM), 1 mL salicylic acid-ethanol (6 mM), 1 mL H_2O_2 (0.1%), were mixed with 1 mL various concentrations samples into 10 mL final reaction volume and incubated for 1 h at 37 ºC. The absorbance of the mixture was measured at 510 nm. Ascorbic acid was taken as the positive control. Scavenging rate (SR) was calculated as the formula (1):

$$SR(\%) = \left\{ 1 - \frac{A_{sample} - A_{control}}{A_{blank}} \right\} \times 100\% \quad , (1)$$

A_{sample} - the absorbance of adding ferrous sulphate, acid - ethanol absorbance, hydrogen peroxide, and the same volume of the sample

$A_{control}$ - the absorbance of adding ferrous sulphate, acid - ethanol absorbance, and the same volume of the sample, without hydrogen peroxide

A_{blank} - blank solution absorbance values, i.e., the absorbance of only adding to join ferrous sulfate, salicylic acid - ethanol, hydrogen peroxide, without the sample

1,1-Diphenyl-2-picrylhydrazyl (DPPH) radical scavenging activity assay DPPH radical scavenging activity was assessed according to Ashley et al. [12], and Kimura et al. [13]. And the tested samples of n-butanol extracts from fermentation were added into 2 mL samples with various concentrations, and were mixed in 2 mL freshly prepared 0.025 mg/mL

DPPH ethanolic solution. The mixture were kept at room temperature for 30 min and measured calorimetrically at 517 nm. The control was established by ethanol instead of samples. The DPPH radical scavenging activity of samples was calculated based on the following equation (2):

$$DPPH\ scavenging\ effect\ (\%) = \left\{ 1 - \frac{A_{sample} - A_{control}}{A_{blank}} \right\} \times 100\% \quad , (2)$$

Where $A_{control}$, A_{sample} and A_{blank} denoted the absorbance of the control, the sample and DPPH without samples, respectively

Fermentation, Isolation and structure determination Secondary metabolites of fungus had a good antioxidant activity. Thin-layer chromatography analysis showed that ethyl acetate parts of H401 contained rich chemical compositions. The fungus was cultured in a 25-liter fermentation system, and selected for further study. Purification was carried out by column chromatography. The structures of the compounds were elucidated primarily by NMR analysis.

RESULTS AND DISCUSION

Isolation of endophytic fungi 13 strains of endophytic fungi were isolated from *Astragalus monadelphus* in this study. Colony morphologies of some typical strains were shown in Figure 1. And they were all stored in 20% glycerol at -80 ºC.

H101   H301

H302   H502
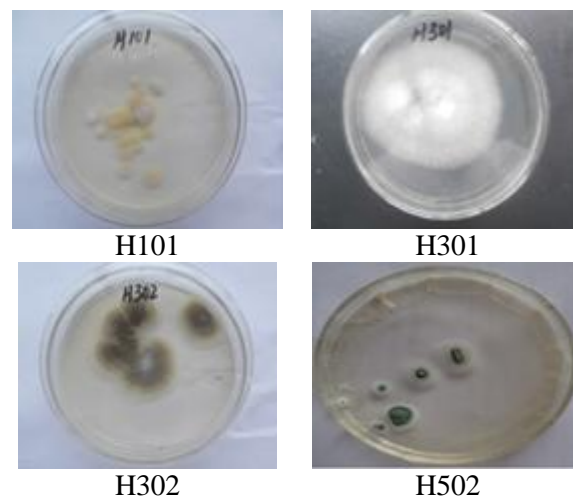
Fig. 1. Colony morphology of some strains.

Antioxidant Activity

The total reducing ability assay The reducing abilities of the samples were determined according to potassium ferricyanide reduction method. The results (Figure 2a) showed that 39 samples (0.05 mg/mL) have different reducing ability. Two parts of extracts of the sample H401 have strong reducing ability with the absorbance values of

2.555 and 2.565, respectively, which were slightly lower than that of the positive control (Vc, 2.636). On the other hand, it could be seen from Figure 2b that the reducing ability enhanced with the increasing of the sample's concentration. According to half-maximum effective concentration (EC_{50}), reducing ability of H401 mycelium were stronger than the ethyl acetate extract parts, and its EC_{50} value was 0.0034 mg/mL ($y=134.73x+0.0361$, $R^2=0.9943$), but the value was still somewhat weak when compared with the positive control Vc (EC_{50} value is 0.0019 mg/mL, $y=233.27x+0.0665$, $R^2=0.9975$).

Hydroxyl radical scavenging activity assay In this study, spectrophotometric assay was introduced to estimate on ·OH scavenging activities of the samples. The results (Figure 3a) illustrated that the scavenging effects on ·OH of 39 samples (0.25 mg/mL) varied, i.e., the scavenging ratios of 3 samples were between 70% and 80%, as to the ethyl acetate extract parts of H401 and H802, and mycelium part of H301, the scavenging ratios of 4 samples were noticed more than 80%, in addition, the scavenging ratios of the mycelium parts of H302, H601, H802 and H803 were 89.93% which is higher than the positive control Vc (89.75%).

The results (Figures 3b, 3c) implied that within the range of 0.02~0.1 mg/mL, the scavenging abilities of ·OH of the tested materials all enhanced with the increasing concentration of the samples.
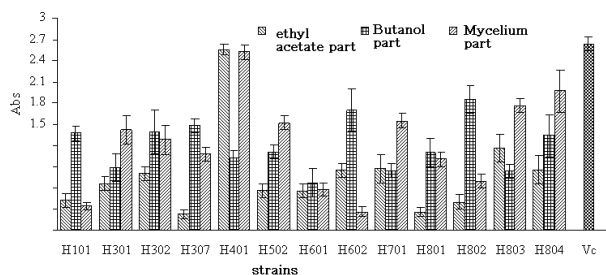
Fig. 2a. The reduction abilities of the samples
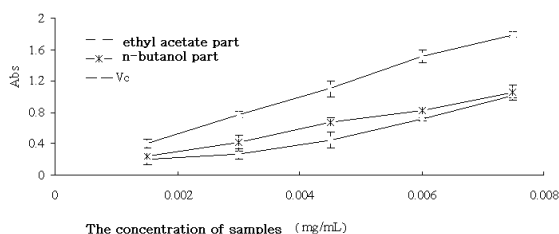
Fig. 2b. The results of concentration gradient experiment.
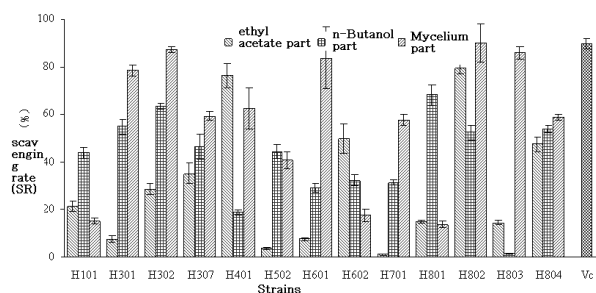
Fig. 3a. The · OH scavenging ratios of the samples
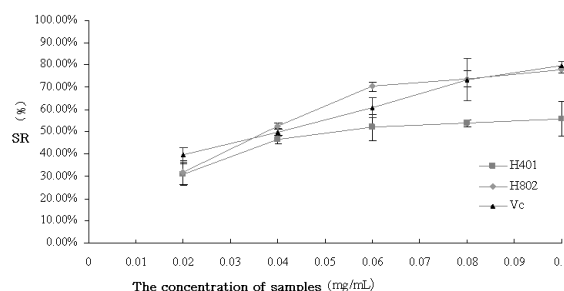
Fig. 3b. The ·OH scavenging ratios of H401 and H802 (Ethyl acetate extract parts)
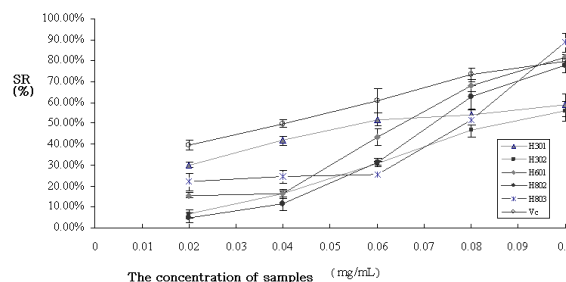
Fig. 3c. The ·OH scavenging ratios of H301, H302, H601, H802 and H803 (mycelium parts)

The results shown in Table 1 showed that ethyl acetate extract parts of H802 has relative strong ·OH scavenging effect (IC_{50} value was 0.0384 mg/mL), which was slightly stronger than the positive control Vc (IC_{50} value was 0.0395 mg/mL). While the ·OH scavenging abilities of other samples were not obvious.

1,1-Diphenyl-2-picrylhydrazyl (DPPH) radical scavenging activity assay The results displayed in Figure 4a that DPPH· scavenging abilities of 39 samples (0.025 mg/mL) were all over 50%, in detail, DPPH· scavenging ratio of ethyl acetate extract of 13 samples were higher than the others, especially, DPPH· scavenging ratio of ethyl acetate parts of H101, H301, H302 and H401 were more than 80%. Among these four samples, the most predominant one was H401 for its scavenging ratio reached 98.52%, which was a little higher than the positive control Vc (98.4%).

Table 1. IC_{50} values and linear relationship of the samples

	Samples	Concentration range （mg/mL）	linear relationship	IC_{50} (mg/mL)
ethyl acetate extract	H401	0.02～0.06	y=5.325x+0.2183(R^2=0.9224)	0.0529
	H802	0.02～0.06	y=9.675x+0.1283(R^2=0.9973)	0.0384
	H301	0.02～0.06	y=5.45x+0.1947(R^2=0.9982)	0.0560
mycelium	H302	0.02～0.1	y=6.74x+0.0365(R^2=0.9982)	0.0688
	H601	0.04～0.1	y=11.02x-0.2469(R^2=0.9831)	0.0678
	H802	0.04～0.1	y=11.48x-0.3447(R^2=0.9841)	0.0738
	H803	0.06～0.1	y=15.73x-0.7045(R^2=0.9891)	0.0766
control	Vc	0.02～0.1	y=5.21x+0.2944(R^2=0.9925)	0.0395
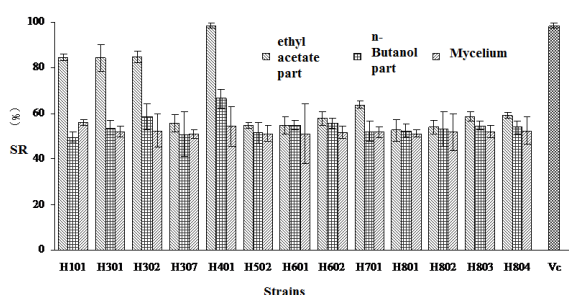
Fig. 4a. The DPPH· scavenging rate of samples.

In general, the abovementioned four samples exhibited significant antioxidant activities in the concentration gradient of 0.002, 0.004, 0.006, 0.008, 0.01 mg / mL. The results (Figure 4b) showed that DPPH· scavenging ratio raised with the increasing concentration of the samples. Within a certain range of the concentrations, most of the samples (except H302) represented an obvious linear relationship with the scavenging ratio.
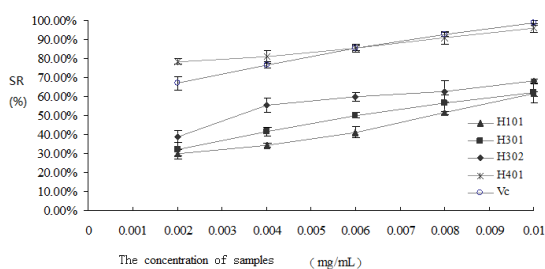
Fig. 4b. The DPPH· scavenging ratios of H101, H301, H302 and H401 (ethyl acetate extract parts).

Moreover, within the range of 0.002~0.01 mg/mL, both of the DPPH· scavenging ratios of H401 and Vc were over 50%. The result of further study focused on H401 (Figure 4c) illustrated that within 0.01~0.05 μg/mL, with the increasing of the concentration of the sample, not only the DPPH· scavenging ratio enhanced, but also a linear relationship (y=8.15x+0.3381 R^2=0.9844) appeared. And the IC_{50} value was 0.0198 μg/mL, which was much lower than Vc of 0.0325 μg/mL

(y=8.86x+0.2112 R^2=0.9958).
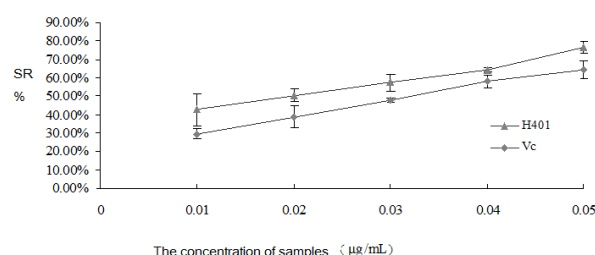
Fig. 4c. The DPPH· scavenging ratios of H401 and Vc.

Fermentation, isolation and structure forecast In order to obtain and identify the major components, the crude ethyl acetate extract of H401 was screened and purified by column chromatography and TLC. However, only one kind of compound was isolated. The structure was elucidated primarily based on HRMS and NMR analyses and confirmed by comparison with published data. And the biological activities of Compound 1 (Figure 5) exhibited significant bioactivities, including antioxidant and anti-atherogenic effect [15], anti-inflammatory and antipyretic activity [16], anthelminthic and antimutagenic activity [17], immunoregulatory activity[18].
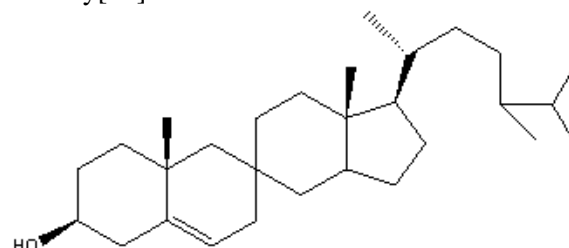
Fig. 5. The structure of Compound 1.

Compound 1 was obtained as white needle-like crystals. Its molecular formula was established as $C_{29}H_{50}O$, by ESI-MS (m/z 414 [M^+]). The ^{1}H-NMR (600 MHz, $CDCl_3$) data showed δ : 3.52 (1H, m, H-3), 5.35 (1H, m, H-6), 0.68 (3H, s, H-18), 1.03 (3H, s, H-19), 0.93 (3H, d, H-21). While the ^{13}C-

NMR (600 MHz, CDCl$_3$) data showed δ (ppm) : 33.2 (C-1), 33.1 (C-2), 71.8 (C-3), 42.2 (C-4), 140.7 (C-5), 121.7 (C-6), 31.9 (C-7), 31.7 (C-8), 50.1 (C-9), 36.5 (C-10), 21.2 (C-11), 39.7 (C-12), 42.3 (C-13), 56.0 (C-14), 24.3 (C-15), 28.2 (C-16), 55.9 (C-17), 19.4 (C-18), 11.9 (C-19), 36.1 (C-20), 18.8 (C-21), 39.9 (C-22), 26.1 (C-23), 45.8 (C-24), 29.1 (C-25), 19.8 (C-26), 19.0 (C-27), 23.1 (C-28), 11.2 (C-29). Besides, combining with the previous published data[19], Compound 1 maybe belongs to β-sitosterol family.

CONCLUSIONS

Endophytic fungi were studied from *Astragalus monadelphus*, and 13 strains were isolated and identified.

The anti-oxidization activities of secondary metabolites and mycelium extracts were investigated. Results showed that secondary metabolites and mycelium extracts from these strains had some promising antioxidant activity. Reducing ability of H401 mycelium extracts were stronger than the ethyl acetate extract parts, and its EC$_{50}$ value is 0.0034 mg/mL, but compared to the positive control Vc (EC$_{50}$ value is 0.0019 mg/mL) is weak. Ethyl acetate parts of H802 has strong ·OH scavenging effect, the IC$_{50}$ value is 0.0384 mg/mL, and less than the positive control Vc (IC$_{50}$ value is 0.0395mg/mL). Especially, in the DPPH radical scavenging activity assay, the IC$_{50}$ value (0.0198μg/mL）of strain H401 (ethyl acetate part) is much lower than Vc (0.0325μg/mL). the DPPH radical scavenging activity test indicated that endophytic fungi can be a good source of radical scavenger. Moreover, based on the NMR date and comparison to literature data, we known that the compound belong to β-sitosterol. These may offer a basis for further development and utilization of endophytic fungi from *Astragalus monadelphus*.

REFERENCES

1. F. Zhou, C. C. Zhang, R. Liu, Y. F. Zhang. *China J. Exp. Tradit. Med. Formulae,* **18**, 125 (2012).
2. W. Ma, X. B. Liu, J. Jiao, L. M. Zhang, W. C. Ren, L. Ma, X. J. Kong, N. Zhang, G, X. W. Zhang, *J. For. Res.,* **25**, 701 (2014).
3. D. Bensky, A. Gamble. Eastland Press, Inc, Seattle, USA. (1993) .
4. A. Stierle, G. A. Strobel, D. Stierle, *Sci.*, **260**, 214 (1993).
5. J. C. Lee, E. Lobkovsky, N. B. Pliam, G. Strobel, J. Clardy, *J. Org. Chem.*, **60**, 7076 (1995).
6. G. A. Strobel, W. M. Hess, *Chem. Biol.*, **4**, 529 (1997).
7. M. D. R. V. Fernandes, T. A. C. E. Silva, L. H. Pfenning, C. M. D. Costa-neto, T. A. Heinfich, S. M. D. Alencar, *Braz. J. Pharm. Sci.*, **45**, 677 (2009).
8. R. Scherer, H. T. Godoy, *Food Chem.*, **112**, 654 (2009).
9. P. R. Murray, E. J. Baron, M. A. Pfaller, F. C. Tenover, R. H. Yolken, ASM Press, Washington D C. 1999.
10. A. L. Carbone-howell, N. D. Stebbins, K. E. Uhrich, *Biomacromolecules*, **15**,1889 (2014).
11. T. Kimura, K. Yamagishi, M. Suzuki, H. Shinmoto, *J. Jpn. Soc. Food Sci.,* **45**, 144 (1998).
12. K. J. Koo, H. J. Park, H. E. Byeon, J. H. Kwak, H. U. Sung, T. K. Soon, K. R. Dong, P. Suhkneung, *J. Food Sci.,* **4**, 719 (2014).
13. M. B. Gupta, R. Nath, N. Srivastava. *Planta Med.*, **39**, 157 (1980).
14. J. H. Lee, J. Y. Lee, J. H. Park, *Vaccine*, **25**, 3834 (2007).
15. I. M. Villasenor, J. Angelada, A. P. Canlas, *Phytother. Res.,* **16**, 417 (2002) .
16. N. H. Tung, H. J. Kwon, J. H. Kim, J. C. Ra, J. A. Kim, Y. H. Kim, *Arch. Pharm. Res.*, **33**, 363 (2010).
17. M. Ivanova, G. Vasilev, S. Stanilova, R. Stoilov, I. Manolova, *J. Balk. Tribol. Assoc.,* **20**, 66 (2014).
18. I. Sheytanov, Ts. Petranova, S. Monova, N. Stoilov, A. Batalov, R. Nestorova, *J. Balk. Tribol. Assoc.,* **19**, 260 (2013).

АНТИОКСИДАНТНА АКТИВНОСТ НА ВТОРИЧНИ МЕТАБОЛИТИ И МИЦЕЛАРНИ ЕКСТРАКТИ ОТ ЕНДОФИТОВИ ГЪБИЧКИ, ИЗОЛИРАНИ ОТ *Astragalus monadelphus*

И.Г. Уанг[1*], Г.Р. Янг[1], Ф. Уанг[2], М.Дж. Янг[1*], Дж. Ли[1], С.Ф. Лю[1], М.Г. Уанг[1], С.Л. Уанг[3]

[1]*Училище за науки за живота и инженерство, Технологичен университет в Ланжоу, 730050 Ланжоу, Китай*
[2] *Институт по биоенергия и биопроцесни технологии, Куингдао, Китайска академия на науките, 266101 Куингдао, Китай*
[3] *Институт по стопанство и фармацевтични науки, Китайска академия на науките, 730050 Ланжоу, Китай*

(Резюме)

Тринадесет щама от ендофитови фунги са изолирани от *Astragalus monadelphus*. Изследвана е активността на техните вторични метаболити и мицеларни екстракти за отстраняване на свободни радикали. Резултатите показват, че те притежават значителна антиоксидантна активност. Редукционната способност на мицеларния екстракт от H401 е по-силна, отколкото екстракта с етилацетат, като неговата EC_{50} стойност е 0.0034 mg/mL. Екстрактът с етилацетат на щама H802 проявява силна способност да отстранява ·OH – радикали с IC_{50} стойност от 0.0384 mg/mL. DPPH-тестът за антирадикалова активност показва, че ендофитовите фунги могат да бъдат добър източник за анти-радикалови средства. Вторичните метаболити, екстрахирани от щама H401 принадлежат към групата на β-ситостерола, което е установено с ЯМР-анализ и от литературни данни.

Experimental study on thermal oxidation of ultra-low concentration methane in a non-catalytic reverse-flow reactor

Z. Li[1], Y. Liu[2*], Z. Wang[1]

[1]School of Energy and Power Engineering, Shandong University, Jinan 250061, China
[2]School of Transportation and Vehicle Engineering, Shandong University of Technology, Zibo 255049, China

A series of experiment were carried out on a 60000 m^3/h non-catalytic reverse-flow reactor for thermal oxidation of ultra-low concentration methane. The start-up performance, methane conversion rate, lowest methane concentration of stable operation, reactor temperature distribution and the yield of super-heated steam were studied. The results show that the temperature distribution on the cross section of the reactor is quite uniform during the whole process including the start-up period, while on the section along the direction of flow, a peak temperature appears at the middle, and temperature falls as it gets farther away from the axis. With the methane concentration at inlet increases from 0.3% to 1.0%, the peak temperature enhances form 990˚C to 1066˚C, while methane conversion rate almost keeps constant (about 98.6%). As the flow of the reactor is 60000 m^3/h, the lowest inlet methane concentration of stable operation is 0.28%.

Keyword: ultra-low concentration methane; thermal oxidation; non-catalytic reverse-flow reactor.

INTRODUCTION

Methane is a kind of conventional energy, and also a kind of greenhouse gas. The huge emission of ventilation air methane (VAM) from coal mine causes serious environmental problem and results in a waste of energy. The ultra-low concentration VAM combustion is difficult to achieve with traditional methods. Nowadays the oxidation technologies of ultra-low concentration VAM are TFRR (thermal reverse-flow reactors) and CFRR (catalytic reverse-flow reactors) [1]. A series of theoretical and experimental study have been done on CFRR [2-8], CFRR achieves relatively low react temperature, however, the reaction activity of the catalyst is greatly affected by temperature, the catalyst is expensive and oxidation process is complex, all of this limit the application of CFRR. TFRR is less expensive and complex; however it needs relatively high reaction temperature. Also, more detailed researches on temperature distribution and methane conversion rate are required for stable and reliable operation of TFRR [9]. While researches on TFRR reported are not enough. Zheng Bin, etc. carried out a series of experimental researches on ultra-low concentration VAM oxidation based on a self-developed pilot regenerative reverse-flow oxidation reactor [10]. Wang Pengfei, etc. established a one dimensional single-temperature model of ultra-low concentration VAM thermal reverse-flow oxidation reactor as well as fractal systems [11, 12, 13]. However, up to now, there is still not any applying plant of TFRR is reported.

A 60000m^3/h non-catalytic reverse-flow reactor for thermal oxidation of ultra-low concentration VAM was proposed, the goal of current paper is to study its performance, including the start-up performance, methane conversion rate, lowest methane concentration of stable operation, and temperature distribution in the reactor.

EXPERIMENT EQUIPMENT AND CONDITIONS

The experiments were carried out on a 60000$m3$/h non-catalytic reverse-flow reactor for thermal oxidation of ultra-low concentration methane, the plant mainly consists of oxidation reactor, heat extraction system, conveying and mixing system, start-up system, deducting and dehumidifying system, monitoring and control system.

Three vertical columns of K-type thermocouples (which were labeled as left, middle and right) were fixed on the flow direction to obtain temperature distribution of oxidation reactor. There were 15 offset temperature measuring point in each column. The schematic diagram of temperature points arrangement show in figure 1.

The fuel gas used for start-up is liquefied petroleum gas. The concentration of ultra-low concentration methane is between 0.3% and 1.0%, which is obtained by mixing coal mine draining methane and VAM from air return ventilation mine shaft. The water used in the experiments is softened water produced by a LMZF-12 automatic water

---

soften system in Julong coal mine methane pumping plant. The soften water is in line with national water supply standards for low pressure boiler. Concentration of methane was measured with a Madur maMos100 methane analyzer, of which the regulation error is 0.025%. Reversing valve actuators (DA-149) were used to achieve the reversing operation. The interval time between two adjacent reversing was 90~150, and the average consuming time of each reversing operation is 2.78s. A plug-in V-cone flow meter was set on the pipeline (DN1200) after the blower to obtain the process capacity. Start-up system consisted of hot air generation, regulation and distribution system, so that the demanding hot air may achieved by adjusting the power of burners and the opening of flow control valve. As core temperature of the reactor reached 800 °C, flow rate was increased, cooperating with which hot air valve was switched off gradually, until the normal operation of the reactor was achieved.
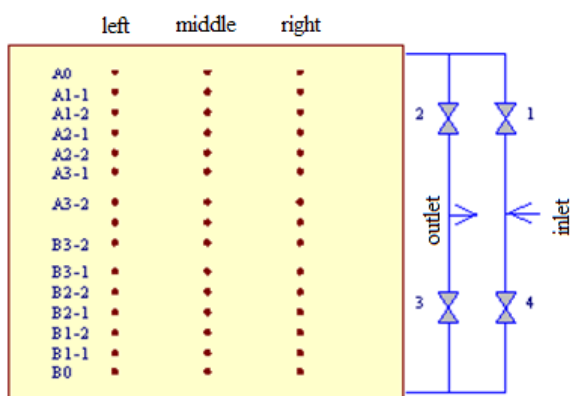
Fig. 1. The schematic diagram of temperature points arrangement.

RESULTS AND DISCUSSION

Start up

To achieve the normal operation of the plant, core temperature of 900~1000 °C and appropriate reactor temperature distribution must be established at first. Therefore, start-up performance experiments were carried out, and the results are shown in Figure 2.

Figure 2 shows that the temperature at the same level are similar, which indicates that during the start-up period temperature at nearly all the points on the same cross section increases synchronously.

However, on the section along the direction of flow, a peak temperature appears at the middle, and temperature falls as it gets farther away from the axis. It is because gas flow direction reverses

periodically, and heat is concentrated at the core of the ceramic regenerator.

(a) after 3 hours

(b) after 12 hours

(c) after 24 hours

(d) after 36 hours

(e) after 48 hours
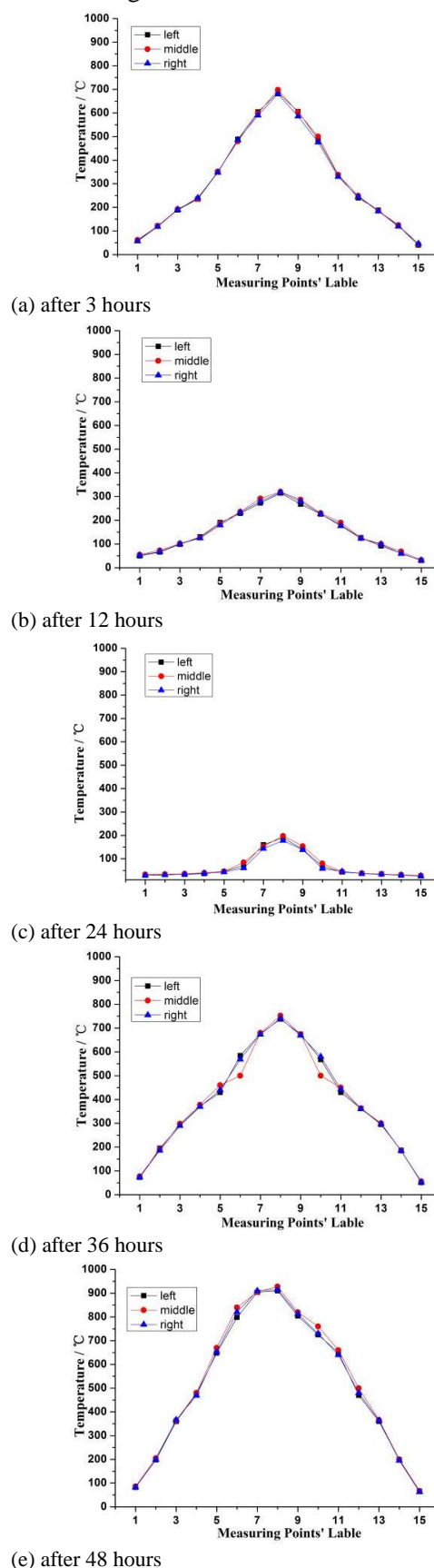
Fig. 2. The temperature distributions of start-up perior.

As more and more heat is sent to the reactor, core temperature increases, and results in the temperature distribution as mentioned above. This temperature distribution is quite similar to that under normal operation conditions, so that the time cost from start up condition to normal operation condition can be controlled.

Methane conversion rate

The experiments were carried out in order to obtain the peak temperature and methane conversion rate under different inlet methane concentration. During these experiments flow rate was $60625\pm385m^3/h$, concentration of methane was adjusted from 0.3% to 1.0%, results are shown in Figure 3.
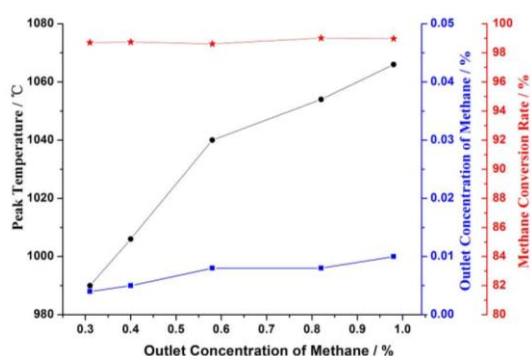
Fig. 3. The effects of methane on peak temperature and methane conversion

Figure 3 shows that as the increase of methane more and more heat is released, so that the peak temperature enhances apparently from 990 °C~1066 °C, meanwhile the outlet methane concentration shows slightly increase (from 0.004% to 0.01%), however methane conversion rates under different inlet methane concentration almost keeps constant, which are all larger than 98.6%, and shows an average value of 98.82%. This indicates that high efficient conversion can be achieved under relative wide range of inlet methane concentration.

The lowest methane concentration of stable operation

Heat released by methane oxidation reaction is partially kept in the reactor to maintain the reaction, and the rest heat may be extracted by the inner heat exchanger. As methane concentration gets too low to maintain the reaction, the temperature may decrease gradually until reaction gets its end. Therefore design of reactor and heat extraction system plays a significant role on the stable operation of the plant. In this experiment, the stable operation condition as following: the flow is about $60000m^3/h$, under a certain inlet methane concentration, after 2 hours continuous operation average temperature of the reactor never falls, the peak temperature is larger than 950˚C, and methane conversion rate is no less than 97%. Table 1 shows several record of the lowest methane concentration of stable operation. The results show that as air flow rate keeps about $60000m^3/h$, the lowest average methane concentration of stable operation is 0.28%.

Uniformity of temperature distribution

Experiments on uniformity of temperature distribution in the reactor were carried out under different methane concentration, which was achieved by adjusting the amount of drainage methane for mixing.

Temperature distribution in Figure 4 under different methane concentration shows that the temperature profiles at different location (left, middle and right) coincide well which reveals the perfect temperature uniformity.

Table1. The lowest methane concentration of the plant stable operation.

Number	Air flow (m³/h)	Peak temperature (˚C)	Lowest methane concentration (%)
1	60258	965	0.27
2	61212	980	0.29
3	60480	976	0.28
4	60650	970	0.28
Average value	/	/	0.28

(a) 0.3%

(b) 0.4%

(c) 0.6%

(d) 0.8%

(e) 1.0%
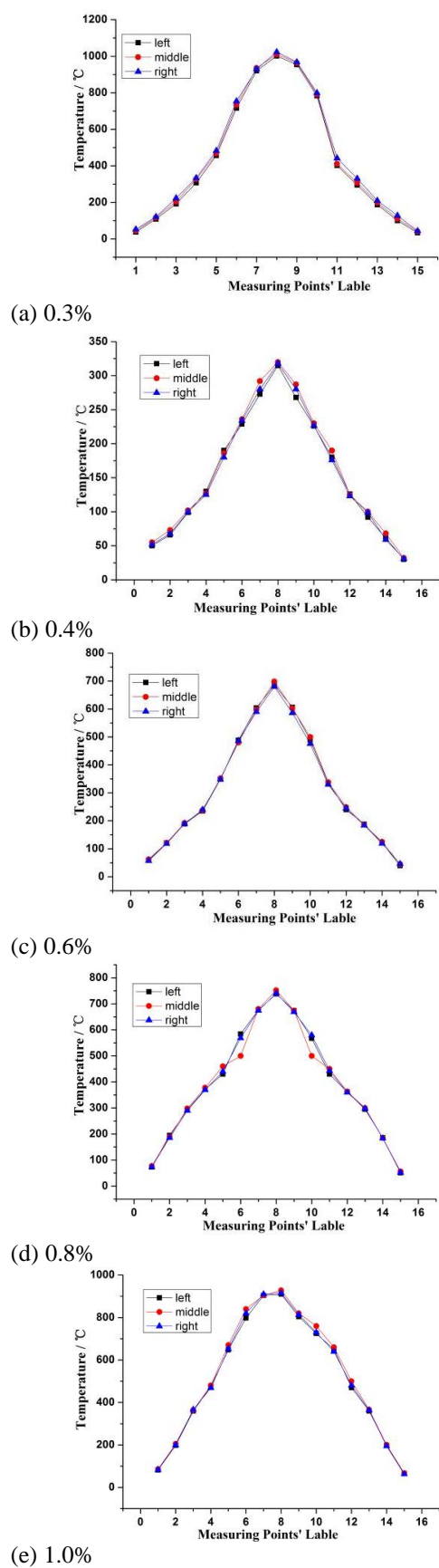
Fig. 4. The effects of methane concentration on the temperature of reactor.

As methane concentration increases, core temperature of the reactor is enhanced, which enlarges the extent of high temperature zone and oxidation zone, and then promotes methane conversion. However, the increase of outlet temperature with concentration can be ignored, which says that the affect of methane concentration variation on heat loss of exhausted gas is little.

CONCLUSION

A series of experiment were carried out on a 60000m^3/h non-catalytic reverse-flow reactor for thermal oxidation of ultra-low concentration methane. With results, following conclusions can be obtained:

(1) Temperature distribution on the cross section of the reactor is quite uniform during start-up period, while on the section along the direction of flow, a peak temperature appears at the middle, and temperature falls as it gets farther away from the axis, which is quite similar to that under normal operation conditions, and helps to achieve normal operation as soon as possible.

(2) The peak temperature enhances apparently from 990~1066 °C, meanwhile the outlet methane concentration shows slightly increase (from 0.004% to 0.01%), however the methane conversion rates under different inlet methane concentration almost keeps constant (98.82%), which indicates that high efficient conversion may achieved under relative wide range of inlet methane concentration.

(3) As the flow is about 60000m^3/h, the lowest methane concentration of stable operation is 0.28%, under which average temperature keeps stable, peak temperature is larger than 950 °C, and methane conversion rate is no less than 97%

(4) Under normal operation conditions, temperature profiles at different location (left, middle and right) coincides well and with the increase of methane concentration high temperature zone and oxidation zone is enlarged, while heat loss of exhausted gas increases little.

REFERENCES

1. K. Özgen, A. Felicia, R. Michael, *Int. J. Coal Geol.*, **86**, 121 (2011).
2. S. Shahamiri I. Wierzba, *Chem. Eng. J.*, **149**, 102 (2009).
3. X.Y. Wang and J. Du, *Coal Technol.*, **27**, 1 (2008).
4. F. Liang, Z.L. Liu, Y.X. Li, *Appl. Therm. Eng.*, **30**, 2804 (2010).
5. G. Krzysztof, S. Yurii, K.W. Matros, *Chem. Eng. Sci.*, **63**, 76 (2012).
6. J. Yin, Y.W. Weng, *Energy Convers. Manage.*, **52**, 1711 (2011).
7. Z.L. Gao, Y.Q. Liu, Q.Q. Su, *J. China Coal Soc.*, **37**, 683 (2012).
8. M. Pablo, A.G.H. Miguel, *Catal. Today*, **105**, 701 (2005).
9. G. Krzysztof, S. M. Yurii, W. Krzysztof, *Chem. Eng. Sci.*, **63**, 5010 (2008).
10. B. Zheng, Y.Q. Liu, and R.X. Liu, *J. China Coal Soc.*, **3**, 1475 (2009).
11. P.F. Wang, T. Feng, X.L. Hao, *J. Min. Saf. Eng.*, **29**, 434 (2012).
12. I. Markovska, D. Rusev, F. Yovkova, *J. Balk. Tribol. Assoc.*, **20**, 75 (2014).
13. D. Balaji, S. Suresh, Oxid. Commun., **39**, 2497 (2016).

ЕКСПЕРИМЕНТАЛНО ИЗСЛЕДВАНЕ НА ТЕРМИЧНОТО ОКИСЛЕНИЕ НА СВРЪХ-НИСКИ КОНЦЕНТРАЦИИ НА МЕТАН В НЕ-КАТАЛИТИЧЕН РЕАКТОР С ОБРАТЕН ПОТОК

З. Ли[1], И. Лю[2*], З. Уанг[1]

[1]*Училище по енергетика и инженерство, Университет Шандонг, Джинан 250061, Китай*
[2]*Училище по транспорт и транспортно инженерство, Технологичен университет Шандонг, Зибо 255049, Китай*

(Резюме)

Проведена е серия от експерименти в не-каталитичен реактор с обратен поток за термичното окисление на свръх-ниски концентрации на метан при дебит 60000 m^3/h. В пусковия период са изследвани степента на превръщане, най-ниската допустима концентрация на метана за устойчива работа, температурния профил и добива на прегрята пара. Резултатите показват, че температурното разпределение по напречното сечение на реактора е почти равномерно по време на целия процес, включвайки и пусковия период, докато по дължината на реактора се наблюдава максимална температура, която спада по-нататък. При повишаване водната концентрация на метана от 0.3% до 1.0% максималната температура се покачва от 990˚C до 1066˚C при постоянна степен на превръщане (около 98.6%). При избрания дебит на газа най-ниската концентрация на метан за стабилна работа е 0.28%.

Study on the extraction, antioxidant activity of polysaccharides from *Piteguo* fruit

C. Lin[1], G. R. Yang[2], Y. G. Wang[1*], M. J. Yang[1*], X. F. Liu[2]

[1] Sports Teaching and Research Department, Lanzhou university of technology, Lanzhou 730050, China
[2] School of Life Science and Engineering, Lanzhou University of Technology, Lanzhou 730050, China

Ultrasonic-assisted extraction (UAE) of polysaccharides from *Piteguo* fruit (*Pyrus sinkiangensis*) was studied. The four parameters, i.e., ratio of water to raw material, extraction time, extraction temperature, and ultrasonic power were optimized by the Box-Behnken design (BBD). The structure of polysaccharide from Piteguo (PTGP) was analyzed preliminarily by infrared spectrum. Antioxidant activities of PTGP were detected in vitro. The results indicated that the extraction ratio of crude PTGP was up to 5.16% ± 1.81% under the optimized extraction conditions as follows: ratio of water to raw material 13:1 mL/g, extraction time 66 min, extraction temperature 70 °C and ultrasonic power 230 W, which is was well matched with the value (5.25%) predicted by the BBD model. Spectroscopic studies illustrated PTGP was composed of Glc with β-type pyranoid type sugar ring. Moreover, the results of antioxidant activity assay indicated that PTGP has antioxidant effect in a certain extent, and could be used as a potential natural antioxidant.

Keywords: Piteguo fruit; Polysaccharide; Ultrasonic-assisted extraction; Response surface methodology; Antioxidative activity

INTRODUCTION

Polysaccharides are polymeric carbohydrate molecules of long chain monosaccharide units, and are of plant and algae origin with the exception of few microbial derived exopolysaccharides [1]. Polysaccharides have important health care functions such as antitumor activity [2], radioprotection activity [3], antioxidant activity [4], *et al.*. As well as, Federico and others [5] found that exopolysaccharides play an indispensable role in enhancing hydraulic conductivity of biological soil crusts.

Piteguo fruit (PTG), which is originally known as Pinangguo fruit (Skins fruit), is classified as Pyrus sinkian-gensis, subfamily Maloideae, family Rosaceae. According to expert research, it proves to have strong plant vigor and environmental adaptation, for it can grow well in poor soil, and resist common diseases and insects. This kind of indigenous fruit contains several kinds of essential amino acids, sugars, crude fiber, vitamins (e.g. C, B1, B2), tannic acid for human beings and essential elements such as potassium, calcium, iron, and *etc*. It is also reported in traditional Chinese medicine theory that *Piteguo* fruit has important health care functions such as nourishing the stomach, moistening the lung, quenching thirsty, and etc. So it is considered as a novel green food with high nutritional value [6].

In our study, we applied ultrasonic-assisted extraction procedure to extract crude polysaccharides from *Piteguo* fruit. Box-Behnken design (BBD) [7], one type of RSM was introduced to optimize ultrasonic-assisted extraction technology condition of crude polysaccharides from *Piteguo* fruit and systematically analyze the effects of extraction parameters on their yields and their interactions. In addition, the structures and activities of polysaccharide were analyzed in order to provide the theoretical basis for application of polysaccharide from *Piteguo* fruit and full development of this kind of undeveloped fruit resource.

MATERIALS AND METHODS

Materials

Piteguo fruit was picked in Hezheng County, Linxia Hui Minority Autonomous Prefecture, Gansu Province in November, 2011. Before eating or application in this study, *Piteguo* fruit has to be treated properly to remove acerbity and become post-mature. Those soluble tannins distributed in the special tannin cells can be transformed into insoluble tannins by CO_2, alcohol and acetaldehyde produced from anaerobic fermentation in sealed containers. After post-maturation, the color of the fruit turns brown and the pulp feels much softer than the unripe one. Then, the treated (post-mature) fruits were transferred and stored at -20 °C for the following extraction experiments.

Methods

Extraction of crude polysaccharides from Piteguo fruit with ultrasonic-assisted treatment The treated *Piteguo* fruits were washed by distilled water

* To whom all correspondence should be sent:
E-mail: 412316788@163.com; yangmj@lut.cn

and the peels were removed before being cut into small pieces. The process of crude polysaccharides extraction from *Piteguo* fruits by ultrasonic-assisted treatment was performed in an ultrasonic processor (KQ-250DB, Kunshan Ultrasonic Instruments Co., Ltd, Jiangsu, China). Then, impurity proteins, vitamins, lipids and other pulp components were separated by centrifugation in a 50 mL centrifuge tube [8]. The supernatant was withdrawn, concentrated in a vacuum concentrator and precipitated with 80% ethanol, and dried to get the crude PTGP by vacuum freeze drying (FD-1A-50, Boyikang Instruments Co., Ltd, Beijing, China).

Determination of the yield of polysaccharides from Piteguo fruit and extraction ratio   The content of polysaccharide extracted from Piteguo fruit was measured by phenol-sulfuric acid method[9]. The freeze-dried polysaccharide sample was dissolved into distilled water, and optical density of this solution at 485 nm (OD_{485}) was measured. The content of polysaccharide in this sample was calculated according to equation of linear regression ($Y=0.0607X-0.0569$, $R^2=0.9977$) based on the standard curve whose horizontal coordinate and vertical coordinate denoted the concentration of glucose (µg/mL) and OD_{485}, respectively. The polysaccharide yield could be calculated as described [9].

Experimental design and statistical analyses   In order to investigate the critical influencing factors in ultrasonic-assisted extraction, single-factor-test was employed in this experiment to determine the preliminary range of the variables including X_1 (ratio of water to raw material), X_2 (extraction time), X_3 (extraction temperature) and X_4 (ultrasonic power). Then, a three-level-four-factor BBD was adopted in the optimization study for the yields of *Piteguo* fruit water-soluble crude polysaccharides. Table 1 represents the coded and non-coded values of the experimental variables and 21 experimental points. Five replicates (17-21) were used to evaluate the pure error. Experimental data shown that response

variables were fitted to a quadratic polynomial model.

FT-IR spectroscopy Infrared spectrum samples were prepared by potassium bromide tabletting. The dried PTGP power and potassium bromide powder were thoroughly ground. The mixed powder was made into a transparent sheet with about 1 mm thickness by a pneumatic tabletting machine. Then the samples were analyzed by a Fourier transform infrared spectrometer (Thermo Scientific Nicolet iN10) at 400 - 4000 cm^{-1} with a resolution of 4 cm^{-1}.

Determination of antioxidant activities in vitro of PTGP

Hydroxyl radical scavenging assay   The 10 mL of reaction mixture contained 2 mL of 200 mM sodium phosphate buffer (pH 7.4), 1.5 mL of 5.0 mM 1, 10-phenanthroline aqueous solution, 1.0 mL of 7.5 mM $FeSO_4$ aqueous solution, 1 mL of 0.1% H_2O_2 aqueous solution, 0.1 mL of the PTGP aqueous solution with different concentration (0.25, 0.5, 0.75, 1.0, 1.5, 2.0, 2.5, 3.0, 3.5 and 4.0mg/mL, respectively) and distilled water. After incubating at 37 °C for 1 h, the absorbance of the mixture was measured at 510 nm. The scavenging activity of hydroxyl radicals production was calculated as described by Jin et al. [10].

Superoxide radical scavenging assay   The sample was diluted to a different concentration (0.25, 0.5, 0.75, 1.0, 1.5, 2.0, 2.5, 3.0, 3.5 and 4.0 mg/mL) with 50 mM Tris-HCl buffer (pH 8.2). Secondly, 5.0 mL of 50 mM Tris-HCl buffer (pH 8.2) and 0.1 mL of samples were incubated at 25 °C for 20 min, then 0.2 mL of 3 mM pyrogallol at the same temperature were added to the mixture and the reaction was kept at 25 ℃ for 4 min, and the rate of absorbance change (A/min) of the solution was measured at 325 nm, with 50 mM phosphate buffer (pH 7.2) instead of sample as the control. The scavenging activity of superoxide radical was calculated according to by the Yuan and Gao [11].

Table 1. Independent variables and their levels used in the response surface design

Variables	Levels		
	-1	0	1
Extraction temperature (X_1) (°C)	65	70	75
Extraction time (X_2) (min)	50	60	70
Ratio of water to raw material (X_3) (mL/g)	10:1	15:1	20:1
Ultrasonic power (X_4) (W)	150	200	250

Effect of scavenging of (DPPH) radicals The solution of 0.2 mM DPPH in 60% ethanol was prepared before UV measurements. Then, 3.0 mL of the samples (0.1, 0.15, 0.20, 0.25, 0.5, 0.75, 1.0, 1.5, 2.0, 2.5, 3.0, 3.5 and 4.0 mg/mL) was added to 1.0 mL DPPH, and kept at room temperature for 30 min in the dark, and the absorbance at 525 nm was then measured against a blank. Ascorbic acid was used as positive controls. The scavenging activity of DPPH radical (%) was calculated according to the Shimada and others [12].

Determination of reducing power The reducing power of PTGP was evaluated according to Oyaizu [13] with necessary modifications. The reaction mixtures contained 2.5 mL phosphate buffer (pH 6.6, 0.2M), 2.5 mL potassium ferricyanide (1%, w/v) and PTGP (0.1, 0.15, 0.20, 0.25, 0.5, 0.75, 1.0, 1.5, 2.0, 2.5, 3.0, 3.5 and 4.0 mg/mL). After incubating at 50 ℃ for 20 min, 2.5 mL of trichloroacetic acid (10%, w/v) was added into the mixture for terminating the reaction, and then centrifuged at $1500 \times g$ for 10 min. An aliquot of 2.5 mL supernatant was collected and mixed with 2.5 mL deionized water and 0.5 mL $FeCl_3$ (0.1%, w/v). After incubating at room temperature for 15 min, the absorbance at 700 nm of the mixture was measured, using ascorbic acid as a positive control. Higher absorbance of the reaction mixture indicated higher scavenging activity of free radicals.

Statistical analysis All the data were exhibited as mean values of three replicate determinations. Difference was considered to be significant when $p<0.05$. Statistical analysis involved use of the Origin Pro software package 8.5 (Origin Lab Corp.) and Design Expert software Version 8.0.5 (Stat-Ease Inc.).

RESULTS AND DISCUSSION

Effect of extraction temperature on extraction yield of polysaccharides In this experiment, the effects of different extraction temperature on the yield of PTPG were studied, while the other extraction conditions such as the ratio of water to raw material, extraction time, ultrasonic power were fixed at 15 mL, 60 min, 150 W respectively. As shown in Figure 1A, the extraction yield of polysaccharides continued to increase with the increasing of extraction temperature and reached at the peak value (5.76%) when extraction temperature was 70 °C. However, the yield was noticed to decrease when the extraction temperature exceeded 70 °C, which may be caused by the degradation of polysaccharides. Thus, the optimum extraction temperature was 70 °C according to the results.
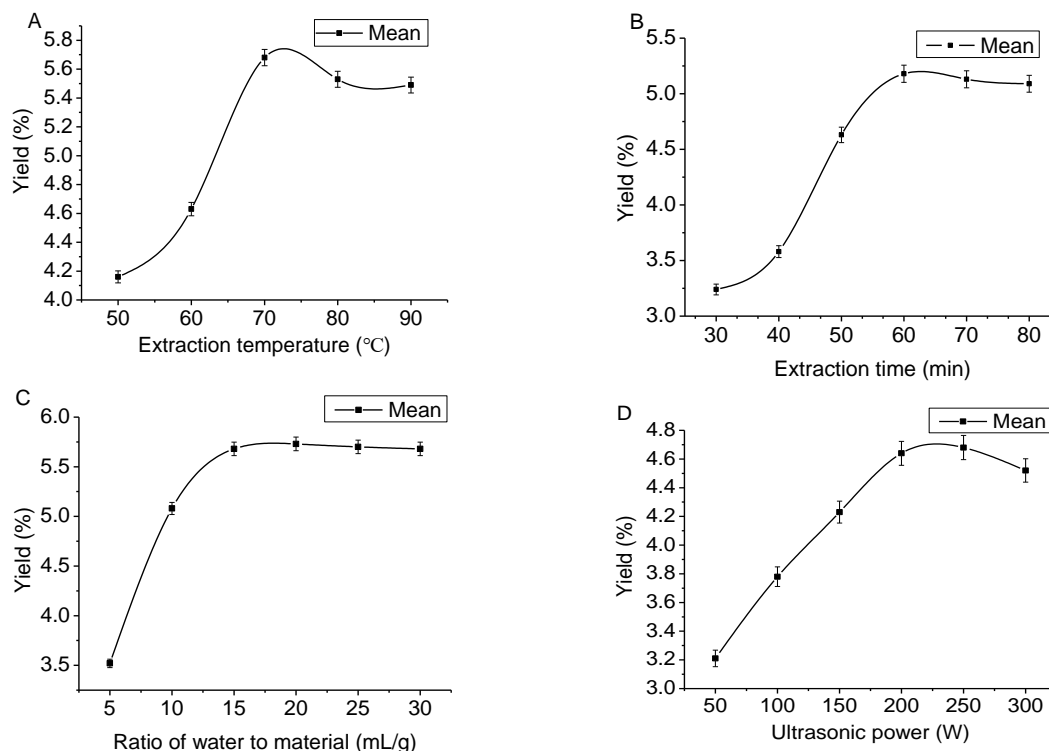
Fig. 1. Effects of different extraction temperature (A), extraction time (B), ratio of water to raw material (C) and ultrasonic power (D) on extraction yield of polysaccharides. All data were mean values of triplicate. The vertical error bars represented the standard deviation of each data point ($P < 0.05$).

Table 2. Box-Behnken design and the response values for the yields of polysaccharides

NO.	X_1 (Extraction temperature, °C)	X_2 (Extraction time, min)	X_3 (Ratio of water to raw material, mL/g)	X_4 (Ultrasonic power, W)	Extraction yield (%)
1	1	1	1	-1	4.11
2	1	1	-1	-1	3.82
3	1	-1	1	1	4.42
4	-1	1	-1	1	4.31
5	1	-1	-1	1	4.26
6	-1	-1	1	-1	4.35
7	-1	1	1	1	4.72
8	-1	-1	-1	-1	4.22
9	-1	0	0	0	4.57
10	1	0	0	0	5.21
11	0	-1	0	0	5.01
12	0	1	0	0	5.17
13	0	0	-1	0	4.73
14	0	0	1	0	5.08
15	0	0	0	-1	4.91
16	0	0	0	1	5.17
17	0	0	0	0	5.17
18	0	0	0	0	5.14
19	0	0	0	0	5.16
20	0	0	0	0	5.15
21	0	0	0	0	5.18

Table 3. Analysis of variance testing the fitness of the regression equation

Source	SS[a]	DF[b]	MS[c]	F-value	p-value
Model	3.89	14	0.28	133.71	<0.0001
X_1	0.20	1	0.20	98.64	<0.0001
X_2	0.013	1	0.013	6.16	0.0476
X_3	0.18	1	0.18	86.48	<0.0001
X_4	0.034	1	0.034	16.28	0.0068
X_1X_2	0.0007225	1	0.0007225	0.35	0.5768
X_1X_3	0.001013	1	0.001013	0.49	0.5111
X_1X_4	0.022	1	0.022	10.41	0.0180
X_2X_3	0.021	1	0.021	10.12	0.0190
X_2X_4	0.32	1	0.32	151.74	<0.0001
X_3X_4	0.002813	1	0.002813	1.35	0.2887
X_1^2	0.26	1	0.26	123.78	<0.0001
X_2^2	0.035	1	0.035	16.92	0.0063
X_3^2	0.23	1	0.23	112.36	<0.0001
X_4^2	0.071	1	0.071	34.41	0.0011
Residual	0.012	6	0.002076		
Lack of fit	0.011	2	0.005729	22.92	0.0064
Pure error	0.001	4	0.00025		
Cor. total	3.90	20			

[a] Sums of squares [b] Degree freedom [c] Mean square $R^2=0.9968$ $R^2_{adj}=0.9894$

Effect of extraction time on extraction yield of polysaccharides The effects of extraction time on the yield of PTGP were shown in Figure 1B. Firstly, the extraction time was set at 30, 40, 50, 60, 70 and 80 min, respectively, while the other extraction parameters were given as the followings: water volume 10 mL, ultrasonic power 150 W and extraction temperature 70 °C. It could be found that the extraction yield increased as extraction time

lasted from 30 to 60 min, maximized at 60 min, and then no longer increased.

Effect of ratio of water to raw material on yield of polysaccharides Different ratio of water to raw material could significantly affect the extraction yield. If ratio of water to raw material is too low, polysaccharides in raw material cannot be completely extracted up. On the other hand, high ratio of water to raw material will cause high process

801

cost [14, 15]. In this study, the effects of ratio of water to raw material on extraction yield of PTGP was investigated. The ratios of water to raw material were set at 5:1, 10:1, 15:1, 20:1 and 25:1, respectively, while other extraction parameters were given as the followings: ultrasonic power 150 W, extraction time 60 min and extraction temperature 70 °C. It could be founded that the extraction yield of PTGP continued to increase obviously with the increasing ratio of water to raw material. But the extraction yield of PTGP started to increase slowly after the ratio of water to raw material exceeded 15:1 (Figure 1C).

Effect of ultrasonic power on yield of polysaccharides Analogously the effects of different ultrasonic power on the yield of PTGP were investigated when the other extraction conditions such as water volume, extraction time, extraction temperature were fixed at 15 mL, 60 min, 70℃ respectively. As shown in Figure 1D, the extraction yield of PTGP increased gradually with the increasing of ultrasonic power and reached the maximal value (5.58%) at 200 W, whereas the yield decreased when the ultrasonic power exceeded 200 W.

Optimization of extraction conditions of polysaccharides

Predicted model and statistical analysis Four independent variables including extraction temperature (X_1), extraction time (X_2), ratio of water to raw material (X_3), and ultrasonic power (X_4) were considered and optimized individually using BBD design. Table 2 shows the small design matrix together with the response values obtained. The yield of PTGP ranged from 3.82 to 5.18%, and reached maximum with the ratio of water to raw material of 15 mL/g, at 200 W, 70 °C, and a 60 min treatment duration. Trials No.17-21 in Table 2 were used to determine the experimental error. According to multiple regression analysis on the experimental data, the model for the predicted yield of polysaccharides (Y) could be expressed by the quadratic polynomial equation (in the form of coded values). Statistical testing of the model was performed in the form of analysis of variance (ANOVA). The ANOVA for the fitted quadratic polynomial model of extraction of PTGP was shown in Table 3. The corresponding variables would be more significant if the *F*-value becomes greater and *p*-value becomes smaller [16,17]. Values of *p*-value less than 0.05 showed model terms were significant. From this analysis, the F-value of 133.71 and *p*-value< 0.0001 indicated the response surface quadratic model was significant. The quadratic

802

regression model showed the value of the determination coefficient (R^2) was 0.9968, which implied that 99.68% of the variations could be explained by the fitted model. For a suitable statistical model, R^2_{adj} should be close to R^2. As shown in Table 3, R^2_{adj} was 0.9894, which indicated that only less 1.1% of the total variations could not be explained by the model. It also implied a high degree of correlation between the observed and predicted values. A relatively low value of *C.V.* (coefficient of variation) (0.96%) indicated a better reliability of the experiments values. Significance of the model was also judged by lack-of-fit test. As shown in Table 3, *F*-value and *p*-value of the lack of fit were 22.92 and 0.0064, respectively, which implied that it was significant. The significance of each coefficient was determined using *F*-value and *p*-value. The results were given in Table 3. It could be seen that the independent variables (X_1, X_3, X_4), the interaction terms (X_2X_4) and all two quadratic terms $(X_1^2, X_2^2, X_3^2, X_4^2)$ affected the yield of PTGP very significantly $(p<0.01)$, the effects of other independent variables (X_2) and interaction terms (X_1X_4, X_2X_3) was significant too $(p<0.05)$. The results also showed that the independent variable X_1 and X_3 were the most significant factor on the experimental yield of PTGP.

Analysis of response surface The relationship between independent and dependent variables was illustrated by the tri-dimensional representation of the response surfaces and the two-dimensional contours generated by the model (shown in Figure 2A-F and 3A-F). Among these four variables (extraction temperature, extraction time, ratio of water to raw material and ultrasonic power), when two variables within the experimental range were depicted in tri-dimensional surface plots, the third variable was kept constant at zero level. The shapes of the contour plots, elliptical or circular, indicated whether the interactions between the corresponding variables were significant or not [16]. An elliptical contour plot means the interactions between the variables are significant while a circular contour plot means otherwise.

Figure 2A and 3A represented the effects of extraction temperature (X_1) and extraction time (X_2) on the yield of PTGP. With the increase of extraction temperature, the yield increased until gradually stable. As far as the effect of extraction time was concerned, the yield initially enhanced as time went by, then decreased slowly. According to the analysis, the optimum PTGP yield should be obtained with an extraction temperature range of 69.5-72.5 °C and an extraction time range of 55.5-60.0 min, respectively, and the effect of extraction temperature was more

significant than that of extraction time. However, the effect of their interaction was not significant.

The effects of extraction temperature (X_1) and ratio of water to raw material (X_3) on the yield of PTGP were shown in Figure 2B and 3B, respectively. It showed that both of the two factors could affect the yield obviously. the production enhanced with the increase of extraction temperature and then remained stable above 70 °C. On the other hand, as the ratio of water to raw material increased from 11.5:1 to 15:1, the yield raised with an increase of extraction temperature from 66.0 to 70 °C.

The conclusions from Figure 2C and 3C demonstrated that extraction temperature (X_1) and ultrasonic power (X_4) represented a significant effect on the yield of PTGP.

When the ratio of water to raw material and extraction time were set at 15:1 and 60 min, respectively, the optimal productivity of PTGP could be gained with an extraction temperature range of 66-70 °C and ultrasonic power range of 185-220 W, and the effect of their interaction on the yield was significant as well as Table. 4 described.

According to Figure 2D and 3D, as the ratio of water to raw material (X_3) increased in the range from 10:1 to 15:1, PTGP yield increased as well. The curve tendency did not level off at low ratio, which indicated that this ratio was well below optimum for PTPG yield. There was a linear increase of the yield with extraction time (X_2) extended from 50 to 60 min, but yet decreased when more than one hour. The effect of extraction time was less significant than the ratio of water to raw material.
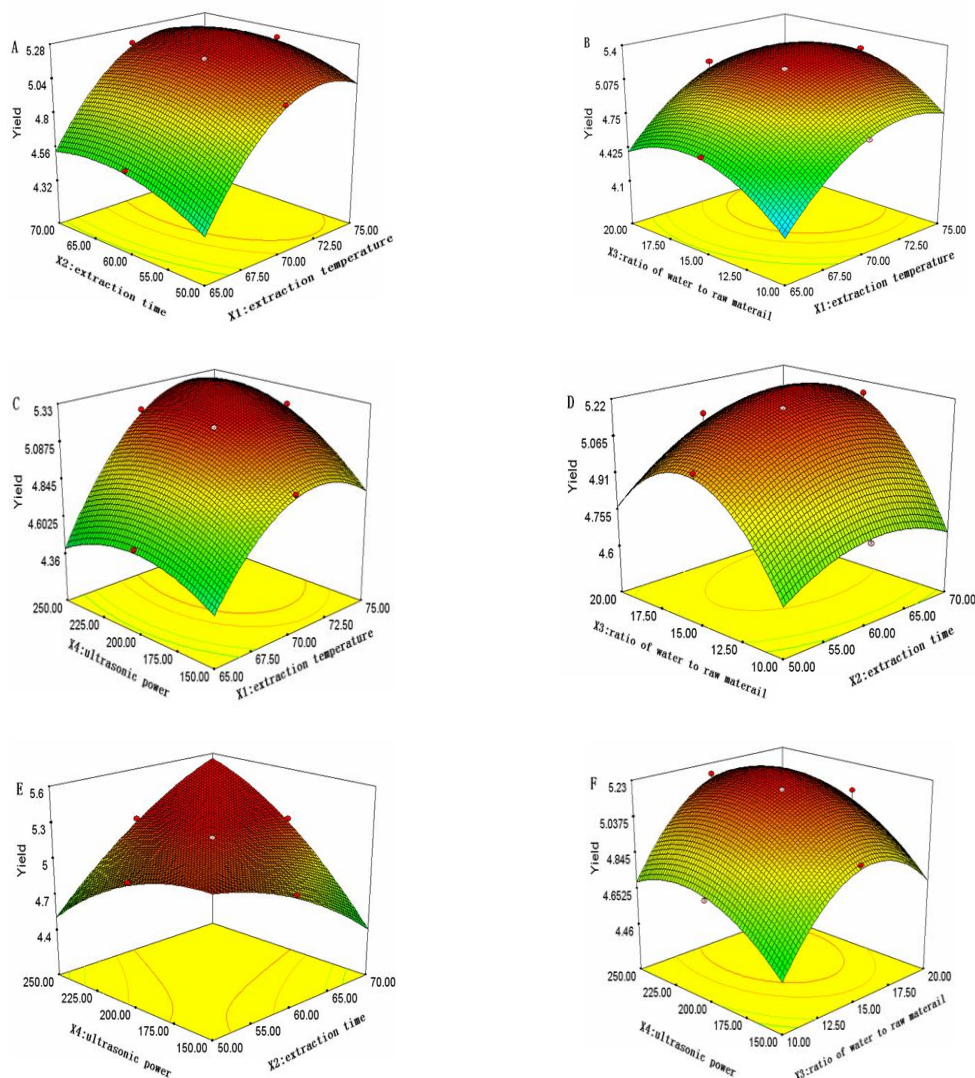
Fig 2. Response surface (3D) showing the effect of different extraction parameters (X_1: extraction temperature, °C; X_2: extraction time, min; X_3: the ratio of water to raw material, mL/g and X_4: ultrasonic power, W) and their interactions on the yield of PTGP.
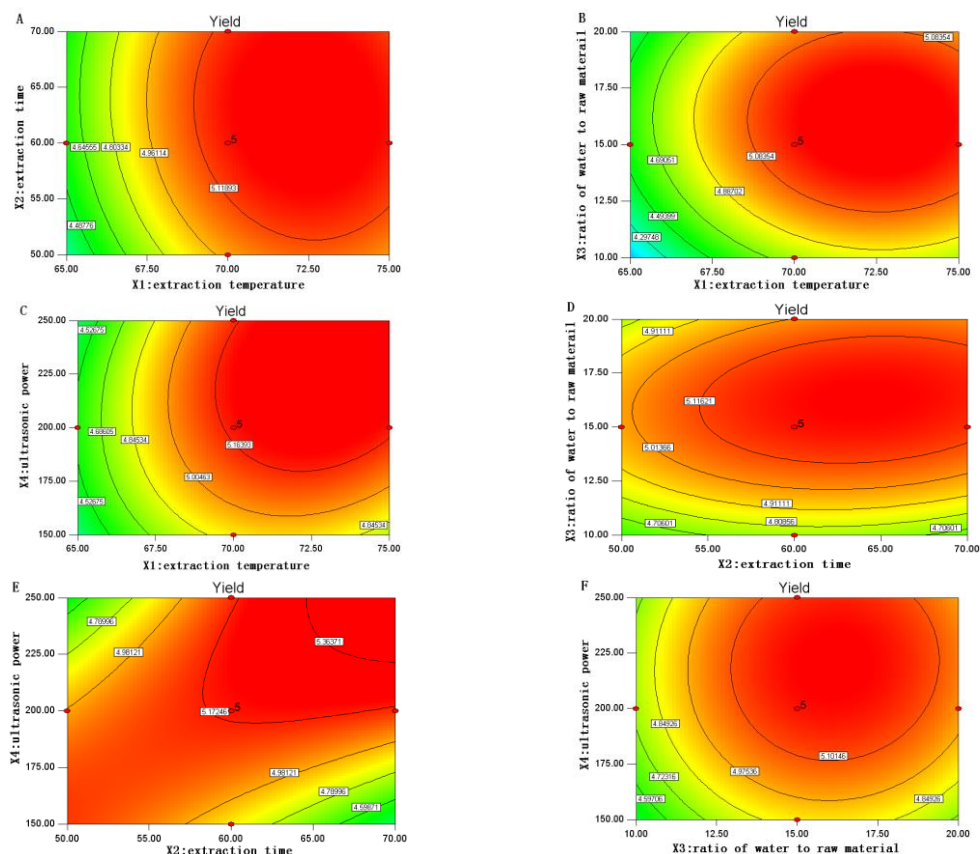
Fig. 3. Contour plots (2D) showing the effect of different extraction parameters (X_1: extraction temperature, °C; X_2: extraction time, min; X_3: the ratio of water to raw material, mL/g and X_4: ultrasonic power, W) and their mutual interactions on the yield of PTGP.

Figure 2E and 3E demonstrated the effects of extraction time (X_2) and ultrasonic power (X_4) on PTGP production. Under the condition of extraction temperature at 70℃ and the ratio of water to raw material at 15:1, the yield increased slowly with the extraction time and ultrasonic power increased until up to a threshold level. However, when extraction time and ultrasonic power exceeded the threshold level, the PTGP production decreased due to partial degradation of polysaccharide, which meant that a suitable ultrasonic power was important for extraction of PTGP.

The effects of the ratio of water to raw material (X_3) and ultrasonic power (X_4) on the yield of PTGP could be seen in Figure 2F and 3F. The lower the ratio of water to material, the lower the PTGP yield. The PTGP yield increased obviously with the ratio of water to raw material in the range of 10:1 to 15:1, then changed little. Similarly, the yield enhanced before ultrasonic power increased up to a threshold level of 200 W, but decreased slightly when ultrasonic power was higher than 200 W. These results were consistent with the preliminary experimental results and could determine the accurate value of the parameter.

Optimization of extraction parameters and validation of the model In this study, the model equation for predicting the optimum response values was tested by using the selected optimal conditions. The predicted optimum conditions for polysaccharides extraction and predicted yield were given as follows: extraction temperature of 70.7 °C, extraction time of 66.87 min, the ratio of water to raw material of 12.23 mL/g and ultrasonic power of 232.52 W, respectively. The maximum predicted theoretical yield was 5.25189%. Considering the operability in actual production, the optimal conditions could be modified as follows: extraction temperature of 70.0 °C, extraction time of 66 min, ratio of water to raw material 13 mL /g, ultrasonic power of 230 W. Under this conditions, the mean value of PTGP yield 5.16% ± 1.81% (n=3) was obtained. These results of analysis confirmed that the response model was adequate for the optimization of extraction process, and the model of equation as follows was accurate.

$$Y = 5.19 + 0.32X_1 + 0.08X_2 + 0.13X_3 + 0.13X_4 - 0.021X_{12} - 0.011X_{13} + 0.12X_{14} + 0.051X_{23} + 0.44X_{24} + 0.019X_{34} - 0.32X_1^2 - 0.12X_2^2 - 0.3X_3^2 - 0.17X_4^2$$

FT-IR analysis The FT-IR spectrum of PTGP was shown in Figure 4.
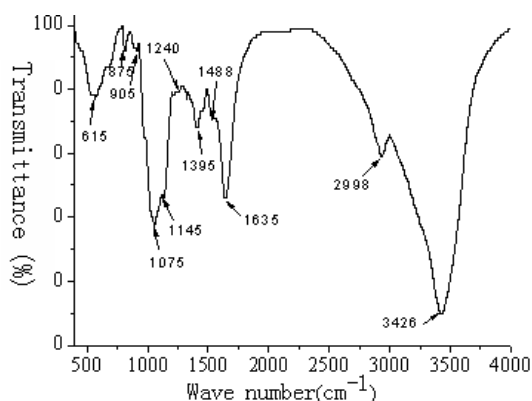
Fig. 4. FT-IR spectrum of PTGP.

A broad band around 3426 cm-1 exhibited O-H stretch vibration [18,19], a weak peak at 2998 cm-1 was assigned to C-H asymmetric stretch vibration [20], a peak at 1635 cm-1 was assigned to the stretching vibrations of the CHO and C=O bonds [18], which was a characteristic absorption band of the bonded water [16,21]. A peak at 1407 cm-1 was regarded as N-H variable angle vibration, which was caused by the -NH3. The peak at 1390 cm-1 was for O-H deformation vibration of CH2O-H. Three stretching peaks at 1240, 1130, and 1060 cm-1 indicated the presence of C-O bonds and pyranose ring in the polysaccharide [22], and the peak broadened due to the C-O stretching vibration. Other stretching peaks 820~950 cm-1 are characteristics absorptions of D-glucose, D-galactose, D-mannose. An obvious absorption peak around 890cm-1 showed that the polysaccharide structure contains β-glucan. These signals all indicated that PTGP had the typical saccharide moiety absorption peaks.

Antioxidant activity of PTGP

Scavenging activity of hydroxyl radical Hydroxyl radicals are highly reactive and undergo chemistry that makes them short-lived. On generation in or exposure of biological systems to these radicals, they can cause damage to cells, including those in humans, where they react with DNA, lipids, and proteins [23]. The result of hydroxyl radical scavenging activities of the polysaccharide was given in Figure 5A, which showed that the difference of scavenging activity between the PTGP with ascorbic acid as a positive control. The scavenging activity increased significantly in a concentration-dependent way at the PTGP concentration range of 0.25-1.5 mg/mL, and achieved maximum scavenging activity of 60.41% at 1.5 mg/mL, which was 30.01% less compared with that of 1.5 mg/mL ascorbic acid (90.42%). Once the value of concentration exceeded 1.5 mg/mL, neither ascorbic acid nor PTGP showed any higher scavenging effects. The results indicated that hydroxyl radicals scavenging activities of PTGP were not obvious at the identical concentration.

Scavenging activity of superoxide radicals The superoxide is a weak oxidant in most organisms, and biologically quite toxic, which could be generated by numerous biological and photo chemical reactions. It could degrade continuously and form other reactive oxygen species (ROS), which contribute to the pathogenesis of many diseases [18]. In this study, scavenging activity of PTGP of superoxide was compared with ascorbic acid, as shown in Figure 5B. The scavenging activity increased gradually along with the concentration. The maximum scavenging ability (89.67%) was obtained at a concentration of 3.5 mg/mL, while ascorbic acid could achieve the maximum scavenging activity of 93.56 % at 1.0 mg/mL. The antioxidant activity of the polysaccharides may be related to monosaccharide component, molecular size, structure and conformation [19, 24].

Scavenging activity of DPPH radicals The methods of scavenging DPPH radical are well acknowledged and widely applied to determinate the free radical scavenging ability of many antioxidants [25, 26, 27]. In this work, DPPH free-radical scavenging effect of PTGP and ascorbic acid were measured respectively as shown in Figure 5C. At the concentration from 0.25 mg/mL to 4.0 mg/mL, the DPPH radical scavenging activity increased with the PTGP concentration until the maximum value of 61.23 % at 3.0 mg/mL. Whereas the maximum scavenging rate of ascorbic acid could reach 84.93 % at 1.0 mg/mL. PTGP scavenging activity of DPPH radicals was not as strong as ascorbic acid.

Reducing power The reducing power, which is regarded as the other one of significant activity indexes, could be assessed by a Fe^{3+}-Fe^{2+} reduction reaction, and is stronger with higher absorbance value in this reaction [18]. The reducing power of PTGP was shown in Figure 5D. The maximum reducing power of ascorbic acid and PTGP were obtained at 0.50 mg/mL (absorbance=1.3226) and 3.0 mg/mL (absorbance=0.5867), respectively.
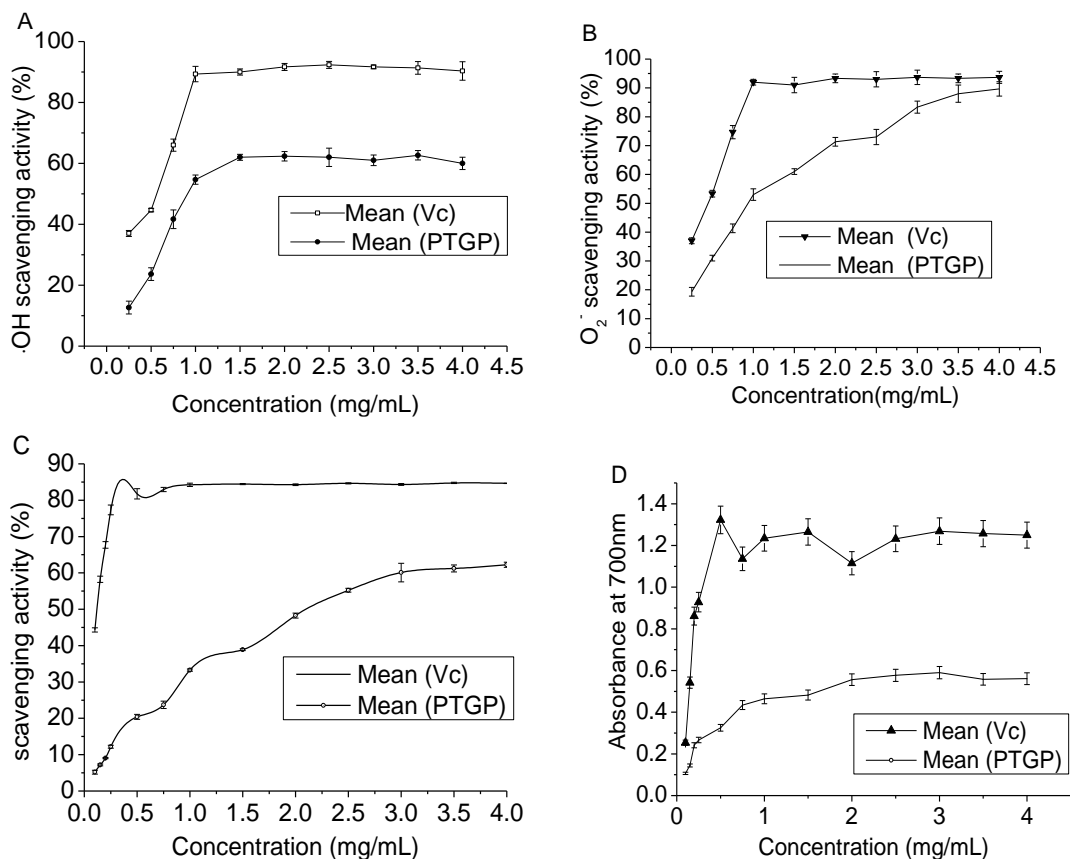
Fig. 5 Antioxidant activities of PTGP. (A) Scavenging ability of hydroxyl radicals. (B) Scavenging ability of superoxide anion. (C) Scavenging activity of DPPH radical. (D) Reducing power. Data were shown as mean (n=3).The vertical bars represented the standard deviation of each data point ($P < 0.05$).

CONCLUSION

Ultrasonic-assisted extraction procedure was used to extract the crude polysaccharides from Piteguo fruit. And Box-Behnken design (BBD) [7] was introduced to optimize the ultrasonic-assisted extraction technology condition. The structures and activities of polysaccharide were analyzed. The results shown the optimized extraction conditions as follows: ratio of water to raw material 13:1 mL/g, extraction time 66 min, extraction temperature 70 °C, and ultrasonic power 230 W, and the extraction ratio of crude PTGP was up to 5.16% ± 1.81%, which is was well matched with the value (5.25%) predicted by the BBD model. PTGP was composed of Glc with β-type pyranoid type sugar ring, displayed certain antioxidant ability and could be used as a potential natural antioxidant.

REFERENCES

1. B. Zisu, N.P. Shsh, *J. Dair. Sci.*, **86**, 3405 (2003).
2. Y.Q. Li, L. Fang, K.C. Zhang, *Carbohyd. Polym.,* **68,** 323 (2007).
3. M.L. Jin, K. Zhao, Q.S. Huang, C.L. Xu, P. Shang, *Carbohyd. Polym.,* **89**, 713 (2012).
4. X.N. Liu, B. Zhou, R.S. Lin, L. Jia, P. Deng, K.M. Fan, G.Y. Wang, L. Wang, J.J. Zhang, *Int. J. Biol. Macromol.,* **47**, 116 (2010).
5. R. Federico, R.M. Potrafka, G.P. Ferran, R.D. Philippis, *Soil Biol. Biochem.*, **46**, 33 (2012).
6. S.K. An, *Food Nutr. China*, **6**, 43 (2005). (in Chinese)
7. S.L. Ferreira, R.E. Bruns, H.S. Ferreira, *Anal. Chem. Acta.*, **597**, 179 (2007).
8. Q. Xia, G. Liu, C. Ge, D.J. Xu, *Anhui. Med. Pharm. J.*, **11**, 1069 (2007). (in Chinese)
9. Q. Zhang, T. M. Zhang, *Shandong Food Sci. Technol.,* **13**, 17 (2004). (in Chinese)
10. M. Jin, Y. Cai, J. Li, H. Zhao, *Prog. Biochem. Biophys.*, **23**, 553 (1996).
11. Z.B. Yuan, R.M. Gao, *Chem. J. Chinese U.*, **18**, 1438 (1997).
12. K. Shimada, K. Fujikawa, K. Yahara, N. Takashi, *J. Agr. Food Chem.*, **40**, 945 (1992).
13. M. Oyaizu, *Japanese J. Nutr.,* **44**, 307 (1986).
14. S. Govender, V. Pillayy, D.J. Chetty, C. M. Dangor, T. Govender, *Int. J. Pharm.*, **306**, 24 (2005).
15. Y. F. Zou, X.F. Chen, W.Y. Yang, S. Liu, V. *Modesta, L.T. Shen, Carbohyd. Polym.*, **84**, 503 (2011).
16. L. Jin, X. Guan, W. Liu, X. Zhang, W. Yan, W.B. Yao, X.D. Gao, *Carbohyd. Polym.*, **90**, 524 (2012).
17. R. V. Murlidhar, R. R. Chirumamil, R. Marchant, P. Nigam, *Biochem. Eng. J.*, **9**, 17 (2001).

18. J. Chen, T. Zhang, B. Jiang, W.M. Mu, M. Miao, *Carbohyd. Polym.*, **87**, 40 (2012).
19. L.C. Wang, K. Zhang, L.Q. Di, R. Liu, H. Wu, *Carbohyd. Polym.*, **86**, 982 (2011).
20. H. Zhang, L. Ye, K. Wang, *Carbohyd. Polym.*, **81**, 953 (2010).
21. Y. Marechal, *J. Mol. Struc.*, **700**, 217 (2004).
22. Y. Yi, M.W. Zhang, S.T. Liao, R.F. Zhang, Y.Y. Deng, Z.C. Wei, X.J. Tang, Y. Zhang, *Carbohyd. Polym.*, **87**, 636 (2012).
23. L. Q. Yang, T. Zhao, H. Wei, M. Zhang, Y. Zou, G. Mao, X. Wu, *Int. J. Biol. Macromol.*, **49**,1124 (2011).
24. J. Wang, J. Zhang, B. Zhao, Y.Q. Wu, C.X. Wang, Y.P. Wang, *Food Chem.*, **120**, 443 (2010).
25. J.F. Yuan, Z.Q. Zhang, Z.C. Fan, J.X. Yang, *Carbohyd. Polym.*, **74**, 822 (2008).
26. H. Li, J. Xua, Y. Liu, S.B. Ai, F. Qin, Z.W. Li, H.R. Zhang, Z.B. Huang, *Carbohyd. Polym.*, **83**, 1821 (2011).
27. I. Sheytanov, Ts. Petranovaa, S. Monova, N. Stoilov, A. Batalov, R. Nestorova, *J. Balk. Tribol. Assoc.,* **19**, 260 (2013).

ИЗСЛЕДВАНЕ НА ЕКСТРАКЦИЯТА И АНТИОКСИДАНТНАТА АКТИВНОСТ ПОЛИЗАХАРИДИ ОТ ПЛОДОВЕ НА *Piteguo*

К. Лин[1], Г.Р. Янг[2], И.Г. Уанг[1*], М.Дж. Янг[1*], С.Ф. Лю[2]

[1] *Департамент за спорт и изследвания, Технологичен университет в Ланжоу, 730050 Ланжоу, Китай*
[2] *Училище за науки за живота и инженерство, Технологичен университет в Ланжоу, 730050 Ланжоу, Китай*

(Резюме)

Изследвана е ултразвуковата екстракция (UAE) на полизахариди от плодовете на *Piteguo* (*Pyrus sinkiangensis*). Четири параметъра (отношението вода/твърда фаза, температура, време на екстракция и мощност на ултразвука) са оптимизирани по плана на Box-Behnken (BBD). Структурата на полизахаридите са предварително анализирани по инфрачервените им спектри. Открита е *in vitro* антиоксидантна активност. Резултатите показват, че екстракционното отношение на суровия плод е до 5.16% ± 1.81% под оптималните условия за екстракция: отношение вода/твърда фаза 13:1 mL/g, време за екстракция 66 мин, температура 70°С и мощност на ултразвука 230 W, което добре се съгласува със стойността (5.25%) предвидена от модела BBD. Спектроскопското изследване показва, че плодовете съдържат съединения Glc с β- пираноиден пръстен. Освен това тестовете показват известна антиоксидантна активност и че плодовете може да се използват като потенциални антиоксиданти.

AUTHOR INDEX

АВТОРСКИ УКАЗАТЕЛ

SUBJECT INDEX

ПРЕДМЕТЕН УКАЗАТЕЛ

BULGARIAN CHEMICAL COMMUNICATIONS

Instructions about Preparation of Manuscripts

General remarks: Manuscripts are submitted in English by e-mail or by mail (in duplicate). The text must be typed double-spaced, on A4 format paper using Times New Roman font size 12, normal character spacing. The manuscript should not exceed 15 pages (about 3500 words), including photographs, tables, drawings, formulae, etc. Authors are requested to use margins of 3 cm on all sides. For mail submission hard copies, made by a clearly legible duplication process, are requested. Manuscripts should be subdivided into labelled sections, e.g. **Introduction, Experimental, Results and Discussion**, *etc*.

The title page comprises headline, author's names and affiliations, abstract and key words.

Attention is drawn to the following:

a) **The title** of the manuscript should reflect concisely the purpose and findings of the work. Abbreviations, symbols, chemical formulas, references and footnotes should be avoided. If indispensable, abbreviations and formulas should be given in parentheses immediately after the respective full form.

b) **The author**'s first and middle name initials, and family name in full should be given, followed by the address (or addresses) of the contributing laboratory (laboratories). **The affiliation** of the author(s) should be listed in detail (no abbreviations!). The author to whom correspondence and/or inquiries should be sent should be indicated by asterisk (*).

The abstract should be self-explanatory and intelligible without any references to the text and containing not more than 250 words. It should be followed by key words (not more than six).

References should be numbered sequentially in the order, in which they are cited in the text. The numbers in the text should be enclosed in brackets [2], [5, 6], [9−12], etc., set on the text line. References, typed with double spacing, are to be listed in numerical order on a separate sheet. All references are to be given in Latin letters. The names of the authors are given without inversion. Titles of journals must be abbreviated according to Chemical Abstracts and given in italics, the volume is typed in bold, the initial page is given and the year in parentheses. Attention is drawn to the following conventions:

a) The names of all authors of a certain publications should be given. The use of "*et al*." in the list of references is not acceptable.

b) Only the initials of the first and middle names should be given.

In the manuscripts, the reference to author(s) of cited works should be made without giving initials, e.g. "Bush and Smith [7] pioneered...". If the reference carries the names of three or more authors it should be quoted as "Bush *et al*. [7]", if Bush is the first author, or as "Bush and co-workers [7]", if Bush is the senior author.

Footnotes should be reduced to a minimum. Each footnote should be typed double-spaced at the bottom of the page, on which its subject is first mentioned.

Tables are numbered with Arabic numerals on the left-hand top. Each table should be referred to in the text. Column headings should be as short as possible but they must define units unambiguously. The units are to be separated from the preceding symbols by a comma or brackets.

Note: The following format should be used when figures, equations, *etc*. are referred to the text (followed by the respective numbers): Fig., Eqns., Table, Scheme.

Schemes and figures. Each manuscript (hard copy) should contain or be accompanied by the respective illustrative material as well as by the respective figure captions in a separate file (sheet). As far as presentation of units is concerned, SI units are to be used. However, some non-SI units are also acceptable, such as °C, ml, l, etc.

The author(s) name(s), the title of the manuscript, the number of drawings, photographs, diagrams, etc., should be written in black pencil on the back of the illustrative material (hard copies) in accordance with the list enclosed. Avoid using more than 6 (12 for reviews, respectively) figures in the manuscript. Since most of the illustrative materials are to be presented as 8-cm wide pictures, attention should be paid that all axis titles, numerals, legend(s) and texts are legible.

The authors are asked to submit **the final text** (after the manuscript has been accepted for publication) in electronic form either by e-mail or mail on a 3.5'' diskette (CD) using a PC Word-processor. The main text, list of references, tables and figure captions should be saved in separate files (as *.rtf or *.doc) with clearly identifiable file names. It is essential that the name and version of

the word-processing program and the format of the text files is clearly indicated. It is recommended that the pictures are presented in *.tif, *.jpg, *.cdr or *.bmp format, the equations are written using "Equation Editor" and chemical reaction schemes are written using ISIS Draw or ChemDraw programme.

The authors are required to submit the final text with a list of three individuals and their e-mail addresses that can be considered by the Editors as potential reviewers. Please, note that the reviewers should be outside the authors' own institution or organization. The Editorial Board of the journal is not obliged to accept these proposals.

EXAMPLES FOR PRESENTATION OF REFERENCES

REFERENCES

1. D. S. Newsome, *Catal. Rev.–Sci. Eng*., **21**, 275 (1980).
2. C.-H. Lin, C.-Y. Hsu, *J. Chem. Soc. Chem. Commun*., 1479 (1992).
3. R. G. Parr, W. Yang, Density Functional Theory of Atoms and Molecules, Oxford Univ. Press, New York, 1989.
4. V. Ponec, G. C. Bond, Catalysis by Metals and Alloys (Stud. Surf. Sci. Catal., vol. 95), Elsevier, Amsterdam, 1995.
5. G. Kadinov, S. Todorova, A. Palazov, in: New Frontiers in Catalysis (Proc. 10th Int. Congr. Catal., Budapest, 1992), L. Guczi, F. Solymosi, P. Tetenyi (eds.), Akademiai Kiado, Budapest, 1993, Part C, p. 2817.
6. G. L. C. Maire, F. Garin, in: Catalysis. Science and Technology, J. R. Anderson, M. Boudart (eds), vol. 6, Springer-Verlag, Berlin, 1984, p. 161.
7. D. Pocknell, *GB Patent* 2 207 355 (1949).
8. G. Angelov, PhD Thesis, UCTM, Sofia, 2001.
9. JCPDS International Center for Diffraction Data, Power Diffraction File, Swarthmore, PA, 1991.
10. CA **127**, 184 762q (1998).
11. P. Hou, H. Wise, *J. Catal.*, in press.
12. M. Sinev, private communication.
13. http://www.chemweb.com/alchem/articles/1051611477211.html.

CONTENTS

СЪДЪРЖАНИЕ

835